The Search for Superluminous Supernovae with the Dark Energy Camera

by

Andreas Papadopoulos

THE THESIS IS SUBMITTED IN PARTIAL FULFILMENT OF THE REQUIREMENTS FOR

THE AWARD OF THE DEGREE OF

DOCTOR OF PHILOSOPHY

OF THE

UNIVERSITY OF PORTSMOUTH

April, 2016

Copyright

To my wife Pantelitsa and our son Kyriakos.

Abstract

We present the search for Superluminous Supernovae (SLSNe) within the Dark Energy Survey (DES), and using the Dark Energy Camera (DECam) in general. We construct empirical selection criteria for the selection of SLSNe from the first year of DES data followed by visual inspection of candidates. We present DES13S2cmm, the first spectroscopically-confirmed SLSN from DES, as a hydrogen-poor SLSN at a redshift of $z = 0.663 \pm 0.001$. We updated our SLSNe search methodology based on our experiences and knowledge gained from this first season of DES data. In combination with the increase of the spectroscopic follow-up resources in the second year of DES operations, we have found 22 SLSNe candidates, 7 of which where spectroscopically confirmed as SLSNe events in the redshift range of $0.47 \leqslant z \leqslant 1.5$. We present in detail the seven confirmed SLSNe and we draw attention to three SNe as the highlights of our SLSNe quest in DES Y2. Firstly, DES14S2qri was discovered at a redshift of $z = 1.5$, as the most luminous SN ($M_z = -22.90$) up to the writing of this thesis. DES14C1rhg was discovered at a redshift of $z = 0.47$ as the least luminous SLSN-I ($M_r = -19.80$), a finding that supports the hypothesis of a continuum that fills the gap between the peak brightness of SNe Ic and SLSNe-I. Lastly, DES14X3taz was detected at a redshift of $z = 0.6$ and is the second ever recorded SLSN to possess a well constrained pre-peak bump, which could be caused by a pre-explosion outburst of the SN. Using the DES Y2 sample of SLSNe we provide a basic calculation of the volumetric SLSNe rate, reporting a value of ~ 206 events Gpc^{-3} yr^{-1} h$_{71}^3$. This value is compatible with other estimates in the literature, considering the simplicity of our method. We fit the bolometric light curves of the entire SLSNe sample discovered by DES with two competing models for SLSNe-I - the radioactive decay of ^{56}Ni, and a magnetar - and find that the magnetar is formally a better fit overall. Using the Magnetar model, we investigate possible correlations between the model parameters. We discovered moderate correlations between the explosion phase (t_{exp}) and the rise-time (τ_m), and between the rise-time (τ_m) and the spin-down time (P). Moreover, we compare the bolometric light-curves of the entire SLSNe sample, without clear evidence of common behaviour, that would point towards a standardization. We find that the short DES observing seasons (~ 5 months per calendar

year) are limiting the discerning between the two models which, at late times (beyond 100 rest frame days), behave significantly differently. We present the Survey Using DECam for Superluminous Supernovae (SUDSS) as a complementary effort to DES SN survey, which operates since April 2014 and aims at obtaining a large and homogeneous sample of SLSNe out to redshift $z \sim 3$, by maximizing its observing seasons in collaboration with DES SN survey.

Preface

The work of this thesis was carried out at the Institute of Cosmology and Gravitation, University of Portsmouth, United Kingdom.

Whilst registered as a candidate for the above degree, I have not been registered for any other research award. The results and conclusions embodied in this thesis are the work of the named candidate and have not been submitted for any other academic award.

Acknowledgements

First and foremost I would like to thank my supervising team composed by Prof. Bob Nichol, Dr. Chris D'Andrea and Dr. Mark Sullivan. I would like to thank my first supervisor Prof. Bob Nichol, for providing me the chance to work within the Dark Energy Survey collaboration and for suggesting the projects undertaken in this thesis. I am very thankful to Dr. Chris D'Andrea who has worked closely with me during the last three years and introduced me to the various concepts and tools of the Dark Energy Survey. I would also like to thank Dr. Mark Sullivan (University of Southampton) who, despite being based in another institution, has helped shape the research and results that are presented herein.

Lastly, I would like to thank my family for their support and love.

Table of Contents

List of Tables

List of Figures

Chapter 1

Introduction

This chapter serves as a brief overview of the cosmological and astrophysical background necessary for the research presented in later chapters of this thesis.

In this chapter, I briefly introduce the current cosmological model starting from the Hubble law and the Friedmann equations, followed by a summary of the contents of the Universe and the description of useful quantities that astronomers and cosmologists use, such as distances and magnitudes of astronomical objects. Then, I present a broad class of astronomical objects called Supernovae (SNe), exploring their nature, types and classification, but most importantly, how these are used in Cosmology via astronomical sky surveys.

Moreover, I present in detail the Dark Energy Survey (DES), a part of which will discover and use a variety of SNe to study Cosmology. I have been actively participating in this project since June 2012, searching for Superluminous SNe (SLSNe).

The chapter then focuses on SLSNe and describes how they were first discovered and classified, while exploring the SLSNe properties and nature, as well as examining how they could be used in Cosmology in the near future.

1.1   Standard Cosmological Model

Cosmology is the study of the Universe using a combination of observations of astrophysical phenomena like stars, supernovae and galaxies and an underlying theoretical framework based on Einstein's theory of General Relativity (Einstein, 1916).

This section will introduce the basic information on the standard Cosmological model, adopted for this thesis.
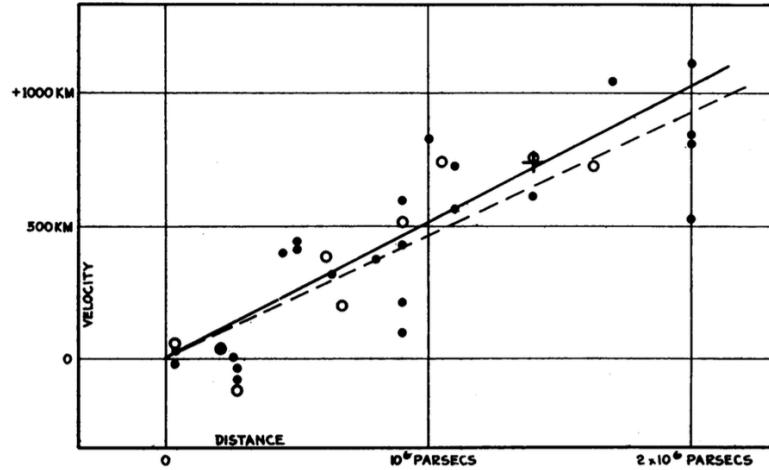
Figure 1.1: The original Hubble diagram, shows the 'roughly linear' relationship between the radial velocities and distances of 'nearby' extragalactic nebulae.

1.1.1 Hubble's Law and Friedmann's Equations

Hubble (1929) introduced the relationship between the radial velocities and distances of few extragalactic 'nebulae'; as illustrated by the original Hubble diagram in Fig. 1.1, and the following equation, named as the 'Hubble law':

$$\upsilon = H_0 \cdot d \tag{1.1}$$

where υ is the apparent velocity of a galaxy, d is the physical distance to that galaxy and $H_0(t = 0)$ is the Hubble parameter today.

The Hubble Space Telescope's (HST) Key Project (Freedman et al., 2001) measured the Hubble constant to be:

$$H_0 = 72 \pm 8 \text{km}^{-1}\text{Mpc}^{-1} \tag{1.2}$$

by using Cepheid calibration on a number of independent, secondary distance determination methods, such as SNe type Ia , the Tully-Fisher relation, the fundamental plane for elliptical galaxies, surface brightness fluctuations and SNe type II.

Komatsu et al. (2009) combined data of the Cosmic Microwave Background (CMB) radiation from WMAP[1] (Wilkinson Microwave Anisotropy Probe) with the Baryonic Acoustic Oscillations (BAO) and type Ia Supernovae, obtaining a value for the Hubble constant equal to:

$$H_0 = 70.1 \pm 1.3 \text{km}^{-1}\text{Mpc}^{-1}. \tag{1.3}$$

---

[1]http://map.gsfc.nasa.gov

Most recently, Planck Collaboration et al. (2014) reported a new estimation of the Hubble constant to be equal to:

$$H_0 = 67.3 \pm 1.2 \text{km}^{-1}\text{Mpc}^{-1}. \tag{1.4}$$

Hubble's law states that the further away an object is, the more rapidly it is receding, thus providing the first confirmation of the prediction of Friedmann (1924) that, an expanding Universe is a valid solution to Einstein's theory of General Relativity (Einstein, 1916).

In general the Hubble parameter could vary with time such as:

$$\dot{r}(t) = H(t) \cdot r(t) \tag{1.5}$$

where $r(t)$ is the physical distance in the radial direction and $\dot{r}(t)$ is its derivative with respect to time.

The physical distance can be defined as:

$$r(t) = \chi \cdot \alpha(t) \tag{1.6}$$

where χ is the comoving distance and $\alpha(t)$ is known as the scale factor.

Then, the Hubble parameter can describe the expansion rate of the Universe, when is written as:

$$H(t) \equiv \frac{\dot{\alpha}(t)}{\alpha(t)}. \tag{1.7}$$

Based on the framework of Einstein's theory of General Relativity (Einstein, 1916); and taking into account the Cosmological principle which states that the Universe, on sufficiently large scales is homogeneous (has the same density) and isotropic (is the same in all directions); and assuming that the content of the Universe can be described by a perfect fluid one can describe the evolution of the Universe using the Friedmann equations (Friedmann, 1924):

$$H^2(t) = \left(\frac{\dot{\alpha}(t)}{\alpha(t)}\right)^2 = \frac{8\pi G\rho}{3} - \frac{k}{a^2} \tag{1.8}$$

$$\frac{\ddot{\alpha}(t)}{\alpha(t)} = -\frac{4\pi G}{3}(\rho + 3p) \tag{1.9}$$

where $H(t)$ and $\alpha(t)$ were defined above as the rate and the scale factor for the relative expansion of the Universe respectively, $\dot{\alpha}(t)$ is the the scale factor derivative with respect to proper time, ρ and p are the the density and pressure of the perfect fluid respectively, G is Newton's gravitational constant, and k is the intrinsic curvature of the Universe.

The contents of the Universe, matter and energy, are what governs k, which can take three possible classes of values, resulting to three possible geometries for the Universe:

- $k = +1$, for a 'closed' Universe with elliptical geometry, described by positive spatial curvature

- $k = 0$, for a 'flat' Universe with Euclidean geometry, described by zero spatial curvature

- $k = -1$, for an 'open' Universe with hyperbolic geometry, described by negative spatial curvature

Using equation 1.8 and considering the first law of thermodynamics for reversible adiabatic expansion of the Universe, one can derive the fluid equation (Liddle, 2003):

$$\dot{\rho} + 3H(\rho + p) = 0 \tag{1.10}$$

which describes how the density of the components of the Universe evolve, as the Universe expands. This perfect fluid, as the only content of the Universe so far in this analysis, can be described by the following simple equation of state:

$$p = w \times \rho \tag{1.11}$$

where w can be treated as a constant; hence the density of the perfect fluid will behave as:

$$\rho(t) \propto \alpha^{-3(1+w)}. \tag{1.12}$$

Critical density (ρ_{crit}) is the density required for a 'flat' Universe (Euclidean geometry, $k = 0$) and can be derived from equation 1.8 as:

$$\rho_{crit} = \frac{3H^2}{8\pi G} \tag{1.13}$$

Density Parameter (Ω) using equations 1.8 and 1.13 can be defined as:

$$\Omega \equiv \frac{\rho}{\rho_{crit}} = 1 + \frac{k}{a^2 H^2} \tag{1.14}$$

and can be used to compare directly the total density (ρ) of the Universe to its critical density (ρ_{crit}), which can result in a closed ($\Omega < 1$), flat ($\Omega = 1$) or open ($\Omega > 1$) Universe.

1.1.2 Contents of the Universe

In Sec. 1.1.1 the Universe was treated as if it contains one perfect fluid. Instead observations (Komatsu et al., 2009; Hinshaw et al., 2013; Planck Collaboration et al., 2014) suggest that we live in a flat Universe ($k = 0$), the contents of which are matter-m (baryonic and dark matter), radiation-γ and dark energy-Λ and can be described using their individual densities (ρ_i) as:

$$\rho = \sum_i \rho_i \tag{1.15}$$

or in terms of their density parameters:

$$\Omega = \Omega_m + \Omega_\gamma + \Omega_\Lambda = \frac{\rho_m}{\rho_{crit}} + \frac{\rho_\gamma}{\rho_{crit}} + \frac{\rho_\Lambda}{\rho_{crit}}. \tag{1.16}$$

Matter

The matter content of the Universe is composed by baryonic and dark matter, both to be treated as pressureless and non-relativistic. Baryonic matter (b) refers to all the atoms, dust, planets, stars, galaxies, gas that exist in the Universe and constitutes around $\sim 4\%$ of the Universe. On the other hand, dark matter (DM) the dominant matter component ($\sim 22\%$ of the Universe), interacts with gravitational forces, but not with electromagnetic ones and is detected using gravitational lensing and galaxy rotation curves.

The latest measurement (Anderson et al., 2014; Betoule et al., 2014) of the matter density parameter is:

$$\Omega_m = \Omega_b + \Omega_{DM} = 0.305 \pm 0.010. \tag{1.17}$$

Radiation

The radiation content of the Universe refers to particles that move at the speed of light (relativistic), like CMB photons and neutrinos, the kinetic energy of which generates radiation pressure. The Universe experienced its radiation domination phase during the

first moments after the Big Bang and today its density parameter value is (Planck Collaboration et al., 2014):

$$\Omega_\gamma < 0.01 \tag{1.18}$$

therefore, radiation's contribution is ignored in the late universe.

Dark Energy

Dark energy was introduced as a possible explanation of the accelerating expansion of the Universe, the evidence of which is explored later in Sec. 1.3. A variety of dark energy models have been proposed, such as the Cosmological constant (Carroll, 2001, and references therein), the quintessence scalar field model (Liddle, 2003, and references therein), the Chevallier-Polarski-Linder model (CPL; Chevallier and Polarski, 2001; Linder, 2003) etc.

Using Eq. 1.12 to determine the value of $\omega(z)$, one can determine the correct model for dark energy. For example, the case of $\omega(z) = -1$ corresponds to a Cosmological constant (Λ) model, in which the density of the dark energy is assumed to be constant through time and space, and its density parameter value is measured (Anderson et al., 2014; Betoule et al., 2014) to be:

$$\Omega_\Lambda = 0.693 \pm 0.010. \tag{1.19}$$

Throughout this thesis, we assume a flat ($k = 0$) Λ-dominated cosmology with $\Omega_\Lambda = 0.693$, $\Omega_m = 0.305$ and $H_0 = 67.3 \, km \, s^{-1} \, Mpc^{-1}$, consistent with recent cosmological measurements (eg. Anderson et al., 2014; Betoule et al., 2014).

1.1.3 Distances and Magnitudes in Cosmology

Observational measurements are needed to constrain the parameters of any cosmological model, as described in Sec. 1.1.1. Distance estimates to astrophysical objects are necessary for such measurements.

Redshift is a frequent measure of distances to astronomical objects and is caused by the expansion of the Universe, which causes light-waves to shift into bluer or redder wavelengths, depending on whether the astronomical objects are moving towards or away from the observer, respectively. It is defined as:

$$z = \frac{\lambda_{obs} - \lambda_{emit}}{\lambda_{emit}} = \frac{\lambda_{obs}}{\lambda_{emit}} - 1 \tag{1.20}$$

where λ_{obs} is the observed by the observer wavelength and λ_{em} is the emitted by the astronomical source wavelength.

The luminosity distance can be defined as:

$$d_L^2 = \frac{L}{4\pi F} \tag{1.21}$$

where L is the luminosity (true brightness) and F is the flux (observed brightness).

The angular diameter distance is defined as:

$$d_A = \frac{l}{\theta} \tag{1.22}$$

where l is the object's dimension and θ is the object's apparent angular size.

The current proper distance can be determined as:

$$d_{PM} = \alpha_0 \times \int_0^{r_0} \frac{dr}{\sqrt{1 - k^2}}. \tag{1.23}$$

Finally, the above distance measurements are connected by the following relationship:

$$d_L = d_{PM} \times (1 + z) = d_{PM} \times (1 + z)^2. \tag{1.24}$$

For a flat ($k = 0$) Universe with a cosmological constant-Λ, a constant equation of state ($\omega = $ constant) and negligible contribution from radiation, the luminosity distance can be written as (Peebles, 1993):

$$d_L = (1 + z) \times \frac{c}{H_0} \int_0^{z'} \frac{dz}{\sqrt{(1 + z)^3 \Omega_m + \Omega_\Lambda}}. \tag{1.25}$$

The apparent (observed) magnitude-m of an astronomical object is given by:

$$m_i = -2.5 \log_{10} \left(\frac{f_i}{f_i^0} \right) \tag{1.26}$$

where f_i is the object's observed flux in the passband-i and f_i^0 is the measured flux of a reference object (i.e. Vega star) in the same passband-i. In modern astronomy, several magnitude systems are used, which have different objects as references; the AB magnitude system is the most commonly used today. In the AB magnitude system, equation 1.26 becomes:

$$m_i = -2.5 \log_{10} f_i - 48.60 \tag{1.27}$$

where the flux-f_i is measured in $\mathrm{erg\,s^{-1}\,cm^{-2}\,Hz^{-1}}$. The constant 48.60 was set as such, so a source with flux density of $f_i = 3631\mathrm{Jy}$ to have zero value for magnitude-$m_i = 0$.

The absolute (true) magnitude-M of an astronomical object can be defined as the apparent magnitude of an astronomical object if it was placed 10pc away from the detector, and is given by the following relation:

$$M = m - 5\log_{10}\left(\frac{d_L}{10pc}\right).\qquad(1.28)$$

The distance modulus-μ can be defined from equation 1.28 as the relation between the apparent and absolute magnitude of an object:

$$\mu(z) = m(z) - M = 5\log_{10}\left(\frac{d_L}{10pc}\right)\qquad(1.29)$$

where d_L is a function of z, Ω_m, Ω_Λ and H_0, equation 1.25.

For objects that we know their intrinsic luminosities (hence their absolute magnitudes-M), we can constrain those cosmological parameters by measuring their apparent magnitudes (m) and redshifts (z), and estimating the distance modulus (μ). Such objects are called 'standard candles'.

Supernovae are the kind of astronomical objects that can be used as standard candles to constrain cosmological models, and in the following sections I will describe how and why SNe are used today for this purpose and what new tools the future may bring.

1.2   Supernovae

The term 'Supernova' (SN) was first used by Baade and Zwicky (1934b,a) to describe newly observed stars (novae) that had extreme brightness, comparable with their host nebula. Supernovae (SNe) are associated with the final stages of stellar evolution, when a star has burned all of its fuel and under the right conditions, explodes. The first recorded supernova is thought to be SN 185 and was recorded by Chinese astronomers in 185 AD (Zhao et al., 2006). A handful of SNe have been observed at such early stages in history, like SN 1006 that was recorded by Chinese and Egyptian astronomers as the brightest event ever recorded; and SN 1572 (Tycho's SN) a type Ia SN in the constellation of Cassiopeia (Krause et al., 2008).

1.2.1   Classification

Minkowski (1941) made the first spectroscopic classification of SNe, reporting nine 'type I' and five 'type II' objects, using the absence or presence of hydrogen (Hα) lines in their
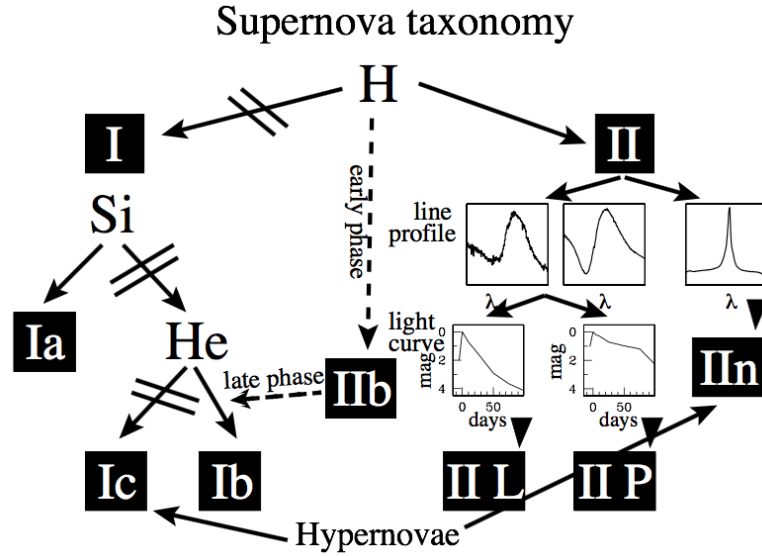
Figure 1.2: SNe classification relies on the identification of spectral features, the analysis of spectral line profiles and the spectral and photometric evolution of each event. Figure is taken from Cappellaro and Turatto (2001).

spectra respectively. Fig. 1.2 shows a diagram of the historically common SN types, as presented by Cappellaro and Turatto (2001), whereas Fig. 1.3 shows different spectral features used for SNe classification.

Type I class of SNe was later divided into three sub-classes: ***type Ia*** show a deep absorption feature produced by silicon (SiII, $\lambda = 6150\mathring{A}$), ***type Ib*** show strong absorption feature of helium (HeI, $\lambda = 5876\mathring{A}$) and ***type Ic*** lack both SiII and HeI features that are seen in the other two sub-classes (Cappellaro and Turatto, 2001).

Barbon et al. (1979) first attempted to divide type II SNe into sub-classes based on their photometric differences. There are four sub-classes of type II events: ***type IIP*** show an after peak plateau of constant luminosity for long periods, ***type IIL*** show a linear decline of their luminosity with time, ***type IIn*** show narrow emission lines on top of their broad spectra features and ***type IIb*** show weak Hα line in their initial spectra, which afterwards fades away and resembles the spectra of a SNe type Ib.

1.2.2 SNe Nature

Type Ia supernovae (SNe type Ia) are believed to be the result of the explosion of a binary system, in which the first star is a white dwarf (WD) that accretes matter from the second star, up until its mass reaches the Chandrasekhar limit ($M_{CH} \sim 1.39 M_\odot$) causing a thermonuclear explosion (Chandrasekhar, 1931; Woosley and Weaver, 1986). The WD material, composed of carbon and oxygen, undergoes nuclear fusion within seconds and an expanding shock wave is formed, travelling with high velocity towards the surface of
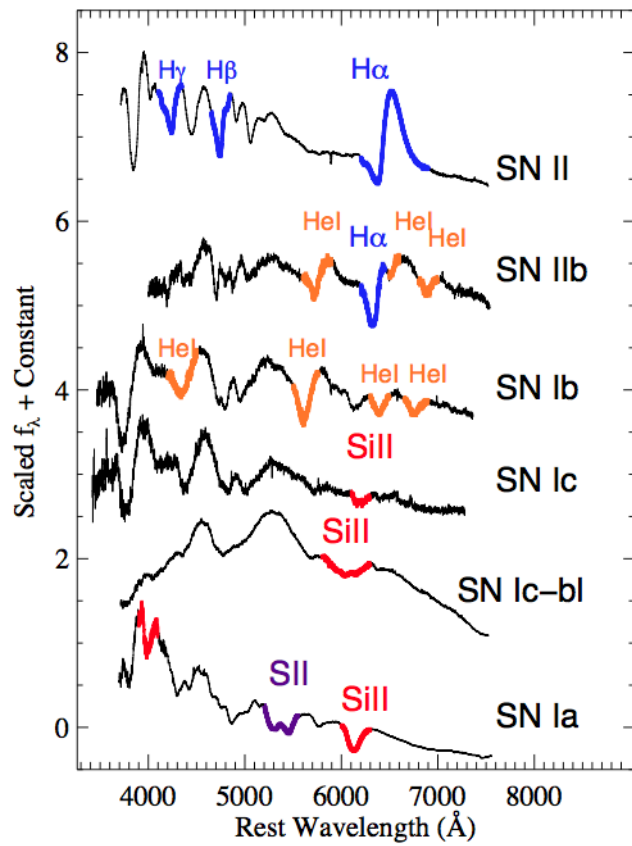
Figure 1.3: SNe classification using different spectral features such as hydrogen in blue, helium in orange, silicon in red and sulfur in purple. Figure is taken from Modjaz et al. (2014).

the star, which will be totally destroyed. The luminosity of the SN would increase to a maximum absolute magnitude of $M \sim -19.3$ in a time-scale of tens of days, and then it would start its decline phase, powered by the radioactive decay of ^{56}Ni$\rightarrow^{56}$Co$\rightarrow^{56}$Fe (Colgate and McKee, 1969).

All the other types of SNe mentioned in 1.2.1 are the results of the collapse of old and massive stars' cores, in which nuclear fusion is no longer able to counterbalance its own gravity and the core collapses, causing an explosion of the whole star; hence a SN to be created. Different initial star masses and metallicities cause different core collapse (CC) mechanisms, resulting in the creation of different types of SNe, and leaving behind different types of remnants (Heger et al., 2003). The Hα features that are seen in their spectra, are created by the outer layers of the star that have been ejected prior to the core collapse, forming a hydrogen envelope (Woosley and Weaver, 1986). Dense circumstellar medium (CSM), created by strong mass loss before the explosion, is ejected during the explosion and converts the kinetic energy of the explosion into radiation, creating narrow emission lines seen in the spectra of SNe type IIn (Cappellaro and Turatto, 2001).

1.3 SNe type Ia & Cosmology

Kowal (1968) was the first person to use 22 SNe type I as luminosity distance estimators for cosmology, as they showed similar peak luminosities with a scatter of ~ 0.6 mags. The concept was to use a uniform ('standard') class of astronomical objects of known luminosity ('candles') at different distances, to probe the expansion rate of the Universe. SNe type Ia properties would prove to be excellent candidates for standard candles.

1.3.1 Standard Candles & Accelerating Universe

The road to the use of SNe type Ia as standard candles opened when Phillips (1993) discovered a relationship between the decline slope of the light-curve and the peak absolute magnitude. Fig. 1.4 shows the original plot from Phillips (1993), which demonstrated the existence of such linear relation between the absolute magnitude (M_{max}) and the decline rate 15 days after peak (Δm_{15}). This linear relation leads to the first correction that makes SNe type Ia standardizable, known as the 'stretch correction'. Also, the different slopes in the three panels of Fig. 1.4 imply that the intrinsic colours of the SNe at peak are also a function of the decline rate (Δm_{15}), which leads to the 'colour correction'. In fact, the 'colour correction' accounts for both the intrinsic colours of the SNe and the effect of dust.

Both corrections, stretch and colour, were studied by Riess et al. (1996) and shown in Fig. 1.5. After correcting the absolute magnitude of SNe type Ia for both stretch and
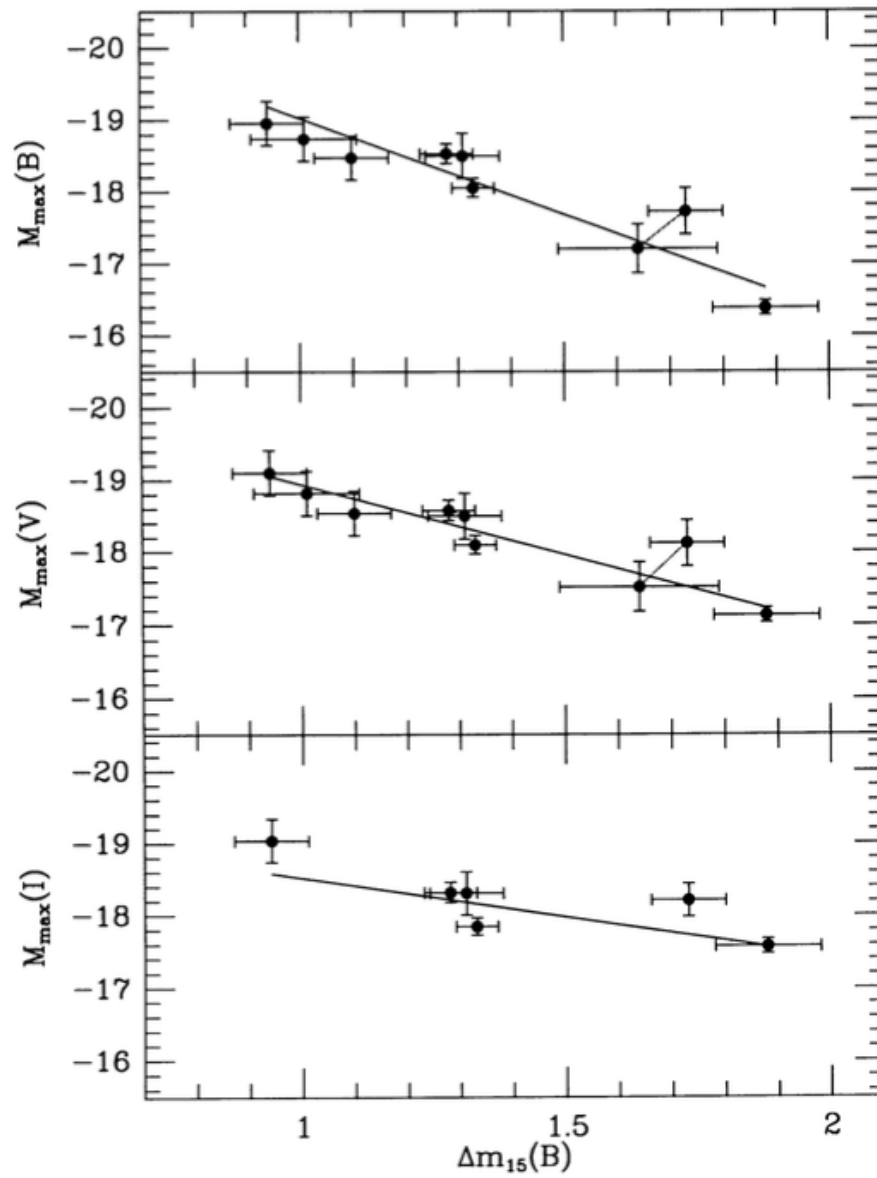
Figure 1.4: Peak absolute magnitudes-M_{max} (in B, V, and I bands) as a function of the decline rate 15 days after peak-$\Delta m_{15}(B)$ (in the observed B-band) and their linear relation. Figure is taken from Phillips (1993).
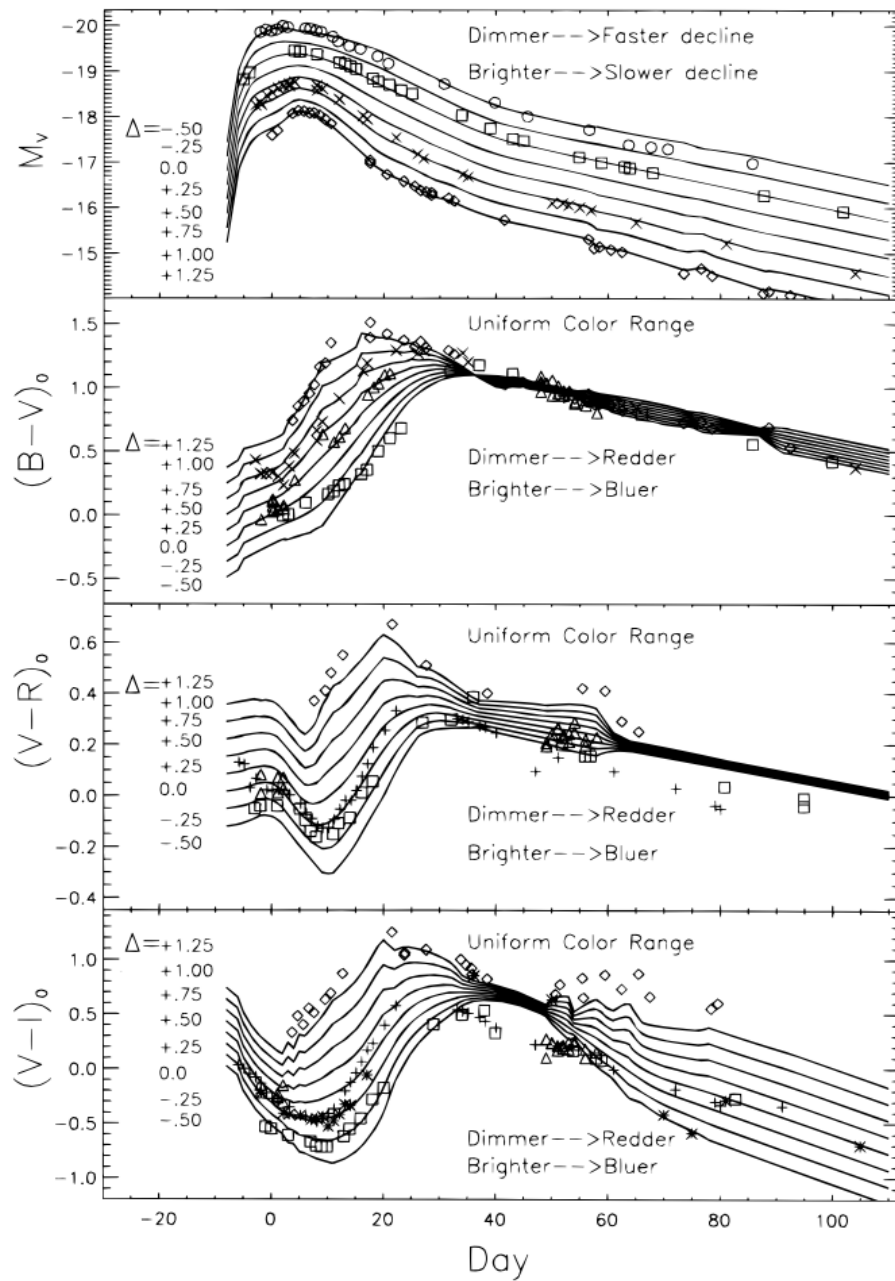
Figure 1.5: Figure is taken from Riess et al. (1996), showing that intrinsically dim type Ia SN are redder and decline faster, whereas bright type Ia SN are bluer and decline slower.
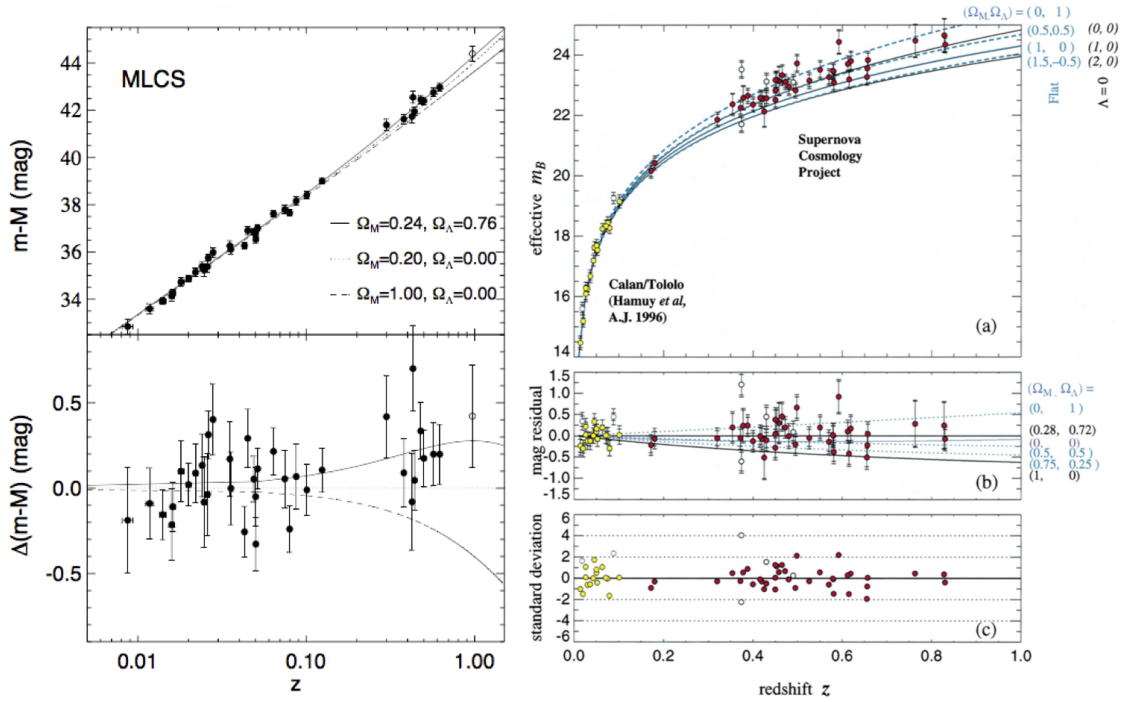
Figure 1.6: Hubble diagrams of SNe type Ia as presented by High-z (*left*; Riess et al., 1998) and SCP (*right*; Perlmutter et al., 1999). Both plots clearly show the inconsistency of SNe type Ia measurements with a Universe that has zero cosmological constant $\Omega_\Lambda = 0$.

colour, the dispersion in the measured distance modulus-μ can be reduced to ~ 0.14 mags (Riess et al., 1996).

As Clocchiatti (2011) emphasized in his review, the tools for standardizing SNe type Ia came at a perfect timing with the development of large mosaic cameras equipped with Charge-Coupled Devices (CCDs) and mounted on large telescopes, ideal for surveying large areas of the night sky.

In the mid-90's two groups of astronomers, the Supernova Cosmology Project (SCP) and the High-z supernova team (High-z), began independently the search and use of SNe type Ia as standard candles. The two teams after collecting data and independently merging and studying each others SNe type Ia samples, published two papers; Riess et al. (1998) for High-z and Perlmutter et al. (1999) for SCP, announcing the discovery of the accelerating expansion of the Universe as the best fit, to explain why their high-z SNe type Ia appeared dimmer than expected. Fig. 1.6 shows the two Hubble diagrams as presented in the two papers, whereas Fig. 1.7 shows the $\Omega_m - \Omega_\Lambda$ plane, which sets limits on the amount of matter (baryonic and DM) and dark energy that the Universe should consist of, as described in Sec. 1.1.2.
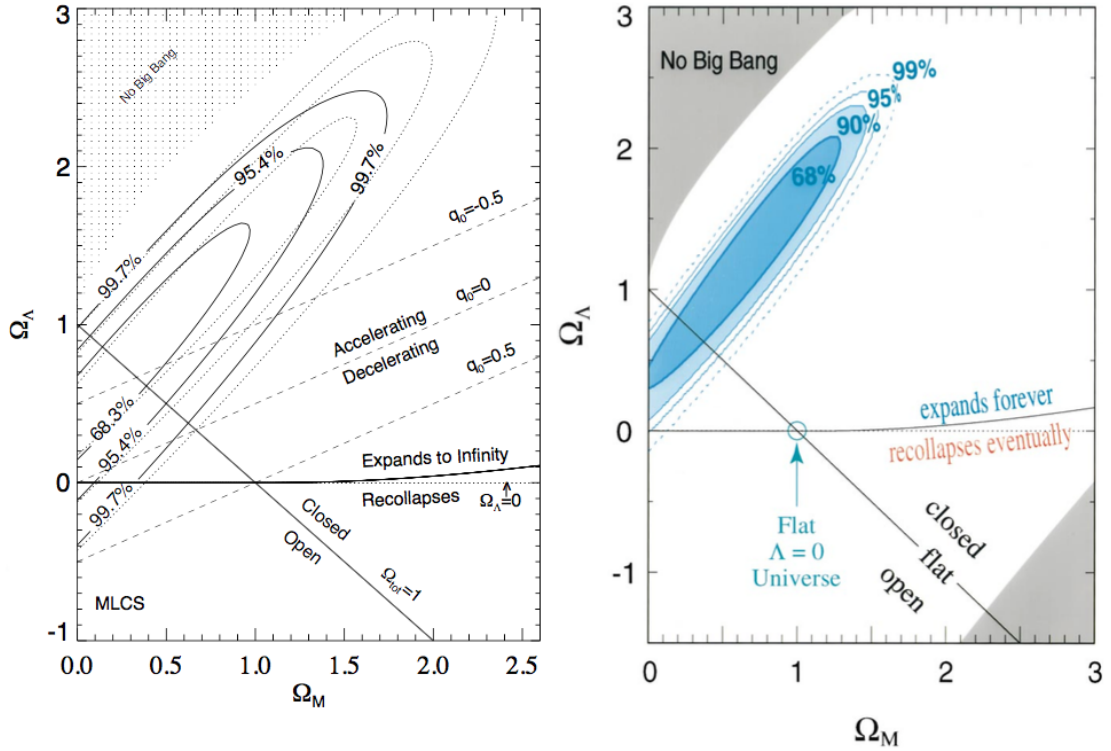
Figure 1.7: The $\Omega_m - \Omega_\Lambda$ plane, as presented by High-z (*left*; Riess et al., 1998) and SCP (*right*; Perlmutter et al., 1999).

On behalf of the SCP and High-z groups, Saul Perlmutter, Adam Riess and Brian Schmidt were awarded the 2011 Nobel prize in Physics for their discovery of the accelerating expansion of the Universe, which is a major breakthrough in modern cosmology.

1.3.2 Second Generation SNe Surveys

The discovery of the accelerated expansion of the Universe stimulated further large surveys of SNe. Such SN surveys reached greater accuracy on the measurement of Ω_Λ in their effort to understand the nature of dark energy by probing the expansion history of the Universe. Some of the biggest SN surveys up to date are:

ESSENCE (Equation of State: SuperNova trace Cosmic Expansion; Wood-Vasey et al., 2007; Miknaitis et al., 2007) used the Blanco 4m telescope at Cerro Tololo Inter-American Observatory (CTIO) and the MOSAIC II camera, between 2002 and 2008, to construct a SNe type Ia survey in the redshift range of $0.15 \leq z \leq 0.75$. ESSENCE used R and I band photometry to discover 102 SNe type Ia and a variety of large telescopes to spectroscopically confirm their spectral type, such as the Keck, VLT, Gemini and Magellan telescopes.
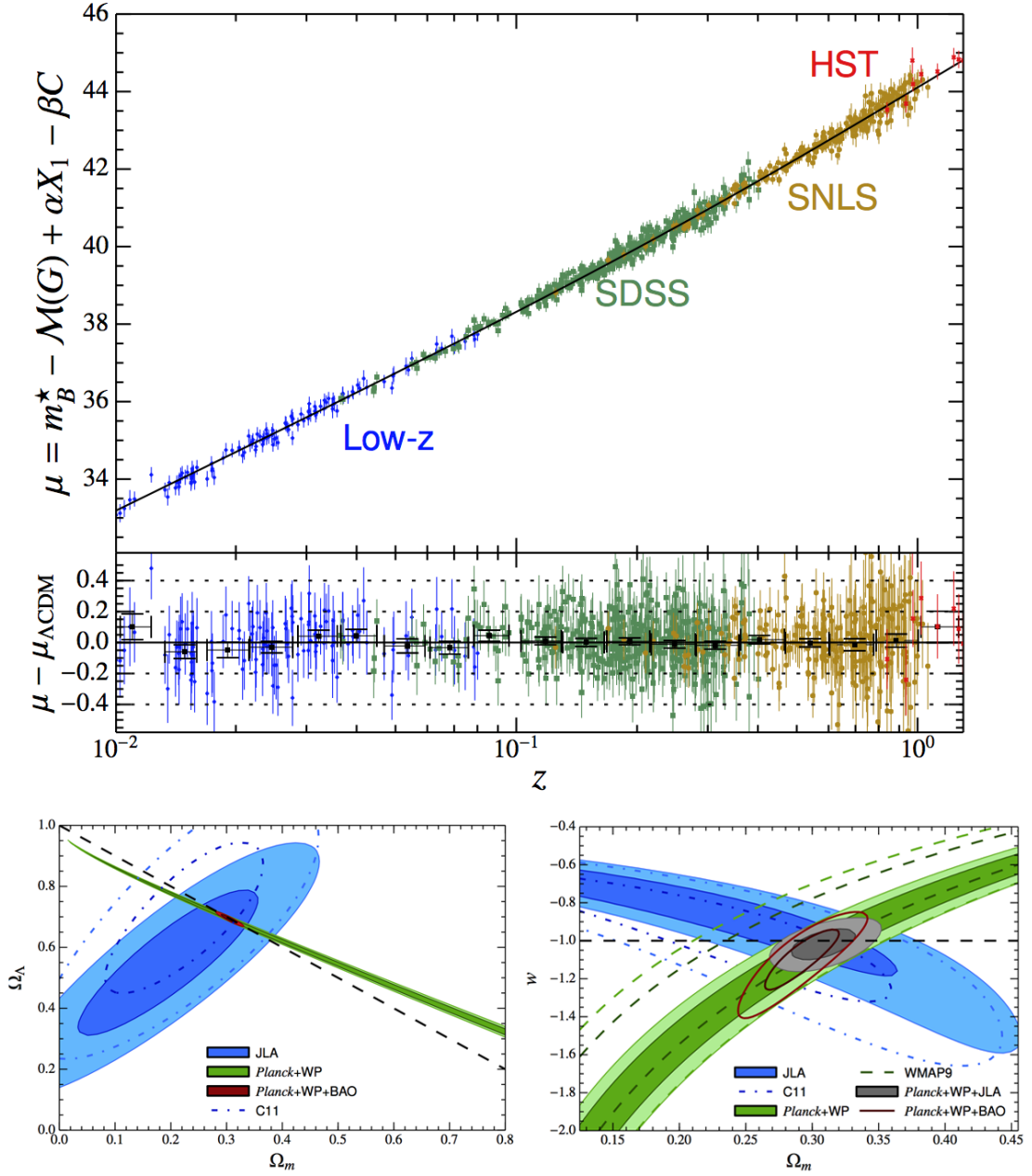
Figure 1.8: Cosmological constrains from the SDSS and SNLS joint analysis of SNe type Ia by Betoule et al. (2014). *Top panel:* the Hubble diagram, *bottom left panel:* $\Omega_m - \Omega_\Lambda$ plane and *bottom right panel:* $\Omega_m - w$ plane. C11 refers to results from the first 3 years of SNLS data as presented by Conley et al. (2011).

SNLS (SuperNova Legacy Survey; Astier et al., 2006; Sullivan et al., 2011) ran from 2003 to 2008 and used the Canada-France-Hawaii Telescope (CFHT) and its Megacam imager to discover and spectroscopically confirm > 500 SNe type Ia in a redshift range of $0.5 \leq z \leq 1.0$. SNLS used $ugriz$ photometric images to discover SNe and a time extensive spectroscopic follow-up program, which was carried out by the world's largest telescopes, namely the Gemini, VLT and Keck telescopes.

SDSS-II (Sloan Digital Sky Survey; Frieman et al., 2008; Sako et al., 2008; Kessler et al., 2009a) ran from 2005 to 2008, from September to November each year and used the dedicated 2.5m wide-angle SDSS telescope at the Apache Point Observatory in New Mexico (Gunn et al., 2006), to discover SNe type Ia at an intermediate redshift range of $0.1 \leq z \leq 0.4$. SDSS also used various telescopes around the world for its spectroscopic follow-up strategy, which resulted in the confirmation of ~ 500 SNe type Ia, which were used for Cosmology (Frieman et al., 2008; Sako et al., 2008).

Campbell et al. (2013) used 752 photometrically classified SNe type Ia obtained from the full SDSS-II SN survey, supplemented with host-galaxy spectroscopy from the SDSS-III BOSS[2] (Baryon Oscillation Spectroscopic Survey; Dawson et al., 2013), and presented an extensive cosmological analysis, leading the way to the new era of SN surveys. More lately, Sako et al. (2014) presented the final SDSS-II data release of SNe type Ia; which included 1443 SNe type Ia with spectroscopic and photometric redshifts and 677 purely-photometric SNe type Ia, all of which were used to constrain the amount of Dark Energy of the Universe.

PTF (Palomar Transient Factory[3]; Rau et al., 2009; Law et al., 2009) used the automated Palomar 60 inch telescope and the 7.26 deg^2 CFHT12k mosaic camera mounted on the Palomar Samuel Oschin 48-inch Schmidt Telescope. The survey ran from 2009 to 2012 and two of its key projects were focused on transients events; one that was performing a rapid cadence SNe search and one with a 5 day cadence. The PTF was designed to provide automated and real-time data of transients events, including classification and follow-up data. The discovery of the youngest SN type Ia (2011fe); the discovery of a pre-explosion outbursts from SNe type IIn and the discovery of some of the first member of the superluminous supernovae class (see also Chap. 2) are listed among the PTF's scientific achievements.

---

[2]http://www.sdss3.org
[3]http://www.astro.caltech.edu/ptf/index.php

In late 2012 PTF was succeeded by the intermediate Palomar Transient Factory (iPTF [4]), which used improved software (eg. data reduction; source classification) and achieved early discoveries and rapid follow-up of transient events.

LSQ   (La Silla-QUEST Low Redshift Supernova Survey; Baltay et al., 2013) uses the 10 deg^2 QUEST camera installed on the 1.0-m Schmidt telescope of the European Southern Observatory [5] (ESO) at La Silla (Chile). Starting in 2011, the LSQ will construct a large sample of low redshift SNe (over 4 years). This survey aims to obtain a similarly large sample of SNe type Ia, as the surveys mentioned before, below a redshift of $z = 0.1$.

Such low-z SNe samples will be complementary to the high-z surveys in two ways. Firstly, the large size of low-z SNe acts as an anchor to the Hubble diagram, as seen in Fig. 1.6, reducing the error on the cosmological parameters. Secondly, the low-z SNe discovered are better-studied than the high-z ones, thus increasing the understanding around the nature and behaviour of these standard candles, leading to more precise cosmological measurements.

SN Compilations

In addition to these SN surveys, several compilations of SNe samples have been created from different SN surveys. Such SNe datasets could be merged together and studied uniformly, extending the redshift coverage and improving the statistics. The 'Union2.1' (Suzuki et al., 2012) is such an example, that brought together 833 SNe from 19 datasets, out to redshift of $z = 1.4$.

More recently, Betoule et al. (2014) constructed a joint analysis from both SDSS and SNLS, using a total sample of 740 spectroscopically confirmed SNe type Ia with high quality light curves and reported a value of $\Omega_m = 0.295 \pm 0.034$ for a flat Λ Cold Dark Matter (ΛCDM) cosmology. Fig. 1.8 shows the Hubble diagram, the $\Omega_m - \Omega_\Lambda$ plane and the $\Omega_m - w$ plane as presented by this joint analysis.

1.4   The Dark Energy Survey

The Dark Energy Survey (DES; The Dark Energy Survey Collaboration, 2005) can be considered as the bridge between the past optical surveys, like SDSS and SNLS and the next generation surveys, like the Large Synoptic Survey Telescope - LSST[6]. This section introduces DES and describes its supernova search (see also Chap. 3 for full details), as it is the main survey used in this research thesis.

---

[4]http://www.ptf.caltech.edu/iptf
[5]http://www.eso.org/
[6]http://www.lsst.org/
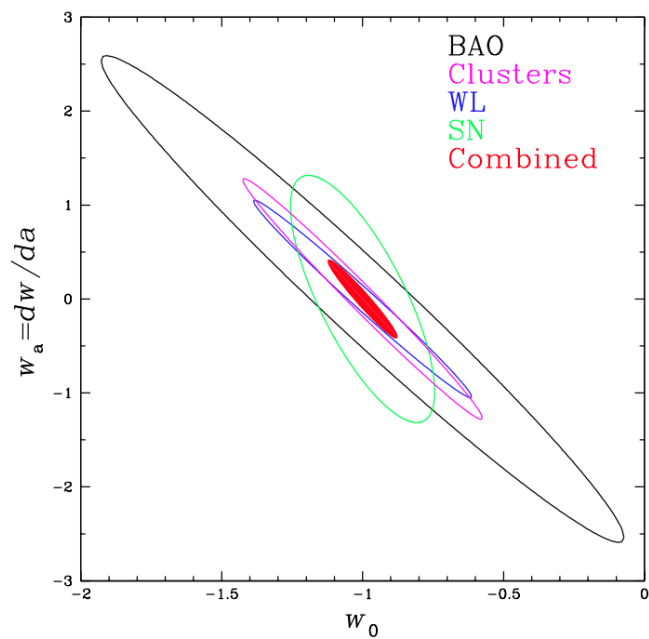
Figure 1.9: DES forecast constrains in the $w_0 - w_\alpha$ plane at 68% confidence level from the four probes: BAO (black), GC (magenta), WL(blue) SNe type Ia(green). Each probe was combined with the Planck CMB prior. The field red region shows the constrains after combining all four DES probes. The plot is taken from the Dark Energy Survey Science Program proposal to the National Science Foundation (NSF) and the Department of Energy (DOE) in December 2006.

DES is an optical/near-infrared (nIR) survey of $5000\,\mathrm{deg}^2$ at the south galactic gap (Fig. 1.13) that was designed to probe the origin of the accelerating Universe and explore the nature of dark energy. In this effort, four dark energy probes will be combined:

- type Ia supernovae (SNe type Ia)

- Baryonic Acoustic Oscillations (BAO)

- Galaxy Clusters (GC)

- Weak Gravitational Lensing (WL)

in order to constrain the dark energy equation of state (Eq. 1.11).

As is well noted in the DES overview (The Dark Energy Survey Collaboration, 2005), the four probes constrain different combinations of the cosmological model parameters and are affected by different systematic errors. By using the same instrument that produces a common data set and a common analysis framework, DES will have cross checks of the systematic errors, allowing a more precise measurement of the cosmological parameters. This is illustrated in Fig. 1.9, where it shows the DES forecast constraints on the $w_0 - w_\alpha$ plane.

1.4.1 The Dark Energy Camera

DES uses the Victor M. Blanco 4m telescope, located at the CTIO in Chile (pictured in Fig. 1.10) and the 570 Megapixels 'Dark Energy Camera' (DECam; Flaugher et al., 2012; Diehl and For the Dark Energy Survey Collaboration, 2012; Flaugher et al., 2015); a purposed-built new imager by the DES consortium. After commissioning DECam, DES was awarded 525 nights, over a period of 5 years, to carry-out the $5000\,\mathrm{deg}^2$ survey.

DECam consists of an optical corrector of five elements, seven filters ($ugrizY$), a 60cm aperture shutter and a 70 CCD mosaic focal plane with a field of view (FoV) of $2.2\,\mathrm{deg}$ diameter. The $250\mu m$ thick fully-depleted CCDs are split into: 62 4kpx×2kpx CCDs for science imaging and 12 2kpx $\times$ 2kpx CCDs used for focusing the entire focal plane and guiding the telescope and camera. The 62 science CCDs were designed and manufactured at Lawrence Berkeley National Laboratory (LBNL[7]) to be more sensitive to the redder part of the optical window than conventional CCDs. This corresponds to filters i and z as seen in Fig. 1.12. Each pixel of the CCDs has a physical size of $15\mu m \times 15\mu m$ and a plate scale of $0.263''$.

The DECam control and data acquisition system is named Survey Image System Process Integration (SISPI; Flaugher et al., 2015, and references therein), and allows

---

[7]http://www.lbl.gov

(a) Blanco 4m dome at CTIO
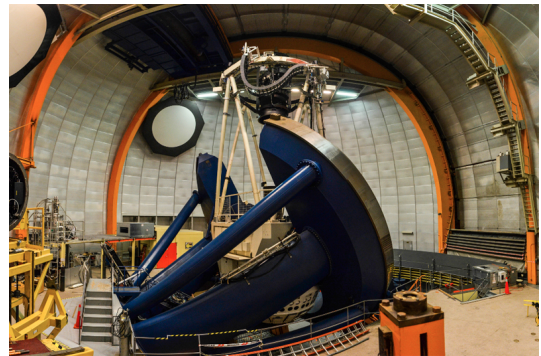
(b) Inside of Blanco 4m dome
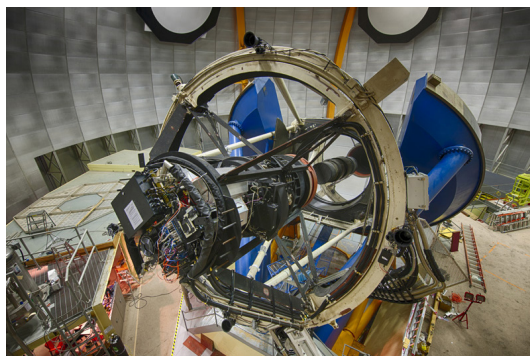
(c) Blanco 4m and DECam
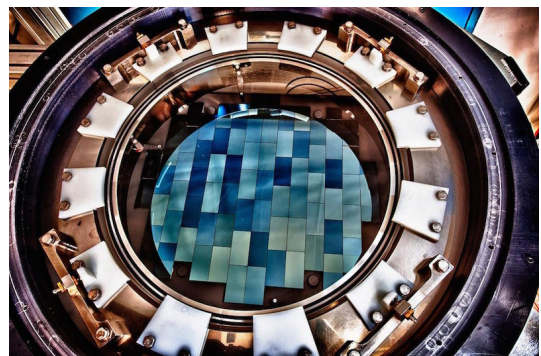
(d) DECam close-up

Figure 1.10: Located at CTIO in Chile are the body (Blanco 4m telescope) and heart(DECam) of DES. *Panel (a):* A panoramic photo of the CTIO located at Cerro-Tololo in Chile, 2207m above sea level. The Blanco 4m telescope sits inside the big, silver-top dome. *Panel (b):* A wide field view of the inside of the Blanco 4m dome, with DECam (black cylindrical structure) mounted on the top of the telescope's cage. I took this composite image on an observing trip back in April 2014. *Panel (c):* The telescope's 4m diameter mirror and DECam stripped-off from its covers. *Panel (d):* The front structure of DECam with the CCD's mosaic in the centre.
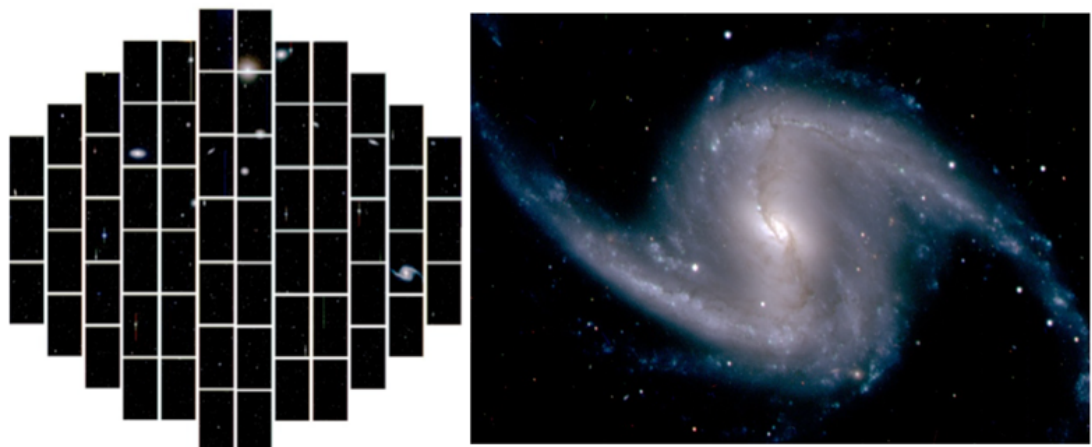
Figure 1.11: DECam's first light images from September 2012. *Left:* the Fornax galaxy cluster imaged over the entire DECam FoV, *right:* zoom-in image of galaxy NGC1365.
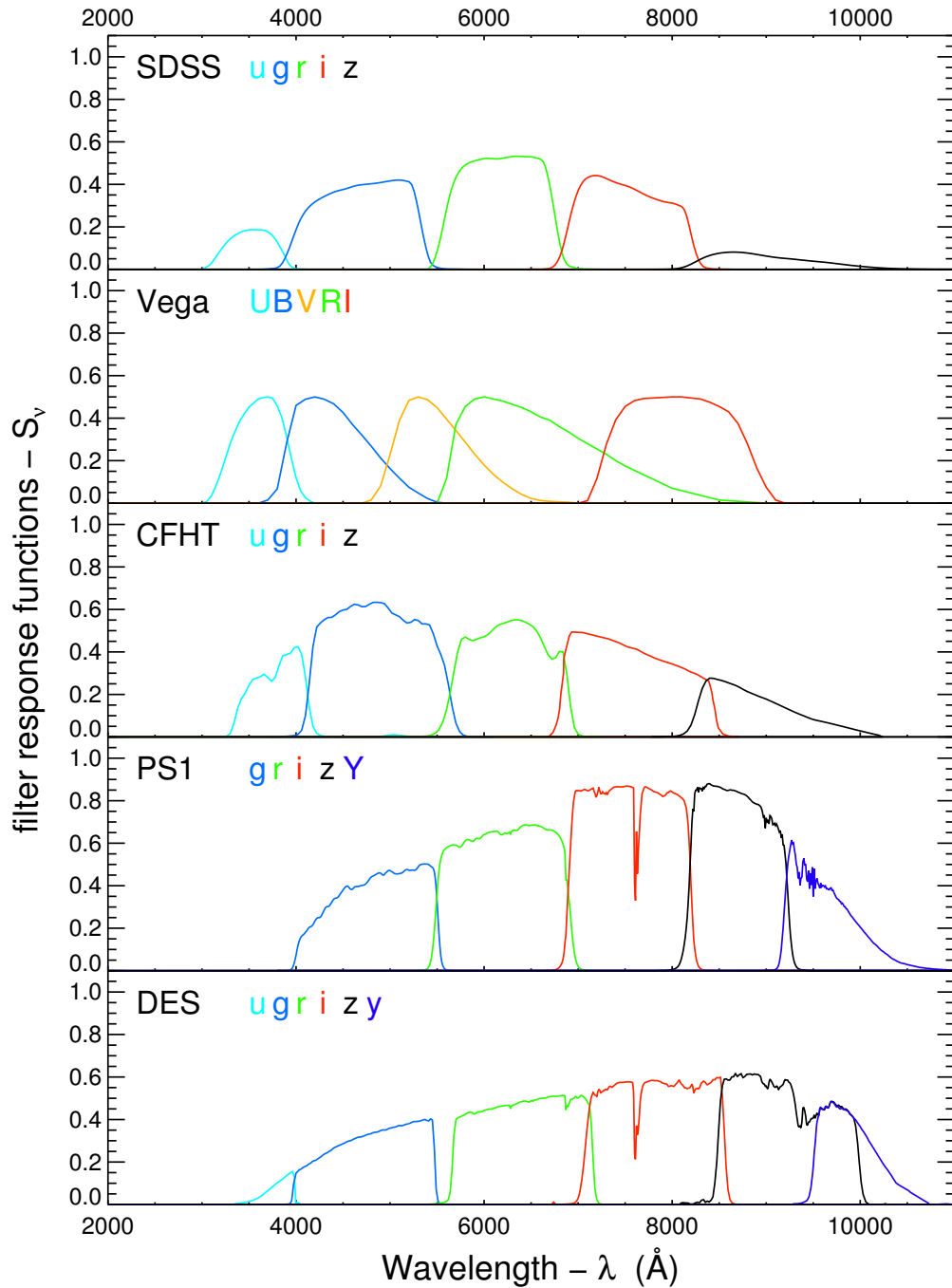
Figure 1.12: The DECam $ugrizY$ filter response functions compared to other surveys such as SDSS, PANSSTARS (PS1), SNLS-CFHT, using the same AB magnitude system. Also the Vega magnitude system filter response functions are shown in the second (from the top) panel.
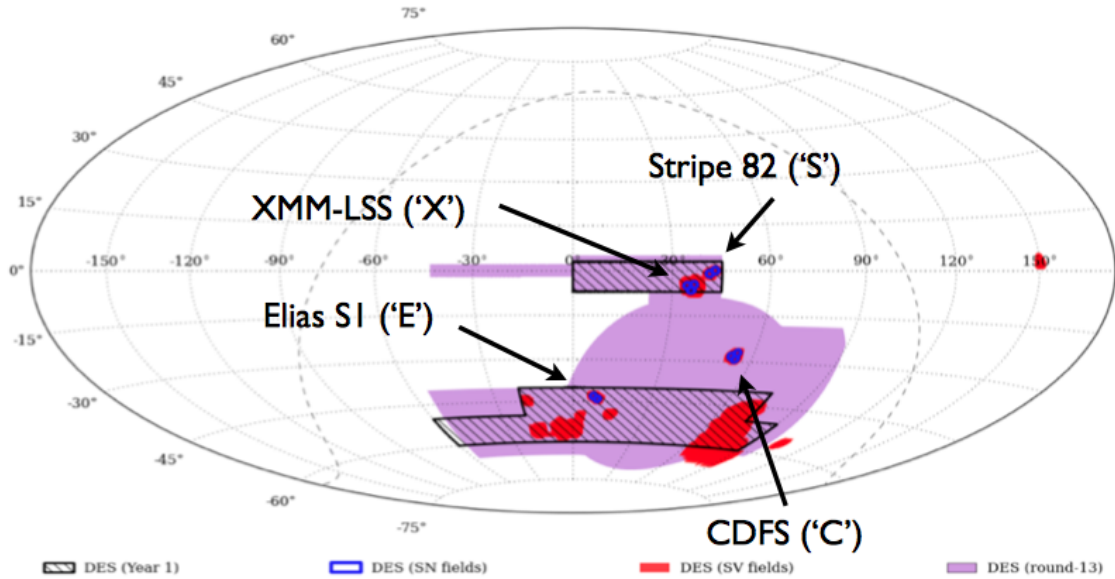
Figure 1.13: The DES footprint shown by the magenta area in equatorial coordinates (ra, dec). Overplotted are the areas observed in the SV season (red) and in Y1 (black shaded) of operations. The blue marked area show the locations of the ten SNe fields spread into four different locations, as listed in Table 3.2. The galactic plane location is marked with the dashed line.

the observers to interact with the telescope/camera using a set of web-based graphical user interfaces (GUIs) running on a multi-screen workstation. DECam's read-out time is ~ 20 seconds and the focusing and alignment are driven by a state-of-the-art hexapod system. A technical description of DECam's engineering, construction, installation and latest status update is given by Flaugher et al. (2015).

The construction of DECam started in 2008 at Fermilab, whereas in 2012 it was completed, shipped and installed at the Blanco 4m telescope. In September 2012 DECam took its first light images which are seen in Fig. 1.11

1.4.2   Strategy and Observations

DES is performing two surveys in parallel: a wide-field, multi-colour ($grizY$) survey of $5000 \, \text{deg}^2$ for the study of GC, WL and BAO; and a deeper, cadenced and multi-colour ($griz$) search for SNe type Ia. Each observing season has 105 nights available, spread between late-August to mid-February, with small gaps of few days in between for engineering work and community allocated time on DECam.

DES conducted science verification (SV) observations from November 2012 to February 2013. Then it began full science operations in mid-August 2013, with year one (Y1; Diehl et al., 2014) running until February 2014, followed by year two (Y2) of operations which lasted six months, starting on the 15th of August 2014. Fig. 1.13 shows the DES
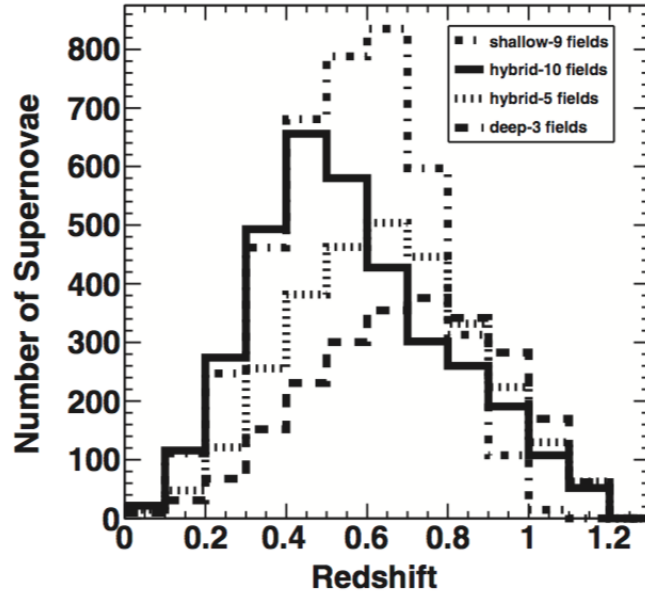
Figure 1.14: Number of SNe type Ia versus redshift for four different strategies from Bernstein et al. (2012). The 'hybrid-10 fields' strategy (*solid black line*) was selected and currently implemented by DES.

wide footprint and DES SNe field locations on the sky, as well as the area covered in SV and Y1 periods.

A detail description of the observational plan execution is given in the first sections of Chap. 3, where I explain the working flow of the SNe survey, from image acquisition all the way down to SNe candidates selection.

1.4.3 DES Supernova Survey

The objective of DES SN survey is to create a homogeneous sample of ~ 3500, high quality SNe type Ia, at a redshift range of $0.05 \leq z \leq 1.2$, as shown in Fig. 1.14 (Bernstein et al., 2012). In order to achieve such goal, DES is monitoring ten fields located in four separate locations within the wide DES footprint, as seen in Fig. 1.13 and listed in Table 3.2, and visits each field every 6 days on average, with an observing window of five and a half months per year.

An external spectroscopic follow-up program (OzDES Yuan et al., 2015) was planned and is currently being executed, which will provide with spectroscopic redshifts for all the host galaxies of the SNe type Ia discovered by DES, after the SNe have fainted away. Moreover, a number of SNe would have to be spectroscopically confirmed from spectra obtained from the SNe, as they would have no host galaxy associated. A detailed description of the SNe strategy, observations, discoveries, follow-up etc. is given in Chap. 3.
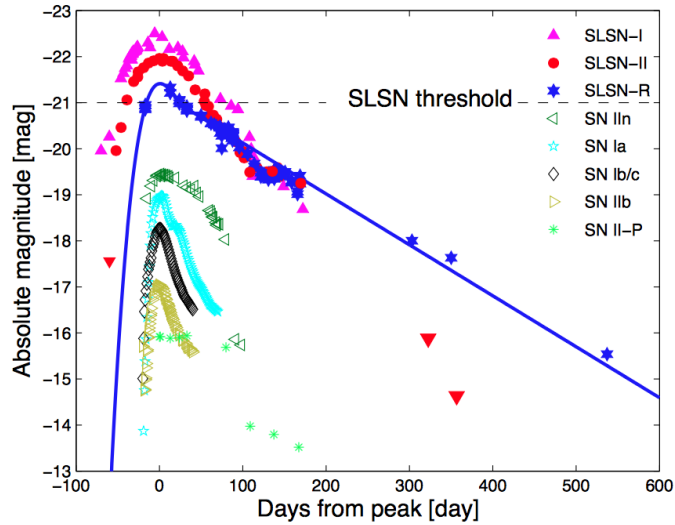
Figure 1.15: The SLSNe light-curves compared with the common SNe classes, which peak at absolute magnitudes $M \geq -19.5$; whereas the SLSNe threshold is placed at $M \leq -21.0$. Figure is taken from Gal-Yam (2012).

1.5 Superluminous Supernova

The last five years have seen the emergence of a new class of ultra-bright stellar explosions: superluminous supernovae (**SLSNe;** Quimby et al., 2011b; Gal-Yam, 2012), some 50 times brighter than classical SNe types presented in Sec. 1.2.1. Such extreme stellar explosions are likely associated with the deaths of the most massive stars in the Universe, that are thought to have lived at earlier times and even contributed to the chemical evolution of the Universe at that time (Gal-Yam, 2012). Any SNe with reported peak absolute magnitude $M \leq -21.0$ in any band would be classified as a SLSN (Gal-Yam, 2012), whereas the typical peak absolute magnitude of SNe type Ia is around $M \sim -19.3$.

Their extreme luminosities in optical and ultra-violet (UV) wavelengths and their observed lifespan, which lasts over a period of several months as shown in Fig. 1.15, make them promising probes of their distant environments, with significant advantages over the short-lived gamma-ray bursts (GRB) and the high-redshift Quasars, which have long-lasting effects on their environments (Gal-Yam, 2012). SLSNe could play a key role in many diverse areas of astrophysics: tracing the evolution of massive stars, driving feedback in low mass galaxies at high redshift and providing potential line-of-sight probes of interstellar medium to their high-redshift hosts (Berger et al., 2012). SLSNe have also been detected to $z \sim 4$ (Cooke et al., 2012), far beyond the reach of the current best cosmological probe, type Ia supernovae (SNe type Ia).

Taking this thought one step further, if SLSNe can be standardized (e.g. Inserra and Smartt, 2014), as is done with SNe Ia (Phillips, 1993; Riess et al., 1996) described in Sec. 1.3.1, then a new era of SN cosmology would be possible, with the potential to

accurately map the expansion rate of the Universe far into the epoch of deceleration (Delubac et al., 2014); or even test other cosmological models besides ΛCDM (e.g Wei et al., 2015). So far only ~ 50 SLSNe events have been reported in the literature (see Chap. 2) and some of them have been poorly studied with incomplete imaging and spectroscopy, leaving many aspects of their observational characteristics and their physical nature, unknown.

1.5.1 Discovery

The first members (e.g. **SN 1999as;** Knop et al., 1999; Hatano et al., 2001) of this class were discovered by first and second generation SNe type Ia surveys and treated as contaminants, as such surveys were targeting SNe type Ia for cosmological use. The breakthrough in discovering SLSNe came when the Texas Supernova Search (TSS; Quimby, 2006b) discovered and published studies for SN 2005ap (Quimby et al., 2007) at a redshift of $z = 0.283$ and SN 2006gy (Ofek et al., 2007; Smith et al., 2007), which occurred in the nearby galaxy NGC 1260. Also, SCP06F6 represents another early member of this class of SNe, which was discovered and studied by Barbary et al. (2009) within the efforts of the Hubble Space Telescope Cluster Supernova Survey (Dawson et al., 2009). Following the excitement of those early discoveries, other surveys such as the Catalina Real-Time Transient Survey (CRTS; Drake et al., 2009a) and the Palomar Transient Factory (PTF; Rau et al., 2009) started to report and study newly discovered luminous supernova. Quimby et al. (2011b) first pointed out that those luminous transients were likely a coherent group of SNe and published the first study of them as a new separate SNe class called the hydrogen-poor SLSNe.

Furthermore, retrospective searches in second generation SNe survey data (e.g. SDSS; SNLS) have also revealed a few SLSNe that passed unnoticed during the time of observations. Such examples are SN 2006oz (Leloudas et al., 2012) and PSN 000123 (Kostrzewa-Rutkowska et al., 2013) from SDSS; SN2213-1745 and SN1000+0216 (Cooke et al., 2012) from SNLS.

In the last couple of years, new SN surveys, such as the Panoramic Survey Telescope And Rapid Response System - Pan-STARRS (PS1; Kaiser et al., 2010), the La Silla QUEST (LSQ; Baltay et al., 2013), the Public ESO Spectroscopic Survey of Transient Objects (PESSTO; Smartt et al., 2013b, 2014) and DES described in Sec. 1.4, are reporting numerous SLSNe discoveries in each observational season. Nowadays, not only has the number of SLSNe discovered increased, but there is also a huge improvement in data quality and light-curve coverage. Also, a lot of effort is put in spectroscopic follow-up programs and on the extensive study of spectral features and evolution.

1.5.2 Classification

Gal-Yam (2012) divided SLSNe using their spectral features and light curve behaviour, into three possible types: SLSN-II, SLSN-I and SLSN-R as seen in Fig. 1.16.

SLSN-II:

SLSNe-II (or 'hydrogen-rich') show strong, narrow and intermediate-width hydrogen features (Balmer lines series) in their spectra, as shown in panel (a) of Fig. 1.16 (Ofek et al., 2007; Smith et al., 2007). Therefore, such stellar explosions are thought to occur inside thick hydrogen envelopes, which convert the explosion and expansion energy into observed radiation. This interaction with the hydrogen-rich CSM is commonly seen in type IIn SNe (Sec. 1.2.1), but with lower peak luminosity than the SLSNe-II. Therefore, SLSNe-II may simply represent the bright end of a continuum SNe type IIn (although this is not well established), which can be translated into the same explosion and energy transfer mechanism of more massive stars than the progenitors of SNe IIn (Smith et al., 2007, 2008a).

This class of SLSNe shows an interesting disparity in redshift distribution. To date, out of the eight reported SLSNe-II, none of them has a redshift greater than 0.289 The only exception, is discovered by DES in Y2 of observations at a redshift of $z = 1.3$ and is described later as part of the research within this thesis (Chap. 5).

SLSN-I:

SLSNe-I (or 'hydrogen-poor') is the most populated class of SLSNe to date, with $>$ 25 events spectroscopically classified as hydrogen free (Quimby et al., 2011b), and is possibly related to Type Ic SNe at late times (Pastorello et al., 2010a). Early time spectra of SLSNe-I (shown in panel (b) of Fig. 1.16) show significant UV flux, accompanied by absorption features of high-excitation low-mass elements, such as OII in the optical and CII, SiII and MgII in the near-UV.

As seen in Fig. 1.15, light-curves of SLSNe-I show slow rise times of around ~ 30 days and decay times inconsistent with the radioactive decay of ^{56}Ni (Pastorello et al., 2010a; Quimby et al., 2011b; Inserra et al., 2013). Many alternative models have been proposed: the injections of energy into a SN ejecta via the spin down of a young magnetar (Kasen and Bildsten, 2010; Woosley, 2010; Inserra et al., 2013); interaction of the SN ejecta with a massive (3-5 $M_\odot$) C/O-rich CSM (Blinnikov and Sorokina, 2010); or collisions between high-velocity shells generated from a pulsational pair-instability event (Woosley et al., 2007). These explanations are still actively debated in the literature.
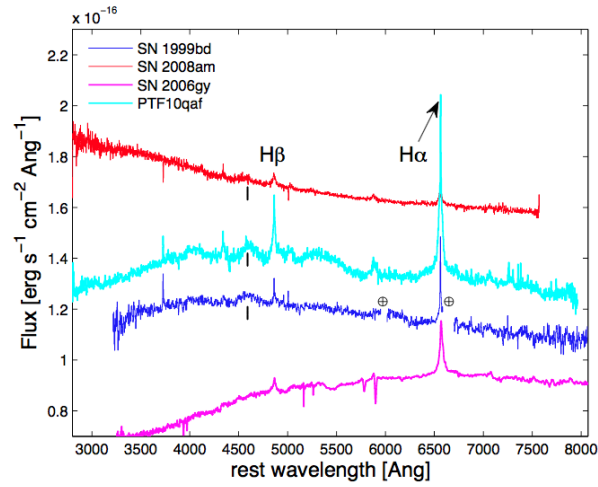
(a) SLSN-II
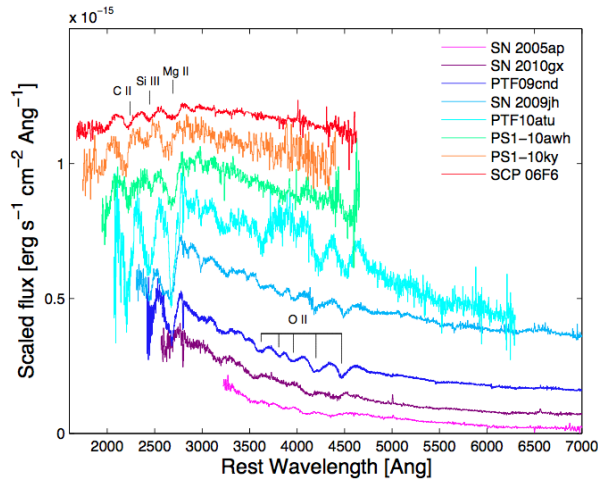
(b) SLSN-I
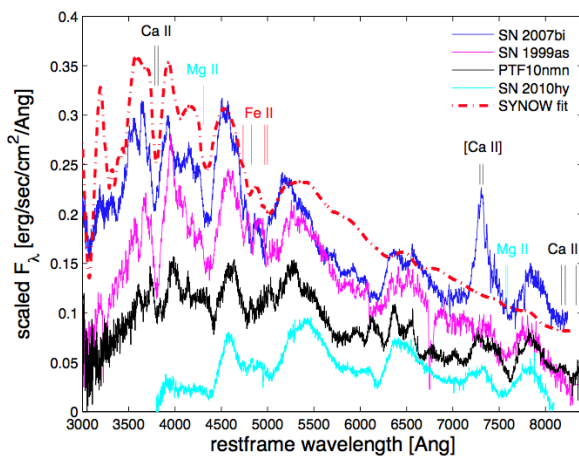
(c) SLSN-R

Figure 1.16: Spectral classification of SLSNe according to Gal-Yam (2012). *Panel (a):* SLSN-II are identified by narrow emission lines of the Balmer series. *Panel (b):* SLSN-I at early times show mixture of OII in the optical and CII, SiII and MgII features in the near-UV. *Panel (c):* SLSN-R show strong absorption features of CaII, MgII and FeII.

SLSN-R:

SLSNe-R (or 'radioactive') are rare and characterized by possessing extremely long, slow-declining light curves (> 200 days in the rest frame) as shown in Fig. 1.15. SLSNe-R originally appeared consistent with the death of $\gtrsim 100 \, M_\odot$ stars via the pair instability mechanism (Gal-Yam et al., 2009). This can explain both their extreme luminosities as well as the slow decline rate of the light curve, consistent with the radioactive decay of ^{56}Co, which lead to the suffix "R" proposed by Gal-Yam (2012).

The first well-observed example of SLSN-R was SN 2007bi (Gal-Yam et al., 2009), discovered by the Nearby Supernova Factory (SNFactory; Aldering et al., 2002) and described in Chap. 2. Their spectra (panel (*c*) of Fig. 1.16) show no signatures of hydrogen, but strong absorption features of CaII, MgII and FeII in resemblance to the spectra of SLSNe-I.

SLSN-Ic:

As noted before, the lack of significant spectral differences between SLSN-I and SLSN-R and recent observations, have challenged the notion that these classes are truly distinct (Nicholl et al., 2013; McCrum et al., 2014) and maybe better described together as SLSNe Ic (Inserra et al., 2013; Nicholl et al., 2013). The label SLSNe-Ic was established because of the late time spectra of SLSNe-I that resemble the spectra of normal type Ic SNe (Pastorello et al., 2010a; Inserra et al., 2013). SLSNe Ic as a distinct class of SNe were used lately for cosmological studies (Inserra and Smartt, 2014; Wei et al., 2015), which are review further in Sec. 1.5.5.

1.5.3 The Nature of Power Sources and Modelling

A handful of models have been used so far in the literature in order to explore all the aspects of SLSNe; from models exploring the power sources that provide their super-bright luminosities, to models describing their light-curve behaviour and even their spectral features. The most promising models are described in the following paragraphs.

Cooling Blackbody

The shape of the SLSNe light curves can be explained by an expanding photosphere, which radiates as a cooling blackbody. This model was first applied by Miller et al. (2009) using SN 2008es photometry and later by Smith et al. (2010) using SN 2006gy spectroscopy. Afterwards, almost every discovery and study of any type of SLSNe involved the fit of an expanding and cooling blackbody, to either the photometric or the spectroscopic data.

Howell et al. (2013) first attempted to quantify this behaviour, by assuming a simple model of a linear expanding photosphere, with the temperature to be linearly decreasing with time. The expanding radius of the photosphere could be described by:

$$R(t) = R_0 + \frac{dR}{dt}t \tag{1.30}$$

where R_0 is the initial radius, $\frac{dR}{dt}$ is the rate of the expansion of the radius with time, and t is time in days. The cooling temperature could be described similarly as:

$$T(t) = T_0 - \frac{dT}{dt}t \tag{1.31}$$

where T_0 is the initial temperature, and $-\frac{dT}{dt}$ is the rate of temperature decrease with time.

This simple model appears to fit the photometry of SLSN well, especially around peak, where it matches the colour evolution and the relative timing of the peaks in each band (Howell et al., 2013). On the other hand, the model fits poorly the light-curve at early ($\lesssim -30$ days) and late ($\gtrsim +50$ days) stages, especially if there is a luminous tail in late times.

Radioactive Decay of ^{56}Ni

The most common example of a SNe powered by ^{56}Ni radioactive decay is SNe type Ia, where the thermonuclear explosion of a WD is capable of producing more than one solar mass ($> M_\odot$) of ^{56}Ni, which later decays to ^{56}Co and later to ^{56}Fe, releasing gamma-ray photons. Those photons are reprocessed and finally diffuse out of the SNe ejecta in the UV, optical and IR wavelengths, with the produced amount of ^{56}Ni mass defining the peak luminosity, and the decay rate of ^{56}Co defining the late time decline rate of the observed light-curve (Arnett, 1982). Inserra et al. (2013) compared this late time decline rate (^{56}Co) and the observed late time light-curves of SLSNe Ic and found that they do not agree, leading to the introduction of different mechanism, which is explored in detail next.

Such power source could also be responsible for SLSNe events, as previous studies have shown (Chatzopoulos et al., 2009; Inserra et al., 2013), following the prescription of Arnett (1982); which is the approximation of an homologously expanding ejecta where the luminosity at any given time (in erg s^{-1}) is given by:

$$L(t) = M_{\text{Ni}}\, e^{-(t/\tau_m)^2} \left[\epsilon_{\text{Ni}} \int_0^t \frac{2u}{\tau_m^2}\, e^{(u/\tau_m)^2}\, e^{-u/\tau_{\text{Ni}}} du \right.$$
$$\left. + \epsilon_{Co} \int_0^t \frac{2u}{\tau_m^2}\, e^{(u/\tau_m)^2} \left(e^{-u/\tau_{\text{Ni}}} - e^{-u/\tau_{Co}} \right) du \right] \delta_\gamma, \tag{1.32}$$

where u is the (time) integration variable. The energy production rate and decay rate for ^{56}Ni are $\epsilon_{Ni} = 3.9 \times 10^{10}$ erg s^{-1} g^{-1} and $\tau_{Ni} = 8.8$ days, while for ^{56}Co these values are $\epsilon_{Co} = 6.8 \times 10^{9}$ erg s^{-1} g^{-1} and $\tau_{Co} = 111.3$ days. The amount of ^{56}Ni produced in the explosion is M_{Ni}. Parameterizing the rise-time of the light curve, τ_m (from eq. 18 and 22 of Arnett, 1982) is the geometric mean of the diffusion and expansion timescales, and is given by:

$$\tau_m = 1.05 \left(\frac{\kappa}{\beta c}\right)^{1/2} \left(\frac{M_{ej}^3}{E}\right)^{1/4} \tag{1.33}$$

Here, E is the explosion energy, M_{ej} is the total amount of ejected mass, κ is the optical opacity (assumed to be 0.1 cm^2 g^{-1} and constant throughout, as in Inserra et al. (2013)), and β is a constant with value ≈ 13.7 (Arnett, 1982).

The gamma-ray deposition function (δ_γ) is denoted as the efficiency with which gamma-rays are trapped within the SN ejecta. xFor this function one can follow Arnett (1982),

$$\delta_\gamma = G[1 + 2G(1-G)(1-0.75G)], \tag{1.34}$$

where $G \equiv \tau_\gamma/(\tau_\gamma + 1.6)$, with the 'optical depth' for gamma-rays approximately given by

$$\tau_\gamma \approx \left(\frac{0.1}{\kappa}\right) \left(\frac{\tau_m^2}{4\tau_{Ni}^2}\right) \left(\frac{5.53 \times 10^{10}}{v_{ej}(0.1 + t/\tau_{Ni})^2}\right). \tag{1.35}$$

Here $v_{ej} = \sqrt{10E_k/3M_{ej}}$ and is in units of cm s^{-1}. The deposition function used in Chatzopoulos et al. (2009) has a functional form that is similar to that used here, but in their approximation τ_γ only deviates from ≈ 1 at much later epochs, resulting in a light-curve decay rate mirroring ^{56}Co and is largely insensitive to changes in the explosion energy or ejecta mass.

Thus, the model can be described by four parameters: the explosion epoch (t_0), the energy of the explosion (E), the total ejected mass (M_{ej}), and the amount of ejected mass which is ^{56}Ni (M_{Ni}). Examples of this model are used to fit SLSNe discovered by DES, as shown in Chap. 4 and 5.

Magnetar

The magnetar model, proposed by Woosley (2010); Kasen and Bildsten (2010), assumes that SLSNe can be powered by the rapid spinning-down of a neutron star with an extreme magnetic field, which deposits its rotational energy into an SNe explosion, which is enhanced in luminosity terms. Inserra et al. (2013) showed that the magnetar model had more success than the radioactive decay of ^{56}Ni, especially at late times of the light-curves of several SLSNe, whereas it maintained the also good fit to the rise time and the peak luminosity.
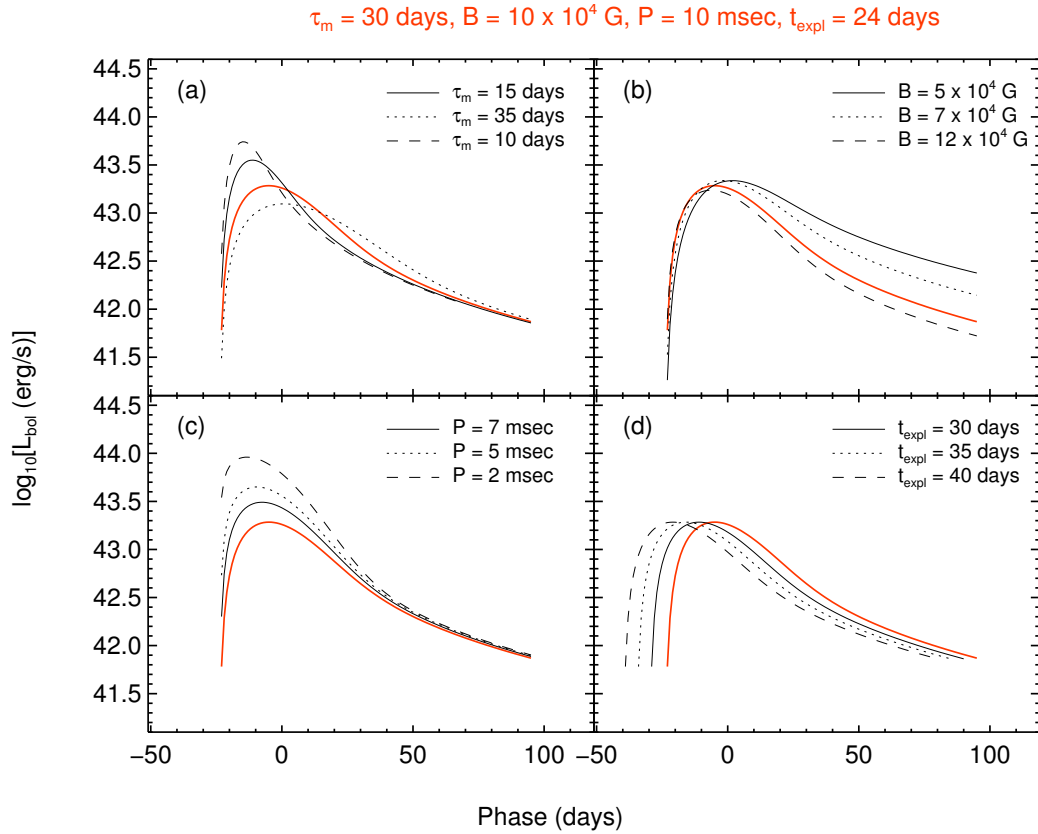
Figure 1.17: Illustration of how the magnetar model's input parameters affect the shape of the corresponding light-curves. For comparison purposes the red light-curve has the same four parameters (τ_m, B, P, t_{expl}) across all panels. *Panel (a):* changes to the rise-time parameter (τ_m) affect the peak luminosity, the rise-time (or the rise-rate) and the decline rate right after peak brightness. *Panel (b):* by increasing the magnetic field strength (B) the decline rate of the light-curves increases as well. *Panel (c):* by increasing the initial spin period (P) the peak brightness and the decline rate decrease. *Panel (d):* by increasing the explosion time (t_{expl}) the peak of the light-curves shifts to negative values.

In the magnetar model the input energy is defined by the initial spin period (P_{ms}, in milliseconds) magnetic field strength (B_{14}, in units of 10^{14} Gauss) of the magnetar, whereas the rise-time parameter (τ_m, see equation 1.33) reflects the combined effect of the explosion energy (E), the ejected mass (M_{ej}), and the opacity (κ). Fig. 1.17 shows how the four parameters, which define the magnetar model, affect the light-curve's properties, such as the rise time, the peak luminosity and the decline rate. An extensive discussion on the model's parameters and their effects is contacted in Chap. 4 and 5, where the magnetar model is fitted to data of SLSNe, that were discovered within the research of this thesis.

Using the semi-analytical model outlined in Inserra et al. (2013), the luminosity of the magnetar model at time t is given (in erg s^{-1}) by:

$$L(t) = 4.9 \times 10^{46} \, e^{-(t/\tau_m)^2} \delta \int_0^t \frac{2u}{\tau_m^2} \, e^{(u/\tau_m)^2} \, \frac{B_{14}^2 \, P_{ms}^{-4}}{(1 + u/\tau_p)^2} du, \qquad (1.36)$$

where u is the (time) integration variable, τ_p is the spin-down timescale, $\tau_p = 4.7 \, B_{14}^{-2} \, P_{ms}^2$ days, and δ is the deposition function for the magnetar radiation; here we assume full trapping (i.e., $\delta = 1$) following Inserra et al. (2013). This model does not include any additional contribution from ^{56}Ni decay. Also, examples of the magnetar model are used to fit SLSNe discovered by DES, as shown in Chap. 4 and 5.

Interaction with Circumstellar Medium

Chevalier and Irwin (2011) proposed that an interaction between the ejected material and pre-existing CSM, could provide the extra energy seen well after the stellar explosion. Such CSM envelope should have been ejected in a relatively big fraction of the progenitor mass and well before the explosion, in order to have time to slow down its expansion (Chomiuk et al., 2011). Then, the explosion causes the ejecta to expand and to collide with the slowly moving CSM, producing the narrow hydrogen emission lines seen in the case of SLSNe-II (SN 2006gy; Smith et al., 2007).

Furthermore, such interaction would boost up the light-curve reaching the level of SLSNe, but at the same time it would slow down the decline rate after peak to many tens to hundreds of days (Ben-Ami et al., 2014). In order for such mechanism to work for other than SLSNe-II events, then narrow emission lines of other than hydrogen elements should be visible in the obtained spectra, as such CSM envelopes would have to be stripped-out of hydrogen.

Pair-Instability Supernova

Barkat et al. (1967) proposed that theoretically, a massive star which has an initial mass $M \geq 100 M_{\odot}$ and an oxygen core of $M_{core} \geq 50 M_{\odot}$, is able to reach such high temperature, which allows the creation of electron-positron pairs from high energy photons. Such action would decrease the core's radiation pressure support and the core will contract, oxygen will ignite, triggering a catastrophic nuclear explosion that can disrupt the entire star and release huge amounts of radioactive ^{56}Ni (Heger and Woosley, 2002). A star that ends its life following this mechanism is called as Pair-Instability SNe (PISN).

SN 2007bi was the first PISN discovered and studied by Gal-Yam et al. (2009), showing a good match between the observations and the theoretical model of PISN. The model also predicts that the peak luminosity is proportional to the amount of ^{56}Ni produced in the explosion, and the late-time decay rate matches well with the theoretical ^{56}Co decay rate.

1.5.4 Host Galaxies Studies

In addition to studying the supernova explosion, several authors have found that SLSNe appear to preferentially inhabit faint dwarf galaxies. In recent years, dedicated efforts and studies of host galaxies of SLSNe have emerged using both photometry and spectroscopy, to look in detail into the stellar environments of such stellar explosions.

Neill et al. (2011) presented the first study of 17 SLSNe hosts, using optical and GALEX[8] NUV photometry and showed that SLSNe prefer to occur in low-mass galaxies with high specific star formation rates (sSFR). Lunnan et al. (2014a) carried out a systematic study of 30 hosts of hydrogen-poor SLSNe, of which 14 objects were discovered by PS1, and span in a redshift range of $0.1 \lesssim z \lesssim 1.6$. They included spectroscopic measurements for 12 of their host in addition to photometric data and determined luminosities, stellar masses, star formation rates, and metallicities of the hosts. Their study concluded that the sample of H-poor SLSNe hosts have low-luminosities $\langle M_B \rangle \simeq -17.3$, low stellar masses $\langle M_* \rangle \simeq 2 \times 10^8 M_{\odot}$ and a high median specific star formation rate $\langle sSFR \rangle \simeq 2 \, \mathrm{Gyr}^{-1}$. They also reported a low median metallicity of: $12 + \log(\mathrm{O/H}) \simeq 8.35 \simeq 0.45 Z_{\odot}$ for the spectroscopic sample. Lunnan et al. (2014a) also argued that the host galaxies of H-poor SLSNe resemble the host galaxies of long-duration gamma-ray bursts (LGRBs) in terms of stellar mass, sSFR, and metallicity.

Lately, Lunnan et al. (2014b) used the HST to image in the rest-frame UV (Fig. 1.18) 16 host galaxies of H-poor SLSNe, 11 of which were discovered by PS1. They showed

---

[8]Galaxy Evolution Explorer: www.galex.caltech.edu/
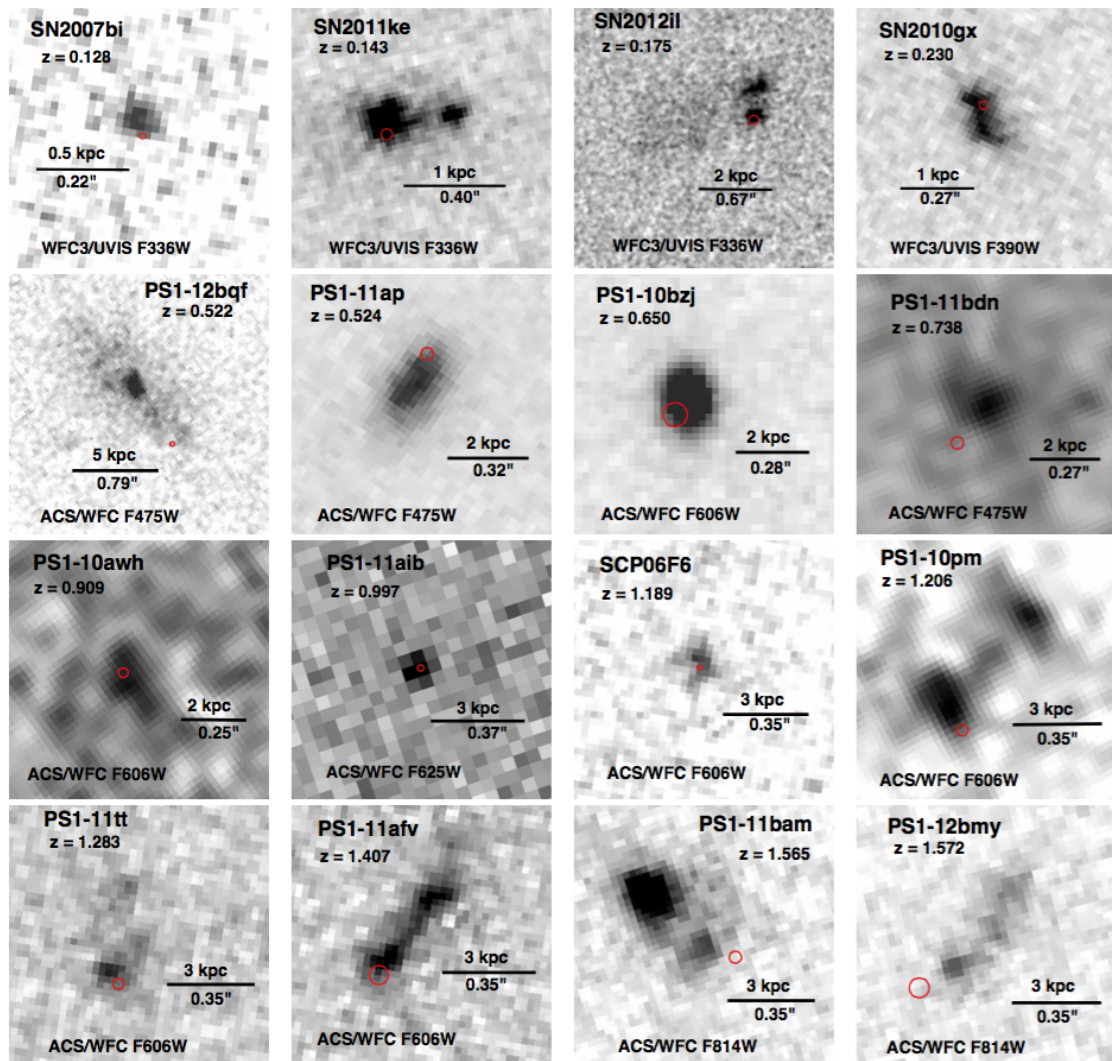
Figure 1.18: HST UV (rest-frame) images of 16 SLSNe hosts from the literature (see Chap. 2). All images are oriented with north up and east pointing to the left, whereas the horizontal bars show the image scale and the red circles correspond to the position of the SNe. Figure taken from Lunnan et al. (2014b).

(a) Mass-sSFR diagram   (b) Mass-Metallicity diagram
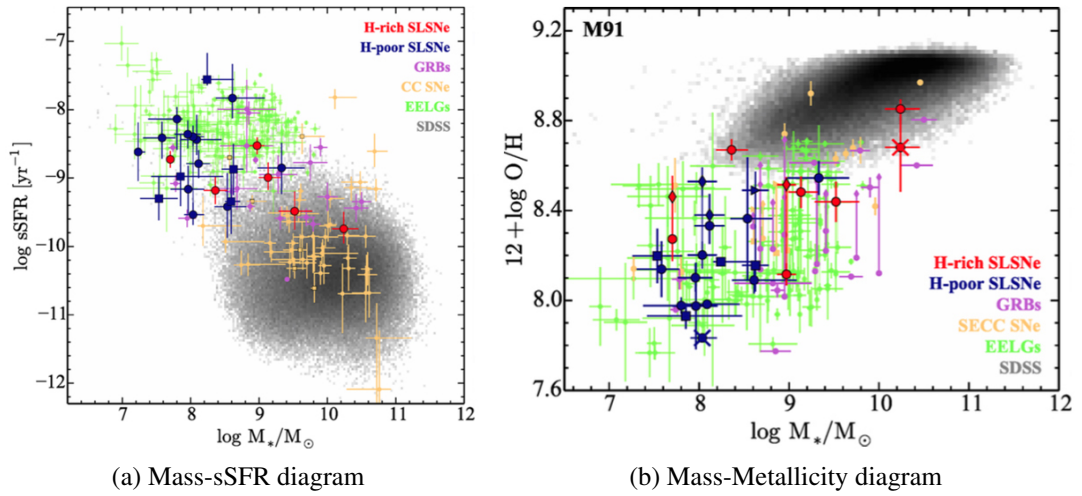
Figure 1.19: SLSNe host galaxies properties as studied by SUSHIES (Leloudas et al., 2015), suggesting that hosts of H-poor and H-rich SLSNe have different environments, pointing towards a different progenitor mechanism for the two SLSNe classes. *Panel (a):* stellar mass - sSFR diagram for various types of host galaxies shown in the legend. *Panel (c):* stellar mass - metallicity diagram for the same sample of host galaxies shown in panel (a).

that those 16 hosts were irregular, compact dwarf galaxies, with a median half-light radius of 0.9 kpc and suggested that a progenitor population of SLSNe could potentially be lower-mass than the one for Long Gamma-Ray Bursts (LGRBs). Leloudas et al. (2015) initiated a new project named SUper-luminous Supernova Host galaxIES (SUSHIES) to study the host of both H-poor and H-rich SLSNe classes. By June 2014, they had collected spectroscopic data for 16 SLSNe hosts, using VLT, GTC and Magellan telescopes, and they also included host spectra from the literature. They argued (see also Fig. 1.19) that often, SLSNe-I and SLSNe-R (H-poor) occur in a class of low-mass, metal-poor, intensively star-forming galaxies with strong nebular emission lines and a hard ionizing radiation field, referred to as Extreme Emission Line Galaxies (EELGs; Atek et al., 2011; Amorín et al., 2014). On the contrary, SLSNe-II (H-rich) occur in more massive, more metal-rich galaxies with softer radiation fields, suggesting that the two populations of SLSNe should have different progenitor mechanisms.

1.5.5 SLSNe Cosmology

Inserra and Smartt (2014) first attempted to standardize SLSNe-Ic for use in cosmology analogous to SNe type Ia, but reaching to higher redshifts using their extreme luminosities. They used a sample of 16 published SLSNe in the redshift range of $0.1 \leq z \leq 1.2$ and introduced two synthetic rest-frame passbands, which they used to investigate the
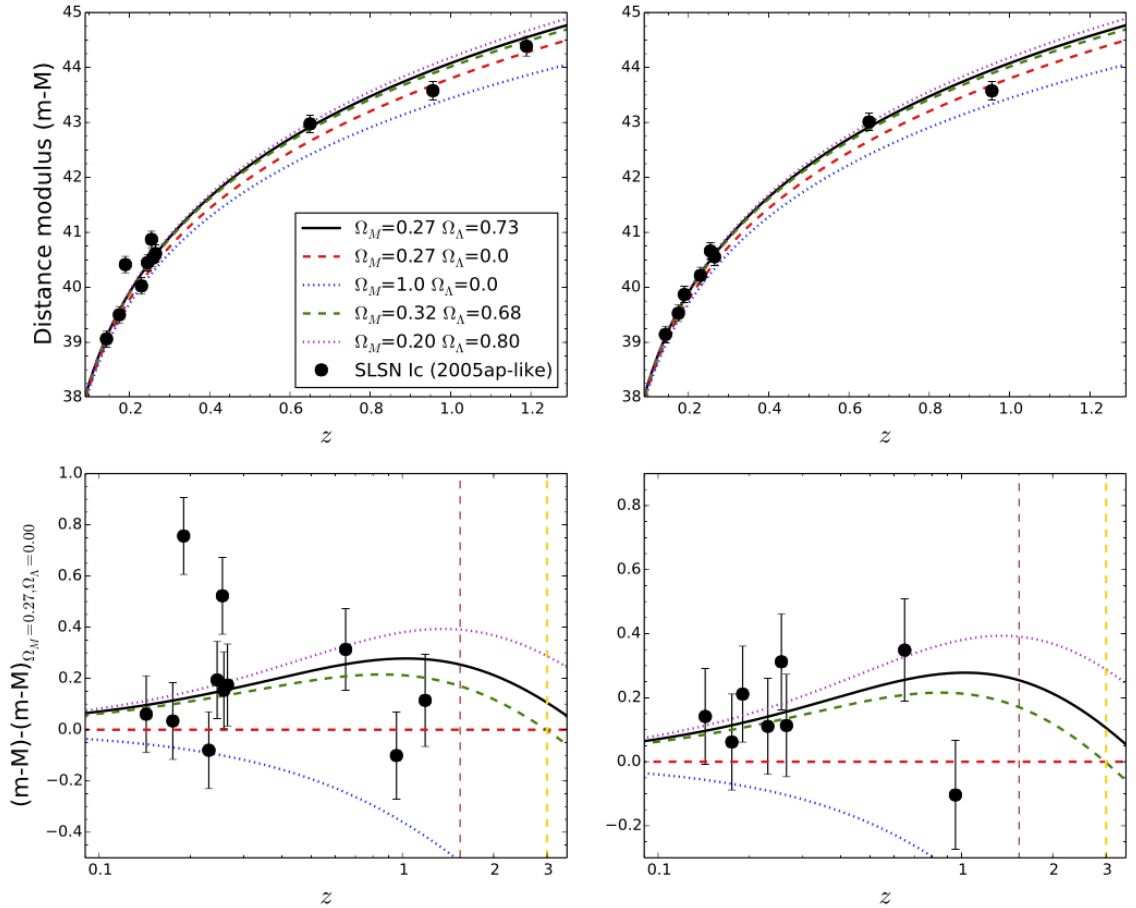
Figure 1.20: Hubble diagrams for SLSNe-Ic, as presented in the analysis of Inserra and Smartt (2014), are shown in the top panels with overplotted different cosmologies, as shown in the legend. The two left-hand-side panels show measurements using the peak magnitude-decline rate relation, whereas the right-hand-side panels show measurements using the the peak magnitude-colour decline relation. The two bottom panels show the residuals of the distance moduli relative to a universe with $\Omega_m = 0.27$ and $\Omega_\Lambda = 0$. The brown and yellow dashed vertical lines represent the upper redshift limits on SNe type Ia and SLSNe-Ic respectively, using current generation telescopes.

correlations between the SLSNe decline rates and peak magnitudes; as well as the correlation between the peak magnitudes and colour evolution, analogous to the corrections found by Phillips (1993) for SNe type Ia (Fig. 1.4).

The results from this first cosmology analysis using SLSNe-Ic were quite encouraging: from the raw mean absolute magnitudes $\langle M \rangle = -21.86 \pm 0.35$, the scatter in standardized peak magnitudes was reduced to ± 0.22 mags by using a magnitude-decline rate relation. Whereas, using a magnitude-colour evolution relation, an even lower scatter of ± 0.13 mags in peak magnitudes appears, showing a promising research area in which the increase in the number of SLSNe would play a key role on testing the standardization of SLSNe for cosmological use. Fig. 1.20 shows two Hubble diagrams using the two empirical relations investigated by Inserra and Smartt (2014).

Motivated by the work of Inserra and Smartt (2014) and using their promising results, Wei et al. (2015) presented tests of cosmological models (besides ΛCDM) using SLSNe Ic. Wei et al. (2015) even run Monte Carlo simulations based on Inserra and Smartt (2014) measurements and estimated that a sample of ~ 240 SLSNe-Ic should be sufficient enough to differentiate between ΛCDM and other cosmological models, like the $R = ct$ model proposed by Wei et al. (2015).

1.6 Strong Gravitational Lensed SNe

The growing number of SLSNe has highlighted a special category of SNe that share some characteristics with SLSNe (extreme brightness), but their nature differs entirely. A gravitational lens, such as massive galaxies or galaxy clusters, could magnify the brightness of a background SN explosion, making it appear as a SLSN event.

For example, Chornock et al. (2013) reported the discovery of PS1-10afx which they classified as a hydrogen deficient SLSNe at $z = 1.388$. Shortly after, Quimby et al. (2013b) argued that PS1-10afx is a normal SNe type Ia, whose flux has been magnified by a gravitational lens by a factor of ~ 30. Going further, Quimby et al. (2014) used the Low-Resolution Imaging Spectrograph (LRIS; Oke et al., 1995) mounted on the Keck-I telescope, to better understand their hypothesis of a gravitational lensed SNe type Ia, by observing the host galaxy and any foreground objects at the sky position of PS1-10afx.

Quimby et al. (2014) found a foreground galaxy, whose redshift and mass suggest that it is fully consistent with a gravitational lens capable of satisfying the observable constraints of PS1-10afx, as set by Quimby et al. (2013b). They concluded that PS1-10afx is not a SLSN but a normal SNIa at $z = 1.3885$ magnified by a strong gravitational lens at $z = 1.1168$, as show in Fig. 1.21.
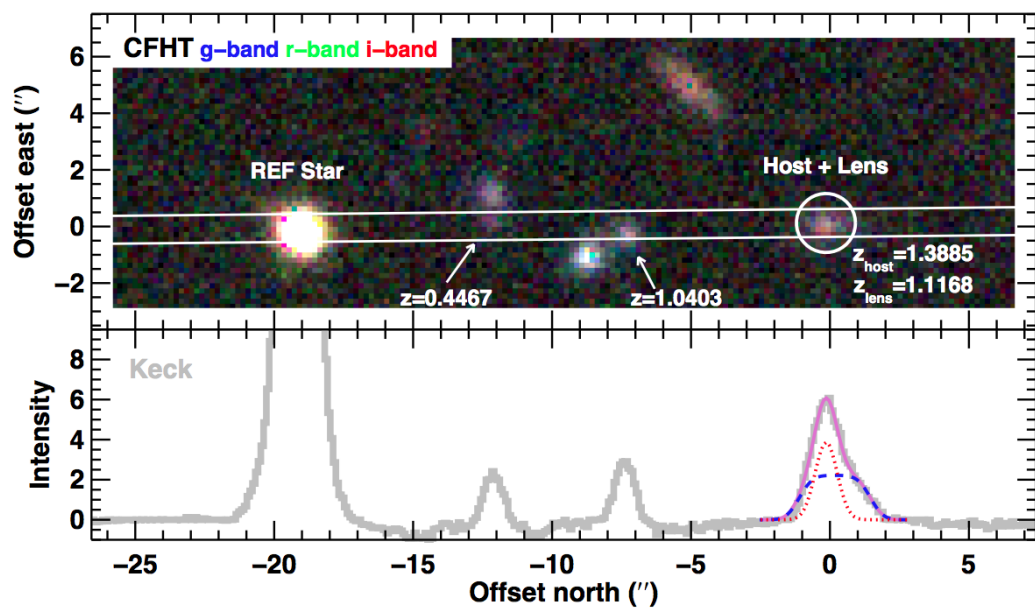
Figure 1.21: A colour-composite image of the sky near PS1-10afx using gri-band data taken prior to the SNe by the CFHT Legacy Survey (Gwyn, 2008). The white lines mark the location of the 1" slit mask deployed for spectroscopy. The location of PS1-10afx is marked with a white circle, and the redshifts of nearby galaxies, as determined from the Keck spectra, are indicated. The lower panel shows the 1-D intensity along the slit as recorded by the Keck observation. The target profile (purple line) was decomposed into a marginally resolved host component (red dotted line) and an extended foreground galaxy component (blue dashed line). *Plot taken from Quimby et al. (2014).*
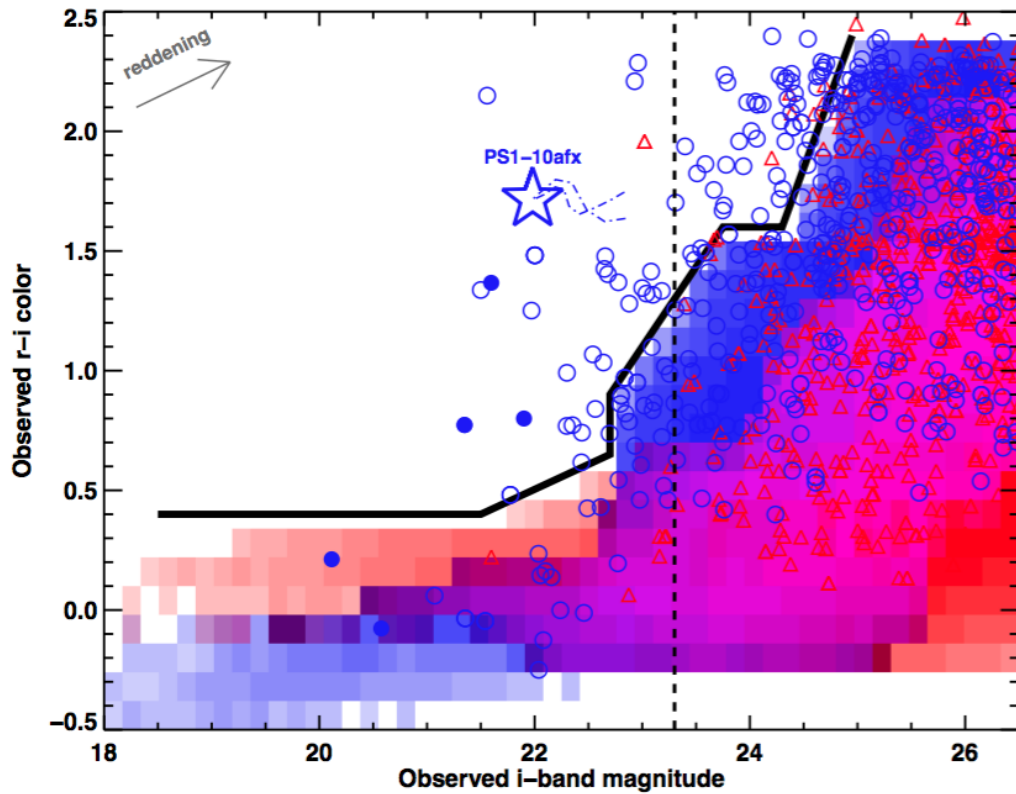
Figure 1.22: colour-magnitude diagram showing how lensed SNe type Ia can be distinguished from un-lensed events. The blue and red shaded areas shows the distribution for un-lensed SNe type Ia and Core-Collapse SNe (CC SNe) respectively. The thick, black line denotes the limit between lensed SNe above the line and unlensed SNe below it. Blue circles and red triangles show the distribution of lensed SNIa and CC SNe respectively, as predicted by Monte Carlo simulations ran by Quimby et al. (2014). Filled symbols indicate objects that could be resolved from ground based telescopes (eg. LSST). Open symbols show objects that require high angular resolution follow-up observations to resolve spatially. The open blue star marks the values corresponding to the peak i-band brightness and the dash-dotted curve shows the colour evolution of PS1-10afx. The vertical dashed line marks the single epoch limit predicted for LSST. The arrow shows the reddening vector, assuming $A_V = 1.0$ mag. *Plot taken from Quimby et al. (2014)*.

Furthermore, Quimby et al. (2014) predicted that in the future, high angular resolution imaging, enabled by adaptive optics (AO) or space-based resources like the Hubble Space Telescope (HST), could be used to spatially resolve the multiple images of gravitational lensed SNIa like PS1-10afx. To emphasize the importance of such events, Quimby et al. (2014) presented the colour-magnitude diagram shown in Fig. 1.22, as a tool for future surveys, allowing them to select such rare events among the vast majority of non-lensed SNe.

1.7 Description of This Thesis

The goal of this thesis is to present the search for SLSNe with DES and DECam. In Chap. 2, I will briefly describe all the SLSNe reported in the literature to date, highlighting the improvement in recent years with more events discovered each year. In Chap. 3, I will present in detail the SNe survey ran by DES in SV and Y1 seasons (2012-2014) and focus on the search for SLSNe, by presenting selection methods, contamination sources, SLSNe candidates and the lessons learned at the end of Y1.

Chap. 4 describes the discovery and study of DES13S2cmm, the first SLSNe discovered by DES in Y1, by showing photometric light-curves, spectra comparisons and model fits to Magnetar and radioactive decay of ^{56}Ni models. In Chap. 5 I will present the improvements and updates on the SLSNe search in Y2 of DES (2014-2015). I will illustrate a more systematic SLSNe candidates selecting process and its results on different samples of SLSNe. Finally, in Chap. 6 I will discuss the results of the search for SLSNe with DES and DECam and also present the Survey Using Decam for Superluminous Supernovae (SUDSS), a new survey currently taking data, which is dedicated to expand the sample of known SLSNe.

Chapter 2

Historical Superluminous Supernovae

2.1 Introduction

In this chapter, I present an overview of all SLSNe reported in the literature to date. Such effort illustrates the emerging properties of these SLSNe and acts as a reference to subsequent analyses in this thesis.

As described in Sec. 1.5.1, the first discoveries of SLSNe were made by sky surveys searching for SNe Ia, which treated SLSNe as contaminants for their cosmological analysis. With the passing of time, the development of new technologies (mosaic CCD cameras) and the application of new tactics (wide-field sky surveys) more astronomical surveys began to discover luminous SNe, until Quimby et al. (2011b) published the first study of hydrogen-poor SLSNe as a group with common properties.

Since then, the scientific interest in discovering and studying SLSNe events has increased, resulting in the doubling of known SLSNe; from 18 objects reviewed by Gal-Yam (2012), to 39 SLSNe presented in Table 2.1. In the upcoming years, the number of SLSNe of all types is expected to increase by a factor of 10 as I will argue at later stages of this thesis. Also, at least 10 more SLSNe events - that had not been published at the time of writing this thesis - have been reported on Astronomer's Telegrams (ATel[1]) and mentioned in other SLSNe studies (Lunnan et al., 2014c).

Most of the SLSNe reported in Table 2.1 come from surveys such as the Texas Supernova Search (**TSS**; Quimby, 2006b), the Sloan Digital Sky Survey (**SDSS**; Frieman et al., 2008), the SuperNova Legacy Survey (**SNLS**; Astier et al., 2006), the Palomar Transient Factory (**PTF**; Rau et al., 2009), Catalina Real-Time Transient Survey (**CRTS**; Drake et al., 2009a), the Panoramic Survey Telescope And Rapid Response System - Pan-STARRS (**PS1**; Kaiser et al., 2010), the La Silla QUEST (**LSQ**; Baltay et al., 2013), the

---

[1]http://www.astronomerstelegram.org

Public ESO Spectroscopic Survey of Transient Objects (**PESSTO**; Smartt et al., 2013b, 2014) and the Dark Energy Survey (**DES**; The Dark Energy Survey Collaboration, 2005).

Table 2.1: Updated list of all SLSNe of all types in the literature; listing the name, the type, the redshift, the reported absolute peak magnitude, the exact location in R.A. and DEC., and the reference under which were first reported or studied.

A/A	Name	type	Redshift - z	Abs. Mag.	RA (J2000)	DEC (J2000)	Reference
1	PTF10hgi	I	0.099	-20.42	$16^h37^m47^s.04$	$+06°12'32''.3$	Inserra et al. (2013)
2	SN 2011ke	I	0.143	-21.42	$13^h50^m57^s.77$	$+26°16'42''.8$	Inserra et al. (2013)
3	SSS120810	I	0.156	-21.60	$23^h18^m01^s.80$	$-56°09'25''.6$	Nicholl et al. (2014)
4	SN 2012il	I	0.175	-21.56	$09^h46^m12^s.91$	$+19°50'28''.7$	Inserra et al. (2013)
5	PTF11rks	I	0.190	-20.76	$01^h39^m45^s.64$	$+29°55'27''.0$	Inserra et al. (2013)
6	SN 2010gx	I	0.230	-21.23	$11^h25^m46^s.71$	$-08°49'41''.4$	Pastorello et al. (2010a)
7	SN 2011kf	I	0.245	-21.73	$14^h36^m57^s.34$	$+16°30'57''.1$	Inserra et al. (2013)
8	LSQ12dlf	I	0.255	-21.77	$01^h50^m29^s.80$	$-21°48'45''.4$	Nicholl et al. (2014)
9	PTF09cnd	I	0.258	-22.03	$16^h12^m08^s.94$	$+51°29'16''.1$	Quimby et al. (2011b)
10	SN 2013dg	I	0.265	-21.54	$13^h18^m41^s.38$	$-07°04'43''.1$	Nicholl et al. (2014)
11	SN 2005ap	I	0.283	-22.73	$13^h01^m14^s.83$	$+27°43'32''.3$	Quimby et al. (2007)
12	MLS121104	I	0.303	-21.30	$02^h16^m42^s.51$	$+20°40'08''.5$	Fatkhullin and Gabdeev (2012)
13	PTF09cwl	I	0.349	-22.03	$14^h49^m10^s.08$	$+29°25'11''.4$	Quimby et al. (2011b)
14	SN 2006oz	I	0.376	-21.53	$22^h08^m53^s.56$	$+00°53'50''.4$	Leloudas et al. (2012)
15	PTF09atu	I	0.501	-22.03	$16^h30^m24^s.55$	$+23°38'25''.0$	Quimby et al. (2011b)
16	PS1-10bzj	I	0.650	-21.40	$03^h31^m39^s.83$	$-27°47'42''.2$	Lunnan et al. (2013)
17	iPTF 13ajg	I	0.740	-22.50	$16^h39^m03^s.95$	$+37°01'38''.4$	Vreeswijk et al. (2014)
18	PS1-10awh	I	0.908	-22.53	$22^h14^m29^s.83$	$-00°04'03''.6$	Chomiuk et al. (2011)
19	PS1-10ky	I	0.956	-22.53	$22^h13^m37^s.85$	$+01°14'23''.6$	Chomiuk et al. (2011)
20	SCP 06F6	I	1.189	-22.30	$14^h32^m27^s.40$	$+33°32'24''.8$	Barbary et al. (2009)
21	PS1-10pm	I	1.206	-21.59	$12^h12^m42^s.20$	$+46°59'29''.5$	McCrum et al. (2015)
22	SNLS-07D2bv	I	1.500	-22.49	$10^h00^m06^s.62$	$+02°38'35''.8$	Howell et al. (2013)
23	PS1-11bam	I	1.566	-22.30	$08^h41^m14^s.19$	$+44°01'56''.9$	Berger et al. (2012)
24	SNLS-06D4eu	I	1.588	-22.70	$22^h15^m54^s.29$	$-18°10'45''.6$	Howell et al. (2013)
25	PTF12dam	R	0.107	-21.40	$14^h24^m46^s.20$	$+46°13'48''.3$	Nicholl et al. (2013)
26	SN 1999as	R	0.127	-21.50	$09^h13^m46^s.28$	$+13°51'36''.9$	Hatano et al. (2001)
27	SN 2007bi	R	0.128	-21.30	$13^h19^m20^s.14$	$+08°55'43''.7$	Gal-Yam et al. (2009)
28	PSN 000123	R	0.281	-21.20	$00^h01^m23^s.36$	$+00°05'04''.2$	Kostrzewa-Rutkowska et al. (2013)
29	PS1-11ap	R	0.524	-21.40	$10^h48^m27^s.75$	$+57°09'09''.3$	McCrum et al. (2014)
30	SN2213-1745	R	2.046	-21.20	$22^h13^m39^s.97$	$-17°45'24''.5$	Cooke et al. (2012)
31	SN1000+0216	R	3.899	-21.60	$10^h00^m05^s.86$	$+02°16'23''.6$	Cooke et al. (2012)
32	SN 2006gy	II	0.019	-22.00	$03^h17^m27^s.06$	$+41°24'19''.5$	Ofek et al. (2007); Smith et al. (2007)
33	SN 2006tf	II	0.074	-20.70	$12^h46^m15^s.82$	$+11°25'56''.3$	Smith et al. (2008a)
34	SN 2008fz	II	0.133	-22.30	$23^h16^m16^s.57$	$+11°42'47''.4$	Drake et al. (2010)
35	CSS100217	II	0.147	-22.70	$10^h29^m12^s.56$	$+40°42'20''.0$	Drake et al. (2011b)
36	SN 2008es	II	0.205	-22.30	$11^h56^m49^s.13$	$+54°27'25''.7$	Gezari et al. (2009); Miller et al. (2009)
37	SN 2008am	II	0.234	-22.39	$12^h28^m36^s.25$	$+15°34'49''.1$	Chatzopoulos et al. (2011)
38	CSS121015	II	0.287	-22.60	$00^h42^m44^s.38$	$+13°28'26''.2$	Benetti et al. (2014)
39	SN 2003ma	II	0.289	-21.52	$05^h31^m01^s.88$	$-70°04'15''.9$	Rest et al. (2011)

2.2 SLSN-I

Here, we present individual transients from the SLSNe-I class, which is the most populous one, by discussing basic information and status for each of the twenty four events listed in Table 2.1. There are few transients that stick out from the rest of the class members, such examples are: SCP 06F6, which was discovered by the HST and was among the very first members of SLSNe studied by Quimby et al. (2011b); SN 2006oz, which showed for the first time a pre-peak 'bump'; iPTF13ajg, which was reported alongside

with a complete time-series of high-quality spectra and of course SNLS-07D2bv, PS1-11bam and SNLS-06D4eu, which are all discovered at high-redshift ($z > 1.5$).

PTF10hgi   was first discovered by PTF on 15th of May 2010, as announced with an ATel, by Quimby et al. (2010a). Three spectra were obtained at +33, +67 and +80 days after its peak, that confirmed its redshift at $z = 0.0985$ and its type as hydrogen-poor SLSN, as described by Inserra et al. (2013). PTF10hgi peaked at an absolute magnitude of $M_g = -20.42$ and occurred at a faint host $M_r = -16.50$.

SN 2011ke   was discovered by multiple surveys almost simultaneously. It was reported on the 30th of March 2011 by Quimby et al. (2011c) as PTF11dij, and on the 6th of April 2011 by Drake et al. (2011b) as CSS110406:135058+261642. Also, on the 15th of April 2011 Smartt et al. (2011) reported it as PS1-11xk. It was given the IAU[2] name SN 2011ke and several spectra were obtained, leading to a classification of a SLSN-I at $z = 0.143$. Photometric and spectroscopic data were published by Inserra et al. (2013), who also reported a host galaxy associated with SN 2011ke, detected at $M_r = -18.42$. SN 2011ke peaked at an absolute magnitude of $M_g = -21.42$.

SSS120810   was discovered by the Siding Spring Survey (SSS), a division of the CRTS on the 11th of August 2012 and its full name is SSS120810:231802-560926. PESSTO classified it as a SLSN-I (Inserra et al., 2012) at $z = 0.156$. A study of this object is given by Nicholl et al. (2014), which includes all the photometric data available, as well as the spectra used to classify this object and obtain the redshift of the host galaxy.

SN 2012il   was first detected and named as PTF12fo by Smartt et al. (2012) on the 19th of January 2012. Few days later, CRTS independently discovered and reported the same event as CSS120121:094613+195028 (Drake et al., 2012a). As shown by Inserra et al. (2013), its redshift of $z = 0.175$ was determined by emission lines from its faint host galaxy ($M_r = -18.18$) and it peaked at $M_g = -21.56$ two weeks after discovery. Three spectra of the SN were obtained and studied by Inserra et al. (2013).

PTF11rks   was discovered by PTF on the 21st of December 2011 (Quimby et al., 2011a). Four spectra were obtained for this SLSN-I (Inserra et al., 2013), with a redshift of $z = 0.190$ secured from the emission lines of the host galaxy, which was detected to have absolute magnitude of $M_r = -19.02$. PTF11rks peaked at $M_g = -20.76$ as shown by Inserra et al. (2013), slightly lower than the SLSNe threshold set by Gal-Yam (2012).

---

[2]International Astronomical Union

SN 2010gx was detected by CRTS as CSS100313:112547-084941 on the 13th of March 2010 (Mahabal et al., 2010). A day later, PTF independently reported the same event as PTF10cwr by Quimby et al. (2010b) as a SLSN at a redshift of $z = 0.23$, obtained by the narrow lines of the host galaxy. PS1 team recovered the transient with the name PS1-1000037, as announced by Pastorello et al. (2010b). A detailed study of SN 2010gx was given by Pastorello et al. (2010a), where a faint host was reported at $M_g = -18.0$, as well as a sequence of spectra that were taken during the SN activity. The absolute peak magnitude of SN 2010gx was reported by Pastorello et al. (2010a) to be $M_B = 21.2$ (Vega system).

SN 2011kf was first reported by CRTS as CSS111230:143658+163057 on the 30th of December 2011 (Drake et al., 2012a). Deep photometry after the SN had fainted, revealed a faint host galaxy at $M_r = -16.52$, whereas SN 2011kf had peaked at an absolute magnitude of $M_g = -21.73$. Its redshift was determined to be $z = 0.245$ from narrow emission lines of the host galaxy (Inserra et al., 2013).

LSQ12dlf was discovered on the 10th of July 2012 by the LSQ (Baltay et al., 2013) as a hostless transient. Almost a month later, the first spectrum was obtained by PESSTO, which showed similarities with a SLSN-I at a phase of +10 days past peak, and at a redshift of $z = 0.25$ (Inserra et al., 2012). After taking more spectra and comparing them with existing SLSNe, its redshift was determine at $z = 0.255 \pm 0.005$, as shown by Nicholl et al. (2014). No host galaxy emission or absorption lines were visible, whereas long after LSQ12dlf had fainted away (+300 days after peak), deep imaging showed a very faint host galaxy, with $M_V \simeq 25$ shown in Fig. 1 of Nicholl et al. (2014).

PTF09cnd was discovered by PTF on the 13th of July 2009 using the Palomar 1.5 m telescope and almost a month later, a spectrum was obtained using the 4.2m William Herschel Telescope (WHT), placing the event at a redshift of $z = 0.258$ (Quimby et al., 2011b). Its host galaxy has a limit magnitude of $M_V \gtrsim -18$, whereas PTF09cnd peaked around $M_u \sim -22$.

SN 2013dg was first discovered by CRTS on the 17th of May 2013. At the beginning of June 2013, PESSTO team used the WHT and the VLT to obtain spectra and classified this object as a SLSN-I at a redshift of $z = 0.265$ (Smartt et al., 2013a; Nicholl et al., 2014). SN 2013dg appeared to be completely hostless, as no host was detected down to magnitude $m_r > 25.6$ from deep imaging long after the SN had faded away (Nicholl et al., 2014).

SN 2005ap was one of the first SLSNe ever reported (Quimby et al., 2007). It was discovered by the TSS on the 3rd of March 2005, using the unfiltered images of the 0.45m ROSTE-IIIb (Robotic Optical Transient Search Experiment) telescope. Its peaked unfiltered absolute magnitude was determined at $M = -22.73$ and occurred few days after the discovery. Its host galaxy was detected at a magnitude of $m_V = 23.9$. Spectra that were obtained using the Hobby-Eberly Telescope (HET) and the Keck telescope, revealed the redshift of the event at $z = 0.283$ (Quimby et al., 2007).

MLS121104 was first reported on ATel#4595 by Drake et al. (2012b) among 46 other SNe candidates discovered by the CRTS. With ATel#4599 Fatkhullin and Gabdeev (2012) announced the spectroscopic classification of $MLS121104 : 021643 + 204009$ (full name) as a SLSN-I, at redshift of $z = 0.303$, that peaked at $M = -21.3$. No further information could be found for this object, such as photometry, spectrum, host galaxy information, etc.

PTF09cwl was first detected by PTF on the 28th of June 2009 (Quimby et al., 2011b). CRTS independently discovered the same object and obtained the IAU name of SN 2009jh (Drake et al., 2009b). On the 25th of August 2011, using the Keck telescope, a spectrum was obtained that classified PTF09cwl as a SLSN-I at a redshift of $z = 0.349$. Its peak magnitude was estimated around $M_u \sim -22$.

SN 2006oz was discovered by the SDSS-II SN Survey (Frieman et al., 2008) close to the end of 2006 observing season and reported by Stritzinger et al. (2006) as a 'possible type Ib' based on a spectrum obtained by the Nordic Optical Telescope (NOT). As more SLSNe spectra became available, Leloudas et al. (2012) presented SN 2006oz as a SLSN-I at a redshift of $z = 0.376$. At such redshift, SN 2006oz would have peaked at an absolute magnitude of $M_u = -21.53$ and its host would be a faint dwarf galaxy with $M_g = -16.9$. Also SN 2006oz was the first SLSNe that showed a pre-peak 'bump' in its light-curve, as seen in Fig. 2.1, which indicates towards the existence of an initial cooling phase related to a recombination wave in the CSM (Leloudas et al., 2012).

PTF09atu was discovered on the 4th of July 2009, during the commissioning of the PTF system (Quimby et al., 2011b). Few days afterwards it was identified as an interesting candidate worth of spectroscopic follow-up and a spectrum was obtained, using the Keck telescope, classifying it as a SLSN-I at a redshift of $z = 0.501$. Its peak magnitude was estimated around $M_u \sim -22$.
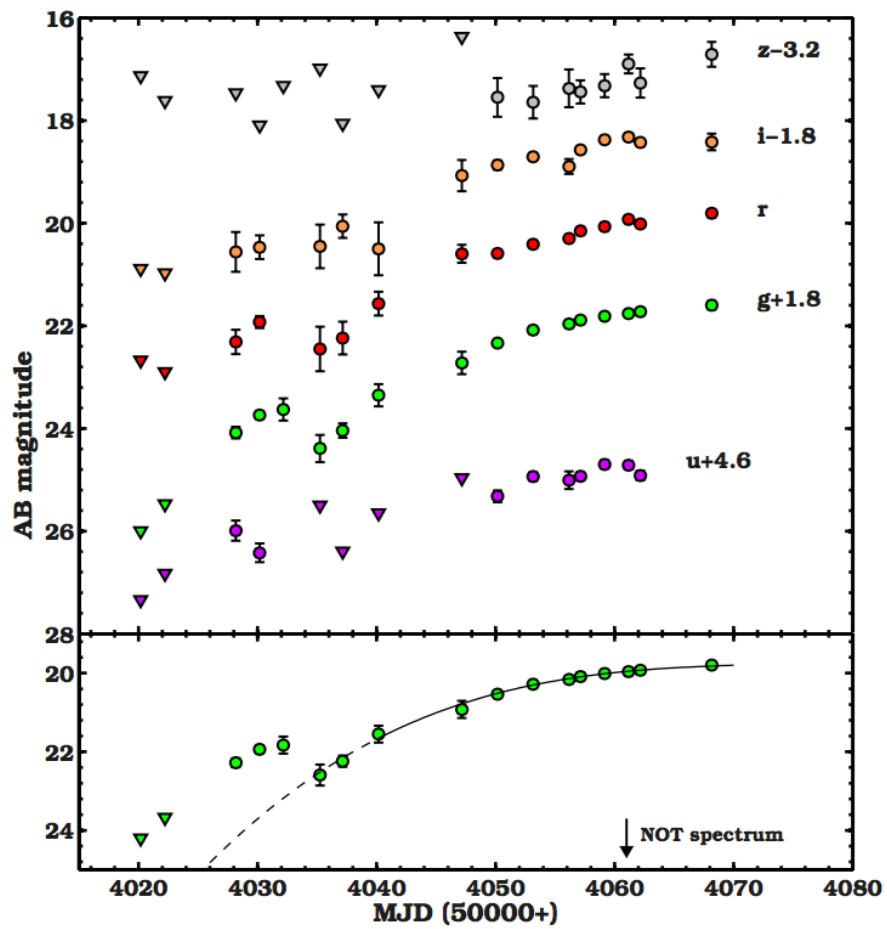
Figure 2.1: Multi-filter (*ugriz*) light-curves of SN 2006oz as obtained by the SDSS SN Survey (Frieman et al., 2008), as published by Leloudas et al. (2012). Triangles denote 3σ upper limits, whereas the lower panel focuses on the *g*-band light evolution showing clearly a pre-peak 'bump' around 38 days before maximum brightness.
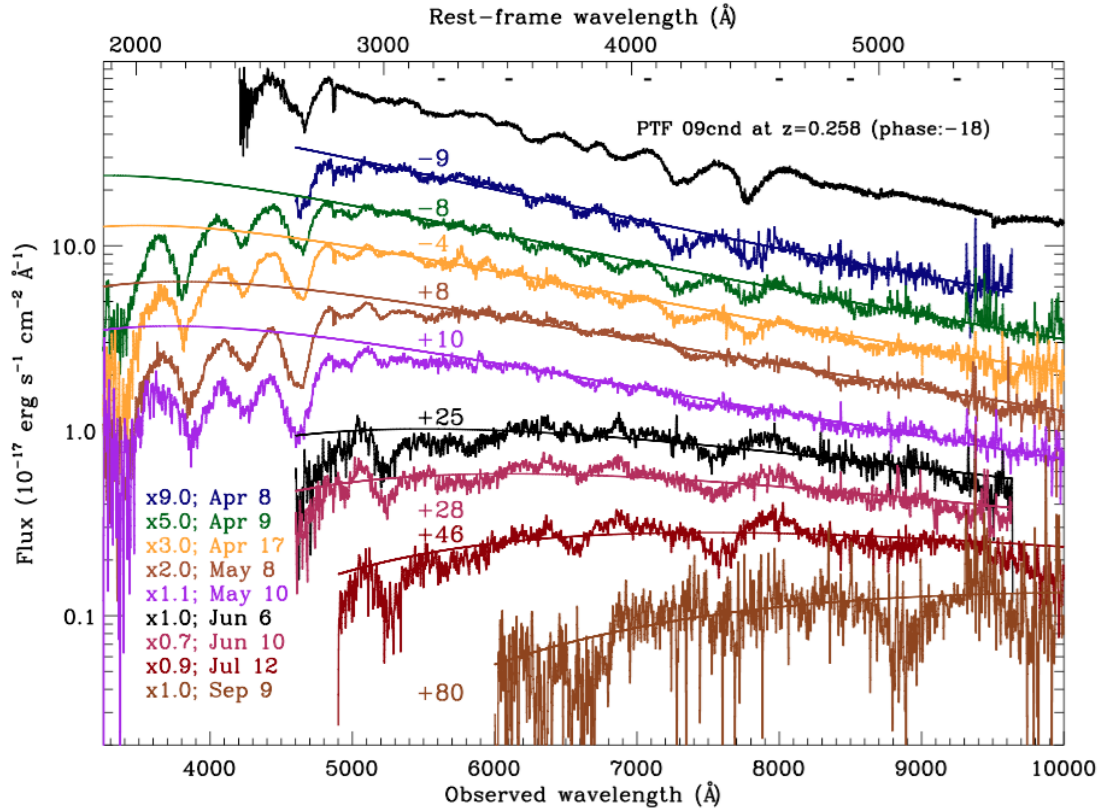
Figure 2.2: Time series of Keck/DEIMOS, Keck/LRIS, and VLT/X-shooter spectra of iPTF 13ajg. Figure taken from Vreeswijk et al. (2014).

PS1-10bzj was discovered in the PS1 Medium Deep Survey on the 16th of December 2010 (Lunnan et al., 2013). Spectroscopic follow-up with Gemini determined its host redshift at $z = 0.650$, placing PS1-10bzj to the SLSNe regime, with a peak absolute magnitude of $M_{Bol} = -21.17$. Its host galaxy was identified as a compact dwarf galaxy ($M_B = -18$).

iPTF13ajg was discovered on the 7th of April 2013 by the iPTF, and the very next night a Keck spectrum was obtained and classified the transient as a SLSN-I at a redshift of $z = 0.740$ (Vreeswijk et al., 2014). iPTF13ajg peaked at an absolute magnitude of $M_u = -22.5$, whereas late time imaging placed a limit on the absolute magnitude of the faint host galaxy at $M_B \gtrsim -17.7$. Nine, high quality spectra were obtained by Keck and VLT telescopes during the life span of the transients' light-curve, as shown in Fig. 2.2.

PS1-10awh was first detected by PS1 in early October 2010 and was observed throughout the end of the observing window of its field in early December 2010 (Chomiuk

et al., 2011). Three optical spectra were obtained, that classified PS1-10awh as a SLSN-I at a redshift of $z = 0.908$, which translates to a peak absolute magnitude around $M_{Bol} \sim -22.50$. Its host galaxy has a limit on its absolute Magnitude of $M_B > -18.4$.

PS1-10ky was discovered right at the start of the observing season of PS1 in June 2010 (Chomiuk et al., 2011). Its light-curve follow-up starts near peak brightness, which reached $M_{Bol} = -22.50$, as the redshift was determined at $z = 0.956$. Four optical spectra were taken just before peak brightness and afterwards. Its host galaxy has a limit on its absolute magnitude of $M_B > -19.4$.

SCP 06F6 was first reported as an unusual optical transient discovered during the Hubble Space Telescope Cluster Supernova Survey (Barbary et al., 2009). It was discovered on the 21st of February 2006 and identified as a hostless event in a field centreed on the galaxy cluster CL1432.5+3332.8, which had a redshift of $z = 1.112$ (Elston et al., 2006). Three spectra were obtained using Subaru, VLT and Keck telescopes, but due to the small number of SLSNe events at the time, Barbary et al. (2009) did not attempt any classification by spectra comparison. Due to the redshift of the targeted cluster ($z = 1.112$), Barbary et al. (2009) mentioned the similarity on the peak brightness of SCP 06F6 with known SLSNe at that time. Quimby et al. (2011b) compared SCP 06F6 spectra with PTF09atu, PTF09cnd, PTF09cwl and SN 2010gx, and came to the conclusion that all five transients belong to the family of SLSNe-I. The redshift of SCP 06F6 was determined at $z = 1.189$ and peaked at an absolute magnitude of $M_u = -22.3$.

PS1-10pm was first detected by PS1 on the 24th of February 2010 and was followed-up until the observing season's end on the 20th of June 2010 (McCrum et al., 2015). Two spectra were obtained with the Gemini North telescope, resulting to a redshift of $z = 1.206$. At such redshift, PS1-10pm reached a peak absolute magnitude of $M_U = -21.59$. The host galaxy remained undetected by PS1, but using deep imaging with the Gemini North telescope at the position of PS1-10pm, it was observed in z-band at $m_z = 24.86$, which corresponds to an absolute magnitude of $M_z = -18.9$.

SNLS-07D2bv was discovered by SNLS on the 22nd of February 2007 as a hostless possible SN type-Ia (Howell et al., 2013). A spectrum of the event was obtained by VLT, that showed a lot of similarities with SCP 06F6 and SNLS-06D4eu, thus placing an estimation on the redshift of about $z = 1.5$. At such redshift, SNLS-07D2bv would have peaked at an absolute magnitude of $M_U = -22.49$.

PS1-11bam was discovered on the 12th of November 2011 by PS1 and was detectable for ~ 110 days after, as reported by Berger et al. (2012). Using the MMT and Gemini telescopes, Berger et al. (2012) obtained three spectra after peak brightness, which showed similarities with other SLSNe-I events and placed the redshift at $z = 1.566$. At such redshift, PS1-11bam peaked at an absolute magnitude of $M_i = -22.3$, whereas its host galaxy absolute magnitude was measured to be $M_{UV} \approx -20.7$.

SNLS-06D4eu was discovered by SNLS on the 20th of August 2006 and was initially thought to be a SN type-Ia (Howell et al., 2013). Spectroscopic follow-up revealed its nature as a SLSN-I at a redshift of $z = 1.588$, which place the peak absolute magnitude of SNLS-06D4eu at $M_U = -22.7$. Its redshift was also confirm via clear emission lines from the host galaxy.

2.3 SLSN-R

Here we present individual SLSNe-R, by discussing basic information and status for each of the seven events listed in Table 2.1. Among the most 'famous' members of this class are: SN 2007bi, which is the first ever pair-instability SNe detected and since then it constitutes the model for this class; as well as the SN with the highest redshift reported to date: SN1000+0216 at $z = 3.899$.

PTF12dam was first reported by PTF on the 23rd of May 2012 (Quimby et al., 2012) and its photometric light-curve was recovered afterwards by PS1 (Nicholl et al., 2013). The decline rate and several spectra that were taken, show extreme similarities with SN 2007bi (Gal-Yam et al., 2009), a PISN, whereas the rise phase of PTF12dam is evolving faster than SN 2007bi. In addition, strong host galaxy lines placed PTF12dam at a redshift of $z = 0.107$.

SN 1999as was discovered on the 18th of February 1999 during the LBNL 1999 nearby supernova campaign and first reported by Hatano et al. (2001), classified as an unusual SN Ic at a redshift of $z = 0.127$. At such redshift, Hatano et al. (2001) noted its extreme brightness, at least $M_V \lesssim -21.5$, but it was Gal-Yam (2012) who first included this object as a SLSN type-R, based on spectral similarities with other members of this group.

SN 2007bi was first detected on the 6th of April 2007 (Chornock et al., 2007), by the SN Factory program (Aldering et al., 2002). It was studied thoroughly by Gal-Yam et al. (2009), who explored its nature as the first pair-instability SNe (PISN) (see also Sec. 1.5.3). It occurred at a redshift of $z = 0.1279$, thus reaching a peak absolute magnitude

of $M_R = -21.3$. Its light curve rose very slowly (~ 77 days) and it was spectroscopically followed-up with several telescopes, even at late times of the light-curve. SN 2007bi host galaxy is a dwarf, metal-poor galaxy with an absolute magnitude of $M_B = -16.3$.

PSN 000123+000504   was presented by Kostrzewa-Rutkowska et al. (2013) as a plausible SLSNe in SDSS Stripe-82 data that was overlooked by the SDSS SN survey. PSN 000123 hereafter, peaked at late September 2005 and was retrieved from the archival data of SDSS. It is associated with an irregular dwarf galaxy with an absolute magnitude of $M_B = -18.2$, at a redshift of $z = 0.281$, derived by late time spectra of the host galaxy from the Keck telescope. At such redshift, PSN 000123 peaked at an absolute magnitude of $M_g = -21.3$. The light-curve behaviour of PSN 000123 resembles other SLSN-R objects, such as SN 2007bi and PTF12dam.

PS1-11ap   was discovered by the PS1 on the 2nd of January 2011 and first reported by Nicholl et al. (2013). A more in detail study, where PS1-11ap photometry was published was given by McCrum et al. (2014). Narrow emission lines from the host galaxy provided a redshift of $z = 0.524$, which leads to a peak absolute magnitude of $M_U = -21.4$. PS1-11ap also falls in the same category as PTF12dam , both objects being similar to SN 2007bi but with a faster evolving rise phase.

SN2213-1745   was discovered after the completion of the SNLS program by modifying the image stacking and analysis technique, as described by Cooke et al. (2012). SN2213-1745 was detected in the 2005 and 2006 observing seasons' stacked images and a late Keck spectrum was obtained (~ 5 years after first detection). Its host galaxy is a Lyman brake galaxy (LBG) at a redshift of $z = 2.046$ and its absolute magnitude reached $M_{FUV} = -21.38$. Its light-curve behaviour lead to classify SN2213-1745 as a SLSN-R or PISN, like SN 2007bi.

SN1000+0216   was also discovered using the same method as SN2213-1745, as shown by Cooke et al. (2012). It was detected from the 2006-2008 image stacks and a late time spectrum (~ 4 years after first detection) was obtained with Keck telescope, placing its LBG host galaxy to a record high redshift of $z = 3.899$. It was also classified as a SLSN-R, similar to SN2213-1745 and SN 2007bi.

2.4 SLSN-II

Here, we present individual SLSNe-II, by discussing basic information and status for each of the eight events listed in Table 2.1. SN 2006gy could be considered as the most
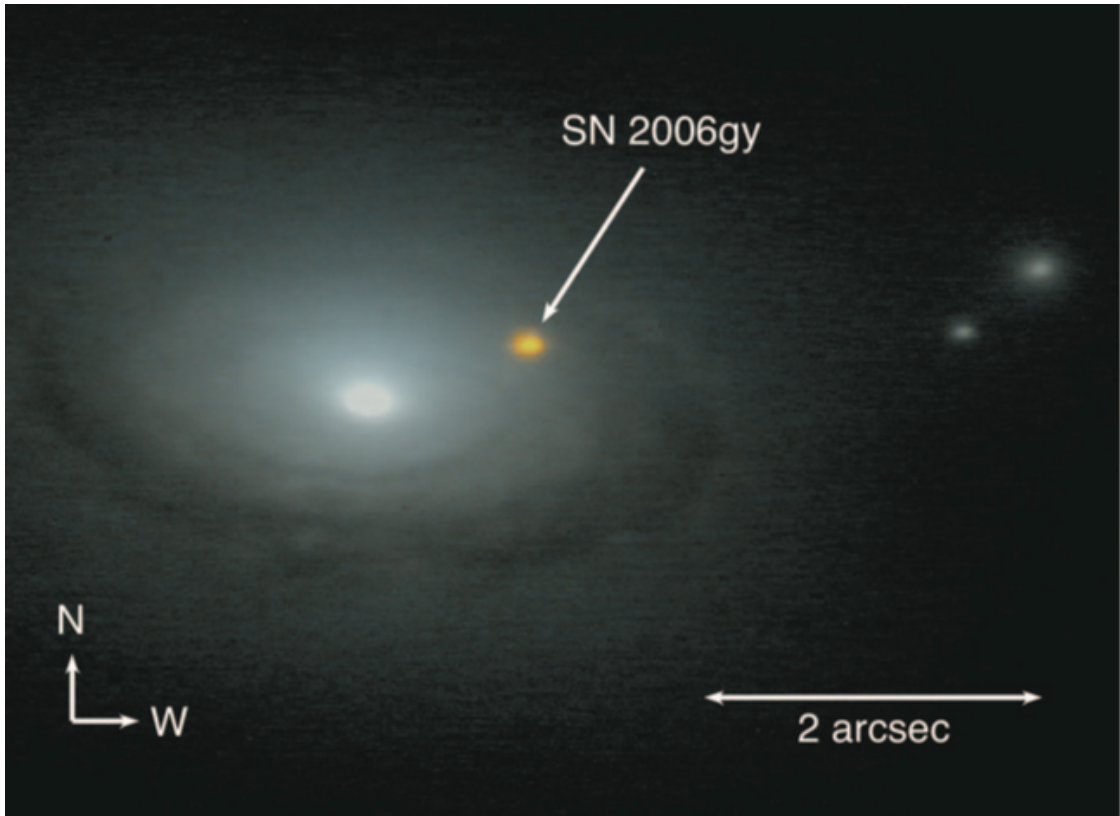
Figure 2.3: False-colour IR image of the core of NGC 1260 and SN 2006gy, generated from Keck LGS/NIRC2 H-band and K0-band observations on 2007 December 1. SN 2006gy is red and very luminous in the near-IR, more than a year after explosion. Figure taken from Smith et al. (2008b).

important event of this class as it occurred in NCG 1260, a nearby galaxy; allowing extensive follow-up studies, which improved our understanding of the behaviour of the SLSNe light-curves.

SN 2006gy   was first detected by the ROSTE-IIIb telescope (Quimby, 2006a), $2''$ away of the centre of NGC 1260, as seen in Fig. 2.3. Two independent analyses were constructed almost simultaneously by Ofek et al. (2007) and Smith et al. (2007), characterizing SN 2006gy the most luminous SNe to that date, placing its peak absolute magnitude at $M = -22.0$, since NGC 1260 has a redshift of $z = 0.019$. Several spectra were obtained (Smith et al., 2010), re-confirming its nature at a SLSNe-II (hydrogen-rich) caused by shock interactions with dense circumstellar medium (CSM). Because SN 2006gy occurred fairly close to us, it was followed-up extensively, even ~ 2 years after its discovery (Smith et al., 2008b; Miller et al., 2010).

SN 2006tf   was discovered on the 12th of December 2006 by the TSS, and was reported as one of the three most luminous SNe to date by Smith et al. (2008a). Its host galaxy is

a faint galaxy with an apparent magnitude of $m_R = 20.68$ and at a redshift of $z = 0.074$. SN 2006tf was discovered after its peak brightness, which led to an upper limit to its peak absolute magnitude of $M < -20.7$. This value is just below the SLSNe threshold of $M_U < -21$ set by Gal-Yam (2012). Smith et al. (2008a) presented several spectra of SN 2006tf that were obtained, showing similarities with SN 2006gy, and led to its classification as a SLSNe-II.

SN 2008fz was first discovered on the 22nd of September 2008 by the CRTS, as reported by Drake et al. (2008). In a detailed study of SN 2008fz, Drake et al. (2010) showed that no host galaxy was detected down to an absolute magnitude limit of $M_r > -17$. Furthermore, three transients' spectra were obtained, showing clear Balmer lines, evidence for a SLSN-II at a redshift of $z = 0.133$, which places the peak absolute magnitude of SN 2008fz at $M_V = -22.3$.

CSS100217:102913+404220 (CSS100217 hereafter) was discovered on the 17th of February 2010 by the CRTS (Drake et al., 2011a). Spectroscopic observations related CSS100217 with a host galaxy at redshift of $z = 0.147$, which translates to a peak absolute magnitude of $M_V = -22.7$. Its extreme luminosity and strong narrow Balmer features place CSS100217 to the SLSN-II class, similar to SN 2006gy.

SN 2008es was first reported on the 26th of April 2008 by Yuan et al. (2008a) as an AGN. Later two independent studies (Gezari et al., 2009; Miller et al., 2009) presented the case for an extremely luminous type-II SNe. Its host galaxy has a redshift of $z = 0.205$ and a absolute magnitude limit of $M_V > -17.4$. SN 2008es peaked at an absolute magnitude of $M_V = -22.3$.

SN 2008am was discovered by the ROSTE-IIIb on the 10th of January 2008 (Yuan et al., 2008b). It was followed-up photometrically in optical and near-IR as presented by Chatzopoulos et al. (2011). Several spectra were obtained with HET and using narrow emission lines SN 2008am was classified as SLSN-II at a redshift of $z = 0.234$. At such redshift SN 2008am peaked at an absolute magnitude of $M = -22.3$. Its host galaxy was determined to be a faint galaxy with an absolute magnitude of $M_r \sim -20$.

CSS121015:004244+132827 (CSS121015 hereafter) was first detected by CRTS on the 15th of September 2012 (Drake et al., 2012c). After first spectrum was obtained, Tomasella et al. (2012) reported an initial redshift estimate of $z \sim 0.286$, starting an extensive follow-up campaign by PESSTO. Benetti et al. (2014) presented the extensive photometric light-curve of CSS121015, as well as a secured redshift of $z = 0.2868$ from
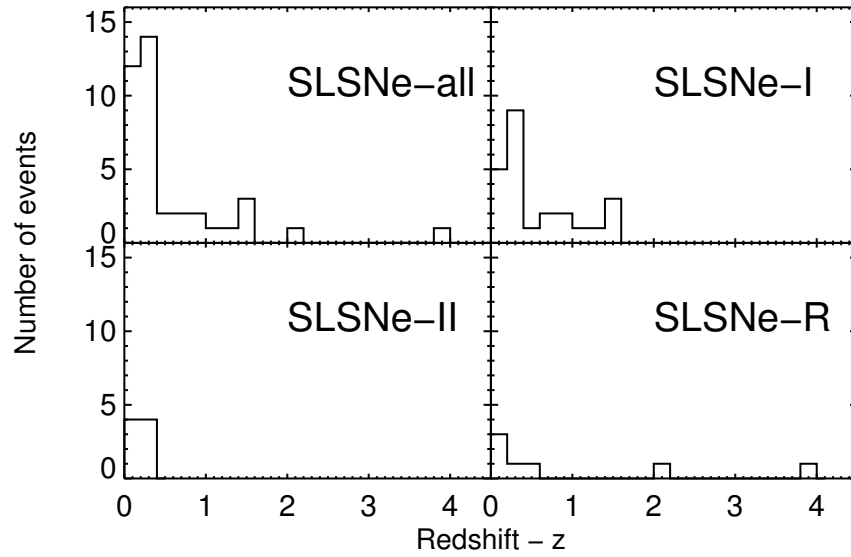
Figure 2.4: The spectroscopic redshift distribution of all the SLSNe events listed in Table 2.1, plotted also as separate types of SLSNe. As noted in Table 2.1, eight SLSNe-II type events have been reported up to a maximum redshift of $z = 0.289$, as shown in the bottom left hand side panel.

narrow emission lines. At such redshift, CSS121015 peaked at an absolute magnitude of $M_B = -22.6$, whereas its faint host galaxy has an absolute magnitude limit of $M_r \gtrsim -17.9$.

SN 2003ma was discovered on the 17th of December 2003 by SuperMACHO microlensing survey and studied by Rest et al. (2011). Its light-curve has a duration of 4.7 years due to the location of SN 2003ma, right behind the Large Magellanic Cloud (LMC), which was monitored for 5 observing seasons by SuperMACHO. SN 2003ma was spectroscopically followed-up for almost 6 years, with several narrow galactic lines identified and placing a redshift of $z = 0.289$, at which SN 2003ma peaked at an absolute magnitude of $M_R = -21.5$.

2.5 Summary

In this chapter, I briefly discussed all confirmed SLSNe that exist in the literature as of June 2015. The list provided in Table 2.1 consists of 39 SLSNe objects, their redshift and absolute magnitude information, as well as the relevant references for each event.

Fig. 2.4 shows the redshift distribution of the 39 SLSNe listed in Table 2.1 altogether, as well as separated in their three classes, introduced by Gal-Yam (2012) and adopted
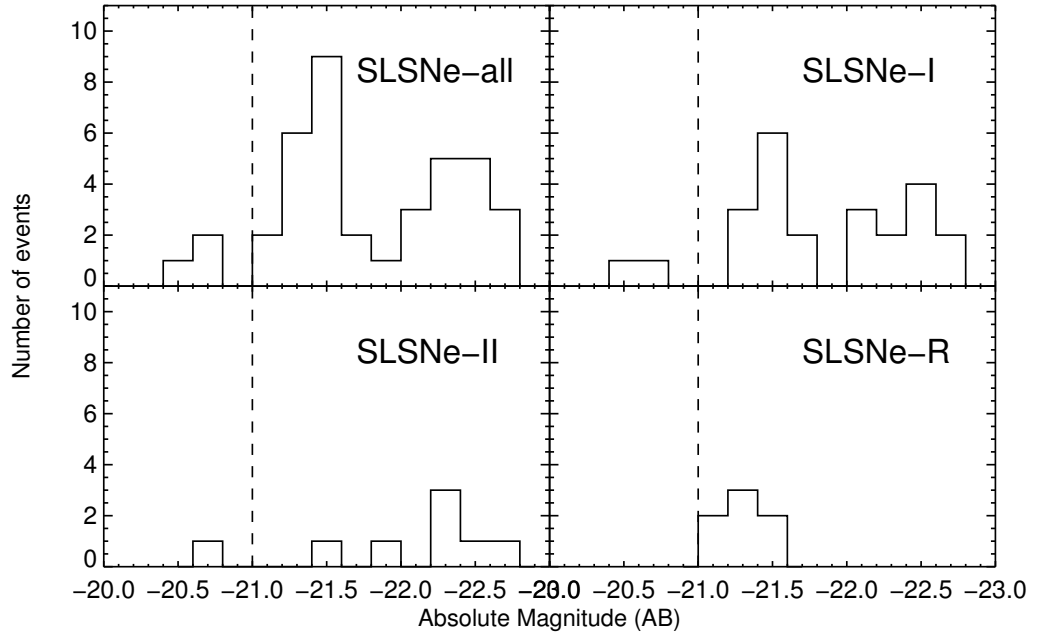
Figure 2.5: The absolute AB magnitude distribution of all the SLSNe events listed in Table 2.1, plotted also as separate types of SLSNe. The dashed line illustrates the absolute magnitude limit of $M < -21$ set by Gal-Yam (2012).

for this thesis (see Sec. 1.5.2). The majority (61.5%) of the events listed were reported as SLSNe-I. Only seven events were reported as SLSNe-R, and this class contains the two more distant events reported to date, at z=2.046 and z=3.899. The remaining eight events were classified as SLSNe-II, and the highest redshift reported was 0.2889. Many studies have already noted this discrepancy on the redshift distribution and rates between the SLSNe classes (Gal-Yam, 2012; McCrum et al., 2015).

Fig. 2.5 shows the reported absolute magnitude distribution of the 39 SLSNe listed in Table 2.1. It is important to note here that the reported absolute magnitude is given in different filters for each event, with the majority to be reported in the U-band (M_U). A few events have absolute magnitudes lower than the SLSNe threshold of $M \leqslant -21$ set by Gal-Yam (2012), whereas the highest absolute magnitude reaches out to -22.73. The reported absolute magnitude distribution of the 24 SLSNe-I (top part of Table 2.1), shows two prominent peaks. Those two peaks could be originated from the existence of two different populations (or sub-categories) within the SLSNe-I class. A similar argument was made by Inserra et al. (2013) and Inserra and Smartt (2014), as they divided the SLSNe-I used in their studies, into two observational groups using the terms: SN2005ap-like and SN2007bi-like for faster and slower evolving events, respectively.

In the following chapters of this thesis, the redshift and absolute magnitude limits reported in this chapter are explored and extended, with newly discovered SLSNe by the Dark Energy Survey.

Chapter 3

The Dark Energy Survey - Year One

3.1 Introduction

This chapter starts with a brief summary of my involvement in the commissioning period of DECam, known as 'Science Verification'. Further in the chapter, I describe in detail the DES SN Survey as it happened in Y1 of operations; including image acquisition, data processing, human and machine scanning of candidates, obtaining spectra using telescopes around the world and finally, discovery and confirmation of SNe. I will then focus on the processes used to select SLSNe events in DES Y1 data and finally, I will end the chapter with the findings and the lessons learned from Y1 of observations.

3.2 Science Verification and Eyeball Squad

The DES SV period started officially on the 12th of September 2012, with the acquisition of the 'first-light' images of DECam seen in Fig. 1.11. The eight years of planning, construction and installation of DECam came to a successful end on that date, marking the beginning of the SV period, at the end of which DECam was deemed ready for science operations.

As stated in the SV (DES-internal) report: *'the purpose of SV was to establish that the camera, telescope, operations, and data-handling systems were producing imaging data of sufficient quality to execute the Dark Energy Survey.'* Therefore all components of the survey, such as the observing operations and strategy, the image transfer and data reduction pipelines, the data management processes and the assessment of the data quality from the various working groups of the collaboration were tested during the SV season.

Such massive effort, required the maximum workforce in order to be completed in time, and as I was at the beginning of my involvement with DES I joined the 'Eyeballing Squad', described in detail in the following subsection.
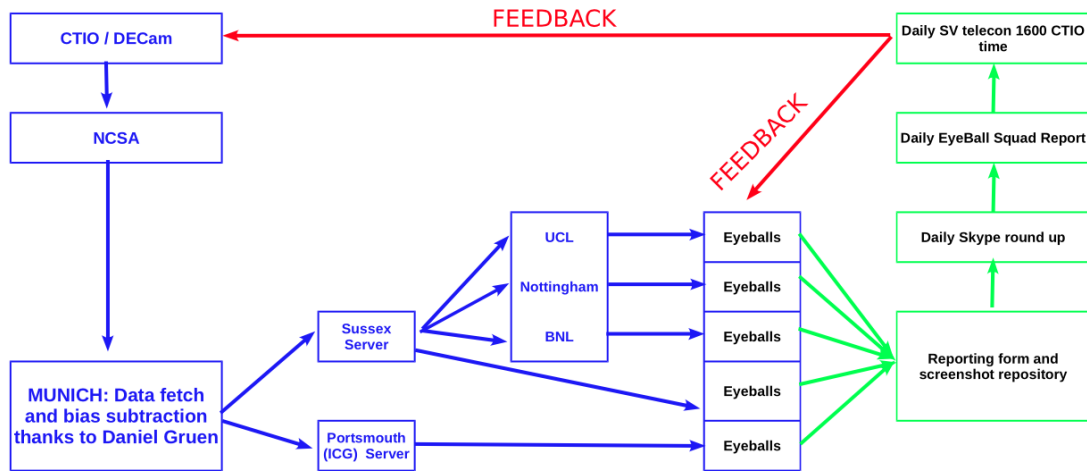
Figure 3.1: Flow chart of the daily operations of the DES Eyeball Squad, which was active during the SV season (November-2013 until Feb-2014) and at the very beginning of Y1 season (September 2014). After the first week of operation, SCIAMA - Portsmouth (ICG) Server became the main storage facility of the daily image income. After the daily Skype round up of the eyeballers and short discussion and sharing of our findings, we reported back to the daily SV operations tele-conference with the observers at Chile. Then, after assessing the feedback from the eyeball squad and checking the observing objectives, the SV operation coordinators would draw the observing plan for the upcoming night. *Flow chart created by Dr.Marisa March.*

3.2.1   Eyeball Squad

The SV observations lasted from November 2012 until February 2013, and during that time I participated in a task force team called 'Eyeball Squad', charged with the task to visually inspect all the images taken by DECam on a daily basis. Our objective was to report any anomalies on the images and inform the observers of any problems before the next observing run.

Fig. 3.1 shows the flow chart of the Eyeball squad's daily operations, which would start immediately after the first images were obtained by DECam in Chile, which were transferred to Germany overnight. There, the raw-images were ran through a quick reduction pipeline, governed by Daniel Gruen. Then, the reduced-images were stored locally on SCIAMA[1] (Sepnet Computer Infrastructure for Astrophysical Modeling and Analysis), a high performance compute cluster, founded by the South East Physics Network (SEPNet) and hosted by the ICG, University of Portsmouth.

Then, volunteers were assigned $\sim 20 - 30$ images each based on a rota, to visually inspect by noon (UK time), at which time a round-up tele-conference (via SKYPE) would take place among the eyeballers to share screen-shots of known and most importantly,

---

[1]http://www.sciama.icg.port.ac.uk

(a) 'Pupil' ghost

(b) 'Arc' ghosts

(c) Edge bleeding

(d) Elongated PSF

(e) Donut shaped PSF

(f) Double PSF-'guider jump'

(g) CCD N31 failure

(h) CCD 'bar code'

(i) CCD 'stripes'

(j) Excessive cosmic rays

(k) Rotating satelite

(l) Orion Nebula
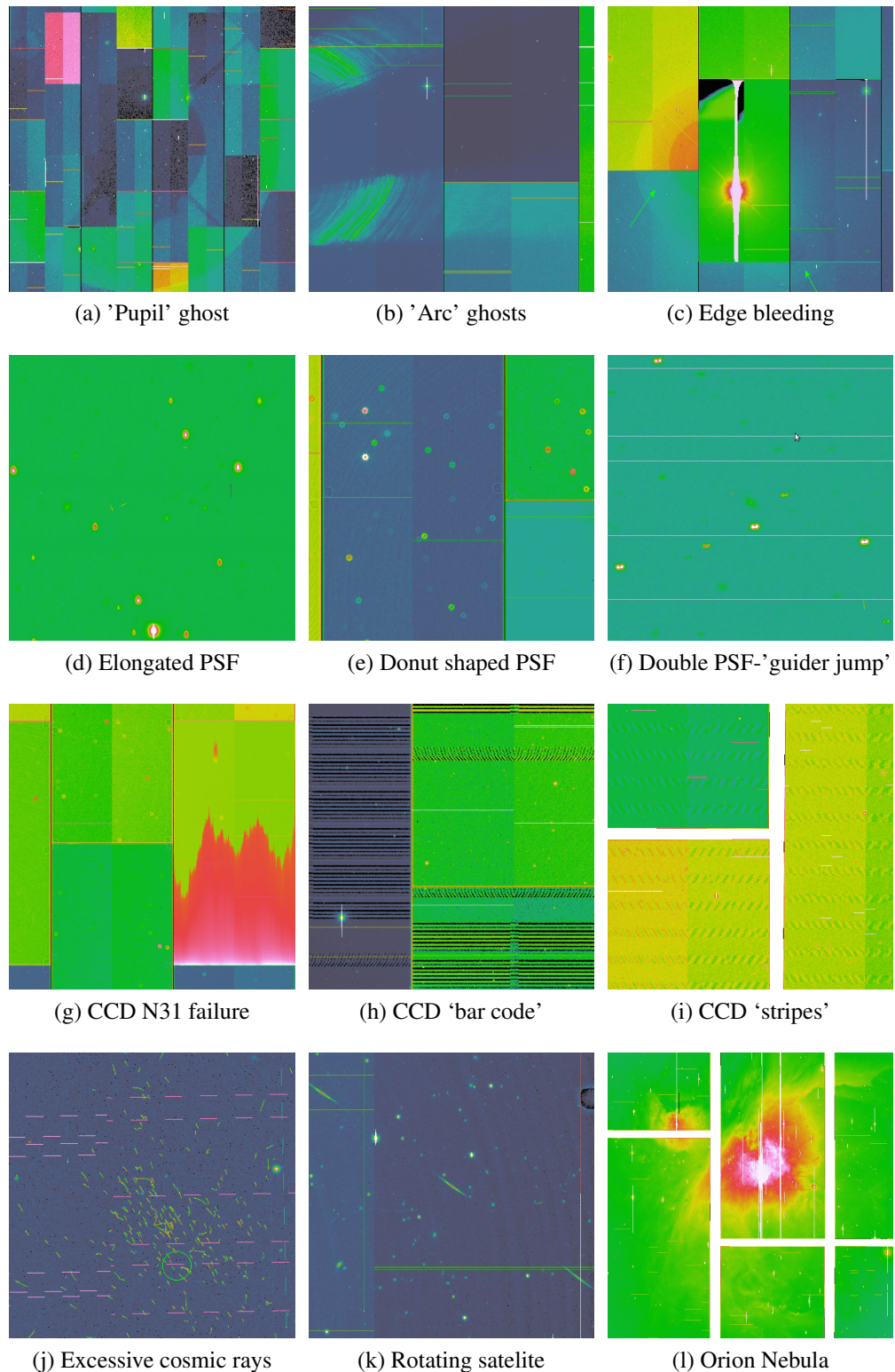
Figure 3.2: Twelve examples of what we discover during the operation of the Eyeball squad. Panels (a) and (b) show examples of 'ghosts', probably caused by scattered light through the lenses of the camera, whereas panel (c) shows an 'edge bleeding' example, caused by the excess photons from a close-by bright star. Panels (d), (e) and (f) show examples of bad formed PSFs, that were the top priority for the Eyeballing squad to report. At the third row, panels (g), (h) and (k), show examples of failure at the CCD read-out process and in particular, panel (g) shows the permanent failure of chip N30. Panels (j), (k) and (l) show examples related to physical objects such as cosmic rays, a rotating satellite and Orion's nebula respectively.

unknown anomalies. Afterwards, a daily 'Eyeball report' was prepared and presented to the daily (16:00 CTIO time) tele-conference, where the observing plan for the imminent night was discussed. The observing strategy was then adjusted to any new anomalies found by the eyeball squad, in order to improve the DECam's image quality.

The visual inspection of the images was carried out using the application SAOIMAGE DS9[2]; and included a quick overview of the entire DECam FoV and a detailed zoomed-in inspection of each of the 62 science CCDs. This daily effort lead to the creation of a key word lexicon for all the different kind of anomalies, which are explained in detail below and seen in Fig. 3.2.

Ghosts are seen in Fig. 3.2 panels (a) and (b). They are named as 'pupil' and 'arcs' ghosts respectively. The cause of such artefacts is scattered light within the camera's filter changer that enters at the extreme edges of the filters. This effect was eliminated by the end of SV period, after shielding the edges of the filter cells, as described in section 6.3 of Flaugher et al. (2015).

Edge bleeding artefact, as seen in Fig. 3.2 panel (c), is caused by the excess in detected photons that are coming from a close-by bright star, in combination with a malfunction during the CCD read-out process. This issue was resolved after the upgrades on DECam's control system, SISPI (Diehl and For the Dark Energy Survey Collaboration, 2012; Flaugher et al., 2015, and Sec.1.4.1).

Point Spread Function - PSF artefacts are shown in the second row of Fig. 3.2 in panels (d), (e) and (f). Such artefacts were reported as top priority to the SV operations team. The elongated and double PSF, panels (d) and (f) respectively, were caused by malfunction of the telescope's guider system and led to the complete dismount and repair of this system within the first engineering window of the SV season. The donut shaped PSFs shown in panel (e) were the result of malfunction of the hexapod's software, which serves as the focusing system of DECam (see also 1.4.1). The malfunction was resolved after updating the hexapod's software.

CCD readout malfunctions are shown in panels (g), (h) and (k) of Fig. 3.2. In particular, panel (g) shows the non-linear behaviour of chip N30, which has not been used in any science images since the SV period. Whereas panels (h) and (k) show two different CCD readout malfunctions, named as 'bar-code' and 'stripes' artefacts respectively, both of which were fixed after updating the CCD readout routines.

---

[2]http://ds9.si.edu/site/Home.html

Miscellaneous   artefacts that are not produced by the telescope's or camera's systems are shown in the fourth row in Fig. 3.2. Excessive cosmic rays activity is shown in panel (j), a rotating satellite that leaves a 3-dashes sky trail is shown in panel (k) and finally the light-saturated centre of Orion's nebula is shown in panel (l) covering multiple CCDs. Such artefacts are masked out from the images using computer algorithms depending on the science goal.

After the first month and a half of the SV period, we noticed that we were not reporting any new and unknown anomalies, which meant that the combination of the telescope's and the camera's systems were working in stable conditions, not producing any new artefacts on the science images. Most of the anomalies reported above were related to software issues, which were resolved, as the data pipelines and the camera's software were updated and finalised (Flaugher et al., 2015). Some major telescope-related issues were address quickly, as a result of this eyeball effort, such as 'double PSFs' and the telescope's guider (Fig. 3.2 panels (d) and (f)), or the permanent failure of CCD N31 (Fig. 3.2 panel (g)).

By the end of the SV season, more than 3000 individual exposures were visually inspected by the members of the Eyeball Squad. The success of this effort led to the repetition of the same actions on a smaller scale at the beginning of the Y1 of operations. This tactic was followed in order to verify the good working condition of the telescope and the camera after the first DES off-season period, when both were used by the wider astronomical community via the CTIO, NOAO observing programs. Within a few days of visual inspection of a couple of hundreds of DECam exposures, we were able to confirm that the telescope and the camera were operating in excellent condition and were producing science quality images (Diehl and For the Dark Energy Survey Collaboration, 2012).

My personal involvement within the eyeball squad could be summarised by the visual inspection of 500 exposures, the training of other eyeballers at ICG-Portsmouth and by the set-up of the shared directories, which were used to store the DECam exposures to the local SCIAMA computer cluster. Finally, when the eyeball squad was reused at the beginning of Y1, I manage to visually inspected ~ 100 DECam exposures.

3.3 DES Supernova Survey

As was briefly stated in Sec. 1.4.3, the objective of DES SN Survey is to create a homogeneous sample of ~ 3500, high quality SNe Ia for use in cosmology, within a redshift range of $0.05 \leq z \leq 1.2$, as illustrated in Fig. 1.14. Bernstein et al. (2012) presented an

Table 3.1: The time optimization of each DES filter in both sets of SN fields, shallow and deep. Also, the corresponding magnitude limits for the reported times are given in the fifth and ninth columns respectively and refer to point source detections at 5σ using a single filter observation, as they were calculated by Bernstein et al. (2012).

Filter	Shallow Fields				Deep Fields			
	# Exp	Exp Time (s)	Total Time (s)	Mag (AB)	# Exp	Exp Time (s)	Total Time (s)	Mag (AB)
g	1	175	175	24.9	3	200	600	25.6
r	1	150	150	24.3	3	400	1200	25.4
i	1	200	200	23.9	5	360	1800	25.1
z	2	200	400	23.8	11	330	3630	24.8

extensive analysis of simulated SNe light-curves in order to finalise the DES SN Survey strategy, including field selection, time optimization, use of the spectroscopic resources, treatment of contamination samples. Finally, Bernstein et al. (2012) estimated the uncertainty on the cosmological parameters that the proposed strategy would be able to deliver at the end of the survey.

The DES SN Survey strategy that was selected and implemented, was named by Bernstein et al. (2012) as 'hybrid-10 fields' and its predicted redshift distribution is illustrated by the solid black line in Fig. 1.14. This section describes in detail the implementation of the proposed 'hybrid-10 fields' SNe strategy by DES in Y1 of operations, as well as the integration of this strategy with the DES-wide survey.

3.3.1   SN Fields

The DES SN Survey monitors 30 deg^2, in $griz$ bands, spread-out to the 10 'hybrid-fields' proposed by Bernstein et al. (2012). The name 'hybrid' was adopted as an indication to the two 'deep' and eight 'shallow' fields, as proposed by Bernstein et al. (2012), as the best choice of strategy in terms of number of SNe discovered within the available fixed time allocation of the DES SN Survey. The depth ('deep/shallow') of the fields is the result of the time optimization seen in Table 3.1, alongside the corresponding magnitude limits, which were calculated by Bernstein et al. (2012) using data simulations.

The fields are located in the XMM-LSS[3], ELAIS-S[4], CDF-S[5] and 'Stripe82' regions. The 10 SN fields names and locations are listed in Table 3.2 and presented in Fig. 1.13 alongside the DES footprint. The names of the 10 SNe fields are constructed using the

---

[3]XMM-Newton Large Scale Structure (XMM-LSS) survey
[4]European Large Area ISO Survey (ELAIS)
[5]Chandra Deep Field South (CDF-S)

Table 3.2: The 10 SN field locations in right ascension and declination, in decimal (2nd and 3rd columns) and sexagesimal (4th and 5th columns) format. The locations on the sky are shown in Fig. 1.13. The two 'deep' SN fields are marked with an asterisk (*).

NAME	RA	DEC	RA	DEC
E1	7.87440	-43.0096	00:31:29.86	-43:00:34.6
E2	9.50000	-43.9980	00:38:00.00	-43:59:52.8
S1	42.82000	0.0000	02:51:16.80	00:00:00.0
S2	41.19440	-0.9884	02:44:46.66	-00:59:18.2
C1	54.27430	-27.1116	03:37:05.83	-27:06:41.8
C2	54.27430	-29.0884	03:37:05.83	-29:05:18.2
C3*	52.64840	-28.1000	03:30:35.62	-28:06:00.0
X1	34.47570	-4.9295	02:17:54.17	-04:55:46.2
X2	35.66450	-6.4121	02:22:39.48	-06:24:43.6
X3*	36.45000	-4.6000	02:25:48.00	-04:36:00.0

first letter of the region (X, E, C and S) and an identification number 1 or 2 for the 'shallow' fields and 3 for the 'deep' fields.

The 10 SNe field locations were selected in order to maximize the overlap with other past or future surveys and the observability of the fields, as seen from the CTIO's side. Furthermore the exact locations of nearby stars, as well as the dust extinction due to the Milky Way (MW) were taken into consideration to minimize light contamination. Fig. 3.3 illustrates the locations of the three DES SN fields in the XMM-LSS region, overplotted with an extinction map of the MW, and relative to other surveys' field locations, such as: VIDEO[6], SWIRE[7] , VVDS[8], CFHTLS[9] and XMM-LSS.

3.3.2 Time optimization

The differences in strategies between the DES-wide survey and DES SN Survey (see Sec. 1.4.2) affect the time optimization of the observations, both on individual exposure duration and long term scheduling. The strategy for the DES wide survey is to cover the $5000\,\text{deg}^2$ to the desired depth after 10 tilings (a tiling is one complete visit to the entire survey area in one filter), in $grizY$ filters. While the time duration of each DECam exposure used for the DES-wide survey remains constant at 90 seconds for each filter, for the SN Survey's exposure times vary based on filters and field's depth, as shown in Table 3.1.

---

[6]VISTA Deep Extragalactic Observations (VIDEO) survey
[7]Spitzer Wide-area InfraRed Extragalactic (SWIRE) survey
[8]VIMOS VLT Deep Survey (VVDS)
[9]Canada-France-Hawaii Telescope Legacy Survey (CFHTLS)
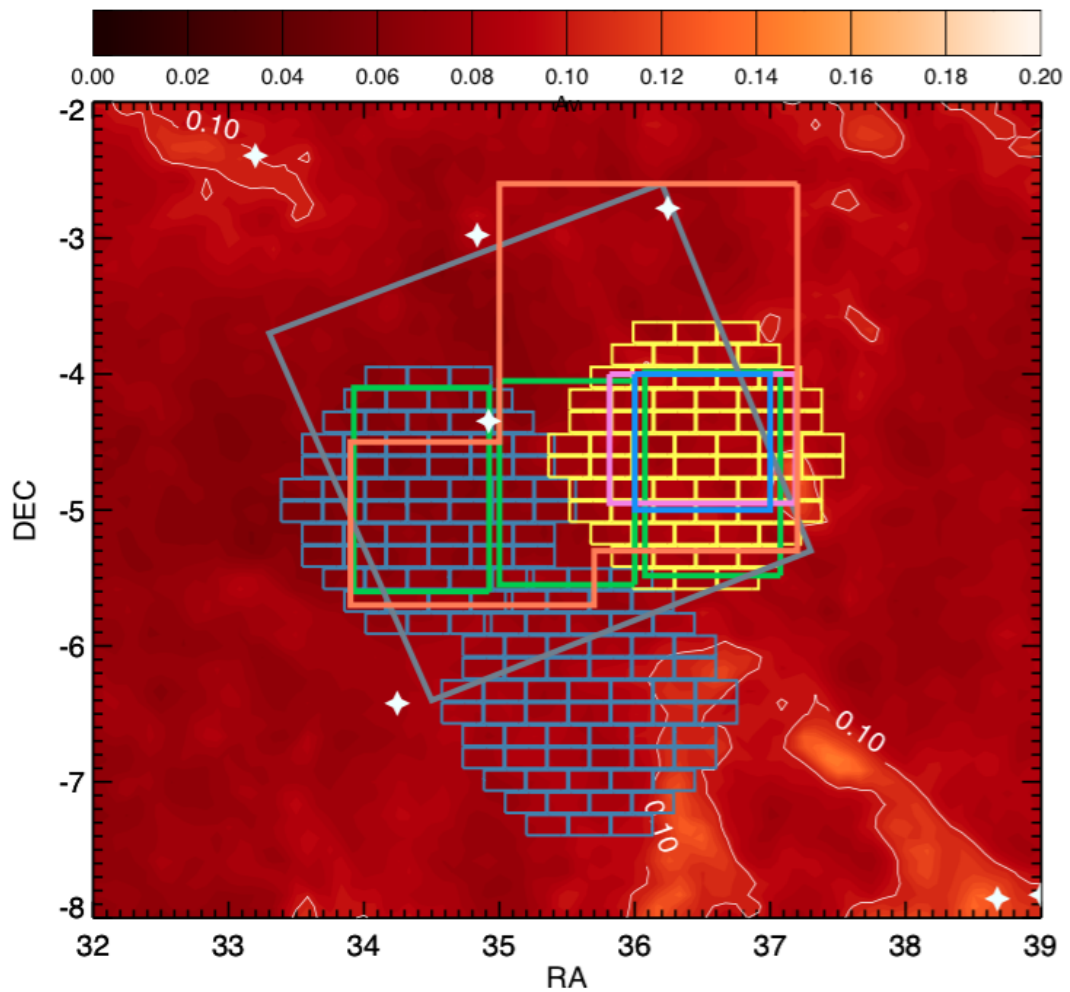
Figure 3.3: SN field locations in the XMM-LSS region, on a red contour map of MW extinction (blue mosaic: X1 and X2, yellow mosaic: X3). The average V-band extinction is illustrated by the legend-colourbar and by the white contours within the plot, whereas several important survey locations are overplotted on the dust maps (*green:* VIDEO, *grey:* SWIRE, *pink:* VVDS, *blue:* CFHTLS, *orange:* XMM-LSS). Plotted in white are stars with V-band magnitude < 7 taken from the HEARSC Bright Star Catalog. *Plot created by Chris DAndrea, Ravi Gupta and Rachel Cane on the 18th of June 2013.*
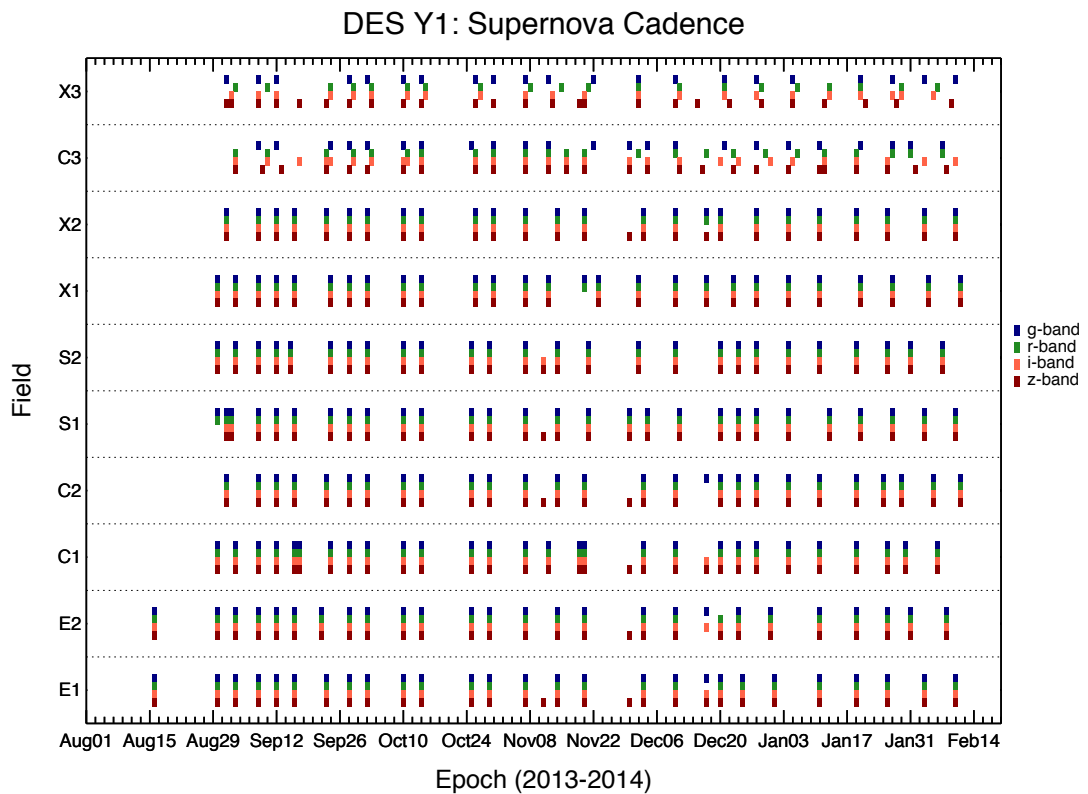
Figure 3.4: The DES SN Survey cadence plot of Y1 of operations. All filters are observed at the same night for the shallow fields, whereas for the deep fields this is not the case, as different filter/exposures can be acquired on different days. Some epochs of the shallow fields show uncompleted filter sequences, due to the poor quality of the data, which resulted in revisiting the same fields on the next available night. *Plot created by Dr. Chris D'Andrea.*
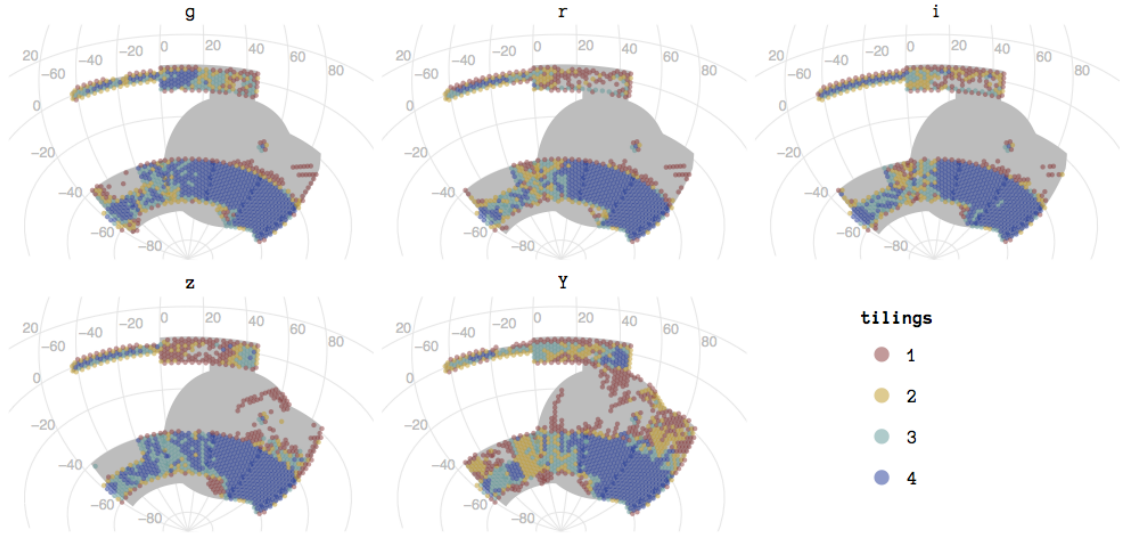
Figure 3.5: The DES wide-survey observed area after the end of Y1 of operations. The grey area shows the entire DES footprint whereas areas coloured with red, yellow, green and blue show the number 1, 2, 3 or 4 of tillings respectively, that were considered as scientific data. *Plot provided by DES operations team.*

Such optimization was set in order to achieve primarily the DES SN Survey science requirements: obtaining well-measured light curves of ~ 3500 SNe Ia out to redshift $z \sim 1.2$, using up to 10% of the photometric survey time and larger fraction of the non-photometric time (Bernstein et al., 2012). Secondly, to accommodate the DES-wide survey science requirements: reaching $g = 24.6$, $r = 24.1$, $i = 24.3$, $z = 23.8$, and $Y = 21.5$ AB at $\geqslant 10\sigma$ SNR in 1.5" apertures with $\leqslant 100$mas accuracy positions, over at least 90% of the wide-survey area (Flaugher, 2005).

Furthermore, on each season's observing schedule the two strategies would have to cooperate to achieve the most efficient use of observational time. This task is handled by the observing tactics (obsTac; Neilsen and Annis, 2014), a component of the DE-Cam control system SISPI (Honscheid et al. 2012) that, based on the night's conditions (weather, seeing, sky brightness, position of the fields available) and the selected strategies, automates the entire DES observation schedule.

ObsTac priorities, as outlined in (Neilsen and Annis, 2014), are governed by two main thresholds: the SNe 'dead-man' switch of seven days and the 'good-seeing' limit of 1.2" and are listed as follows:

1. If there are SNe fields that have passed the 'dead-man' limit of seven days since their last observation, and the current conditions are good for observations, then trigger at highest priority.

2. If the seeing is better than the 'good-seeing' threshold and the moon is down, then select a DES wide-survey exposure in g, r, or i bands, and give priority to fields that set earliest.

3. If the seeing is better than the 'good-seeing' threshold and the moon is up, then select a DES wide-survey exposure in i, z, or Y bands and give priority to fields that set earliest.

4. Observe the SNe fields sequence that was completed least recently.

Those priorities do not exclude observations under all seeing conditions, but any exposures (for the wide or the SN Survey) resulting to data products that do not meet with the science requirements listed above, will have to be retaken.

Implementing obsTac over the entire period of DES Y1 of operations, resulted in ~ 25 visits on average for each SNe field as shown in Fig. 3.4 and 14457 wide-survey science exposures were taken, covering part of the survey's footprint as illustrated in in Fig. 3.5.

3.3.3 Data processing and Supernovae discoveries

All DES SN survey imaging data are de-trended and co-added using a standard photometric reduction pipeline at the National Centre for Supercomputing Applications (NCSA) via the DES Data Management system (DESDM; Mohr et al., 2012; Desai et al., 2012), producing approximately 30 'search images' per field (in all filters) over the duration of the five-month DES season. We performed difference imaging (Kessler et al., 2015) on each of these search images, using deeper template images for each field created from the co-addition of several epochs of data obtained during previous seasons observations (ie. in Y1 the templates were constructed from images taken in SV season). Before differentiating, the search and template images were convolved to the same point spread function (PSF).

Objects were selected from the difference images using SEXTRACTOR v2.18.10 (Bertin and Arnouts, 1996), and previously unknown transient candidates were identified and examined using visual inspection (or 'human scanning') by DES SN group members. Moreover, using the publicly available SNANA light curve simulations (Kessler et al., 2009b), 'fake SNe Ia' were created and injected into the raw images, in order to monitor survey efficiency as described in detail by Kessler et al. (2015).

Fig. 3.6 shows the scanning web interface used during Y1 for visual scanning of SNe candidates, in which $13" \times 13"$ cut-out images called 'postage-stamps' were used. Each scanner had a certain load of objects (~ 100) to scan per night, with the options available
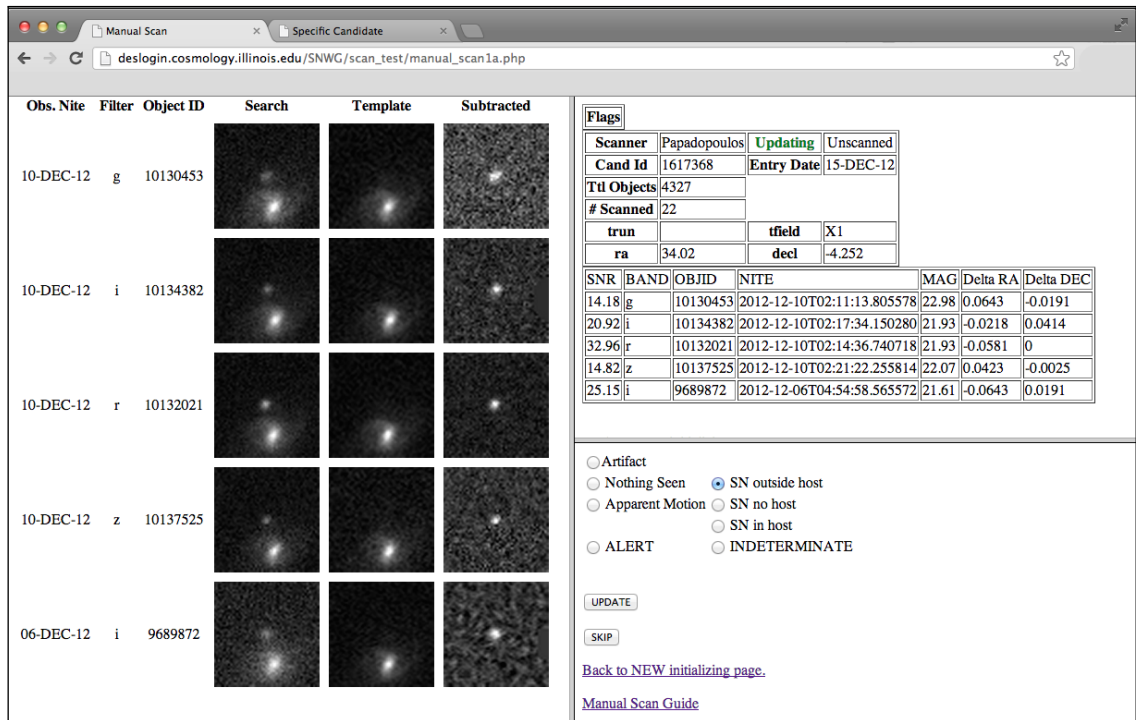
Figure 3.6: The Y1 scanning web interface used for visual inspection of a SN candidate. The left-hand side panel shows a time series of five filter/epoch triplets, each composed of three $13" \times 13"$ cut-out images, called 'postage-stamps', representing the search image on the left, the template image on the centre and the difference image on the right. The upper right panel consists two tables with general information about the current scanning session (scanner name, status, total objects unscanned, number of objects scanned in this session) and basic information about the SNe candidate (candidate ID number, ra dec, field). The second table lists information about each one of the filter/epoch search entries (signal to noise ration, band, time of observation, magnitude). The bottom, right-hand panel hosts the scanning selection options and operation buttons, which are used by the scanner in order to enter the desired classification to the system.

being: 'SN (inside/outside host, hostless, indeterminate)', 'artefact', 'Apparent Motion', 'Nothing Seen' and 'ALERT', as seen in the bottom right-hand side panel of Fig. 3.6. As a scanner myself, I helped scan for SNe candidates in SV and Y1 seasons and I have visually inspected ~ 10000 and ~ 18000 candidates respectively.

During Y1 of operations on any given scanning session contacted by a single scanner, the average outcome was a majority of artefacts and a handful of real and fakes SNe (see postage-stamps on Fig. 3.7). On average, the ratio between the SNe and artefacts reached 85%, a relatively high percentage which forced certain updates within the data pipeline described in Sec. 5.3 and the development of a machine learning algorithm.

An automated machine learning algorithm (AUTOSCAN; Goldstein et al., 2015) was developed and implemented in order to improve the efficiency of selecting real transients. Postage-stamps examples classified by the AUTOSCAN algorithm are shown in Fig. 3.7, for a variety of signal-to-noise ratios. As shown by Goldstein et al. (2015), the AUTOSCAN algorithm improved the number of transient candidates eligible for human scanning by a factor of 13.4, while only 1% of 'fake SNe Ia' were lost, most of which were very faint events.

Up to this data processing stage, the pipeline is known as the 'Search' photometric pipeline, as it searches through the photometric data (DECam images) and produces a list of newly discovered astrophysical transients.

DES transient names are formatted following the convention DESYYFFaaaa, where YY are the last two digits of the year in which the observing season began (i.e. 13), FF is the two character field name (i.e. S2), and the final characters (all letters, maximum of four) provide a running candidate identification, unique within an observing season, as is traditional in SN astronomy (i.e. abc).

Finally, DES transients were photometrically classified using the Photometric SN IDentification software (PSNID; Sako et al., 2008, 2011) to determine the likely SN type. As described by Sako et al. (2011), PSNID uses the observed photometry, calculates the reduced χ^2 against a grid of SN Ia light-curve models and CC SNe templates, and identifies the best-matching SN type and set of parameters with, and without host galaxy redshift as priors in the grid search. For the SN Ia models, there are five model parameters: redshift (z), V-band host galaxy extinction (A_V), time of maximum light (T_{max}), B-band decline rate 15 days after peak (Δm_{15}^B; Phillips, 1993) and distance modulus (μ; Eq. 1.29).

PSNID is run on data derived from the 'Forced' photometric pipeline, which differs from the 'Search' described above. The 'Forced' photometric pipeline takes the coordinates of an object of interest and performs aperture photometry at the same position in every difference image available in the database, old and new. Thus creating a more complete sample of photometric data which can include upper limits as well for each
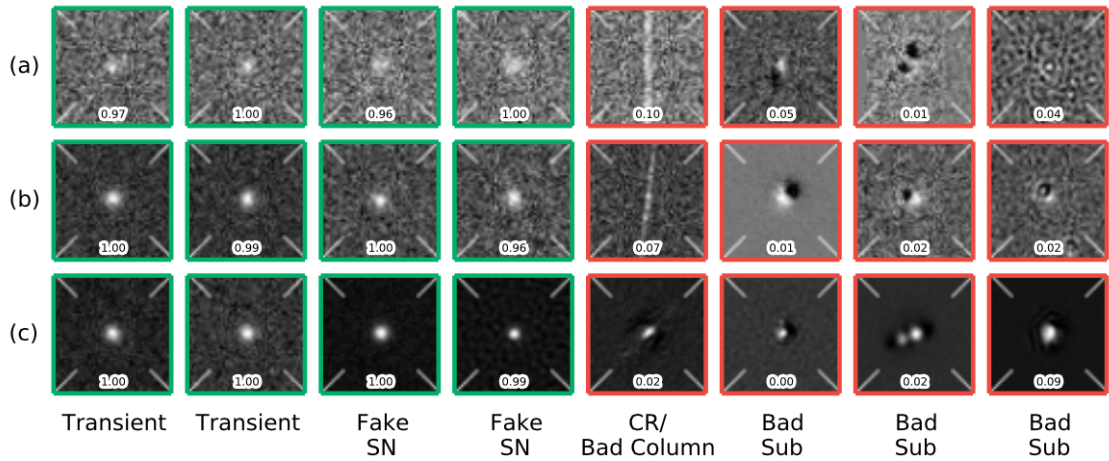
Figure 3.7: Postage-stamps, centered on legitimate (green boxes) and spurious (red boxes) objects, at a variety of signal-to-noise ratios: (a) SNR$\leqslant 10$, (b) $10 <$SNR$\leqslant 30$, (c) $30 <$SNR$\leqslant 100$. The postage-stamps are subclassed to illustrate both the visual diversity of spurious objects and the homogeneity of authentic ones. Objects in the 'Transient' columns are real astrophysical transients that subtracted cleanly. Objects in the 'Fake SN' columns are fake SNe Ia injected into transient search images to monitor survey efficiency. The column labeled 'CR/Bad Column' shows detections of cosmic rays (rows b and c) and a bad column on the CCD detector (row a). The columns labeled 'Bad Sub' show non-varying astrophysical sources that did not subtract cleanly; this can result from poor astrometric solutions, shallow templates, or bad observing conditions. The numbers at the bottom of each cut-out indicate the score that each detection received from AUTOSCAN; a score of 1.0 indicates that the algorithm is perfectly confident that the detection is not an artefact, while a score of 0.0 indicates the opposite. *Plot is taken from Goldstein et al. (2015).*

transient, as it performs the aperture photometry regardless of the existence of the transient.

These SNe candidates were stored in an online SQL database hosted by NCSA, alongside associated data products of the two pipelines ('search' and 'force'), and then the SNe were prioritized for spectroscopic follow-up by the Spectroscopic Marshall (Dr. Chris D'Andrea in Y1), according to the goals and time allocations available at the time, as explained in detail in the following section.

3.4 Spectroscopic Follow-Up

As discussed by Campbell et al. (2013), in new SN Surveys such as the DES SN survey, real-time spectroscopy of all the SNe type-Ia discoveries will be impractical due to the vast amount of such objects. An alternative solution is to use photometry to classify all discovered SNe and collect redshifts for the majority SNe-like transients from spectroscopic follow-up of the associated host galaxies, after the SN has faded away (Lidman et al., 2013; Campbell et al., 2013). This strategy was selected as the main method for the DES SN Survey for obtaining SN redshifts for use in cosmology, as stated in Bernstein et al. (2012).

Getting real-time spectra of SNe would have to work as a complementary method and could focus on specific categories such as hostless events or interesting and peculiar SNe (e.g. SLSNe or lensed SNe). Such spectroscopically confirmed SNe transients would be announced officially by DES via the Astronomer's Telegram (ATel)[10]. Moreover, the spectroscopic follow-up of live SNe would be creating test samples of live SNe for testing the survey's photometric classification and ultimately helping to train the photometric selection techniques.

3.4.1 SNe host galaxies

The OzDES program (Yuan et al., 2015) was created precisely to cover the spectroscopic strategy mentioned above. The AAOmega spectrograph, coupled with the Two Degree Field (2dF) multi-object 400-fiber-positioning system (Lewis et al., 2002) on the Anglo-Australian Telescope (AAT) was the perfect fit to this task, as both AAT and Blanco telescopes share the same design and are equipped with instruments with similar field-of-view (FoV) area. As shown in Fig. 3.4.1, the similarity of the two FoV allows them to align almost perfectly on top of each other, making the spectroscopic follow-up of DES SNe hosts very efficient, as on each exposure, AAT + AAOmega are able to target hundreds of DES targets.

---

[10]http://www.astronomerstelegram.org
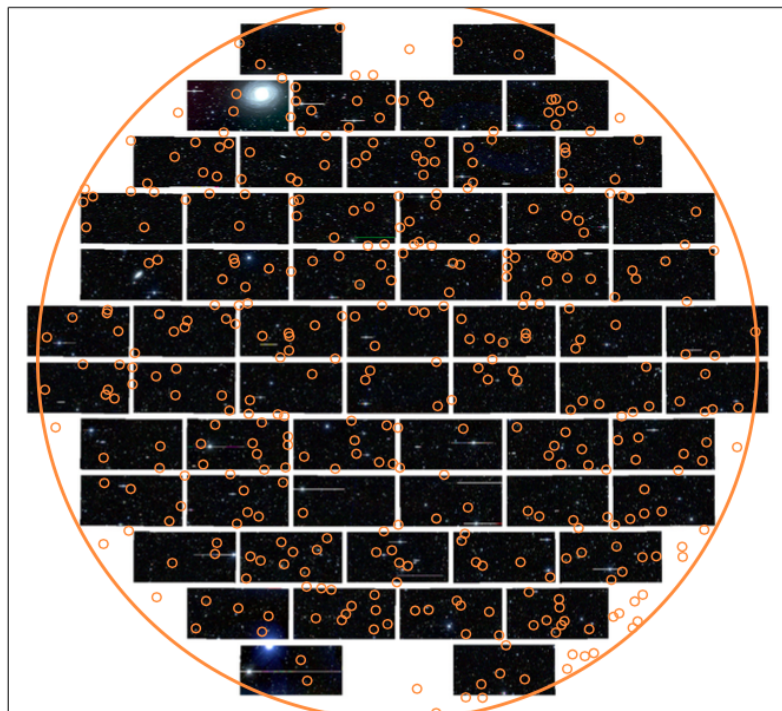
Figure 3.8: The DECam FoV (image mosaic in the background), that is composed by 60 CCDs, is well matched by the 2dF spectrograph FoV (large orange circle). The small, orange circles show the position of the 392 optical fibers of 2dF that were targeted in one AAT observation, highlighting the efficiency of the OzDES program. *Plot taken from Yuan et al. (2015)*.
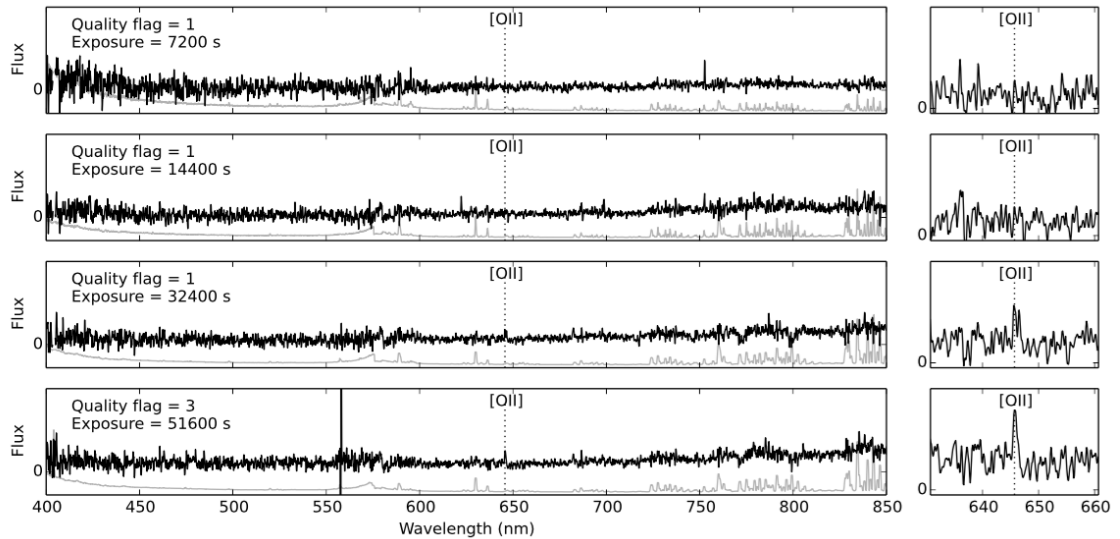
Figure 3.9: Co-added spectra of a SN host target of r-band magnitude 23.7 and redshift 0.732. The significance of the candidate [OII] feature appears to have increased with exposure time. Quality flag of 1, translates to an unsecured redshift estimation, whereas quality flag of 3 means that the redshift is well secured. *Plot taken from Yuan et al. (2015).*

The number of 400-fibers of 2dF also allows more science goals than SNe cosmology to be pursued, such as reverberation mapping of AGN (King et al., 2015), calibration of DES photometric redshifts (Sánchez et al., 2014) and following radio galaxies and galaxy clusters as described in detail in Yuan et al. (2015).

Moreover, OzDES program offers a unique strategy of repeated targeting, dynamic fibre allocation, and stacking, as described in detail by (Lidman et al., 2013; Yuan et al., 2015). Multiple observations of the same DES field allow brighter targets to be deselected between the observing runs when redshifts are secured; while fainter targets remain in the queue. Stacking across many observing runs, allows OzDES to go deeper than otherwise possible with the 4m AAT. Fig. 3.9 shows an example of stacked spectra, for a SN host target of r-band magnitude 23.7 and redshift 0.732, published by Yuan et al. (2015). The stacking technique can be also applied on many observing runs across different observing seasons of DES-OzDES.

3.4.2 Live SNe spectroscopy

For real-time spectroscopy of DES SNe, the strategy was shaped based on the public-access time available on various telescopes around the world. Dr. Chris D'Andrea was appointed as spectroscopic marshal charged with the responsibilities of constructing an

Table 3.3: Spectroscopic resources during DES Y1 of operations, listing the telescope's name, the telescope's instrument, the time allocated during Y1 and short comments on the objectives of each program.

Telescope	Instrument	Time Available	Objectives
GTC	OSIRIS [a]	15.6h (ToO)	ambiguous SNe $m_r < 23.5$
SALT	RSS [b]	22.1h (ToO)	low-z high SNR $m_r < 21.7$
Gemini	GMOS [c]	18.0h (ToO)	Velocity-Colour-Relation of type-Ia
HET	LRS [d]	14.0h (ToO)	SNe type-Ia $m_r < 21.5$
Keck	LRIS [e]	2n	random sample of SNe with good SNR $m_i < 24$
	DEIMOS [f]	2n	
Magellan	IMACS [g]	3n	piggyback to photo-z program
AAT	AAOmega/2dF [h]	14n	OzDES program for SNe hosts

[a] Optical System for Imaging and low-Intermediate-Resolution Integrated Spectroscopy
[b] Robert Stobie Spectrograph
[c] Gemini Multi-Object Spectrographs
[d] Low Resolution Spectrograph
[e] Low Resolution Imaging Spectrometer
[f] DEep Imaging Multi-Object Spectrograph
[g] Inamori Magellan Areal Camera and Spectrograph
[h] AAOmega spectrograph Two Degree Field system

operation plan for each DES season, leading the telescope proposals and finally allocating targets to available telescopes/programs accordingly, to maximize discovery and classification efficiency.

A variety of telescopes were selected to carry out different programs based on the combination between instruments/telescopes specifications and SNe targets available. For example the GTC telescope (Gran Telescopio Canarias), equipped with a 10.4 m mirror and OSIRIS slit-spectrograph (Optical System for Imaging and low-Intermediate-Resolution Integrated Spectroscopy), were selected to follow-up photometrically ambiguous SNe, with limiting magnitude of $m_r < 23.5$. The proposal was awarded 15.6 hours in total (12 pointings $\times$ 1.3 hours) to be used as ToO (Target of Opportunity) during DES Y1 of operations. Another example was the use of Keck telescopes, equipped with LRIS (Low Resolution Imaging Spectrometer) and DEIMOS (DEep Imaging Multi-Object Spectrograph), to spectroscopically classify a random sample of SNe with good SNR and limiting magnitude of $m_i < 24$. The program was awarded two nights in each instrument. The full list of available spectroscopic time during DES Y1 is listed in Table 3.3

Also, through the OzDES program for spectroscopic follow-up of host galaxies, all live DES transients with limiting magnitude of $m_r < 22.5$, will be able to be targeted with a fiber, as such events were made top priority. The predicted number of such targets was not exceeding ~ 10 events per SNe field, per pointing of the AAT/2dF.

3.5 Selecting SLSNe candidates in Year One

The remaining of this chapter focuses on the methodology and results of the search of SLSNe, which I led during the Y1 of DES operations. I will present in detail the selection process, the contamination sources and finally, the results and lessons learned from this first attempt of discovering SLSNe.

3.5.1 Methodology

During the first season of DES, I used the sequence of actions described below for selecting SLSNe candidates from the pool of DES transients, which were discovered and named as described in Sec. 3.3.3.

Every time new SN data were obtained, new DES transients were created, visually scanned, passed through AUTOSCAN, PSNID and named as described in Sec. 3.3.3. Shortly after these initial events, I would perform a semi-automatic search for SLSNe using the newly inserted data, as well as the data already in the database. As the two data pipelines ('search' and 'force' photometry) were filling the SQL database with auxiliary information for each DES transient, such as coordinates, flux measurements and uncertainties, host galaxy details, PSNID fits etc., I would create a separate SLSN-specific database myself.

This personal database had an entry for each DES transient discovered during Y1, containing the following information: the $griz$ peak fluxes created by the 'force' photometry pipeline, the number of epochs and observations created by the 'search' photometry pipeline and host galaxy information where applicable, such as photometric or spectroscopic redshifts, separation and $griz$ magnitudes. The $griz$ peak fluxes were transformed into peak observed magnitudes using Eq. 1.27, whereas Fig. 3.10 shows the single-band peak magnitude distributions.

Then, all DES transients were split into two major categories: those related to a host galaxy and those without one, called hostless. Afterwards, the following five broad criteria, which are satisfied by most SLSNe, while eliminating many of the possible contaminating sources (Active Galactic Nuclei-AGNs, normal types of SNe, artefacts etc.), were used:

1. At least one month of multi-colour data, i.e., typically five to six detections ($S/N > 3.5$) in each of $griz$.

2. A low PSNID fit probability to any of the standard SN sub-classes (Ia, Ib, II-P, ll-L).

3. Located greater than one pixel (1 pixel = 0.27" for DECam) from the centroid of the host galaxy.
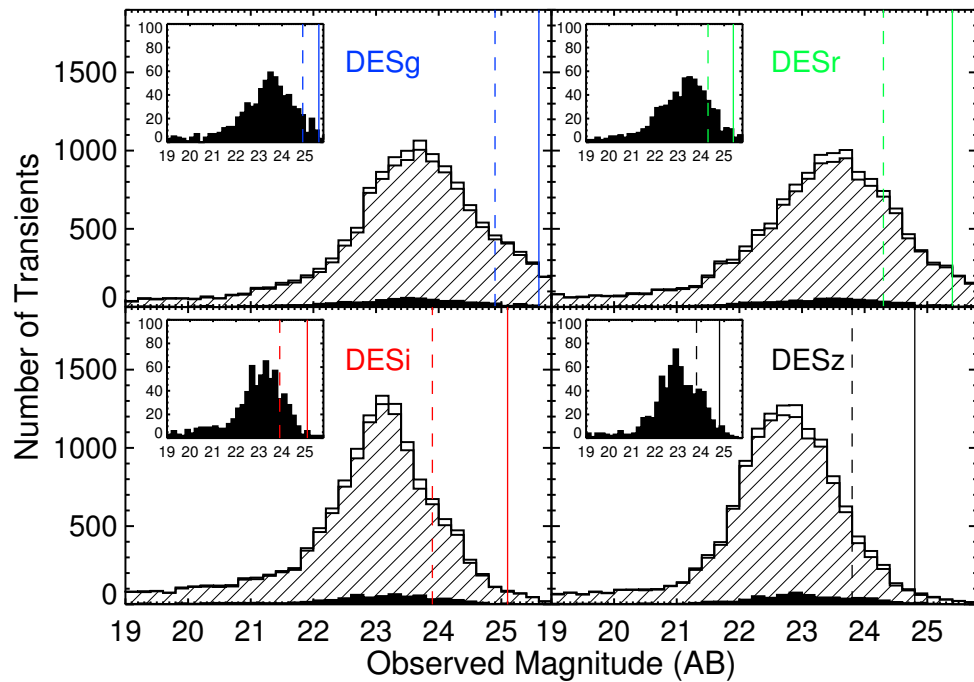
Figure 3.10: The histograms show the peak magnitude distribution of all named DES transients from Y1, in the four DES filters - $griz$. The shaded and black histograms refer to transients associated with a host galaxy and hostless transients, respectively. Because of the smaller number of hostless transients compared to transients associated with host galaxies, their histograms (solid black area) are zoomed and overplotted. The dashed and solid vertical lines show the magnitude limit for the DES SN shallow and deep fields respectively, as listed in Table 3.1.

4. Peak observed brightness no fainter than one magnitude below that of its host galaxy.

5. Peak absolute magnitude $M_{griz} < -20.5$, SLSNe threshold ($M < -21$; Gal-Yam, 2012)

The first criterion aimed at selecting events with long rising times, a clear characteristic seen in many historic SLSNe, shown in Chap. 2. The second and third criteria were placed in order to eliminate possible contamination sources like 'normal' types of SNe (eg. Ia, Ib, II-P, ll-L) and AGNs/QSOs[11]/artefacts respectively. The fourth criterion was implemented to help with the spectroscopic follow-up of the SLSNe candidate, as candidates much fainter than their host would be difficult to be classified since the host spectrum would be dominant over any SNe features. The last criterion was determined using Eq. 1.28, the $griz$ peak observed magnitudes and the host photometric redshift (z_{photo}), or spectroscopic redshift (z_{spec}) when available for each DES transient.

The first two criteria were applied to all DES transients, both hostless and those associated with a host galaxy, whereas the latter three criteria were additionally applied to DES transients associated with a host galaxy. The selection process described so far, provided the capability to scale down the visual inspection load from thousands of SN-like candidates to $\sim 30 - 50$ transients, every time SNe images were processed through the data processing pipelines described in Sec. 3.3.3.

The next step was the visual examination of the observed light-curves of the $\sim 30-50$ transients that passed the selection cuts above. Fig. 3.11 shows the visual inspection panel used to select SLSNe candidates during DES Y1, illustrating how a confirmed SLSNe (DES13S2cmm; Chap. 4) was behaving by the end of Y1. I created this visual inspection panel in order to consist the following two plots: one that shows the transient's light-curve in the DES apparent magnitudes and one that shows the absolute magnitude at peak, given the z_{photo} or z_{spec} of the host or the SN itself, when available. The former plot was used to inspect the rise time to peak of each transient and a minimum of ~ 25 days was required for the transient to become a SLSNe candidate. Whereas the latter plot was used to inspect the peak absolute magnitude in all four bands (criterion no.5), using equation Eq. 1.28 for simplicity and assuming the z_{photo} or z_{spec} related to the host or the SN itself, as the redshift of the transient.

By the end of DES Y1, late-February 2014, the number of named DES transients were ~ 26.000, which I narrowed down to less than ~ 1500 possible SLSNe candidates using the selection stages described above. Implementing the visual inspection of all the possible SLSNe candidates revealed that the majority were artefacts (i.e. mis-subtractions of

---

[11]Quasi-Stellar Objects
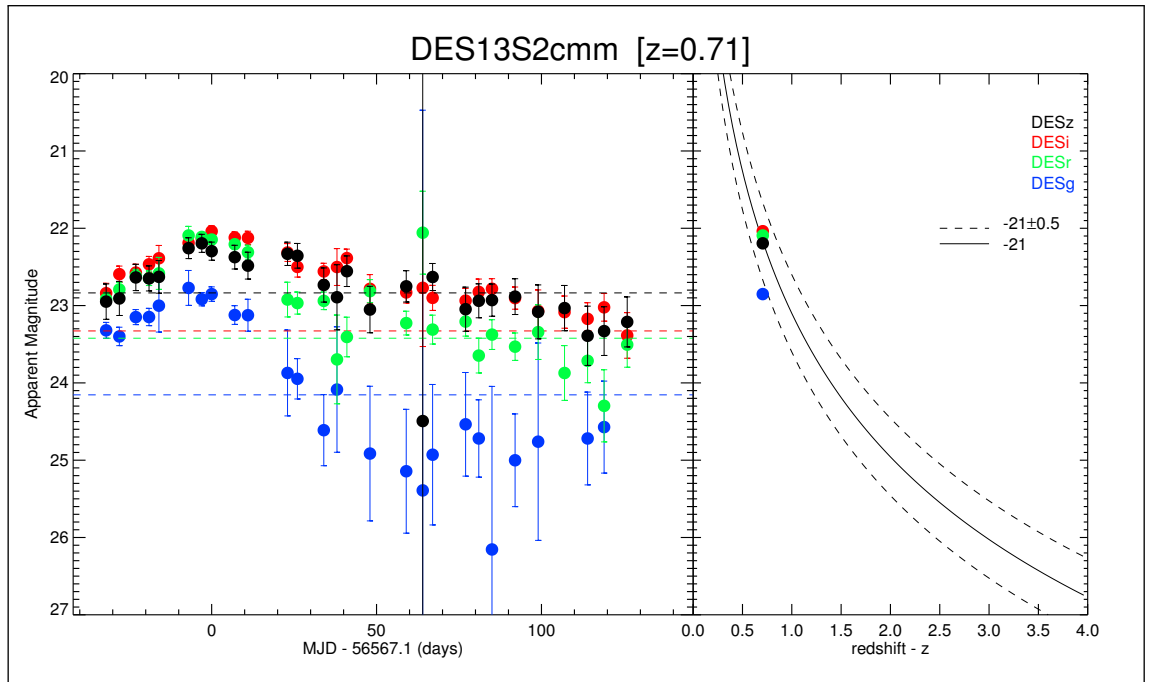
Figure 3.11: Visual inspection panel for SLSNe candidates used in DES Y1. *Left:* Apparent magnitude light-curves of a SLSNe candidate in $griz$ as a function of the observed phase from peak brightness. The dashed lines represents the host galaxy magnitudes in the four DES filters $griz$. *Right:* Using the z_{photo} of the host galaxy and the peak apparent magnitude of the candidate, we were able to calculate the expected absolute magnitude (Eq. 1.28) at peak. The solid black line shows the absolute magnitude of $M = -21.0$, which is the SLSNe threshold set by Gal-Yam (2012), whereas the dashed lines represent the $M = -21.0 \pm 0.5$.

galaxies, hot-pixels, bad masked areas etc), leaving only ~ 300 real transients, of which a large proportion appeared to be AGN/QSO and a small minority to be real SNe of some type. Those types of non-SLSNe objects would be referred as contamination sources and they are explored in detail in the following section (Sec. 3.5.2).

The end result of the entire SLSNe selection process described in this section, was the classification of 12 SNe as SLSNe candidates, listed in Table 3.4 and described in detail in Sec. 3.5.3.

3.5.2 Contamination sources

With the term 'contamination sources' I refer to named DES transients, that passed through 'search pipeline', human scanning and AUTOSCAN and also passed partly or as a whole the SLSNe selection process described in Sec. 3.5.1, but never made it to the final SLSNe candidates list (Table 3.4). There are three main categories of contamination sources, examples of which are shown in Fig. 3.12 (light-curves) and in Fig. 3.13 (postage-stamps).

AGN

The main contamination sources were AGNs/QSOs, which passed all the selection criteria set in Sec. 3.5.1. The number of such objects increase dramatically as we relax the host separation limit, which was set to 1 pixel (0.27" for DECam) away from the host galaxy centre. But even when using that separation limit of 1 pixel away from the host centre, a significant number of AGNs/QSOs ended up into the final SLSNe candidates list. A light-curve example of such contamination source (DES13C2adf) is shown in the fourth row of Fig. 3.12 and its postage stamps are shown in panel (d) of Fig. 3.13.

DES13C2adf was classified as an AGN at $z_{spec} = 0.66$ and was selected as an example to be directly compared to DES13S2cmm (SLSNe at $z_{spec} = 0.66$), emphasizing their similarities and differences, as both occurred in similar redshifts. Looking at Fig. 3.12, both objects show long-lived light-curves in all bands with high SNR, but in the case of DES13C2adf no colour evolution can be seen as the light-curve progresses. Moreover, in both cases the host z_{photo} that was used in each case, placed both objects beyond the SLSNe peak absolute magnitude threshold of $M_{griz} < -21$. Visual comparison of panels (a) and (d) in Fig. 3.13, can not distinguish the different nature of the two objects, as both appear to be close to their host centre and the subtraction images show similar results.

As noted before, AGNs/QSOs were the dominant source of contamination in Y1 and actions had to be taken during the off-season, in order to improve the SLSNe discovery efficiency for Y2. Actions such as the creation of an AGN veto catalogue, updates on the data pipelines and on AUTOSCAN are discussed in Chap. 5.
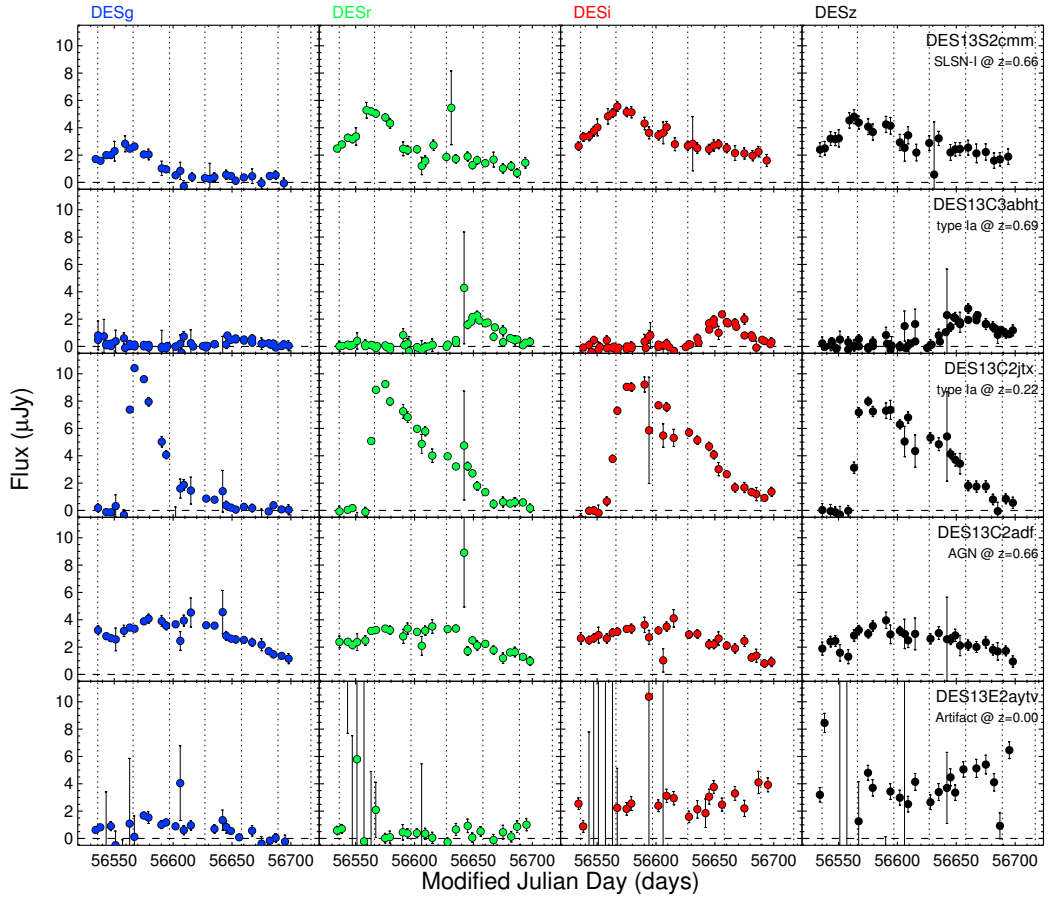
Figure 3.12: DES multi-band light-curves in flux space of five DES transient objects. *First row:*DES13S2cmm is a SLSN-I at redshift $z = 0.663$ confirmed by VLT (see Chap. 4 for full detail). *Second row:* DES13abht is the highest spectroscopic confirmed SN type-Ia from DES Y1 at a redshift of $z = 0.69$ obtained by Gemini-South. *Third row:* DES13C2jtx is a SN type-Ia in the 'nearby Universe', which translates to a redshift of $z = 0.223$. *Fourth row:* DES13C2adf is an AGN at redshift $z = 0.66$ confirmed by the OzDES program and accounted for the main look-a-like competitor to SLSNe in DES Y1.*Fifth row:* DES14E2aytv is an artefact out of thousands that were created from the image differencing pipeline, and accounted for the main source of contamination in the search for SLSNe. The doted vertical lines represent the beginning of each month of DES Y1, starting from 1-September-2013 and ending 1-March-2014. They can serve as a ruler of 30 days rising to peak, a property of SLSNe. The dashed horizontal line shows the zero flux level of each light-curve.
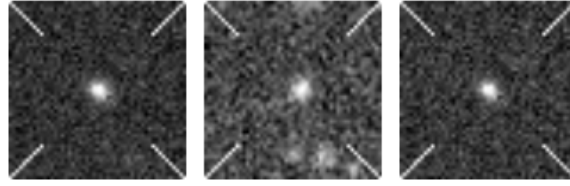
(a) DES13S2cmm (SLSN)
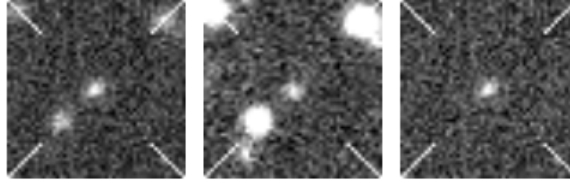
(b) DES13C3abht (SN Ia)
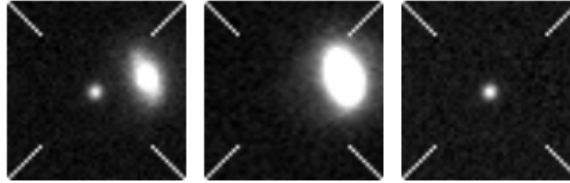
(c) DES13C2jtx (SN Ia)
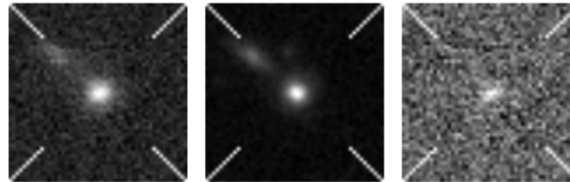
(d) DES13C2adf (AGN)
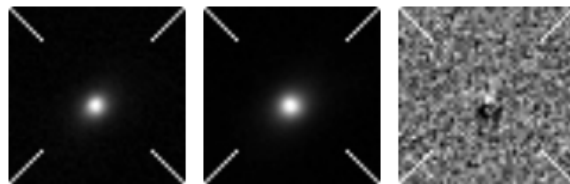
(e) DES13E2aytv (Artefact)

Figure 3.13: 'Postage-stamps' of DES transients, each created by a $13" \times 13"$ cutout of DECam images, taken in r-band and close to their peak brightness. The three columns corresponds to the search, template and difference images, respectively. *Panel (a):* DES13S2cmm, the first SLSNe discovered and spectroscopically confirmed by DES (see Chap. 4). *Panel (b):* DES13C3abht, a SNe Ia at $z_{spec} = 0.69$ that was initially considered as a SLSNe candidate. *Panel (c):* DES13C2jtx, a SN Ia at $z_{spec} = 0.223$. *Panel (b):* DES13C2adf, an AGN at $z_{spec} = 0.66$ that was initially selected as a SLSNe candidate. *Panel (e):* DES13E2aytv, an artefact that was misclassified and selected as a SLSNe candidate.

Artefacts

Another popular source of contamination during Y1 were artefacts, which are objects created by some malfunction of the 'search pipeline', probably during the stage of image differencing or template convolution (Kessler et al., 2015). Most of the artefacts' cases that were selected as SLSNe candidates, were scanned by a human scanner as a real transient at least once during their entire life span, but at later stages showed bad subtraction stamps, as in panel (e) of Fig. 3.13. Their light-curve evolution, shown in the fifth row in Fig. 3.12, shows erratic behaviour accompanied with large errorbars in some measurements.

The main reason for such objects to become SLSNe candidates, was some isolated high flux measurements with high SNR, generated by bad subtractions of galaxies in the 'search' pipeline. A combination of such high flux measurements with a high value of the host galaxy's z_{photo}, can produce a SLSNe candidate that could pass the SLSN selection criteria. Various changes and updates of the data processing pipelines and general SNe candidates selection methods, during the off-season after Y1 (see details in Chap. 5) were able to reduce the number of artefact passing as real transients to a minimum.

Other SNe types

The last source that contaminated the SLSNe candidates list were other types of 'normal' SNe. They were mainly caused by the behaviour of their light-curves in early stages, combined with misleading z_{photo} of the host galaxy, that boosted the transient's luminosity. Such an example is DES13C3abht, a spectroscopically confirmed SNe Ia at $z_{spec} = 0.69$, that was originally thought to be a SLSNe at $z_{photo} = 0.95$. Its light-curve is shown at the second row of Fig. 3.12, and its postage-stamps are shown in panel (b) of Fig. 3.13.

In this category we include also hostless transients that were classified as 'normal' type SNe but also showed some similarities with SLSNe in the early stages of their light-curves.

3.5.3 Results

Using the SLSNe selection process described in Sec. 3.5.1, a final 'DES Y1 SLSNe candidates list' was created which contains 12 transients, listed in Table 3.4. Fig. 3.14 presents the observed light-curves of those SLSNe candidates, whereas Fig. 3.15 shows their 'postage-stamp' triplets.

Unfortunately, we only secured a usable spectrum for one of the SLSNe candidates, DES13S2cmm, which was classified as a SLSN-I and is discussed in detail in Chap. 4,

Table 3.4: List of the 12 SLSNe candidates selected during the DES Y1 of operations, showing the DES transient name, the SNe field, the CCD number where the SN was discovered, the equatorial coordinates (RA,DEC), the host z_{photo} and z_{spec} where available and a column with status and comments on the specific candidate.

#	Fig. 3.15 panel	Transient Name	field	chip	RA	DEC	host z_{photo}	host z_{spec}	Status/Comments
1	a	DES13S2cmm	S2	46	40.637	-01.358	0.863±0.134	0.663(VLT)	SLSN-I, ATel5603
2	b	DES13E1maj	E1	15	7.807	-42.566	0.786±0.062	0.67 (AAT)	AGN (AAT - Y2)
3	c	DES13C1gjb	C1	57	53.971	-27.809	1.028±0.045		AAT - Y2 unidentified
4	d	DES13S1ih	S1	57	6.784	-43.065	0.944±0.078	2.435(AAT)	AGN (AAT)
5	e	DES13C3absw	C3	6	35.777	-4.079	0.178±0.065		SN-Ia outlier
6	f	DES13X3aajk	X3	44	35.777	-4.079	0.178±0.065	0.294 (AAT)	possible lensed SN
7	g	DES13C3baf	C3	32	51.483	-28.218	hostless		
8	h	DES13X3obu	X3	27	36.245	-4.535	hostless		
9	i	DES13E1nkg	E1	11	8.131	-42.431	hostless		
10	j	DES13X3beu	X3	11	36.676	-4.051	hostless		
11	k	DES13X3bcg	X3	8	35.777	-4.079	hostless		
12	l	DES13E1xe	E1	32	42.758	- 0.695	hostless	0.306(AAT)	AGN (AAT)

while two others (DES13S1ih, DES13E1xe) were classified as AGNs via the OzDES program during its first year of operations (Yuan et al., 2015). Nine more SLSNe candidates lack spectroscopic confirmation, either directly from the SNe or the host galaxy where available. The main reasons behind this was the limited amount of the spectroscopic resources during Y1 (Sec. 3.4) and the focus of the spectroscopic follow-up strategy around the main goal of the DES SN Survey, which is the discovery of SNe Ia for use in cosmology.

During DES Y2 of operations, we attempted to gain spectroscopy of the host galaxies of the remaining nine unclassified SLSNe candidates, but in several cases this has proven to be challenging, as no host was detected in the DES deep template images for some of our SLSN candidates (DES13X3obu, DES13E1nkg, DES13X3beu and DES13X3bcg). In more detail, in Y2 of OzDES observations (16 nights spread out during DES Y2), a fiber was placed at the location of each of the nine SLSNe candidates which had faded, hoping to detect even faint traces of emission lines coming from the underlying faint galaxy. The results of this effort was to classify one of the nine remaining SLSNe candidates (DES13E1maj) as an AGN at $z_{spec} = 0.67$, and secure a host redshift of $z_{spec} = 0.294$ for another candidate (DES13X3aajk), which strongly suggests it is a normal SN. The remaining seven SLSNe candidates have no secure redshift information.

This section, contains detailed descriptions of all the SLSNe candidates in the order listed in Table 3.4, except of DES13S2cmm which is described in-depth in Chap. 4.

DES13E1maj was first discovered in early December 2013 as a SN transient, but it was close to the end of Y1 observations (early January 2014), that it became a SLSNe candidate. The arguments in support of it being a SLSN were the long rise time to peak (~ 40 days) and the host galaxy $z_{photo} = 0.786$. Moreover it showed minor colour
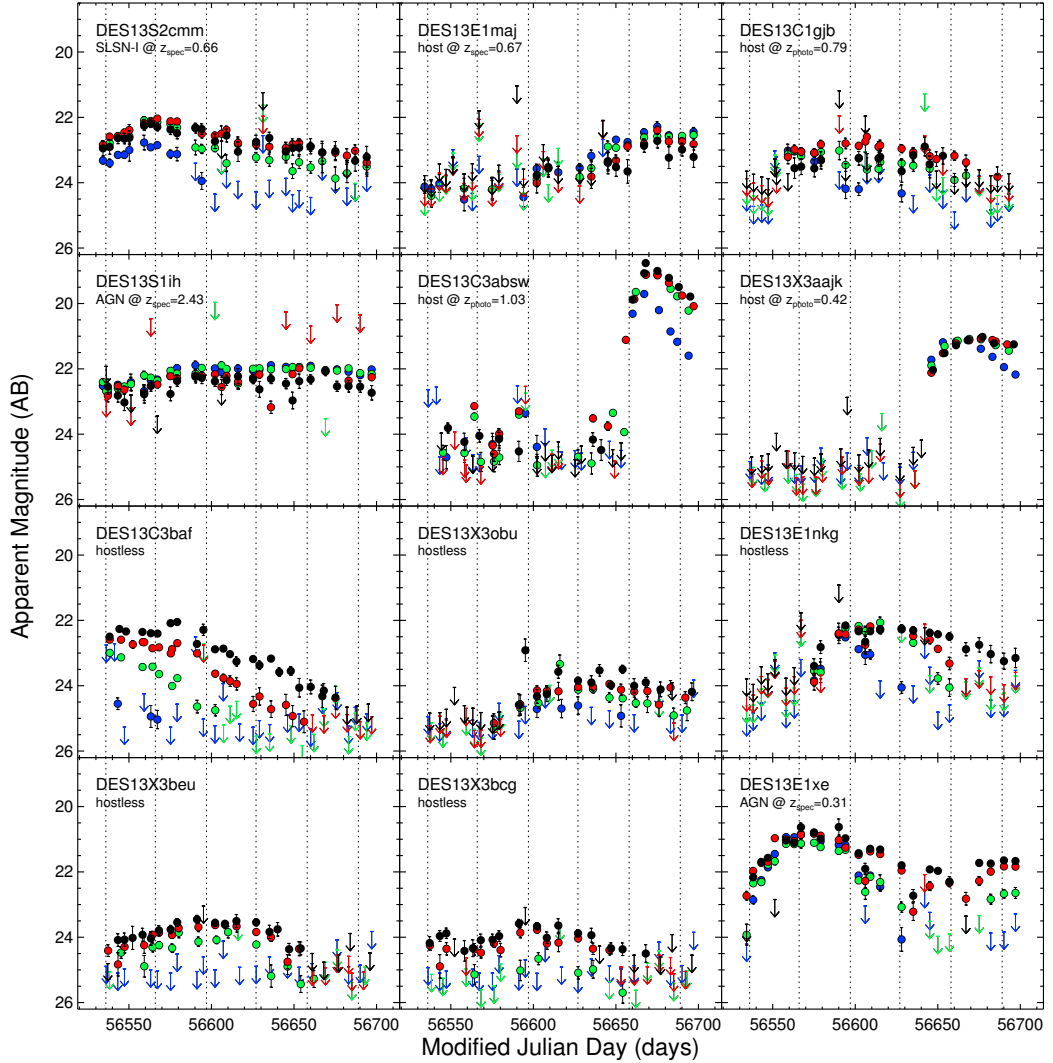
Figure 3.14: DES multi-band, AB apparent magnitude light-curves of the 12 SLSNe candidates from DES Y1, listed in Table 3.4. Only DES13S2cmm (*top left corner panel*) was confirmed to be a SLSN at $z_{spec} = 0.663$. The errorbars represent 1-σ uncertainties, and the arrow symbols are 3-σ upper limits.The doted vertical lines represent the beginning of each month of DES Y1, starting from 1-September-2013 and ending 1-March-2014. They can serve as a ruler of 30 days rising to peak, a property of SLSNe. The dashed horizontal line shows the zero flux level of each light-curve.

(a) DES13S2cmm

(b) DES13E1maj

(c) DES13C1gjb

(d) DES13S1ih

(e) DES13C3absw

(f) DES13X3aajk

(g) DES13C3baf

(h) DES13X3obu

(i) DES13E1nkg

(j) DES13X3beu

(k) DES13X3bcg

(l) DES13E1xe
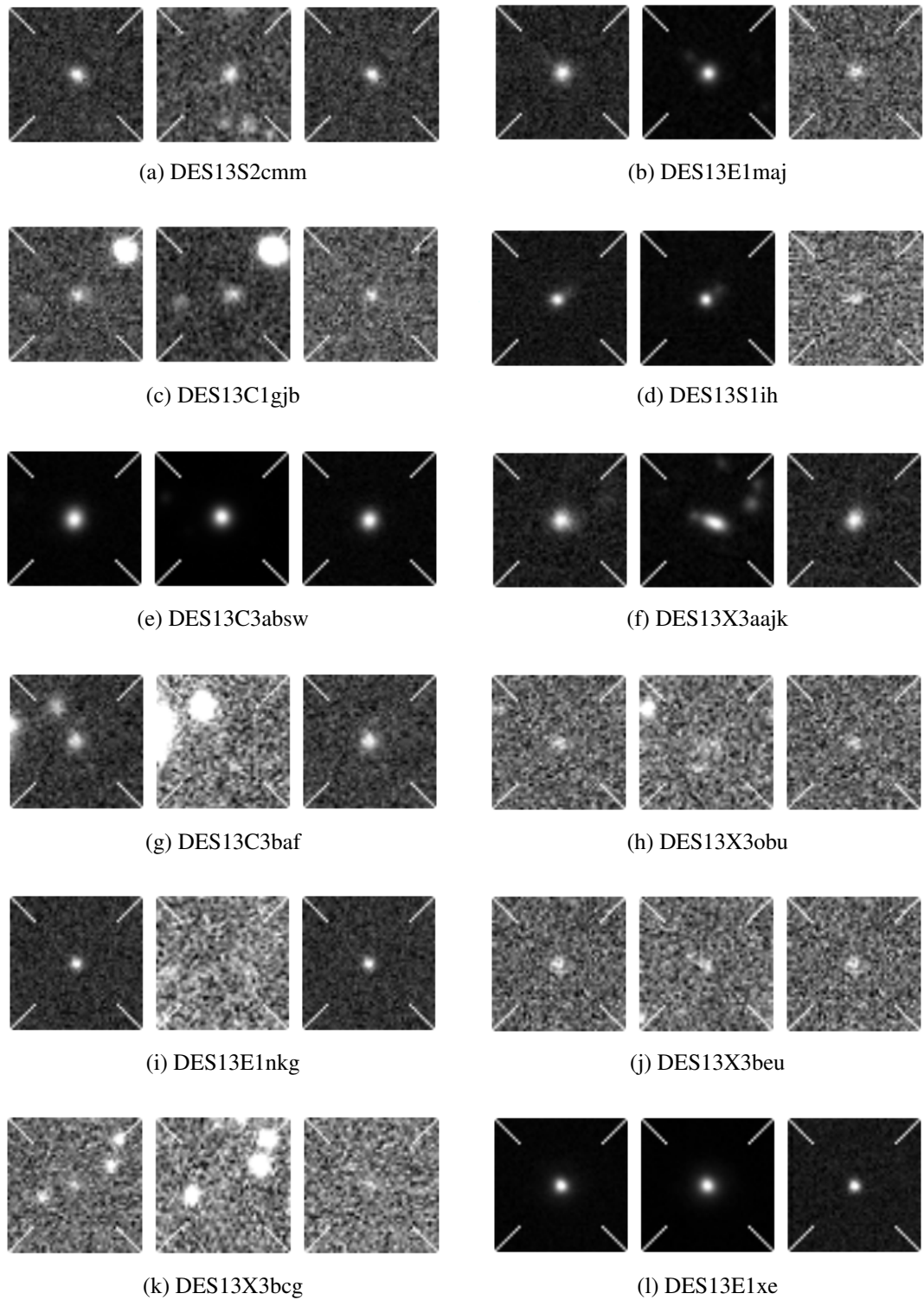
Figure 3.15: 'Postage-stamps' triplets of the 12 SLSNe candidates selected in Y1 listed in Table 3.4. Each triplet was created by a $13" \times 13"$ cutout of r-band DECam images acquired close to the transients' peak brightness and shows the search, template and difference images, respectively.

evolution of its light curve. Due to DES13E1maj being discovered late in the observing season, we were not able to obtain a spectrum of the SN, but we observed its host galaxy in Y2 with the OzDES program. This resulted in identifying the host galaxy as an AGN at $z_{spec} = 0.67$, eliminating the possibility for a SLSN.

DES13C1gjb was discovered and scanned by early October 2013 as a SN and one month later it was selected as SLSN candidate for three good reasons: the high $z_{photo} = 1.03$ of its host, the rising trend of the light curve at that time and the colour evolution of the light-curve. Specifically, as the light-curve evolved with time, the g-band dropped to upper-limits in few days after peak, whereas the r-band was reduced by half a magnitude compared to the i-band and z-band. The candidate peaked at $m_r \sim 23.0$, which made it difficult to be placed in any of the available telescopes' queues for spectroscopic follow-up time. In Y2 season, and using the OzDES program, we obtained three spectra of the identified host galaxy without any success at extracting the redshift of it. As a result of that, this host galaxy will remain at the OzDES list, named as 'SN_{host}', until further data are collected and combined to secure a redshift.

DES13S1ih was one of the first transients discovered by DES. It was scanned and classified as a real transient event in early September 2013. It was selected as a SLSN candidate around a month later and was inserted to the OzDES schedule for spectral observations. By the time that OzDES took a spectrum of this transient, in early November 2013, we had become confident that DES13S1ih was an AGN. This was because of the flatness in the light-curve in all four bands and because of the colourless evolution after the peak.Two consecutive spectra that were taken with OzDES confirmed it as an AGN at $z_{spec} = 2.44$, as expected.

DES13C3absw shows clearly SNe light-curve behaviour and was not selected during Y1 operations because of a data processing error. The fault occurred within the module responsible for naming new transients with the designated DES name, described in Sec. 3.3.3, leaving several real transients 'un-discovered'. The fault was revealed later after re-processing the entire Y1 data-set with the use of updated pipelines and DES13C3absw was classified as potential SN type-Ia. As such, it was used in various cosmology analysis samples, where it was treated as an outlier of the Hubble diagram. At that point, it came to my attention its luminous peak brightness ($M_r \sim -20.6$), which was inferred from its host $z_{photo} = 0.18$. After examining closely its postage-stamps, I realized that the SNe was associated with the wrong host, and its real host has a redshfit of $z = 0.07$, which agrees with the SN PSNID classification as a SN Ia at low redshift.
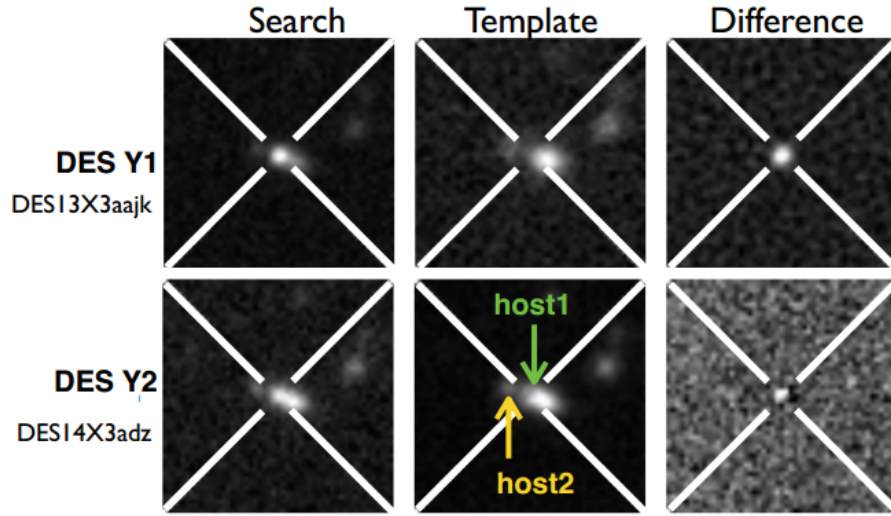
Figure 3.16: The triplet (search, template and difference) postage stamps of the same SN, discovered as two different candidates (*top:* DES13X3aajk, *bottom:* DES14X3adz), in the two consecutive DES seasons (*top:* Y1, *bottom:* Y2). The location of the SN, between the two close-by host galaxies (*green:* host1 at $z_{photo} = 0.44$) and *yellow:* host2 at $z_{photo} = 1.01$) could be explained as a strong gravitational lensed SNe.

DES13X3aajk falls in a similar category as DES13C3absw, in the sense that was not discovered during the Y1, but afterwards. The explosion happened in mid-December 2013 and the light-curve showed clear evidence of SNe activity, and even some hints of a second bump in z-band, signature of SN type-Ia. The interesting fact about this candidate is that it was discovered in Y2 data using all the tools developed for Y2 SLSNe and SNe search. Fig. 3.16 shows the triplet (search, template and difference) postage stamps of the same SNe, discovered as two different candidates, in the two consecutive DES seasons; Y1 in top row and Y2 in bottom row.

The fact that a SN could be visible and detectable in two consecutive seasons of DES, automatically indicated a long lasting light-curve. Combining that detail with the two closest hosts at $z_{photo} = 0.44$ (host1-*green*) and $z_{photo} = 1.01$ (host2-*yellow*), made this a very interesting candidate.

The proximity of the two close-by galaxies, and the location of the SN between the two galaxies, suggested it could be a lensed SN. Such events are rare, but have already been detected (Chornock et al., 2013; Quimby et al., 2013b; Kelly et al., 2015, and Sec. 1.6 of this thesis). We targeted the closest host galaxy (host1-*green*) with the OzDES Y2 program in late December 2014 and obtained a redshift at $z_{spec} = 0.295$ which ruled out the possibility of a SLSN. Also, the case of a lensed SN was dismissed, based on the photometric redshifts of the hosts and the resulted Einstein radius expected, which is significantly smaller than what we observed.

DES13C3baf was one the most promising hostless transients discovered in Y1, with the closest galaxy to be ~ 4 arcseconds away at $z_{photo} = 0.675$. It was discovered at the beginning of Y1 and its light-curve showed minor slow rise in all four bands, then remained flat for almost a month in the i and z bands, whereas in g and r bands started dropping. Because of the absence of a second bump in any of the filters and the long life span of its light-curve, this transient was considered to be an excellent SLSNe candidate (Fig 3.14).

In early October 2013, it peaked at $m_z = 22.05$ and from that time on, the light-curve was fading slowly throughout the rest of the season, showing clear evidence of colour evolution. DES13C3baf was also considered to be a high redshift SN type-Ia candidate, as the results from PSNID showed a moderate fit to SN Ia at $z_{photo} = 1.2$. During Y1 we attempted to obtain a live spectrum of the transient with the Gemini South telescope, but due to bad weather conditions it was never observed. Furthermore, we included the location of DES13C3baf to the OzDES Y2 program (Sec. 5.3.2), tagged as a 'SN host faint' target after the transient had faded away, with the condition to be observed once in case any faint emission lines from the faint host galaxy were detected. This attempt did not secure a redshift for this candidate, either.

DES13X3obu was classified as a SLSN candidate around mid-November 2013, because of its long rise time up to peak and the fact that it appeared to be hostless. Due to its faint peak magnitude $_z = 23.65$, any live spectroscopic follow-up would be impossible given the evidence of almost no colour evolution of the light curve. It was also targeted with OzDES in Y2, which obtained two spectra on the location of the transient. Even after combining the two spectra together a redshift estimation was not possible.

DES13E1nkg became a hostless SLSN candidate around its peak, in early November 2013, because of the ~ 30 days rise time in r, i and z bands. Also, at the decline phase it showed significant colour evolution, as the g band dropped to zero flux quickly after peak, compared to the other three bands. It was observed with OzDES on 30 November 2013 as part of the live transients follow-up component of the program, but no secure redshift or classification was obtained. Furthermore, in Y2, the location of the transient was targeted again as a 'SN host faint' object and additional three spectra were taken without any luck at securing a redshift of the faint host.

DES13X3beu had a slow and long rise time up to the beginning of November 2013, when it was selected as SLSN. The light-curve showed minor colour evolution, which is a sign for AGN activity. In addition, this transient was not detected down to 3σ limit in

g band at any point of its light-curve. Its faint peak at $_z = 23.21$, made it difficult for the object to be included to any live spectroscopic follow-up telescope queue.

DES13X3bcg was another faint and hostless SLSN candidate. It showed similar behaviour as DES13X3beu, but in this case were only a handful of detections (r band) over 3σ. It reached peak at the beginning of October 2013 and the light-curve reached zero flux in i and z bands by the end of January 2014, close to the end of Y1. It was targeted by OzDES in Y2 as a 'SN host faint' object, which obtained a tentative redshift of $z_{spec} = 0.636$, due to the low SNR of the data. At this redshift ($z_{spec} = 0.636$), DES13X3bcg would not be as bright as a SLSNe (which would require a redshift of $z > 1.1$).

DES13E1xe was detected early in Y1 season as a transient and classified as SLSN candidate by the end of September 2013, when it peaked after 30 days of rising in all four bands. After peak it showed minor colour evolution, which resulted in being targeted with the OzDES live spectroscopic follow-up program. Almost a month later, when three spectra were taken, we classified this object as an AGN at $z_{spec} = 0.306$.

3.6 Summary

In this chapter, I presented my initial contribution to the DES collaboration, which started right after DECam's first light during the SV period of operations. I was actively involved in the 'Eyeball Squad', responsible for the visual inspection of all images acquired and the report of any anomalies, in order for the operations team to finish the commissioning of DECam.

This chapter also shows the DES SN survey strategy and operations during Y1, including the SNe fields and time optimization, the data pipelines ('search' and 'force' photometry), the discovery and archiving astronomical transients and the spectroscopic follow-up plans and actions. After the end of DES Y1, a series of updates on the difference imaging pipeline (Kessler et al., 2015) took place, described in detail in Sec. 5.3.1. The Y1 data were re-reduced and passed through the steps described in Sec. 3.3.3, with the final outcome internally released to the DES SN working group in August 2014.

The impact of such updates was noticeable for the entire DES SN Survey as the total number of named DES transients was only 14.500, compared to the ~ 26.000 transients named during observations in Y1. Also, the total number of possible SLSNe candidates was 702 objects related to a host galaxy and 114 hosless objects, compared to the total of ~ 1.500 possible SLSNe candidates I visually inspected during Y1. Those updates

taught a few lessons to the entire DES SN Survey, which helped us to be prepared for the DES Y2 observations as described in Sec. 5.3.

The bulk of this chapter focuses on the search for SLSNe within the data from Y1 of operations, which I constructed using tools provided by the SNe working group. The SLSNe search was operational during the entire DES Y1 of observations, between August 2013 and February 2014. This search involved a series of selection cuts on the existing DES transients database, in order to lower the amount of available transients that could be considered as SLSNe. Then, a visual inspection was placed in order to reject the obvious, non-SLSNe objects, leading to the creation of a final 'SLSNe candidates' list, which consists of 12 objects.

The final part of this chapter presents the results of the SLSNe search in DES Y1, alongside with light-curves and images of all the SLSNe candidates. Of those 12 SLSNe candidates, only one of them (DES13S2cmm) was confirmed to be a SLSN, and Chap. 4 is a detailed description of this object, similar to what was published by Papadopoulos et al. (2015).

Chapter 4

DES13S2cmm

4.1 Introduction

In this chapter, I discuss the discovery, confirmation process and modelling of the first SLSNe detected with DECam during the first season of DES operations in 2013. Moreover, I introduce the construction and use of bolometric light-curves in the study of SLSNe. The work outlined in this chapter, was constructed in collaboration with Dr. Chris D'Andrea, Dr. Mark Sullivan and Prof. Bob Nichol and was published in Papadopoulos et al. (2015).

My role in this section could be summarized in the discovery (via scanning, see Sec. 3.3.3) of DES13S2cmm, the photometric monitoring of the transient and the construction of the bolometric light-curve of DES13S2cmm and other SLSNe from the literature, which led to the direct comparison of those bolometric light-curves. Also, I contributed to the write-up of the spectroscopic follow-up proposal and I verified the power source model fits to the bolometric light-curve of DES13S2cmm, as well as the estimation of the peak absolute U-band magnitude.

4.2 Discovery

DES13S2cmm is located at $\mathrm{RA}(2000) = 02^h42^m32^s.82$, $\mathrm{Dec.}(2000) = -01^o21'30''.1$, and its official IAU name is **SN 2013hy**. However, we continue to use the DES name throughout this thesis so as to be consistent with other DES transients.

DES13S2cmm was first detected on 27th of August 2013 in the DES SN 'S2' field located in the Stripe 82 region (Table 3.2), and it was placed as a transient candidate to the queue for human scanning, as was the practice in DES Y1 (see Chap. 3) on the second epoch of observations of Y1 season. It was scanned as a SN by the end of September, and in early October of 2013 it was selected as a SLSN candidate, as it had been rising for
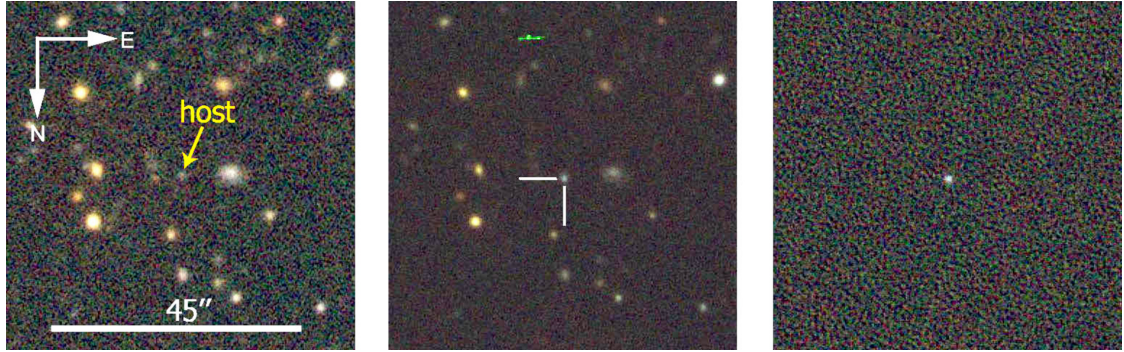
Figure 4.1: Colour images (*riz*) of the field surrounding DES13S2cmm. *Left:* Deep template image created from the co-addition of several epochs of data obtained during the DES Science Verification period in late 2012; the likely host galaxy is indicated by the arrow. *Centre:* The search image taken close to maximum light (28-Sept-2013) with the position of DES13S2cmm indicated. *Right:* The difference of the two previous images, clearly identifying DES13S2cmm at center. This image demonstrates the quality of difference images used for discovery and monitoring during the DES observing season.

~ 30 days and the host galaxy's photometric redshift at $z = 0.863 \pm 0.134$ was suggesting the high luminosity of this object. Fig. 4.1 presents DES *riz* imaging data at the position of DES13S2cmm: pre-explosion, post-explosion, and their difference image.

4.3   Light Curve

Fig. 4.2 shows the multi-colour light curve for DES13S2cmm, constructed from DES Y1 of observations. The light-curves does not include upper limits from the earlier, pre-explosion epochs available from the DES SV period in 2012-2013, as these data were taken hundreds of days prior to the data shown in Fig. 4.2 and are already used to create the reference template image for this field used in the difference imaging detection of the SNe.

The photometric pipeline from Sullivan et al. (2011) was used to reduce the DES photometric data for DES13S2cmm (also used in Maguire et al., 2012; Ofek et al., 2013). This pipeline is based on difference imaging, subtracting a deep, good seeing, pre-explosion reference image from each frame the SN is present in. The photometry is then measured from the differenced image using a PSF-fitting method, with the PSF determined from nearby field stars in the unsubtracted image. This average PSF is then fit at the position of the SN event, weighting each pixel according to Poisson statistics, yielding a flux, and flux error, for the SN.

We calibrated the flux measurements of DES13S2cmm to a set of tertiary standard stars produced by the DES collaboration (Wyatt et al., in preparation), intended to be in the AB photometric system (Oke and Gunn, 1983). The photometry shown in Fig. 4.2
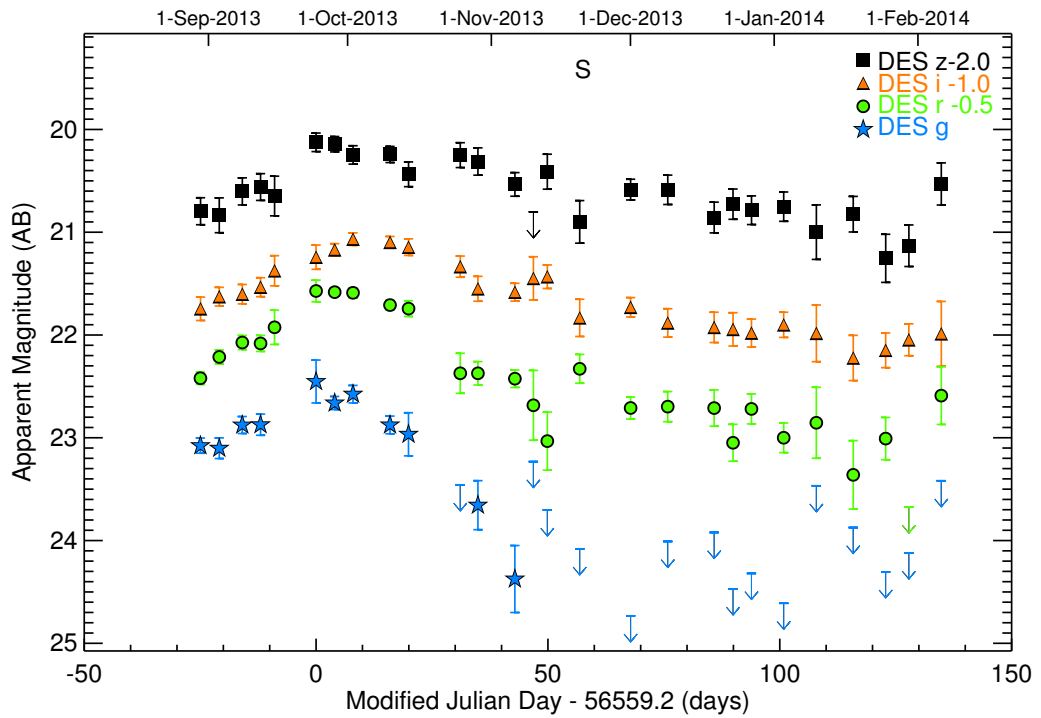
Figure 4.2: The observed AB magnitude light curve of DES13S2cmm in the four DES SN search filters ($griz$) as a function of the observed phase. 'S' denotes the epoch when the ESO VLT spectrum was obtained. The errorbars represent 1-σ uncertainties, and the arrow symbols are 3-σ upper limits. The phase relative to peak was defined using the observed-frame r-band. We have artificially offset (in magnitudes) the r, i and z band data for clarity.

has also been checked against the standard DES detection photometry, described in detail in Sec. 3.3, and found to be in good agreement. The light-curve data are presented in Table 4.1.

We corrected for Galactic extinction using the maps of Schlafly and Finkbeiner (2011), which estimate $E(B - V) = 0.028$ at the location of DES13S2cmm, leading to extinction values of 0.123, 0.070, 0.051 and 0.039 magnitudes in the DES $griz$ filters respectively. We did not include these corrections in the values reported in Table 4.1, but did correct for extinction in all figures and analysis herein, including Figure 4.2.

4.4   Spectroscopy

On the 5th of November 2013, DES13S2cmm was placed to Gemini South Target of opportunity (ToO) queue, but due to bad weather and higher priority targets, the observation was delayed. So, on the 12th November 2013, we requested Director's Discretionary Time at the European Southern Observatory (ESO) Very Large Telescope (VLT) to observe DES13S2cmm, and were awarded ToO time within days. The closeness of the object to the moon and instrument scheduling issues, conspired to delay observations until the 21st of November 2013, at which point DES13S2cmm was approximately 30 days after peak brightness (rest frame). A spectrum was obtained with the FOcal Reducer and low dispersion Spectrograph (FORS2; Appenzeller et al., 1998) using the GRIS_300I+11 grism, the OG590 order blocker, and a 1" slit, with an exposure time of 3600s (3×1200s). This configuration provided an effective wavelength coverage of 5950 Å to 9400 Å.

The reduction of the FORS2 data followed standard procedures using the Image Reduction and Analysis Facility[1] environment (v2.16), and the pipeline described in Ellis et al. (2008). This pipeline includes an optimal, two-dimensional (2D) sky subtraction technique as outlined in Kelson (2003), subtracting a 2D sky frame constructed from a sub-pixel sampling of the background spectrum and a knowledge of the wavelength distortions determined from 2D arc comparison frames. The extracted 1D spectra were then scaled to the same flux level, the host-galaxy emission lines were interpolated over, and the spectra were combined using a weighted mean and the uncertainties in the extracted spectra.

Fig 4.3 presents the reduced 2D FORS2 spectrum, where wavelength increases to the right along the horizontal axis and the vertical axis is distance along the slit. We highlight the obvious narrow nebular emission lines in the host galaxy of DES13S2cmm, specifically [O II] $\lambda3727$ Å, Hβ $\lambda4861$ Å, and [O III] $\lambda4959, 5007$ Å. One can assume that these

---

[1] The Image Reduction and Analysis Facility (IRAF) is distributed by the National Optical Astronomy Observatories, which are operated by the Association of Universities for Research in Astronomy, Inc., under cooperative agreement with the National Science Foundation.

Table 4.1: Light curve data for DES13S2cmm used in Fig. 4.2. We provide the observed calendar date, modified Julian Day (MJD), observed phase relative to peak MJD (defined relative to peak flux in the *r*-band), and fluxes (not corrected for Galactic extinction) with 1-σ uncertainties in the DES *griz* passbands. These fluxes can be converted to AB magnitudes using $mag_{AB} = -2.5 \log_{10}(f) + 31$.

Date	MJD	Phase (days)	f_g	f_r	f_i	f_z
30-AUG-2013	56534.3	-25	1138±77	1705±94	1730±181	1913±231
3-SEP-2013	56538.3	-21	1112±103	2063±129	2234±186	1845±288
8-SEP-2013	56543.3	-16	1369±104	2348±148	2285±198	2285±277
12-SEP-2013	56547.2	-12	1373±130	2329±167	2433±207	2376±284
15-SEP-2013	56550.2	-9	±	2691±413	2818±380	2193±389
24-SEP-2013	56559.2	0	2022±388	3727±363	3183±346	3548±295
28-SEP-2013	56563.2	4	1668±97	3688±133	3400±187	3488±241
2-OCT-2013	56567.2	8	1805±141	3666±166	3742±209	3169±261
10-OCT-2013	56575.2	16	1370±108	3285±137	3636±192	3182±230
14-OCT-2013	56579.1	20	1260±243	3182±223	3482±259	2663±295
25-OCT-2013	56590.3	31	886±346	1782±319	2924±277	3163±352
29-OCT-2013	56594.1	35	667±146	1782±187	2398±267	2987±366
6-NOV-2013	56602.1	43	344±103	1698±132	2326±185	2433±257
10-NOV-2013	56606.1	47	803±426	1338±418	2633±510	1817±634
13-NOV-2013	56609.1	50	-312±276	970±252	2672±281	2726±426
20-NOV-2013	56616.1	57	347±195	1855±239	1848±307	1739±331
1-DEC-2013	56627.0	68	184±107	1306±129	2032±176	2322±216
9-DEC-2013	56635.0	76	259±208	1322±178	1766±225	2318±304
19-DEC-2013	56645.1	86	302±226	1305±211	1697±230	1808±248
23-DEC-2013	56649.1	90	261±136	956±157	1667±248	2038±276
27-DEC-2013	56653.1	94	41±156	1295±174	1613±201	1930±248
3-JAN-2014	56660.0	101	252±119	1000±132	1736±196	1993±261
10-JAN-2014	56667.1	108	310±343	1144±364	1609±408	1586±387
18-JAN-2014	56675.0	116	-75±236	717±220	1290±261	1863±297
25-JAN-2014	56682.0	123	306±158	992±188	1382±215	1254±270
30-JAN-2014	56687.0	128	345±188	523±179	1518±217	1404±261
6-FEB-2014	56694.0	135	-346±359	1459±376	1602±465	2443±461

Figure 4.3: The reduced VLT FORS2 two-dimensional spectrum for DES13S2cmm. The key nebular emission lines used to derive the redshift of the host galaxy, and therefore supernova, are labelled.

lines originate from the underlying host galaxy as their spatial extent along the vertical axis is greater than the observed trace of the main supernova spectrum. This observation does not exclude the possibility that such emission lines come from the supernova, but it is difficult to address this issue with the low resolution, and low signal-to-noise, data. We note that the observed emission lines are not significantly broadened or asymmetrical, as witnessed in type IIn supernovae.

No evidence of any further emission lines could be seen, from the SN and/or host galaxy. Therefore, it is unlikely that DES13S2cmm is a type II supernova (normal or superluminous).

Using these nebular emission lines, we determined a redshift of $z = 0.663 \pm 0.001$ for the host galaxy of DES13S2cmm, where the uncertainty is derived from the wavelength dispersion between individual emission lines. This measurement is consistent with the redshift of the SN based on identifications of the broad absorption features seen in the spectrum. As the redshift derived from the host-galaxy spectrum is significantly more precise, henceforth we adopt this value as the redshift to DES13S2cmm.

The spectral classification for DES13S2cmm is based on the SUPERFIT program (Howell et al., 2005), which compares observed spectra of SNe to a library of template SN spectra (via χ^2 minimisation), while accounting for the possibility of host-galaxy contamination in the data. We added as template spectra of SLSNe-I (PTF09atu, PTF09cnd and PTF10nmn; Quimby et al., 2011b) and SLSN-R (SN 2007bi; Gal-Yam et al., 2009) to SUPERFIT to facilitate our classification. We found that the highest-ranked fits to DES13S2cmm were these SLSNe templates, preferred over templates of normal SN types (e.g., SN Ia). The SLSNe-I templates were slightly better fits to DES13S2cmm than SN 2007bi (SLSN-R), although this may be due to not having a template for SN 2007bi at a similar phase to our spectrum for DES13S2cmm.

We show the spectrum of DES13S2cmm in Fig. 4.4, alongside spectra from other well-studied SLSNe in the literature at a similar phase in their light curves (Quimby et al., 2011b; Inserra et al., 2013; Gal-Yam et al., 2009). There is a deficit of spectra for SLSNe in the literature at these late phases for a robust comparison. However, the broad resemblance between the spectra of PTF10hgi, SN 2011kf, SN 2011ke and DES13S2cmm, all taken at approximately $+30$ days past peak, suggests DES13S2cmm is a similar object to these other SLSNe-I. The spectrum of DES13S2cmm is also similar to the spectrum of SN 2007bi (a SLSN-R in Gal-Yam et al., 2009), although the differences between Type I and Type R SLSNe remains unclear (Inserra et al., 2013), and either classification would be interesting given the sparseness of the data. Also, Fig. 4.4 contains the spectrum of SN 2007if, a 'super-Chandrasekhar' SN Ia (Scalzo et al., 2010), an over-luminous
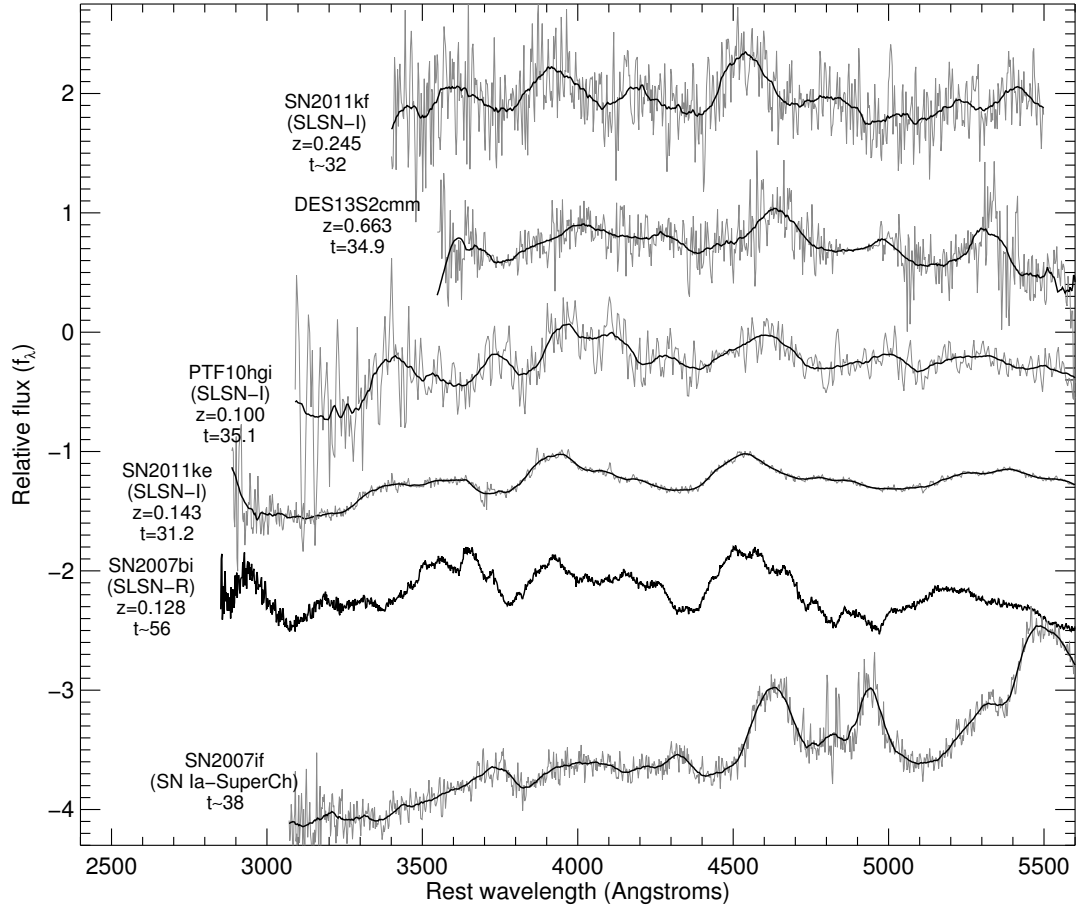
Figure 4.4: The VLT FORS2 spectrum of DES13S2cmm (second from top) compared to other SLSNe of similar phase in their light curves. From top to bottom, we also show SN 2011kf (Inserra et al., 2013), PTF10hgi (Quimby et al., 2011b), SN 2011ke (Inserra et al., 2013) and SN 2007bi(classified as Type R in Gal-Yam et al., 2009); as discussed in Sec. 4.4, SUPERFIT identifies these SLSNe as some of the best-fitting spectral templates to DES13S2cmm. In each case, the light grey shows the raw data and the solid line is a Savitsky-Golay smoothed version of the spectrum. The spectra are labelled with the SN name, SLSN type (except DES13S2cmm), redshift, and the phase when the spectrum was taken. We show the spectrum of the 'super-Chandrasekhar' SN Ia SN 2007if as discussed in Scalzo et al. (2010). Note that the spectrum for 2007bi, while at a later phase than the other data, is the earliest spectral observation of this SN.

($M_V = -20.4$) and likely thermonuclear SN located in a faint host galaxy. This comparison clearly shows that DES13S2cmm is unlikely to be a super-Chandrasekhar SN Ia.

4.5 Host-galaxy properties

The host galaxy of DES13S2cmm is detected in our reference images that contain no SN light. Using SEXTRACTOR in dual-image mode and the i-band image as the detection image, we measured host-galaxy magnitudes of $g = 24.24 \pm 0.13$, $r = 23.65 \pm 0.10$, $i = 23.31 \pm 0.10$ and $z = 23.26 \pm 0.17$ (AB MAG_AUTO magnitudes). The large photometric errors are due to the relatively shallow depth, and poor seeing, of the template image generated from the DES SV data.

The estimated photometric redshift of the host galaxy at the time of discovery was $z_{photo} = 0.86 \pm 0.13$ (68 percentile error). This photometric redshift was derived by the DESDM neural network photo-z module code, with uncertainties estimated from the nearest neighbour method, using data taken during SV (Sánchez et al., 2014). Photometric redshifts (when available) are used when selecting SLSN candidates for spectroscopic follow-up, and for DES13S2cmm this redshift implied that the event was brighter than $M_U^{peak} = -21$ (typical for SLSNe; Gal-Yam, 2012). Since the start of the first DES observing season, the photometric catalogue derived from SV data has improved and presently the DESDM photo-z for the host of DES13S2cmm has improved to $z_{photo} = 0.71 \pm 0.06$. This is in better agreement with our measured spectroscopic redshift ($z = 0.663 \pm 0.001$).

Using the DES host-galaxy photometry and the spectroscopic redshift from VLT, we estimated that the stellar mass of the host galaxy is $\log(M/M_\odot) = 9.3 \pm 0.3$ using stellar population models from PEGASE.2 (Fioc and Rocca-Volmerange, 1997), and $\log(M/M_\odot) = 9.0 \pm 0.3$ using the stellar population templates from Maraston (2005) (both corrected for Milky Way extinction and fixing the redshift of the templates to $z = 0.663$). Such a low stellar-mass host galaxy is consistent with the findings for other SLSNe (Neill et al., 2011; Chen et al., 2013; Lunnan et al., 2014b).

The host-galaxy metallicity was estimated from the VLT spectrum using the double-valued metallicity indicator R_{23}, defined as ([OII] $\lambda 3727$ + [OIII] $\lambda 4959, 5007$)/$H\beta$. Fluxes and uncertainties are derived individually for each emission line from fits of a gaussian plus a first-order polynomial, with the assumption that there is no contamination of the galaxy emission lines from the SN. We computed metallicities using the calibrations of Kobulnicky and Kewley (2004) and McGaugh (1991), and used the formulae derived in Kewley and Ellison (2008) to convert these metallicities into the calibration of

Kewley and Dopita (2002) – a step that allows for direct comparison between different methods. We note that since $H\alpha$ and NII $\lambda6584$ are redshifted to wavelengths beyond our spectral coverage, we cannot determine the branch of the R_{23} function that the metallicity lies on. However, the derived value for R_{23} is close to its theoretical maximum, which minimizes the difference in metallicity estimates between the two branches.

Assuming the lower (upper) branch, we find a metallicity ($12 + \log[\text{O/H}]$) of 8.30 (8.38) from McGaugh (1991) and 8.30 (8.42) from Kobulnicky and Kewley (2004), which is consistent with the median metallicity of 8.35 found by Lunnan et al. (2014b) for a sample of 31 SLSNe host galaxies. The total uncertainty is dominated by the calibration (~ 0.15 dex), while the statistical uncertainty and the scatter induced by the conversion to Kewley and Dopita (2002) are comparatively negligible. We thus find a host-galaxy abundance ratio that is distinctly sub-solar (8.69; Asplund et al., 2009), though not as extremely low as has been seen for other SLSNe, such as SN2010gx ($12 + \log[\text{O/H}]$=7.5; Chen et al., 2013).

4.6 Bolometric light-curve of DES13S2cmm

Fig. 4.5 shows the bolometric light curve of DES13S2cmm. This single light curve was constructed by fitting a single blackbody Spectral Energy Distribution (SED) to the DES multi-colour data (requiring measurements in a minimum of three photometric bandpasses for a fit), at each epoch of the light-curve (Table 4.1), as illustrated in Fig. 4.6.

In detail, we redshift blackbody spectra to the observer frame and integrate these spectra through the response functions of the DES filters. We then determined the best-fitting parameters (temperature and radius) for a black body to the extinction-corrected photometry, and integrate this spectrum in the rest frame to obtain the bolometric luminosity per epoch (Fig. 4.6).

This procedure benefits from the homogeneity of the DES data, as we possess approximately equally-spaced epochs across the whole light curve – typically in four DES passbands – due to our rolling search. The errors on the bolometric luminosities were calculated from the fitting uncertainties on the blackbody spectra.

We visually checked our best-fit blackbody curves for each epoch of the DES13S2cmm light curve against the observed $griz$ photometry, and found them to be reasonable within the errors (Fig. 4.6). The largest discrepancies were seen in the g-band, where some epochs were below the fitted curves, possibly due to UV absorption in the underlying spectral energy distributions relative to a blackbody curve. Inserra et al. (2013) compared the predicted UV flux (from a blackbody curve) for two SLSNe with SWIFT UV observations, and found that the fluxes were consistent within the error. Therefore, we
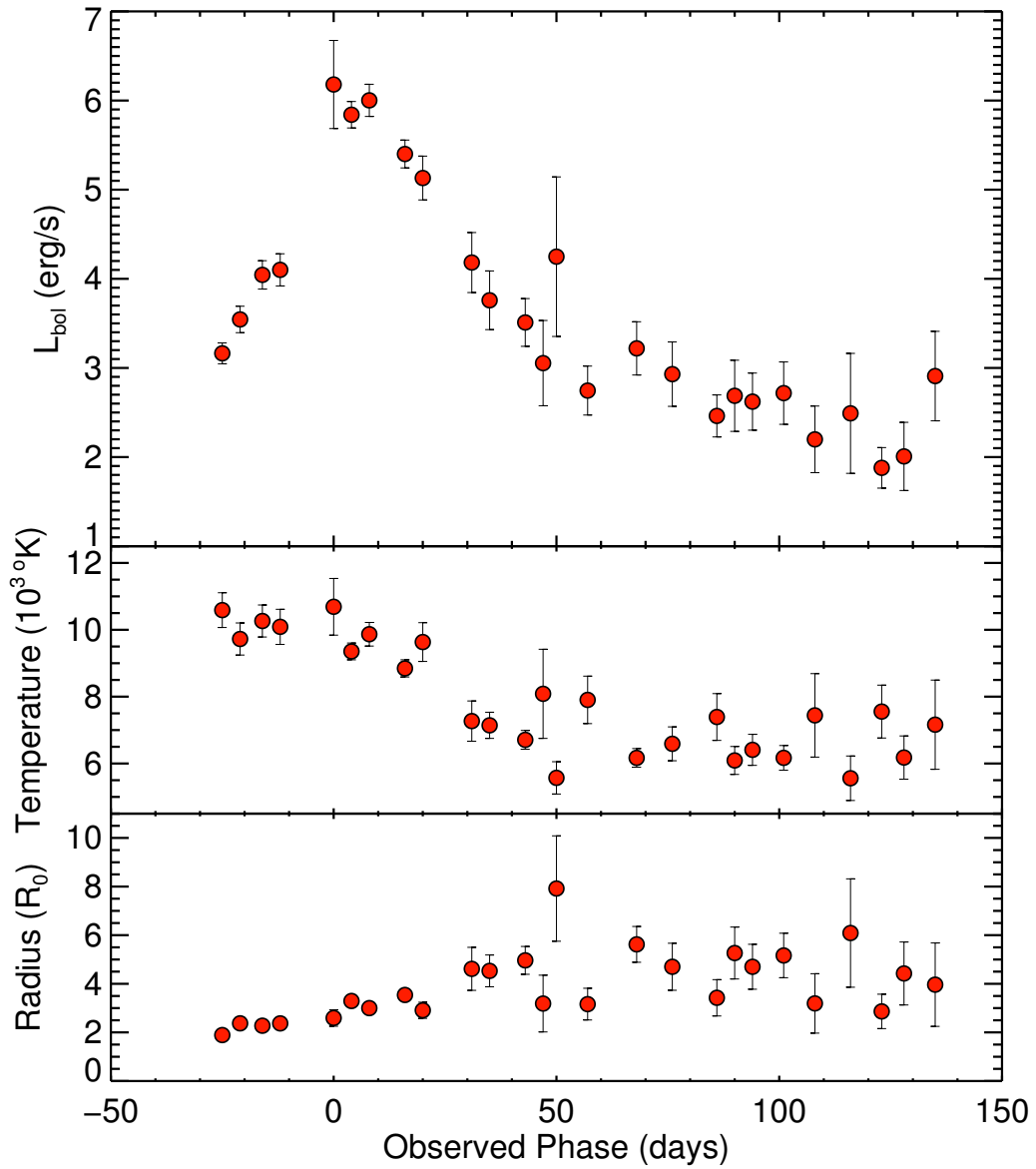
Figure 4.5: *Top panel:* The bolometric light curve of DES13S2cmm ploted against the observer frame phase. *Middle and Bottom panels:* Temperature and radius evolution of the best-fitting blackbody to each photometric epoch which is used to construct the bolometric light curve.
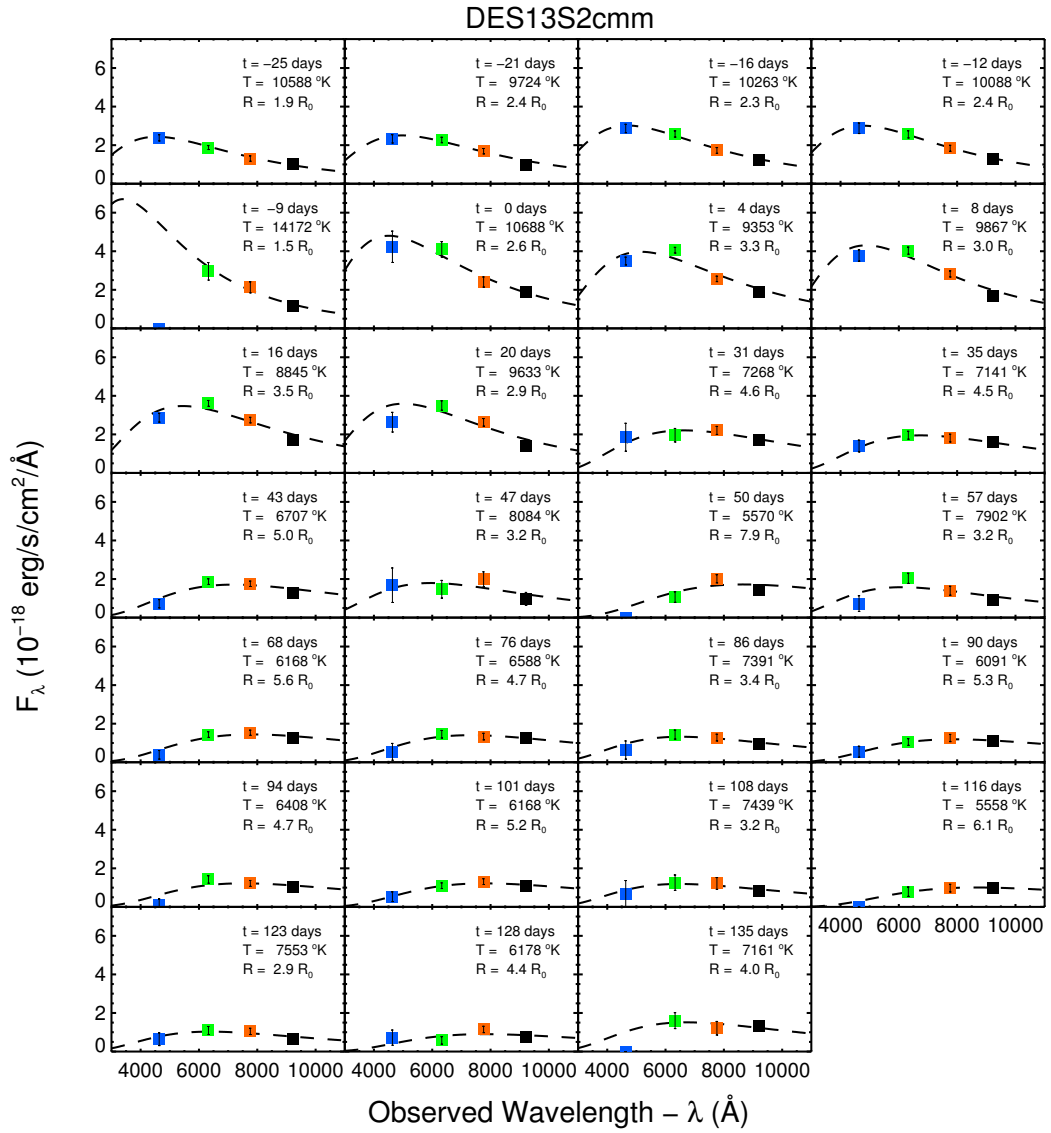
Figure 4.6: The blackbody SED fits to each epoch of DES13S2cmm photometry, constructed by the best fit Temperature ($T[^oK]$) and Radius ($R[R_0 = 10^{15}cm]$), which are reported on each panel. The phase (t) refers to the observer's frame phase.

make no additional correction to the derived bolometric light curve, but note that quantifiable systematic errors in the bolometric luminosity require spectral templates, which in turn requires more spectral data of SLSNe than is currently publicly available.

Using the bolometric light curve of DES13S2cmm, we can determine the peak luminosity of the event and compare it to the definition of a SLSNe in Gal-Yam (2012). This was achieved by integrating the best-fitting blackbody spectra through a standard U-band filter response function (on the Vega system) to obtain the rest-frame absolute magnitude in U-band (M_U). We find that the 24th of September 2013 epoch ($t = 0$ relative phase in Table 1) gives the largest (peak) absolute U-band magnitude of $M_U^{peak} = -21.05^{+0.10}_{-0.09}$, which is consistent with the SLSNe threshold of $M_U^{peak} < -21$ in Gal-Yam (2012).

This result was checked using a model-independent estimate based on the observed r-band peak magnitude. At the redshift of DES13S2cmm, the observer-frame r band maps into the rest frame as a synthetic filter with an effective wavelength of ≈ 3800Å, slightly redward of the standard U-band. Defining a synthetic filter as such, means the k-correction is independent of the SN spectral energy distribution, and since we are in the AB system the correction is simply $2.5 \log(1 + z)$. We apply this k-correction to the observed r-band peak magnitude, as well as corrections for Galactic extinction and distance modulus, to yield an estimated peak absolute magnitude of -20.47 (AB), or -20.74 (Vega) in our synthetic filter (where we have computed the AB to Vega conversion for our filter). While this is fainter than our blackbody-based estimate, Vega magnitudes are sensitive to the exact shape of the filter in this region, due to the jump in Vega from 3700-3900Å; thus even the small difference in effective wavelength between U band and our synthetic filter can result in significant offsets. The absolute magnitude in our synthetic filter from the best-fitting blackbody method yields $M_{\text{synthetic}} = -20.59$, proving that our model-independent estimate is consistent with our results from the blackbody fitting.

We note that the peak magnitude (Vega) for DES13S2cmm classifies it as a SLSN, provided the magnitude is intrinsic to the SN and not enhanced by other effects. Visual inspection of the images in Fig. 4.1 (including the surrounding areas) shows little evidence for strong gravitational lensing, which could affect the observed brightness of this SN (we note that the host galaxy would have to be lensed as well). We cannot conclusively rule out the possibility of strong lensing, as in the case of PS1-10afx (Quimby et al., 2014), but as discussed above the spectrum and extended light curve of DES13S2cmm are inconsistent with a normal SN, while the probability of such a strong lensing event in our DES data is less than the probability of discovering a SLSN, based on the lensing statistics given in Quimby et al. (2014), the lower redshift of DES13S2cmm and smaller search area of DES. Moreover, the observed $r - i$ peak colour of DES13S2cmm is consistent with the expected colours of other unlensed SNe (including SLSNe) shown in

Fig. 1.22 (same as figure 4 of Quimby et al. (2014)), i.e., DES13S2cmm is located below the thick, black line in this plot.

4.7 Comparison of bolometric light-curves

For comparison with DES13S2cmm, we show in Fig. 4.7 the bolometric light curves for 14 SLSNe-I from the literature, all of which were described in Chap. 2: PS1-10ky, PS1-10awh (Chomiuk et al., 2011) and PS1-10bzj (Lunnan et al., 2013); SN 2010gx (Pastorello et al., 2010a); PTF 10hgi, SN 2011ke, PTF 11rks, SN 2011kf and SN 2012il (Inserra et al., 2013); SNLS 06D4eu and SNLS 07D2bv (Howell et al., 2013); and LSQ 12dlf, SSS 120810 and SN 2013dg (Nicholl et al., 2014). We exclude from this figure, and our analysis, other SLSNe-I that do not possess data for at least three passbands for each epoch (defined as being taken within a 24 hour window) over a majority of their light curves. This criterion, was defined to ensure well-constrained bolometric light-curve fits, excludes namely PTF 09atu, PTF 09cnd, and PTF 09cwl (Quimby et al., 2011b); SCP 06F6 (Barbary et al., 2009); and SN 2006oz (Leloudas et al., 2012).

The full bolometric light curves for these SLSNe-I were calculated using the same methodology as described above for DES13S2cmm (i.e. using the published photometric data and requiring three or more passbands per epoch). As a check, our bolometric light curves for PTF 10hgi, SN 2011ke, PTF 11rks, SN 2011kf and SN 2012il are similar to those published in Inserra et al. (2013), with any offsets attributed to differences in the integration of the blackbody curve; we integrate over all wavelengths, while Inserra et al. (2013) integrate over the wavelength range of their observed optical passbands (we are able to reproduce their luminosities if we follow their procedure). Our bolometric light-curves for PS1-10ky, PS1-10awh, and PS1-10bzj are also similar to those published in the literature.

In Fig. 4.7, the phase relative to peak for DES13S2cmm was defined as the peak of the observer-frame r-band, which occurred on MJD 56563.2, while for other SLSNe-I we simply used the phase relative to peak as reported by the individual literature studies. In the case of SNLS 06D4eu and SNLS 07D2bv, Howell et al. (2013) reported a phase based on their calculation of the bolometric light curves, which we use herein, but note that there may be greater uncertainty in the definition of the time of peak for these light curves.

The top panel of Fig. 4.7 shows that DES13S2cmm is one of the faintest SLSNe-I around peak compared to the other SLSNe-I in the literature, and possesses one of the slowest declining tails (beyond approximately +30 rest-frame) of the SLSNe studied herein. In the bottom panel of Fig. 4.7, we compare DES13S2cmm to possible Type R
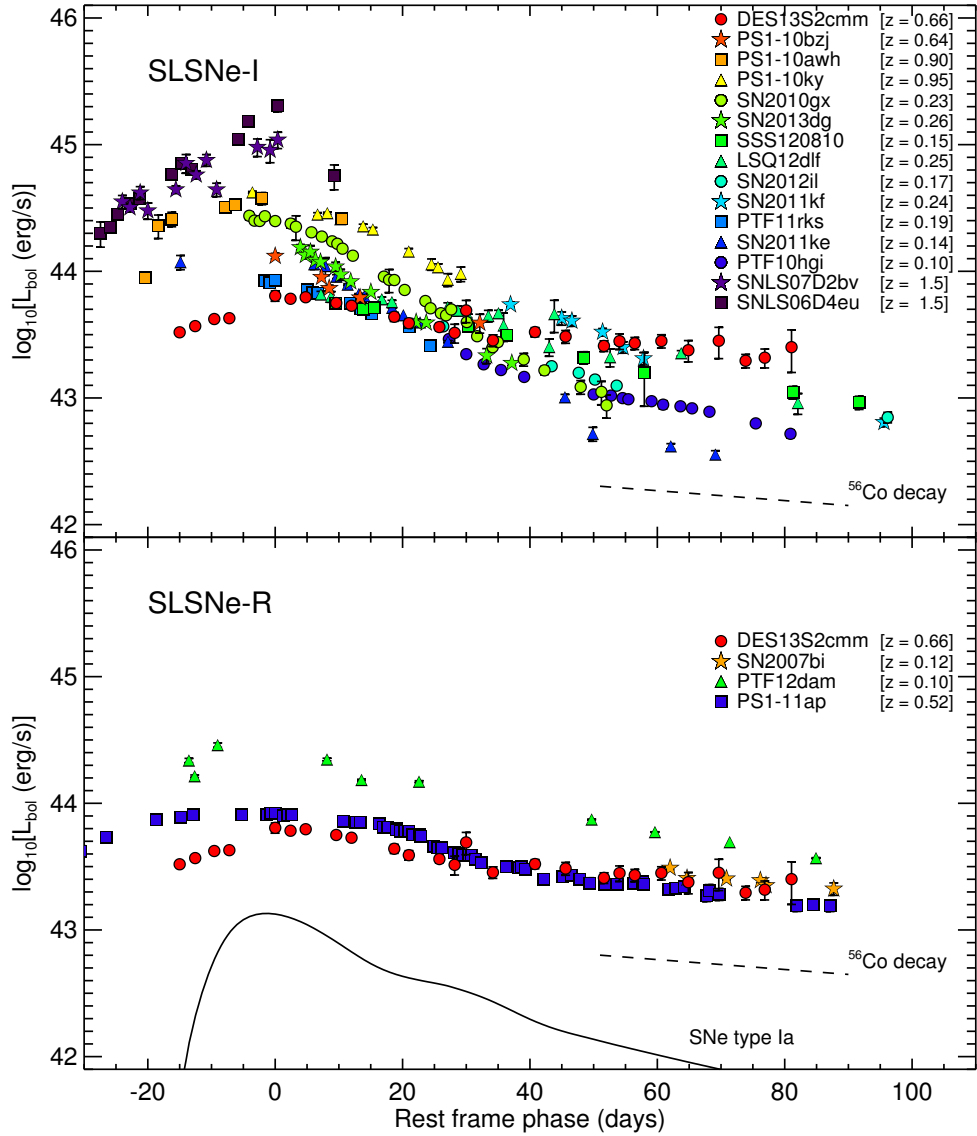
Figure 4.7: The bolometric light curve of DES13S2cmm (red circles) compared to other SLSNe in the literature (see text for explanation). These bolometric light curves were constructed by fitting a single blackbody spectrum to the multicolour data available per epoch (requiring at least three photometric measurements per epoch), and then by integrating the blackbody spectral energy distribution to produce the bolometric luminosity per rest-frame epoch (described in detail in Section 4.7). We show statistical errors on the blackbody fits to each epoch of these light curves, but in most cases this error is smaller than the plotting symbol. We stress that these errors do not account for systematic uncertainties involved in the bolometric calculation (e.g., assuming a blackbody for the spectral energy distribution of SLSNe, especially for the UV part of the rest-frame spectral energy distribution). The phase relative to peak (y-axis) for the literature SLSNe is taken directly from the published individual studies and not recalculated herein. The dashed lines shown in both panels represent the expected ^{56}Co decay rate at late times. In the lower panel, we show the bolometric light curve expected for a typical Type Ia SNe (solid line) to again illustrate the extraordinary brightness, and extended duration, of these SLSNe

SLSNe (to be consistent with the classification scheme of Gal-Yam, 2012) and find the late-time light curve of DES13S2cmm to be similar to both PS1-11ap (McCrum et al., 2015) and SN2007bi (Gal-Yam et al., 2009), highlighting the possible overlap between these two SLSNe types, as discussed in Section 4.4 and Inserra et al. (2013).

Fig. 4.7 also demonstrates that the fifteen SLSNe-I light curves (top panel) have similar luminosities at approximately +25 days (rest frame) past peak, close to the inflection point in the light curves when their extended tails begin to appear. We calculate the dispersion, as a function of relative phase, for the SLSNe-I light curves shown in Fig. 4.7, linearly interpolating between large gaps in each light curve to provide an evenly sampled set of data. We find a minimum dispersion of $\sigma(\log_{10}L_{\mathrm{bol}}) = 0.11$ (equivalent to 0.29 magnitudes) around +30 days past peak (rest frame), to be derived from the nine SLSNe in Fig. 4.7 constraining this phase. This dispersion in the light-curves can be decreased to $\sigma(\log_{10}L_{\mathrm{bol}}) = 0.083$, or 0.20 magnitudes, at approximately +25 days past peak (rest frame) if we exclude the four highest redshift SLSNe-I above $z \simeq 1$ (SNLS 06D4eu, SNLS 07D2bv, PS1-10ky. PS1-10awh). The bolometric luminosities of these SLSNe-I are more difficult to estimate because of the uncertainties associated with modelling the UV part of the spectrum by assuming a simple blackbody curve. There could also be evolution in the population with redshift. As commented in Quimby et al. (2011b), such light curve characteristics could point towards a possible 'standardisation' of SLSNe-I, as with SNe Ia, leading to their use as high-redshift 'standard candles' for cosmological studies (King et al., 2014).

As noted in Sec. 1.5.5, Inserra and Smartt (2014) proposed a 'standardisation' of the peak magnitude of 16 SLSNe using a stretch-luminosity correction similar to the Δm_{15} relationship of Phillips (1993) for SNe Ia. They found that SLSNe that are brighter at peak have slower declining light curve over the first 30 days after peak (rest frame) and, correcting for this correlation, the dispersion of the peak magnitude of SLSNe can be reduced to $\sigma \simeq 0.2$. This is similar in size to the dispersion between +25 to +30 days past peak seen in Fig. 4.7, and is worse by only a factor of two compared to the dispersion obtained for standardised SNe Ia.

Both Fig. 4.7 and Inserra and Smartt (2014) suggest that some standardisation of SLSNe light curves is possible, but further observations and analyses are required to find the best approach. For example, the light curve of DES13S2cmm does not appear to follow the correlation found by Inserra and Smartt (2014), as it has a faint peak magnitude relative to other SLSNe, but is also slowly declining towards +30 days after peak. A direct comparison to Inserra and Smartt (2014) is difficult as our study uses different sample selection criteria (only 9 of their 16 SLSNe are included here because of our requirement to have three passbands per epoch), while Inserra and Smartt (2014) estimate

a common synthetic peak magnitudes for all their SLSNe using their own time-evolving spectral template.

4.8 Power source of DES13S2cmm

The details of the power source of SLSN-I remain unclear and are much debated (see Sec. 1.5.3). Here, we investigate the two popular explanations in the literature for SLSNe-I: radioactive decay of ^{56}Ni and energy deposition from a Magnetar.

4.8.1 Radioactive ^{56}Ni model

As can been seen in Fig. 4.7, the decline rate of DES13S2cmm is approximately that expected from the decay of ^{56}Co (dashed line). This is suggestive of the SN energy source being the production and subsequent decay of large quantities of ^{56}Ni produced in the explosion. To test this theory, we fit the bolometric light curve of DES13S2cmm to a model of ^{56}Ni, which is given by Eq. 1.32 and described in full detail in Sec. 1.5.3.

The model can be constructed using four parameters: the explosion epoch (t_0), the energy of the explosion (E), the total ejected mass (M_{ej}), and the amount of ejected mass which is ^{56}Ni (M_{Ni}). We define the fraction of the ejecta mass that is in ^{56}Ni as $f_{Ni} = M_{Ni}/M_{ej}$. We fit our model to the data with a variety of upper limits on f_{Ni}, varying from 0.3 to 1.0. However, we follow Inserra et al. (2013) in assuming a physically motivated upper limit on f_{Ni} of 0.5, which they base on the prevalence of intermediate-mass elements in their spectra of lower-z SLSNe, and the calculations of ^{56}Ni production in core-collapse SNe by Umeda and Nomoto (2008). We report the best-fitting parameters and goodness of fit for these models in Table 4.2, while showing the range of f_{Ni} models in Fig. 4.8 to illustrate the scale of uncertainties in the theoretical modelling.

We found that the ^{56}Ni model is not a good fit to the bolometric light curve, as the best-fitting model has a $\chi^2/dof = 2.7$ (χ^2 of 59 for 22 degrees of freedom), and is physically unrealistic ($f_{Ni} = 1$). As can be seen in Table 4.2, the model prediction for M_{Ni} is relatively robust ($3.8 - 4.4 M_{\odot}$), as this parameter is primarily constrained by the peak luminosity of the light curve. However, to match the late time ($t > 30$ days) flattening of the light curve, a large amount of ejecta mass or low explosion energy (see Eqn. 1.33) is required to increase the diffusion time-scale, which simultaneously makes the fit to the post-peak decline poor while predicting a much longer rise time than is seen. We also note that these parameters are poorly constrained individually, as E and M_{ej} are correlated (Equation 1.33), and this degeneracy cannot be broken without the presence of high-quality spectral data (Mazzali et al., 2013).
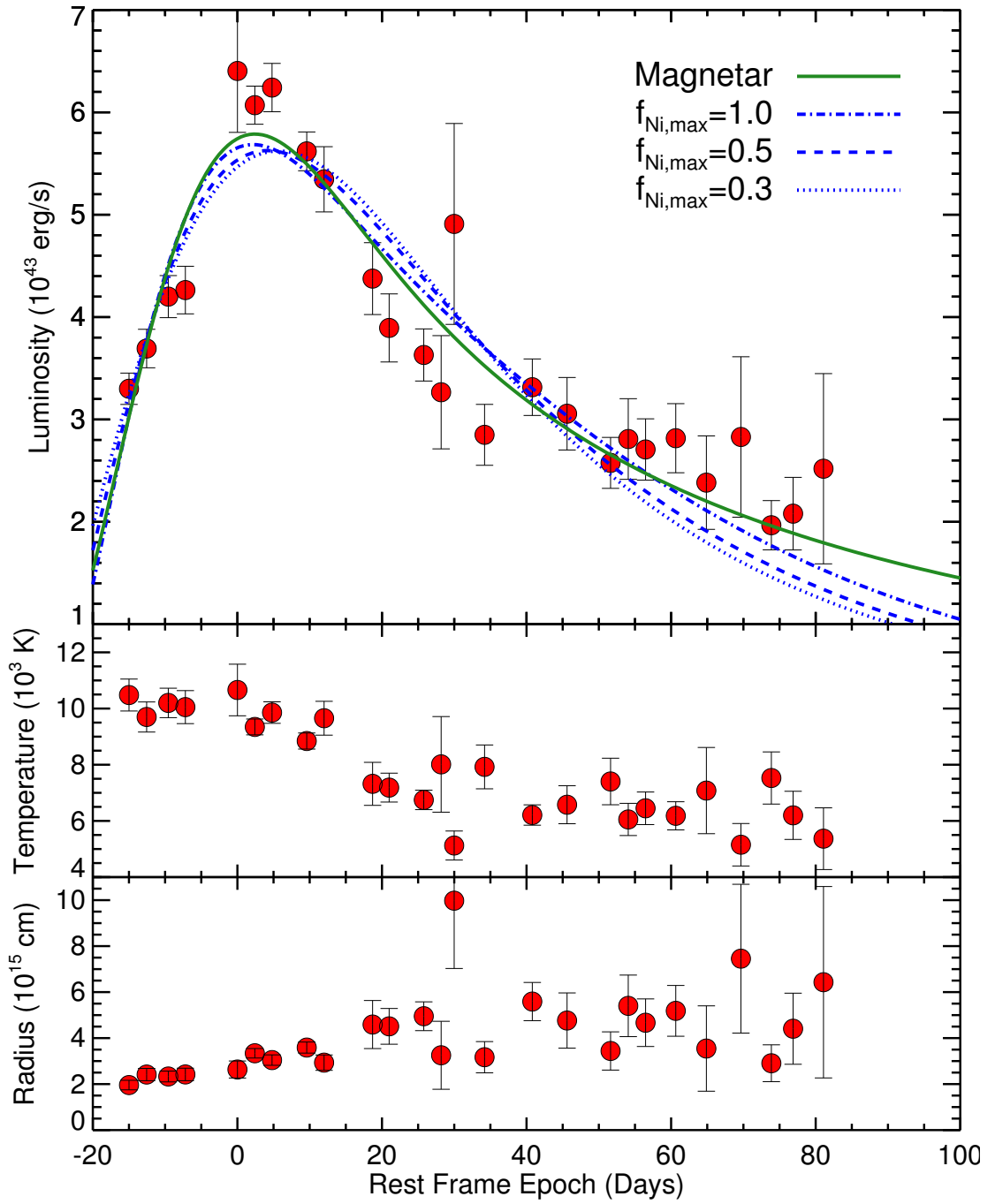
Figure 4.8: *Top panel:* Bolometric light curve of DES13S2cmm, with the best-fit magnetar model (green solid line) and three ^{56}Ni models with different $f_{Ni,max}$ (blue lines) overplotted. The magnetar model is a better match to the data than the best-fit ^{56}Ni, and has a significantly better χ^2 than the models with a more realistic $f_{Ni,max}$ (see text). However both models have difficulty reproducing the peak luminosity, the post-peak decline, and the late-time flattening. *Middle and Bottom panels:* Temperature and radius evolution of the best-fitting blackbody to each photometric epoch, which is used to construct the bolometric light curve.

Table 4.2: Best-fitting parameters for a variety of ^{56}Ni model fits to the bolometric light curve for DES13S2cmm. $f_{\text{Ni,max}}$ is the maximum fraction of ^{56}Ni allowed in the ejecta for each fit; for DES13S2cmm the best-fitting model always maximizes this value. Ejecta and ^{56}Ni masses are given in units of solar masses. There are 22 degrees of freedom for each fit.

$f_{\text{Ni,max}}$	$E(10^{51}$ erg$)$	M_{ej}	M_{Ni}	t_0 (MJD)	χ^2
0.30	31.88	14.77	4.43	56508.8	81.5
0.40	14.83	10.59	4.23	56510.4	76.0
0.50	8.22	8.21	4.10	56511.5	71.5
0.60	5.08	6.68	4.01	56512.4	67.9
0.70	3.38	5.62	3.93	56513.1	65.0
0.80	2.38	4.84	3.88	56513.7	62.7
0.90	1.74	4.25	3.83	56514.2	60.9
1.00	1.32	3.79	3.79	56514.6	59.4

We do not provide uncertainties on the best fit parameters for each f_{Ni} model in Table 4.2. This is because the formal uncertainties on parameters (such as M_{Ni}) are smaller for each fit than they are between fits with different constraints on f_{Ni}. This is due to the simplicity of the ^{56}Ni model; we do not consider herein Ni mixing, non-standard density profiles, nor other possible variations in this basic model that could yield different light-curve shapes. For example, it has been noted that a two-component model that is denser in the inner component would produce a quicker flattening post-peak (Maeda et al., 2003).

4.8.2 Magnetar model

As an alternative to the radioactive decay of ^{56}Ni, we also fit our derived bolometric light curve for DES13S2cmm to a magnetar model (also described in Sec. 1.5.3), where the model's bolometric luminosity as function of time is given by Eq. 1.36. The four parameters needed to construct such model are: the initial spin period (P_{ms}, in milliseconds), the magnetic field strength (B_{14}, in units of 10^{14} Gauss) of the magnetar, the rise-time parameter (τ_m, Eqn. 1.33) and the explosion epoch (t_0).

In Fig. 4.8 we include the best-fitting magnetar model to the bolometric light curve of DES13S2cmm. The best-fitting parameters of this model are a magnetic field of 1.43×10^{14} Gauss, an initial spin period of 5.28 ms, a diffusion timescale of 22.9 days, and an explosion date of MJD 56511.0. This model has a $\chi^2/dof = 2.0$ (χ^2 of 44 for 22 degrees of freedom) and is therefore a significantly better fit to our data than the ^{56}Ni model. However, it is still clear that the model does not fit well: it is unable to reproduce the factor of two drop in luminosity post-peak within 30 days of explosion (although it

does a better job than ^{56}Ni). Intriguingly, the late-time epochs seem to fit the magnetar model well. Our time coverage of DES13S2cmm allows us to determine whether either model is able to reproduce detailed features of the light curve, but discerning between the two models would be improved by an even longer time-scale over which the two models cannot mimic one another; DES alone will unlikely provide longer light curve coverage as its observing season is typically not much more than 5 months a year.

4.9   Summary and Discussion

In this chapter, we have explored DES13S2cmm, the first spectroscopically-confirmed SLSN from DES SN survey, as it was presented in Papadopoulos et al. (2015). Using spectroscopic data obtained from the VLT, we measured a redshift of $z = 0.663 \pm 0.001$, and assigned a classification of SLSN-I. However, we cannot exclude the possibility that DES13S2cmm is a type R (Fig. 4.4 and 4.7), if this is in fact a distinct SLSN type.

Using this redshift and correcting for Milky Way extinction, we find the rest-frame U-band absolute magnitude of DES13S2cmm at peak to be $M_U^{peak} = -21.05^{+0.10}_{-0.09}$, consistent with the SLSNe definition of Gal-Yam (2012). Like other SLSNe (Lunnan et al., 2014a), DES13S2cmm is located in a faint, low stellar-mass host galaxy $(\log(M/M_\odot) = 8.9 \pm 0.3)$ with sub-solar metallicity.

In Fig. 4.7, we compare the bolometric light curve of DES13S12cmm to fourteen similarly well-observed SLSNe-I light curves in literature, and see that DES13S2cmm has one of the slowest declining tails (beyond $+30$ rest frame past peak) of all SLSNe-I studied herein, while most likely being the faintest at peak. We further find that the dispersion between the bolometric light curves of all SLSNe-I shown in Fig. 4.7 has a minimum of 0.29 magnitudes around $+30$ days past peak (rest frame). This reduces to 0.20 magnitudes around $+25$ days if we remove the four SLSNe-I above $z \simeq 1$ from the measurement, because of the increased uncertainty in their rest-frame UV luminosities. This observation raises the tantalising possibility of 'standardising' these SLSNe like SNe Ia (Quimby et al., 2011b; Inserra and Smartt, 2014) and starting a new era of supernova cosmology (King et al., 2014). Further study is required to confirm if SLSNe can be standardised and to investigate further the k-corrections of SLSNe, which would be needed to use SLSNe as robust distance indicators.

In Fig. 4.8, we fit the bolometric light curve of DES13S2cmm with two possible models for the power source of these extreme events; the radioactive decay of ^{56}Ni and a magnetar (e.g. see Inserra et al., 2013). We find that the ^{56}Ni model is not a good fit to the bolometric light curve, as the best-fitting model has a $\chi^2/\text{DoF} = 2.7$ with an unrealistic fraction of ^{56}Ni to ejected mass $(f_{\text{Ni}} = 1)$. The model does provide a relatively robust

prediction for the overall ^{56}Ni mass ($3.8 - 4.4M_\odot$), as this is primarily constrained by the peak luminosity of the light curve, but is unable to reproduce the late time ($t > 30$ days) evolution of the light curve. The Magnetar model provides a smaller χ^2 (for the same degrees of freedom) than ^{56}Ni, but is likewise not a good fit to the data, as it is unable to fully reproduce the drop in luminosity within 30 days of explosion.

Chapter 5

Dark Energy Survey - Year Two

5.1 Introduction

In this chapter, I will briefly present a status update of the Dark Energy Survey (wide + SNe), after the end of year two (Y2) of operations. I will explore the improvements on the SN Survey that were implemented prior to the start of Y2 and I will concentrate on the results from the search of SLSNe using Y2 data. I will present in detail the selection process, discoveries and modelling of SLSNe discovered in DES Y2 data. The findings described in this chapter, were the result of the collaboration with Dr. Chris D'Andrea, Dr. Mat Smith, Dr. Mark Sullivan and Prof. Bob Nichol.

5.2 Dark Energy Survey Status

The second year of DES operations started on the 15th of August 2014 and ended six months later, on the 15th of February 2015. The goal of the DES wide survey for Y2 was to observe the entire DES footprint (5000 deg^2) in four tiles depth in all 5 filters ($grizY$). Exceptionally poor weather at the beginning of Y2 cost around 15% of the available telescope time, resulting in a 89% completeness of the Y1+Y2 goals. Fig. 5.1 shows the survey's area coverage at the end of Y2.

The poor weather conditions at the beginning of Y2 also affected the DES SN Survey, as the mean cadence of 6.2 days achieved during the Y1 increased to 6.4 days in Y2. As a result, and in order to help the wide survey to recover the area coverage, DES SN survey stopped observing most of the SN fields from the beginning of February 2015, except C1, C2 and C3. This modification translates to the loss of at least one epoch in the SNe light-curves from the dropped fields, but with uncertain measurements, as those fields would have been observed at high air-mass, especially the X-fields. Fig. 5.2 shows the final cadence plot for the SN Survey at the end of Y2 of operations.
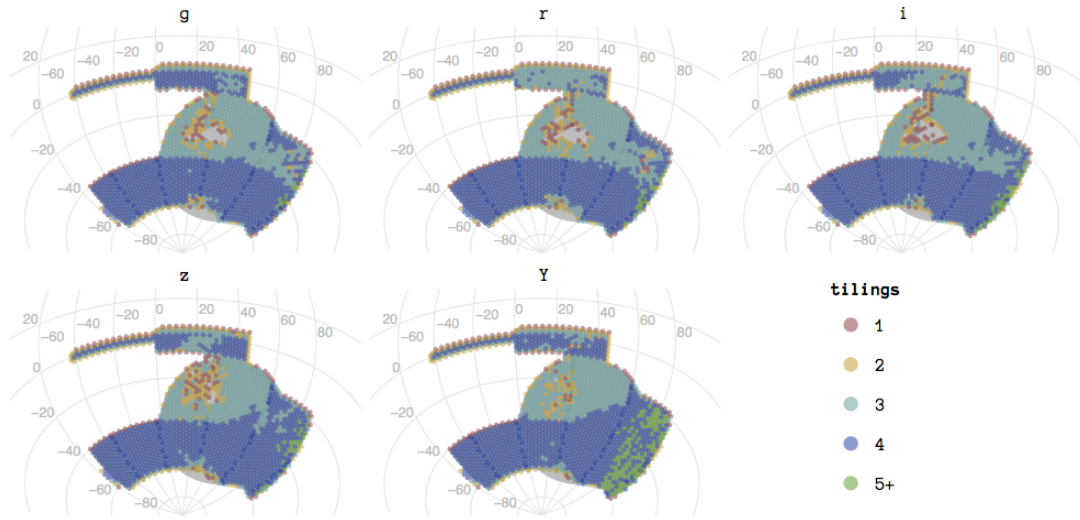
Figure 5.1: The DES wide-survey observed area at the end of Y2 of operations. The grey area shows the entire DES footprint, whereas the observed area is coloured-coded, based on the number of tiles acquired so far. *Plot provided by the DES operations team.*
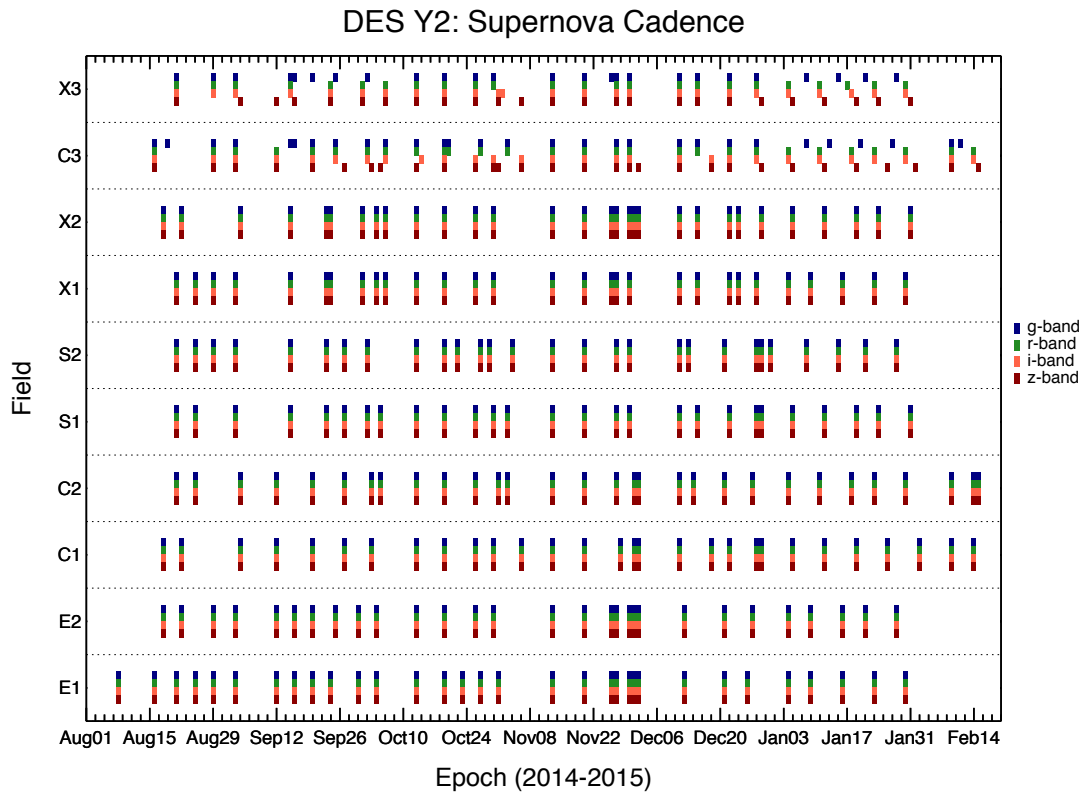
Figure 5.2: The DES SN Survey cadence plot from the Y2 of operations. All filters are observed on the same night for the shallow fields, whereas for the deep fields this is not the case, as different filter/exposures can be acquired on different days. Some epochs of the shallow fields show uncompleted filter sequences due to the poor quality of the data, which resulted to revisiting the same fields on the next available night. *Plot created by Dr. Chris D'Andrea.*
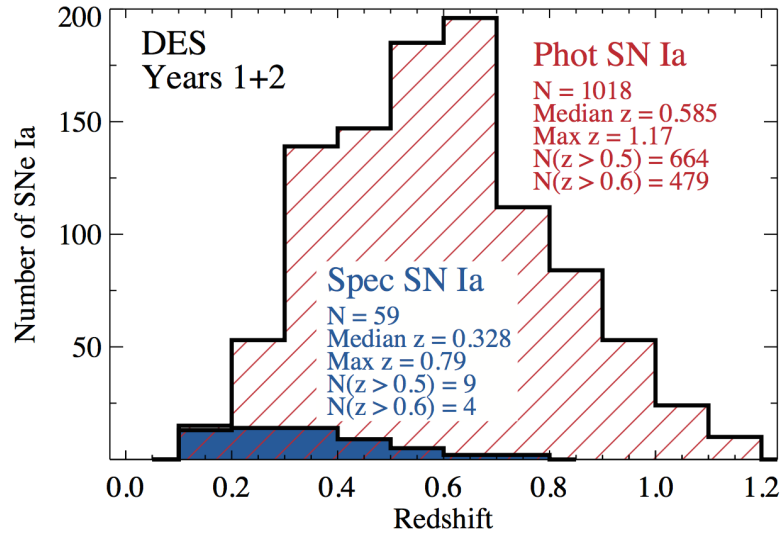
Figure 5.3: Redshift distribution of photometrically classified (red hashed; 1018 SNe) and spectroscopically classified (blue filled; 59 SNe) SN Ia from DES Y1 and Y2, as used in various telescopes' proposals for Y3 of DES. The majority of the spectroscopic confirmations were obtained in Y2, in which we had access to more telescope time and the OzDES program observed host galaxies of SNe Ia discovered both in Y1 and Y2. *Plot created by Dr. Ryan Foley for the 2015B semester Gemini proposal.*

5.3 Supernova Survey in Year Two

This section describes the updates and preparation work done between the two DES seasons, as well as the final results in terms of SNe Ia discovered and confirmed for use in cosmology.

5.3.1 Pipeline updates

Between Y1 and Y2, the SN search pipeline under went a major update in order to be more streamlined and automated. Each of the search pipeline's steps and subroutines were re-visited and updated in order for the pipeline as a whole to incorporate changes that were made on the DESDM side, which included improving file tracking and provenance information.

All the updates were in place and tested using data from Y1 in time, before the beginning of Y2 of operations. For the SN search pipeline, tests showed that we were getting better difference images, and this had a major impact on reducing the number of artefacts that were reaching the human scanners. Moreover, updates and retraining of AUTOSCAN with a new version of postage-stamps improved its effectiveness, such as the number of transient candidates eligible for human scanning decreased by a factor of 13.4, while only 1% of the artificial SNe Ia injected into search images to monitor survey efficiency were

Table 5.1: List of spectroscopic resources during DES Y2 of operations, listing the telescope's name and instrument, the time allocated during Y2 and short comments on the objectives of each program.

Telescope	Instrument	Time Available	Objectives
GTC	OSIRIS [a]	13.0h(ToO)	ambiguous SNe $m_r < 23.5$
SALT	RSS [b]	9.0h(ToO)	low-z high SNR SNe Ia $m_r < 21.7$
Keck	DEIMOS [c]	1.0n+8.0h(ToO)	random sample of SNe with good SNR $m_i < 24$;
	LRIS [d]	4.5n (ToO)	Hostless SNe Ia; Interesting and rare transients
Magellan	IMACS [e]	6.5n (classical)	piggyback to photo-z program; pre-peak $z \sim 0.5$ SNe Ia
AAT	AAOmega/2dF [f]	16.0n (classical)	OzDES program for SNe hosts
VLT	X-Shooter	7.1n (classical)	Hostless SNe Ia and other transients
MMT	Blue Channel Spectrograph	4.5n (classical)	pre-peak $z \sim 0.5$ SNe Ia; RAISIN2

[a] Optical System for Imaging and low-Intermediate-Resolution Integrated Spectroscopy
[b] Robert Stobie Spectrograph
[c] DEep Imaging Multi-Object Spectrograph
[d] Low Resolution Imaging Spectrometer
[e] Inamori Magellan Areal Camera and Spectrograph
[f] AAOmega spectrograph Two Degree Field system

lost, most of which were faint events (Goldstein et al., 2015). As a result, AUTOSCAN replaced human scanning as the last step in the search pipeline before a candidate becomes a transient, and human scanning remained as a training mechanism for AUTOSCAN.

Another updated part of the SN pipeline that had a positive effect on the SNe discovery efficiency, was the implementation of deeper template images. In Y1 the templates were created by selecting 10 images from the SV season in each filter with the best seeing. Similarly, the Y2 templates were created by using 10 good seeing images from each filter that were observed in Y1. But because Y1 season lasted longer than SV, the number of images with good seeing had increased. As a result, the average seeing of the 10 images per filter decreased, resulting in deeper templates and hence, the subtractions were cleaner, creating fewer artefacts in Y2 than in Y1.

5.3.2 Y2 Spectroscopic Follow-up Updates

The spectroscopic strategy for the SN Survey, discussed in detail in Sec. 3.4, remained unchanged with few more additions to our resources, as listed in Table 5.1. An example of proposal that were awarded classical observing nights is the VLT/X-shooter proposal led by Dr. Mark Sullivan. This proposal was awarded 7.1 classical observing nights, split into four different sessions throughout the Y2 season. Also, we increased our spectroscopic resources by signing various new external collaboration agreements. For example, we shared 4.5 classical observing nights on the Multiple Mirror Telescope (MMT) and its Blue Channel Spectrograph, granted through RAISIN2, a HST program that obtains restframe NIR photometry of high-redshift SNe Ia.

Furthermore, the OzDES program (Yuan et al., 2015) described in Sec. 3.4.1, on each subsequent season will increase its efficiency, by collecting spectroscopic data for a growing sample of SNe Ia hosts. This was a planned feature of OzDES, as the number of observing nights in each season increases. Namely, in Y1 we had 12 nights which increased to 16 nights in Y2, 20 nights for Y3, 24 nights for Y4 and 28 nights for the last year of DES operations.

Also, the discovery and study of DES13S2cmm (Chap. 4), as well as the unclassified SLSNe candidates sample (Chap. 3), had a positive impact on the spectroscopic resources' objectives. Programs like GTC, Keck and VLT were primarily targeting hostless or faint SN Ia, of which some could be proven to be SLSNe, but at the same time those programs were targeting ambiguous, rare and interesting SNe, such as SLSNe or gravitationally lensed SNe.

5.3.3 Results

In Y2 the discovery and classification efficiency of the SN survey improved as a result of all the reasons presented above. This was translated to 76 spectroscopically confirmed SNe, more than 600 host galaxies with secured z_{spec} (OzDES) and a handful of rare and interesting transients like SLSNe, Tidal Disruption Event (TDE; Foley et al., 2015) etc.

The 76 spectroscopically confirmed SNe from Y2 are listed in Table 5.2 as reported within 22 separate ATels, whereas Fig. 5.3 shows the redshift distribution of SNe Ia discovered and classified in both Y1 and Y2, that have either a z_{spec} or z_{photo}. Fig. 5.3 was used in recently submitted telescope proposals, in order to continue and extend our spectroscopically follow-up plan in Y3 and beyond.

5.4 Methodology for Selecting SLSNe Candidates in Year Two

The methodology used for the search of SLSNe in Y2 data, followed the same logic and strategy as in Y1 (Sec. 3.5) with the addition of some updates, mostly developed in order to minimize the diverse sources of contamination described in Sec. 3.5.2. The updated methodology used in Y2 is illustrated by the flow diagram in Fig. 5.4, and described in this section.

Table 5.2: List of spectroscopically confirmed SNe from DES Y2, as reported in multiple ATels released during the observing season.

Num	Name	RA (J2000)	Dec (J2000)	Disc. Date (UT)	Disc. m_r	Spectrum Date (UT)	Redshift	Type	Phase	Telescope
1	DES14X2fna	02:23:15.64	-07:05 20.8	2014 Sep 30	19.1	2014 Nov 21	0.045	IIb	+37	AAT
2	DES14C3aol	03:30:09.97	-28:42:27.4	2014 Sep 02	21.7	2014 Sep 23	0.075	II	+25	Magellan
3	DES14C2pw	03:38:02.38	-29:19:49.2	2014 Aug 20	21.2	2014 Sep 23	0.101	Ia	+80	Magellan
4	DES14E1rph	00:27:25.54	-42:51:01.5	2014 Dec 11	20.9	2014 Dec 30	0.1054	Ia	+7	AAT; SALT
5	DES14S2qg	02:42:21.44	-01:21:42.9	2014 Aug 20	19.7	2014 Aug 31	0.11	Ia	+30	VLT
6	DES14X1qt	02:16:51.50	-04:09:15.2	2014 Aug 20	21.7	2014 Oct 30	0.139	II	+62	AAT
7	DES14X2bnz	02:25:01.24	-06:16:42.8	2014 Sep 14	20.4	2014 Oct 15	0.147	Ia	+20	MMT
8	DES14C1qty	03:34:06.22	-27:37:55.6	2014 Dec 09	22.3	2014 Dec 19	0.148	Ia	-7	Magellan
9	DES14E1anf	00:33:56.13	-43:20:59.1	2014 Sep 02	21.6	2014 Sep 17-20	0.149	Ia	+2-5	AAT
10	DES14C2fkd	03:33:45.34	-29:40:36.2	2014 Sep 26	21.7	2014 Oct 22	0.160	Ia	+12	MMT
11	DES14C1kia	03:34:47.49	-26:19:35.0	2014 Nov 11	22.2	2014 Dec 19	0.162	TDE		Magellan
12	DES14S1td	02:52:22.94	+00:37:20.0	2014 Aug 20	22.3	2014 Sep 23	0.170	galaxy		Magellan
13	DES14C1jkw	03:39:37.63	-27:48:46.9	2014 Oct 18	22.4	2014 Nov 19	0.1729	Ia	+13	AAT
14	DES14C2ikn	03:35:23.57	-29:35:30.4	2014 Oct 18	23.1	2014 Dec 19	0.180	Ia	+38	Magellan
15	DES14S2bnq	02:43:40.05	-00:45:43.0	2014 Sep 14	22.6	2014 Sep 30	0.18531	Ia	Peak	AAT
16	DES14E2aqu	00:40:10.75	-44:01:48.8	2014 Sep 11	23.0	2014 Sep 23	0.193	blue cont.		Magellan
17	DES14X2dm	02:23:29.96	-06:38:16.1	2014 Aug 17	20.6	2014 Oct 28	0.196	II	>+60	AAT
18	DES14X2eei	02:22:53.77	-06:15:24.5	2014 Sep 22	22.6	2014 Oct 22	0.197	Ia	+15	MMT
19	DES14C2gwx	03:33:35.18	-29:11:26.3	2014 Oct 12	22.4	2014 Oct 29	0.198	Ia	+2	AAT
20	DES14S1rah	02:48:57.46	-00:24:30.3	2014 Dec 09	22.7	2014 Dec 19	0.199	Ia	-5	Magella n
21	DES14C3tsg	03:28:25.74	-28:09:50.7	2015 Jan 02	23.8	2015 Jan 27	0.21	II	+20-25	VLT
22	DES14C1es	03:36:41.40	-27:50:24.0	2014 Aug 17	20.9	2014 Sep 23	0.219	Ia	+26	Magellan
23	DES14C3cxt	03:27:21.32	-28:07:30.0	2014 Sep 19	23.1	2014 Oct 01	0.2153	Ia	-7	Keck
24	DES14C3gqv	03:28:38.86	-27:08:31.8	2014 Oct 23	24	2014 Oct 24	0.22	Ia	peak	Keck
25	DES14C3hud	03:28:39.14	-28:06:29.7	2014 Oct 18	22.5	2014 Nov 15	0.225	Ia	+8-11	Magellan
26	DES14E2ag	00:39:22.19	-44:04:03.4	2014 Aug 17	21.2	2014 Sep 01	0.2263	Ic	+20	VLT
27	DES14S1qid	02:51:56.62	-00:31:23.0	2014 Nov 28	23.2	2014 Dec 19	0.228	Ia	+3	Magellan
28	DES14X2cy	02:22:51.25	-07:11:18.3	2014 Aug 17	22.1	2014 Sep 23	0.232	II	+200	Magellan
29	DES14S2pkz	02:43:27.38	-01:36:13.1	2014 Nov 25	23.4	2014 Dec 19	0.234	Ia	+6	Magellan
30	DES14S2dbi	02:41:04.30	-00:57:18.9	2014 Sep 22	21.7	2014 Oct 22	0.236	Ia	+19	MMT
31	DES14X2raq	02:23:36.76	-05:28:53.2	2014 Dec 09	21.5	2014 Dec 19	0.239	Ia	+3	Magellan
32	DES14S2qb	02:43:59.72	-00:54:22.1	2014 Aug 20	22.1	2014 Sep 18	0.24	Ia	+20	AAT
33	DES14E2am	00:39:57.94	-44:52:30.9	2014 Aug 17	22.5	2014 Aug 30	0.2470	II?	peak	VLT
34	DES14X3amb	02:23:17.03	-05:10:55.6	2014 Sep 14	23.0	2014 Oct 22	0.259	Ia	+20	MMT
35	DES14C3cwp	03:27:10.88	-27:49:19.6	2014 Sep 19	23.7	2014 Oct 29	0.279	Ia	+17	AAT
36	DES14X2rao	02:24:01.90	-06:48:38.2	2014 Dec 09	22.1	2014 Dec 19	0.283	Ia	-2	Magellan
37	DES14E2u	00:37:51.13	-43:43:17.2	2014 Aug 17	23.0	2014 Aug 31; Sep 17	0.2923	Ia	peak;+15	VLT; AAT
38	DES14X1oes	02:19:19.90	-05:47:22.0	2014 Nov 25	22.4	2014 Dec 19	0.30	Ia	+8	SALT
39	DES14X2ags	02:24:00.58	-06:29:51.8	2014 Sep 03	21.6	2014 Sep 18	0.30	Ia	+3	AAT
40	DES14C2apq	03:40:21.49	-29:02:54.9	2014 Sep 03	23.3	2014 Sep 23	0.303	II		Magellan
41	DES14X3aeb	02:24:24.61	-04:40:29.7	2014 Sep 02	21.2	2014 Sep 23	0.314	Ia	+13	Magellan
42	DES14X1fnt	02:18:11.14	-05:00:36.5	2014 Sep 30	23.5	2014 Oct 15,22	0.315	Ia	+4	MMT
43	DES14S1kdq	02:49:04.83	+00:34:56.5	2014 Oct 29	23.1	2014 Nov 15	0.3275	Ia	+4	Magellan
44	DES14C3rap	03:31:11.39	-27:57:33.5	2014 Dec 09	24.1	2014 Dec 30	0.330	Ia	+1	SOAR
45	DES14X2gxr	02:21:10.71	-06:27:47.2	2014 Oct 12	23.0	2014 Nov 21	0.332	Ia	+19	AAT
46	DES14C2kct	03:39:35.46	-28:54:38.8	2014 Oct 30	23.0	2014 Nov 19	0.333	Ia	+2	AAT
47	DES14C3foo	03:28:09.10	-27:31:58.5	2014 Oct 01	23.1	2014 Oct 29	0.338	Ia	+11	AAT
48	DES14C3mpt	03:33:12.20	-28:01:29.5	2014 Nov 12	24.3	2014 Dec 19	0.3339	Ia	+14	AAT
49	DES14C3rhw	03:27:16.30	-28:43:51.4	2014 Dec 13	24.9	2015 Jan 28	0.3407	II	+34-37	VLT
50	DES14E2f	00:42:01.13	-43:31:27.7	2014 Aug 17	21.6	2014 Sep 23	0.349	galaxy		Magellan
51	DES14X3ftq	02:26:39.29	-04:58:14.7	2014 Oct 05	23.4	2014 Oct 28	0.35	Ia	+7	AAT
52	DES14S1aot	02:51:12.85	-00:40:08.8	2014 Sep 02	22.9	2014 Sep 23	0.364	Ia	peak	Magellan
53	DES14E1tb	00:28:48.01	-43:33:44.2	2014 Aug 15	22.9	2014 Sep 17-20	0.37	Ia	~+10	AAT
54	DES14C1fkl	03:40:24.63	-26:43:19.5	2014 Sep 26	22.5	2014 Oct 22	0.385	Ia	+10	MMT
55	DES14C2fkf	03:35:38.75	-28:19:09.6	2014 Sep 26	23.7	2014 Oct 22	0.386	Ia	+7	MMT
56	DES14C1eu	03:38:53.58	-27:54:18.1	2014 Aug 17	22.2	2014 Aug 30	0.39	Ia	peak	VLT
56	DES14S2boa	02:44:19.15	-00:27:01.3	2014 Sep 14	22.2	2014 Sep 28	0.398	Ia	-2	GTC
58	DES14S2pon	02:41:12.39	-00:45:51.7	2014 Nov 25	24.0	2014 Dec 25	0.414	Ia?	+10	GTC
59	DES14S1lfk	02:50:26.63	-00:21:42.2	2014 Nov 11	22.4	2014 Nov 15	0.439	Ia	+0	Magellan
60	DES14X2dl	02:22:44.29	-06:03:48.9	2014 Aug 17	22.5	2014 Aug 30	0.44	Ia	+9	VLT
61	DES14C1bdv	03:34:52.66	-27:49:58.1	2014 Sep 11	23.3	2014 Sep 23	0.443	Ia	-1	Keck
62	DES14C3nj	03:34:03.05	-28:19:05.4	2014 Aug 15	23.8	2014 Aug 31	0.45	Ia	-5	VLT
63	DES14E1gw	00:26:45.80	-43:26:02.5	2014 Aug 07	22.0	2014 Aug 31	0.4533	Ia	+22	VLT
64	DES14S1rag	02:50:15.02	-00:44:41.9	2014 Dec 09	22.7	2014 Dec 18	0.47	Ia	+1	GTC
65	DES14S1aow	02:50:35.72	+00:56:16.6	2014 Sep 02	23.1	2014 Sep 23	0.472	Ia	peak	Magellan
66	DES14X3jmx	02:24:14.02	-05:09:52.5	2014 Oct 25	23.9	2014 Nov 15	0.502	Ia	+3	Magellan
67	DES14X3tdv	02:23:42.32	-04:01:07.9	2014 Dec 28	-	2015 Jan 21	0.52	Ia	peak	Keck
68	DES14S1aoz	02:50:27.57	-00:52:18.4	2014 Sep 02	23.2	2014 Sep 23	0.525	Ia	+6	Keck
69	DES14C3tvk	03:28:16.64	-28:03:49.2	2014 Dec 26	24.7	2015 Jan 28	0.53	Ia	+8	VLT
70	DES14C2vnf	03:35:34.85	-29:02:52.8	2015 Jan 09	23.1	2015 Jan 27	0.5421	Ia	+5	VLT
71	DES14X3taz	02:28:04.46	-04:05:12.7	2014 Dec 09	23.1	2015 Jan 26; Feb 06	0.60	SLSN-I		GTC
72	DES14X3ajv	02:24:58.40	-04:15:03.1	2014 Sep 03	23.4	2014 Sep 23	0.613	Ia	+3	Keck
73	DES14C3uje	03:29:08.18	-28:57:05.6	2015 Jan 09	24.3	2015 Jan 27	0.78	Ia	+3	VLT
74	DES14X2byo	02:23:46.93	-06:08:12.3	2014 Sep 22	23.4	2014 Oct 22-23	0.869	SLSN-I		GTC, Keck, MMT
75	DES14C1fi	03:33:49.80	-27:03:31.6	2014 Aug 24	–	2014 Oct 24	1.3	SLSN-II		Keck
76	DES14S2qri	02:43:32.14	-01:07:34.2	2014 Nov 18	23.2	2015 Jan 21	1.5	SLSN-I		GTC
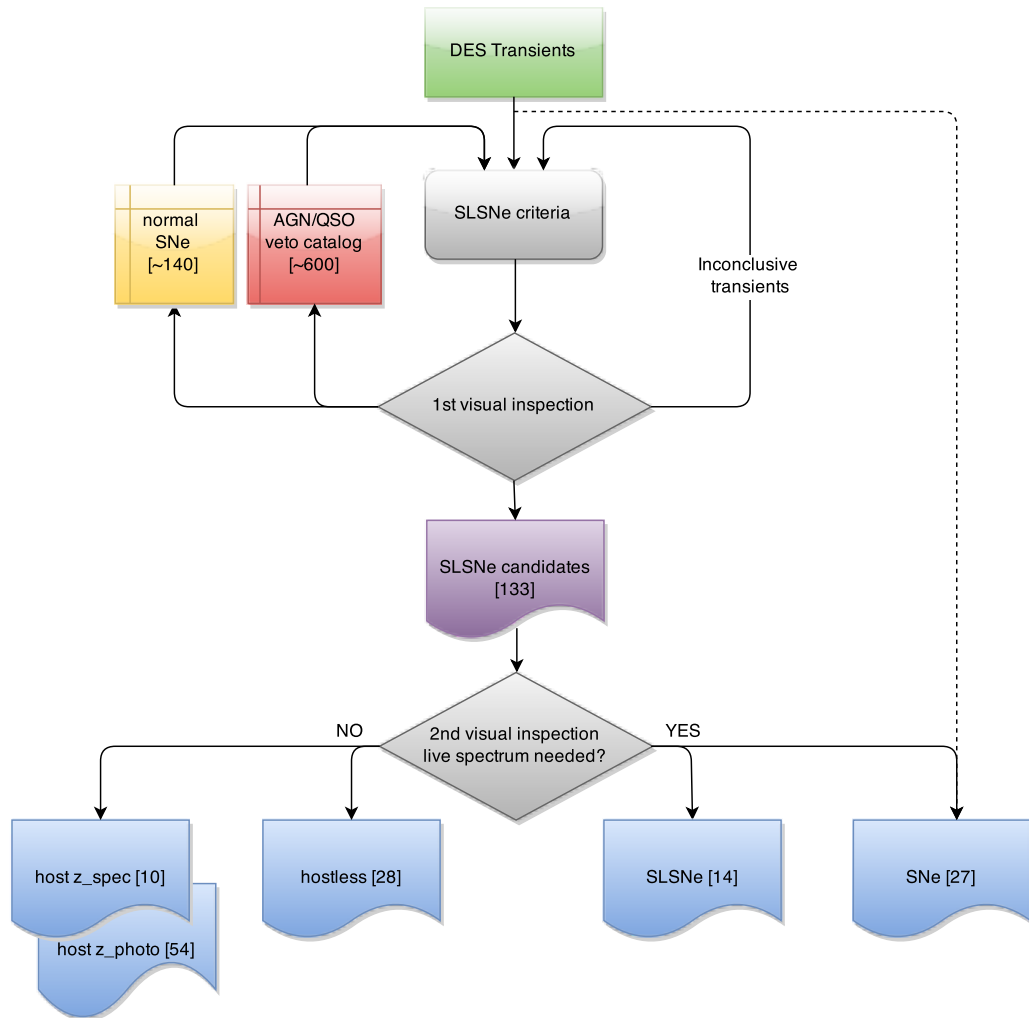
Figure 5.4: Flow diagram of the methodology used for discovering SLSNe in DES Y2 data. After the creation of the DES transients by the automated SN pipeline (*green rectangular;* Sec. 3.3.3), a series of selection processes (Sec. 5.4) were applied in order to end up with various selection samples (*blue lists;* Sec. 5.5) according to the spectroscopic follow-up strategy. The number of the relative transients selected in each step are reported within square brackets.

5.4.1 Updates on Methodology

The experience gained during Y1 (Sec. 3.5.1) indicated that updates were needed on two main parts of the whole SLSNe selection process: the way one determines the peak magnitude of a transient and the SLSNe selection criteria used afterwards.

In the flow diagram of Fig. 5.4, the implementation of the updated SLSNe criteria is shown as a grey box at the top, whereas the updated peak magnitude determination could be considered as part of the DES transients green box, because it is a process applied to all transients at the very beginning.

Peak Magnitude and Signal-to-Noise Ratio limit

For all DES transients detected by the automated pipeline (sections 3.3.3 and 5.3), I selected their peak flux in each individual band, using a limit of Signal-to-Noise Ratio (SNR) $\geqslant 5$. Later that flux was transformed into an apparent peak magnitude using Eq. 1.27. The SNR limit was applied in order to eliminate the large number of artefacts, which possessed only a handful of high flux measurements accompanied with large uncertainties, an example of which (DES13E2aytv) is shown in Fig. 3.12 and Fig. 3.13.

Fig. 5.5 shows the DES multi-band peak magnitude distributions of all named transients in Y2, using three different SNR limits: panel (a) for $\geqslant 3$, panel (b) $\geqslant 5$ (the one selected) and panel (c) for $\geqslant 7$. All three limits were used in parallel at the beginning of Y2, with the limit of SNR $\geqslant 5$ being selected as the best of the three and implemented from October 2014 onwards. The efficient performance of the SNR $\geqslant 5$ limit can be seen in Fig. 5.5. Through the comparison of the three panels it is evident that SNR $\geqslant 5$ eliminates more artefacts than SNR $\geqslant 3$ and does not changes the shape of the distribution, unlike the stricter limit of SNR $\geqslant 7$ does.

SLSNe selection criteria

At this stage, an updated version of the SLSNe criteria used in Y1 (see Sec. 3.5.1) were implemented, as a first step for selecting SLSNe candidates. As stated before, this process is illustrated as a grey box in the flow diagram of Fig. 5.4, and was implemented right after all DES transients were created and their peak apparent magnitudes were calculated. Then, all DES transients were split into two categories: hostless and transients associated with one or more host galaxies; and they were filtered through the following four criteria:

1. Number of epochs $\geqslant 4$.

2. Number of observations $\geqslant$ (Number of epochs-2)$\times$ (Number of filters -1).

3. Host galaxy - transient separation $\geqslant 1$pixel ($= 0.27$" for DECam).
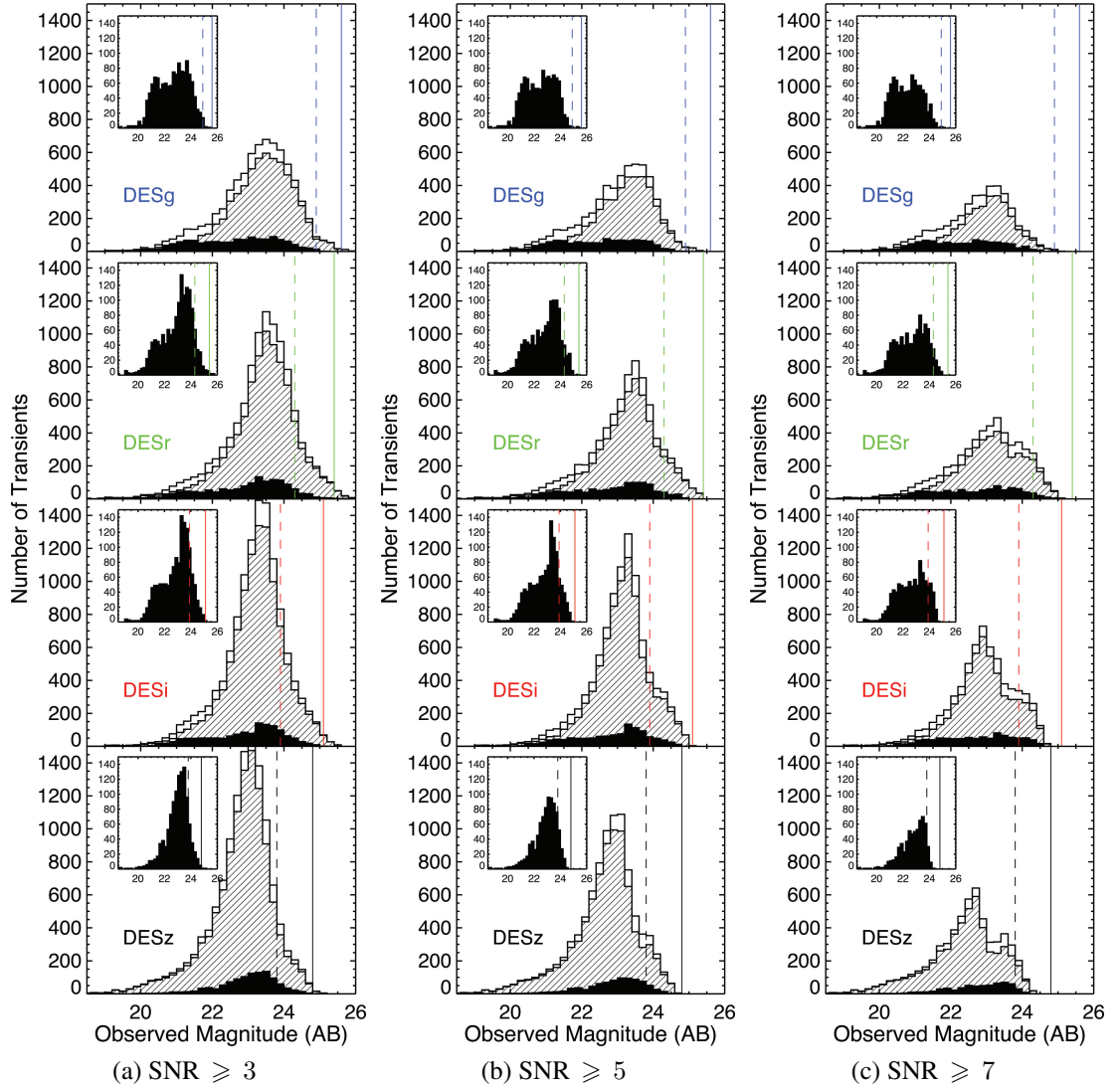
Figure 5.5: Histograms show the peak magnitude distribution of all named DES transients from Y2, in the four DES filters - $griz$, using three different thresholds on SNR; $\geqslant 3$ in panel (a), $\geqslant 5$ which was the one used in panel (b) and $\geqslant 7$ in panel (c). The shaded and black histograms refer to transients associated with a host galaxy and hostless transients, respectively. Because of the smaller number of hostless transients compared to transients associated with host galaxies, their histograms (solid black area) are zoomed and overploted. The dashed and solid vertical lines show the magnitude limit for the DES SNe shallow and deep fields respectively, as listed in Table 3.1. The SNR $\geqslant 5$ was selected and used throughout the Y2, because it is more efficient at eliminating the number of artefacts than SNR $\geqslant 3$, and at the same time it does not exaggerate as SNR $\geqslant 7$, which is illustrated by the change in shape of the distribution.

4. Absolute magnitude at peak; $M_{peak} \leqslant -20.0$ in any band.

For hostless transients only the first two criteria were applied, whereas all four of the criteria were applied to transients associated with a host galaxy.

The number of epochs is created by the search pipeline, which is used for the initial discovery of each transient, and is used with a threshold of 4 epochs in order to select objects with at least 24 days of rise time [4 epochs $\times 6$ days which is the simulated mean cadence as set by Bernstein et al. (2012)].

The number of observations refers to the number of times a transient was recovered by the search pipeline in any filter, at any given epoch. For example, if a bright transient was observed 5 times, and the search pipeline had discovered and recovered the transients in each image of each filter, then the perfect score for number of observations would be 20. But due to weather, bad subtractions, hot pixels and also the fact that a transient may be too faint in one or more filters, the threshold for the the number of observations was chosen to be less than its perfect score. The formula shown in the second criterion was adopted as a threshold for each transient, in order to account for these variations from the perfect score in the number of observations. The number of epochs was reduced by two, to account for the cases of bad weather and/or entire field observations that did not pass the minimum data acceptance limit, which was set by DESDM. Also, the number of detections in the four filters was reduced by one, to account for the cases of high redshift transients in which the bluer bands would not be automatically detected by the search pipeline, due to low SNR. Thus, for the transients that passed the first criterion threshold with number of epochs of 4, 5, 6 etc, the second criterion threshold would be 6, 9, 12 instead of 16, 20, 24 which would be the perfect score.

The third criterion remained unchanged as in Y1, as it showed reasonable effectiveness at removing most of the AGN/QSOs and variable stars, that show irregular fluctuation in their brightness, but that are also consistent with the central region of their host galaxy.

Finally, the last criterion, which refers directly to the SLSNe absolute magnitude threshold set by Gal-Yam (2012), was performing more effectively in Y2 because the number of host galaxies with secured z_{spec} had increased; as the OzDES program was observing through the season. Also, in Y2 we relaxed the value of M_{peak} to be $\leqslant -20.0$, instead of -20.5 that was used in Y1 (see Sec. 3.5.1), in order not to exclude SLSNe that would appear less luminous at peak, due to the incorrect z_{photo} of their host galaxies.

5.4.2 First Visual Inspection

On average, each night that SN data was collected, around ~ 500 candidates were named as DES transients, after passing all the steps in the SN selection process described in

```
=========================================================
---------------------------------------------------------
Selection configuration:
# epochs              =           4        5        6
# obs                 =           6        9       12
MAG_lower_limit       =    -20.0000
host separation(arcsec) =    0.260000
---------------------------------------------------------
Transients TOTAL #                          =     14111
Transients + hostless                       =      1892
Transients + hostless + (#epo+#obs)         =       103
Transients + host                           =     12219
Transients + host + sepa(1px)               =      8524
Transients + host + sepa(1px) + (#epo+#obs) =      1264
Transients + host + sepa(1px) + (#epo+#obs) + MAG=   361
~~~~~~~~~~~~~~~~~~~~~~~~~~~~~~~~~~~~~~~~~~~~~~~~~~~~~~~~~~~~~~~~~~~~~~~~~~~~~~~~~~~~~~~~~~~~~~~~
A/A   Name        snid | photo-z   spec-z      | <mag>  mag_g  mag_r  mag_i  mag_z |#epo #obs |arcsec |status
----------------------------------------------------------------------------------------------------------
  1)  DES14E2q      5487 |  0.60   1.23 NED         | -15.74 -20.99 -21.03 -20.93   0.00 |  18   31 |  0.37 |
 26)  DES14X3rb    12571 |  0.28   0.34 SDSS        | -19.84 -19.80 -19.84 -20.00 -19.71 |  27   59 |  7.51 |
 27)  DES14X3yg    12574 |  0.79   0.00            | -20.88 -20.77 -20.92 -20.97 -20.87 |  37   70 |  0.39 |
 28)  DES14X3yk    12653 |  0.94   0.70 PanSTARRS_MM | -20.38 -20.68 -20.40 -20.20 -20.21 |  41   86 |  0.35 |
260)  DES14X2dl     6306 |  0.64  -9.99 DES_AAOmega | -19.99 -18.87 -20.41 -20.46 -20.23 |   5   11 |  0.32 | SL-SNe
261)  DES14C1fi     6783 |  1.19  -9.99 DES_AAOmega | -22.33 -21.98 -22.34 -22.51 -22.50 |  27   79 |  0.64 | SL-SNe
262)  DES14C1fs     6904 |  0.74   0.00            | -20.67 -19.97 -20.59 -20.94 -21.18 |  24   60 |  0.82 | SL-SNe
265)  DES14C3oz    14082 |  1.25   0.00            | -22.87 -22.08 -22.95 -23.20 -23.26 |  52  103 |  2.73 | SL-SNe
277)  DES14X3fpy   77395 |  0.87   0.82 DES_AAOmega | -15.03   0.00 -19.70 -20.34 -20.06 |   8   18 |  1.29 | SL-SNe
304)  DES14X1rbi  192464 |  0.69   0.72 VIPERS      | -20.43 -19.92 -20.41 -20.70 -20.71 |  10   28 |  2.14 | SL-SNe
321)  DES14S1rwf   26795 |  0.10   0.07 SDSS        | -18.99 -18.65 -18.88 -18.31 -20.12 |  24   70 |  0.65 |    sne
322)  DES14C2bfg   33473 |  0.66  -9.99 DES_AAOmega | -19.87 -19.13 -20.12 -20.18 -20.03 |   5   13 |  0.50 |    sne
323)  DES14E1bgh   37394 |  0.66   0.67 PRIMUS      | -15.09   0.00 -19.64 -20.03 -20.68 |   4    8 |  0.66 |    sne
325)  DES14C2cpo   39173 |  0.53   0.00            | -20.05 -19.95 -20.08 -20.16 -20.02 |   9   26 |  0.26 |    sne
335)  DES14X3mos  160359 |  0.99   1.05 VVDS_DEEP   | -14.92   0.00 -19.06 -20.18 -20.46 |   4    7 |  1.18 |    sne
~~~~~~~~~~~~~~~~~~~~~~~~~~~~~~~~~~~~~~~~~~~~~~~~~~~~~~~~~~~~~~~~~~~~~~~~~~~~~~~~~~~~~~~~~~~~~~~~
 A/A    Name        snid | #epo  #obs |status
-----------------------------------------------
   1)   DES14E2wfk    5937 |  22   41 |
   2)   DES14E2up     9937 |  19   40 |
  25)   DES14X3qzo  186659 |  19   33 |
  27)   DES14S2sz     7483 |  18   50 | SL-SNe
  34)   DES14C1coz   39114 |  15   44 | SL-SNe
  36)   DES14X2byo   45950 |  23   57 | SL-SNe
  50)   DES14S2qri  175982 |  11   30 | SL-SNe
  51)   DES14C1rhg  184587 |  11   34 | SL-SNe
  52)   DES14S1rah  187878 |  10   40 | SL-SNe
  58)   DES14E2slp  197238 |   7   27 | SL-SNe
  61)   DES14C1eu     6656 |   7   20 |    sne
  62)   DES14E1gw     7423 |   5   12 |    sne
  65)   DES14C2tz     9430 |   4    9 |    sne
  66)   DES14S2qg    11170 |  20   62 |    sne
  67)   DES14E1ani   23884 |   6   17 |    sne
~~~~~~~~~~~~~~~~~~~~~~~~~~~~~~~~~~~~~~~~~~~~~~~~~~~~~~~~~~~~~~~~~~~~~~~~~~~~~~~~~~~~~~~~~~~~~~~~
```

Figure 5.6: An example of the output list at the first visual inspection step in the process of selecting SLSNe candidates. The very top lines show the selecting configuration, which is done using the four criteria described in Sec.5.4.1 and then the number of transients selected from those criteria are shown. The first, multi-column table shows a short sub-sample of the SLSNe candidates associated with a host galaxy, whereas a sub-sample of the hostless SLSNe candidates is listed in the bottom table. Notice that the status column was filled after the first visual inspection of each candidate.

Sec. 3.3. Using the steps described so far for selecting SLSNe candidates, this number of all DES transients was reduced to $\sim 40 - 50$ SLSNe possible candidates. Those steps were implemented with the use of a semi-interactive IDL [1] routine. This allowed the downloading and updating an initial DES transients list after each SNe field observation. After implementing the first selection criteria the semi-interactive routine was printing a first-cut list of SLSNe candidates for visual inspection. An example of such first-cut output list of this IDL routine is shown in Fig. 5.6.

At this stage (top grey diamond in flow diagram of Fig. 5.4), I performed the first visual inspection of the transients listed in Fig. 5.6, using the search panel in Fig. 5.7.

---

[1] Interactive Data Language; http://www.exelisvis.com/ProductsServices/IDL.aspx

The search panel shows the multi-band light-curve in apparent AB-magnitude space for each transient, the colour evolution, a diagram of the inferred absolute magnitude given the host z_{photo} or z_{spec} and a colour-magnitude diagram as introduced by Quimby et al. (2014) and used for selecting gravitational lensed SNe Ia, as described in Sec. 1.6.

In Appendix A several examples of visual inspection panels are presented, showing the variety of transients that have undergone this process. Also, Appendix A presents six transient examples, which were used to investigate whether the colour-colour parameter space can be used as a SLSNe identification method, alongside with the colour evolution plot that exist in the search panel shown in Fig. 5.7. The six colour-colour plots, presented in Appendix A, at the time of this search for SLSNe did not show any evidence in support for using them to identify SLSNe.

Also, for this first visual inspection step I used a secondary search panel, shown in Fig. 5.8, which presents the transient's light-curve in flux space, using both multi-season (Y1+2) and single season (Y2 only) data. The light-curve plots in flux space were implemented as an update in the Y2 methodology, firstly because they illustrate the zero flux point in each band, which helps visual inspection when looking for long rise times of f $\sim$ 30 days, seen in most SLSNe. The second reason for the use of the flux light-curves was to facilitate the detection of multi-season (Y1+2) activity, which greatly improves our ability to detect AGN/QSO variability.

The comparison in figure 5.8, between the left-hand-side and the right-hand-side panels, demonstrates that a likely AGN/QSO event (*panel c+d*) would show activity in both observing seasons, whereas a SNe (*panel a+b*) would have on average a flat and zero flux in Y1. When using the flux light-curves constructed with Y2 data only, then the similarities between a SN (*panel b*) and an AGN/QSO event (*panel d*) resulted to the inclusion of both objects as possible SLSNe and to the contamination of the selection sample.

The semi-interactive IDL routine had 4 status options to select for each transient listed and plotted. Transients that show unambiguous multi-season activity (*panel (c)* of Fig. 5.8) were marked as AGN/QSO and were vetoed from any future SLSNe list.The second option was for 'normal SNe types', like SNe Ia recognized by their second bump in redder bands or other non-luminous SNe recognized by their quick ($\lesssim 15$ days) rise time and under-luminous ($\gtrsim -19.5$) peak magnitudes.

The third option was for SLSNe candidates, given to any transient that showed any evidence for superluminous behaviour in this first round of visual inspection. Such evidence where the long rise time of $\gtrsim 30$ days or the inferred peak absolute magnitude, given the host z_{photo} or z_{spec}. The fourth and last option was to leave the status entry empty. This was applied for inconclusive transients that could not be typed within the previous three options, so the transient in review would return to the initial list in order to be revisited when new observational data were available. The most common example of
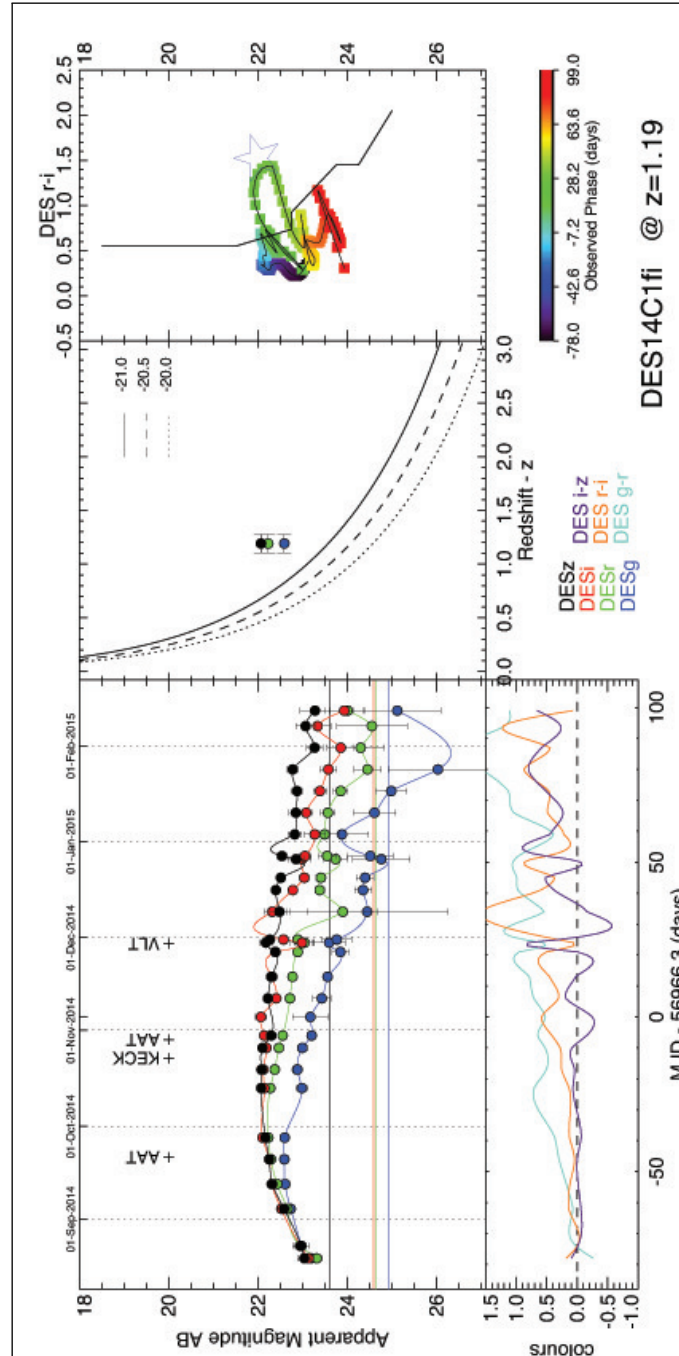
Figure 5.7: Visual inspection panel for SLSNe candidates used in DES Y2. *Top-left:* Apparent magnitude light-curve of a SLSNe candidate as a function of the observed phase from peak brightness. The solid, horizontal lines represent the host galaxy magnitudes in $griz$ filters, whereas the dotted vertical lines show the first of each calendar month, serving as a ~ 30 days ruler. For each spectrum that was obtained, the name of the relative telescope and the spectrum date are marked with a cross. *Top-middle:* Absolute peak magnitude-M_{griz} (equation 1.28) versus host z_{photo} or z_{spec}. The solid, dashed and dotted black lines show the absolute magnitude of $M = [-21.0, -20.5, -20.0]$ respectively. *Top-right:* A colour-magnitude diagram used for detection of gravitational lensed SNe Ia (Quimby et al., 2014, see also Sec. 1.6). The colour evolution with observed phase follows the colour-bar under the plot. The black crooked-line divides the diagram into unlensed (left) and possibly lensed (right) SNe Ia. The open blue star marks the values corresponding to PS1-10afx (Chornock et al., 2013; Quimby et al., 2013a), a lensed SNe Ia. *Bottom-left:* Multi-colour evolution plot of the transient created by using spline interpolation (IDL) on the data from the magnitude light-curve on top.
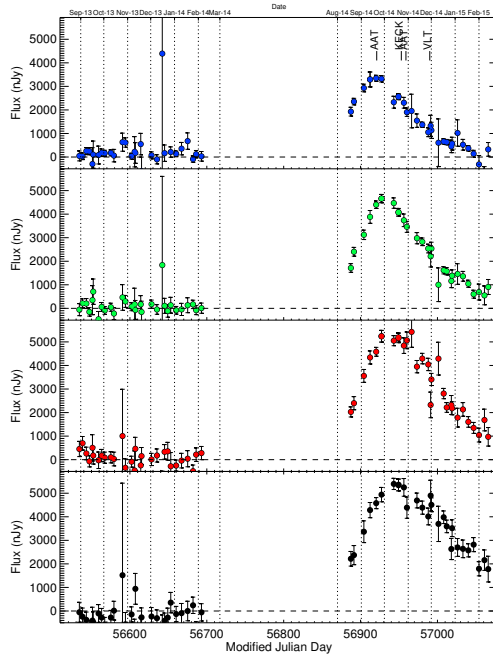
(a) DES14C1fi Y1+2
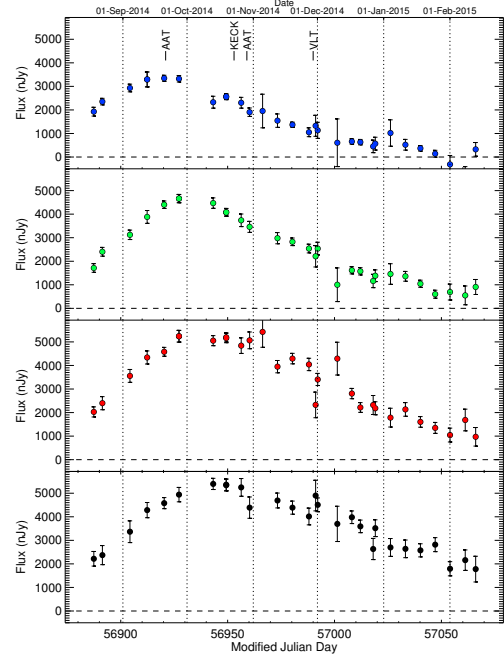
(b) DES14C1fi Y2 only
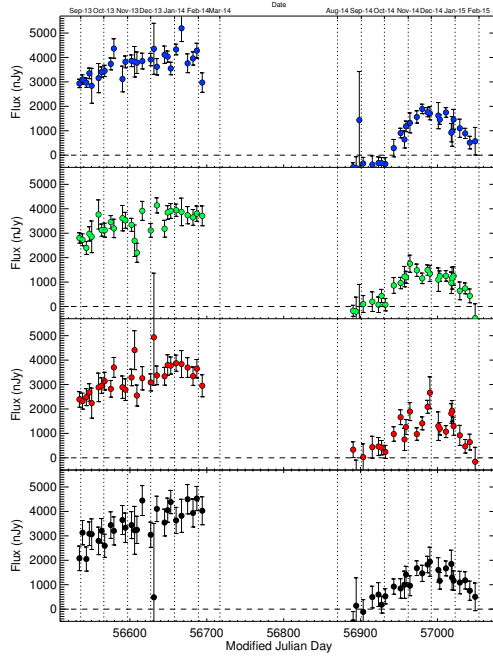
(c) DES14S2jct Y1+2
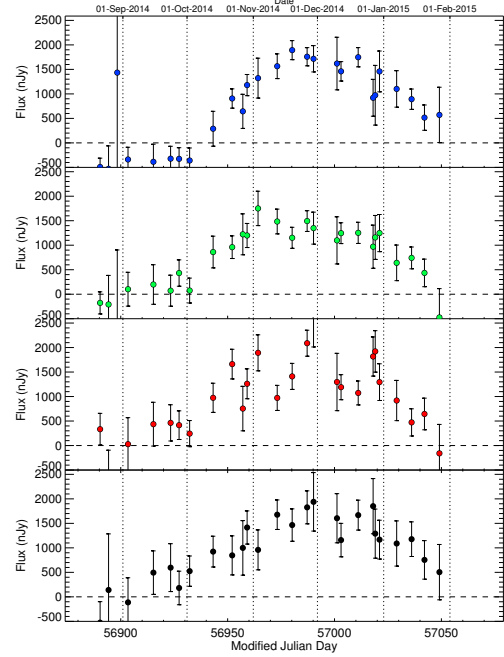
(d) DES14S2jct Y2 only

Figure 5.8: Light-curve plots in flux space of two SLSNe candidates from Y2; **DES14C1fi** *(top row)* and **DES14S2jct** *(bottom row)*, that served as auxiliary panels to the main visual inspection panel of Fig. 5.7. Individual DES filter (blue-g, green-r, red-i, black-z) light-curves where plotted in separate sub-panels from top to bottom, whereas the horizontal dashed lines show the zero flux limit, and the vertical dotted lines show the beginning of each month, that DES was observing. *Left panels:* multi-season (Y1+2) flux light-curves, *right panels:* single season (Y2 only) flux light-curves.

such case would be a transient that was discovered and selected by the selection process at an early stage of its light-curve, then more data would be needed for a final decision.

By the end of DES Y2 in mid-February 2015, I had visually inspected through this process more than 1000 transients that had passed the SNR limit and the four SLSNe criteria, described before. The majority ($\sim$ 650) were classified as AGNs/QSOs and were placed into a veto catalogue which excluded them from future SLSN selection; 140 transients were classified as definite 'normal SNe', most of which were detected and classified by the SNe Ia search, and finally 133 transients were classified as SLSNe candidates.

Fig. 5.9 shows flux light-curve plots of such examples: SLSNe, normal SNe, AGN and artefacts, whereas their respective triplet postage-stamps are shown in Fig. 5.10. Most of the time, the differences between those classes of objects were easy to identified (e.g. DES14X1kjg designated as artefact in Fig. 5.9 shows zero flux in g and r bands, constant flux in i band and chaotic behaviour in z band flux). On the other hand, cases like DES14C3rhw (bottom panel of Fig. 5.9) can mimic the behaviour of a SLSNe light-curve at early times, leading to a misclassification at this selection stage.

As stated before, in Appendix A several examples of the those main candidate categories (SLSNe, 'normal SNe', AGNs) are presented in the form of the visual inspection panel, shown in Fig. 5.7.

The number of 133 SLSNe candidates that were selected from this process step by the end of DES Y2, could be considered high, given the number of historic SLSNe presented in Chap. 2. On the other hand, the main goal of the SLSNe search to this stage, was to eliminate the majority of transients that show clear evidence of their non-SLSN nature. So, the expectation at the time was that the following selection-cut steps would be able to decrease the total number of SLSNe candidates by a factor of $\sim$ 10.

5.4.3 Second Visual Inspection

At this stage of the SLSNe selection process, a second visual inspection was found to be necessary and thus was implemented (bottom grey diamond in flow diagram of Fig. 5.4). Such a step was put in place to achieve the most efficient use of the spectroscopic follow-up time and meet the spectroscopic strategy described in Sec. 5.3.2. As stated before, a portion of the spectroscopic follow-up time was to be invested towards the confirmation and study of interesting and rare SNe, such as SLSNe. That time was limited, so each SLSNe candidate that was targeted for spectroscopic follow-up would have to possess a confident classification. In addition, some of the SLSNe candidates were expected to be targeted already as live-transients within the OzDES program, which targets any transient brighter than $m_r < 21.5$.
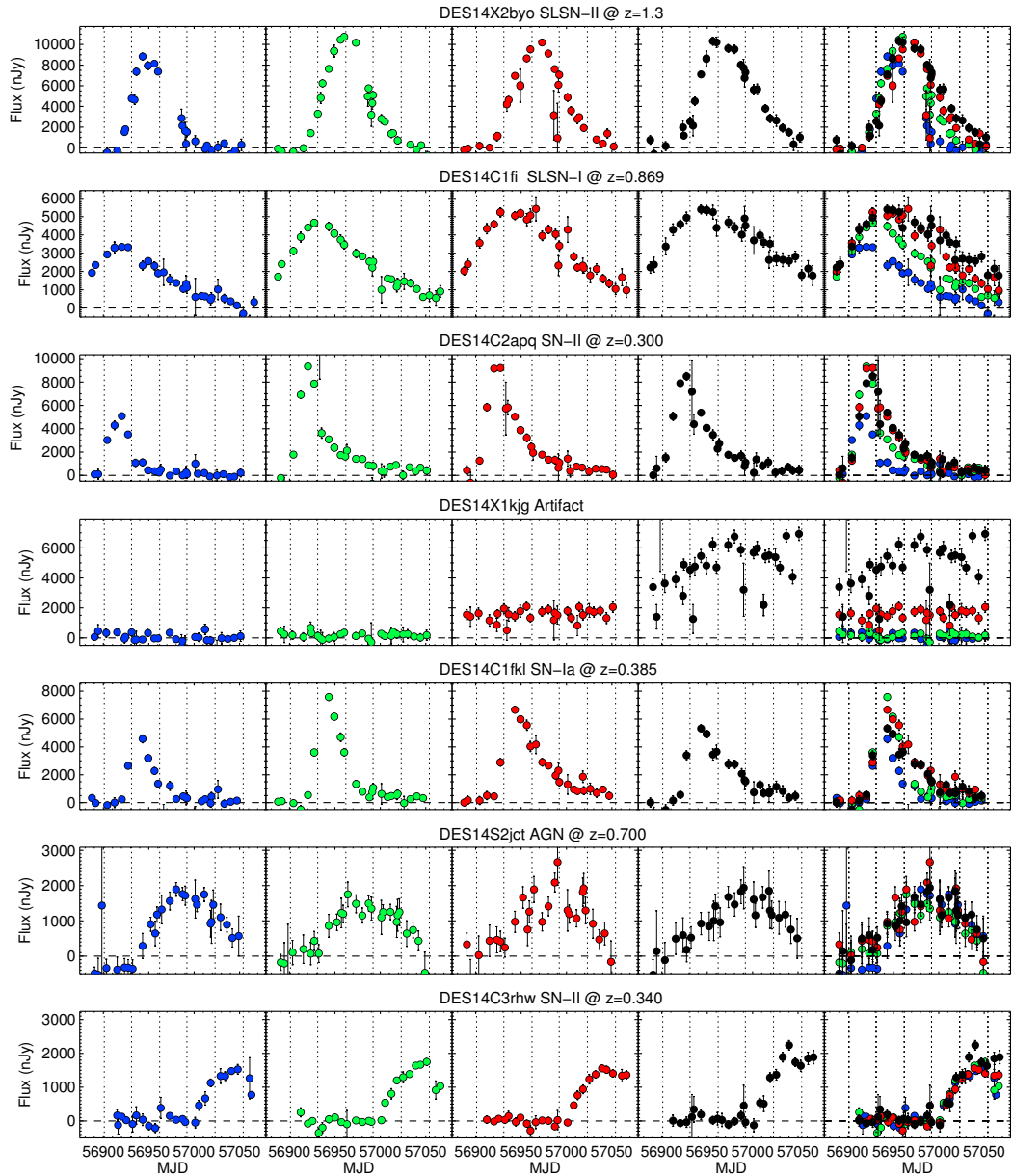
Figure 5.9: Flux light-curves of 7 different DES transients discovered in Y2, that passed the SLSNe selection criteria and finally were visually inspected as described in Sec. 5.4. For each transient the four panels show the isolated time evolution of the measured flux in each DECam filter, whereas the fifth panel shows a composite overplot of all the filters in order to demonstrate the colour evolution. The horizontal dashed lines show the zero flux limit, and the vertical dotted lines show the beginning of each month, that DES was observing. The first visual inspection process (subsection 5.4.2) aimed at distinguishing the differences between the light-curves behaviour of those 7 examples.
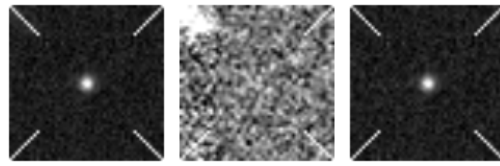
(a) DES14X2byo
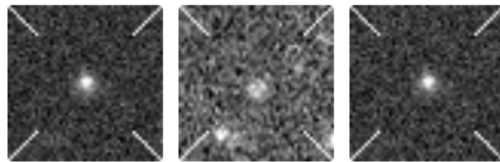
(b) DES14C1fi
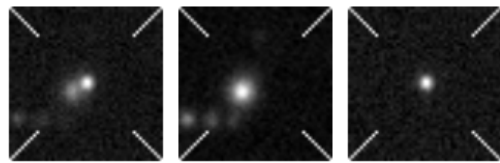
(c) DES14C2apq
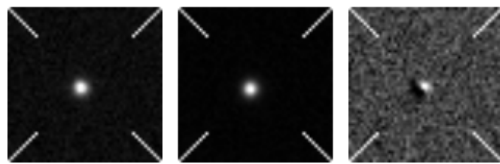
(d) DES14X1kjg
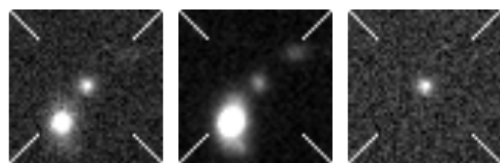
(e) DES14C1fkl
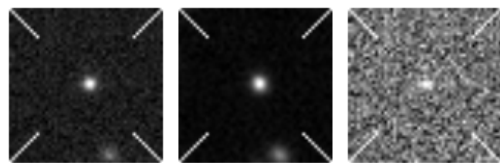
(f) DES14S2jct
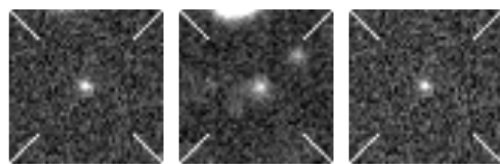
(g) DES14C3rhw

Figure 5.10: 'Postage-stamps' of 7 DES transients in the order presented in Fig. 5.9. Each stamp was created by a $13" \times 13"$ cutout of DECam images, taken in r-band and close to their transient's peak brightness. The three columns correspond to the search, template and difference images, respectively.
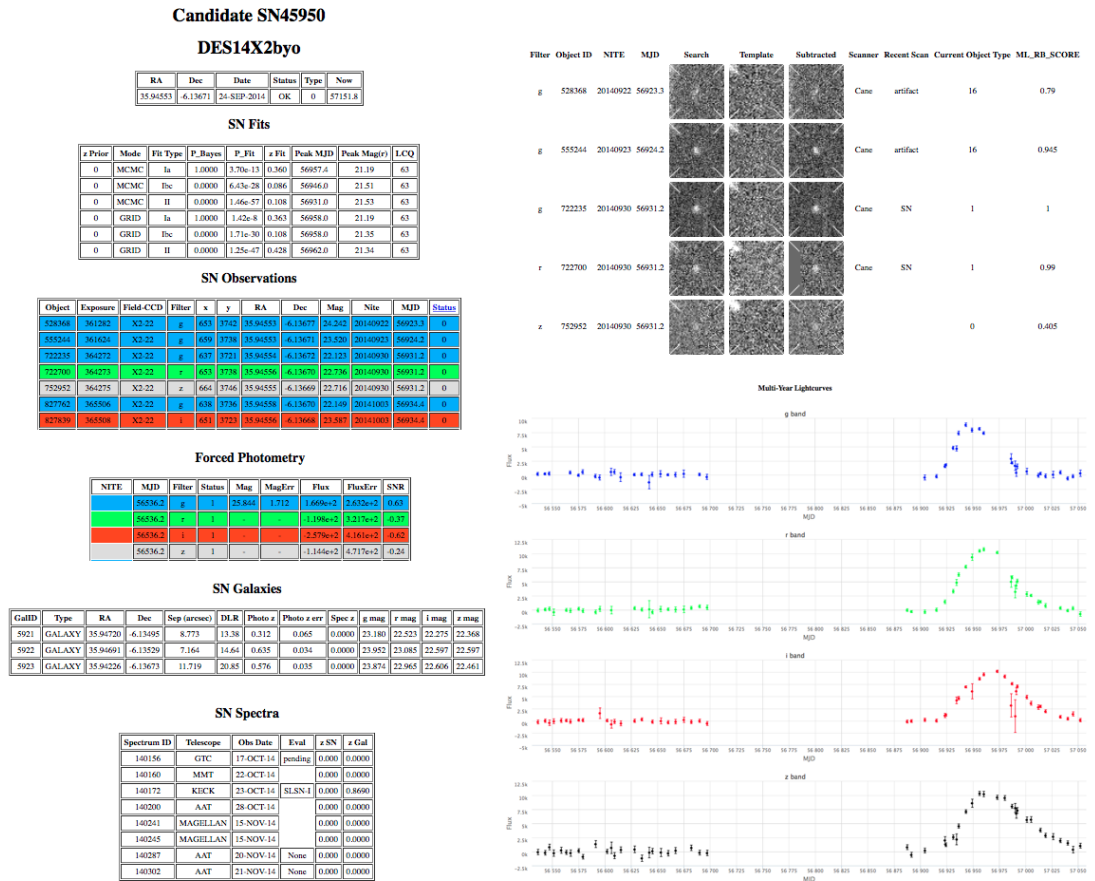
Figure 5.11: Each DES transient's data were presented by individual web-pages containing the transient's coordinates, model fits, observed measurements, host galaxy details, spectral information, postage-stamps with AUTOSCAN scores and multi-season light-curve plots. The 'candidates-page' was developed by Dr. John Fischer as part of the DES SNe search, in order to assist the SNe-Ia candidates selection.
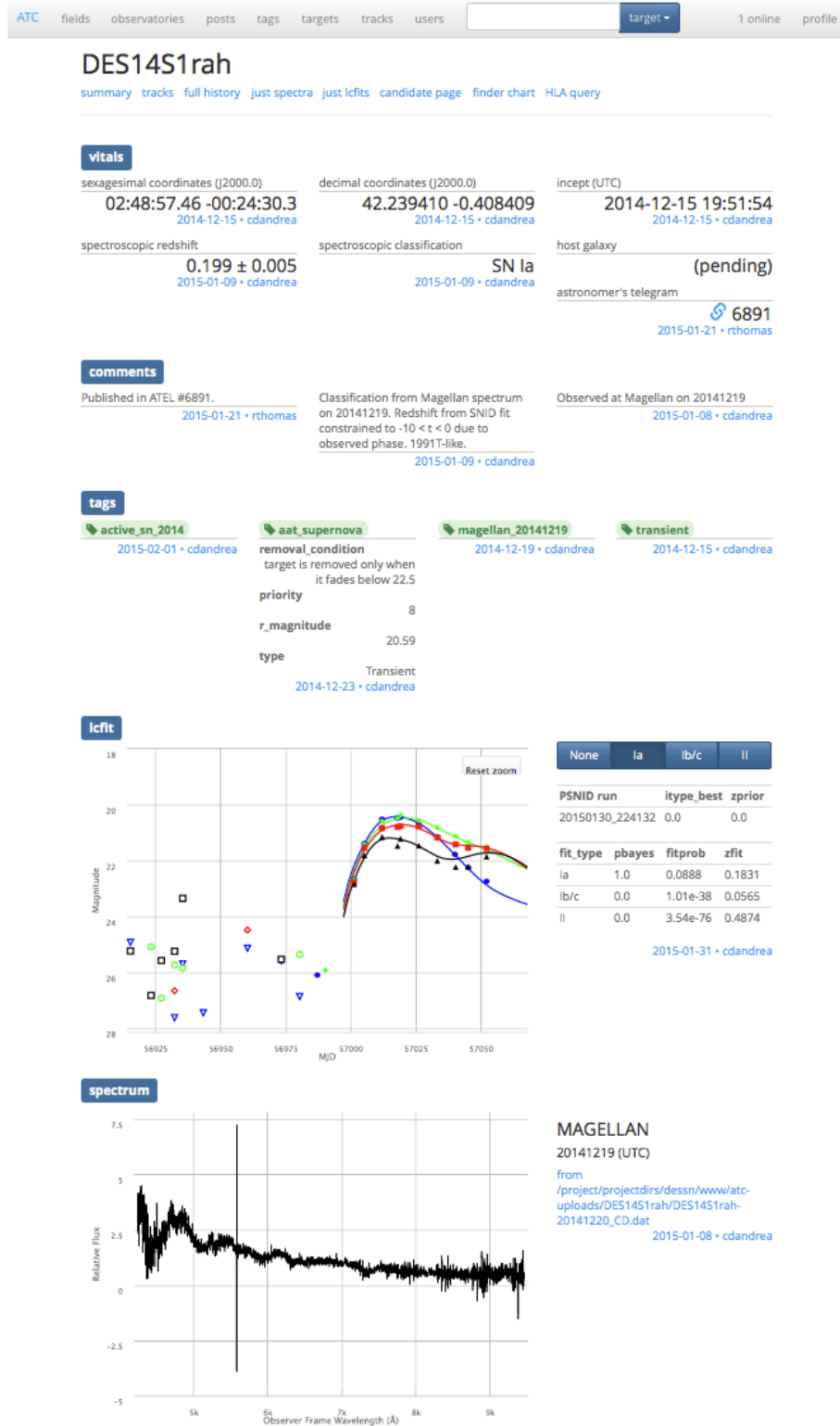
Figure 5.12: The ATC is a web application designed to assist the observer on the spectroscopic follow-up observations. It presents information for the location of each DES transient, provides a detailed finder chart of the surrounding area, shows interactive plots of the light-curves and previous spectra and finally, it allows multiple users to comment or tag information about the transient. The 'ATC-page' was designed and developed by Dr. Rollin Thomas.

The second visual inspection process involved a more careful study of each of the 133 SLSNe candidates, in order to select the best sample to be sent to the telescopes for spectroscopic confirmation. All the tools described in the previous steps (visual inspection panel - fig.5.7; flux light-curves - fig.5.8) were used to assist this effort. At the same time, two additional tools were in service to help as well. First was the 'candidate-page' seen in Fig. 5.11, which was developed by Dr. John Fischer as part of the DES SNe search, in order to assist the SNe-Ia candidates selection. The 'candidate-page' is used as a visualization web-page of the available data for each DES transient. As seen in Fig. 5.11, the web-page contains various tables with each transient's information: coordinates, date of discovery, search observations/measurements, force photometry measurements, SNe model fits, host galaxy details, spectroscopic observations details, DECam postage-stamps from the area around the transient and multi-season flux light-curves.

The 'ATC-page' shown in Fig. 5.12, was the second auxiliary tool and was developed by Dr. Rollin Thomas as an assisting visualization tool for observers undertaking spectroscopic follow-up of SN candidates. The 'ATC-page' is a web application, which gathers and presents critical information for each DES transient e.g. coordinates (both in decimal and sexagesimal format), interactive light-curve and spectrum plots, finder charts with pointing stars and visibility plots for various observatories. Also, it offers useful auxiliary information about the transient to be observed, like its observing history, links to host galaxy information, previous comments from other observers, fits to various SNe models to the light-curves etc.

Another semi-interactive IDL routines, similar to that described in the previous section, was used for this second stage. For each of the 133 SLSNe candidates, I visually reviewed all available data provided from all the tools described above. The first objective was to select objects that presented strong evidence of being superluminous in nature and not a normal type SNe (e.g. Ia, II, Ibc), as the light-curve of each candidate was evolving each night.

SLSNe candidates that were showing any evidence of 'normal SNe type' behaviour were placed at a lower priority. Such evidence were the quick rise time to peak brightness seen mostly in SNe-II, the lower flux peak and the second bump in the redder bands for SNe-Ia. Moreover, the results of a light-curve model fitter (PSNID; Sako et al., 2008, 2011) were available within the 'candidate-page' and the 'ATC-page' for every transient. The PSNID fitter provided the best model fits for any given transient's light-curve – with or without a prior on the redshift to accommodate both hostless and SNe with host galaxies – but only included normal SN models (e.g. Ia, Ib/c and II). That information was provided in the format of a table with the best fit parameters (e.g. probability, redshift estimation, peak magnitude etc.) in the 'candidate page' (fig. 5.11); and in a plotted format alongside the photometric light-curve in the 'ATC-page' (fig. 5.12).

Table 5.3: List of 14 DES transients from Y2, that were selected primarily as SLSNe candidates and were sent to the listed telescopes for spectroscopic follow-up. The outcome results of the spectral classifications are listed in the last column. In the telescopes' column, the telescope names in bold show the first one that secured the SNe classification. In the transient's name column, the names in bold refers to those transients classified as SLSNe.

#	Name	M_r	host z_{photo}	host z_{spect}	host separ.(")	# epochs	# obs.	Telescope(s)	Comments
1	**DES14C1fi**	-22.34	1.191 ± 0.085	Pending (OzDES)	0.64	27	79	AAT; **VLT**; Keck	SLSN-II; $z_{host} = 1.3$
2	DES14C1fs	-20.59	0.744 ± 0.050		0.82	24	60	VLT	Uncertain
3	DES14C3oz	-22.95	1.253 ± 0.079	Pending (OzDES)	2.73	52	103	AAT; VLT	AGN; SN-IIP
4	DES14C1kyz	-22.06	0.982 ± 0.065	Pending (OzDES)	1.36	8	23	AAT	Pending
5	DES14X3phi	-20.59	0.550 ± 0.046		1.13	23	40	AAT	Pending; SN-Ia?
6	DES14C3qzz	-21.35	1.148 ± 0.139		0.26	22	38	VLT	Uncertain; SN-Ic?
7	DES14S2sz					18	50	AAT	Pending
8	DES14C1coz					15	44	AAT; VLT	SN-II $z = 0.385$
9	DES14S1dch					15	39	VLT	Uncertain
10	**DES14X2byo**			Hostless		23	57	AAT; VLT; GTC; MMT; **Keck**; Magellan	SLSN-I; $z = 0.869$
11	**DES14S2qri**					11	30	GTC	SLSN-I; $z = 1.5$
12	**DES14C1rhg**					11	34	AAT; **VLT**	SLSN-I; $z = 0.47$ underluminous?
13	DES14E1rpk					6	18	VLT	SN-Ia $z = 0.57$
14	**DES14E2slp**					7	27	VLT	SLSN-I; $z = 0.6$

After a SLSNe candidate had passed all the previous steps and I had sufficient evidence that it was not a 'normal SN', but had a rather long rising time ($\gtrsim$ 30 days) and a host z_{photo} or z_{spec} that would put the candidate to the superluminous regime, the SLSNe candidate was placed in one of the selection samples described in the following section, to be sent to the telescopes for obtaining a spectrum. The SLSNe candidate selection samples were available and updated on the internal DES collaboration web-services ('wikipage') and each SLSNe candidate was tagged on the 'ATC-page' as 'superluminous-cand'. After coordinating with Dr. Chris D'Andrea, the spectroscopic marshal of the SN Survey, the SLSNe candidates would be chosen and sent to the selected telescopes for spectroscopic follow-up. The final selection of the targets and the telescopes/instruments was made by the spectroscopic marshal, who was in a position to decide the most efficient use of the spectroscopic time for the purposes of the entire SN Survey.

5.5 Selection Samples

The selection samples analysed in this section, are the final outcome of the selection process described above and illustrated in the flow diagram in Fig. 5.4 as the blue lists at the bottom end of the diagram.

5.5.1 Spectral Classification

Out of the 133 SLSNe candidates that passed the selection process described above, 41 transients were deemed to be high priority and placed in the observing queues of various telescopes, and one or more spectra were obtained. Tables 5.3 and 5.4 summarize the
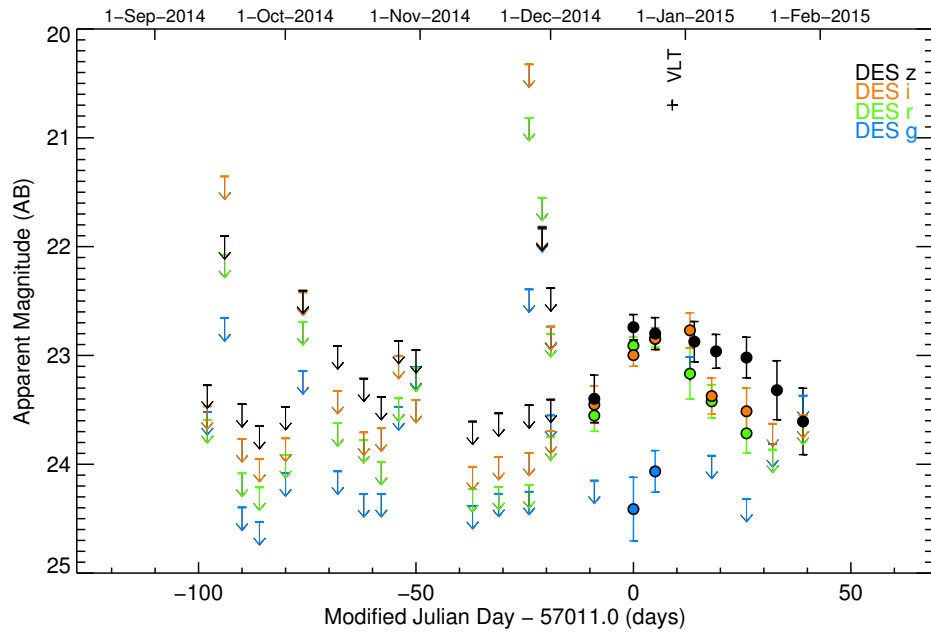
(a) DES14E1rpk light-curve
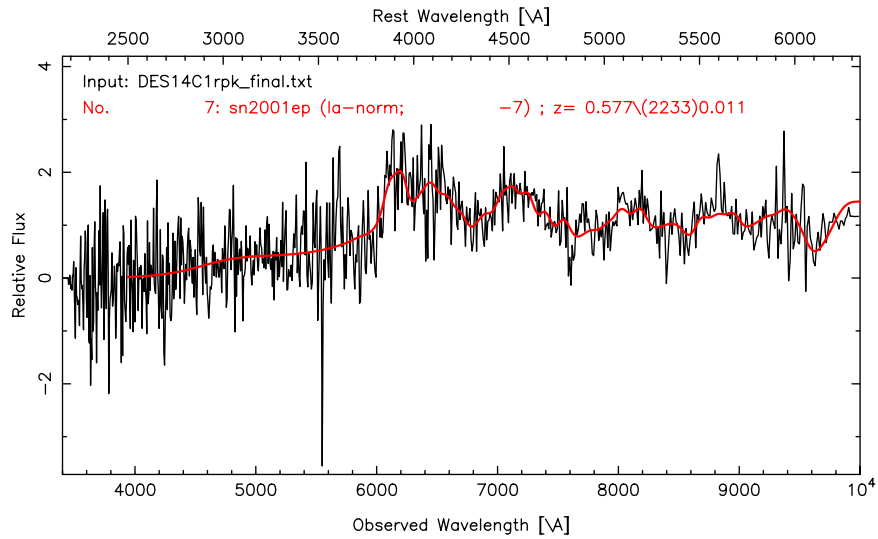
(b) DES14E1rpk spectra

Figure 5.13: The observed light-curve (*panel a*) and VLT spectrum (*panel b*) of **DES14E1rpk**. The spectrum was used to classify DES14E1rpk as a SNe-Ia at a redshift of $z = 0.57$, as seen in the bottom panel created by Dr. Mat Smith with the use of SNID (Blondin and Tonry, 2007).
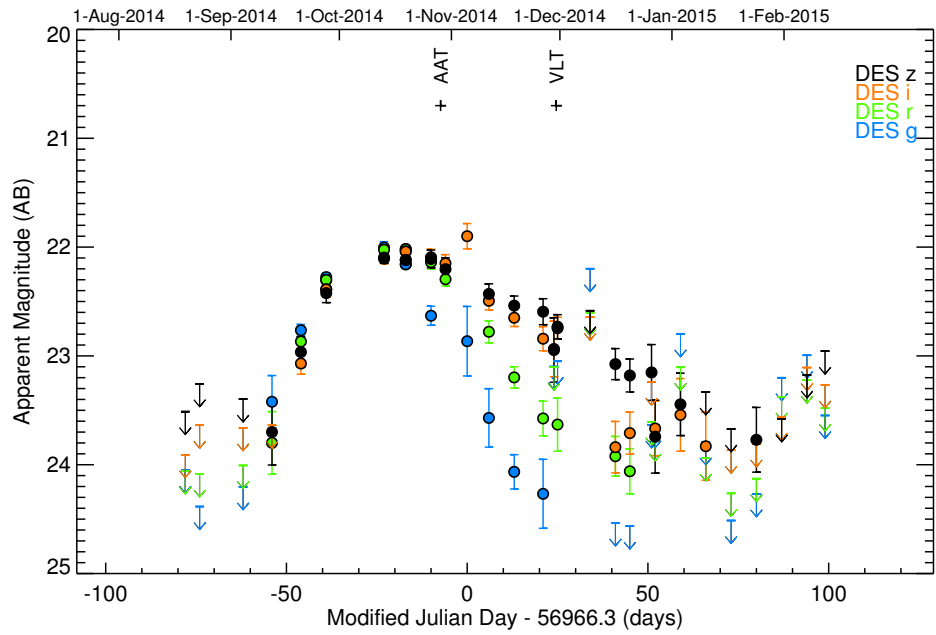
(a) DES14C1coz light-curve
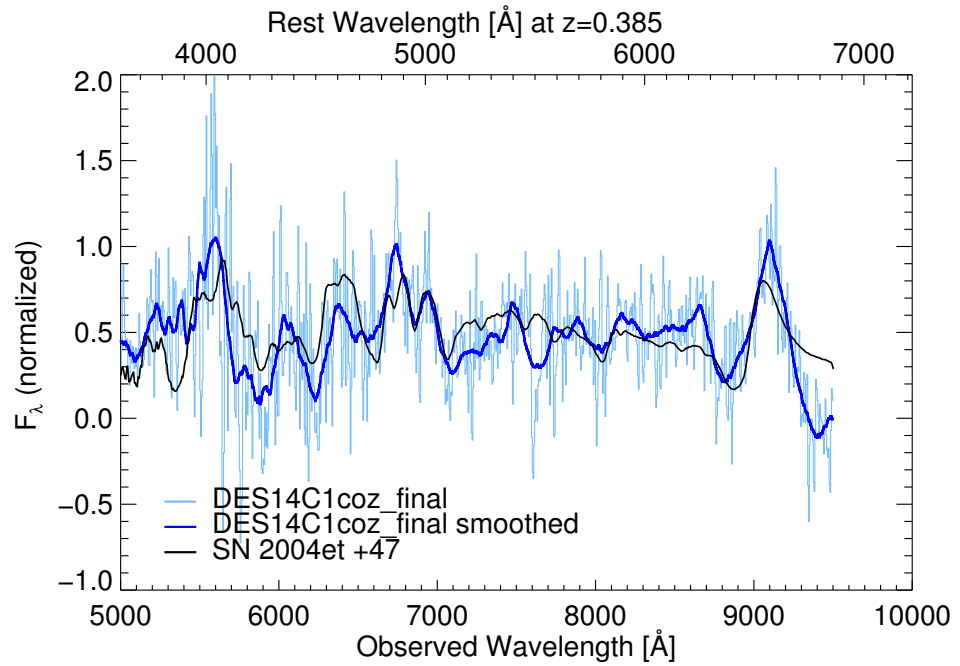
(b) DES14C1coz spectra

Figure 5.14: The observed light-curve (*panel a*) and VLT spectrum (*panel b*) of **DES14C1coz**. The spectrum was used to classify DES14C1coz as a SNe-II at a redshift of $z = 0.385$, as seen in the bottom panel created with the use of SUPERFIT (Howell et al., 2005), although the light-curve is in good agreement with a SLSNe at higher redshift.

results of the spectroscopic follow-up of those 41 SLSNe candidates. Fourteen objects were targeted primarily as SLSNe (Table 5.3). The rest were originally targeted as SNe Ia (Table 5.4), but later in their light curves became good SLSNe candidates as they met enough of the SLSN criteria discussed above.

Both tables show separately the hostless candidates from those associated with a host galaxy, as this segregation was necessary for the different spectroscopic resources available in Y2 as described in Sec. 5.3.2. For example, the VLT program was primarily targeting hostless SNe, whereas the OzDES program was targeting by design the host galaxies of as many SNe candidates as possible.

Out of the 14 SLSNe candidates listed in Table 5.3, 4 SLSNe events were spectroscopically confirmed, and one more SLSNe had an indirect identification, after securing its host redshift. A detailed description and study of those objects can be found in later sections. Two objects were spectroscopically identified as non-SLSNe, namely: DES14E1rpk that was classified as SNe-Ia at $z = 0.57$ as seen in Fig. 5.13, and DES14C1coz, whose spectrum is in good agreement with a SNe-II at $z = 0.385$, although its light-curve mimics almost perfectly a SLSNe at higher redshift, as seen in Fig. 5.14. Moreover, 6 objects remain uncertain as fits to their spectra (using (eg. SUPERFIT, SNID; Howell et al., 2005; Blondin and Tonry, 2007)) could not find an unambiguous classification to any SN class. One last object, DES14C3oz, was spectroscopically classified as SN-IIP using a VLT spectrum at late times, but earlier spectra obtained by the OzDES program had identified it as an AGN.

Table 5.4 lists the 27 transients that were originally selected as SNe Ia for spectroscopic follow-up, as part of the main goal of the DES SN Survey. Some of those objects were then selected as SLSNe candidates in the first visual inspection but remained ambiguous in the second, more detailed examination. Some others were selected as SLSNe candidates, after the first attempt at obtaining a spectrum had failed to reach a secure classification and their light-curve developed similar characteristics as a SLSNe; such an example is the transient named DES14X2agp, seen in panel (a) of Fig. 5.15. Eleven objects from Table 5.4 were subsequently classified as SNe Ia, either by their spectra features or by the combination of the host z_{spec} and the PSNID light-curve fits. Two objects were classified as SNe-II and 12 more had unclassified spectra, most of which are cases where the host galaxy brightness was dominating over the SNe spectral features, like DES14E2ffb seen in panel (b) of Fig. 5.15.

One particular transient, DES14X3taz, was targeted at first as an interesting SN-Ia candidate, as it showed a pre-peak prominent bump in its light-curve, and was sent to the GTC for spectral confirmation. When the spectrum was obtained and analysed, there was minimal evidence in support of a SNe Ia classification, whereas I proposed the preliminary spectrum was more consistent with a SLSN-I candidate at $z \sim 0.6$. At a later

Table 5.4: List of 27 DES transients from Y2, that were selected primarily as SNe-Ia and were sent to the listed telescopes for spectroscopic follow-up. At a later stage, the listed transients were also selected as possible SLSNe candidates. The outcome of the spectral classifications are listed in the last column, and the names of the transients highlighted in bold are those spectroscopically confirmed to be SLSNe. In the telescopes' column, the highlighted (bold) name of the telescope refer to the first one that secured the SNe classification. In the transient's name column, the names in bold refers to those transients classified as SLSNe.

#	Name	M_r	host z_{photo}	host z_{spect}	host separ.(")	# epochs	# obs.	Telescope(s)	Comments
1	DES14X2dl	-20.41	0.636 ± 0.067	Pending (OzDES)	0.32	5	11	VLT	SN-Ia; $z = 0.437$
2	**DES14X1ps**	-21.31	0.610 ± 0.085	Pending (OzDES)	0.48	21	55	AAT	SLSN-II ?; $z = 0.61$
3	DES14X3rb	-19.84	0.282 ± 0.038	0.343 (SDSS)	7.51	27	59	AAT	Pending; SN-Ia?
4	DES14X3afj	-18.88	0.307 ± 0.062	0.288 (OzDES)	0.37	19	43	AAT	Pending; SN-Ia? secured host z_{spect}
5	DES14X2agp	-18.70	0.335 ± 0.046	0.304 (OzDES)	0.10	17	50	AAT; MMT	Pending; secured host z_{spect}
6	DES14E2ffb	-20.09	0.213 ± 0.066	0.209 (OzDES)	1.29	21	68	AAT	Pending; secured host z_{spect}
7	DES14C1gdz	-19.12	0.315 ± 0.084	Pending (OzDES)	2.38	13	36	AAT	Pending
8	DES14C3gym	-19.90	0.387 ± 0.068	Pending (OzDES)	0.39	31	65	AAT	Pending
9	DES14C2kdr	-21.09	0.695 ± 0.085	Pending (OzDES)	0.70	10	24	AAT	Pending
10	DES14E1mli	-19.30	0.326 ± 0.063		1.96	13	47	AAT	Pending
11	DES14C3mpr	-19.96	0.691 ± 0.051		0.34	15	26	VLT	SN-Ia; $z = 0.79$
12	DES14C3oci	-19.68	0.716 ± 0.056		0.39	14	24	VLT	Uncertain
13	DES14X1oes	-21.97	0.706 ± 0.079		1.27	13	44	SALT	SN-Ia; $z = 0.3$
14	DES14X3oir	-19.91	0.458 ± 0.071	0.435 (OzDES)	0.32	20	39	AAT	Pending; SN-Ia; secured host z_{spect}
15	DES14C2rsq	-20.48	0.629 ± 0.071	Pending (OzDES)	0.65	9	28	AAT; VLT	Uncertain
16	**DES14X3taz**	-22.10	0.747 ± 0.079		0.15	17	25	GTC	SLSN-I; $z = 0.6$; pre-peak bump
17	DES14C3tsg	-19.75	0.534 ± 0.083		0.49	17	25	VLT	SN-II; $z = 0.21$;
18	DES14S2usy	-18.66	0.280 ± 0.060		0.54	4	15	Magellan	Pending
19	DES14C2vnf	-20.08	0.644 ± 0.060		0.69	6	17	VLT	SN-Ia; $z_{host} = 0.542$;
20	**DES14E2ap**					11	32	VLT	SLSN-I ?; $z = 0.6$
21	DES14E1tb					10	32	AAT	SN-Ia; $z = 0.372$
22	DES14C3nm					23	44	VLT	SN-II
23	DES14C1jnc			Hostless		12	29	AAT	Pending
24	DES14X2nzt					16	53	VLT	Uncertain
25	DES14S1rah					10	40	Magellan	SN-Ia; $z = 0.199$
26	DES14X2rao					10	38	**Magellan;** VLT	SN-Ia; $z = 0.283$
27	DES14E2slo					7	23	VLT	SN-Ia
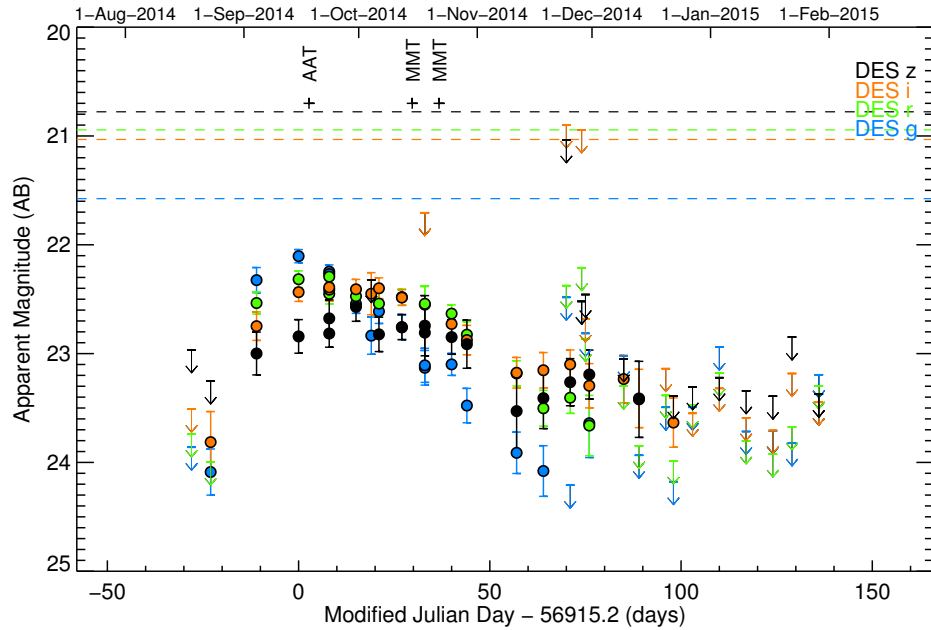
(a) DES14X2agp light-curve
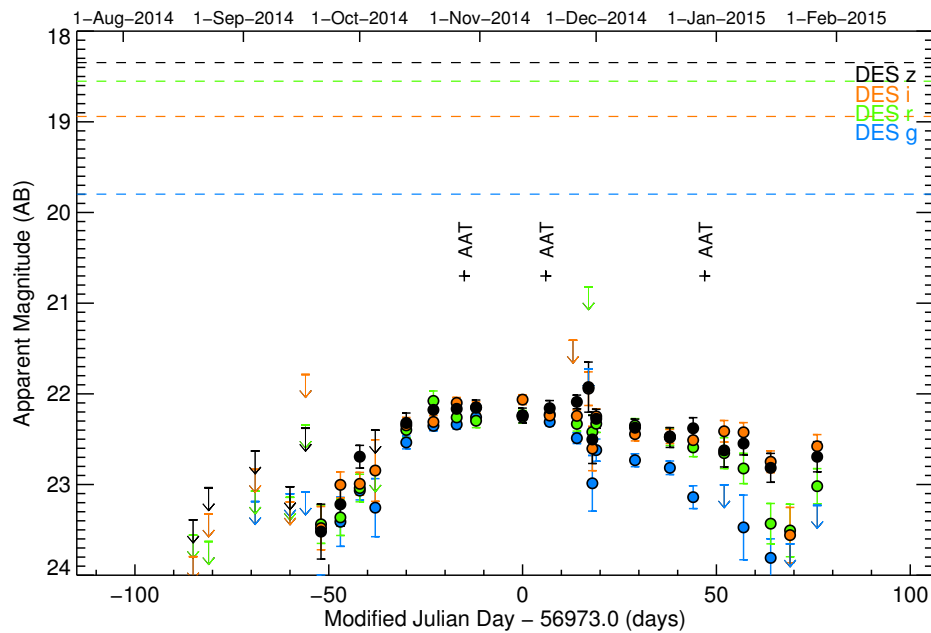
(b) DES14E2ffb light-curve

Figure 5.15: The observed light-curves of **DES14X2agp** (*panel a*) and **DES14E2ffb** (*panel b*). Neither transient could be securely classified as SLSNe, even thought spectra data were obtained for both of them. The horizontal dashed lines show the magnitude measurements of the host galaxies, where the black crosses mark the phase where spectra were obtained. The errorbars represent 1-σ uncertainties, and the arrow symbols are 3-σ upper limits. DES14E2ffb was more than two magnitudes fainter than its host galaxy, so the spectral classification is almost impossible, whereas DES14X2agp show strong signs (second bump) of a SNe-Ia.

Table 5.5: List of SLSNe candidates from Y2, that did not get a spectroscopic observation of the transient, but are associated with a host galaxy that has a secured z_{spec}. Those host z_{spec} were secured mostly by the OzDES program during Y1 of operations and by using public archival data from past surveys. The one transient (DES14X1rbi) that was confirmed as a SLSNe by using the light-curve and its host z_{spec} is highlighted in bold fonts.

#	Name	M_r	host z_{photo}	host z_{spect}	host separ.(")	# epochs	# obs.	Comments
1	DES14C2dmc	-21.52	0.659 ± 0.028	0.731 (OzDES)	0.59	4	11	SN-Ia ?
2	DES14E2fly	-19.17	0.440 ± 0.070	0.515 (OzDES)	1.13	5	10	SN-Ia
3	DES14X3fpy	-19.70	0.866 ± 0.038	0.818 (OzDES)	1.29	8	18	SN-Ia?
4	DES14X3kvs	-20.04	0.577 ± 0.042	0.610 (OzDES)	2.25	12	29	SN-Ia?
5	DES14C1mek	-20.15	0.675 ± 0.028	0.743 (OzDES)	1.01	8	15	SN-II
6	DES14C3ocl	-19.13	0.668 ± 0.036	0.678 (VVDS[a])	0.36	9	16	Uncertain
7	DES14C1pjy	-22.14	0.748 ± 0.029	0.854 (OzDES)	0.27	4	8	SN-Ia
8	**DES14X1rbi**	-20.69	0.689 ± 0.033	0.717 (VIPERS[b])	2.14	10	28	SLSN
9	DES14X2tbf	-20.01	0.685 ± 0.026	0.678 (OzDES)	0.33	5	9	SN-Ia
10	DES14C1wcy	-20.54	0.661 ± 0.057	0.670 (ATLAS[c])	0.40	7	17	SN-Ia
11	DES14C3vno	-22.14	0.845 ± 0.135	2.142 (NED[d])	1.54	8	11	AGN/QSO

[a]VIMOS-VLT Deep Survey
[b]VIMOS Public Extragalactic Redshift Survey
[c]VLT Survey Telescope 'ATLAS' survey
[d]NASA/IPAC Extragalactic Database

time, Dr. Mat Smith re-reduced the spectral data with a new version of spectral reduction pipeline and discovered a perfect fit to a SLSN-I at $z = 0.6$.

Other interesting cases are DES14X1ps and DES14E2ap. The latter is a transient that was first selected and targeted as a promising SN-Ia candidate, but the spectrum obtained by the VLT was very noisy and a secured classification was beyond reach. After the end of Y2 and the re-reduction of the spectral data, DES14E2ap could be classified as a SLSNe at $z = 0.6$. DES14X1ps light-curve and the photometric redshift of its host galaxy at $z_{photo} = 0.61$ point towards a SLSNe, even though its noisy and featureless spectrum obtained with the OzDES program, adds no additional information. More detailed descriptions and studies of DES14X3taz, DES14E2ap and DES14X1ps are given in later sections.

5.5.2 Photometric Classification

Out of the total 133 SLSNe candidates, 92 did not make it to a telescope's target list for various reasons. The most common reason was the candidate in question had faded by the time we had access to observing time with particular telescopes, mostly with VLT and AAT (OzDES). Also, the allocated Target-of-Opportunity (ToO) spectroscopic time over the entire Y2 was limited, so priority was given towards the main DES SNe goal of confirming SNe-Ia. Furthermore, some SLSNe candidates had noisy and low SNR light-curves so that, their classification could not be sufficiently trusted to risk a spectroscopic

observation. Finally, a handful of SLSNe candidates were one or more magnitudes fainter than the host galaxy, so targeting such transients would not provide more information than available from the host galaxy redshift (z_{spec}), which could be provided later on by the OzDES program.

The 92 SLSNe candidates that did not get a spectrum can be divided into three groups, described below:

Group A

The first group consists of SLSNe candidates that are associated with host galaxies with secured z_{spec}, via the OzDES program or other archival data. A list of those 11 transients can be seen in Table 5.5, most of which show good agreement between their photometry and PSNID fits of 'normal SNe'. Five of them have been classified as SNe-Ia in the redshift range of $0.52 \leqslant z_{spec} \leqslant 0.85$, one object (DES14C3vno) was classified as a possible high-redshift AGN at $z_{spec} = 2.14$, and one object DES14X1rbi can be classified as a SLSN that peaked at $M_i = -20.7$ at a host redshift of $z_{spec} = 0.72$.

Group B

The second group consists of SLSNe candidates without a secured spectroscopic redshift of their host galaxy, because their host galaxies have not been targeted yet or the OzDES program needs more observations to secure the redshift of those hosts. Table 5.6 lists the 54 SLSNe candidates that fall into this group. After considering their fit results from PSNID, and using their host z_{photo}, one can make a stricter selection as to what could be considered a SLSN and what could be a normal SN, in most cases type Ia. After re-examining the light-curve of those 54 SLSNe candidates and focusing on the disagreement between the host z_{photo} and the fitted redshift from PSNID, 9 transients were selected which can be considered as SLSNe candidates. All 9 of them are poorly fit by any 'normal SNe' model of PSNID at high redshift, and their light-curves show long rising time-scales, accompanied by high peak brightnesses, considering their host galaxies z_{photo}.

In Table 5.6, the hosts that are designated with 'Pending (OzDES)' are going to remain in the target list of the OzDES program for the Y3 of operations – until a secured redshift is obtained – by stacking multiple spectra together and increasing the spectra SNR. As for the rest of the sample, the host galaxies that are associated with real SNe transients and fulfil the magnitude limits of the OzDES program, will be targeted in Y3 in order to obtain a secured host z_{spec}. Through this process, transients that were on the borderline between SLSNe or SNe-Ia at high redshift (e.g. DES14X3ehq; DES14S2emj), would be classified more confidently.

Table 5.6: List of SLSNe candidates from Y2, that did not get a spectroscopic observation of the transient, but are associated with a host galaxy that has an estimation of its z_{photo}. Almost half of the hosts were observed by OzDES, but a secured redshift was not delivered. Hence, they remain in the targeting list of OzDES for further spectra to be obtained in the future. Also, the rest of the hosts that are clearly associated with a real transient, are probably going to be targeted with OzDES in Y3 of operations. Highlighted in bold are the names of the transients that show significant evidence (light-curve, host z_{photo}, bad PSNID fits etc) of their SLSNe nature. The last column shows comments after the final classification of the 54 transients.

| #	Name	M_r	host z_{photo}	host z_{spect}	host separ.(")	# epochs	# obs.	Comments
1	DES14C1gm	-19.50	0.522 ± 0.060		0.47	24	40	possible SLSN; only late times light-curve
2	**DES14E1hk**	-20.91	0.531 ± 0.045	Pending (OzDES)	0.94	13	34	possible SLSN;
3	DES14X1uh	-21.07	1.067 ± 0.049	Pending (OzDES)	0.28	20	39	flux in Y1 from first epochs; could be SLSN
4	DES14X3ajy	-19.88	0.534 ± 0.040	Pending (OzDES)	0.79	19	38	SN-Ia
5	DES14C3asw	-22.22	1.150 ± 0.041		0.47	45	89	AGN
6	DES14X3avr	-19.44	0.420 ± 0.069		1.14	18	32	SN-Ia
7	DES14S1bno	-20.29	0.613 ± 0.060	Pending (OzDES)	0.90	6	17	SN-Ia
8	DES14X2axy	-20.37	0.677 ± 0.045	Pending (OzDES)	2.61	7	19	SN-Ia
9	DES14E2cmo	-20.43	0.882 ± 0.034	Pending (OzDES)	0.64	5	12	SN-Ia
10	**DES14E2bhn**	-21.09	0.973 ± 0.072	Pending (OzDES)	2.44	6	12	possible SLSN
11	**DES14X1brr**	-20.63	0.651 ± 0.060	Pending (OzDES)	0.97	11	31	possible SLSN
12	DES14X3ehq	-19.45	1.010 ± 0.083	Pending (OzDES)	1.02	6	12	possible SLSN or high-z SN-Ia
13	DES14X3ehz	-19.61	0.940 ± 0.063		0.35	5	10	high-z SN-Ia
14	DES14S2elt	-20.28	0.863 ± 0.043	Pending (OzDES)	0.99	4	6	SN-Ia faint
15	DES14S2emb	-20.56	0.703 ± 0.029	Pending (OzDES)	0.47	5	11	SN-Ia
16	DES14S2emj	-20.25	0.824 ± 0.051	Pending (OzDES)	1.56	5	10	SN-Ia or Ib/c faint
17	**DES14S1ewv**	-21.98	1.230 ± 0.085		0.66	16	40	SLSN; no colour evolution
18	DES14X1gwm	-20.90	0.959 ± 0.065		0.40	5	9	SN-Ia faint
19	**DES14X3gyr**	-19.81	0.948 ± 0.049	Pending (OzDES)	0.87	9	20	possible SLSN or high-z SN-Ia
20	DES14X3pcw	-20.29	0.746 ± 0.065		10.20	15	24	SN-Ia
21	DES14S1jza	-20.10	0.679 ± 0.050		0.67	4	9	SN-Ia
22	DES14X3jmy	-19.37	0.809 ± 0.037	Pending (OzDES)	2.59	7	15	SN-Ia
23	DES14X2jqt	-19.86	0.699 ± 0.032		6.98	10	18	SN-II
24	DES14X2jsk	-20.14	0.658 ± 0.045		0.78	5	11	SN-Ia
25	DES14C3kfo	-19.89	0.658 ± 0.062		0.59	15	31	SN-Ia or SLSNe
26	DES14C3kzv	-20.29	0.768 ± 0.027		1.37	11	26	SN-Ib/c
27	DES14C3lac	-19.06	1.013 ± 0.066		0.34	5	9	high-z SN-Ia
28	DES14C3lae	-18.98	0.908 ± 0.031		0.53	5	9	high-z SN-Ia
29	DES14X2mgn	-20.19	0.907 ± 0.037		0.40	4	8	faint SN-Ia
30	DES14X2mgq	-20.24	0.394 ± 0.061		0.28	15	48	SN-Ia
31	**DES14X3mjf**	-20.03	0.829 ± 0.066	Pending (OzDES)	0.38	20	39	SLSN strong case high-z
32	DES14X3lfs	-19.28	0.953 ± 0.040		0.39	8	18	high-z SN-Ia
33	DES14S1mkz	-19.93	0.802 ± 0.063		0.32	4	9	high-z SN-Ia
34	DES14S2lim	-19.68	0.700 ± 0.043		0.67	4	8	SN-Ia
35	DES14C2mnd	-20.71	0.586 ± 0.037	Pending (OzDES)	0.27	12	37	SN-Ia
36	DES14C3mpp	-19.77	0.853 ± 0.079		0.89	9	17	SN-Ia faint
37	DES14X2mrr	-20.29	0.450 ± 0.092		0.30	16	46	SN-Ia
38	DES14C2ncy	-21.95	0.971 ± 0.074	Pending (OzDES)	0.93	5	10	noisy and faint light-curve
39	DES14C2ocp	-21.36	0.682 ± 0.058	Pending (OzDES)	3.43	5	16	SN-Ia
40	DES14C2ocs	-19.55	0.783 ± 0.046		0.45	4	6	SN-Ia
41	**DES14C1ngk**	-20.95	0.813 ± 0.033	Pending (OzDES)	1.03	13	23	SLSN strong case high-z
42	DES14E2pkg	-20.44	0.776 ± 0.037		1.32	5	11	SN-Ia
43	DES14C3oko	-20.20	0.927 ± 0.050		0.82	9	16	revisit
44	DES14X1qzi	-19.72	0.623 ± 0.062		1.52	7	17	SN-Ib/c
45	**DES14E1rpi**	-20.97	1.048 ± 0.066		1.81	6	14	promising SLSN or high-z SNIa
46	DES14X2rbx	-21.78	1.223 ± 0.134		0.62	9	21	SN-II
47	DES14S2tax	-20.97	0.915 ± 0.031		0.76	6	10	SN-Ibc
48	DES14S1tbi	-20.41	0.775 ± 0.078		1.24	5	14	SN-Ia
49	DES14E2ssz	-20.40	0.791 ± 0.061		0.27	4	6	AGN
50	**DES14C3tny**	-20.41	0.788 ± 0.082		0.45	15	32	potential SLSN
51	DES14C1ter	-21.37	0.726 ± 0.043		0.66	7	10	noisy light-curve
52	DES14C1vok	-19.90	0.730 ± 0.045		1.34	4	11	SN-Ia
53	DES14C2vra	-20.46	0.430 ± 0.090		1.00	6	23	SN-Ia
54	DES14C1vsn	-21.88	1.121 ± 0.115		0.26	6	18	AGN?
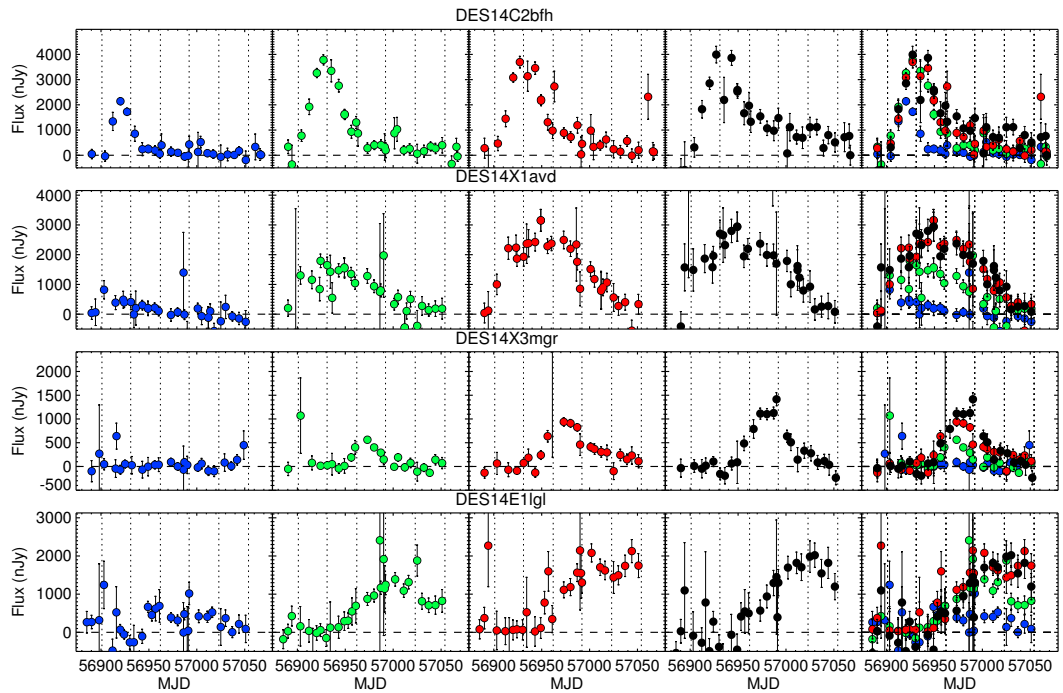
Figure 5.16: Flux light-curves of four hostless SLSNe candidates that lack spectroscopic observations, selected as described in Sec. 5.5.2. For each transient, the first four panels show the isolated time evolution of the measured flux in each DECam filter, whereas the fifth panel shows a composite overplot of all the filters in order to demonstrate the colour evolution. The horizontal dashed lines show the zero flux limit, and the vertical dotted lines show the beginning of each month that DES was observing. Such plots were used in order to select the best cases for SLSNe (eg. DES14X1avd, DES14E1lgl).

Table 5.7: List of hostless SLSNe candidates from Y2 that did not get a spectroscopic observation of the transient. Highlighted in bold, are the names of the transients that show significant evidence (light-curve, bad PSNID fits etc.) of their SLSNe nature. The columns under the PSNID caption show the results of fitting 'normal SNe' models to the photometry of the transients. The last column shows comments after the final classification of the 54 transients.

#	Name	# epochs	# obs.	PSNID results							Comments
				best type	Ia fit prob.	Ib/c fit prob.	II fit prob.	Ia fit z_{photo}	Ib/c fit z_{photo}	II fit z_{photo}	
1	DES14X2vk	5	9	Ia	0.977	0.801	0.888	0.676	0.633	0.721	SN-Ia?
2	DES14X3aab	4	6	Ia	0.876	0.500	0.798	0.901	0.401	1.257	SN-Ia?
3	**DES14C3nn**	24	39	Ib/c	0.352	0.643	0.144	0.360	0.108	0.796	SLSNe; visible host
4	DES14C3aaw	5	9	Ia	0.997	0.572	0.945	0.881	0.849	1.257	SN-Ia
5	DES14C2apm	4	8	Ia	0.816	0.229	0.659	0.958	0.414	1.177	SN-Ia?
6	DES14C2bfh	9	21	none	0.302	0.393	0.000	0.507	0.428	0.538	SN-Ia/Ibc; missed host
7	**DES14X1avd**	15	33	II	0.001	0.000	0.525	0.779	0.112	0.166	SLSNe; visible host
8	DES14S1awy	6	14	Ia	0.260	0.089	0.093	0.345	0.128	0.388	SN-Ia
9	DES14X1egp	6	13	Ia	0.978	0.148	0.676	0.736	0.593	0.937	SN-Ia
10	DES14E1hek	7	17	Ia	0.847	0.171	0.094	0.659	0.487	0.676	SN-Ia; missed host
11	DES14E1hey	4	9	Ia	0.966	0.660	0.875	0.568	0.155	0.796	SN-Ia
12	DES14S1ktk	4	9	none	0.551	0.145	0.634	0.898	0.177	0.968	noisy light-curve
13	DES14E2lbh	4	10	Ia	0.998	0.843	0.417	0.665	0.654	0.745	SN-Ia
14	DES14X3mgr	6	12	Ia	0.864	0.101	0.038	1.101	0.428	1.216	SN-Ia
15	**DES14E1lgl**	13	26	II	0.000	0.000	0.749	0.329	0.092	0.128	SLSN
16	DES14S1mlv	4	9	Ia	0.942	0.514	0.414	0.662	0.520	0.770	SN-Ia
17	DES14X3mot	4	7	Ia	0.968	0.973	0.578	1.634	1.103	1.342	SN-Ia?
18	DES14C3mpo	4	7	Ia	0.905	0.044	0.261	1.518	1.342	1.742	SN-Ia?
19	DES14C3oaz	6	12	Ia	0.642	0.038	0.197	0.873	0.401	1.342	SN-Ia
20	DES14X1qhf	4	11	Ia	0.987	0.821	0.888	0.509	0.520	0.796	SN-Ia
21	DES14S2qrg	4	6	none	0.144	0.144	0.363	1.025	0.238	1.139	noisy light-curve
22	DES14X3qhy	13	21	Ia	0.250	0.000	0.005	0.714	0.428	0.822	SN-Ia
23	DES14X3qzw	17	29	Ia	0.112	0.000	0.000	0.721	0.078	0.770	SN-Ia; unidentified host
24	DES14S2rpx	7	22	Ia	0.676	0.248	0.041	0.500	0.132	0.555	SN-Ia
25	DES14X1rbk	7	16	Ia	0.958	0.325	0.845	0.669	0.633	0.721	SN-Ia
26	DES14E1ufo	5	19	Ia	0.731	0.000	0.000	0.334	0.055	0.069	SN-Ia; high SNR ligth-curve
27	DES14C3ufw	11	16	Ia	0.551	0.041	0.497	0.834	0.183	1.103	SN-Ia
28	DES14X1vpq	4	11	Ib/c	0.000	0.101	0.000	0.334	0.388	0.166	AGN?

Group C

The last group, which lacks any spectroscopic information, consists of 28 hostless SLSNe candidates listed in Table 5.7. The absence of an associated galaxy, hence the lack of both z_{photo} and z_{spec}, makes these SLSNe candidates even more difficult to be classified. Fig. 5.16 shows 4 examples of transients from group C: DES14X1avd and DES14E1lgl were selected as SLSNe (due to their long rise time and colour evolution), whereas DES14C2bfh and DES14X3mgr show more similarities to 'normal SNe' types. Guided only by the shape of their light curves and the poor fit results of PSNID fitter, I was able to identify 3 possible SLSNe within this group.

The future plan for such candidates is to select those that show clear evidence of SNe activity and tag them within the OzDES program as 'SN faint host'. This translates into targeting the location of the SNe, under the condition that it is observed just once, with the expectation that the faint host galaxy redshift could be secured from galaxy emission lines after the SNe had faded away. This method was applied by OzDES in Y2, targeting hostless SNe that were discovered in Y1 and resulted in securing a portion of the redshifts in question.

Table 5.8: The final selection list of 22 SLSNe from DES Y2. The table is divided by horizontal lines in three parts: SLSNe that were spectroscopically confirmed, those that were classified by the use of their host z_{spec} and the events whose host z_{photo} was used for the classification.

#	Name	M_g	M_r	M_i	M_z	SNe	host z_{photo}	host z_{spect}	host separ.(")	m_g	m_r	m_i	m_z	Comments
1	DES14S2qri	-21.50	-22.51	-22.84	-22.92	1.500			4.97	24.28	25.41	23.72	24.47	SLSN-I
2	DES14X2byo	-22.19	-23.64	-22.34	-22.98	0.869			8.77	23.18	22.52	22.27	22.37	SLSN-I
3	DES14E2slp	-21.22	-21.27	-21.32	-21.29	0.640	0.550 ± 0.031		3.93	23.50	22.57	22.20	22.06	SLSN-I
4	DES14E2ap	-20.17	-20.49	-20.42	-20.43	0.600			4.26	24.80	23.23	22.85	22.52	SLSN-I
5	DES14X3taz	-21.15	-21.52	-21.41	-21.36	0.600	0.747 ± 0.079		0.15	26.25	25.13	24.99	25.04	SLSN-I
6	DES14C1rhg	-19.74	-19.80	-19.59	-19.79	0.470			2.97	99.00	26.98	25.87	24.41	SLSN-I
7	DES14C1fi	-22.52	-22.58	-22.75	-22.74		1.191 ± 0.085	1.3 (VLT)	0.64	24.93	24.64	24.59	23.61	SLSN-II
8	DES14X1rbi	-19.92	-20.69	-20.70	-20.71		0.689 ± 0.033	0.717 (VIPERS)	2.14	23.20	21.70	20.78	20.36	SLSN
9	DES14S1ewv	-22.12	-21.98	-22.01	-22.43		1.230 ± 0.085		0.66	22.69	22.53	22.33	21.88	
10	DES14E1rpi	-20.92	-20.97	-21.32	-22.10		1.048 ± 0.066		1.81	24.85	23.77	23.31	22.50	
11	DES14C3nn	-20.89	-21.01	-21.54	-21.29		1.026 ± 0.081		2.30	24.70	24.45	24.02	23.65	
12	DES14E2bhn	-20.41	-21.09	-22.07	-21.23		0.973 ± 0.072	pending (OzDES)	2.44	23.24	22.95	22.51	22.26	
13	DES14X3gyr	-19.88	-19.81	-20.41	-21.29		0.948 ± 0.049	pending (OzDES)	0.87	23.97	23.10	22.08	21.61	
14	DES14X1avd	-20.87	-20.46	-20.97	-21.86		0.835 ± 0.031		10.22	23.39	22.74	22.10	21.86	
15	DES14X3mjf	-20.55	-20.03	-20.50	-20.44		0.829 ± 0.066	pending (OzDES)	0.38	24.05	23.61	23.19	23.06	
16	DES14C1ngk	-19.44	-20.95	-20.46	-20.84		0.813 ± 0.033	pending (OzDES)	1.03	22.83	21.84	20.89	20.53	
17	DES14C3tny	-26.89	-20.41	-20.23	-20.90		0.788 ± 0.082		0.45	25.72	25.13	24.70	24.43	
18	DES14C1fs	-21.97	-20.59	-20.94	-21.18		0.744 ± 0.050		0.82	24.70	24.00	23.32	23.29	
19	DES14E1lgl	-19.38	-20.10	-20.03	-19.91		0.673 ± 0.033		6.60	23.35	22.44	21.94	21.70	
20	DES14X1brr	-20.42	-20.63	-20.51	-20.46		0.651 ± 0.060	pending (OzDES)	0.97	24.96	24.03	23.73	23.52	
21	DES14X1ps	-20.88	-21.31	-21.29	-21.51		0.610 ± 0.085	pending (OzDES)	0.48	24.63	24.52	24.53	24.93	
22	DES14E1hk	-20.31	-20.91	-20.83	-20.73		0.531 ± 0.045	pending (OzDES)	0.94	23.76	22.48	21.98	21.56	

5.6 Results

At the end of DES Y2, a total number of 22 SLSNe were selected after all the steps described above, out of a sample of 133 SLSNe candidates that passed the first visual inspection, described in Sec. 5.4.2. Those 22 SLSNe are listed in Table 5.8 and should be considered as the final sample of SLSNe discovered by DES in Y2, for the remaining of this thesis.

This section provides a detailed summary of each of the 7 spectroscopic confirmed SLSNe, accompanied with light-curves and spectral plots. Appendix B contains several figures, illustrating finder-charts and postage-stamps of these 7 SLSNe.

5.6.1 DES14C1fi

DES14C1fi is located at R.A.= $03^h33^m49^s.80$, Dec.= $-27^o03'31''.6$ and was discovered shortly after the beginning of Y2 observing season, on the 21th of August 2014 at $m_r = 23.1$, among the very first DES transients in Y2. The DES photometric light-curve of DES14C1fi is shown in Fig. 5.17, whereas the finder chart in Fig. B.1, created by the ATC application (Fig. 5.12) shows the sky around the target, accompanied with useful information for further follow-up observations.

The photometric redshift of host galaxy ($z_{photo} = 1.19$) and the pre-peak light-curve behaviour led to the selection of DES14C1fi as a SLSN candidate a month after discovery. By the 22nd of September 2014, it was automatically selected as a spectroscopic target for the OzDES program, as its brightness reached a magnitude of $m_r = 22.3$. The first
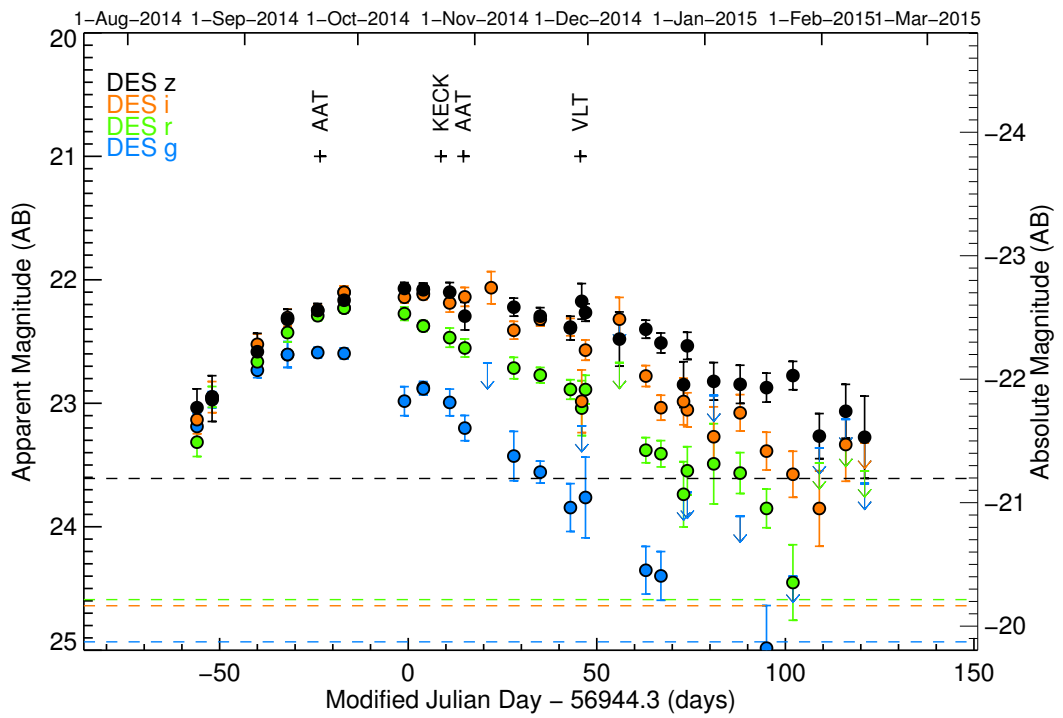
Figure 5.17: The observed AB magnitude light curve of **DES14C1fi** in the four DES SN search filters ($griz$) as a function of the observed phase. The crosses denote the epochs of spectral observations as follows: OzDES, Keck, OzDES and VLT. The errorbars represent 1-σ uncertainties, and the arrow symbols are 3-σ upper limits. The horizontal dashed lines show the host galaxy apparent magnitudes in the four DES filters ($griz$.)
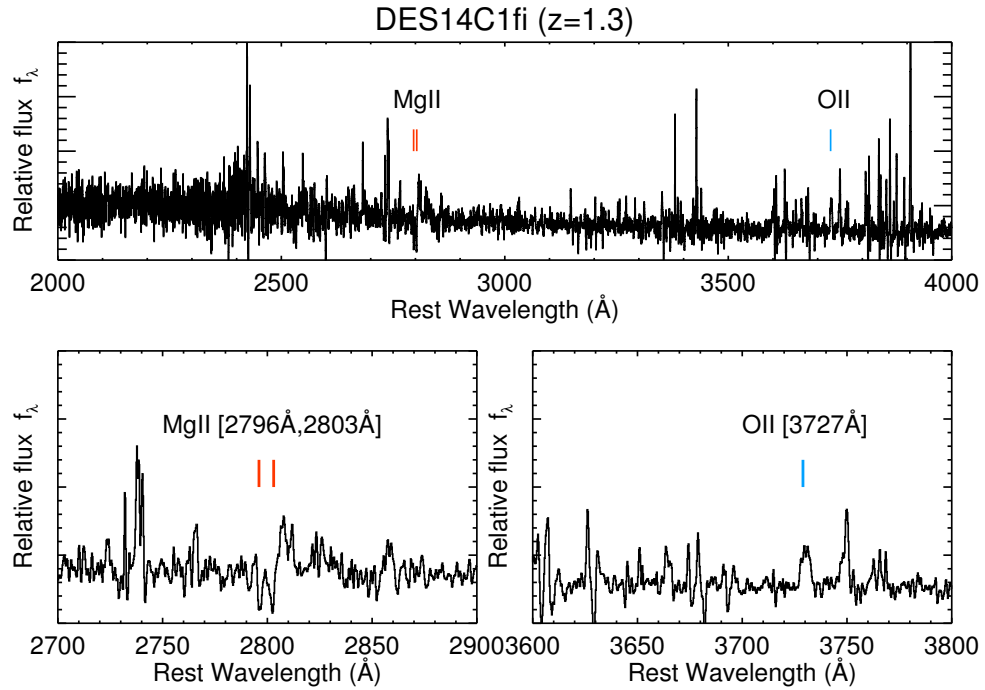
Figure 5.18: *Top panel:* The rest-frame spectrum of **DES14C1fi** obtained on the 23rd of October 2014 (+9 days past peak) by the LRIS spectrograph on the Keck telescope. Using the host galaxy emission lines of O II[$\lambda 3727\,\text{Å}$] and the doublet absorption features of Mg II[$\lambda 2796, 2803\,\text{Å}$], we were able to secure the redshift of the host galaxy at $z = 1.3$. *Bottom panels:* Zoom-in plots to the wavelength range, so the two sets of spectral features used to derive the host galaxy redshift, can been seen clearly.
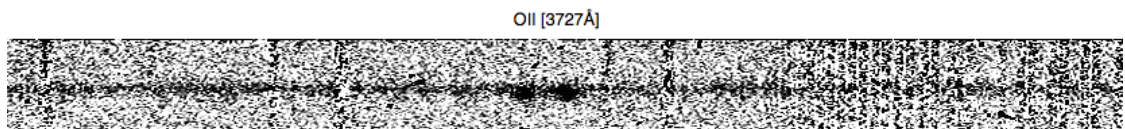
Figure 5.19: The reduced VLT/FORS2 two-dimensional spectrum of **DES14C1fi** taken on the 29th of November 2014, almost +50 days past peak. The nebular emission lines of O II[$\lambda 3727\,\text{Å}$], used to derive the host galaxy redshift, are labeled.

attempt on spectral classification, using the spectrum provided by OzDES proved to be inconclusive, as the spectrum showed no clear SNe features of any type.

As we continued to follow the light-curve evolution of DES14C1fi, we noticed that by mid-October – almost a month after the first spectral observation – the bluer bands started to decline faster than the redder bands, which seemed to have flattened out, indicating that the transient had reached peak brightness. At that point we triggered on the Keck telescope's ToO time available for the Y2, and requested a spectrum to be taken with the LRIS spectrograph. Keck observed DES14C1fi on the 24th of October 2014, when the phase of the SNe was around +9 days past peak and had faded to $m_r = 22.5$. The spectrum, despite the high SNR provided by the unmatched combination of LRIS and Keck, was still featureless with no signs of SNe activity.

After ruling out the possibility of an error in the finding chart, I proposed an alternative explanation which was that DES14C1fi was a hydrogen rich SLSN (type II) at a redshift greater than the host galaxy photometric redshift $z > z_{photo} = 1.19$. Thus the Hβ [$\lambda 4861$ Å] and Hα [$\lambda 6563$ Å] features of a SLSN-II at redshift of $z = 1.19$ (10645 Å and 14372 Å respectively) would fall out of the observing window of the visible spectrum of LRIS ($3400 - 10275$ Å). This hypothesis became stronger when, a few days afterwards when the team that constructed the Keck observations (lead by Prof. Peter Nugent and Dr. Melissa Graham) re-reduced the obtained spectrum and discovered clear evidence of the host galaxy redshift. As seen in Fig. 5.18, the strong nebular emission line of O II[$\lambda 3727$ Å] and the doublet absorption features of Mg II[$\lambda 2796, 2803$ Å] were used to derive the host galaxy redshift of $z_{spec} = 1.3$.

At such redshift, DES14C1fi peaked at $M_r = -22.57$ and can be placed among the most luminous SNe to date (Table 2.1). Furthermore, another spectrum was later obtained with the OzDES program with similar results as the first attempt. On the 29th of November 2014 one more spectrum was obtained using the VLT and the X-Shooter spectrograph, a 2-dimensional version which is shown in Fig. 5.19. This spectrum contains data from all three arms of X-Shooter (UV-visible-NIR), but apart from the confirmation of the host galaxy's redshift, no obvious hydrogen emission is recognizable.

Finally, the observed light-curve of DES14C1fi lasted longer than the entire DES Y2 observing season, as the SNe pipeline was able to detect the transient in the redder bands even on the last observing night of DES in mid-February 2015. This impressive long-lived light-curve can be seen also in flux space in panels (a) and (b) of Fig. 5.8.

5.6.2 DES14X2byo

DES14X2byo is located at R.A.= $02^h23^m46^s.93$, Dec.= $-06^o08'12''.3$ (Fig. B.2) and was discovered on the 24th of September 2014 at $m_r = 23.4$ as a hostless SNe candidate.
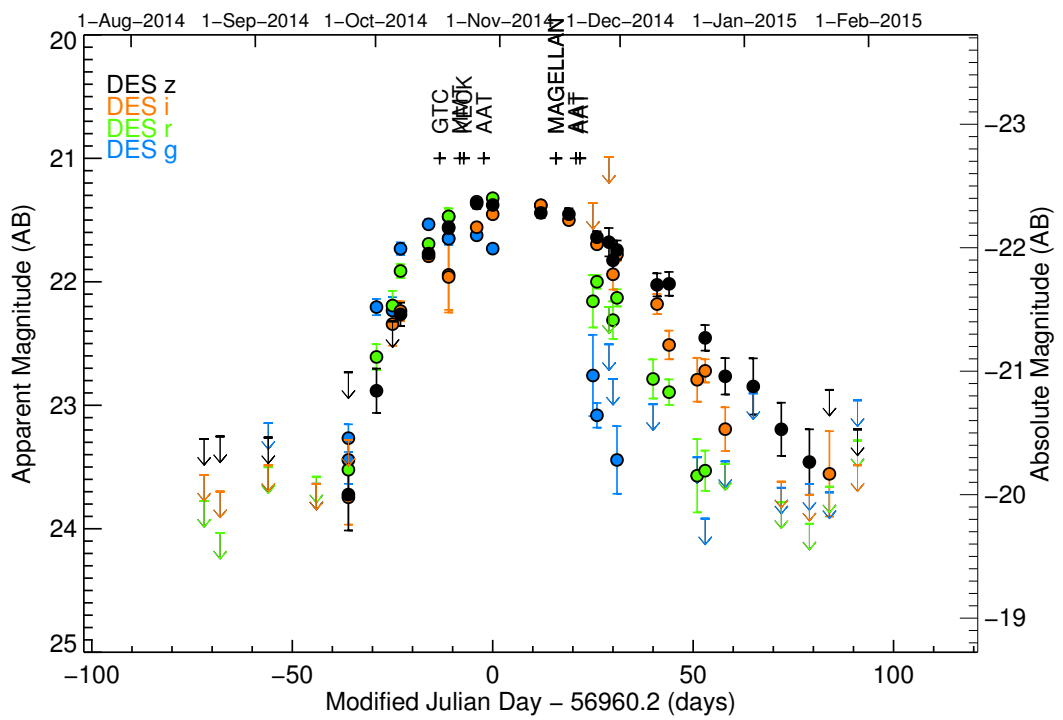
Figure 5.20: The observed AB magnitude light curve of **DES14X2byo** in the four DES SN search filters ($griz$) as a function of the observed phase. The crosses denote the epochs of spectral observations as following: GTC, MMT, Keck, OzDES, Magellan and 2 more times with OzDES. The errorbars represent 1-σ uncertainties, and the arrow symbols are 3-σ upper limits.

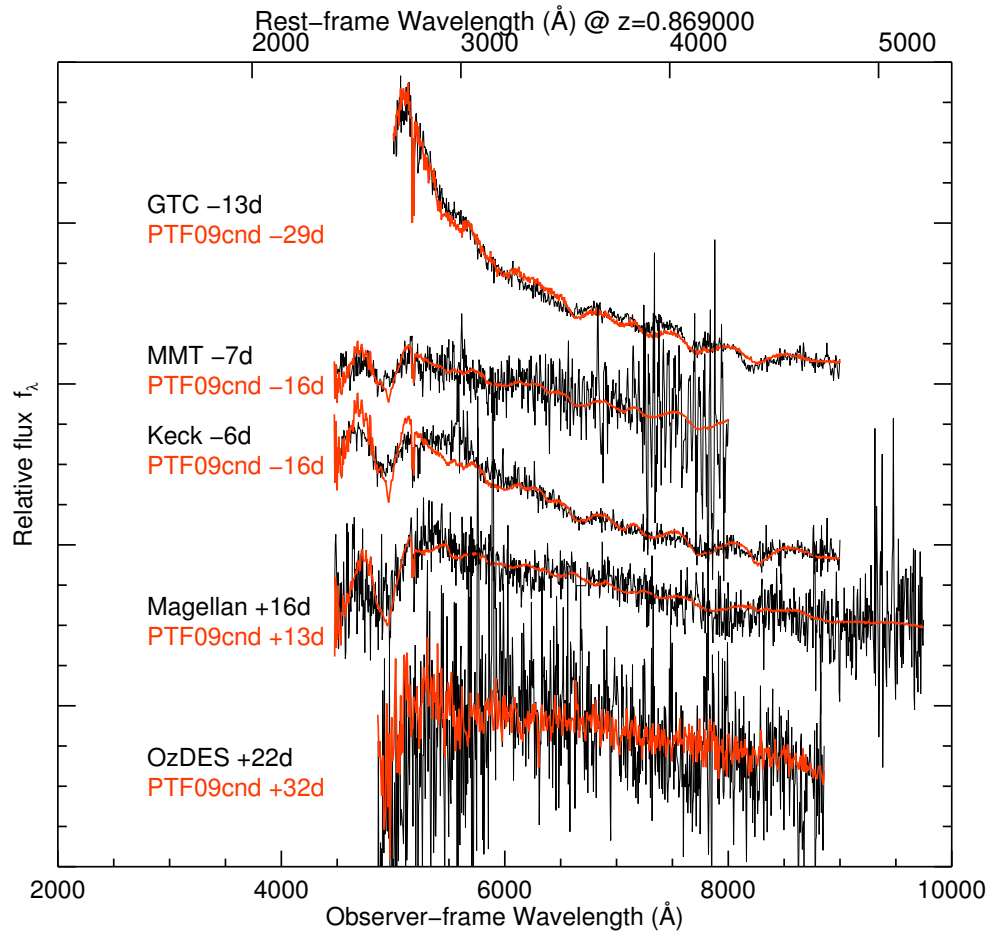Figure 5.21: The spectra of **DES14X2byo** as obtained in different epochs of the SNe, from the different spectrographs/telescopes, are plotted in black. Over-plotted in orange are the SUPERFIT best-fits of several spectral templates to DES14X2byo. Two of the OzDES spectra, one obtained at -3 days before peak and one +21 days past peak, are not plotted due to poor quality of the data. The spectra are labeled with the respective telescope, the phase relative to peak and the name and phase of the SUPERFIT spectral templates.

By mid-October it was identified as a SLSN candidate based on the long rise time of the light-curve, which is shown in Fig. 5.20. On the 17th of October it was placed in the queue of the GTC for spectroscopic follow-up as a hostless, bright ($M_r = 21.77$) transient and a first spectrum was obtained with the OSIRIS spectrograph, resulting in a SLSN-I classification at a redshift of $z \sim 0.85$.

At that stage, DES14X2byo was selected for observations using the Blue Channel Spectrograph on the MMT and the LRIS spectrograph on Keck telescope on the 22nd and 23rd of October, respectively. The high-SNR spectrum obtained by the Keck telescope, secured the classification of a SLSN-I near maximum, at a redshift of $z = 0.869$, consistent with narrow Mg II 2800 Å absorption clearly detected at $z = 0.869$. An astronomer's telegrams (ATel #6635; Graham et al., 2014) was released shortly afterwards, announcing both the discovery and the spectral classification.

Furthermore, a spectrum (+13 days past peak) was obtained using the IMACS spectrograph on the Magellan telescope on the 15th of November 2014; and also DES14X2byo was automatically placed into the targeting list of the OzDES program due to its brightness ($m_r = 21.47$). Hence three spectra were obtained during the Y2. Fig. 5.21 shows the available spectra obtained by the different telescopes for DES14X2byo.

The light-curve continued to rise until early November, when it reached a peak magnitude of $M_r = -22.34$ and then started to decline slowly until the beginning of February, when it was last detected close to the zero flux limit in z band and the X2 field was close to visibility limits from the CTIO. Like most SLSNe, DES14X2byo light-curve dropped first and more rapidly in g band with the redder bands following later, with a slower decline rate, as seen in Fig. 5.20. No host galaxy is visible up to this stage in DES deep template imaging, which is complete down to $m_r = 24.0$.

5.6.3 DES14S2qri

DES14S2qri is located at R.A.= $02^h43^m32^s.14$, Dec.= $-01^o07'34''.2$ and was discovered on the 26th of November 2014 at $m_i = 23.7$ as a hostless SN candidate, as seen in Fig. B.3. By late December it was identified as a SLSN candidate based on the long rise time of the light-curve, mostly seen in z band, shown in panel (a) of Fig. 5.22. At first DES14S2qri was not a convincing SLSN candidate due to its odd light-curve behaviour. Usually, SLSNe show no colour evolution in pre-peak epochs, and soon after peak the bluer bands drop faster than the redder bands, creating a visually recognizable colour evolution of the post-peak light-curve (similar to what was seen in DES14X2byo light-curve in Fig. 5.20). The light-curve of DES14S2qri showed a different behaviour, as it reached peak first in the redder bands (i and z) and then in bluer bands (g and r).
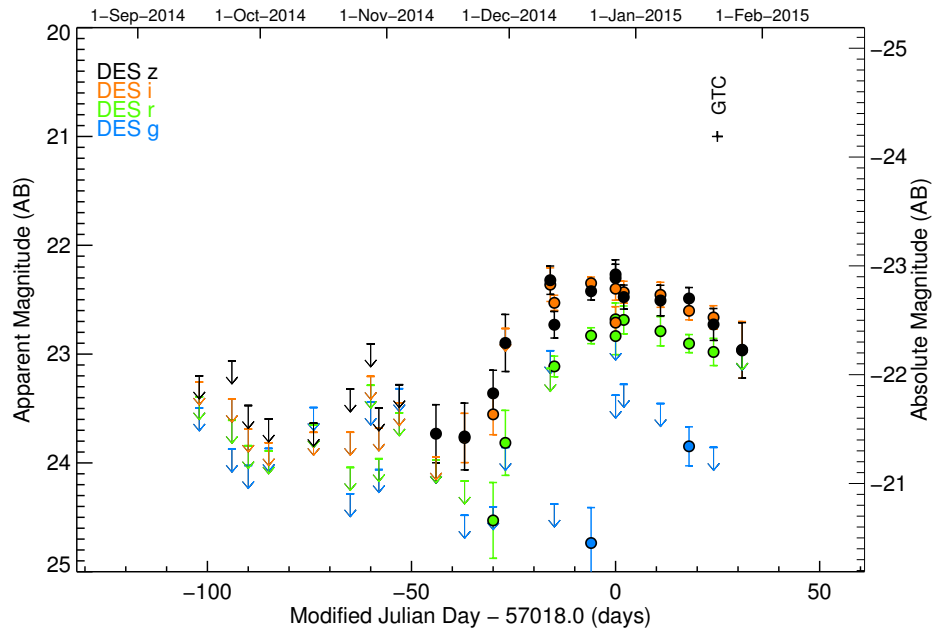
(a) DES14S2qri light-curve
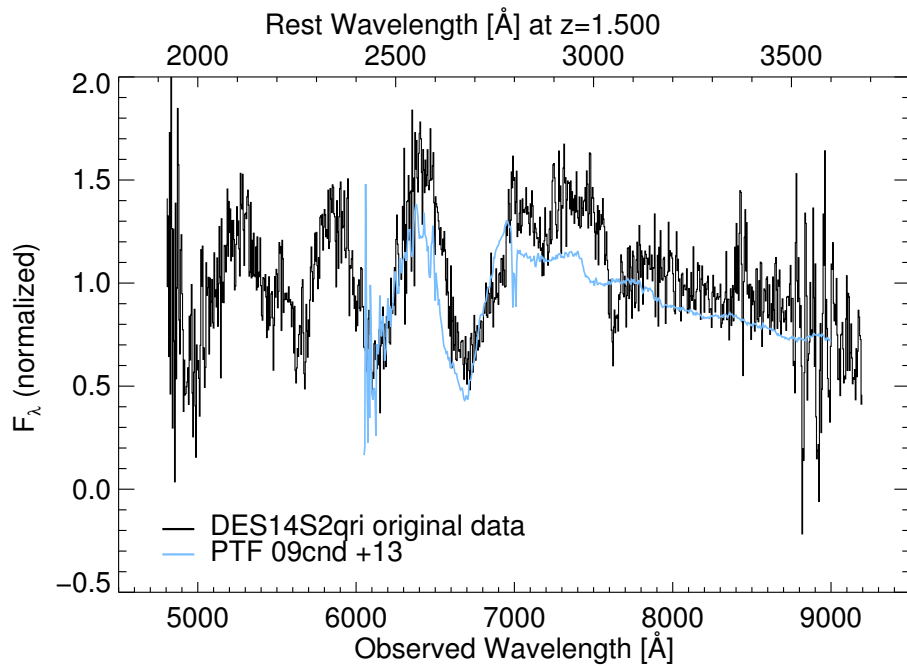
(b) DES14S2qri spectra

Figure 5.22: *Panel a:* The observed AB magnitude light curve of **DES14S2qri** in the four DES SN search filters ($griz$) as a function of the observed phase. The cross denotes the epoch of spectroscopic observations with GTC. The errorbars represent 1-σ uncertainties, and the arrow symbols are 3-σ upper limits. *Panel b:* The observed spectrum (black) of DES14S2qri as obtained by the GTC with the OSIRIS spectrograph on the 21st of January 2015, +25 days past peak brightness. Also, plotted in blue, is the SUPERFIT best-fit spectral template, which was used to classify DES14S2qri as a SLSN-I at a redshift of $z = 1.5$.

At the beginning of January 2015, after coordinating with the SN survey's spectroscopic marshal, DES14S2qri was placed on both VLT and GTC telescopes' target lists, as an interesting hostless transient. On the 15th of January, using the OSIRIS spectrograph on the GTC, we obtained a spectrum that was initially misclassified as a SNe Ia at a redshift of $z \sim 0.8$. The fact that the first spectral data reduction was poor and at such redshift the transient would be in the superluminous regime ($M > -21$), indicated that something was wrong with the first classification attempt.

In March 2015, Dr. Mat Smith had re-reduced the data and obtained a secure classification of DES14S2qri as a SLSN-I at a redshift of $z = 1.5$, which was announced by ATel # 7199 (Castander et al., 2015). At such redshift, DES14S2qri peaked at $M_z = -22.9$, placing itself as the most luminous SLSNe to date (Table 2.1).

5.6.4 DES14X3taz

DES14X3taz is located at R.A.= $02^h28^m04^s.46$, Dec.= $-04^o05'12''.7$ and was discovered on the 21st of December 2014 at $m_r = 23.3$ as SN candidate $0.15''$ away from its host galaxy, as seen in Fig. B.4. DES14X3taz was not initially selected as a SLSN candidate because it violated one of the SLSNe criteria (Sec. 5.4.1), namely within 1 pixel of the host centre. It was instead selected as an interest normal SN Ia candidate. By mid-Januray 2015, the light-curve of DES14X3taz showed unusual behaviour presented in panel (a) of Fig. 5.23. After initially rising for a few days, the light-curve peaked and then it started rising again, leading to a second peak which is very unusual in SNe light curves. This rare behaviour has been seen before as a pre-explosion outburst in SNe IIn (Ofek et al., 2013; Margutti et al., 2014; Smith et al., 2014), as well as in a SLSN presented by Leloudas et al. (2012), see SN 2006oz in chapter 2.

DES14X3taz was selected for spectroscopic follow-up observation with the GTC as an interesting and rare SNe with obvious signs of a pre-explosion outburst, and on the 21st of January 2015 a spectrum was obtained and DES14X3taz was classified as SLSN-I at a redshift of $z = 0.6$. Panel (b) of Fig. 5.23 shows the spectral comparison carried out with SUPERFIT, revealing the SLSN nature and redshift of DES14X3taz.

5.6.5 DES14C1rhg

DES14C1rhg is located at R.A.= $03^h38^m07^s.27$, Dec.= $-27^o42'45''.7$ and was discovered on the 1st of December 2014 at $m_r = 23.8$ as a hostless SN candidate (Fig. B.5). After 20 days of rising, it reached its peak brightness of $m_r = 22.3$, as seen in panel (a) of Fig. 5.24. At first, DES14C1rhg was placed on the OzDES target list as a hostless SNe
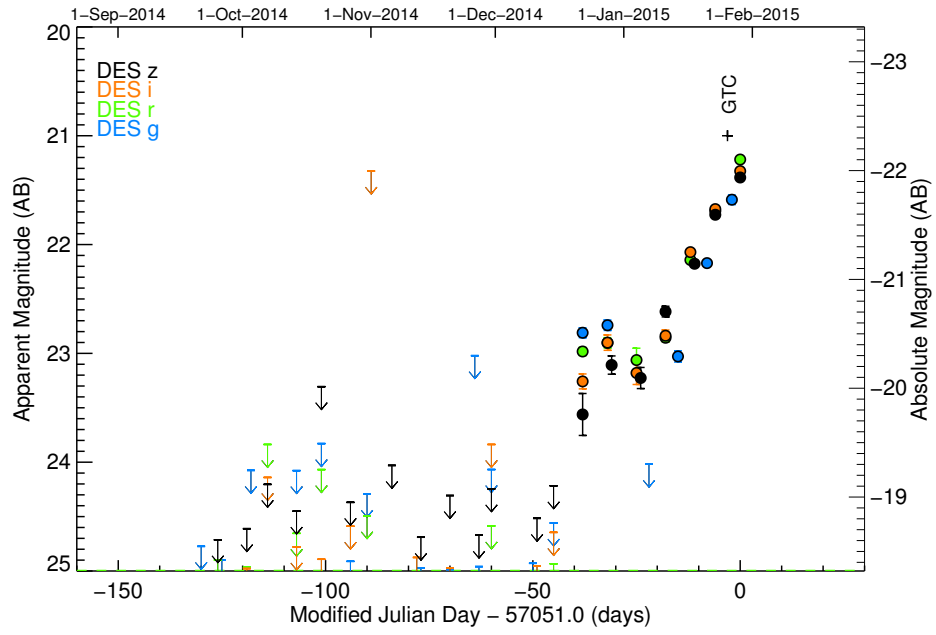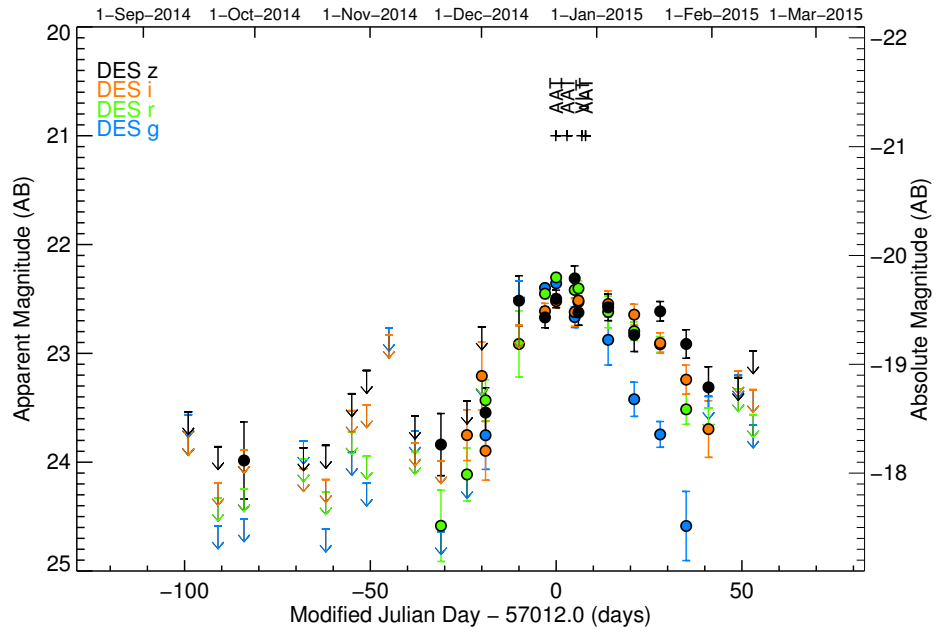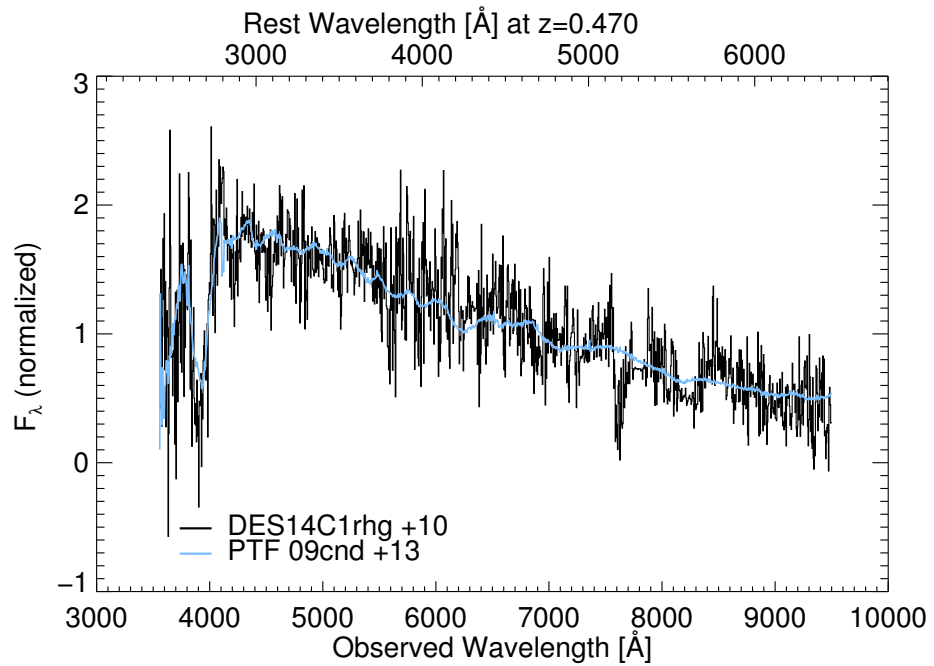
(a) DES14X3taz light-curve
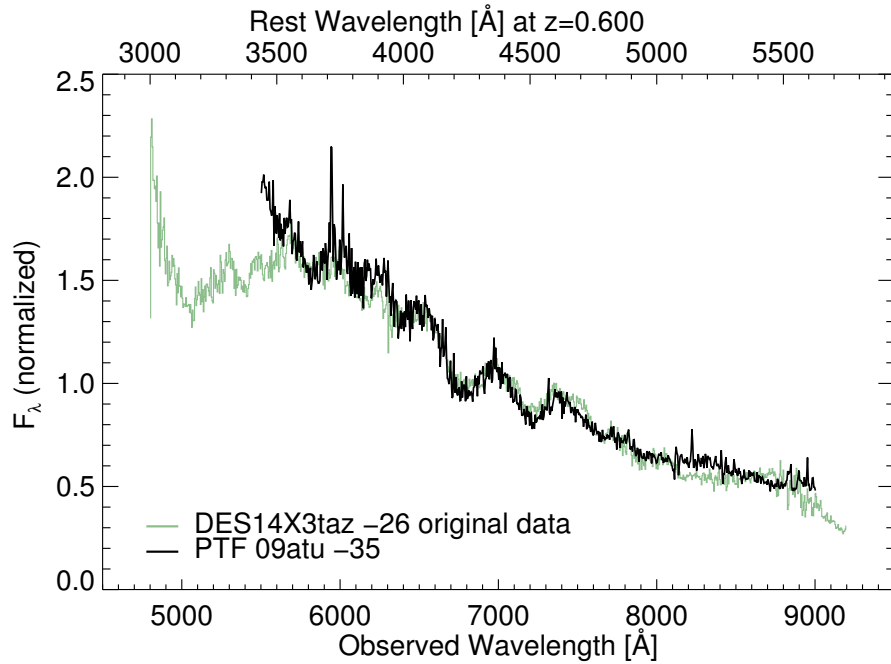
(b) DES14X3taz spectra

Figure 5.23: *Panel a:* The observed AB magnitude light curve of **DES14X3taz** in the four DES SN search filters ($griz$) as a function of the observed phase. The cross denotes the epoch of spectroscopic observations with GTC. The errorbars represent 1-σ uncertainties, and the arrow symbols are 3-σ upper limits. *Panel b:* The observed spectrum (black) of DES14X3taz as obtained by the GTC with the OSIRIS spectrograph on the 21st of January 2015. Also, plotted in blue, is the SUPERFIT best-fit spectral template, which was used to classify DES14X3taz as a SLSN-I at a redshift of $z = 0.6$.

(a) DES14C1rhg light-curve

(b) DES14C1rhg spectra

Figure 5.24: *Panel a:* The observed AB magnitude light curve of **DES14C1rhg** in the four DES SN search filters ($griz$) as a function of the observed phase. The crosses denote the epoch of spectroscopic observations. The errorbars represent 1-σ uncertainties, and the arrow symbols are 3-σ upper limits. *Panel b:* The observed spectrum (black) of DES14C1rhg as obtained by the VLT with the X-Shooter spectrograph on the 28th of December 2015. Plotted in blue is the SUPERFIT best-fit spectral template, which was used to classify DES14C1rhg as a SLSN-I at a redshift of $z = 0.47$.

Ia candidate. Two spectra were taken on the 21st and 24th of December with the AAT and 2dF spectrograph, resulting in a featureless spectrum.

Soon after, DES14C1rhg was identified as a SLSN candidate due to its ~ 30 days of rise time, and was selected for spectroscopic follow-up observations for the VLT/X-Shooter program. A spectrum was obtained on the 28th of December 2014, shown in panel (b) of Fig. 5.24, which led to the secure classification of DES14C1rhg as a SLSN-I at a redshift of $z = 0.47$.

The post-peak behaviour of the light-curve, in which the bluer bands start to decline quicker and more rapidly than the redder bands, was another confirmation of the superluminous nature of the transient. At this point one must highlight the fact that DES14C1rhg peaked at an absolute magnitude of $M_r = -19.80$, which is the lowest value to be reported to date for a spectroscopically confirmed SLSN of any type (see Table 2.1). Such 'underlunimous-SLSNe' could support the argument that the SLSNe absolute magnitude limit of $M < -21$, set by Gal-Yam (2012) (see Sec. 1.5 of this thesis), was arbitrarily chosen in the lack of SLSNe at lower peak magnitudes.

An explanation for this, could be the limited sensitivity of the other surveys that have discovered SLSNe up to this date. Although, PTF10hgi, PTF11rks (Inserra et al., 2013) and SN 2006tf (Smith et al., 2008a) were characterized as 'underlunimous-SLSNe', as they peaked at $M = -20.24, -20.76$ and -20.70 respectively (slightly lower than the SLSNe limit of $M < -21$), any further discoveries of such 'underluminous-SLSNe' could indeed reveal the existence of a continuum that will fill the gap between the peak brightness of SNe Ic and SLSNe.

As noted in Sec. 5.4.1, a selection cut at the absolute peak magnitude was applied during the selection process of SLSNe, with a value of $M_{peak} \leqslant -20.0$. Thus DES14C1rhg was initially selected as a hostless SNe Ia and did not pass the SLSNe selection process described in Sec. 5.4.1. By relaxing the value of the absolute peak magnitude cut to $M_{peak} \leqslant -19.5$ the number of transients selected for the first visual inspection process increased by a factor of ~ 2 and by a factor of ~ 3 when the limit was set to $M_{peak} \leqslant -19.0$.

5.6.6 DES14E2slp

DES14E2slp is located at R.A$= 00^h33^m04^s.08$, Dec.$= -44^o11'42''.8$ and was first detected on the 19th of December 2014 at $m_r = 23.4$ as a hostless candidate, despite the existence of two nearby galaxies at $3.5''$ and $3.9''$ away, as seen in Fig. B.6. DES14E2slp brightness was rising in all four bands for almost 30 days, until it reached its maximum on the 19th of January 2015, whereas the last observed night of the light-curve took placed a week after, on the 26th of January, as seen in panel (a) of Fig. 5.25. The last two epochs
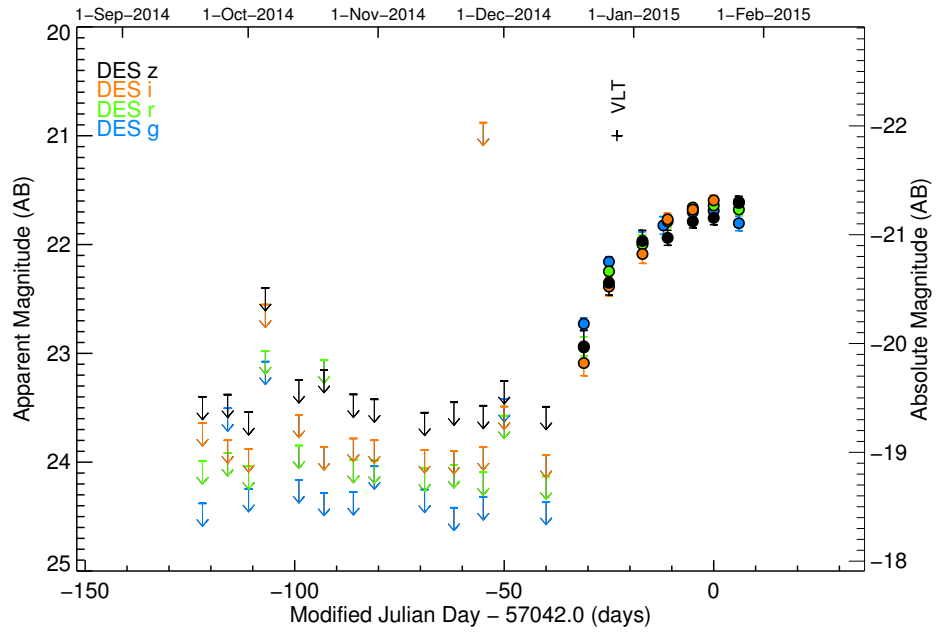
(a) DES14E2slp light-curve
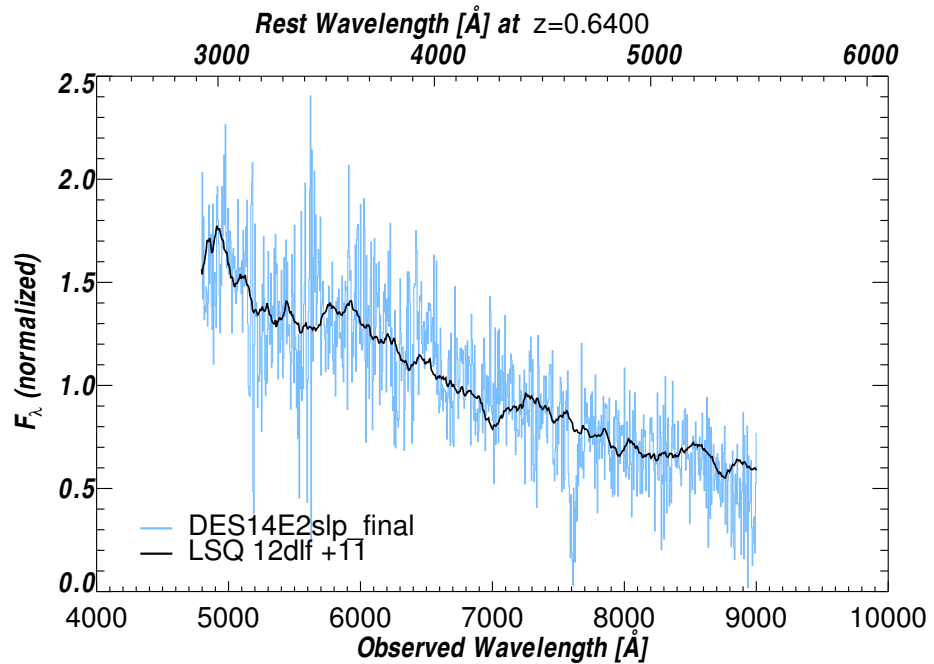
(b) DES14E2slp spectra

Figure 5.25: *Panel a:* The observed AB magnitude light curve of **DES14E2slp** in the four DES SN search filters ($griz$) as a function of the observed phase. The cross denotes the epoch of spectroscopic observations with VLT. The errorbars represent 1-σ uncertainties, and the arrow symbols are 3-σ upper limits. *Panel b:* The observed spectrum (blue) of DES14E2slp as obtained by the VLT with the Xshooter spectrograph, around 25 days before peak brightness. Plotted in black is the SUPERFIT best-fit spectral template, which was used to classify DES14E2slp as a SLSN-I at a redshift of $z = 0.64$.

of the light-curve provide some evidence of the SLSN nature of this transients, as the g band starts to decline faster than the redder bands.

At an early stage of its light-curve, DES14E2slp was placed as a target for VLT towards the end of December 2014, and a spectrum was obtained on the 28th, around 20 days before peak brightness. The first attempt of classification was unsuccessful, but subsequent re-analysis of the data by Dr. Mat Smith, indicates that the spectrum shows some similarities to a SLSN-I at redshift of $z = 0.64$, as seen in panel (b) of Fig. 5.25. For this thesis, DES14E2slp would be considered as a SLSN-I even though there is some disagreement with the comparison spectrum (LSQ12dlf; Nicholl et al., 2014) which was taken as a different phase in the light curve (+11 days past peak). It is worth stressing that spectra of the early pre-peak phase of SLSNe is quite rare and therefore this spectrum has value for comparisons with other future SLSNe.

5.6.7 DES14E2ap

DES14E2ap is located at R.A= $00^{h}38^{m}59^{s}.36$, Dec.= $-43^{o}35'45''.5$ as seen in Fig. B.7. It was discovered at the beginning of DES Y2, on the 21st of August 2014 at $m_r = 22.2$ as a hostless candidate and close to its maximum brightness, as seen in panel (a) of Fig. 5.26. Its light-curve evolution showed a slow decline, with the g band fading away quicker than the redder bands, similar to that expected from other SLSNe. We were able to detect this transient up to mid-November 2014, when it had faded below the detection limit.

Soon after detection, DES14E2ap was targeted with the VLT for spectroscopic observations and on the 30th of August 2014 a spectrum was obtained. The preliminary data reduction revealed a noisy and low SNR spectrum, without a good classification. The spectrum of DES14E2ap was later re-reduced and a moderate match with a SLSN-I at a redshift of $z = 0.6$ and at the phase of +37 days past peak, was found (using SUPERFIT; Howell et al., 2005). At such redshift, DES14E2ap peaked at an absolute magnitude of $M_r = -20.49$, which is slightly smaller than the SLSNe limit of $M \leqslant -21$ adopted by Gal-Yam (2012).
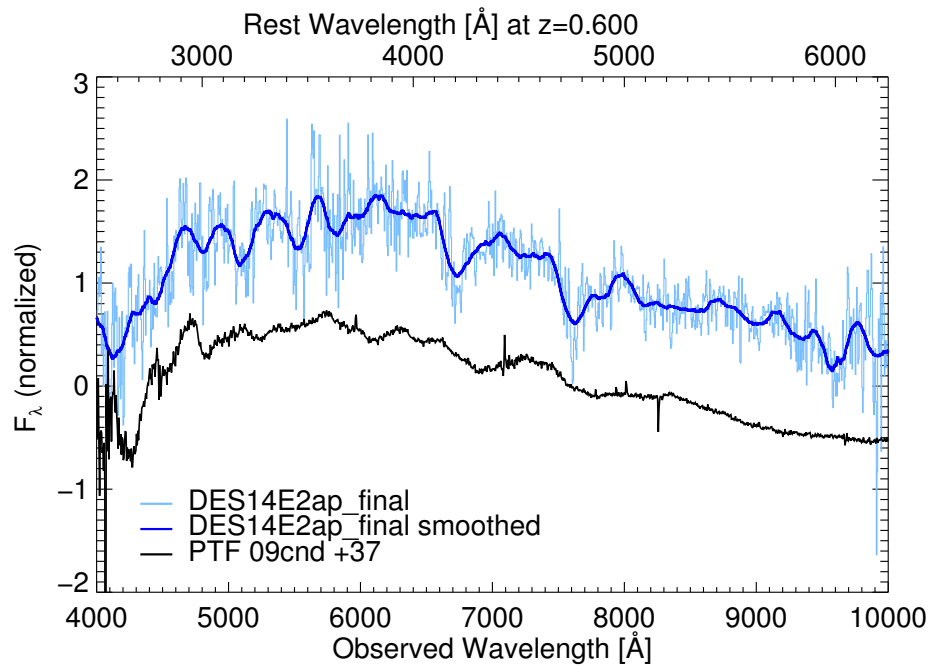
For the purpose of this thesis, I will consider DES14E2ap as a SLSN-I at a redshift of $z = 0.6$, based on its light curve behaviour and spectral classification.

5.7 Modeling

Using the 22 SLSNe (Table 5.8) discovered in DES Y2, we attempt to explore the properties of their nature, by constructing their bolometric light-curves and fitting different
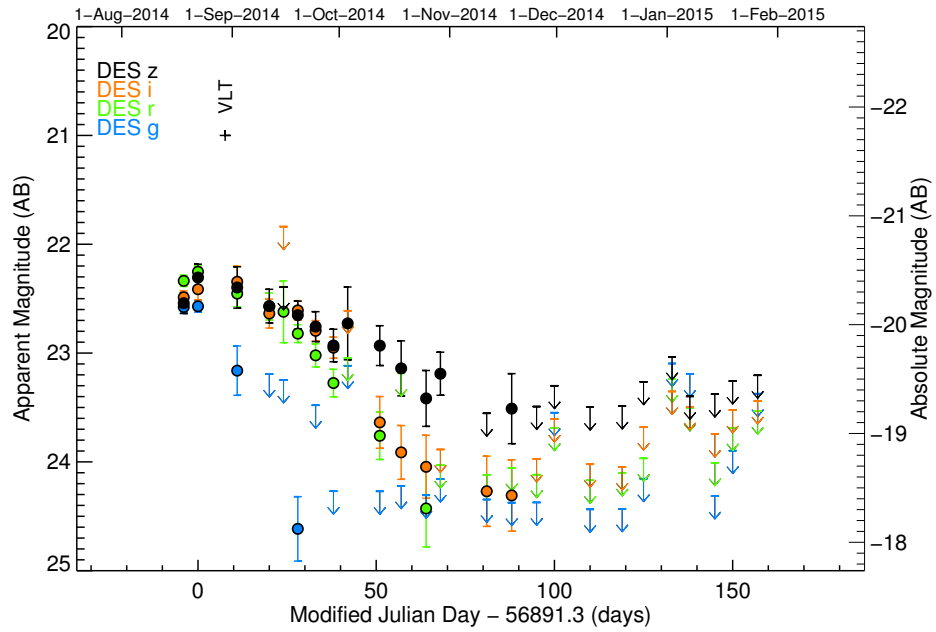
(a) DES14E2ap light-curve

(b) DES14E2ap spectra

Figure 5.26: *Panel a:* The observed AB magnitude light curve of **DES14E2ap** in the four DES SN search filters ($griz$) as a function of the observed phase. The cross denotes the epoch of spectroscopic observations with VLT. The errorbars represent 1-σ uncertainties, and the arrow symbols are 3-σ upper limits. *Panel b:* The observed spectrum (blue) of DES14E2ap as obtained by the VLT with the Xshooter spectrograph, around 5 days past peak brightness. Also, plotted in black is the SUPERFIT best-fit spectral template, which was used to classify DES14E2ap as a SLSN-I at a redshift of $z = 0.6$. The two telluric absorption features at 6700 and $7600\,\text{Å}$ were ignored by the fitting routine, as they are caused by the Earth's atmosphere.

power source models to them, as described in Sec. 1.5.3 and adopted in Chap. 4 for DES13S2cmm.

5.7.1 Bolometric Light-Curves

We follow the methodology outlined in Sec. 4.6 to construct bolometric light curves for all 22 SLSNe candidates. A single blackbody SED is fit to the DES multi-colour data, for each epoch of the light-curve that has minimum three distinct filter observations. Firstly, the blackbody SED is redshifted to the observer frame and integrated through the response functions of each DES filter. Then, the best-fitting parameters that synthesize the blackbody SED, namely the temperature and radius, are determined by the fit to the observed photometry.

Finally, the best-fit blackbody SED for each epoch is integrated in the rest frame, over the wavelength range of $5 - 50000 \, \mathring{A}$ to obtain the bolometric luminosity of the specific epoch. The errors on the bolometric luminosities were calculated from the fitting uncertainties of the blackbody parameters.

Fig. 5.27 shows the 26 blackbody SED fits to the observed DES photometry for the SLSNe named DES14C1fi. Whereas, Fig. 5.28 shows the bolometric light-curve of DES14C1fi, plotted as a function of the observed-frame phase from peak magnitude. Also in the same figure, the panels at the bottom show the time evolution of the two fit parameters (temperature and radius). Later data points on the light-curve have larger errorbars, as a result of low flux values in bluer bands at such epochs, which cause larger uncertainties on constraining the blackbody SED, as seen in the last five panels of Fig. 5.27.

For the rest of the SLSNe discovered in Y2 (Table 5.8), the respective figures of the blackbody fits and the derived bolometric light-curves are shown in Appendix C.

Fig. 5.29 shows the bomometric light-curves, temperature and radius evolution of 8 SLSNe from Y2 that have a spectroscopic confirmation, or a host galaxy z_{spec}, plus DES13S2cmm from Y1 (Chap. 4). The plot reveals the similarities and differences between those 9 spectroscopically confirmed SLSNe from DES; as the temperature and radius evolution seem to follow the same evolution pattern, close to the linear relations described by the cooling blackbody (see Sec. 1.5.3) introduced by Howell et al. (2013).

5.7.2 Power Source Models

Following the process used for DES13S2cmm in Chap. 4, we investigate two SLSNe power source models for the sample of 22 SLSNe discovered in Y2 (Table 5.8): the radioactive decay of ^{56}Ni, and the energy deposition from a Magnetar.
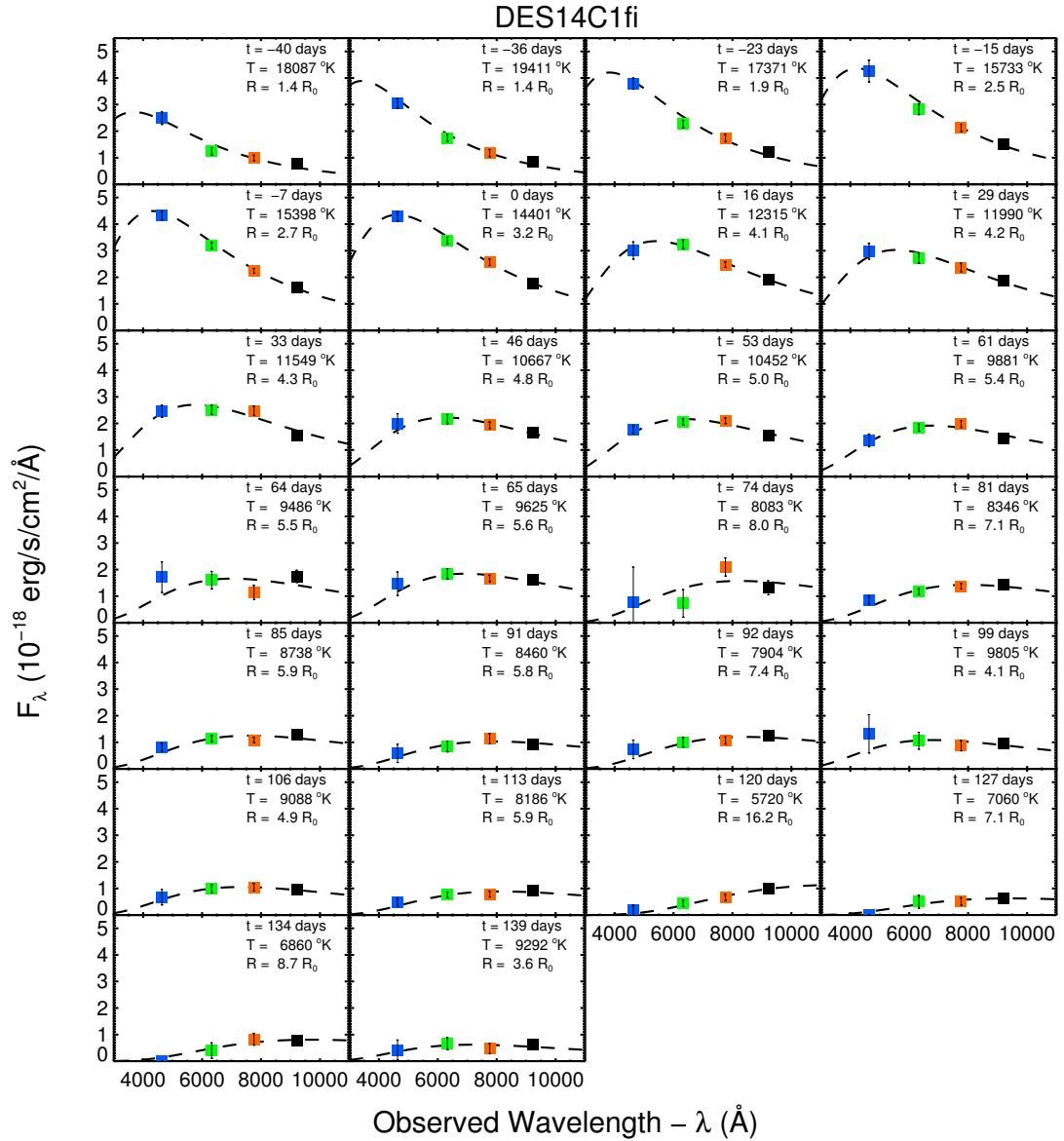
Figure 5.27: Blackbody fits (*dashed lines*) to the 26 observed epochs of the DES multi-band photometry (*coloured squares*) for **DES14C1fi**. The legend of each panel states the observed phase-t in days from peak magnitude, and the blackbody best-fit parameters: temperature-$T(^oK)$ and radius-$R(R_0 = 10^{15}$cm$)$. The respective figures of the blackbody fits of the rest of the SLSNe discovered in Y2 are shown in Appendix C.
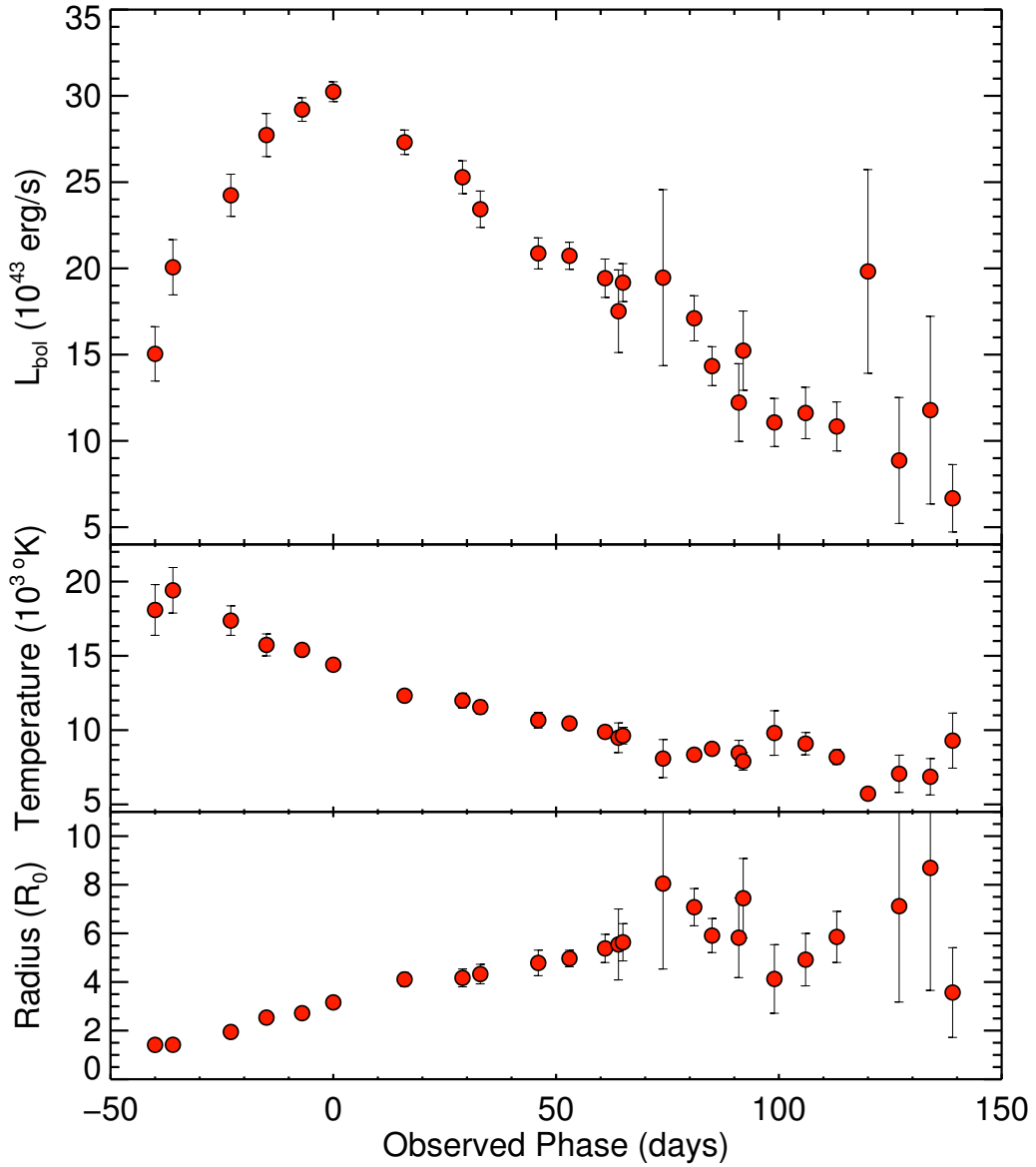
Figure 5.28: *Top panel:* The bolometric light-curve of **DES14C1fi** in units of 10^{43} erg s^{-1} as a function of the observed phase. *Middle panel:* The temperature evolution with observed phase, as obtained by the best-fit blackbody SED on the photometry of each epoch. *Bottom panel:* The radius evolution with observed phase, also obtained by the best-fit blackbody SEDs, in units of 10^{15} cm. The respective figures of the derived bolometric light-curves of the rest of the SLSNe discovered in Y2 are shown in Appendix C.
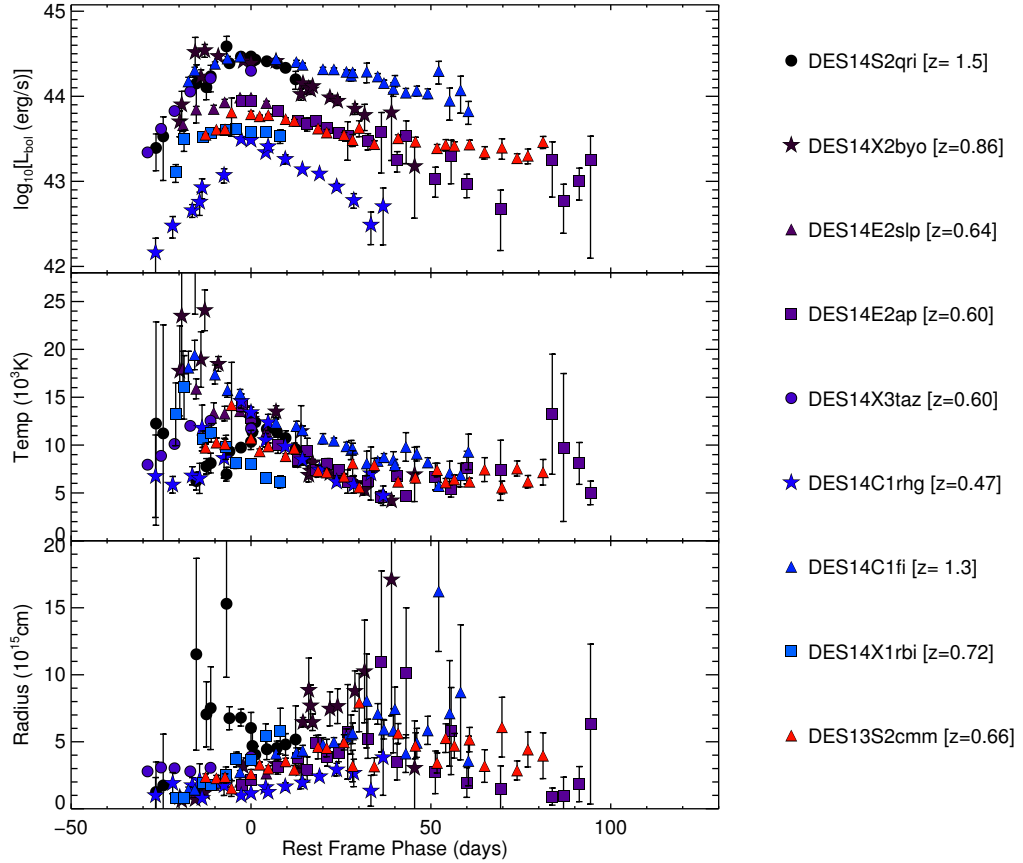
Figure 5.29: The bolometric light-curve (top panel) of 8 spectroscopically confirmed SLSNe from Y2 and DES13S2cmm from Y1, as derived from the temperature (middle panel) and the radius (bottom panel) time evolution in rest-frame phase. Note here, that the temperature evolution is better constrained than the radius one. This is not surprising as DES gains good colour evolution for such SLSNe, which directly constraints the temperature. Also note, that the late time ($> +50$ days) behaviour of the radius appears to decrease slightly with time. The colours and plotting symbols were selected to match the following plots in this thesis.

Table 5.9: List of 22 SLSNe discovered in Y2 and DES13S2cmm from Y1, reporting the best-fit Magnetar models' parameters values (τ_m, B, P and t_{exp}), as well as the fits' results (χ^2_{red}, χ^2 and DoF). The table is separated into four sections: 6 SLSNe that were spectroscopically confirmed, 2 SLSNe that have a host z_{spec}, 14 events that were photometrically selected as SLSNe and DES13S2cmm. The SLSNe are ordered based on their redshift and this order was kept throughout the chapter for clarity in reference and plotting.

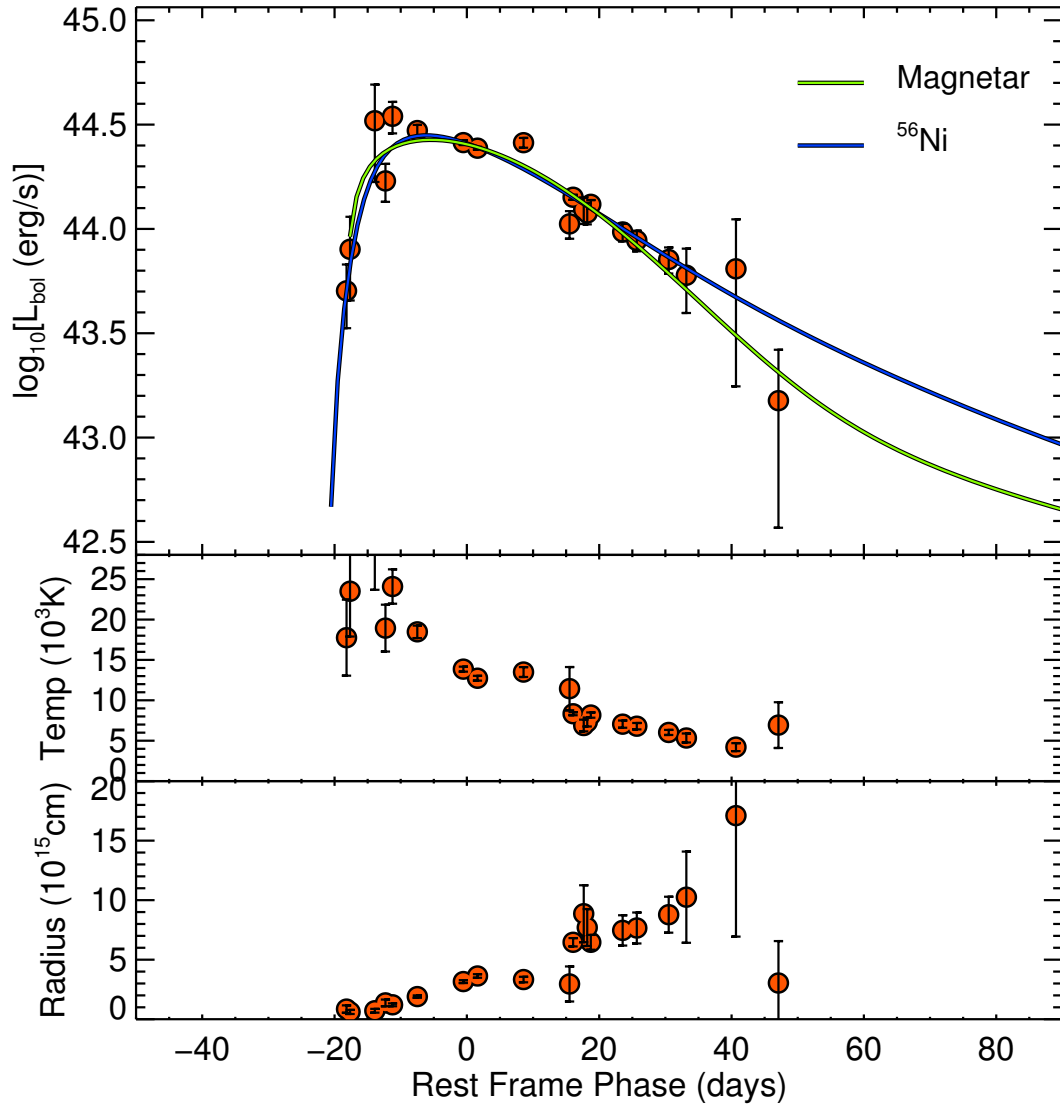| #	Name	z	τ_m	B	P	t_{exp} (days)	χ^2_{red}	χ^2	DoF
1	DES14S2qri	1.500	17.11	1.12	3.02	24.78	0.803	8.83	11
2	DES14X2byo	0.869	31.67	4.73	0.98	18.67	2.440	39.04	16
3	DES14E2slp	0.640	26.14	2.43	4.69	29.13	2.637	7.91	3
4	DES14E2ap	0.600	43.94	3.59	2.33	45.06	0.650	11.05	17
5	DES14X3taz	0.600	32.29	0.26	1.69	25.52	15.976	31.95	2
6	DES14C1rhg	0.470	20.38	5.33	10.95	17.83	9.723	126.40	13
7	DES14C1fi	1.300	27.02	0.84	2.45	32.25	0.810	17.01	21
8	DES14X1rbi	0.720	14.33	1.42	6.28	26.05	0.356	1.78	5
9	DES14S1ewv	1.230	23.48	1.92	3.08	22.90	1.296	15.56	12
10	DES14E1rpi	1.050	13.40	4.26	8.87	15.42	0.257	1.29	5
11	DES14C3nn	1.030	12.32	3.13	6.93	12.65	0.140	1.12	8
12	DES14E1lgl	1.000	48.90	0.91	4.67	40.70	0.656	6.56	10
13	DES14E2bhn	0.970	10.30	3.27	9.48	18.61	0.346	3.12	9
14	DES14X3gyr	0.950	27.49	3.31	8.97	28.24	0.086	0.43	5
15	DES14X1avd	0.840	45.61	4.21	4.83	26.37	0.772	10.81	14
16	DES14X3mjf	0.830	29.78	0.24	3.28	31.64	0.296	1.48	5
17	DES14C1ngk	0.810	49.33	0.86	4.41	41.75	0.690	6.90	10
18	DES14C3tny	0.790	13.37	1.05	6.07	22.87	0.987	3.95	4
19	DES14C1fs	0.740	58.61	2.08	4.32	39.36	0.819	15.57	19
20	DES14X1brr	0.650	12.16	4.79	9.98	16.03	0.882	12.35	14
21	DES14X1ps	0.610	40.67	2.72	3.76	47.78	1.516	33.35	22
22	DES14E1hk	0.530	24.05	5.62	6.83	21.33	0.517	8.26	16
23	DES13S2cmm	0.663	24.71	1.51	5.39	29.19	3.736	82.19	22

Figure 5.30: *Top panel:* The bolometric light-curve of **DES14X2byo** as a function of the rest-frame phase, fitted with the Magnetar (green) and ^{56}Ni (blue) models. *Middle panel:* The temperature evolution with rest-frame phase, as obtained by the blackbody SED best-fit of the photometry of each epoch. *Bottom panel:* The radius evolution with rest-frame phase, also obtained by the best-fit blackbody SEDs, in units of 10^{15} cm
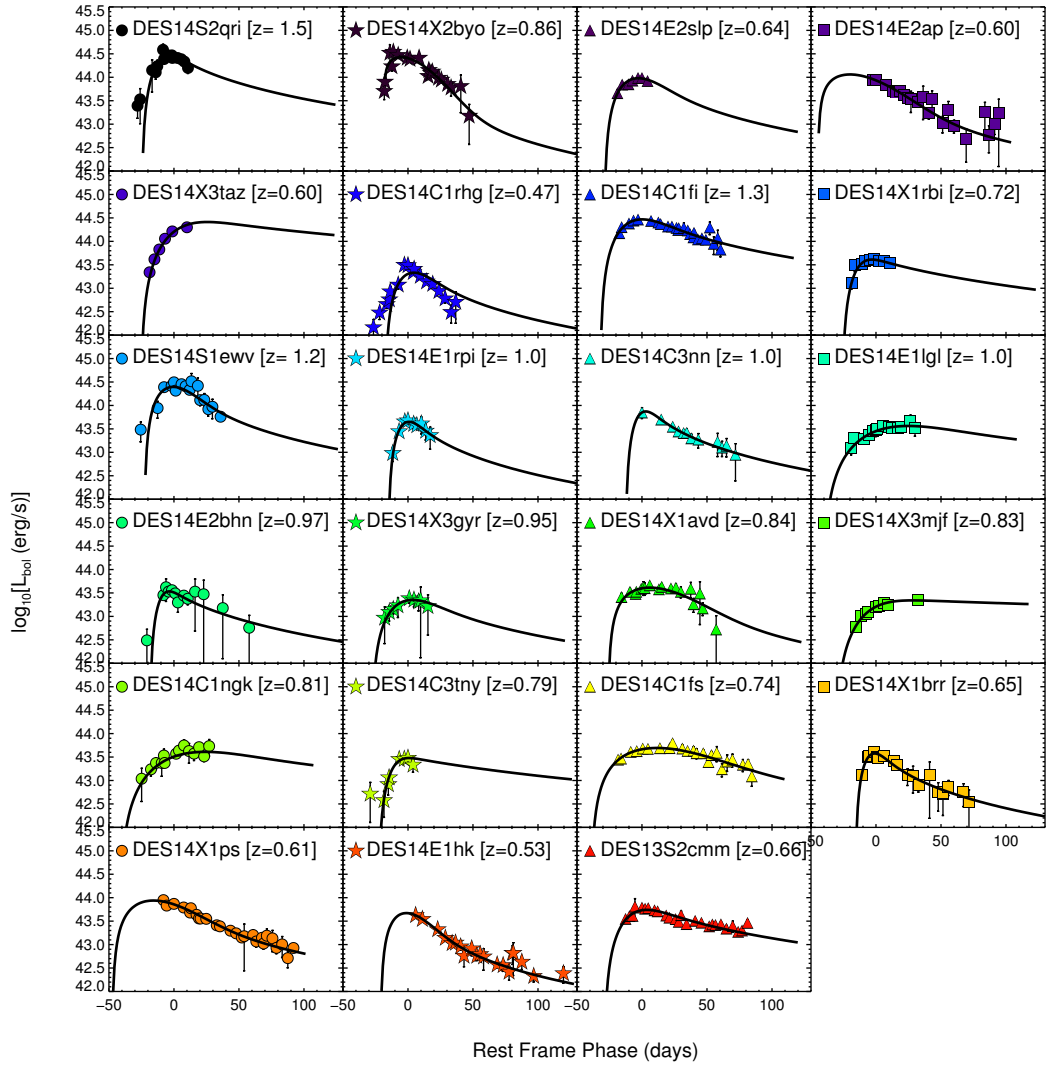
.

Figure 5.31: Rest-frame bolometric light-curves of the 23 SLSNe listed in Table 5.9, overplotted with the best-fit Magnetar model for each SLSNe. The plotting symbols and colours are kept constant for the remaining of this thesis.

Both models were described in detail in Sec. 1.5.3, where equations 1.32 and 1.36 give the bolometric luminosity as a function of time for the Magnetar and decay of ^{56}Ni models respectively. We fit the bolometric light-curve of the SLSNe discovered in Y2 (Table 5.8) with the two models, using the MPFITFUN routine (Markwardt, 2009) within IDL.

Fig. 5.30 shows the best fitting curves of the two models discussed here (green - magnetar, blue - ^{56}Ni) for the bolometric light-curve of DES14X2byo. Both models show identical behaviour to +20 days (rest-frame) past peak, but at later times the magnetar model drops quicker than ^{56}Ni which is a well-known difference between the models, and is often cited as evidence favouring the magnetar explanation (see Cap.4 and Inserra et al., 2013).

Appendix D contains the respective plots with the best fitting curves of the two models for the rest of the SLSNe sample discovered in Y2. Overall, the magnetar model appears to fit better than the ^{56}Ni to the whole sample of SLSNe, especially in late times, a result that confirms the findings from Inserra et al. (2013). A formal 'goodness of fit' test between the two models has not been done within this thesis, but such a project could be the subject of future publications. Table 5.9 gives the best fit parameters for the magnetar model (τ_m, B, P and t_{exp}), as well as the fits' results (χ^2_{red}, χ^2 and DoF) for the sample of 22 SLSNe in Y2, plus DES13S2cmm.

Focusing on the Magnetar model, we present Fig. 5.31 which shows the best fitting curves of the magnetar model on the rest-frame bolometric light-curves of the 23 SLSNe, listed in Table 5.9. A general commend from Fig. 5.31 is that the Magnetar model can fit fairly well light-curves with a range of different shapes. This could be explained by the diversity of the physical parameters of the model as described in Sec. 1.5.3 and presented in Fig. 1.17. The fact that the physical parameters' space of the Magnetar model is not strictly constrained by the theory (Woosley, 2010; Kasen and Bildsten, 2010), results to the good agreement between the data and the models. In the other hand, the decay of ^{56}Ni models for example, have a physical constrain in the amount of ^{56}Ni that is produced during the SN explosion.

We note that several magnetar fits have very small χ^2_{red} values produced by MPFITFUN. Such values indicated over-fitting (Andrae et al., 2010), namely there are a small number of data points (eg. DES14X3gyr) with unexpected large errors and/or the model has too many degrees of freedom. This over-fitting then translates into large errorbars on the best-fit parameters of the model. Such large errorbars are not to be trusted, while one can argue, based on visual inspection of the best-fit models in Fig. 5.31, that the produced parameters values are reasonable and compatible with the ones coming from more sensible fits.

Moreover, we note that most of the 23 SLSNe in this sample (Table 5.9) do not possess enough data points to cover both before and after peak epochs of the light-curve, resulting in insufficient fits of the Magnetar model, although visually one can argue that the model fits the data well enough e.g. DES14E2slp, DES14X3taz, DES14C3nn and DES14X3mjf etc. This situation is currently unavoidable, due to the predefined observing season of DES, which is limited to a maximum of five and a half months per calendar year. Because of time dilation, the observing window decreases with redshift and as a result, the SLSNe that were not discovered early in the observing season and at an early stage of their life, will have incomplete light-curves, leading to inadequate model fits.

We attempt to explore correlation in the Magnetar model's parameter space using Fig. 5.32, which shows six cross-reference plots between the four fitting parameters of the Magnetar model for the SLSNe sample discovered in Y1 and Y2. A clear correlation between the four parameters is difficult to be seen visually, though there is evidence for a (linear) correlation between the explosion phase (t_{exp}) and the rise-time parameter (τ_m, Eqn. 1.33), plotted in the bottom left hand side panel of Fig. 5.32.

We note the large errorbars derived for the fit parameters of some of the SLSNe shown in those plots. As explained above, those are the results of the MPFITFUN routine's over-fitting (Andrae et al., 2010). Using the following selection-cut: $\chi^2_{red} < 0.6$ and $\chi^2_{red} > 5.0$ the SLSNe possessing the large errorbars were selected and replaced with the median errorbars derived from the whole SLSNe sample. The result of this is shown in Fig. 5.33. Such action can be justified by a previous argument, that despite the large errorbars the derived parameters' values are reasonable and compatible with the ones coming from SLSNe with more sensible fits.

Furthermore, we explore possible correlations in Fig. 5.33 using a Pearson and Spearman test using pre-defined routines in IDL. For Pearson and Spearman tests the correlation coefficient could have any value within the following limits: $+1$ (total positive correlation), 0 (no correlation), and -1 (total negative correlation). Two sets of parameters shows significant correlations (one negative and one negative), whereas the rest of the parameters' combinations were inconclusive. Namely the rise-time (τ_m) and the spin-down time (P) resulted to coefficient values of -0.58 and -0.63 for the Pearson and Spearman tests respectively. Also, for the correlation between the explosion phase (t_{exp}) and the rise-time (τ_m), the Pearson test resulted to a coefficient value of 0.56, whereas the Spearman test gave a coefficient value of 0.65.

We applied a selection-cut based on the values of the χ^2_{red} of Table 5.9, using $0.6 < \chi^2_{red} < 5.0$ – which resulted to the exclusion of 9 SLSNe from Table 5.9 – and performed the Pearson and Spearman tests again. The correlation between the rise-time (τ_m) and the spin-down time (P) was weakened significantly. In the other hand, the positive correlation between the the explosion phase (t_{exp}) and the rise-time (τ_m) was slightly
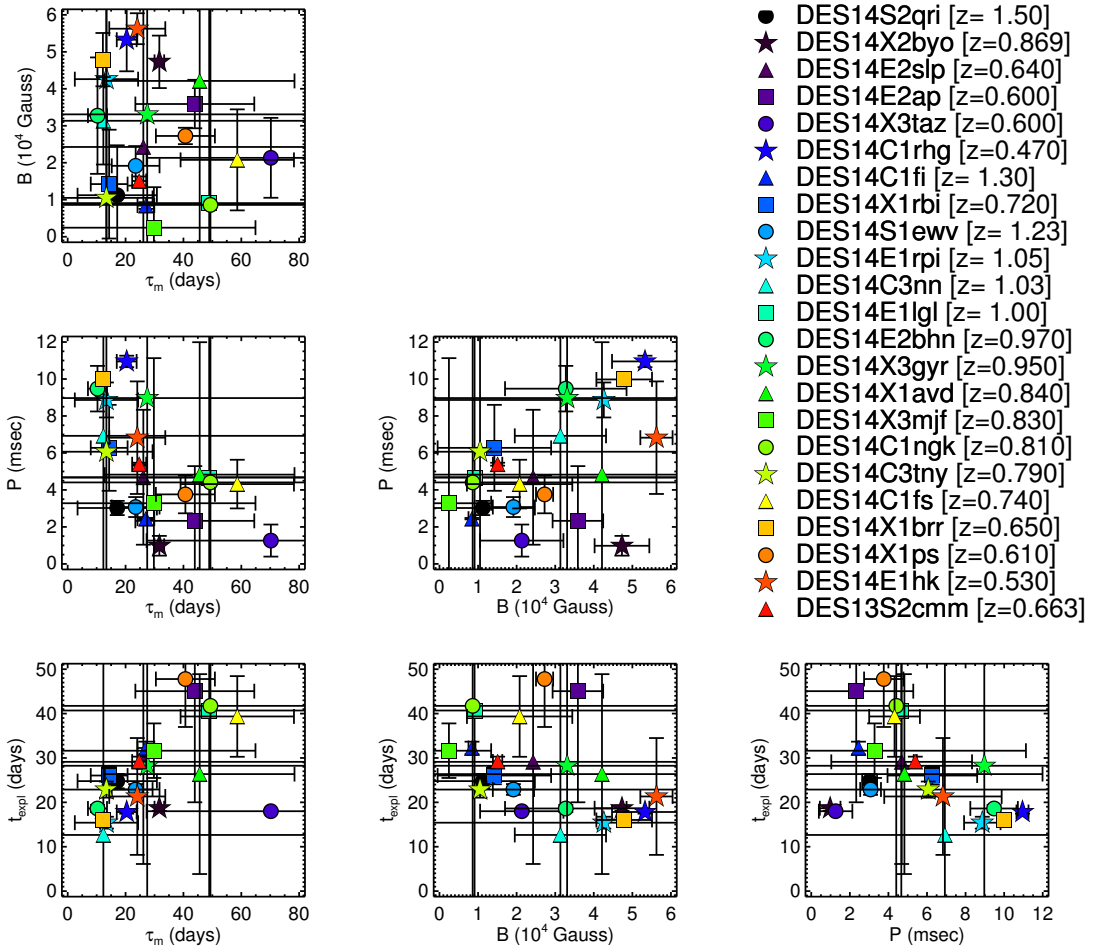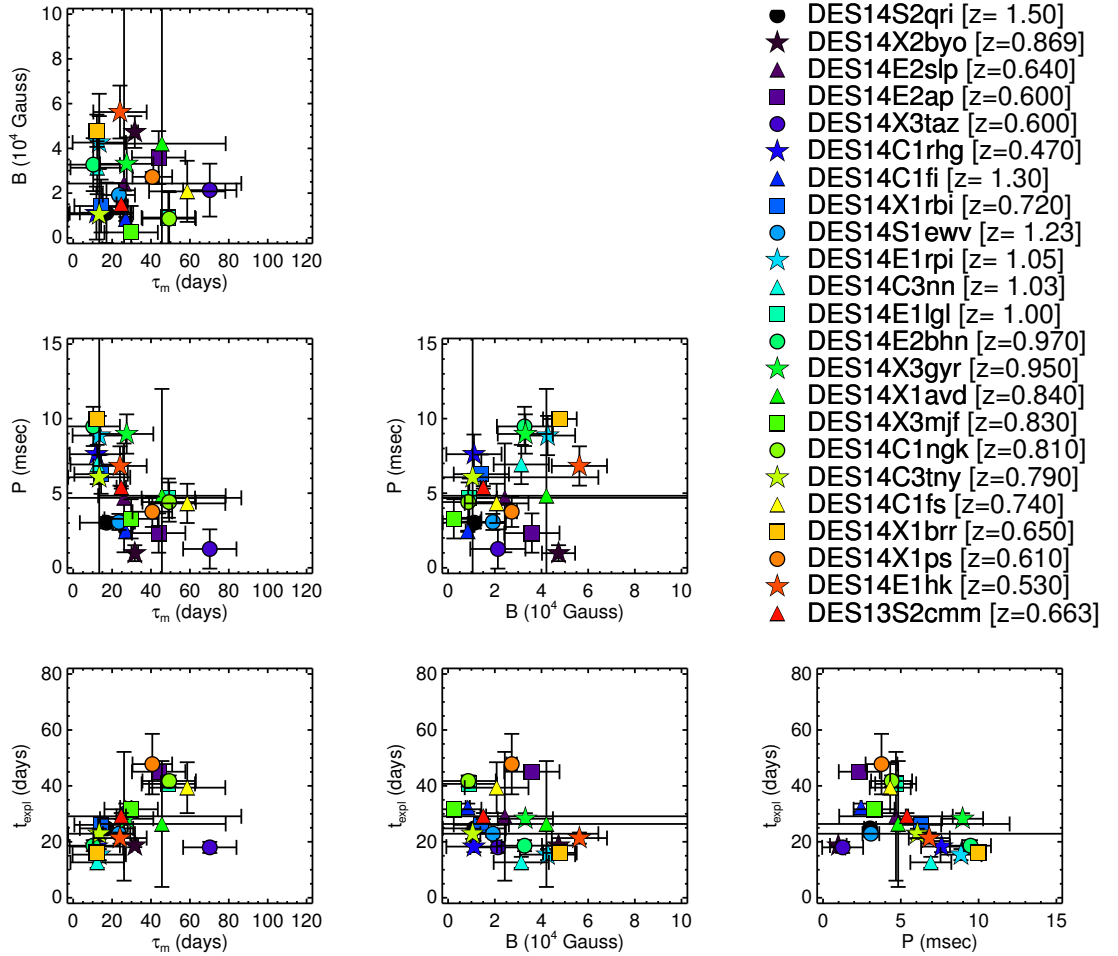
Figure 5.32: The four parameters (τ_m, B, P and t_{exp}) of the best-fit Magnetar models of the 23 SLSNe listed in Table 5.9, plotted against each other. There is visual evidence of a (linear) correlation in some of these relations, which is to be expected as some of the parameters will be correlated. Such a correlation can be seen between the τ and t_{exp} parameters (bottom left panel). Unfortunately the errors are large making clear conclusions hard. The plotting symbols and colours are kept constant as in previous plots and for the remaining of this thesis.

Figure 5.33: The four parameters (τ_m, B, P and t_{exp}) of the best-fit Magnetar models of the 23 SLSNe listed in Table 5.9, plotted against each other, as in Fig. 5.32, but with adjusted errorbars for the SLSNe that passed the χ^2_{red} selection cut. The plotting symbols and colours are kept constant as in previous plots and for the remaining of this thesis.
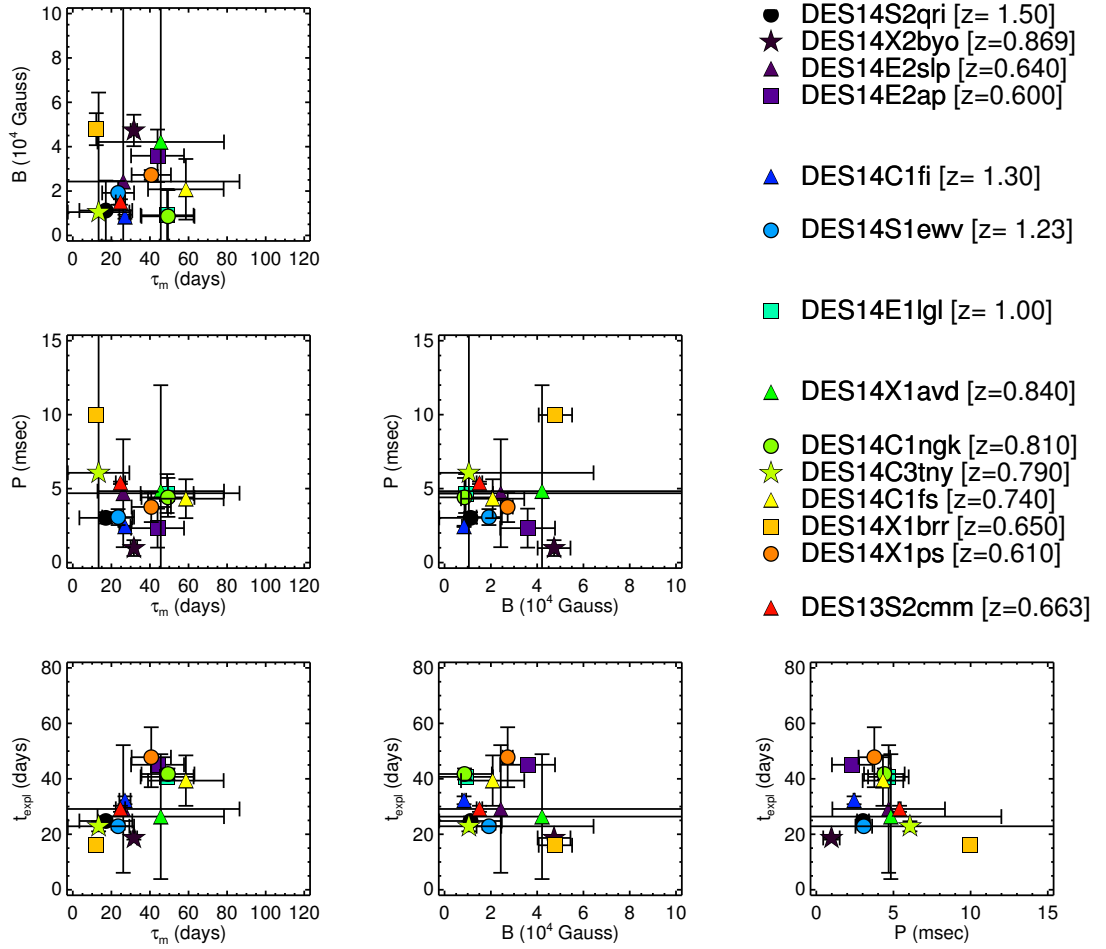
Figure 5.34: The four parameters (τ_m, B, P and t_{exp}) of the best-fit Magnetar models of the 14 SLSNe selected as described in Sec. 5.7.2, plotted against each other. Pearson and Spearman correlation tests revealed the possible correlations between the explosion phase (t_{exp}) and the rise-time (τ_m). The plotting symbols and colours are kept constant as in previous plots and for the remaining of this thesis.
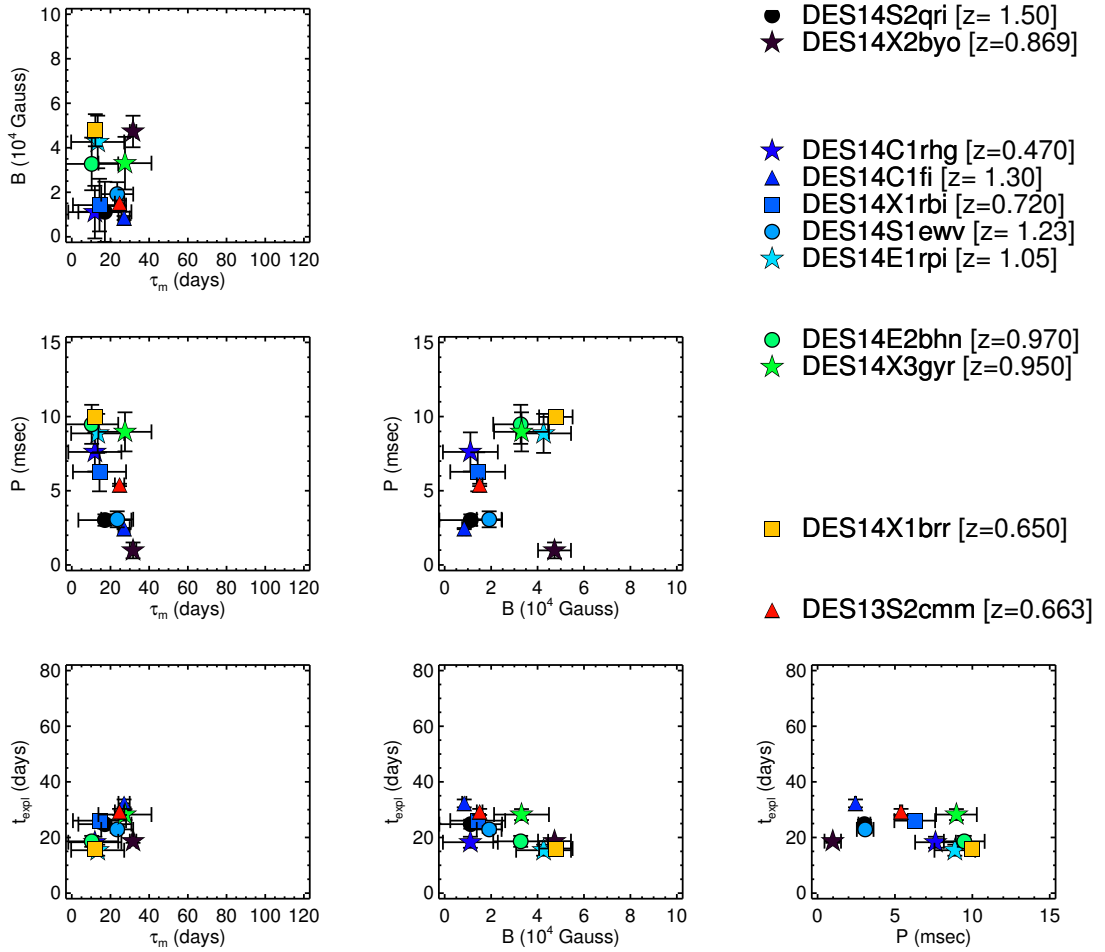
Figure 5.35: The four parameters (τ_m, B, P and t_{exp}) of the best-fit Magnetar models of the 11 SLSNe selected as described in Sec. 5.7.2, plotted against each other. Pearson and Spearman correlation tests revealed the existence of two possible correlations, one between the explosion phase (t_{exp}) and the rise-time (τ_m); and between the spin down time (P) and the rise-time (τ_m). The plotting symbols and colours are kept constant as in previous plots and for the remaining of this thesis.

strengthened, resulting to coefficient values of 0.65 and 0.66 for the Pearson and Spearman tests respectively. Fig. 5.34 shows the six cross-reference plots of the Magnetar model's parameters for the 14 SLSNe that passed this χ^2_{red} selection cut.

An alternative method for selecting a more robust sample of SLSNe light curves is to select based on light curve coverage. The best light curves have coverage before and after peak, which significantly improves the constraints on the magnetar model parameters. Using the light-curves of the 23 SLSNe as presented in Fig. 5.31, one can select those SLSNe that have at least 2 pre-peak epochs and several past-peak epochs, that reach at least a minimum of +30 days (rest-frame). Clear examples of such cases would be DES14X2byo and DES14C1fi, whereas events such as DES14X3taz and DES14E2ap would fail to pass this selection cut. Other events, such as DES14E1lgl and DES14X3mjf, appear to have enough data points around peak, but at the same time the shape of the light-curve at peak and its slow evolution, push these specific SNe examples outside the selection cut. Other SNe that fall in the latter category are DES14C1ngk and DES14C1fs.

Using the latter selection cut, we re-run the Pearson and Spearman tests again and find coefficient values of 0.59 and 0.65 respectively, for the correlation between the explosion phase (t_{exp}) and the rise-time (τ_m). Also, the latter selection cut re-emerged the correlation between the spin down time (P) and the rise-time (τ_m), with coefficient values equal to -0.67 and -0.65 for the Pearson and Spearman tests respectively. All other correlations tested provided an inconclusive result for the Pearson and Spearman test (e.g. coefficient values close to zero). Fig. 5.35 shows the six cross-reference plots of the Magnetar model's parameters for the 11 SLSNe that passed the light-curve coverage selection cut.

This exploration of the correlation in the Magnetar model's parameter space revealed that, one correlation is robust as it appears in all the selection cuts. Namely, the correlation between the explosion phase (t_{exp}) and the rise-time (τ_m) showed consistent coefficient values (for both Pearson and Spearman tests). Also, the correlation between the spin down time (P) and the rise-time (τ_m) was tentative and depended on the selection cuts applied, while the remained parameters combinations showed no correlation. Thus, a more detailed analysis is required to investigate further these possible correlations to 'standardise' these SLSNe as discussed in Inserra and Smartt (2014).

5.8 Comparison of Bolometric Light-Curves

By plotting the bolometric light-curves of SLSNe on the same panel, we explored the potential of seeing common behaviour in the evolution of the SLSNe, as we have dis-
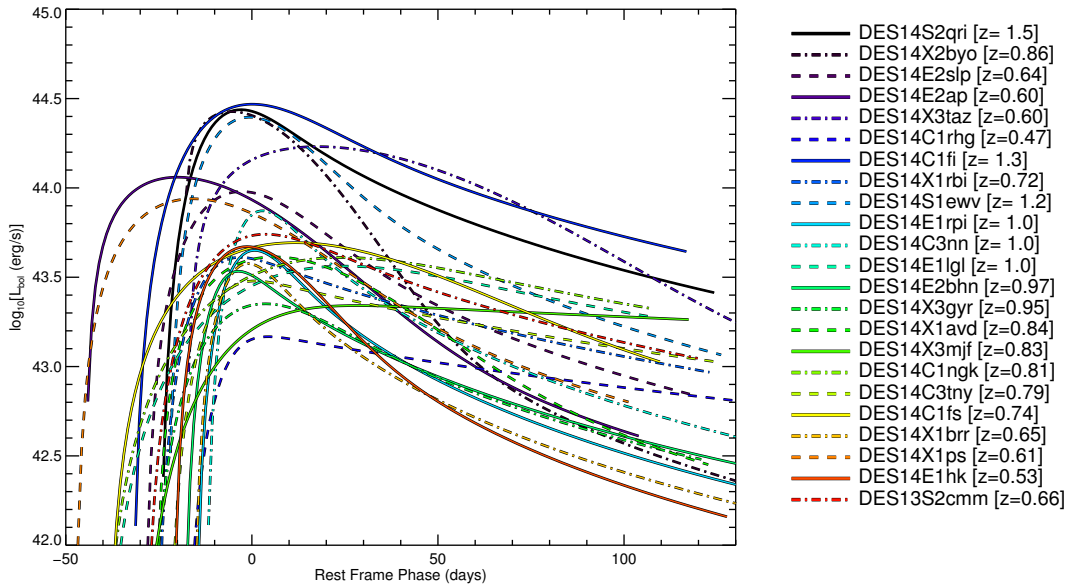
Figure 5.36: Rest-frame bolometric light-curves, constructed by using the Magnetar model, of the 23 SLSNe listed in Table 5.8, plotted on the same panel in order to spot common behaviour. The complete sample of 23 SLSNe does not show a particular common behaviour, whereas some sub-samples could be identified by such plot. The colour-coding of the SLSNe was adopted and kept constant from previous plots.
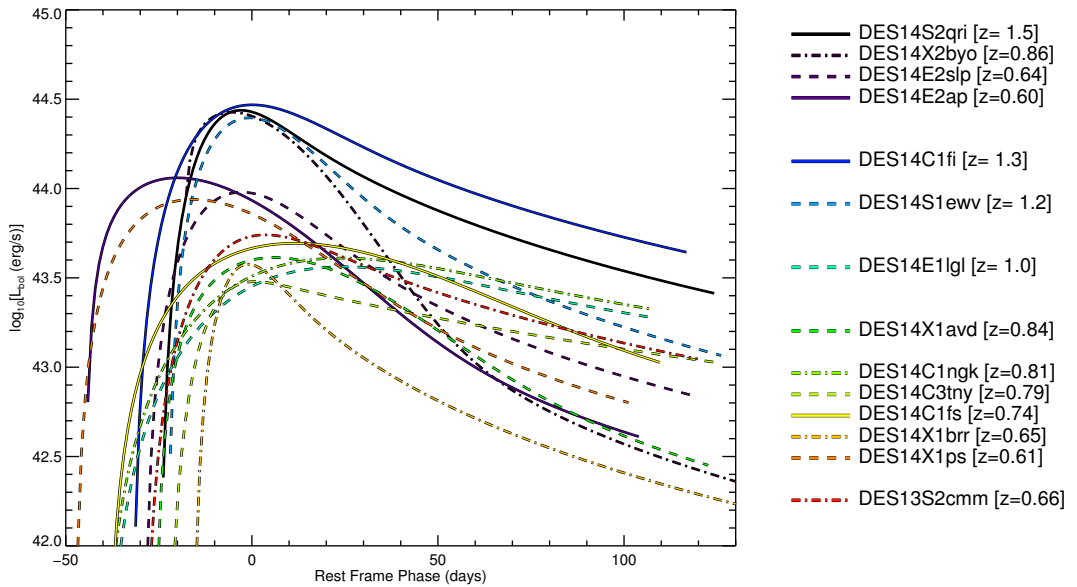

Figure 5.37: Rest-frame bolometric light-curves, constructed by using the Magnetar model, of the 14 SLSNe that passed the χ^2_{red} selection cut, plotted on the same panel in order to spot common behaviour. The diversity between the light-curves can be easily spotted. The colour-coding of the SLSNe was adopted and kept constant from previous plots.
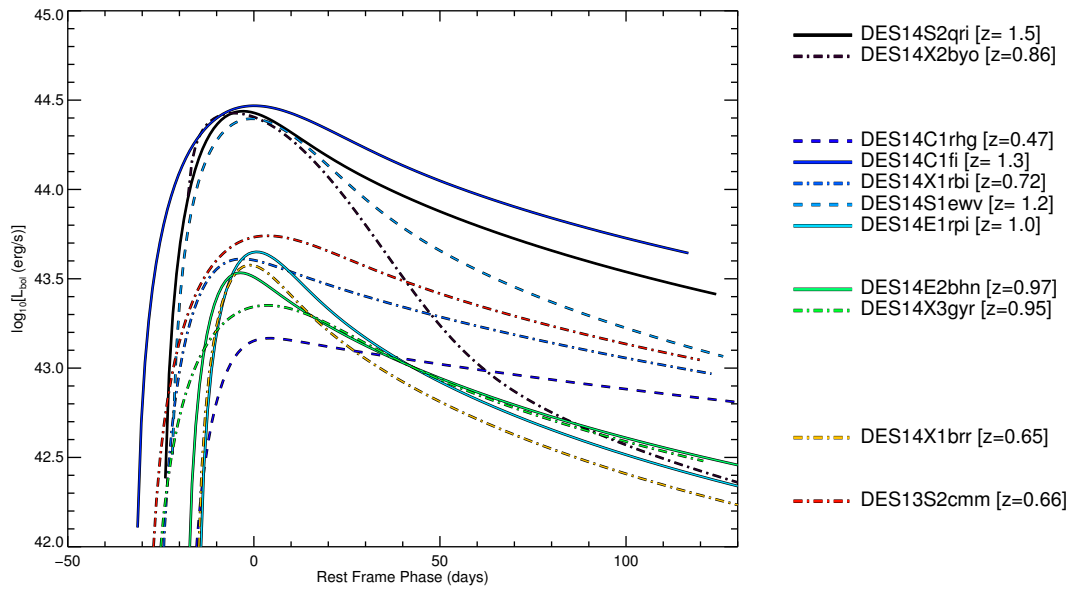
Figure 5.38: Rest-frame bolometric light-curves, constructed by using the Magnetar model, of the 14 SLSNe that passed the χ^2_{red} selection cut, plotted on the same panel in order to spot common behaviour. The diversity between the light-curves can be easily spotted, especially around peak brightness, whereas the only common behaviour appears at very late time, where the light-curves have the same slow decline rate. The colour-coding of the SLSNe was adopted and kept constant from previous plots.

cussed previously in Sec. 4.7 for DES13S3cmm, which we include here in our overall
DES SLSN sample.

In Fig. 5.36 we attempt the first direct comparison of the 22 SLSNe listed in Table 5.8 plus DES13S2cmm, by using their rest-frame bolometric light-curves as constructed from their best fit magnetar model. The whole sample of 23 SLSNe does not show any obvious common behaviour. Instead, it reveals a diversity between the 23 light-curves, in contrast to what we have seen in Fig. 4.7, where the SLSN light curves showed some similarities at approximately $+25$ days (rest frame) past peak.

Moreover, figures 5.37 and 5.38 illustrate the direct comparison of the bolometric light-curves created by the Magnetar model, after applying the two selection cuts mentioned in the previous section, namely the χ^2_{red} limits and light-curve coverage respectively. By using those selection cuts, the SLSNe sample hopefully becomes more robust, as the events that fail to pass the selection cuts are the less likely to be true SLSNe, as we do not possess spectroscopic confirmation for the whole sample and/or have lower quality light curves (so worse magnetar model fits). Even though the two sub-samples can be considered purer than the 23 SLSNe of Table 5.8, the bolometric light-curve comparison does not reveal any strong correlation in their time evolution.

One can argue that, for the sample with the light-curve coverage cut applied, illustrated in Fig. 5.38, the light-curves at very late times $> +100$ days (rest frame) past peak, have similar slopes. This argument is preliminary, as for such late rest-frame times most of the SLSNe do not have any measurements, as seen in Fig. 5.31, and the slopes at those late times are governed purely by the mathematical form of the magnetar model. A more detailed statistical test is required to fully understand this sample of SLSNe and what possible correlations could be seen.

5.9   Rates and Distributions of SLSNe

The redshift distribution of the 22 SLSNe discovered in Y2 by DES, is illustrated in Fig. 5.39, whereas the apparent and absolute magnitude distributions can be seen in panels (a) and (b) of Fig. 5.40, respectively.

From the absolute U magnitude distribution plot, one would notice that around half of our sample of the 22 SLSNe is distributed below the SLSNe absolute magnitude limit of $M \leq -21.0$, set by Gal-Yam (2012). As noted before, this limit was arbitrarily set at the beginning of the quest for SLSNe, and the discovery of events with absolute magnitudes less than -21 could explain the existence of a continuum between the SLSNe and type Ic class ($-17.8 \leq M \leq -18.3$). Pastorello et al. (2010a) first showed that late time spectra of SLSNe resemble the spectra of SNe Ic, pointing towards a common physical
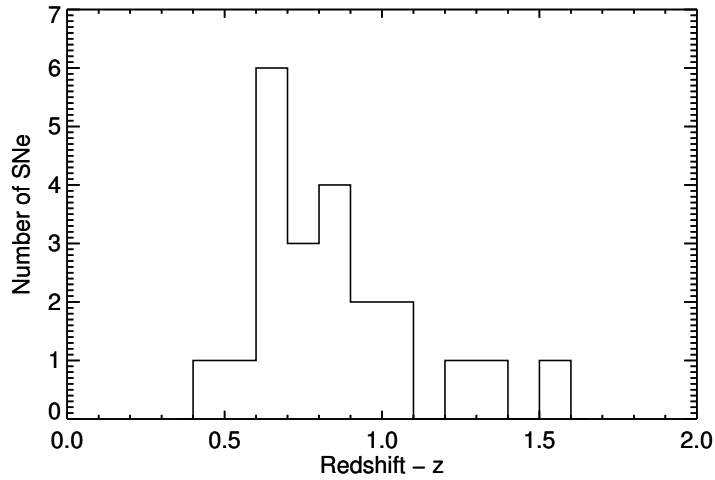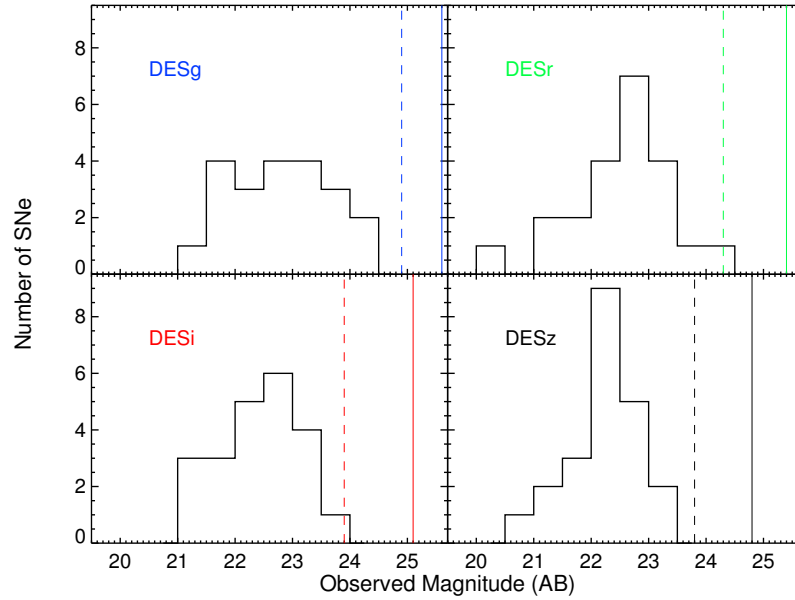
Figure 5.39: Redshift distribution of the 22 SLSNe discovered in Y2 by DES as listed in Table 5.8. The redshift bins size is set to 0.1.

origin scenario (massive Wolf-Rayet stars) with a different energy source to power the high luminosity of SLSNe. The use of a bigger sample of SLSNe with well covered light-curves and extensive spectroscopic follow-up, is necessary in the near future in order to investigate thoroughly this common progenitor scenario between SLSNe and SNe Ic.

Moreover, as presented in panel (b) of Fig. 5.40, the distribution of absolute peak magnitude could be bimodal, suggesting two populations of SLSNe-I. A similar distribution is seen in Fig. 2.5, for SLSNe-I taken from the literature. Note, that a more detailed and robust statistical test is required to confirm this visual impression, as well as a larger samples of SLSNe.

Cooke et al. (2012) estimated the rate of SLSNe at high redshift ($2 < z < 4$), using two SLSNe, SNLS-07D2bv and SNLS-06D4eu, from archival SNLS data as described in Sec. 2.2, and reported a lower limit of ~ 400 events Gpc^{-3} yr^{-1} h$_{71}^3$. Furthermore, Quimby et al. (2013b) used 19 SLSNe-like events and estimated the volumetric rate in the local volume $\overline{z} \sim 0.2$, of 199_{-86}^{+137} events Gpc^{-3} yr^{-1} h$_{71}^3$.

Both studies by Cooke et al. (2012) and Quimby et al. (2013b) have adopted complicated and detailed calculations in order to reach to their reported SLSNe rate values illustrated in Fig. 5.41. Both used Monte Carlo simulations to mimic the respective surveys' strategies, observations and efficiency in detecting SLSNe via simulated SLSNe light-curves, whereas we adopted a much simpler, but less accurate process.

(a) Apparent Magnitude histograms
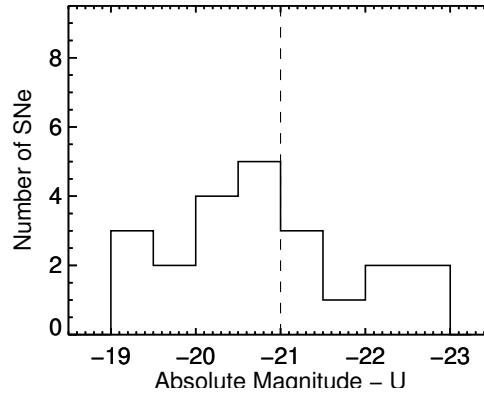
(b) Absolute U Magnitude histogram

Figure 5.40: *Panel a:* The apparent magnitude distribution of the 22 SLSNe discovered in Y2, separated in the four DES filters ($griz$). The vertical lines show the magnitude limits in the shallow (dashed lines) and deep (solid lines) SNe fields, as listed in Table 3.1. *Panel b:* The peak absolute U magnitude distribution of the 22 SLSNe discovered in Y2. The dashed, vertical line denotes the SLSNe limit ($M_U \leq -21.0$) set by Gal-Yam (2012) (see Sec. 1.5).
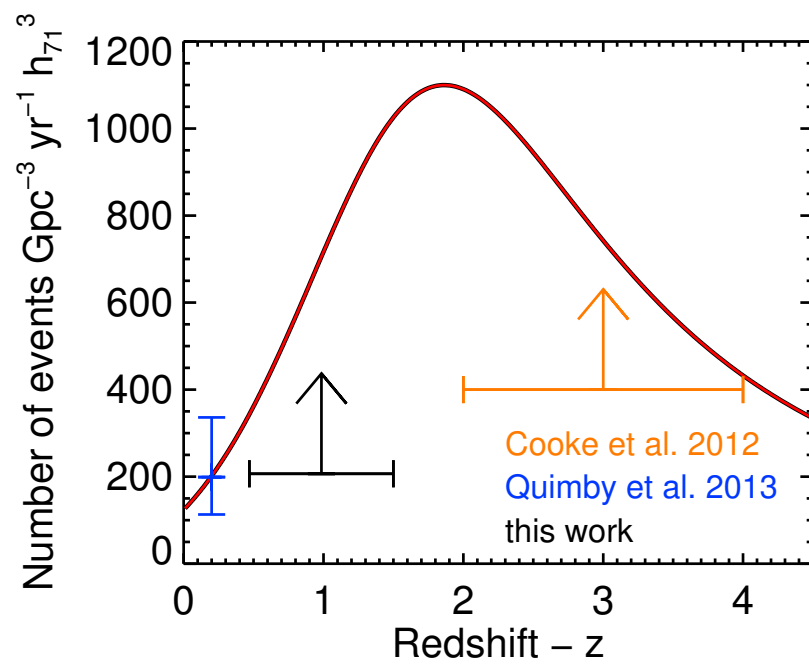
Figure 5.41: Rates of SLSNe-like events as a function of redshift, as reported by Quimby et al. (2013b) (*blue*) for the local Universe, by Cooke et al. (2012) (*orange*) for the high redshift range and by this work's rough estimate for indeterminate redshifts. The red line represents the cosmic Star Formation History (SFH), as presented by Madau and Dickinson (2014), anchor to the SLSNe rate value of Quimby et al. (2013b).

Using the 22 SLSNe-like events we discovered in Y2, as listed in Table 5.8, we attempted a basic calculation of the volumetric SLSNe rate, using the following equation:

$$R = \sum_{i=1}^{N} \frac{1}{V_{eff,i}} \tag{5.1}$$

where N is the total number of SLSNe and $V_{eff,i}$ is the effective volume element for each event.

In order to calculate each $V_{eff,i}$, we adopt a few assumptions. First, in order to determine the maximum volume element in which each of the 22 SLSNe was detected, we redshifted the observed light-curve flux to the detection limits of DECam, as listed in Table 3.1, thus determining the maximum redshift at which each event would be detectable. Secondly, for each event we take into account the survey's sky coverage and the survey's available observing window. The survey's observing window of ~ 6 months per year shrinks as it is redshifted to the maximum redshift at which each SLSNe would be detectable.

After applying the above assumptions, we calculated a lower limit for the SLSNe rate of ~ 206 events Gpc^{-3} yr^{-1} h$_{71}^{3}$, illustrated in Fig. 5.41, as compared to rates reported in the literature to date. We found a good compatibility with what is reported in the literature, which indicates that the number of SLSNe found during Y2 is compatible with reasonable expectations in the literature. In Fig. 5.41, we also compared the cosmic Star Formation History (SFH), as presented by Madau and Dickinson (2014), after we anchor it to the SLSNe rate value at $\overline{z} \sim 0.2$ (Quimby et al., 2013b). This comparison was constructed in analogy to the estimation of the Core-Collapse SNe rate from the cosmic SFH, presented in Fig.10 of Madau and Dickinson (2014).

Moreover, Perrett et al. (2012) measured the evolution of the volumetric SNe Ia rate of SNLS (Astier et al., 2006; Sullivan et al., 2011), within the redshift range $0.1 \leqslant z \leqslant 1.1$. They reported a SNe Ia rate of $59 \cdot 10^3$ events Gpc^{-3} yr^{-1} h$_{71}^{3}$ at $\langle z \rangle = 0.7$; which compared to the SLSNe rate we reported above translates to one SLSNe event every ~ 290 SNe Ia events.

A more detailed and in-depth calculation of the rate of SLSNe, similar to Cooke et al. (2012) and Quimby et al. (2013b), extends beyond the scope of this thesis, and could be the subject of future publications.

5.10 Summary and Discussion

In this chapter, I have described in detail the search for SLSNe during the DES Y2 of operations. Moreover, I explored the improvements on the DES SN survey that took

place during the off-season period, involving updates on data-pipelines and spectroscopic follow-up resources.

Furthermore, I presented in detail the updated methodology used for the SLSNe search in Y2, illustrated by the flow-chart in Fig. 5.4, involving the reformation of the selection criteria; enhanced with a SNR limit on the selection of the peak fluxes (Sec. 5.4.1) and the introduction of a semi-interactive IDL routine responsible for two steps of visual inspection processes (Sec. 5.4.2, 5.4.3). During the visual inspections of SLSNe candidates, new tools were developed and used, such as the search panel for SLSNe (Fig. 5.7 and App. A), the AGN/QSO veto catalogue using the multi-season flux light-curve panels (Fig. 5.8), as well as the 'candidates-page'(Fig. 5.11) and 'ATC' web application(Fig. 5.12).

All those tools and process lead to the discovery of 22 SLSNe in Y2, 7 of which were spectroscopically confirmed and presented in detail in Sec. 5.6. Also, Sec. 5.7 presents the construction the bolometric light-curves of all the 22 SLSNe, which were then fitted by two power-source models: the Magnetar and ^{56}Ni decay as described in Sec. 1.5.3. The model fits revealed that overall, the Magnetar model was more successful, and that was prominent when the observed light-curve was covered with both pre-peak and late-time data.

In the quest for standardizing SLSNe in order to use them as 'standard candles', the entire sample of SLSNe discovered by DES (Y1+Y2) was used and fitted by the Magnetar model in Sec. 5.7.2, to explore the possible correlations between the model's parameters. Moderate correlations between the explosion phase (t_{exp}) and the rise-time (τ_m), and between the spin down time (P) and the rise-time (τ_m), were discovered. Moreover, the bolometric light-curves of the DES SLSNe sample were compared (Sec. 5.8), without tracing any common behaviour similar to what was seen between DES13S2cmm and other historic SLSNe, explained in Sec. 4.7 and by Papadopoulos et al. (2015).

Finally, using the Y2 sample of SLSNe I performed a basic calculation of the volumetric SLSNe rate, presented in Sec. 5.9, concluding that the number of SLSNe found during Y2 is compatible with reasonable expectations in the literature.

The standardization of SLSNe remains an open question, as the model's parameters' correlations were subjected to different selection cuts and could not be generalized to the DES sample of SLSNe, while the bolometric light-curve comparison did not reveal any common behaviour.

Chapter 6

Summary and Conclusions

In this thesis, I present a new, dedicated search for Superluminous Supernova within the Dark Energy Survey. I started this search at the beginning of Y1 (August 2013) and continued it until the end of Y2 of operations (February 2015). To date, it has been a successful search providing eight new spectroscopically confirmed SLSNe including DES13S2cmm, which was the first SLSN confirmed by DES and was studied in detail Papadopoulos et al. (2015) and Chap. 4. The remaining seven SLSNe are as yet unpublished and are presented together in this thesis for the first time. These seven new SLSNe include interesting objects like DES14X3taz which appear to have a pre-peak bump in its light curve like SN 2006oz.

In Chap. 3, I present the infrastructure work I performed during the DES Science Verification period. This period was dedicated to ensuring the DECam could deliver the quality of data required for DES and involved the visual inspection of every image obtained by DECam over a three month period. This chapter also outlines my contributions to the visual inspection of DES SNe candidates, which in Y1 involved scanning hundreds of possible transients a day. Chap. 3 also presents an overview of the DES SN survey including details of the survey design and implementation (including plans for spectroscopic follow-up). Finally, in Chap. 3 I present my research in designing an algorithm for selecting SLSNe candidates from the pool of DES SNe candidates in Y1. I present details of the common SLSNe contaminants, as well as show the first 12 SLSNe candidates selected from Y1 data.

Chap. 4 presents a detailed examination of DES13S2cmm ($z = 0.663$) the only spectroscopically confirmed SLSN from DES Y1. The presented was published in Papadopoulos et al. (2015) and includes a careful examination of the SN light curve and possible models for powering such massive explosion. We find the Magnetar model (the rapid spin-down of a magnetic neutron star) is the best explanation, but it is not a good fit to the bolometric light curve of DES13S2cmm.

In Chap. 5, I present my search for SLSNe in Y2 of DES, building upon the success in Y1 and upgrading various parts of my search algorithm. We also had additional spectroscopic resources in Y2, allowing us to spectroscopically confirm 7 new SLSNe from my sample of SLSN candidates. Major improvements in Y2 included a better, more automated, algorithm for selecting transients from DES data, which significantly reduced the number of data artefacts in my candidates (thus reducing the visual inspection load), as well as stricter criteria on identifying SLSNe candidates, especially to reduce AGN contamination. Over Y2, I selected 133 SLSNe candidates from the stream of DES SN candidates. These candidates required a further, more detailed examination to decide on their priority for spectroscopic follow-up, to maximise this limited resource. After much consideration, I present in Table 5.8 a list of 22 SLSNe from Y2 which I am confident of their classification. This table includes 6 spectroscopically confirmed SLSNe, 2 SLSNe confirmed from spectroscopic redshifts of their host galaxies, and 14 SLSNe classified using their light curves and host galaxy photometric redshifts.

Chap. 5 also presents a preliminary study of the population statistics of the 23 DES SLSNe presented in this thesis (22 discovered in Y2, plus DES13S2cmm in Y1). This is already one of the largest samples of SLSNe studied together and presented a number of interesting initial results:

- I discover many SLSNe with peak absolute magnitudes below the defined threshold of $M_U = -21$. This threshold is probably arbitrary and my work suggests there maybe a continuum of SLSN peak magnitudes towards the fainter normal SNe e.g. normal Type Ic supernova.

- I find the Magnetar model is consistently a better fit to the bolometric light curves of my sample, primarily because of the long tails which the ^{56}Ni model is unable to explain. This is consistent with recent studies (see Inserra et al., 2013) and strengthens the case for this central engine power source.

- The distribution of SLSNe peak magnitudes could be bimodal, suggesting two populations of SNe. This is seen both in Fig. 5.40 for my sample of 23 DES SLSNe and in Fig. 2.5 for SLSNe taken from the literature. A more detailed statistical test is required to confirm this visual impression, as well as a larger samples of SLSNe.

- Using the Magnetar model, I investigate possible correlations between the model parameters and the shape and amplitude of the observed light curves. Apart from a correlation between explosion phase and the rise-time, I found no evidence for strong correlations and the data showed a diversity of light curve shapes. A more detailed analysis is required to seek possible correlations to 'standardise' these SLSNe as discussed in Inserra and Smartt (2014).

- I present a crude measurement of the rates of SLSNe and find that it is consistent with other measurements, but with a large uncertainty at present. This exercise does confirm that the number of SLSNe found in DES over the last two seasons (e.g. $\simeq 30$ reasonable SLSNe candidates in Y1+Y2) is realistic and my search was efficient.

- My search has highlighted important issues for future searches, including the importance of a AGN veto catalogue (the biggest contaminant) and the need for semi-automated algorithms to detect and priorities SLSNe targets for spectroscopic follow-up. The increase in spectroscopically-confirmed SLSNe in DES Y2 was because of my improved, quicker search algorithm.

6.1 Future plans and SUDSS

DES has three more seasons to run and Y3 started in August 2015. I expect the quality of the SLSNe candidates to improve in future seasons, based on my experience from the last two years. I also expect an increase in the amount of available spectroscopic follow-up time, meaning DES will likely obtain many more spectroscopically-confirmed SLSNe.

However, since Y1, it has been clear that the efficiency of detecting SLSNe in DES data has suffered from temporal edge-effects due to the DES observing window (~ 4.5 months). These edge-effects result in curtailing many of the long SLSNe light curves, especially at high redshift where time dilation can extend the observed light curves to many months. These issues have a big impact on the modelling of the bolometric light curves (see Chap. 4), as it is difficult to obtain meaningful fits to the Magnetar and ^{56}Ni decay models without data before and after peak magnitude. As seen in Fig. 5.31, several SLSN light curves are incomplete because of these edge-effects.

To ease this problem, I have been involved in a complementary programme called 'Survey Using DECam for Superluminous Supernovae' (SUDSS) since Y1 of DES. SUDSS is designed to extend the observing window of the DES SN Survey, thus reducing the temporal edge-effects and helping to provide complete light curves. I discuss SUDSS below.

Survey Using DECam for Superluminous Supernovae

The 'Survey Using DECam for Superluminous Supernovae' (SUDSS) was begun in February 2013, at the end of Y1 DES. SUDSS was designed to obtain a large and homogeneous sample of SLSNe out to a redshift of $z \sim 3$ using DECam. In order to fully capture such slowly evolving SLSNe, SUDSS was required to have a long observing season of 8-9 months per field, approximately a factor of two longer than the nominal DES
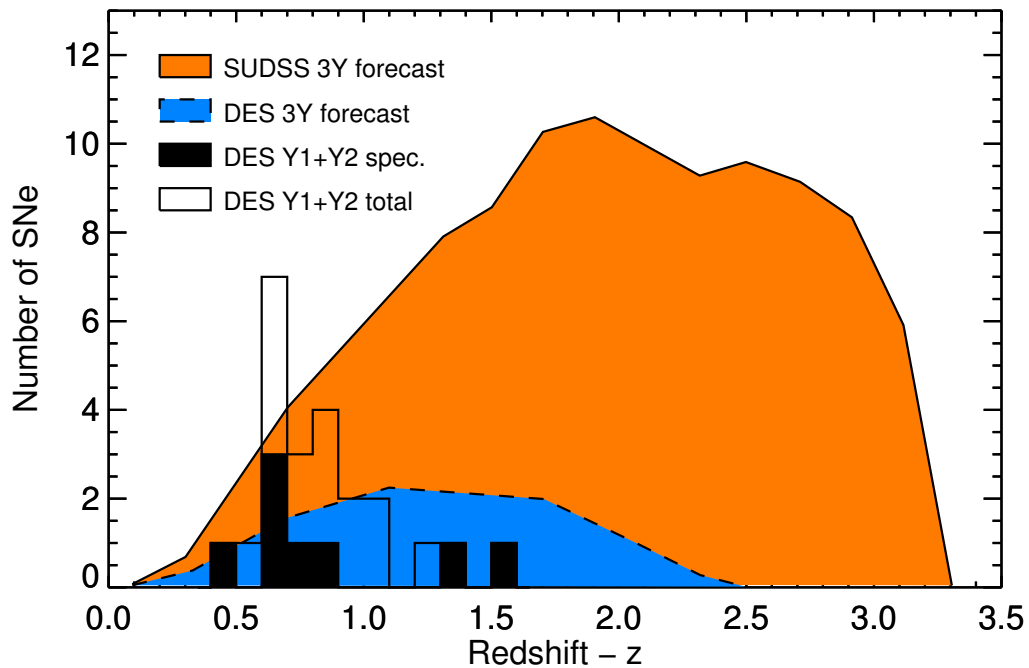
Figure 6.1: The redshift histogram (N(z)) of SLSNe from SUDSS, all in bins of 0.2 in redshift. The orange area shows the simulated N(z) from SUDSS after three years of operations, the blue area shows the simulated N(z) from DES after three years of operations, the uncoloured histogram shows the distribution of our 23 SLSNe candidates from DES Y1+Y2, and the black area shows the redshift distribution of the 8 spectroscopically confirmed SLSNe from DES Y1+Y2.

SN Survey. Likewise, we determined that we could reduce the cadence for observing such long-lived light curves and decided that 15 days was sufficient to give homogeneous, complete light curves.

SUDSS is now under-way and Fig. 6.1 shows the expected performance of this new survey after three full years. This figure was created by assuming the SLSNe rates reported by Quimby et al. (2013b); Cooke et al. (2012) and the SUDSS observing strategy as discussed above (assuming an exposure time that is midway between the DES shallow and deep fields). In Fig. 6.1, we show the redshift distribution of SLSNe using SUDSS+DES (orange) and DES alone (blue). For comparison, I also show the redshift distributions of known DES SLSNe as presented in this thesis. Overall, SUDSS should detect ~ 200 SLSNe (of all types) out to $z \sim 2.5$, which is approximately a factor of 5 more SLSNe than DES alone.

I am a member of SUDSS and helped create the first DECam observing script files, for the first SUDSS observing run in 2013. These scripts define exposure sequences, including controlling the telescope and instrument parameters (e.g. filter changes, exposure

times, etc). I was also twice a SUDSS observer (16th of April and 8th of May 2014), and both runs were successfully.

In Fig. 6.2, I show an updated light curve of DES14X3taz, which was discovered and confirmed as a SLSN in DES Y2 (see Chap. 5). The original DES data (circles) used to detect the early light curve of the SN is shown, including the pre-peak bump discussed in Chap. 5. This figure also shows the additional SUDSS photometry (triangles), which extends the light curve to second peak, confirming DES14X3taz as a SLSN. Therefore SUDSS will not only discover more SLSNe, but will also improve the light curves of existing SLSNe in DES. A comparison between the number of discovered SLSNe within this thesis and the number of historical SLSNe, as they were presented in Chap. 2, suggests that by the end of DES in 2018, the synergy of SUDSS and DES SN program would be a leading factor in the research of SLSNe. Furthermore, the increase of the number of SLSNe with high quality data, good light-curve coverage and extensive spectroscopic follow-up is a necessity for the near future, in order to understand the underlying physical mechanism that powers SLSNe and to explore thoroughly the possibility of using them as 'standard candles'.
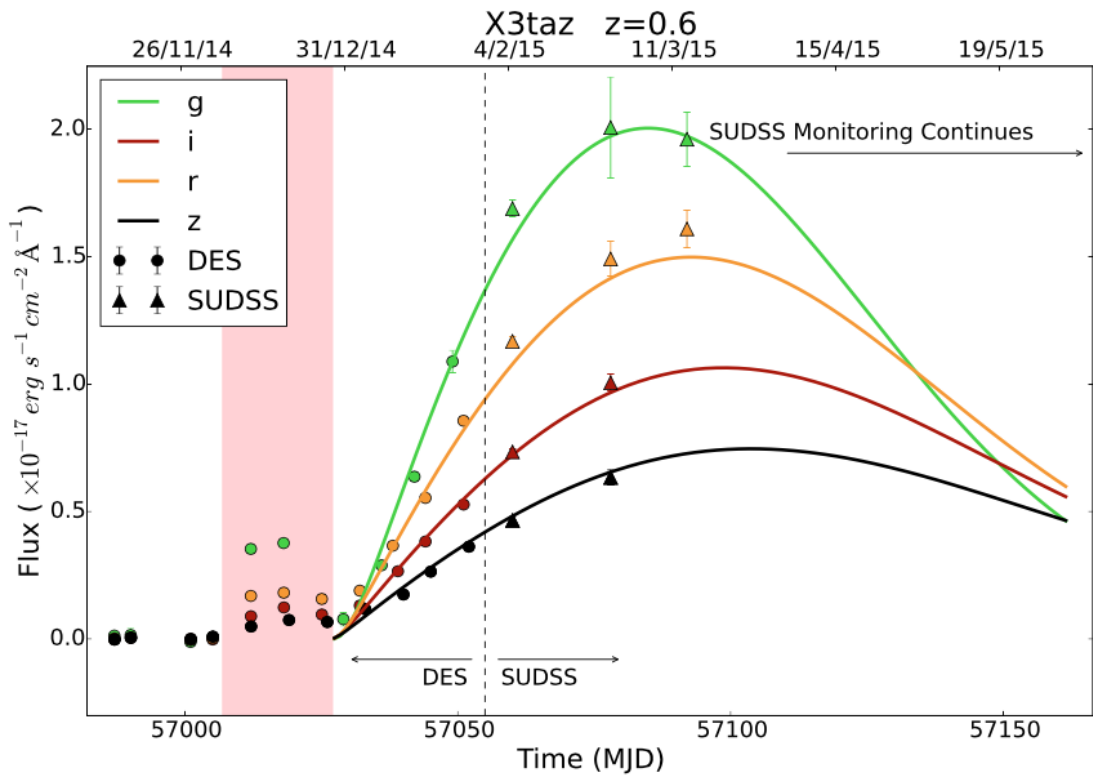
Figure 6.2: Example of SUDSS (triangles) and DES (circles) $griz$ flux light-curves illustrating the power of SUDSS. Where over-plotted, the solid line is the magnetar model fitted-curves (*Created by PhD student, Szymon Prajs*). DES14X3taz has a puzzling and unexplained 'bump' in the light curve prior to the rise of the main light curve, highlighted by the red band. Without SUDSS, the peak of the light curve would not be observed. *Plot created by Dr. Mark Sullivan*.

Appendix A

Examples of Transients Discovered in DES Y2

This appendix presents 9 examples of DES transients discovered during Y2 which passed the first visual inspection process, described in Sec.5.4.2. Those 9 examples are constructed by three transients from the three main categories of results of this first visual inspection: SLSNe candidates (Fig. A.1), AGN/QSO (Fig. A.2) and 'normal SNe type' (Fig. A.3).

The 9 visual inspection panels shown here, similar to Fig. 5.7, consist of four plot panels each. *Top-left panel:* Apparent magnitude light-curve of a SLSNe candidate as a function of the observed phase from peak brightness. The solid horizontal lines represent the host galaxy magnitudes in $griz$ filters, whereas the dotted vertical lines show the first of each calendar month, serving as a ~ 30 days ruler. For each spectrum that was obtained, the name of the relative telescope and the spectrum date are marked with a cross. *Top-middle panel:* Absolute peak magnitude-M_{griz} (equation 1.28) versus host z_{photo} or z_{spec}. The solid, dashed and dotted black lines show the absolute magnitude of $M = [-21.0, -20.5, -20.0]$ respectively. *Top-right panel:* A colour-magnitude diagram used for detection of gravitational lensed SNe Ia (Quimby et al., 2014, see also Sec. 1.6). The colour evolution with the observed phase follows the colour-bar under the plot. The black crooked-line divides the diagram into unlensed (left) and possibly lensed (right) SNe Ia. The open blue star marks the values corresponding to PS1-10afx (Chornock et al., 2013; Quimby et al., 2013a), a lensed SNe Ia. *Bottom-left panel:* Mutli-colour evolution plot of the transient created by using spline interpolation (IDL) on the data from the magnitude light-curve on top.
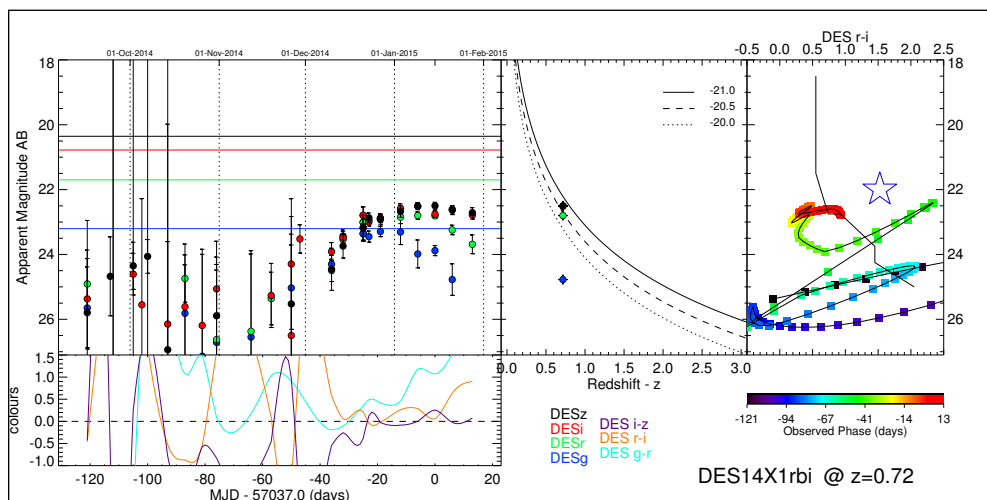
Also this appendix presents colour-colour plots of both SLSNe and 'normal SNe types', that were discussed in Sec. 5.4.2. For each of the six SNe examples presented
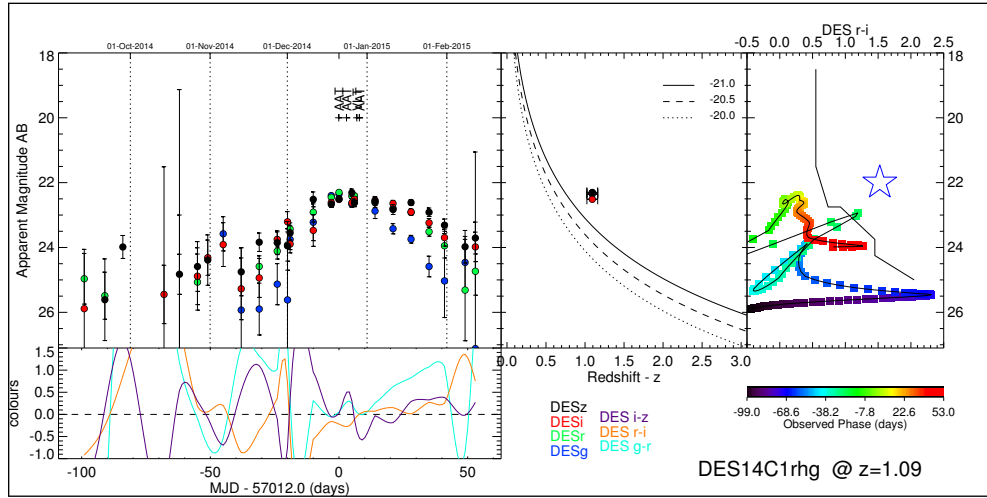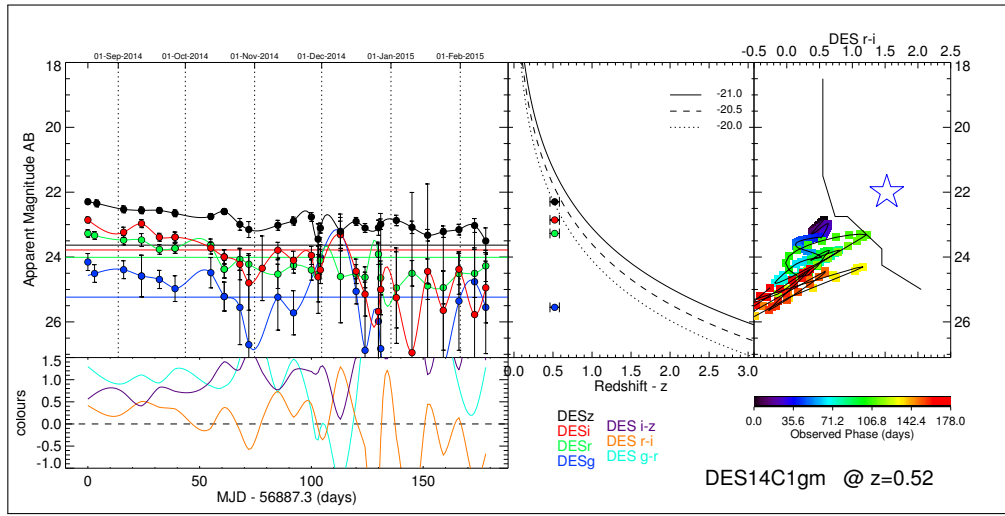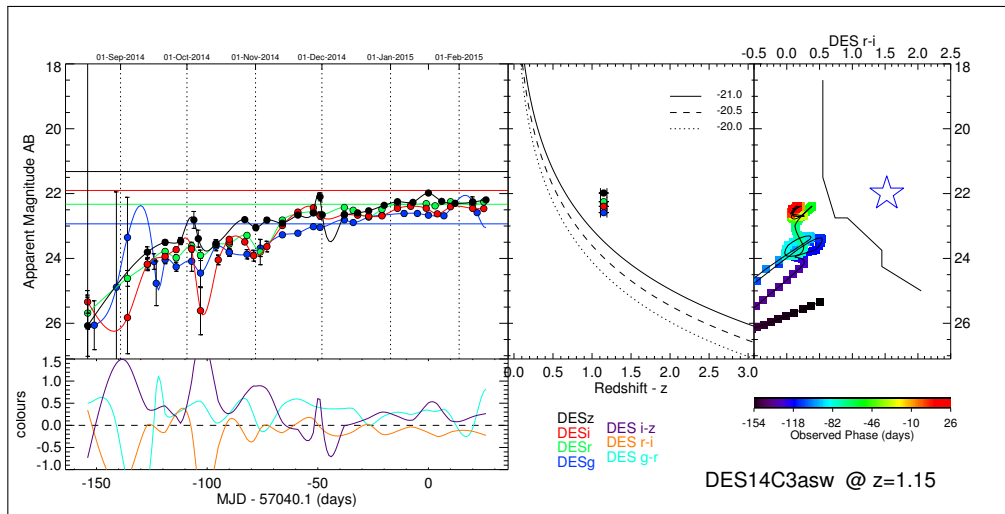
(a) DES14C1rhg
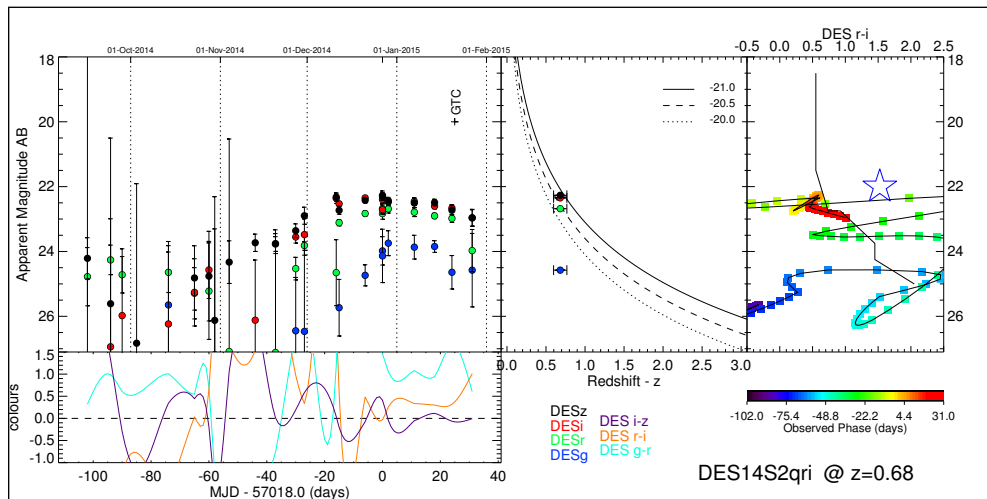
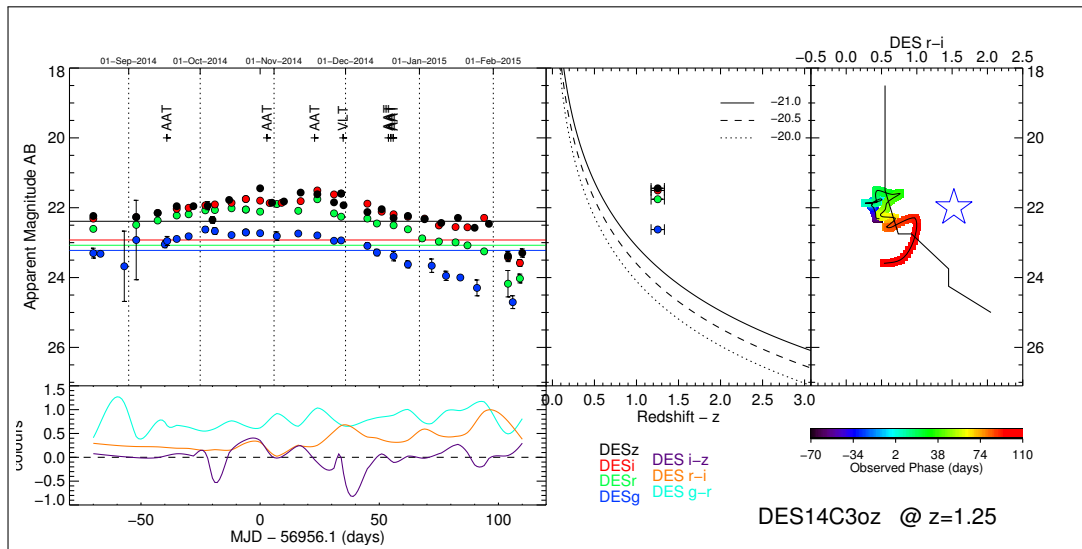

(b) DES14S2qri

(c) DES14X1rbi

Figure A.1: The visual inspection panels used in DES Y2, similar to Fig. 5.7, for three examples of SLSNe candidates.
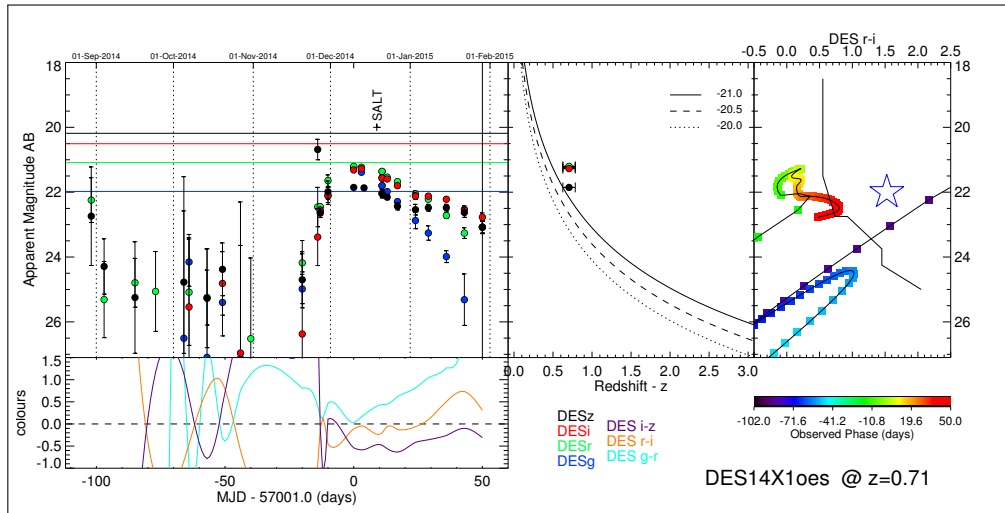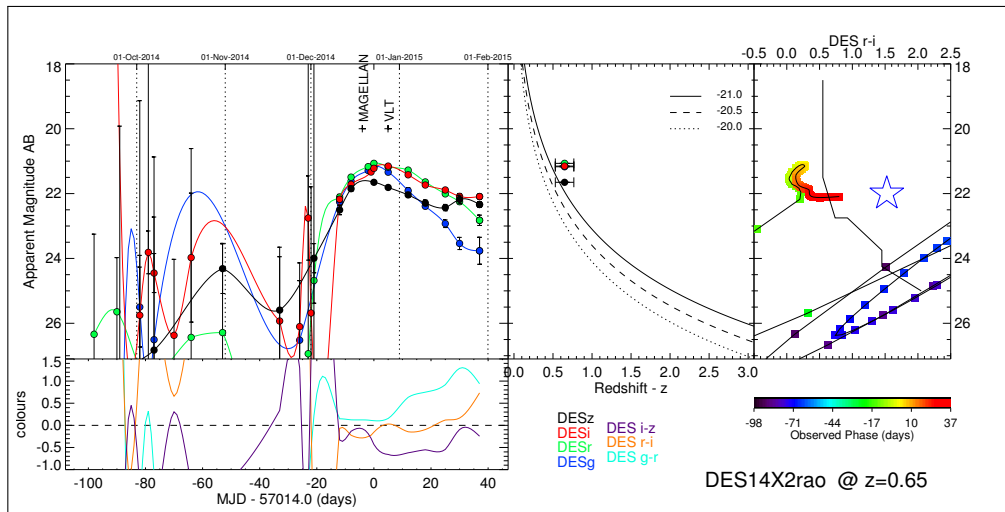
(a) DES14C1gm

(b) DES14C3asw
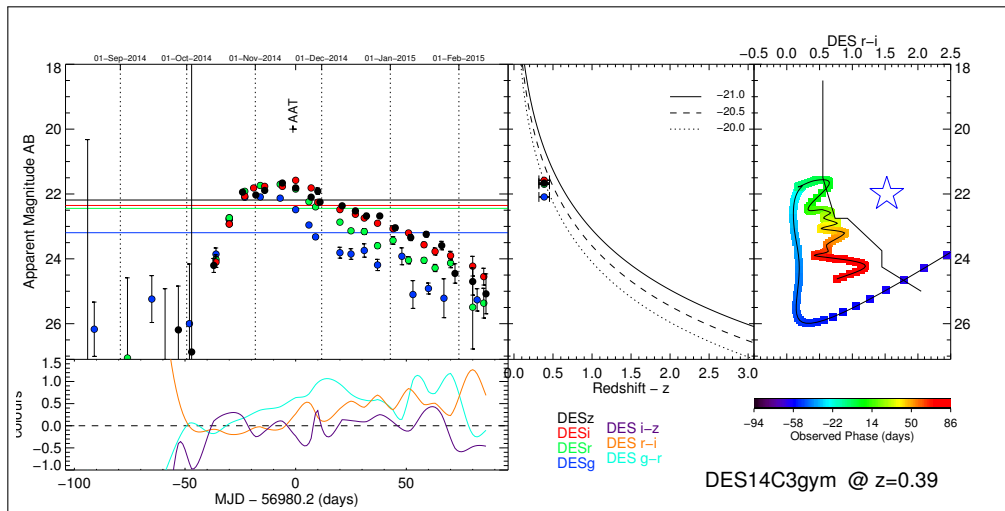

(c) DES14C3oz

Figure A.2: The visual inspection panels used in DES Y2, similar to Fig. 5.7, for three AGN/QSOs examples.
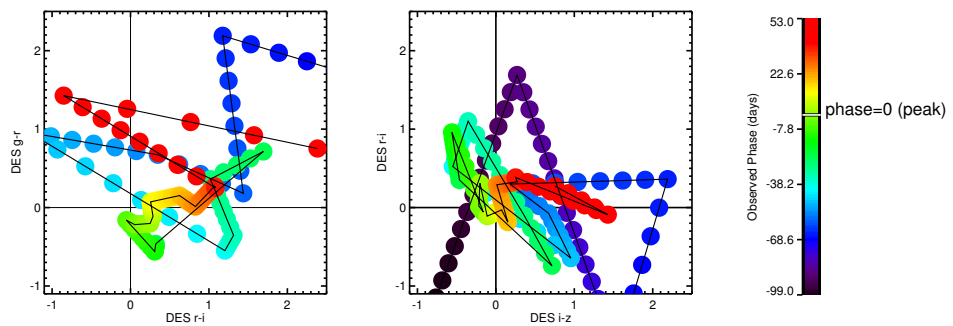
(a) DES14X1oes

(b) DES14X2rao

(c) DES14C3gym

Figure A.3: The visual inspection panels used in DES Y2, similar to Fig. 5.7, for three 'normal SNe' examples.

here, two panels show the DES *r-i* versus *g-r* and *i-z* versus *r-i* colour-colour space evolution, with the phase of each data point to be represented by the colour bar on the right hand side of the two plots. The comparison of the six plots, suggests that the SLSNe do not uniquely occupy a certain part of the colour-colour space, thus such tools were not used as a SLSNe identification method at the time. On the other hand, a larger sample of SLSNe with better light-curve data coverage could be used in the future to explore the use of colour-colour parameters as SLSNe selection tool.
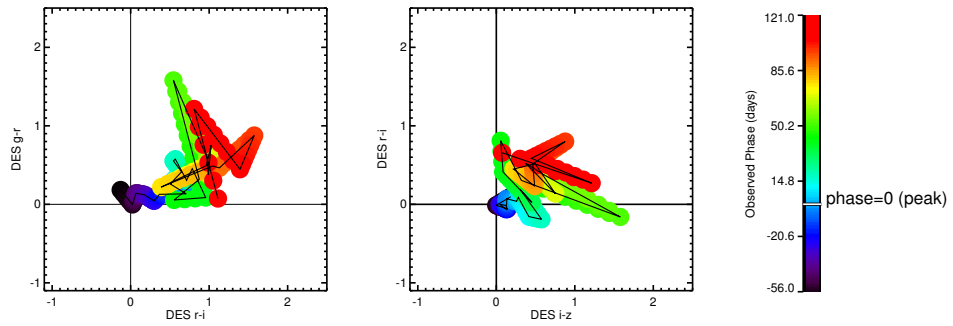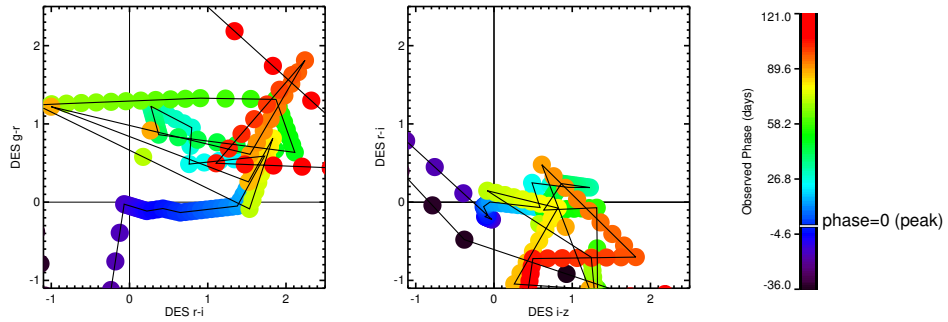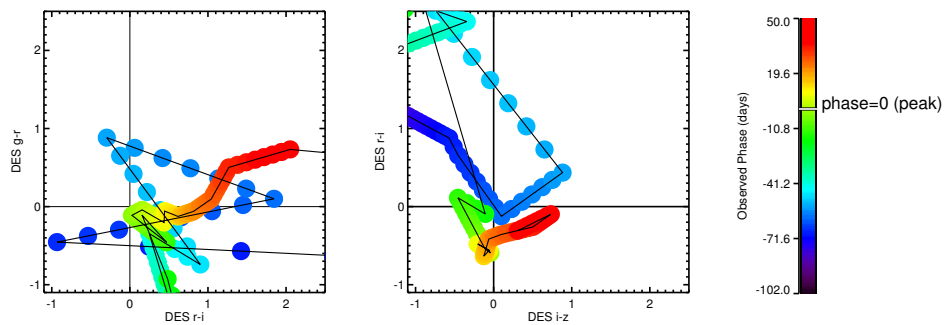
(a) DES14C1fi

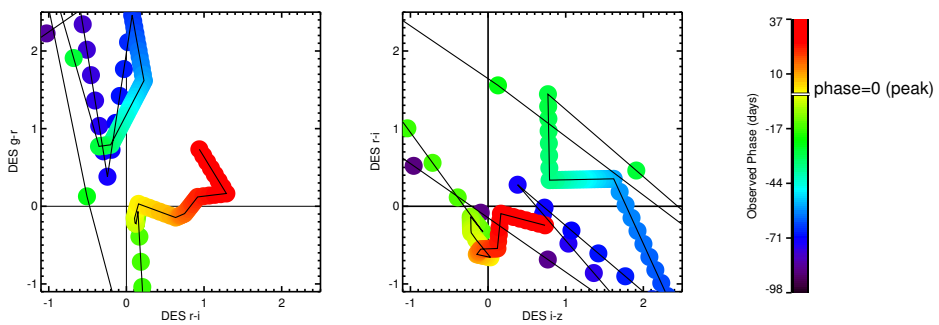
(b) DES14C1rhg
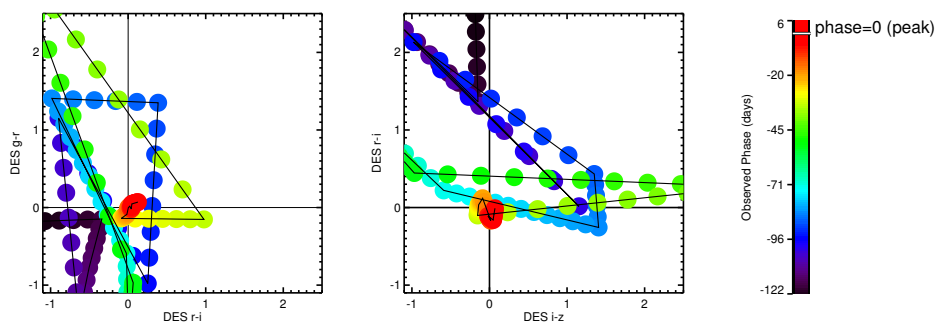
(c) DES14E2slp

Figure A.4: Colour-colour plots of three SLSNe, where the phase evolution is colour-coded based on the colour bar on the right-hand-side. *Left:* DES *r-i* versus *g-r* plot. *Right:* DES *i-z* versus *r-i* plot.

(a) DES14S2boa

(b) DES14X1oes

(c) DES14X2roa

Figure A.5: Colour-colour plots of three SNe Ia, where the phase evolution is colour-coded based on the colour bar on the right-hand-side. *Left:* DES *r-i* versus *g-r* plot. *Right:* DES *i-z* versus *r-i*

.

Appendix B

Images of SLSNe

This Appendix contains images of the sky area around the 7 spectroscopically confirmed SLSNe discovered in DES Y2 and listed in Table 5.8, presented in three different ways. For DES14C1fi, Fig. B.1 shows a finder chart created automatically by the ATC web application (Fig. 5.12), consisting of helpful information for any observer who wants to construct spectroscopic follow-up observations.

For DES14X2byo, DES14S2qri and DES14X3taz, Fig. B.2, B.3 and B.4 respectively, show colour triplet images of the surrounding sky areas. Those images were created using SAOIMAGE DS9[1] software and image products provided by the DESDM group.

Finally, Fig. B.5, B.6 and B.7 illustrate the 'postage-stamps' triplets in separate filters for DES14C1rhg, DES14E2slp and DES14E2ap respectively, as generated by the 'candidate-page' (Fig. 5.11).

The order of appearance of the plots in this Appendix follows the order of presentation in Sec. 5.6.

---

[1]http://ds9.si.edu/site/Home.html

DES14C1fi (22.3)
03:33:49.795 -27:03:31.61

◇ (host)	03:33:49.748 -27:03:31.45
Offset (arcsec)	0.6
P.A. from Target (degrees)	284.2
E/W *from* Target (arcsec)	0.6 W
N/S *from* Target (arcsec)	0.2 N
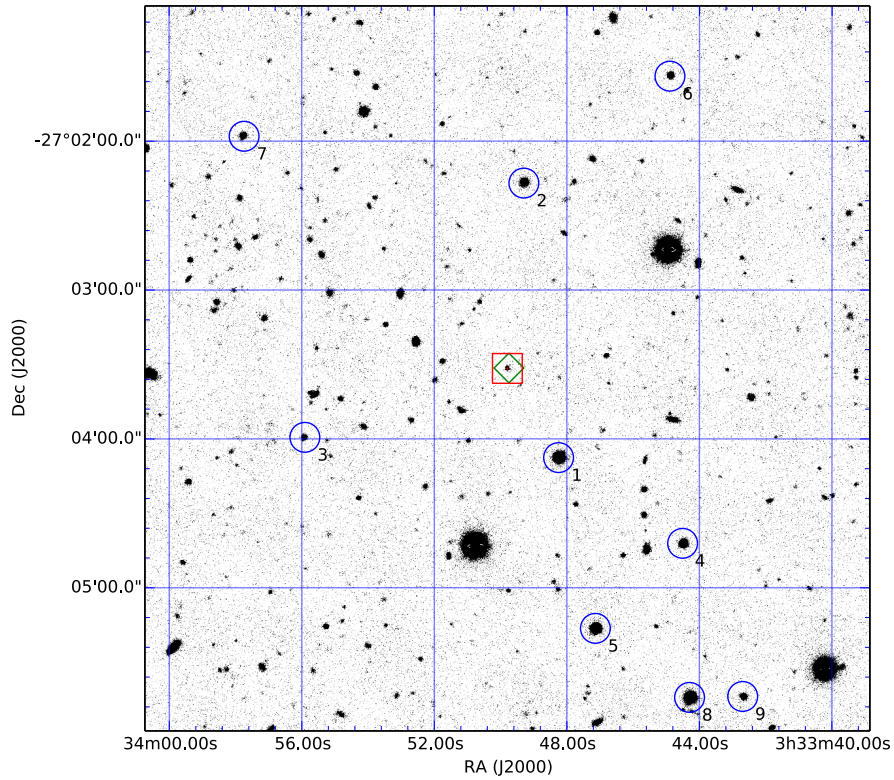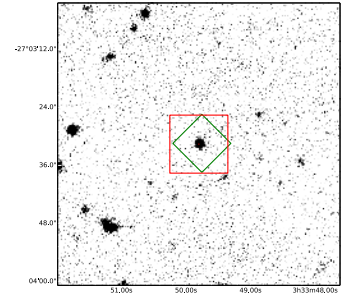
Label	Mag.	R.A.	Dec.	Offset (arcsec)	P.A. from Target (degrees)	E/W to Target (arcsec)	N/S to Target (arcsec)
1	17.3	03:33:48.250	-27:04:07.55	41.5	209.9	20.6 E	35.9 N
2	18.8	03:33:49.297	-27:02:16.91	75.0	354.9	6.7 E	74.7 S
3	20.7	03:33:55.906	-27:03:59.38	86.2	108.8	81.6 W	27.8 N
4	18.6	03:33:44.507	-27:04:42.11	99.8	225.1	70.6 E	70.5 N
5	17.6	03:33:47.139	-27:05:16.39	110.6	198.7	35.5 E	104.8 N
6	19.9	03:33:44.891	-27:01:33.81	134.8	330.9	65.5 E	117.8 S
7	20.0	03:33:57.738	-27:01:58.03	141.5	48.6	106.1 W	93.6 S
8	17.1	03:33:44.296	-27:05:44.21	151.6	209.0	73.4 E	132.6 N
9	19.8	03:33:42.691	-27:05:43.82	162.7	215.7	94.9 E	132.2 N

Figure B.1: Finder chart for targeting **DES14C1fi** (red square) and its host galaxy (green diamond), with information on the location of the target of interest, as well as on the nine surrounding pointing stars (blue circles). The ATC web application (Fig. 5.12) automatically generates a finder chart for each DES transient.
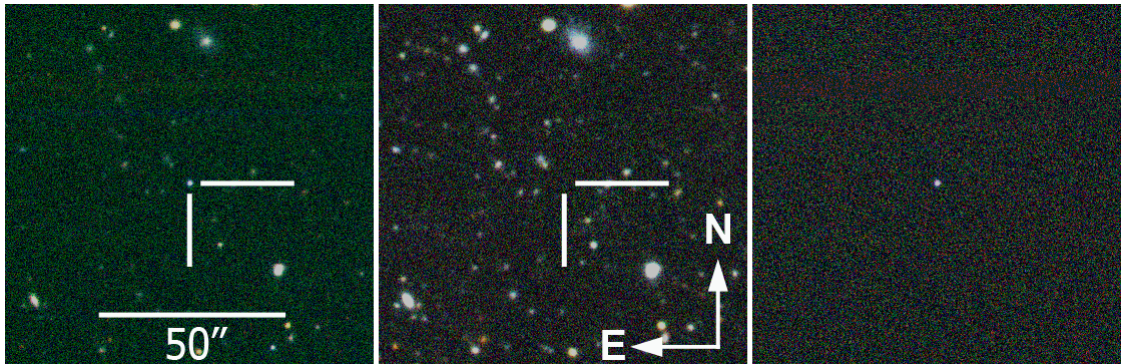
Figure B.2: Colour images (riz) of the sky area around **DES14X2byo**. *Left:* The search image was taken close to peak brightness (1-November-2014), with DES14X2byo in the centre. *Centre:* The deep template image of the same sky area, showing no signs of a host galaxy associated with the transient. *Right:* The difference of the two previous images, clearly identifying DES14X2byo at the centre.
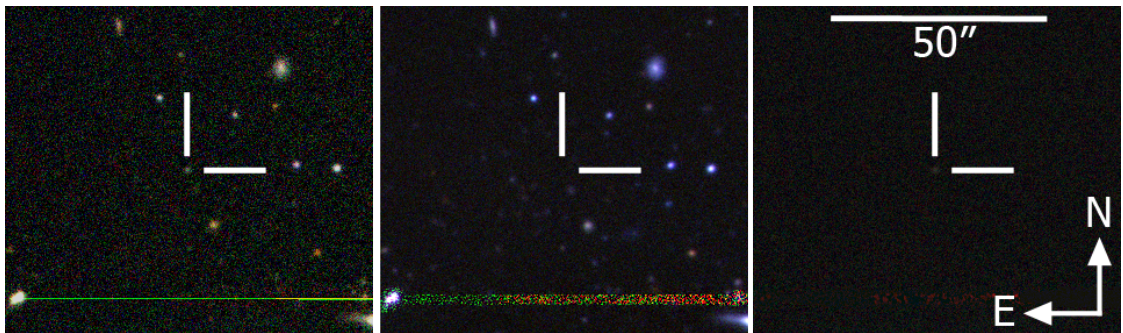

Figure B.3: Colour images (riz) of the sky area around **DES14S2qri**. *Left:* The search image was taken close to peak brightness (late-December 2014), with DES14S2qri in the centre. *Centre:* The deep template image of the same sky area, showing no signs of a host galaxy associated with the transient. *Right:* The difference of the two previous images, identifying the faint trace of DES14S2qri at the image centre.

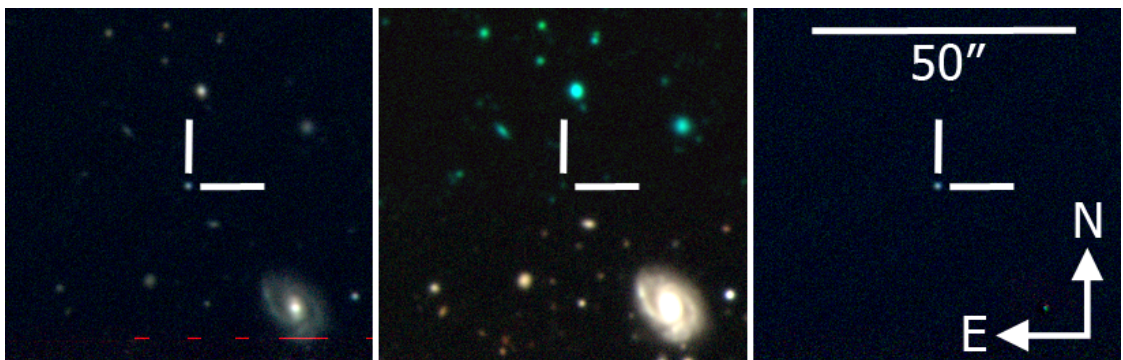Figure B.4: Colour images (riz) of the sky area around **DES14X3taz**. *Left:* The search image was taken close to peak brightness (1-November-2014), with DES14X3taz in the centre. *Centre:* The deep template image of the same sky area, showing no signs of a host galaxy associated with the transient. *Right:* The difference of the two previous images, clearly identifying DES14X3taz at centre.
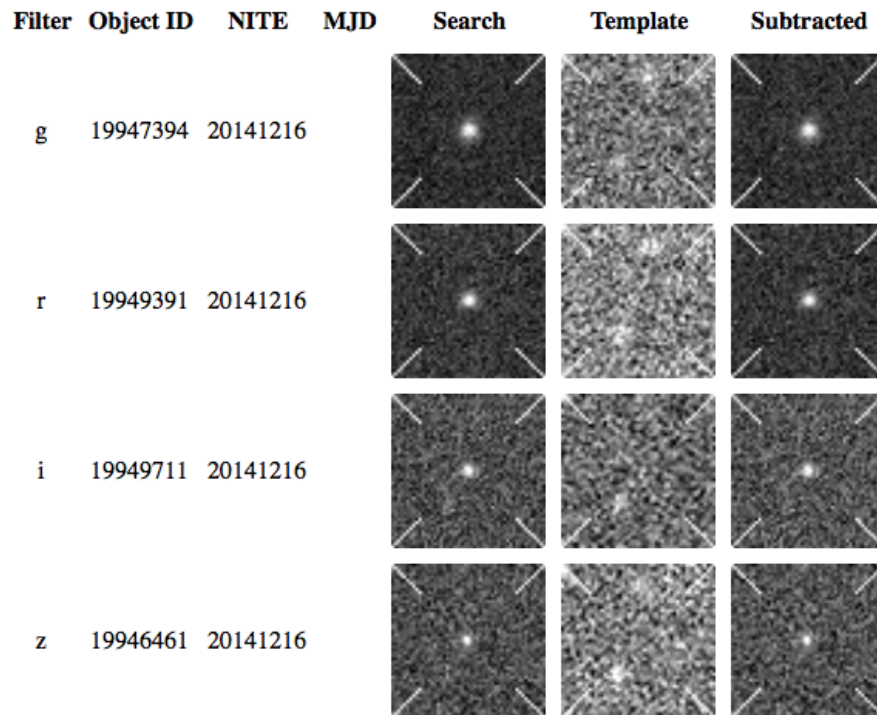
Filter	Object ID	NITE	Search	Template	Subtracted
g	19947394	20141216			
r	19949391	20141216			
i	19949711	20141216			
z	19946461	20141216			

Figure B.5: Multi-filter postage-stamps from the first detection of **DES14C1rhg** on the 17th of August 2014. The 'postage stamps' are centred on DES14C1rhg.

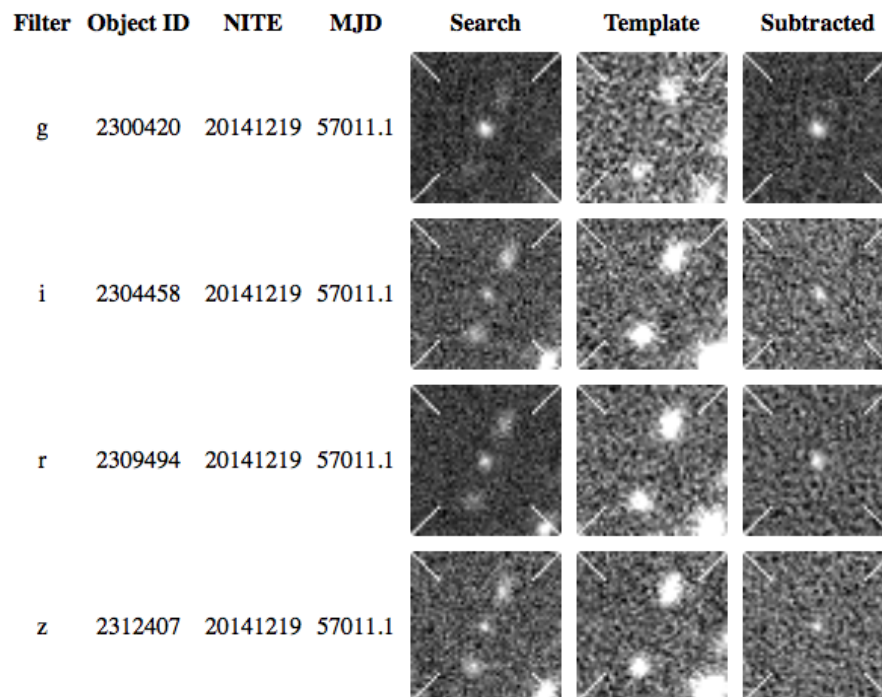| Filter	Object ID	NITE	MJD	Search	Template	Subtracted
g	2300420	20141219	57011.1			
i	2304458	20141219	57011.1			
r	2309494	20141219	57011.1			
z	2312407	20141219	57011.1			

Figure B.6: Multi-filter postage-stamps from the first detection of **DES14E2slp** on the 19th of December 2014. The 'postage stamps' are centred on DES14E2slp, and in the search and template images the two closest host can be seen in opposite positions from the transient.
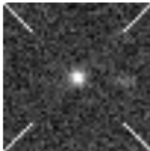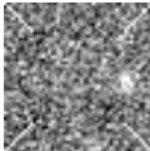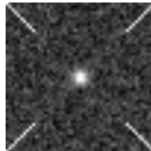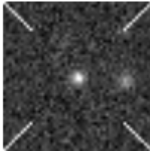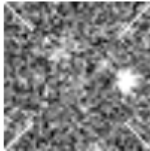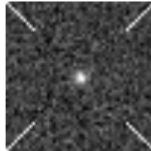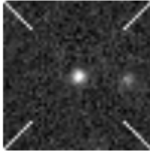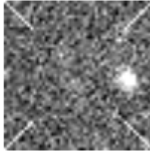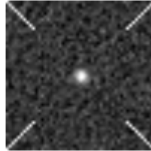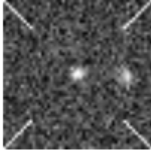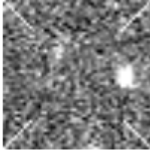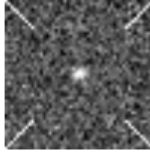
Filter	Object ID	NITE	MJD	Search	Template	Subtracted
g	76188	20140817	56887.2			
i	80339	20140817	56887.2			
r	77891	20140817	56887.2			
z	149913	20140817	56887.2			

Figure B.7: Multi-filter postage-stamps from the first detection of **DES14E2ap** on the 17th of August 2014. The 'postage stamps' are centred on DES14E2ap.

Appendix C

Construction of the bolometric light-curves

This appendix presents the blackbody SED fits and the derived bolometric light-curves of the SLSNe sample discovered in Y2 (table C.1), for completeness of section 5.7.

For each of the SLSNe in table C.1 we show two separate plots: one multi-panel plot that contains all the blackbody SED fits to each epoch observed, and one plot that contains three panels with the observed phase evolution of the temperature and radius of the fitted blackbody and of the subsequent bolometric luminosity.

Table C.1: The final selection list of 22 SLSNe from DES Y2. The table is divided by horizontal lines in three parts: SLSNe that were spectroscopically confirmed, those that were classified by the use of their host z_{spec} and the events of which the host z_{photo} were used for the classification.

#	Name	M_g	M_r	M_i	M_z	Redshift			host separ.(")	Host galaxy				Comments
						SNe	host z_{photo}	host z_{spect}		m_g	m_r	m_i	m_z	
1	DES14S2qri	-21.50	-22.51	-22.84	-22.92	1.500			4.97	24.28	25.41	23.72	24.47	SLSN-I
2	DES14X2byo	-22.19	-23.64	-22.34	-22.98	0.869			8.77	23.18	22.52	22.27	22.37	SLSN-I
3	DES14E2slp	-21.22	-21.27	-21.32	-21.29	0.640	0.550 ± 0.031		3.93	23.50	22.57	22.20	22.06	SLSN-I
4	DES14E2ap	-20.17	-20.49	-20.42	-20.43	0.600			4.26	24.80	23.23	22.85	22.52	SLSN-I
5	DES14X3taz	-21.15	-21.52	-21.41	-21.36	0.600	0.747 ± 0.079		0.15	26.25	25.13	24.99	25.04	SLSN-I
6	DES14C1rhg	-19.74	-19.80	-19.59	-19.79	0.470			2.97	99.00	26.98	25.87	24.41	SLSN-I
7	DES14C1fi	-22.52	-22.58	-22.75	-22.74		1.191 ± 0.085	1.3 (VLT)	0.64	24.93	24.64	24.59	23.61	SLSN-II
8	DES14X1rbi	-19.92	-20.69	-20.70	-20.71		0.689 ± 0.033	0.717 (VIPERS)	2.14	23.20	21.70	20.78	20.36	SLSN
9	DES14S1ewv	-22.12	-21.98	-22.01	-22.43		1.230 ± 0.085		0.66	22.69	22.53	22.33	21.88	
10	DES14E1rpi	-20.92	-20.97	-21.32	-22.10		1.048 ± 0.066		1.81	24.85	23.77	23.31	22.50	
11	DES14C3nn	-20.89	-21.01	-21.54	-21.29		1.026 ± 0.081		2.30	24.70	24.45	24.02	23.65	
12	DES14E2bhn	-20.41	-21.09	-22.07	-21.23		0.973 ± 0.072	pending (OzDES)	2.44	23.24	22.95	22.51	22.26	
13	DES14X3gyr	-19.88	-19.81	-20.41	-21.29		0.948 ± 0.049	pending (OzDES)	0.87	23.97	23.10	22.08	21.61	
14	DES14X1avd	-20.87	-20.46	-20.97	-21.86		0.835 ± 0.031		10.22	23.39	22.74	22.10	21.86	
15	DES14X3mjf	-20.55	-20.03	-20.50	-20.44		0.829 ± 0.066	pending (OzDES)	0.38	24.05	23.61	23.19	23.06	
16	DES14C1ngk	-19.44	-20.95	-20.46	-20.84		0.813 ± 0.033	pending (OzDES)	1.03	22.83	21.84	20.89	20.53	
17	DES14C3tny	-26.89	-20.41	-20.23	-20.90		0.788 ± 0.082		0.45	25.72	25.13	24.70	24.43	
18	DES14C1fs	-21.97	-20.59	-20.94	-21.18		0.744 ± 0.050		0.82	24.70	24.00	23.32	23.29	
19	DES14E1lgl	-19.38	-20.10	-20.03	-19.91		0.673 ± 0.033		6.60	23.35	22.44	21.94	21.70	
20	DES14X1brr	-20.42	-20.63	-20.51	-20.46		0.651 ± 0.060	pending (OzDES)	0.97	24.96	24.03	23.73	23.52	
21	DES14X1ps	-20.88	-21.31	-21.29	-21.51		0.610 ± 0.085	pending (OzDES)	0.48	24.63	24.52	24.53	24.93	
22	DES14E1hk	-20.31	-20.91	-20.83	-20.73		0.531 ± 0.045	pending (OzDES)	0.94	23.76	22.48	21.98	21.56	

Figure C.1: Blackbody fits (*dashed lines*) to the 26 observed epochs of the DES multi-band photometry (*coloured squares*) for the SLSNe DES14X2byo. The legend of each panel states the observed phase-t in days from peak magnitude, and the blackbody best-fit parameters: temperature-$T(^oK)$ and radius-$R(R_0 = 10^{15}cm)$.

Figure C.2: *Top panel:* The bolometric light-curve of DES14X2byo in units of $10^{43} \, erg/s$ as a function of the observed phase. *Middle panel:* The temperature evolution with the observed phase, as obtained by the best-fit blackbody SED on the photometry of each epoch. *Bottom panel:* The radius evolution with the observed phase, also obtained by the best-fit blackbody SEDs, in units of $10^{15} \, cm$

.

Figure C.3: Blackbody fits (*dashed lines*) to the 26 observed epochs of the DES multi-band photometry (*coloured squares*) for the SLSNe DES14S2qri. The legend of each panel states the observed phase-t in days from peak magnitude, and the blackbody best-fit parameters: temperature-$T(^oK)$ and radius-$R(R_0 = 10^{15}cm)$.

Figure C.4: *Top panel:* The bolometric light-curve of DES14S2qri in units of $10^{43}\ erg/s$ as a function of the observed phase. *Middle panel:* The temperature evolution with the observed phase, as obtained by the best-fit blackbody SED on the photometry of each epoch. *Bottom panel:* The radius evolution with the observed phase, also obtained by the best-fit blackbody SEDs, in units of $10^{15}\ cm$

.
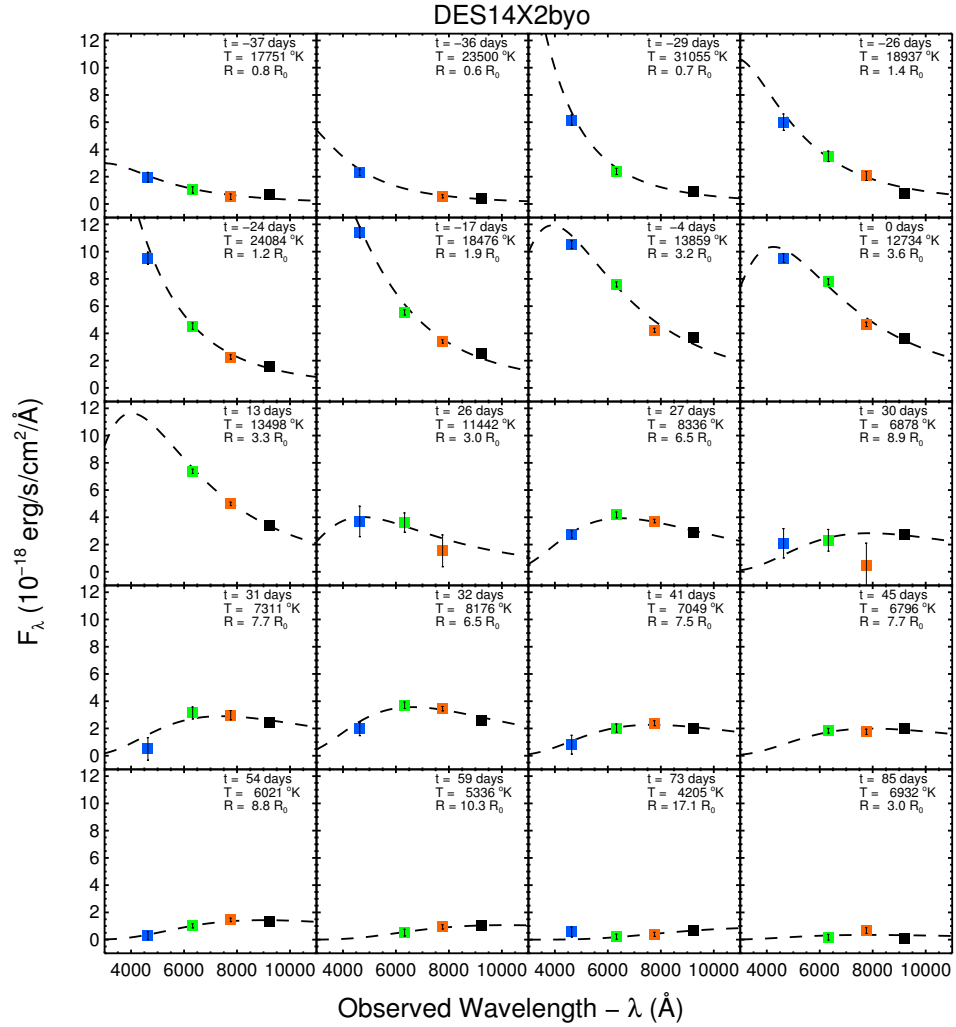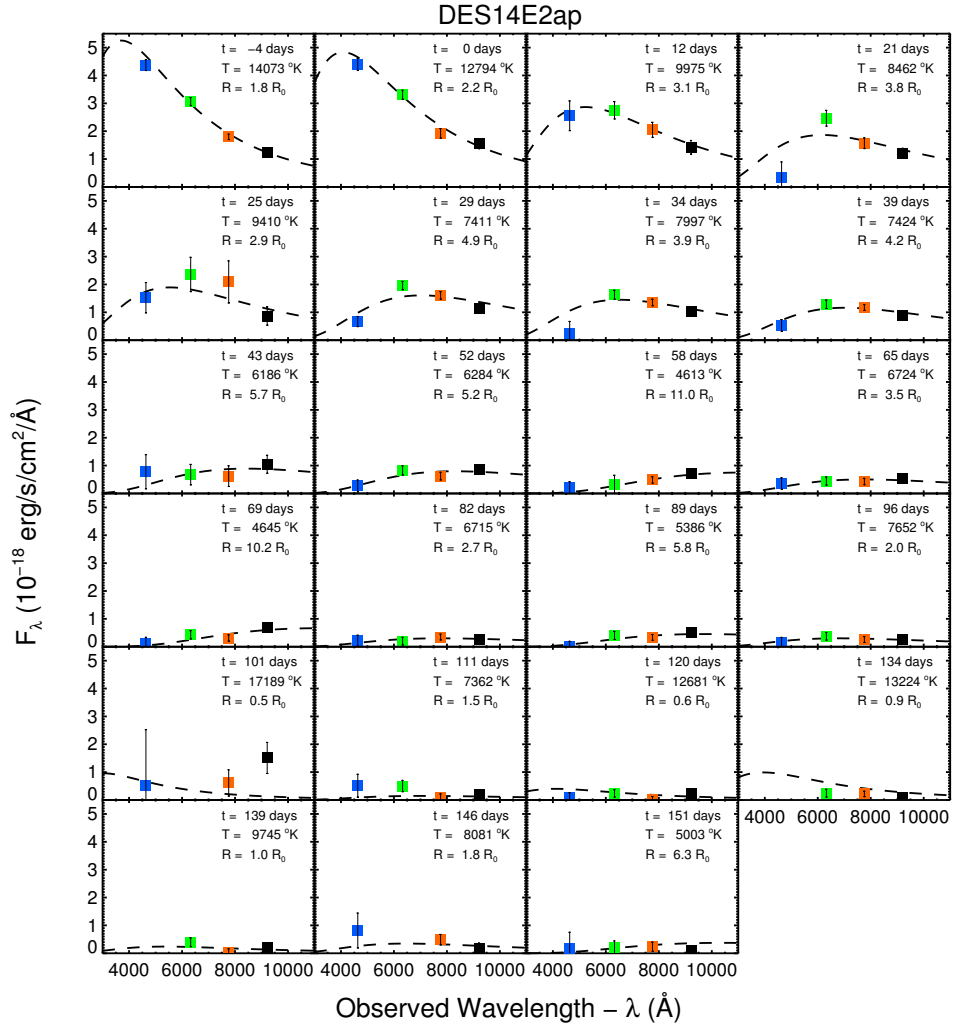
Figure C.5: Blackbody fits (*dashed lines*) to the 26 observed epochs of the DES multi-band photometry (*coloured squares*) for the SLSNe DES14E2ap. The legend of each panel states the observed phase-t in days from peak magnitude, and the blackbody best-fit parameters: temperature-$T(^oK)$ and radius-$R(R_0 = 10^{15}cm)$.
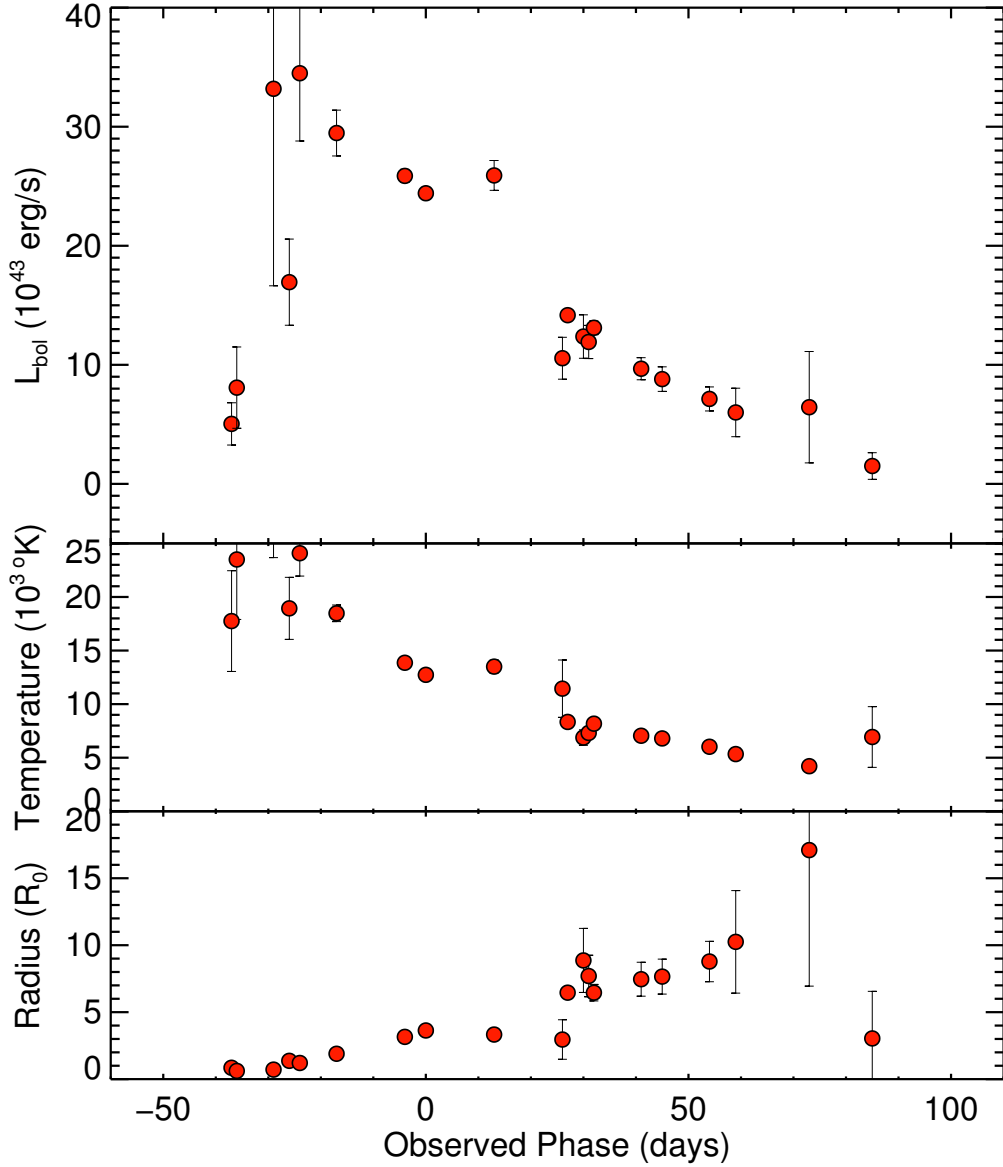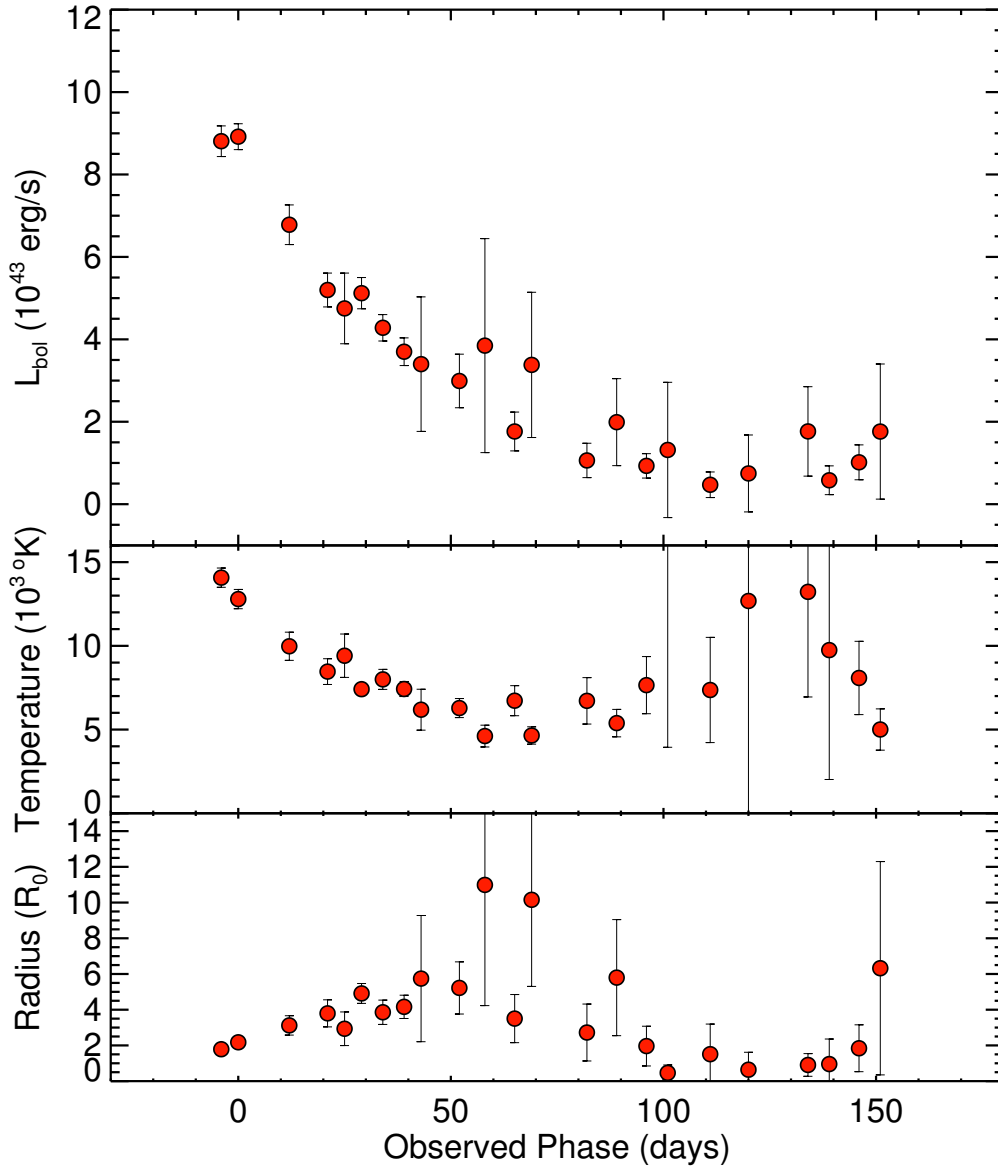
Figure C.6: *Top panel:* The bolometric light-curve of DES14E2ap in units of $10^{43}\ erg/s$ as a function of the observed phase. *Middle panel:* The temperature evolution with the observed phase, as obtained by the best-fit blackbody SED on the photometry of each epoch. *Bottom panel:* The radius evolution with the observed phase, also obtained by the best-fit blackbody SEDs, in units of $10^{15}\ cm$
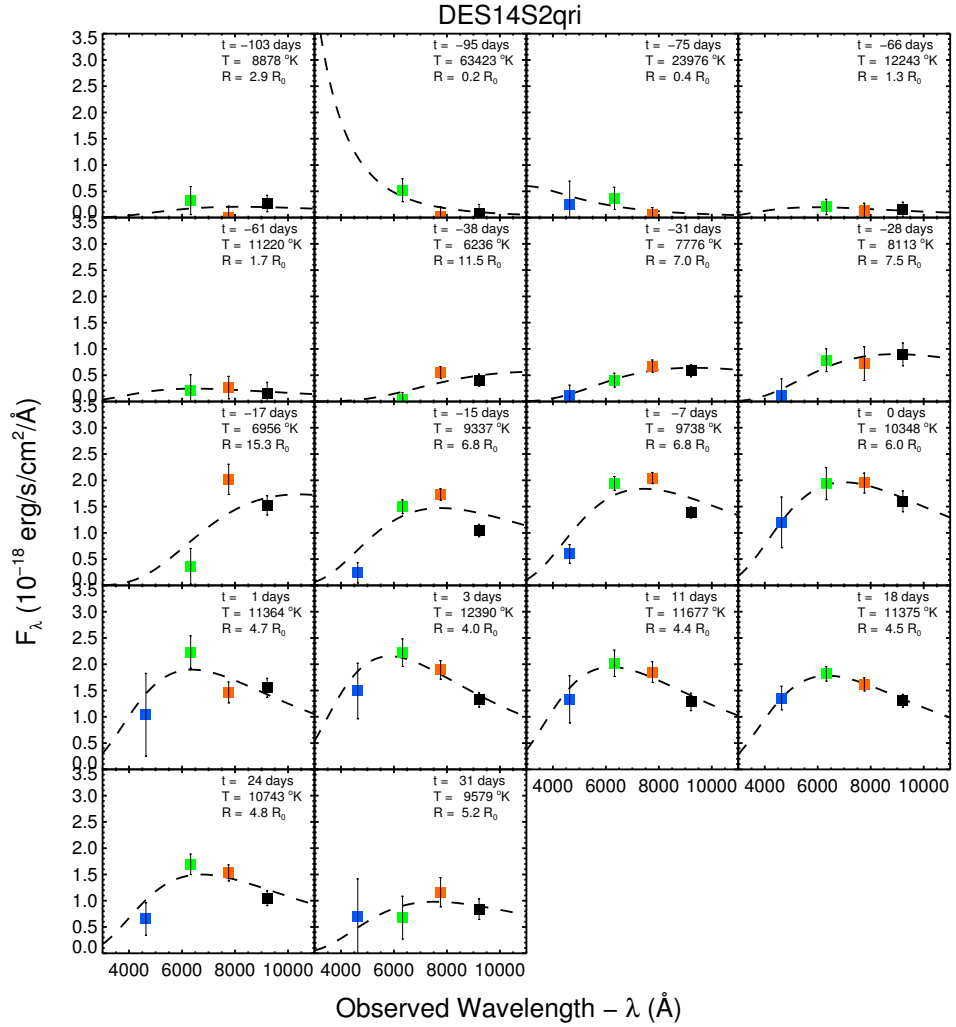
.
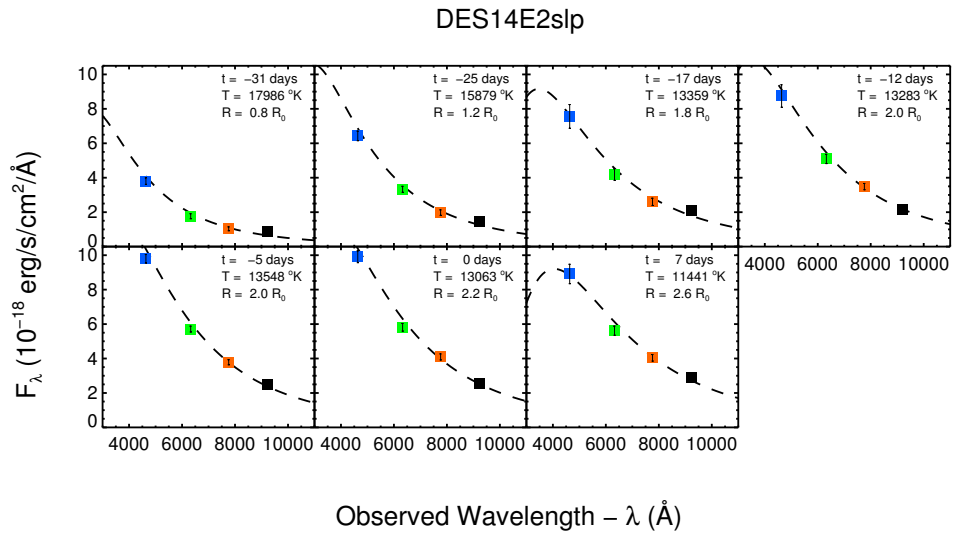
Figure C.7: Blackbody fits (*dashed lines*) to the 26 observed epochs of the DES multi-band photometry (*coloured squares*) for the SLSNe DES14E2slp. The legend of each panel states the observed phase-t in days from peak magnitude, and the blackbody best-fit parameters: temperature-$T(^oK)$ and radius-$R(R_0 = 10^{15} cm)$.
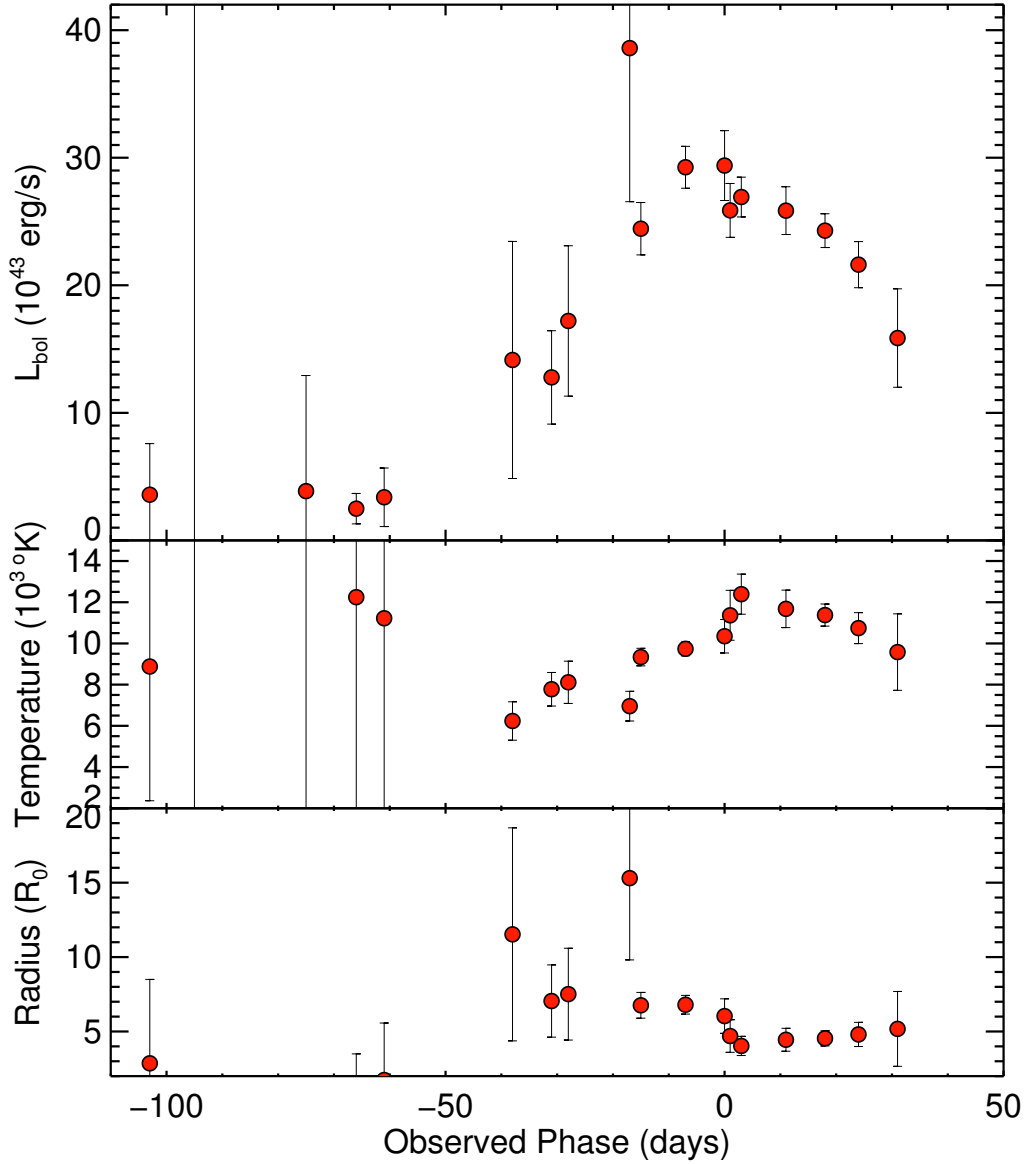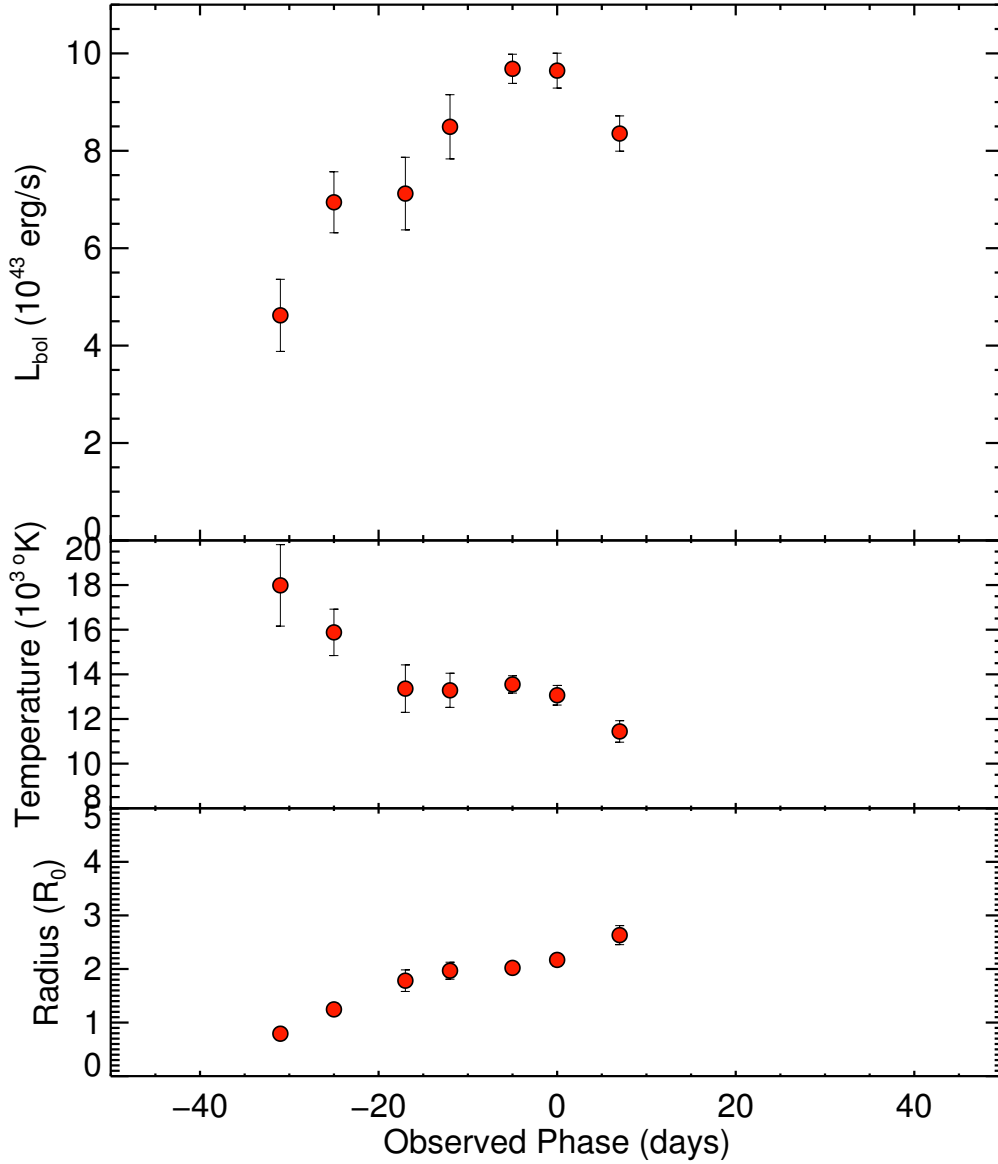
Figure C.8: *Top panel:* The bolometric light-curve of DES14E2slp in units of $10^{43}\,erg/s$ as a function of the observed phase. *Middle panel:* The temperature evolution with the observed phase, as obtained by the best-fit blackbody SED on the photometry of each epoch. *Bottom panel:* The radius evolution with the observed phase, also obtained by the best-fit blackbody SEDs, in units of $10^{15}\,cm$

.

Appendix D

Model fits of the bolometric light-curves

For completeness of Sec. 5.7.2, this appendix consist of the plots of the power source models fits to the bolometric light-curves of all the 22 SLSNe discovered during DES Y2, as listed in Table 5.8.

The plots' order of appearance follows the listing order in Table 5.8, which we report again in Table D.1, listing the best-fit Mangetar models' parameters values (τ_m, B, P and t_{exp}), as well as the fits' results (χ^2_{red}, χ^2 and DoF). Each plot panel shows the bolometric light-curve (orange circles) of each SLSN and the best-fit of the two compelling power source models, the Magnetar (green line) and the decay of ^{56}Ni (blue line).

Table D.1: List of 22 SLSNe discovered in Y2 and DES13S2cmm from Y1, reporting the best-fit Magnetar models' parameters values (τ, B, P and t_{exp}), as well as the fits' results (reduced χ^2, χ^2 and DoF). The table is separated into four sections: 6 SLSNe that were spectroscopically confirmed, 2 SLSNe that have a host z_{spec}, 14 events were photometrically selected as SLSNe and DES13S2cmm. The SLSNe are ordered based on their redshift and this order was kept throughout the chapter for clarity in reference and plotting.

#	Name	z	τ	B	P	t_{exp} (days)	reduced χ^2	χ^2	DoF
1	DES14S2qri	1.500	17.11	1.12	3.02	24.78	0.803	8.83	11
2	DES14X2byo	0.869	31.67	4.73	0.98	18.67	2.440	39.04	16
3	DES14E2slp	0.640	26.14	2.43	4.69	29.13	2.637	7.91	3
4	DES14E2ap	0.600	43.94	3.59	2.33	45.06	0.650	11.05	17
5	DES14X3taz	0.600	32.29	0.26	1.69	25.52	15.976	31.95	2
6	DES14C1rhg	0.470	20.38	5.33	10.95	17.83	9.723	126.40	13
7	DES14C1fi	1.300	27.02	0.84	2.45	32.25	0.810	17.01	21
8	DES14X1rbi	0.720	14.33	1.42	6.28	26.05	0.356	1.78	5
9	DES14S1ewv	1.230	23.48	1.92	3.08	22.90	1.296	15.56	12
10	DES14E1rpi	1.050	13.40	4.26	8.87	15.42	0.257	1.29	5
11	DES14C3nn	1.030	12.32	3.13	6.93	12.65	0.140	1.12	8
12	DES14E1lgl	1.000	48.90	0.91	4.67	40.70	0.656	6.56	10
13	DES14E2bhn	0.970	10.30	3.27	9.48	18.61	0.346	3.12	9
14	DES14X3gyr	0.950	27.49	3.31	8.97	28.24	0.086	0.43	5
15	DES14X1avd	0.840	45.61	4.21	4.83	26.37	0.772	10.81	14
16	DES14X3mjf	0.830	29.78	0.24	3.28	31.64	0.296	1.48	5
17	DES14C1ngk	0.810	49.33	0.86	4.41	41.75	0.690	6.90	10
18	DES14C3tny	0.790	13.37	1.05	6.07	22.87	0.987	3.95	4
19	DES14C1fs	0.740	58.61	2.08	4.32	39.36	0.819	15.57	19
20	DES14X1brr	0.650	12.16	4.79	9.98	16.03	0.882	12.35	14
21	DES14X1ps	0.610	40.67	2.72	3.76	47.78	1.516	33.35	22
22	DES14E1hk	0.530	24.05	5.62	6.83	21.33	0.517	8.26	16
23	DES13S2cmm	0.663	24.71	1.51	5.39	29.19	3.736	82.19	22

(a) DES14S2qri
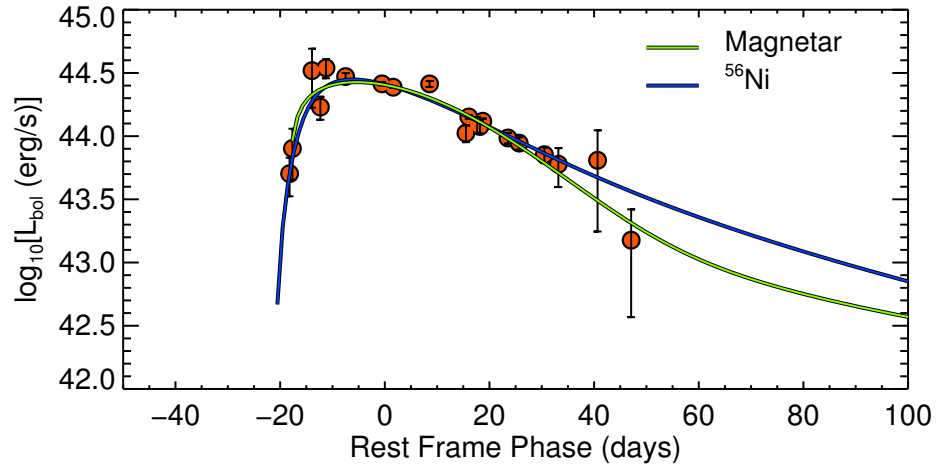
(b) DES14X2byo
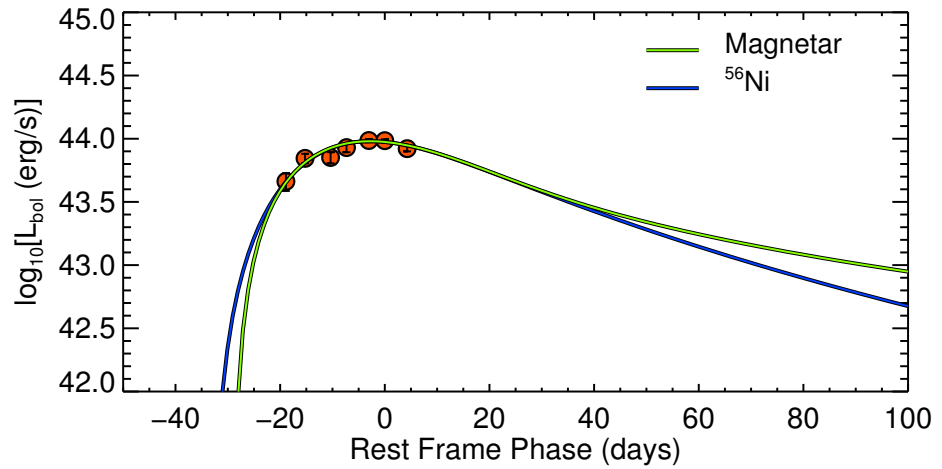
(c) DES14E2slp

Figure D.1: The bolometric light-curve of three SLSNe as a function of the rest-frame phase, fitted with the Magnetar (green) and ^{56}Ni (blue) models, as described in Sec. 5.7.2.

(a) DES14E2ap

(b) DES14X3taz

(c) DES14C1rhg

Figure D.2: The bolometric light-curve of three SLSNe as a function of the rest-frame phase, fitted with the Magnetar (green) and ^{56}Ni (blue) models, as described in Sec. 5.7.2.

(a) DES14C1fi

(b) DES14X1rbi

(c) DES14S1ewv

Figure D.3: The bolometric light-curve of three SLSNe as a function of the rest-frame phase, fitted with the Magnetar (green) and ^{56}Ni (blue) models, as described in Sec. 5.7.2.

(a) DES14E1rpi

(b) DES14C3nn

(c) DES14E1lgl

Figure D.4: The bolometric light-curve of three SLSNe as a function of the rest-frame phase, fitted with the Magnetar (green) and ^{56}Ni (blue) models, as described in Sec. 5.7.2.

(a) DES14E2bhn

(b) DES14X3gyr

(c) DES14X1avd

Figure D.5: The bolometric light-curve of three SLSNe as a function of the rest-frame phase, fitted with the Magnetar (green) and ^{56}Ni (blue) models, as described in Sec. 5.7.2.

(a) DES14X3mjf

(b) DES14C1ngk
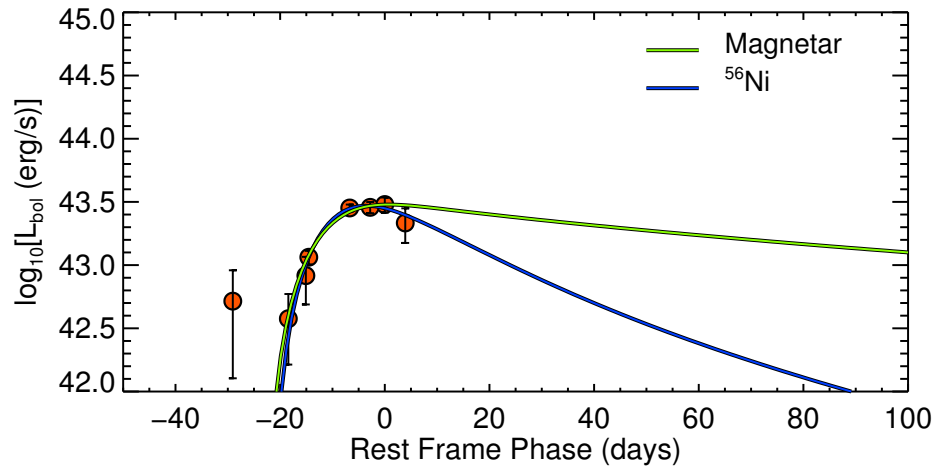
(c) DES14C3tny

Figure D.6: The bolometric light-curve of three SLSNe as a function of the rest-frame phase, fitted with the Magnetar (green) and ^{56}Ni (blue) models, as described in Sec. 5.7.2.
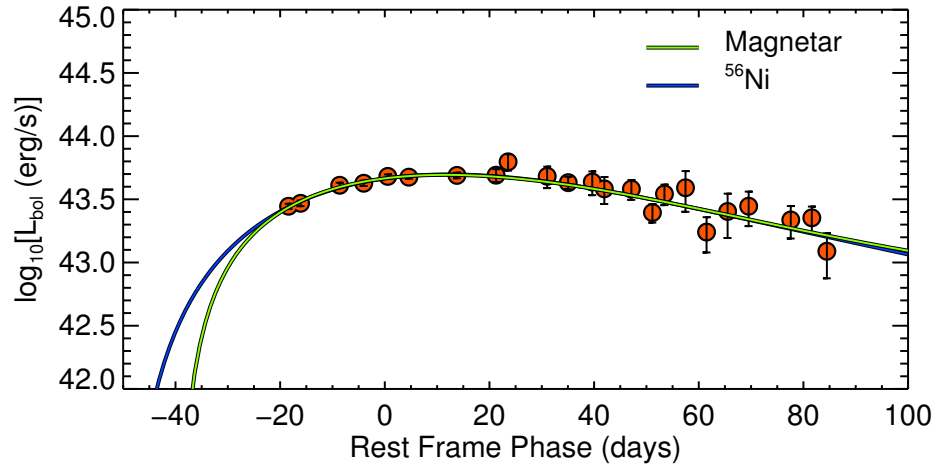
(a) DES14C1fs
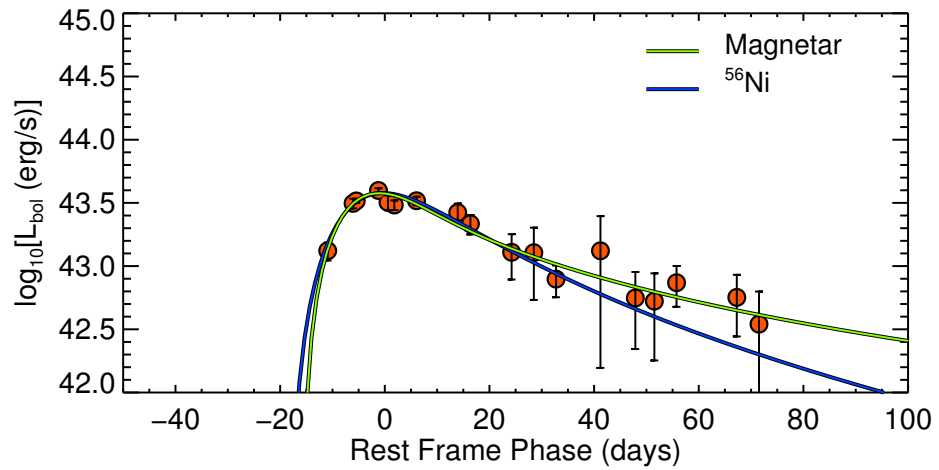
(b) DES14X1brr

Figure D.7: The bolometric light-curve of two SLSNe as a function of the rest-frame phase, fitted with the Magnetar (green) and ^{56}Ni (blue) models, as described in Sec. 5.7.2.
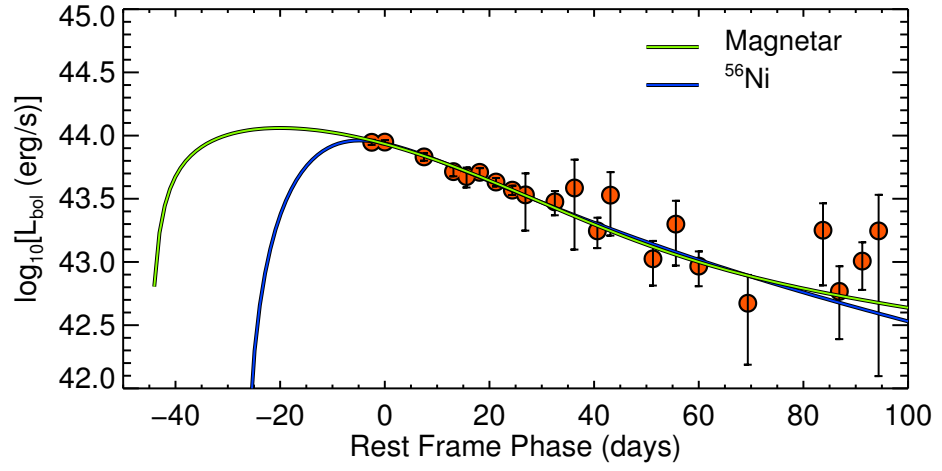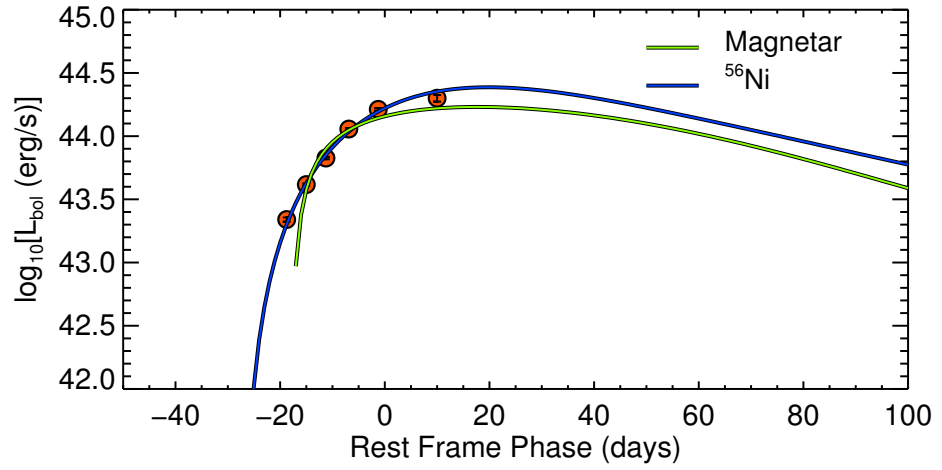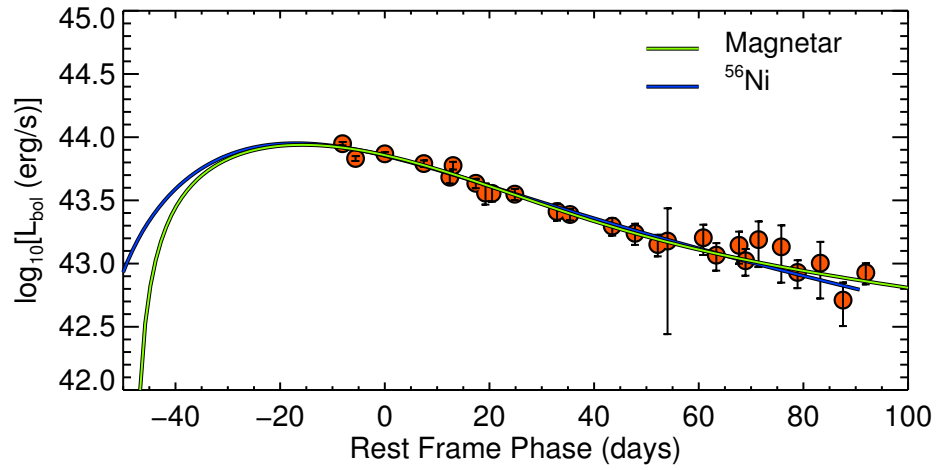
(a) DES14X1ps
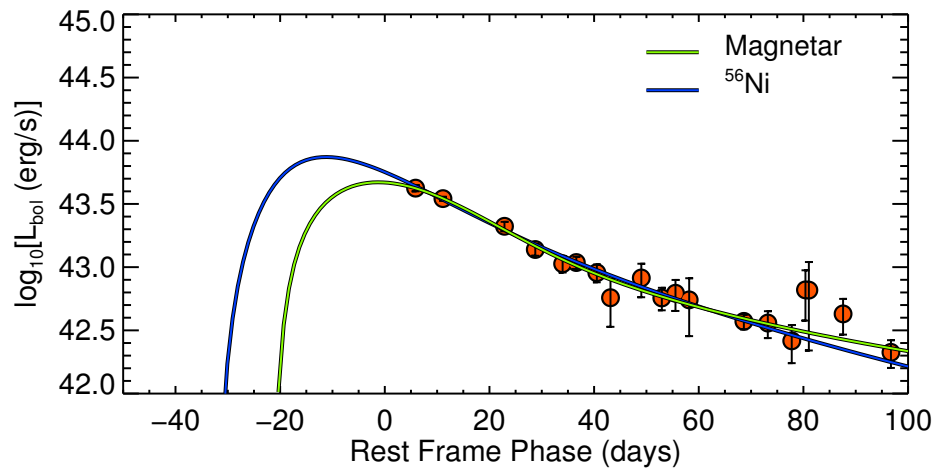
(b) DES14E1hk
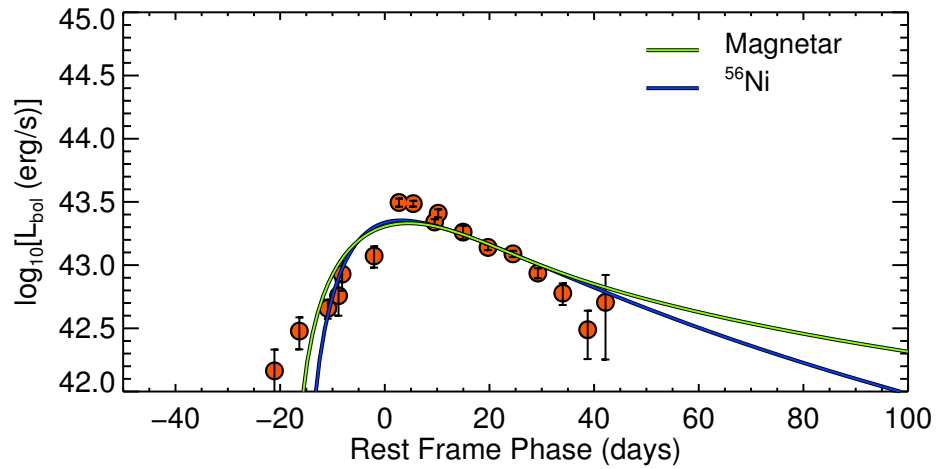
Figure D.8:]
The bolometric light-curve of two SLSNe as a function of the rest-frame phase, fitted
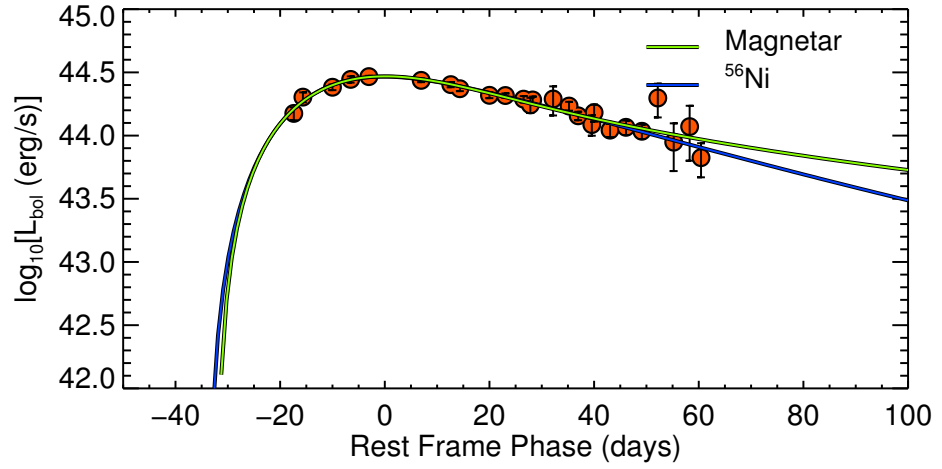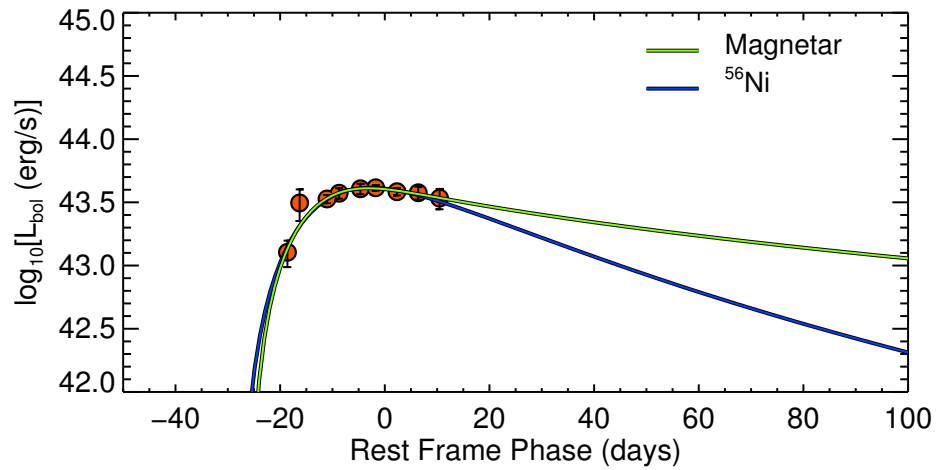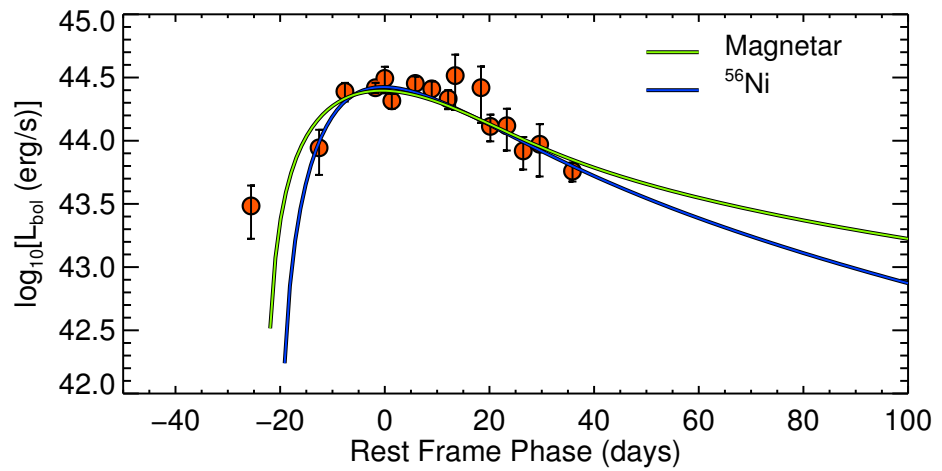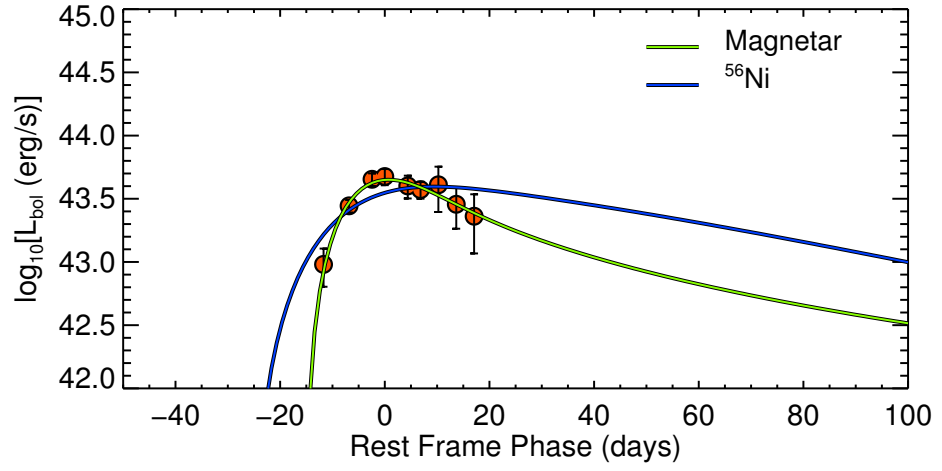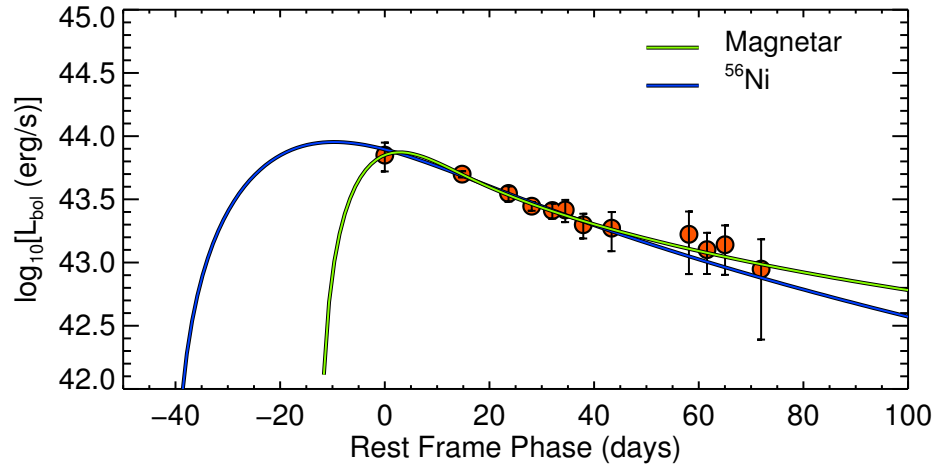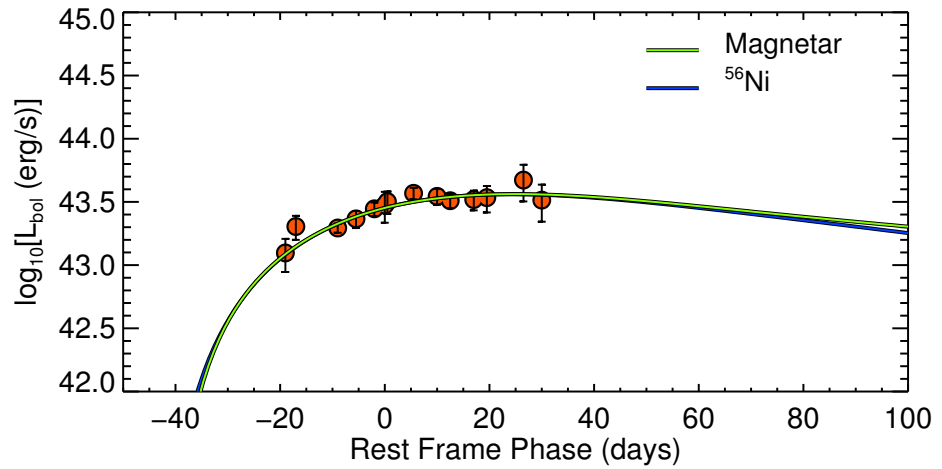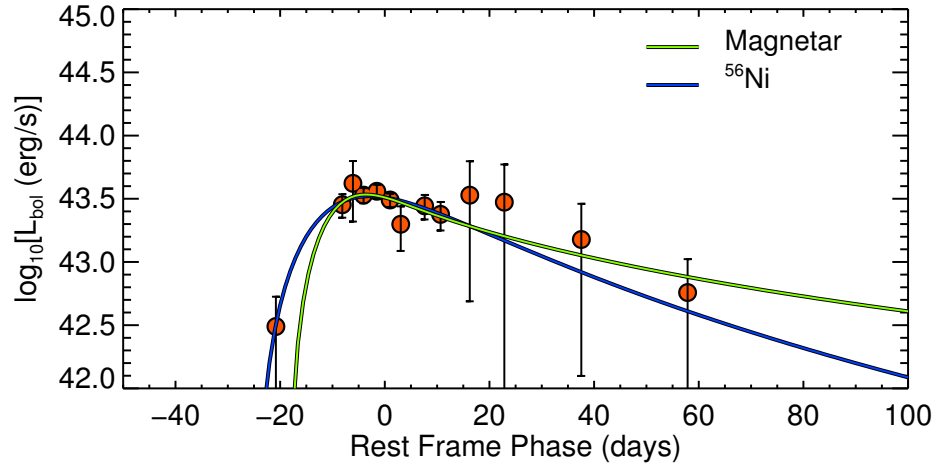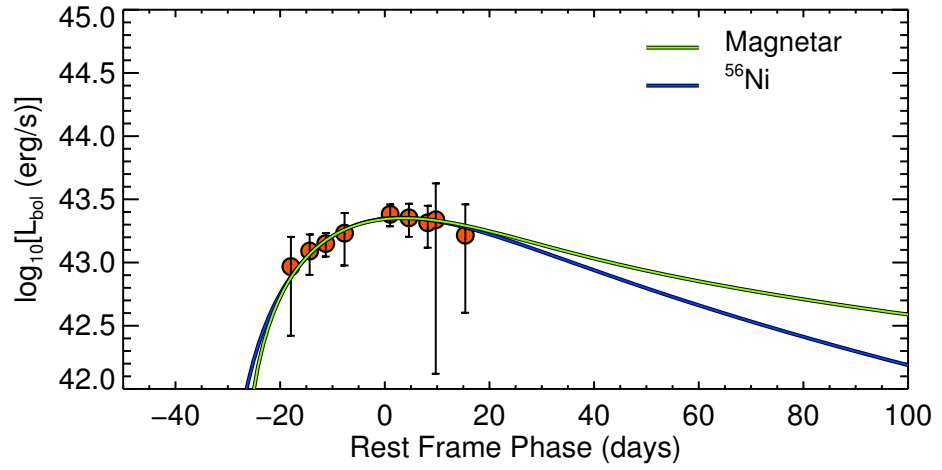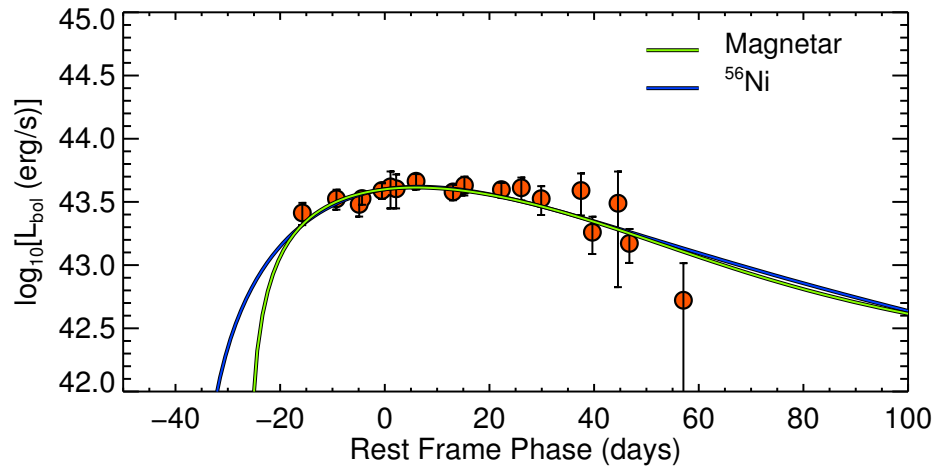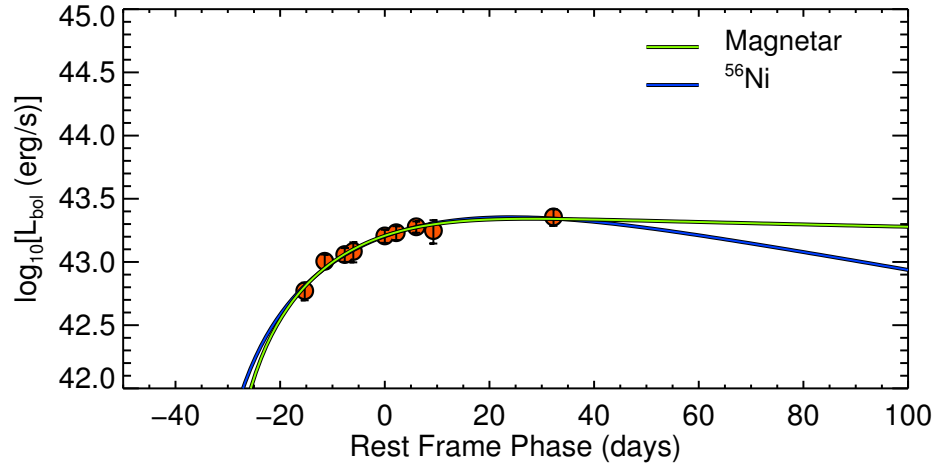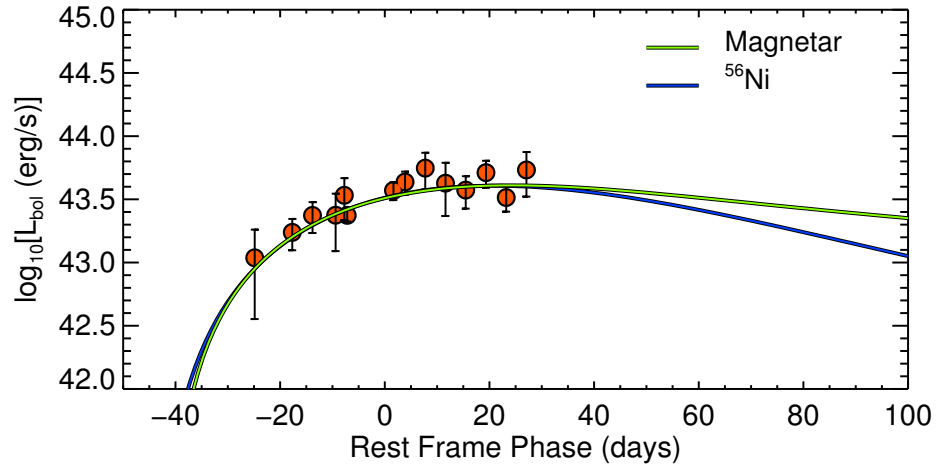with the Magnetar (green) and ^{56}Ni (blue) models, as described in Sec. 5.7.2.

DES13S2cmm: The First Superluminous Supernova from the Dark Energy Survey

A. Papadopoulos[1]⋆, C. B. D'Andrea[1], M. Sullivan[2], R. C. Nichol[1], K. Barbary[3], R. Biswas[4], P. J. Brown[5], R. A. Covarrubias[6] D. A. Finley[7], J. Fischer[8], D. Goldstein[9,10], R. R. Gupta[4], R. Kessler[11,12], A. G. Kim[10], E. Kovacs[4], S. E. Kuhlmann[4], C. Lidman[13], M. March[8], P. E. Nugent[9,10], M. Sako[8], R. C. Smith[14], H. Spinka[4], W. Wester[7],T. M. C. Abbott[14], F. Abdalla[15], S. S. Allam[6,16], M. Banerji[15], J. P. Bernstein[4], R. A. Bernstein[17], A. Carnero[18,19], L. N. da Costa[18,19], D. L. DePoy[5], S. Desai[20,21], H. T. Diehl[7], T. Eifler[22], A. E. Evrard[23,24], B. Flaugher[7], J. A. Frieman[7,11], D. Gerdes[23], D. Gruen[25,26], K. Honscheid[27], D. James[14], K. Kuehn[13], N. Kuropatkin[7], O. Lahav[15], M. A. G. Maia[18,19], M. Makler[28], J. L. Marshall[5], K. W. Merritt[7], C. J. Miller[23,24], R. Miquel[29,30], R. Ogando[18,19], A. A. Plazas[31] N. A. Roe[10], A. K. Romer[32], E. Rykoff[33], E. Sanchez[34], B. X. Santiago[19,35], V. Scarpine[7], M. Schubnell[23], I. Sevilla[33], M. Soares-Santos[7], E. Suchyta[27], M. Swanson[6], G. Tarle[23], J. Thaler[36], D. L.Tucker[7], R. H. Wechsler[37] J. Zuntz[38]

10 September 2014

ABSTRACT

We present DES13S2cmm, the first spectroscopically-confirmed superluminous supernova (SLSN) from the Dark Energy Survey (DES). We briefly discuss the data and search algorithm used to find this event in the first year of DES operations, and outline the spectroscopic data obtained from the European Southern Observatory (ESO) Very Large Telescope to confirm its redshift ($z = 0.663 \pm 0.001$ based on the host-galaxy emission lines) and likely spectral type (type I). Using this redshift, we find $M_U^{peak} = -21.05^{+0.10}_{-0.09}$ for the peak, rest-frame U-band absolute magnitude and find DES13S2cmm is located in a faint, low metallicity (sub-solar), low stellar-mass host galaxy ($\log(\mathrm{M}/\mathrm{M}_\odot) = 9.3 \pm 0.3$); consistent with what is seen for other SLSNe-I. We compare the bolometric light curve of DES13S2cmm to eleven similarly well-observed SLSNe-I in the literature and find it possesses one of the slowest declining tails (beyond $+30$ days rest frame past peak), and is the faintest at peak. Moreover, we find the bolometric light curves of the twelve SLSNe-I studied herein possess a minimum dispersion of 0.21 magnitudes at $+25$ days after peak (rest frame), which could be important for 'standardising' such supernovae, as is done with the more common type Ia. We fit the bolometric light curve of DES13S2cmm with two competing models for SLSNe-I – the radioactive decay of ^{56}Ni, and a magnetar – and find that while the magnetar is formally a better fit, neither model provides a compelling match to the data. Although we are unable to conclusively differentiate between these two physical models for this particular SLSN-I, further DES observations of more SLSNe-I should break this degeneracy, especially if the light curves of SLSNe-I can be observed beyond 100 days in the rest frame of the supernova.

Key words: surveys - stars: supernovae: general - stars: supernovae: DES13S2cmm

1 INTRODUCTION

The last five years have seen the emergence of a new class of ultra-bright stellar explosions: superluminous supernovae (SLSNe; for

⋆ E-mail: andreas.papadopoulos@port.ac.uk

a review see Gal-Yam 2012), some 50 times brighter than classical supernova (SN) types. Data on these rare and extreme events are still sparse, with only ∼50 SLSN detections reported in the literature. These events have generally been poorly studied with incomplete imaging and spectroscopy, leaving many aspects of their observational characteristics, and their physical nature, unknown.

Yet these SLSNe could play a key role in many diverse areas of astrophysics: tracing the evolution of massive stars, driving feedback in low mass galaxies at high redshift, and providing potential line-of-sight probes of interstellar medium to their high-redshift hosts (Berger et al. 2012). SLSNe have also been detected to $z \sim 4$ (Cooke et al. 2012), far beyond the reach of the current best cosmological probe, type Ia supernovae (SNe Ia). If SLSNe can be standardised (e.g. Inserra & Smartt 2014), as is done with SNe Ia (Tripp 1998; Phillips 1993; Riess et al. 1996), then a new era of SN cosmology would be possible, with the potential to accurately map the expansion rate of the universe far into the epoch of deceleration (Delubac et al. 2014).

SLSNe have been divided into three possible types: SLSN-II, SLSN-I and SLSN-R (see Fig. 1 of Gal-Yam 2012). SLSNe-II show signs of interactions with CSM via narrow hydrogen lines (e.g., Ofek et al. 2007; Smith et al. 2007), and thus may simply represent the bright end of a continuum of Type IIn SNe (although this is not well established).

SLSN-I are spectroscopically classified as hydrogen free (Quimby et al. 2011), and are possibly related to Type Ic SNe at late times (Pastorello et al. 2010), but normal methods of powering such SNe (e.g., the radioactive decay of ^{56}Ni or energy from the gravitational collapse of a massive star) do not appear to be able to simultaneously reproduce their extreme brightness, slowly-rising light curves, and decay rates (Inserra et al. 2013). Many alternative models have been proposed: the injections of energy into a SN ejecta via the spin down of a young magnetar (Kasen & Bildsten 2010; Woosley 2010; Inserra et al. 2013); interaction of the SN ejecta with a massive (3-5 $M_\odot$) C/O-rich circumstellar material (CSM; e.g., Blinnikov & Sorokina 2010); or collisions between high-velocity shells generated from a pulsational pair-instability event (Woosley et al. 2007). These explanations are still actively debated in the literature.

SLSNe-R are rare and characterised by possessing extremely long, slow-declining light curves (> 200 days in the rest frame). SLSNe-R originally appeared consistent with the death of $\gtrsim 100\,M_\odot$ stars via the pair instability mechanism (Gal-Yam et al. 2009). However, new observations – and the lack of significant spectral differences between SLSN-I and SLSN-R – have challenged the notion that these classes are truly distinct (Nicholl et al. 2013) and maybe better described together as Type Ic SLSNe (Inserra et al. 2013).

In summary, the origin of the power source for SLSNe (of all types) remains unclear, with the possibility that further sources of energy may be viable. A more detailed understanding requires an increase in both the quantity and quality of the data obtained on these events. However, finding more SLSNe (of any type) with existing transient searches is challenging, especially in the local universe where the rates are only $\simeq 10^{-4}$ that of the core-collapse SN rate (Quimby et al. 2013; McCrum et al. 2014) thus making it hard to assemble large samples of events over reasonable timescales, even from large surveys. For example, McCrum et al. (2014) detected only 10 SLSN candidates over $0.3 \leqslant z \leqslant 1.4$ within the first year of the PanSTARRS1 Medium Deep Survey.

Searches for SLSNe at higher redshifts may be more profitable as the rates of SLSNe appear to rise by a factor of ∼10-15

at $z > 1.5$ (Cooke et al. 2012), perhaps tracking the increased cosmic star-formation rate and/or decreasing cosmic metallicity: SLSNe are preferentially found in faint, low-metallicity galaxies (Neill et al. 2011; Chen et al. 2013; Lunnan et al. 2014). Moreover, the peak of a SLSN's energy output is located in the UV region of the electromagnetic spectrum, which is redshifted to optical wavelengths at high redshift.

In this paper, we outline our first search for SLSNe in the Dark Energy Survey (DES). In Section 2, we discuss details of DES and our preliminary search, while in Section 3, we describe the first SLSN detected in DES and provide details of its properties, including our spectroscopic confirmation. In Section 4, we compare our SLSN to other events in the literature and explore the possible power sources for our event. We conclude in Section 5. Throughout this paper, we assume a flat Λ-dominated cosmology with $\Omega_M = 0.28$ and $H_0 = 70\,\mathrm{km\,s^{-1}\,Mpc^{-1}}$, consistent with recent cosmological measurements (e.g. Anderson et al. 2014; Betoule et al. 2014).

2   THE DARK ENERGY SURVEY

The Dark Energy Survey (DES; Flaugher 2005) is a new imaging survey of the southern sky focused on obtaining accurate constraints on the equation-of-state of dark energy. Observations are carried out using the Dark Energy Camera (DECam; Flaugher et al. 2012; Diehl & For the Dark Energy Survey Collaboration 2012) on the 4-metre Blanco Telescope at the Cerro Tololo Inter-American Observatory (CTIO) in Chile. DECam was successfully installed and commissioned in 2012, and possesses a 3 deg^2 field-of-view with 62 fully depleted, red-sensitive CCDs.

2.1   DES Supernova Survey

DES conducted science verification (SV) observations from November 2012 to February 2013, and then began full science operations in mid-August 2013, with year one running until February 2014. DES is performing two surveys in parallel: a wide-field, multi-colour ($grizY$) survey of 5000 deg^2 for the study of clusters of galaxies, weak lensing and large scale structure; and a deeper, cadenced multi-colour ($griz$) search for SNe. In this paper we focus on this DES SN Survey, as outlined in Bernstein et al. (2012), which surveys 30 deg^2 over 10 DECam fields (two 'deep', eight 'shallow') located in the XMM-LSS, ELAIS-S, CDFS and 'Stripe82' regions. The DES SN Survey has already discovered hundreds of SN Ia candidates, some of which have been followed up using several telescopes around the world.

This rolling search for SNe Ia is also ideal for discovering other transient phenomena including SLSNe. Using the light curve of SNLS-06D4eu (a SLSN-I; Howell et al. 2013), we calculate that DES could detect such an event to $z = 2.5$ given the limiting magnitudes for the DES deep fields. For example, assuming a volumetric rate of $32\,\mathrm{Gpc^{-3}\,yr^{-1}}$ from Quimby et al. (2013) and correcting for time dilation, we estimate DES should find approximately 3.5 SLSN-I events per DES season (five months) in the deep fields and many more in the shallow fields (although at a lower redshift). This basic prediction is uncertain because: i) We have not corrected for 'edge effects' that will reduce the number of SLSNe with significant light-curve coverage; ii) The volumetric rates themselves may evolve with redshift (e.g., Cooke et al. 2012) and have large uncertainties (McCrum et al. 2014); and iii) We have not included any corrections for survey completeness.

2.2 Selecting SLSNe candidates

We began our search for SLSNe using the data products from the DES SN Survey. All imaging data were de-trended and co-added using a standard photometric reduction pipeline at the National Center for Supercomputing Applications (NCSA) using the DES Data Management system (DESDM; Mohr et al. 2012; Desai et al. 2012), producing approximately 30 'search images' per field (in all filters) over the duration of the five-month DES season. We perform difference imaging on each of these search images, using deeper template images for each field created from the co-addition of several epochs of data obtained during the SV period in late 2012. Before differencing, the search and template images were convolved to the same point spread function (PSF).

Objects were selected from the difference images using SEX-TRACTOR (Bertin & Arnouts 1996) v2.18.10, and previously unknown transient candidates were identified and examined using visual inspection (or 'scanning') by DES team members. Over the course of the first year of DES approximately $25,000$ new transient candidates were selected in this manner, including many data artefacts in addition to legitimate SN-like objects. A machine learning algorithm (Goldstein et al., in preparation) was used to improve our efficiency of selecting real transients. Transient candidates were photometrically classified using the Photometric SN IDentification software (PSNID; Sako et al. 2008, 2011) to determine the likely SN type based on fits to a series of SN templates. These SN candidates were stored in a database and prioritized for their spectroscopic follow-up.

During the first season of DES, PSNID only included templates for the normal SN types Ib/c, II and Ia, so a fully automated classification of SLSN candidates was not possible. Therefore, for this first season of DES, we searched for candidate SLSNe using the following criteria: i) At least one month of multi-colour data, i.e., typically five to six detections ($S/N > 3.5$) in each of $griz$; ii) A low PSNID fit probability to any of the standard SN subclasses; iii) Located greater than one pixel from the centroid of the host galaxy (to eliminate AGN); and iv) Peak observed brightness no fainter than one magnitude below that of its host galaxy. These broad criteria will be satisfied by most SLSNe, while also helping to eliminate many of the possible contaminating sources.

Using this methodology, we selected 10 candidate SLSNe over the course of the first season. We secured a useable spectrum for one of our SLSN candidates, DES13S2cmm, which is discussed in detail in Section 3, while none of the other candidates were spectroscopically confirmed. We will attempt to gain spectroscopy of the host galaxies of these other candidates, but in several cases this will be challenging as no host is detected in our images for a few of our SLSN candidates .

3 DES13S2CMM

In Fig. 1 we show DES riz imaging data at the position of DES13S2cmm: pre-explosion, post-explosion, and their difference image. DES13S2cmm is located at RA(2000) $= 02^{\mathrm{h}}42^{\mathrm{m}}32^{\mathrm{s}}_{.}82$, Dec. (2000) $= -01°21'30''_{.}1$, and was first detected on 2013 August 27 in the DES SN 'S2' field (a 'shallow' field) located in the Stripe 82 region. DES transient names are formatted following the convention DESYYFFaaaa, where YY are the last two digits of the year in which the observing season began (13), FF is the two character field name (S2), and the final characters (all letters, maximum of 4) provide a running candidate identification, unique within an observing season, as is traditional in SN astronomy (cmm).

3.1 Light Curve

In Fig. 2 we present the multi-colour light curve for DES13S2cmm constructed from the first year of DES observations. We have not included upper limits from the earlier, pre-explosion epochs available from the DES SV period in 2012-2013, as these data were taken hundreds of days prior to the data shown in Fig. 2 and are already used to create the reference template image for this field used in the difference imaging detection of the SNe. We use the photometric pipeline from Sullivan et al. (2011) (also used in Maguire et al. 2012; Ofek et al. 2013) to reduce the DES photometric data for DES13S2cmm. This pipeline is based on difference imaging, subtracting a deep, good seeing, pre-explosion reference image from each frame the SN is present in. The photometry is then measured from the differenced image using a PSF-fitting method, with the PSF determined from nearby field stars in the unsubtracted image. This average PSF is then fit at the position of the SN event, weighting each pixel according to Poisson statistics, yielding a flux, and flux error, for the SN.

We calibrate the flux measurements of DES13S2cmm to a set of tertiary standard stars produced by the DES collaboration (Wyatt et al., in preparation), intended to be in the AB photometric system (Oke & Gunn 1983). The photometry shown in Fig. 2 has also been checked against the standard DES detection photometry, used to find and classify all candidates for follow-up, and found to be in good agreement. The light-curve data are presented in Table 1.

We correct for Galactic extinction using the maps of Schlafly & Finkbeiner (2011), which estimate E(B − V) $= 0.028$ at the location of DES13S2cmm, leading to extinction values of 0.123, 0.070, 0.051 and 0.039 magnitudes in the DES $griz$ filters respectively. We do not include these corrections in the values reported in Table 1, but do correct for extinction in all figures and analysis herein, including Figure 2.

3.2 Spectroscopy

On 2013 November 12, we requested Director's Discretionary Time at the European Southern Observatory (ESO) Very Large Telescope (VLT) to observe DES13S2cmm, and were awarded target-of-opportunity time within days. The closeness of the object to the moon and instrument scheduling issues conspired to delay observations until 2013 November 21, at which point DES13S2cmm was approximately 30 days after peak brightness (rest frame). A spectrum was obtained with the FOcal Reducer and low dispersion Spectrograph (FORS2 Appenzeller et al. 1998) using the GRIS_300I+11 grism, the OG590 order blocker, and a $1''$ slit, with an exposure time of 3600s (3×1200s). This configuration provided an effective wavelength coverage of $5950\,\text{Å}$ to $9400\,\text{Å}$.

The reduction of the FORS2 data followed standard procedures using the Image Reduction and Analysis Facility[1] environment (v2.16), using the pipeline described in Ellis et al. (2008). This pipeline includes an optimal two-dimensional (2D) sky subtraction technique as outlined in Kelson (2003), subtracting a 2D sky frame constructed from a sub-pixel sampling of the background spectrum and a knowledge of the wavelength distortions determined from 2D arc comparison frames. The extracted 1D spectra were then scaled to the same flux level, the host-galaxy emission

---

[1] The Image Reduction and Analysis Facility (IRAF) is distributed by the National Optical Astronomy Observatories, which are operated by the Association of Universities for Research in Astronomy, Inc., under cooperative agreement with the National Science Foundation.
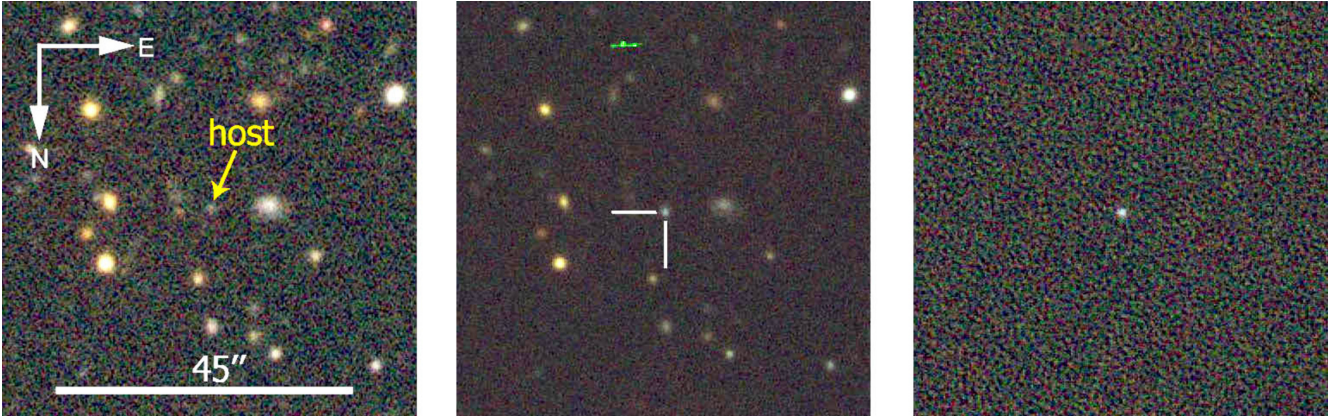
Figure 1. Colour images (*riz*) of the field surrounding DES13S2cmm. *Left:* Deep template image created from the co-addition of several epochs of data obtained during the DES Science Verification period in late 2012; the likely host galaxy is indicated by the arrow. *Centre:* The search image taken close to maximum light (28-Sept-2013) with the position of DES13S2cmm indicated. *Right:* The difference of the two previous images, clearly identifying DES13S2cmm at center. This image demonstrates the quality of difference images used for discovery and monitoring during the DES observing season.
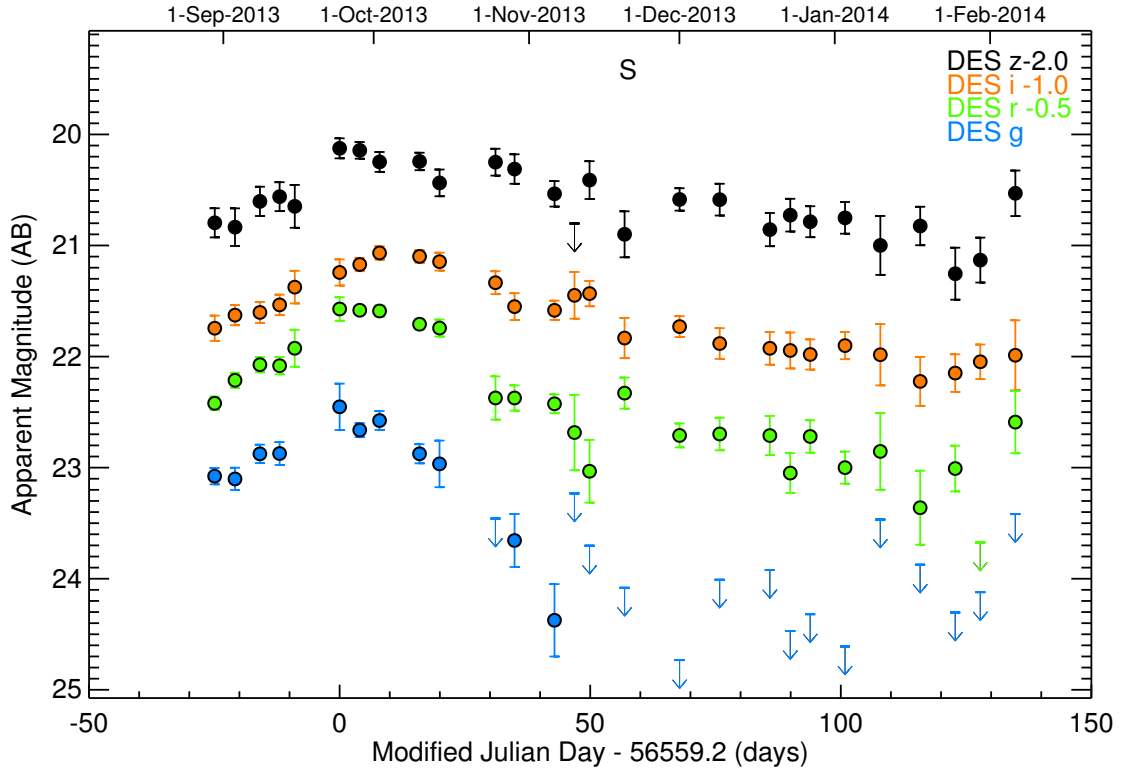
Figure 2. The observed AB magnitude light curve of DES13S2cmm in the four DES SN search filters ($griz$) as a function of the observed phase. 'S' denotes the epoch when the ESO VLT spectrum was obtained. The error-bars represent 1-σ uncertainties, and the arrow symbols are 3-σ upper limits. The phase relative to peak was defined using the observed-frame r-band. We have artificially offset (in magnitudes) the i and z band data for clarity.

Figure 3. The reduced VLT FORS2 two-dimensional spectrum for DES13S2cmm. The key nebular emission lines used to derive the redshift of the host galaxy, and therefore supernova, are labelled.

Table 1. Light curve data for DES13S2cmm used in Fig. 2. We provide the observed calendar date, modified Julian Day (MJD), observed phase relative to peak MJD (defined relative to peak flux in the *r*-band), and fluxes (not corrected for Galactic extinction) with 1-σ uncertainties in the DES *griz* passbands. These fluxes can be converted to AB magnitudes using $\mathrm{mag_{AB}} = -2.5 \log_{10}(f) + 31$.

Date	MJD	Phase (days)	f_g	f_r	f_i	f_z
30-AUG-2013	56534.3	-25	1138±77	1705±94	1730±181	1913±231
3-SEP-2013	56538.3	-21	1112±103	2063±129	2234±186	1845±288
8-SEP-2013	56543.3	-16	1369±104	2348±148	2285±198	2285±277
12-SEP-2013	56547.2	-12	1373±130	2329±167	2433±207	2376±284
15-SEP-2013	56550.2	-9	±	2691±413	2818±380	2193±389
24-SEP-2013	56559.2	0	2022±388	3727±363	3183±346	3548±295
28-SEP-2013	56563.2	4	1668±97	3688±133	3400±187	3488±241
2-OCT-2013	56567.2	8	1805±141	3666±166	3742±209	3169±261
10-OCT-2013	56575.2	16	1370±108	3285±137	3636±192	3182±230
14-OCT-2013	56579.1	20	1260±243	3182±223	3482±259	2663±295
25-OCT-2013	56590.3	31	886±346	1782±319	2924±277	3163±352
29-OCT-2013	56594.1	35	667±146	1782±187	2398±267	2987±366
6-NOV-2013	56602.1	43	344±103	1698±132	2326±185	2433±257
10-NOV-2013	56606.1	47	803±426	1338±418	2633±510	1817±634
13-NOV-2013	56609.1	50	-312±276	970±252	2672±281	2726±426
20-NOV-2013	56616.1	57	347±195	1855±239	1848±307	1739±331
1-DEC-2013	56627.0	68	184±107	1306±129	2032±176	2322±216
9-DEC-2013	56635.0	76	259±208	1322±178	1766±225	2318±304
19-DEC-2013	56645.1	86	302±226	1305±211	1697±230	1808±248
23-DEC-2013	56649.1	90	261±136	956±157	1667±248	2038±276
27-DEC-2013	56653.1	94	41±156	1295±174	1613±201	1930±248
3-JAN-2014	56660.0	101	252±119	1000±132	1736±196	1993±261
10-JAN-2014	56667.1	108	310±343	1144±364	1609±408	1586±387
18-JAN-2014	56675.0	116	-75±236	717±220	1290±261	1863±297
25-JAN-2014	56682.0	123	306±158	992±188	1382±215	1254±270
30-JAN-2014	56687.0	128	345±188	523±179	1518±217	1404±261
6-FEB-2014	56694.0	135	-346±359	1459±376	1602±465	2443±461

lines interpolated over, and the spectra combined using a weighted mean and the uncertainties in the extracted spectra.

In Fig 3 we present our reduced 2D FORS2 spectrum, where wavelength increases to the right along the horizontal axis and the vertical axis is distance along the slit. We highlight the obvious narrow nebular emission lines in the host galaxy of DES13S2cmm, specifically [O II] $\lambda 3727$ Å, Hβ $\lambda 4861$ Å, and [O III] $\lambda 4959, 5007$ Å. We assume these lines originate from the underlying host galaxy as their spatial extent along the vertical axis is greater than the observed trace of the main supernova spectrum. This observation does not exclude the possibility that such emission lines come from the supernova, but it is difficult to address this issue with our low resolution, and low signal-to-noise, data. We note the observed emission lines are not significantly broadened or asymmetrical, as witnessed in type IIn supernovae.

We see no evidence of any further emission lines, from the SN and/or host galaxy. Therefore, it is unlikely DES13S2cmm is a type II supernova (normal or superluminous).

Using these nebular emission lines, we determine a redshift of $z = 0.663 \pm 0.001$ for the host galaxy of DES13S2cmm, where the uncertainty is derived from the wavelength dispersion between individual emission lines. This measurement is consistent with the redshift of the SN based on identifications of the broad absorption features seen in the spectrum. As the redshift derived from the host-galaxy spectrum is significantly more precise, henceforth we adopt this value as the redshift to DES13S2cmm.

The spectral classification for DES13S2cmm is based on the SUPERFIT program (Howell et al. 2005), which compares un-

known observed spectra of SNe against a library of template SN spectra (via χ^2 minimisation), including the possibility of host-galaxy contamination in the observed spectra. The spectra of the SLSNe PTF09atu, PTF09cnd, PTF10nmn and SN 2007bi were added to SUPERFIT to facilitate our classification and these SLSNe spectra were found to be the highest ranked fitted templates to DES13S2cmm and in preference to normal SN types (e.g., SN Ia).

We show our spectrum of DES13S2cmm in Fig. 4, alongside spectra from other well-studied SLSNe in the literature at a similar phase in their light curves (Quimby et al. 2011; Inserra et al. 2013; Gal-Yam et al. 2009). There is a deficit of spectra for SLSNe in the literature at these late phases for a robust comparison. However, the broad resemblance between the spectra of PTF10hgi, SN 2011kf, SN 2011ke and DES13S2cmm, all taken at approximately +30 days past peak, suggests DES13S2cmm is a similar object to these other SLSNe-I. The spectrum of DES13S2cmm is also similar to the spectrum of SN 2007bi (a SLSN-R in Gal-Yam et al. 2009), although the differences between Type I and Type R SLSNe remains unclear, and either classification would be interesting given the sparseness of the data. We also show in Fig. 4 the spectrum of SN 2007if, a 'super-Chandrasekhar' SN Ia (Scalzo et al. 2010), an over-luminous ($M_V = -20.4$) and likely thermonuclear SN located in a faint host galaxy. This comparison clearly shows that DES13S2cmm is unlikely to be a super-Chandrasekhar SN Ia.
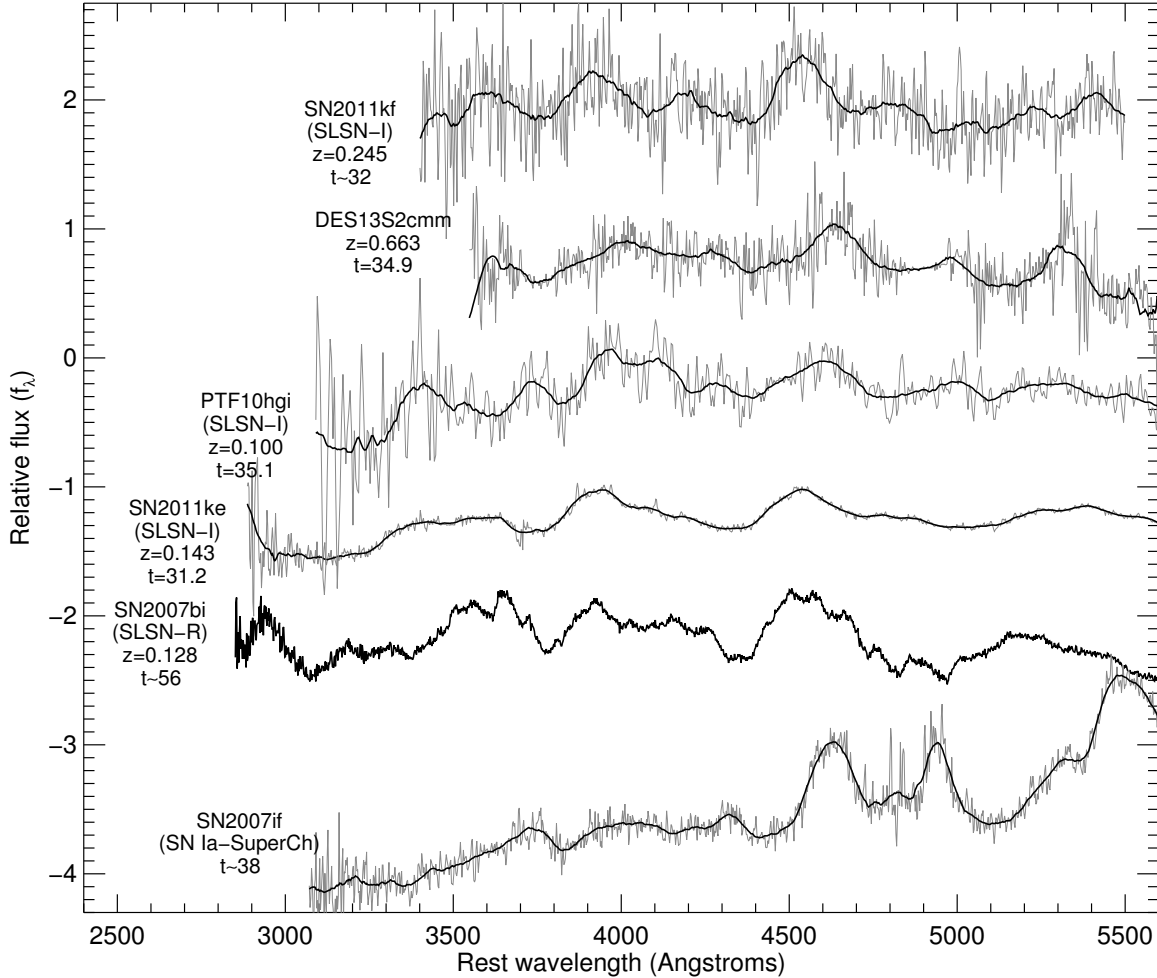
Figure 4. The VLT FORS2 spectrum of DES13S2cmm (second from top) compared to other SLSNe of similar phase in their light curves. From top to bottom, we also show SN 2011kf (Inserra et al. 2013), PTF10hgi (Quimby et al. 2011), SN 2011ke (Inserra et al. 2013) and SN 2007bi(classified as Type R in Gal-Yam et al. 2009); as discussed in Section 3.2, SUPERFIT identifies these SLSNe as some of the best-fitting spectral templates to DES13S2cmm. In each case, the light grey shows the raw data and the solid line is a Savitsky-Golay smoothed version of the spectrum. The spectra are labelled with the SN name, SLSN type (except DES13S2cmm), redshift, and the phase when the spectrum was taken. We show the spectrum of the 'super-Chandrasekhar' SN Ia SN 2007if as discussed in Scalzo et al. (2010). Note that the spectrum for 2007bi, while at a later phase than the other data, is the earliest spectral observation of this SN.

3.3 Host-galaxy properties

The host galaxy of DES13S2cmm is detected in our reference images that contain no SN light. Using SEXTRACTOR in dual-image mode and the i-band image as the detection image, we measure host-galaxy magnitudes of $g = 24.24 \pm 0.13$, $r = 23.65 \pm 0.10$, $i = 23.31 \pm 0.10$ and $z = 23.26 \pm 0.17$ (AB MAG_AUTO magnitudes). The large photometric errors are due to the relatively shallow depth, and poor seeing, of the template image from the DES SV data – we cannot use the DES first-year data for the host photometry as all epochs of this data contain some light from DES13S2cmm.

The estimated photometric redshift of the host galaxy at the time of discovery was $z_{\mathrm{photo}} = 0.86 \pm 0.13$ (68 percentile error). This photometric redshift was derived by the DESDM neural network photo-z module code, with uncertainties estimated from the nearest neighbour method, using data taken during SV (Sánchez et al. 2014). Photometric redshifts (when available) are used when selecting SLSN candidates for spectroscopic follow-up, and for DES13S2cmm this redshift implied the event was brighter than $M_U^{\mathrm{peak}} = -21$ (typical for SLSNe; Gal-Yam 2012). Since the start

of the first DES observing season the photometric catalog derived from SV data has improved, and presently the DESDM photo-z for the host of DES13S2cmm has improved to $z_{\mathrm{photo}} = 0.71 \pm 0.06$, which is in better agreement with our measured spectroscopic redshift ($z = 0.663 \pm 0.001$).

Using the DES host-galaxy photometry and the spectroscopic redshift from VLT, we estimate that the stellar mass of the host galaxy is $\log(M/M_\odot) = 9.3 \pm 0.3$ using stellar population models from PEGASE.2 (Fioc & Rocca-Volmerange 1997), and $\log(M/M_\odot) = 9.0 \pm 0.3$ using the stellar population templates from Maraston (2005) (both corrected for Milky Way extinction and fixing the redshift of the templates to $z = 0.663$). Such a low stellar-mass host galaxy is consistent with the findings for other SLSNe (Neill et al. 2011; Chen et al. 2013; Lunnan et al. 2014).

We estimate the host-galaxy metallicity from our VLT spectrum using the double-valued metallicity indicator R_{23}, defined as $([\mathrm{OII}]\ \lambda3727 + [\mathrm{OIII}]\ \lambda\lambda4959, 5007)/H\beta$. Fluxes and uncertainties are derived individually for each emission line from fits of a gaussian plus a first-order polynomial, with the assumption that

there is no contamination of the galaxy emission lines from the SN. We compute metallicities using the calibrations of Kobulnicky & Kewley (2004) and McGaugh (1991), and use the formulae derived in Kewley & Ellison (2008) to convert these metallicities into the calibration of Kewley & Dopita (2002) – a step that allows for direct comparison between different methods. We note that since $H\alpha$ and NII $\lambda6584$ are redshifted to wavelengths beyond our spectral coverage, we cannot determine the branch of the R_{23} function that the metallicity lies on. However, the derived value for R_{23} is close to its theoretical maximum, which minimizes the difference in metallicity estimates between the two branches.

Assuming the lower (upper) branch, we find a metallicity (12 + log[O/H]) of 8.30 (8.38) from McGaugh (1991) and 8.30 (8.42) from Kobulnicky & Kewley (2004), which is consistent with the median metallicity of 8.35 found by Lunnan et al. (2014) for a sample of 31 SLSNe host galaxies. The total uncertainty is dominated by the calibration ($\sim$ 0.15 dex), while the statistical uncertainty and the scatter induced by the conversion to Kewley & Dopita (2002) are comparatively negligible. We thus find a host-galaxy abundance ratio that is distinctly sub-solar (8.69; Asplund et al. 2009), though not as extremely low as has been seen for other SLSNe, such as SN2010gx (12 + log[O/H]=7.5; Chen et al. 2013).

4 RESULTS

4.1 Bolometric light-curve of DES13S2cmm

We show in Fig. 5 the bolometric light curve of DES13S2cmm. This single light curve was constructed by fitting a single black-body spectrum to the DES multi-colour data (requiring measurements in a minimum of three photometric bandpasses for a fit), on each epoch in the light curve (Table 1). In detail, we redshift black-body spectra to the observer frame and integrate these spectra through the response functions of the DES filters. We then determine the best-fitting parameters for a black body to the extinction-corrected photometry and integrate this spectrum in the rest frame to obtain the bolometric luminosity per epoch. This procedure benefits from the homogeneity of the DES data as we possess approximately equally-spaced epochs across the whole light curve – typically in four DES passbands – due to our rolling search. The errors on the bolometric luminosities were calculated from the fitting uncertainties on the black-body spectra.

We visually checked our best-fit blackbody curves for each epoch of the DES13S2cmm light curve against the observed $griz$ photometry and found them to be reasonable within the errors. The largest discrepancies were seen in the g-band where some epochs were below the fitted curves, possibly due to UV absorption in the underlying spectral energy distributions relative to a blackbody curve. Inserra et al. (2013) compared the predicted UV flux (from a blackbody curve) for two SLSNe with SWIFT UV observations, and found the fluxes were consistent within the error. Therefore we make no additional correction to the derived bolometric light curve, but note that quantifiable systematic errors in the bolometric luminosity require spectral templates, which in turn requires more spectral data of SLSNe than is currently publicly available.

Using the bolometric light curve of DES13S2cmm, we can determine the peak luminosity of the event and compare it to the definition of a SLSNe in Gal-Yam (2012). This was achieved by integrating the best-fitting black-body spectra through a standard U-band filter response function (on the Vega system) to obtain the rest-frame absolute magnitude in U-band (M_U). We find

the 2013 September 24 epoch ($t = 0$ relative phase in Table 1) gives the largest (peak) absolute U-band magnitude of $M_U^{peak} = -21.05^{+0.10}_{-0.09}$, which is consistent with the SLSNe threshold of $M_U^{peak} < -21$ in Gal-Yam (2012).

We check this result using a model-independent estimate based on the observed r-band peak magnitude. At the redshift of DES13S2cmm, the observer-frame r band maps into the rest frame as a synthetic filter with an effective wavelength of ≈ 3800Å, slightly redward of the standard U-band. Defining a synthetic filter as such means the k-correction is independent of the SN spectral energy distribution, and since we are in the AB system the correction is simply $2.5 \log(1 + z)$. We apply this k-correction to the observed r-band peak magnitude, as well as corrections for Galactic extinction and distance modulus, to yield an estimated peak absolute magnitude of -20.47 (AB), or -20.74 (Vega) in our synthetic filter (where we have computed the AB to Vega conversion for our filter). While this is fainter than our blackbody-based estimate, Vega magnitudes are sensitive to the exact shape of the filter in this region due to the jump in Vega from 3700-3900Å; thus even the small difference in effective wavelength between U band and our synthetic filter can result in significant offsets. The absolute magnitude in our synthetic filter from the best-fitting blackbody method yields $M_{\rm synthetic} = -20.59$, proving that our model-independent estimate is consistent with our results from the blackbody fitting.

We note that the peak magnitude (Vega) for DES13S2cmm classifies it as a SLSN, provided the magnitude is intrinsic to the SN and not enhanced by other effects. Visual inspection of the images in Fig. 1 (including the surrounding areas) shows little evidence for strong gravitational lensing which could affect the observed brightness of this SN (we note that the host galaxy would have to be lensed as well). We cannot conclusively rule out the possibility of strong lensing, as in the case of PS1-10afx (Quimby et al. 2014), but as discussed above the spectrum and extended light curve of DES13S2cmm are inconsistent with a normal SN, while the probability of such a strong lensing event in our DES data is less than the probability of discovering a SLSN, based on the lensing statistics given in Quimby et al. (2014), and the lower redshift of DES13S2cmm and smaller search area of DES. Moreover, the observed $r - i$ peak colour of DES13S2cmm is consistent with the expected colours of other unlensed SNe (including SLSNe) shown in Figure 4 of Quimby et al. (2014), i.e., DES13S2cmm is located below the thick black line in this plot. Therefore, we do not consider gravitational lensing further in this paper, but higher-resolution imaging data should be obtained for DES13S2cmm, after the SN event has vanished, to provide better constraints on possible strong lensing as discussed in Quimby et al. (2014).

4.2 Comparison of bolometric light-curves

For comparison with DES13S2cmm, we also show in Fig. 5 the bolometric light curves for eleven well-observed SLSNe-I (or Ic, as discussed in Inserra et al. 2013) in the literature: SN 2010gx (Pastorello et al. 2010); PTF 10hgi, SN 2011ke, PTF 11rks, SN 2011kf and SN 2012il (Inserra et al. 2013); SNLS 06D4eu and SNLS 07D2bv (Howell et al. 2013); and LSQ 12dlf, SSS 120810 and SN 2013dg (Nicholl et al. 2014). We exclude from this figure other SLSNe-I that do not possess data for at least three passbands for each epoch over a majority of their light curves, namely PTF 09atu, PTF 09cnd and PTF 09cwl (Quimby et al. 2011); SCP 06F6 (Barbary et al. 2009); SN 2006oz (Leloudas et al.
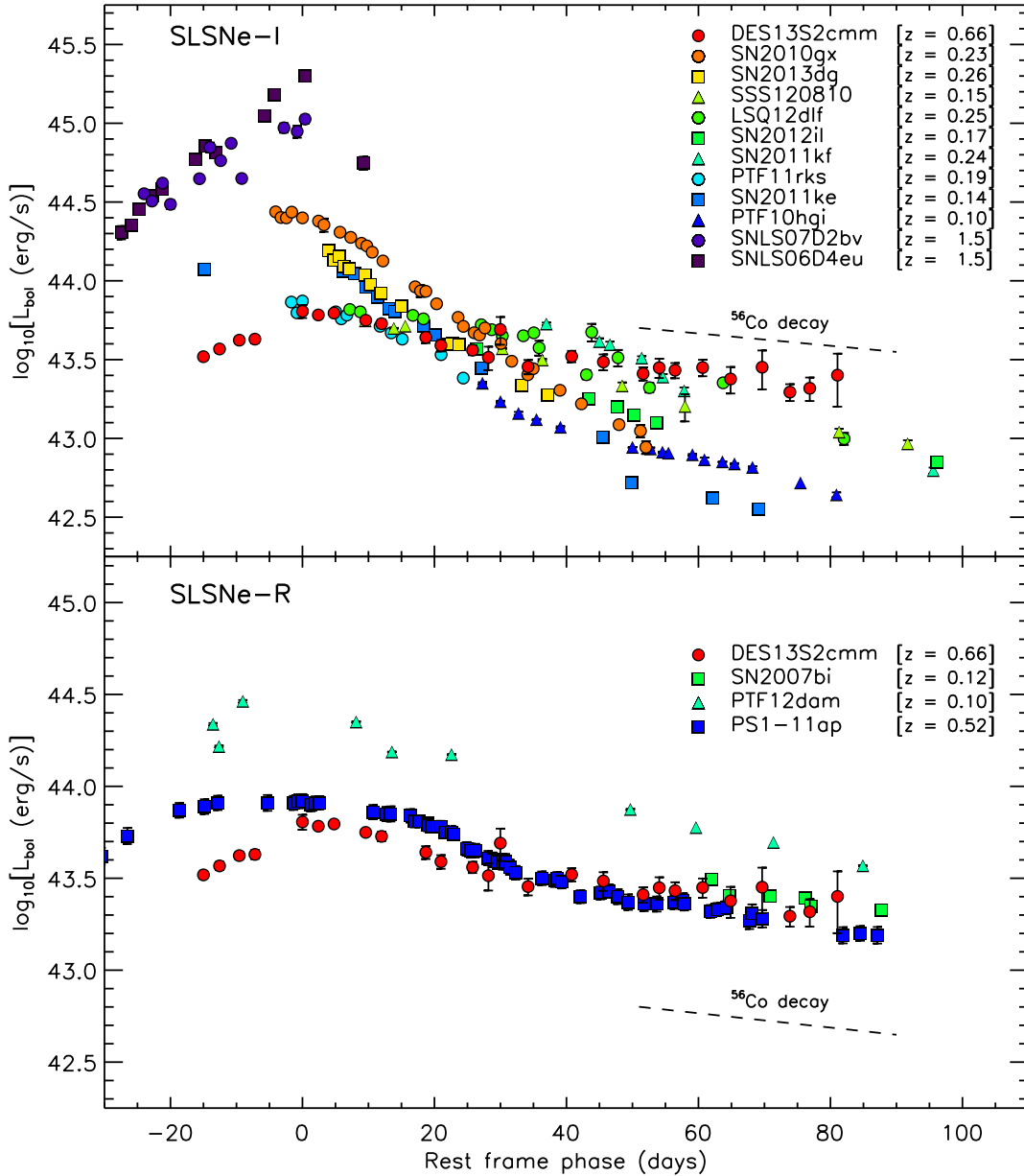
Figure 5. The bolometric light curve of DES13S2cmm (red circles) compared to other SLSNe in the literature (see text for explanation). These bolometric light curves were constructed by fitting a single black-body spectrum to the multicolour data available per epoch (requiring at least three photometric measurements per epoch), and then by integrating the black-body spectral energy distribution to produce the bolometric luminosity per rest-frame epoch (described in detail in Section 4.2). We show statistical errors on the blackbody fits to each epoch of these light curves, but in most cases this error is smaller than the plotting symbol. We stress that these errors do not account for systematic uncertainties involved in the bolometric calculation (e.g., assuming a blackbody for the spectral energy distribution of SLSNe). The phase relative to peak (y-axis) for the literature SLSNe is taken directly from the published individual studies and not recalculated herein. The dashed lines shown in both panels represent the ^{56}Co decay rate at late times.

2012); PS1-10ky and PS1-10awh (Chomiuk et al. 2011); and PS1-10bzj (Lunnan et al. 2013).

The full bolometric light curves for these eleven literature SLSNe-I were calculated using the same methodology as described above for DES13S2cmm (i.e. using the published photometric data and requiring three or more passbands per epoch). As a check, our bolometric light curves for PTF 10hgi, SN 2011ke, PTF 11rks,

SN 2011kf and SN 2012il are similar to those published in Inserra et al. (2013), with any offsets due to differences in the integration of the blackbody curve; we integrate over all wavelengths, while Inserra et al. (2013) integrate over the wavelength range of their observed optical passbands (we are able to reproduce their luminosities if we follow their procedure).

In Fig. 5, the phase relative to peak for DES13S2cmm was de-

fined as the peak of the observer-frame r-band, which occurred on MJD 56563.2, while for other SLSNe-I we simply used the phase relative to peak as reported by the individual literature studies. In the case of SNLS 06D4eu and SNLS 07D2bv, Howell et al. (2013) reported a phase based on their calculation of the bolometric light curves, which we use herein, but note there may be greater uncertainty in the definition of the time of peak for these light curves; these SLSNe are at significantly higher redshifts than the others in Fig. 5, and as such their bolometric light-curve is based exclusively on data bluewards of rest-frame *g*-band.

The top panel of Fig. 5 shows that DES13S2cmm is one of the faintest SLSNe-I around peak compared to the other SLSNe-I in the literature, and possesses one of the slowest declining tails (beyond approximately +30 rest-frame) of the SLSNe studied herein. In the bottom panel of Fig. 5, we compare DES13S2cmm to possible Type R SLSNe (to be consistent with the classification scheme of Gal-Yam 2012) and find the late-time light curve of DES13S2cmm is similar to both PS1-11ap (McCrum et al. 2014) and SN2007bi (Gal-Yam et al. 2009), highlighting the possible overlap between these two SLSNe types, as discussed in Section 3.2 and Inserra et al. (2013).

Fig. 5 also demonstrates that the twelve SLSNe-I light curves (top panel) have similar luminosities at approximately +25 days (rest frame) past peak, close to the inflection point in the light curves when their extended tails begin to appear. We calculate the dispersion, as a function of relative phase, for the twelve SLSNe-I light curves shown in Fig. 5, linearly interpolating between large gaps in each light curve to provide an evenly sampled set of data. We find a minimum dispersion of $\sigma(\log_{10} L_{bol}) = 0.084$ – equivalent to 0.21 magnitudes – at +25 days past peak (rest frame), derived from the seven SLSNe in Fig. 5 constraining this phase. As commented in Quimby et al. (2011), such light curve characteristics could point towards a possible 'standardisation' of SLSNe-I, as with SNe Ia, leading to their use as high-redshift 'standard candles' for cosmological studies (King et al. 2014).

Recently, Inserra & Smartt (2014) has proposed a 'standardisation' of the peak magnitude of 16 SLSNe using a stretch-luminosity correction similar to the Δm_{15} relationship of Phillips (1993) for SNe Ia. They find that SLSNe that are brighter at peak have slower declining light curve over the first 30 days after peak (rest frame) and, correcting for this correlation, the dispersion of the peak magnitude of SLSNe can be reduced to $\sigma \simeq 0.2$. This is similar in size to the dispersion at +25 days past peak seen in Fig. 5 and is only a factor of two worse than the dispersion obtained for standardised SNe Ia.

Both Fig. 5 and Inserra & Smartt (2014) suggest some standardisation of SLSNe light curves is possible but further observations and analyses are required to find the best approach. For example, the light curve of DES13S2cmm does not appear to follow the correlation found by Inserra & Smartt (2014) as it has a faint peak magnitude, relative to other SLSNe, but is also slowly declining towards +30 days after peak. A direct comparison to Inserra & Smartt (2014) is difficult as our study uses different sample selection criteria (only 7 of their 16 SLSNe are included here because of our requirement to have three passbands per epoch), while Inserra & Smartt (2014) estimate a common synthetic peak magnitudes for all their SLSNe using their own time-evolving spectral template. A more detailed comparison will be possible with further DES SLSNe.

4.3 Power source of DES13S2cmm

The details of the power source of SLSN-I remain unclear and are much debated (see Section 1). Here we investigate the two popular explanations in the literature for SLSNe-I: radioactive decay of ^{56}Ni, and energy deposition from a Magnetar.

4.3.1 Radioactive ^{56}Ni model

As can been seen in Fig. 5, the decline rate of DES13S2cmm is approximately that expected from the decay of ^{56}Co (dashed line). This is suggestive of the SN energy source being the production and subsequent decay of large quantities of ^{56}Ni produced in the explosion. To test this theory we fit the bolometric light curve of DES13S2cmm to a model of ^{56}Ni, following the prescription of Arnett (1982), which is the approximation of an homologously expanding ejecta (Chatzopoulos et al. 2009; Inserra et al. 2013) where the luminosity at any given time (in erg s^{-1}) is given by

$$L(t) = M_{Ni}\, e^{-(t/\tau_m)^2} \left[\epsilon_{Ni} \int_0^t \frac{2u}{\tau_m^2} e^{(u/\tau_m)^2} e^{-u/\tau_{Ni}} du \right.$$
$$\left. + \epsilon_{Co} \int_0^t \frac{2u}{\tau_m^2} e^{(u/\tau_m)^2} \left(e^{-u/\tau_{Ni}} - e^{-u/\tau_{Co}} \right) du \right] \delta_\gamma. \quad (1)$$

The energy production rate and decay rate for ^{56}Ni are $\epsilon_{Ni} = 3.9 \times 10^{10}$ erg s^{-1} g^{-1} and $\tau_{Ni} = 8.8$ days, while for ^{56}Co these values are $\epsilon_{Co} = 6.8 \times 10^9$ erg s^{-1} g^{-1} and $\tau_{Co} = 111.3$ days. The amount of ^{56}Ni produced in the explosion is M_{Ni}, while the rise-time of the light curve τ_m (from Eqns 18, 19, and 22 of Arnett 1982) is given by

$$\tau_m = 1.05 \left(\frac{\kappa}{\beta c} \right)^{1/2} \left(\frac{M_{ej}^3}{E} \right)^{1/4} \quad (2)$$

Here E is the explosion energy, M_{ej} is the total amount of ejected mass, κ is the gamma-ray opacity (assumed to be 0.1 and constant throughout), and β is a constant with value ≈ 13.7 (Arnett 1982).

We use δ_γ to denote the gamma-ray deposition function: the efficiency with which gamma-rays are trapped within the SN ejecta. For this function we follow Arnett (1982), which is also used by Inserra et al. (2013) and uses the deposition function defined in Colgate et al. (1980),

$$\delta_\gamma = G[1 + 2G(1 - G)(1 - 0.75G)], \quad (3)$$

where $G \equiv \tau_\gamma/(\tau_\gamma + 1.6)$, with the 'optical depth' for gamma-rays approximately given by

$$\tau_\gamma \approx \left(\frac{0.1}{\kappa} \right) \left(\frac{\tau_m^2}{4\tau_{Ni}^2} \right) \left(\frac{5.53 \times 10^{10}}{v_{ej}(0.1 + t/\tau_{Ni})^2} \right). \quad (4)$$

Here $v_{ej} = \sqrt{10 E_k/3 M_{ej}}$ and is in units of cm s^{-1}. We note that the deposition function used in Chatzopoulos et al. (2009) has a functional form that is similar to that used here, but in their approximation τ_γ only deviates from ≈ 1 at much later epochs, resulting in a light-curve decay rate mirroring ^{56}Co and largely insensitive to changes in the explosion energy or ejecta mass.

We thus have four parameters in our model: the explosion epoch (t_0), the energy of the explosion (E), the total ejected mass (M_{ej}), and the amount of ejected mass which is ^{56}Ni (M_{Ni}). Since high S/N spectra of SLSNe display predominantly intermediate-mass elements, it is clear that there must be an upper limit to the fraction of the ejecta mass which can be in ^{56}Ni ($f_{Ni} = M_{Ni}/M_{ej}$): otherwise these elements would be subdominant to Fe-group elements. Inserra et al. (2013) assumed an upper limit of 50% on the

Table 2. Best-fitting parameters for a variety of ^{56}Ni model fits to the bolometric light curve for DES13S2cmm. $f_{Ni,max}$ is the maximum fraction of ^{56}Ni allowed in the ejecta for each fit; for DES13S2cmm the best-fitting model always maximizes this value. Ejecta and ^{56}Ni masses are given in units of solar masses. There are 22 degrees of freedom for each fit.

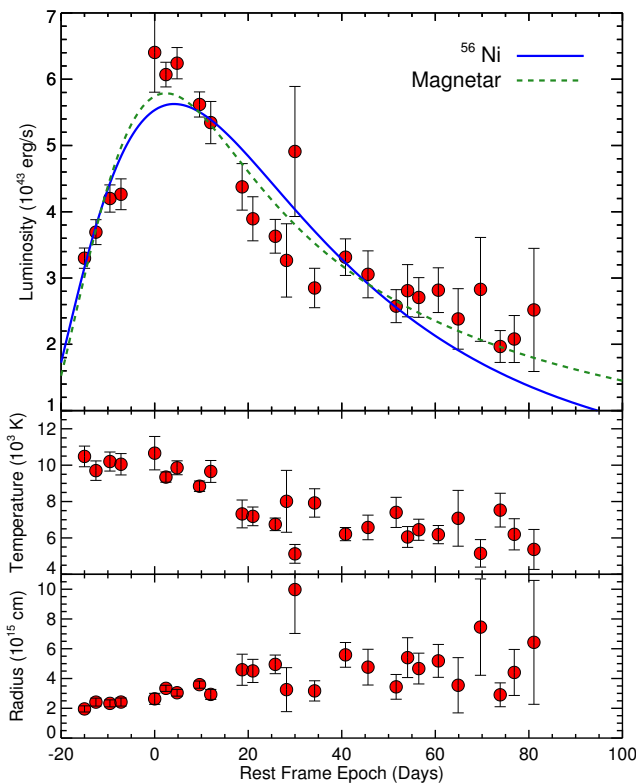| $f_{Ni,max}$	$E(10^{51}$ erg$)$	M_{ej}	M_{Ni}	t_0 (MJD)	χ^2
0.30	31.88	14.77	4.43	56508.8	81.5
0.40	14.83	10.59	4.23	56510.4	76.0
0.50	8.22	8.21	4.10	56511.5	71.5
0.60	5.08	6.68	4.01	56512.4	67.9
0.70	3.38	5.62	3.93	56513.1	65.0
0.80	2.38	4.84	3.88	56513.7	62.7
0.90	1.74	4.25	3.83	56514.2	60.9
1.00	1.32	3.79	3.79	56514.6	59.4

Figure 6. *Upper panel:* Bolometric light curve with ^{56}Ni (blue solid line) and magnetar (green dashed line) best-fitting models. We plot here the ^{56}Ni model with $f_{Ni,max} = 0.5$. The magnetar model is the better fit (see text). However both models have difficulty reproducing the peak luminosity, the post-peak decline, and the late-time flattening. *Middle and Bottom panels:* Temperature and radius evolution of the best-fitting blackbody to each photometric epoch which is used to construct the bolometric light curve.

ejecta mass as being ^{56}Ni. Without a strong theoretical limit on this value, we fit the model to the data with a variety of upper limits on f_{Ni}, varying from 0.3 to 1.0. We report the best-fitting parameters and goodness of fit for these models in Table 2.

We find that the ^{56}Ni model is not a good fit to the bolometric light curve, as the best-fitting model has a $\chi^2/\mathrm{dof} = 2.7$ (χ^2 of 59 for 22 degrees of freedom), and is physically unrealistic ($f_{Ni} = 1$). As can be seen in Table 2, the model prediction for M_{Ni} is relatively robust ($3.8 - 4.4 M_\odot$), as this parameter is primarily constrained by

the peak luminosity of the light curve. However, to match the late time ($t > 30$ days) flattening of the light curve a large amount of ejecta mass or low explosion energy (see Eqn. 2) is required to increase the diffusion time-scale, which simultaneously makes the fit to the post-peak decline poor while predicting a much longer rise time than is seen.

4.3.2 Magnetar model

As an alternative to the radioactive decay of ^{56}Ni, we also fit our derived bolometric light curve for DES13S2cmm to a magnetar model, which proposes that SLSNe are powered by the rapid spinning-down of a neutron star with an extreme magnetic field (Woosley 2010; Kasen & Bildsten 2010). In this model the input energy is defined by the initial spin-down time (P_{ms}, in milliseconds) and magnetic field strength (B_{14}, in units of 10^{14} Gauss) of the magnetar, and the diffusion timescale (τ_m, Eqn. 2) reflects the combined effect of the explosion energy (E), the ejected mass (M_{ej}), and the opacity (κ). We use the semi-analytical model outlined in Inserra et al. (2013). The luminosity of the magnetar model (in erg s^{-1}) is given by

$$L(t) = 4.9 \times 10^{46} \, e^{-(t/\tau_m)^2} \delta_\gamma \int_0^t \frac{2u}{\tau_m^2} \, e^{(u/\tau_m)^2} \, \frac{B_{14}^2 \, P_{ms}^{-4}}{(1 + u/\tau_p)^2} \, du, \tag{5}$$

where τ_p is the spin-down timescale, $\tau_p = 4.7 \, B_{14}^{-2} \, P_{ms}^2$ days. We do not include any additional contribution from ^{56}Ni decay in this model.

In Fig. 6 we include the best-fitting magnetar model to the bolometric light curve of DES13S2cmm. The best-fitting parameters of this model are a magnetic field of 1.43×10^{14} Gauss, an initial spin period of 5.28 ms, a diffusion timescale of 22.9 days, and an explosion date of MJD 56511.0. This model has a $\chi^2/\mathrm{dof} = 2.0$ (χ^2 of 44 for 22 degrees of freedom) and is therefore a significantly better fit to our data than the ^{56}Ni model. However, it is still clear that the model does not fit *well*: it is unable to reproduce the factor of two drop in luminosity post-peak within 30 days of explosion (although it does a better job than ^{56}Ni). Intriguingly the late-time epochs seem to fit the magnetar model well. Our time coverage of DES13S2cmm allows us to determine whether either model is able to reproduce detailed features of the light curve, but discerning between the two models would be improved by an even longer time-scale over which the two models cannot mimic one another; DES alone will unlikely provide longer light curve coverage as its observing season is typically less than 5 months a year.

5   CONCLUSIONS

In this paper we have presented DES13S2cmm, the first spectroscopically-confirmed superluminous supernova (SLSN) from the Dark Energy Survey. Using spectroscopic data obtained from the ESO Very Large Telescope, we measured a redshift of $z = 0.663 \pm 0.001$, and assigned a classification of SLSN-I. However, we cannot exclude the possibility that DES13S2cmm is a type R (Fig. 4 and 5) if this is in fact a distinct SLSN type.

Using this redshift and correcting for Milky Way extinction, we find the rest-frame U-band absolute magnitude of DES13S2cmm at peak to be $M_U^{peak} = -21.05^{+0.10}_{-0.09}$, consistent with the SLSNe definition of Gal-Yam (2012). Like other SLSNe

(Lunnan et al. 2014), DES13S2cmm is located in a faint low stellar-mass host galaxy ($\log(\mathrm{M/M_\odot}) = 8.9 \pm 0.3$) with sub-solar metallicity.

In Fig. 5, we compare the bolometric light curve of DES13S12cmm to eleven similarly well-observed SLSNe-I light curves in literature, and see that DES13S2cmm has one of the slowest declining tails (beyond +30 rest frame past peak) of all SLSNe-I studied herein, as well as likely being the faintest at peak. We further find that the dispersion between the bolometric light curves of all twelve SLSNe-I shown in Fig. 5 has a minimum of 0.21 magnitudes at +25 days past peak (rest frame), thus raising the tantalising possibility of 'standardising' these SLSNe like SNe Ia (Quimby et al. 2011; Inserra & Smartt 2014) and starting a new era of supernova cosmology (King et al. 2014). Further study is required to confirm if SLSNe can be standardised.

In Fig. 6, we fit the bolometric light curve of DES13S2cmm with two possible models for the power source of these extreme events; the radioactive decay of ^{56}Ni and a magnetar (e.g. see Inserra et al. 2013). We find that the ^{56}Ni model is not a good fit to the bolometric light curve, as the best-fitting model has a $\chi^2/\mathrm{DoF}= 2.7$ with an unrealistic fraction of ^{56}Ni to ejected mass ($f_{\mathrm{Ni}} = 1$). The model does provide a relatively robust prediction for the overall ^{56}Ni mass ($3.8 - 4.4 M_\odot$), as this is primarily constrained by the peak luminosity of the light curve, but is unable to reproduce the late time ($t > 30$ days) evolution of the light curve. The Magnetar model provides a smaller χ^2 (for the same degrees of freedom) than ^{56}Ni, but is likewise not a good fit to the data as it is unable to fully reproduce the drop in luminosity within 30 days of explosion.

In the future, DES should find many more SLSN-I. Such data should allow us to further test these two models, especially if we can measure the (rest frame) light curves to > 100 days (see Fig. 6 and Inserra et al. 2013). Therefore, we have begun a new project entitled 'SUrvey with Decam for Superluminous Supernovae' (SUDSS), which will enable extended monitoring of some DES SN fields (in addition to several non-DES fields) to over 8 months, greatly enhancing both our ability to detect many more SLSNe and measure their long light curves.

REFERENCES

Anderson L. et al., 2014, MNRAS, 441, 24
Appenzeller I. et al., 1998, The Messenger, 94, 1
Arnett W. D., 1982, ApJ, 253, 785
Asplund M., Grevesse N., Sauval A. J., Scott P., 2009, ARA&A, 47, 481
Barbary K. et al., 2009, ApJ, 690, 1358
Berger E. et al., 2012, ApJ, 755, L29
Bernstein J. P. et al., 2012, ApJ, 753, 152
Bertin E., Arnouts S., 1996, A&AS, 117, 393
Betoule M. et al., 2014, arxiv:1401.4064
Blinnikov S. I., Sorokina E. I., 2010, arxiv:1009.4353
Chatzopoulos E., Wheeler J. C., Vinko J., 2009, ApJ, 704, 1251
Chen T.-W. et al., 2013, ApJ, 763, L28
Chomiuk L. et al., 2011, ApJ, 743, 114
Colgate S. A., Petschek A. G., Kriese J. T., 1980, ApJ, 237, L81
Cooke J. et al., 2012, Nature, 491, 228
Delubac T. et al., 2014, arxiv:1404.1801
Desai S. et al., 2012, ApJ, 757, 83
Diehl H. T., For the Dark Energy Survey Collaboration, 2012, Physics Procedia, 37, 1332
Ellis R. S. et al., 2008, ApJ, 674, 51
Fioc M., Rocca-Volmerange B., 1997, A&A, 326, 950
Flaugher B., 2005, International Journal of Modern Physics A, 20, 3121
Flaugher B. L. et al., 2012, in Society of Photo-Optical Instrumentation Engineers (SPIE) Conference Series, Vol. 8446, Society

of Photo-Optical Instrumentation Engineers (SPIE) Conference Series

Gal-Yam A., 2012, Science, 337, 927

Gal-Yam A. et al., 2009, Nature, 462, 624

Howell D. A. et al., 2013, ApJ, 779, 98

Howell D. A. et al., 2005, ApJ, 634, 1190

Inserra C., Smartt S. J., 2014, in prep

Inserra C. et al., 2013, ApJ, 770, 128

Kasen D., Bildsten L., 2010, ApJ, 717, 245

Kelson D. D., 2003, PASP, 115, 688

Kewley L. J., Dopita M. A., 2002, ApJS, 142, 35

Kewley L. J., Ellison S. L., 2008, ApJ, 681, 1183

King A. L., Davis T. M., Denney K. D., Vestergaard M., Watson D., 2014, MNRAS, 441, 3454

Kobulnicky H. A., Kewley L. J., 2004, ApJ, 617, 240

Leloudas G. et al., 2012, A&A, 541, A129

Lunnan R. et al., 2014, ApJ, 787, 138

Lunnan R. et al., 2013, ApJ, 771, 97

Maguire K. et al., 2012, MNRAS, 426, 2359

Maraston C., 2005, MNRAS, 362, 799

McCrum M. et al., 2014, arxiv:1402.1631

McGaugh S. S., 1991, ApJ, 380, 140

Mohr J. J. et al., 2012, in Society of Photo-Optical Instrumentation Engineers (SPIE) Conference Series, Vol. 8451, Society of Photo-Optical Instrumentation Engineers (SPIE) Conference Series

Neill J. D. et al., 2011, ApJ, 727, 15

Nicholl M. et al., 2014, ArXiv e-prints

Nicholl M. et al., 2013, Nature, 502, 346

Ofek E. O. et al., 2007, ApJ, 659, L13

Ofek E. O. et al., 2013, Nature, 494, 65

Oke J. B., Gunn J. E., 1983, ApJ, 266, 713

Pastorello A. et al., 2010, ApJ, 724, L16

Phillips M. M., 1993, ApJ, 413, L105

Quimby R. M. et al., 2011, Nature, 474, 487

Quimby R. M. et al., 2014, Science, 344, 396

Quimby R. M., Yuan F., Akerlof C., Wheeler J. C., 2013, MNRAS, 431, 912

Riess A. G., Press W. H., Kirshner R. P., 1996, ApJ, 473, 88

Sako M. et al., 2008, AJ, 135, 348

Sako M. et al., 2011, ApJ, 738, 162

Sánchez C. et al., 2014, arxiv:1406.4407

Scalzo R. A. et al., 2010, ApJ, 713, 1073

Schlafly E. F., Finkbeiner D. P., 2011, ApJ, 737, 103

Smith N. et al., 2007, ApJ, 666, 1116

Sullivan M. et al., 2011, ApJ, 732, 118

Tripp R., 1998, A&A, 331, 815

Woosley S. E., 2010, ApJ, 719, L204

Woosley S. E., Blinnikov S., Heger A., 2007, Nature, 450, 390

AFFILIATIONS

[1] Institute of Cosmology and Gravitation, Dennis Sciama Building, University of Portsmouth, Burnaby Road, Portsmouth, PO1 3FX, UK

[2] School of Physics and Astronomy, University of Southampton, Southampton, SO17 1BJ, UK

[3] Berkeley Center for Cosmological Physics, University of California at Berkeley, Berkeley, CA 94720, USA

[4] Argonne National Laboratory, 9700 S. Cass Avenue, Argonne, IL 60439, USA

[5] George P. & Cynthia Woods Mitchell Institute for Fundamental Physics & Astronomy, Texas A. & M. University, Dept. of Physics & Astronomy, College Station, TX, USA

[6] National Center for Supercomputing Applications, 1205 West Clark St., Urbana, IL 61801, USA

[7] Fermi National Accelerator Laboratory, P.O. Box 500, Batavia, IL 60510, USA

[8] Dept. of Physics & Astronomy, University of Pennsylvania 209 South 33rd Street, Philadelphia, PA 19104, USA

[9] Astronomy Dept., University of California at Berkeley, Berkeley, CA 94720, USA

[10] Lawrence Berkeley National Laboratory, 1 Cyclotron Road, Berkeley, CA 94720, USA

[11] Kavli Institute for Cosmological Physics, University of Chicago, Chicago, IL 60637, USA

[12] Department of Physics & Astronomy, 5640 South Ellis Avenue, University of Chicago, Chicago, IL 60637, USA

[13] Australian Astronomical Observatory, PO Box 915, North Ryde NSW 1670, Australia

[14] Cerro Tololo Inter-American Observatory, National Optical Astronomy Observatory, Casilla 603, La Serena, Chile

[15] Department of Physics and Astronomy, University College London, London WC1E 6BT, UK

[16] Space Telescope Science Institute (STScI), 3700 San Martin Drive, Baltimore, MD 21218, USA

[17] Carnegie Observatories, 813 Santa Barbara St., Pasadena, CA 91101, USA

[18] Observatório Nacional, Rua Gal. José Cristino 77, Rio de Janeiro, RJ - 20921-400, Brazil

[19] Laboratório Interinstitucional de e-Astronomia - LIneA, Rua Gal. José Cristino 77, Rio de Janeiro, RJ - 20921-400, Brazil

[20] Department of Physics, Ludwig-Maximilians-Universität, Scheinerstr. 1, 81679 München, Germany

[21] Excellence Cluster Universe, Boltzmannstr. 2, 85748 Garching, Germany

[22] Jet Propulsion Laboratory, California Institute of Technology, 4800 Oak Grove Drive, Pasadena, 91109 CA

[23] Department of Physics, University of Michigan, Ann Arbor, MI 48109, USA

[24] Department of Astronomy, University of Michigan, Ann Arbor, MI 48109, USA

[25] University Observatory Munich, Scheinerstrasse 1, 81679 Munich, Germany

[26] Max Planck Institute for Extraterrestrial Physics, Giessenbachstrasse, 85748 Garching, Germany

[27] Department of Physics, The Ohio State University, Columbus, OH 43210, USA

[28] ICRA, Centro Brasileiro de Pesquisas Físicas, Rua Dr. Xavier Sigaud 150, CEP 22290-180, Rio de Janeiro, RJ, Brazil

[29] Institut de Física d'Altes Energies, Universitat Autònoma de Barcelona, E-08193 Bellaterra, Barcelona, Spain

[30] Institució Catalana de Recerca i Estudis Avançats, E-08010 Barcelona, Spain

[31] Brookhaven National Laboratory, Dept of Physics, Bldg 510A, Upton, NY 11973

[32] Department of Physics and Astronomy, Pevensey Building, University of Sussex, Brighton, BN1 9QH, UK

[33] SLAC National Accelerator Laboratory, Menlo Park, CA 94025, USA

[34] Centro de Investigaciones Energéticas, Medioambientales y Tecnológicas (CIEMAT), Avda. Complutense 40, Madrid, Spain

[35] Instituto de Física, UFRGS, Caixa Postal 15051, Porto Alegre, RS - 91501-970, Brazil

[36] Department of Physics, University of Illinois, 1110 W. Green St., Urbana, IL 61801, USA

[37] Kavli Institute. for Particle Astrophysics & Cosmology, Stanford University, Stanford, CA 94305, USA

[38] Jodrell Bank Centre for Astrophysics, University of Manchester, Manchester M13 9PL, UK.

This paper has been typeset from a TEX/ LATEX file prepared by the author.

FORM UPR16
Research Ethics Review Checklist

Please include this completed form as an appendix to your thesis (see the Postgraduate Research Student Handbook for more information

University of **Portsmouth**

Postgraduate Research Student (PGRS) Information		Student ID:	641093
PGRS Name:	Andreas Papadopoulos		
Department:	ICG	**First Supervisor:**	Prof. Bob Nichol
Start Date: (or progression date for Prof Doc students)		October 2012	

Study Mode and Route:	Part-time	☒	MPhil	☐	MD	☐
	Full-time	☐	PhD	☒	Professional Doctorate	☐

Title of Thesis:	The search for Superluminous Supernova with the Dark Energy Camera
Thesis Word Count: (excluding ancillary data)	63957

If you are unsure about any of the following, please contact the local representative on your Faculty Ethics Committee for advice. Please note that it is your responsibility to follow the University's Ethics Policy and any relevant University, academic or professional guidelines in the conduct of your study

Although the Ethics Committee may have given your study a favourable opinion, the final responsibility for the ethical conduct of this work lies with the researcher(s).

UKRIO Finished Research Checklist:
(If you would like to know more about the checklist, please see your Faculty or Departmental Ethics Committee rep or see the online version of the full checklist at: http://www.ukrio.org/what-we-do/code-of-practice-for-research/)

a)	Have all of your research and findings been reported accurately, honestly and within a reasonable time frame?	YES NO	☒ ☐
b)	Have all contributions to knowledge been acknowledged?	YES NO	☒ ☐
c)	Have you complied with all agreements relating to intellectual property, publication and authorship?	YES NO	☒ ☐
d)	Has your research data been retained in a secure and accessible form and will it remain so for the required duration?	YES NO	☒ ☐
e)	Does your research comply with all legal, ethical, and contractual requirements?	YES NO	☒ ☐

Candidate Statement:

I have considered the ethical dimensions of the above named research project, and have successfully obtained the necessary ethical approval(s)

Ethical review number(s) from Faculty Ethics Committee (or from NRES/SCREC):	113B-E952-7E2B-F5A4-155A-CAB2-14D8-357E

If you have *not* submitted your work for ethical review, and/or you have answered 'No' to one or more of questions a) to e), please explain below why this is so:

Signed (PGRS):		Date: 29-09-2015

References

Aldering, G., Adam, G., Antilogus, P., Astier, P., Bacon, R., Bongard, S., Bonnaud, C., Copin, Y., Hardin, D., Henault, F., Howell, D. A., Lemonnier, J.-P., Levy, J.-M., Loken, S. C., Nugent, P. E., Pain, R., Pecontal, A., Pecontal, E., Perlmutter, S., Quimby, R. M., Schahmaneche, K., Smadja, G., and Wood-Vasey, W. M. (2002). Overview of the Nearby Supernova Factory. In Tyson, J. A. and Wolff, S., editors, *Survey and Other Telescope Technologies and Discoveries*, volume 4836 of , pages 61–72.

Amorín, R., Sommariva, V., Castellano, M., Grazian, A., Tasca, L. A. M., Fontana, A., Pentericci, L., Cassata, P., Garilli, B., Le Brun, V., Le Fèvre, O., Maccagni, D., Thomas, R., Vanzella, E., Zamorani, G., Zucca, E., Bardelli, S., Capak, P., Cassará, L. P., Cimatti, A., Cuby, J. G., Cucciati, O., de la Torre, S., Durkalec, A., Giavalisco, M., Hathi, N. P., Ilbert, O., Lemaux, B. C., Moreau, C., Paltani, S., Ribeiro, B., Salvato, M., Schaerer, D., Scodeggio, M., Talia, M., Taniguchi, Y., Tresse, L., Vergani, D., Wang, P. W., Charlot, S., Contini, T., Fotopoulou, S., López-Sanjuan, C., Mellier, Y., and Scoville, N. (2014). Discovering extremely compact and metal-poor, star-forming dwarf galaxies out to z ˜ 0.9 in the VIMOS Ultra-Deep Survey. , 568:L8.

Anderson, L., Aubourg, É., Bailey, S., Beutler, F., Bhardwaj, V., Blanton, M., Bolton, A. S., Brinkmann, J., Brownstein, J. R., Burden, A., Chuang, C.-H., Cuesta, A. J., Dawson, K. S., Eisenstein, D. J., Escoffier, S., Gunn, J. E., Guo, H., Ho, S., Honscheid, K., Howlett, C., Kirkby, D., Lupton, R. H., Manera, M., Maraston, C., McBride, C. K., Mena, O., Montesano, F., Nichol, R. C., Nuza, S. E., Olmstead, M. D., Padmanabhan, N., Palanque-Delabrouille, N., Parejko, J., Percival, W. J., Petitjean, P., Prada, F., Price-Whelan, A. M., Reid, B., Roe, N. A., Ross, A. J., Ross, N. P., Sabiu, C. G., Saito, S., Samushia, L., Sánchez, A. G., Schlegel, D. J., Schneider, D. P., Scoccola, C. G., Seo, H.-J., Skibba, R. A., Strauss, M. A., Swanson, M. E. C., Thomas, D., Tinker, J. L., Tojeiro, R., Magaña, M. V., Verde, L., Wake, D. A., Weaver, B. A., Weinberg, D. H., White, M., Xu, X., Yèche, C., Zehavi, I., and Zhao, G.-B. (2014). The clustering of galaxies in the SDSS-III Baryon Oscillation

Spectroscopic Survey: baryon acoustic oscillations in the Data Releases 10 and 11 Galaxy samples. , 441:24–62.

Andrae, R., Schulze-Hartung, T., and Melchior, P. (2010). Dos and don'ts of reduced chi-squared. *ArXiv e-prints*.

Appenzeller, I., Fricke, K., Fürtig, W., Gässler, W., Häfner, R., Harke, R., Hess, H.-J., Hummel, W., Jürgens, P., Kudritzki, R.-P., Mantel, K.-H., Meisl, W., Muschielok, B., Nicklas, H., Rupprecht, G., Seifert, W., Stahl, O., Szeifert, T., and Tarantik, K. (1998). Successful commissioning of FORS1 - the first optical instrument on the VLT. *The Messenger*, 94:1–6.

Arnett, W. D. (1982). Type I supernovae. I - Analytic solutions for the early part of the light curve. , 253:785–797.

Asplund, M., Grevesse, N., Sauval, A. J., and Scott, P. (2009). The Chemical Composition of the Sun. , 47:481–522.

Astier, P., Guy, J., Regnault, N., Pain, R., Aubourg, E., Balam, D., Basa, S., Carlberg, R. G., Fabbro, S., Fouchez, D., Hook, I. M., Howell, D. A., Lafoux, H., Neill, J. D., Palanque-Delabrouille, N., Perrett, K., Pritchet, C. J., Rich, J., Sullivan, M., Taillet, R., Aldering, G., Antilogus, P., Arsenijevic, V., Balland, C., Baumont, S., Bronder, J., Courtois, H., Ellis, R. S., Filiol, M., Gonçalves, A. C., Goobar, A., Guide, D., Hardin, D., Lusset, V., Lidman, C., McMahon, R., Mouchet, M., Mourao, A., Perlmutter, S., Ripoche, P., Tao, C., and Walton, N. (2006). The Supernova Legacy Survey: measurement of Ω_M, Ω and w from the first year data set. , 447:31–48.

Atek, H., Siana, B., Scarlata, C., Malkan, M., McCarthy, P., Teplitz, H., Henry, A., Colbert, J., Bridge, C., Bunker, A. J., Dressler, A., Fosbury, R. A. E., Hathi, N. P., Martin, C., Ross, N. R., and Shim, H. (2011). Very Strong Emission-line Galaxies in the WFC3 Infrared Spectroscopic Parallel Survey and Implications for High-redshift Galaxies. , 743:121.

Baade, W. and Zwicky, F. (1934a). Cosmic Rays from Super-novae. *Proceedings of the National Academy of Science*, 20:259–263.

Baade, W. and Zwicky, F. (1934b). On Super-novae. *Proceedings of the National Academy of Science*, 20:254–259.

Baltay, C., Rabinowitz, D., Hadjiyska, E., Walker, E. S., Nugent, P., Coppi, P., Ellman, N., Feindt, U., McKinnon, R., Horowitz, B., and Effron, A. (2013). The La Silla-QUEST Low Redshift Supernova Survey. , 125:683–694.

Barbary, K., Dawson, K. S., Tokita, K., Aldering, G., Amanullah, R., Connolly, N. V., Doi, M., Faccioli, L., Fadeyev, V., Fruchter, A. S., Goldhaber, G., Goobar, A., Gude, A., Huang, X., Ihara, Y., Konishi, K., Kowalski, M., Lidman, C., Meyers, J., Morokuma, T., Nugent, P., Perlmutter, S., Rubin, D., Schlegel, D., Spadafora, A. L., Suzuki, N., Swift, H. K., Takanashi, N., Thomas, R. C., and Yasuda, N. (2009). Discovery of an Unusual Optical Transient with the Hubble Space Telescope. , 690:1358–1362.

Barbon, R., Ciatti, F., and Rosino, L. (1979). Photometric properties of type II supernovae. , 72:287–292.

Barkat, Z., Rakavy, G., and Sack, N. (1967). Dynamics of Supernova Explosion Resulting from Pair Formation. *Physical Review Letters*, 18:379–381.

Ben-Ami, S., Gal-Yam, A., Mazzali, P. A., Gnat, O., Modjaz, M., Rabinak, I., Sullivan, M., Bildsten, L., Poznanski, D., Yaron, O., Arcavi, I., Bloom, J. S., Horesh, A., Kasliwal, M. M., Kulkarni, S. R., Nugent, P. E., Ofek, E. O., Perley, D., Quimby, R., and Xu, D. (2014). SN 2010mb: Direct Evidence for a Supernova Interacting with a Large Amount of Hydrogen-free Circumstellar Material. , 785:37.

Benetti, S., Nicholl, M., Cappellaro, E., Pastorello, A., Smartt, S. J., Elias-Rosa, N., Drake, A. J., Tomasella, L., Turatto, M., Harutyunyan, A., Taubenberger, S., Hachinger, S., Morales-Garoffolo, A., Chen, T.-W., Djorgovski, S. G., Fraser, M., Gal-Yam, A., Inserra, C., Mazzali, P., Pumo, M. L., Sollerman, J., Valenti, S., Young, D. R., Dennefeld, M., Le Guillou, L., Fleury, M., and Léget, P.-F. (2014). The supernova CSS121015:004244+132827: a clue for understanding superluminous supernovae. , 441:289–303.

Berger, E., Chornock, R., Lunnan, R., Foley, R., Czekala, I., Rest, A., Leibler, C., Soderberg, A. M., Roth, K., Narayan, G., Huber, M. E., Milisavljevic, D., Sanders, N. E., Drout, M., Margutti, R., Kirshner, R. P., Marion, G. H., Challis, P. J., Riess, A. G., Smartt, S. J., Burgett, W. S., Hodapp, K. W., Heasley, J. N., Kaiser, N., Kudritzki, R.-P., Magnier, E. A., McCrum, M., Price, P. A., Smith, K., Tonry, J. L., and Wainscoat, R. J. (2012). Ultraluminous Supernovae as a New Probe of the Interstellar Medium in Distant Galaxies. , 755:L29.

Bernstein, J. P., Kessler, R., Kuhlmann, S., Biswas, R., Kovacs, E., Aldering, G., Crane, I., D'Andrea, C. B., Finley, D. A., Frieman, J. A., Hufford, T., Jarvis, M. J., Kim, A. G., Marriner, J., Mukherjee, P., Nichol, R. C., Nugent, P., Parkinson, D., Reis, R. R. R., Sako, M., Spinka, H., and Sullivan, M. (2012). Supernova Simulations and Strategies for the Dark Energy Survey. , 753:152.

Bertin, E. and Arnouts, S. (1996). SExtractor: Software for source extraction. , 117:393–404.

Betoule, M., Kessler, R., Guy, J., Mosher, J., Hardin, D., Biswas, R., Astier, P., El-Hage, P., Konig, M., Kuhlmann, S., Marriner, J., Pain, R., Regnault, N., Balland, C., Bassett, B. A., Brown, P. J., Campbell, H., Carlberg, R. G., Cellier-Holzem, F., Cinabro, D., Conley, A., D'Andrea, C. B., DePoy, D. L., Doi, M., Ellis, R. S., Fabbro, S., Filippenko, A. V., Foley, R. J., Frieman, J. A., Fouchez, D., Galbany, L., Goobar, A., Gupta, R. R., Hill, G. J., Hlozek, R., Hogan, C. J., Hook, I. M., Howell, D. A., Jha, S. W., Le Guillou, L., Leloudas, G., Lidman, C., Marshall, J. L., Möller, A., Mourão, A. M., Neveu, J., Nichol, R., Olmstead, M. D., Palanque-Delabrouille, N., Perlmutter, S., Prieto, J. L., Pritchet, C. J., Richmond, M., Riess, A. G., Ruhlmann-Kleider, V., Sako, M., Schahmaneche, K., Schneider, D. P., Smith, M., Sollerman, J., Sullivan, M., Walton, N. A., and Wheeler, C. J. (2014). Improved cosmological constraints from a joint analysis of the SDSS-II and SNLS supernova samples. , 568:A22.

Blinnikov, S. I. and Sorokina, E. I. (2010). Supernova Explosions inside Carbon-Oxygen Circumstellar Shells. *arxiv:1009.4353*.

Blondin, S. and Tonry, J. L. (2007). Determining the Type, Redshift, and Age of a Supernova Spectrum. , 666:1024–1047.

Campbell, H., D'Andrea, C. B., Nichol, R. C., Sako, M., Smith, M., Lampeitl, H., Olmstead, M. D., Bassett, B., Biswas, R., Brown, P., Cinabro, D., Dawson, K. S., Dilday, B., Foley, R. J., Frieman, J. A., Garnavich, P., Hlozek, R., Jha, S. W., Kuhlmann, S., Kunz, M., Marriner, J., Miquel, R., Richmond, M., Riess, A., Schneider, D. P., Sollerman, J., Taylor, M., and Zhao, G.-B. (2013). Cosmology with Photometrically Classified Type Ia Supernovae from the SDSS-II Supernova Survey. , 763:88.

Cappellaro, E. and Turatto, M. (2001). Supernova Types and Rates. In Vanbeveren, D., editor, *The Influence of Binaries on Stellar Population Studies*, volume 264 of *Astrophysics and Space Science Library*, page 199.

Carroll, S. M. (2001). The cosmological constant. *Living Reviews in Relativity*, 4(1).

Castander, F. J., Casas, R., Garcia-Alvarez, D., Perez-Valladares, D., Miquel, R., Smith, M., Ahn, E., Finley, D. A., Frieman, J., Marriner, J., Wester, W., Aldering, G., Kim, A. G., Thomas, R. C., Barbary, K., Bloom, J. S., Goldstein, D., Nugent, P., Perlmutter, S., Foley, R. J., Castander, F. J., Desai, S., Paech, K., Smith, R. C., Schubnell, M., Kessler, R., Scolnic, D., Covarrubias, R. A., Brout, D. J., Fischer, J. A., Gladney, L., March, M., Sako, M., Wolf, R. C., Brown, P. J., Krisciunas, K., Suntzeff, N., D'Andrea, C., Nichol, R., Papadopoulos, A., Sullivan, M., Maartens, R., Gupta, R., Kovacs, E., Kuhlmann, S., and Spinka, H. (2015). GTC Classification of DES Supernova Candidates. *The Astronomer's Telegram*, 7199:1.

Chandrasekhar, S. (1931). The Maximum Mass of Ideal White Dwarfs. , 74:81.

Chatzopoulos, E., Wheeler, J. C., and Vinko, J. (2009). Modeling the Light Curve of the Transient SCP06F6. , 704:1251–1261.

Chatzopoulos, E., Wheeler, J. C., Vinko, J., Quimby, R., Robinson, E. L., Miller, A. A., Foley, R. J., Perley, D. A., Yuan, F., Akerlof, C., and Bloom, J. S. (2011). SN 2008am: A Super-luminous Type IIn Supernova. , 729:143.

Chen, T.-W., Smartt, S. J., Bresolin, F., Pastorello, A., Kudritzki, R.-P., Kotak, R., McCrum, M., Fraser, M., and Valenti, S. (2013). The Host Galaxy of the Super-luminous SN 2010gx and Limits on Explosive ^{56}Ni Production. , 763:L28.

Chevalier, R. A. and Irwin, C. M. (2011). Shock Breakout in Dense Mass Loss: Luminous Supernovae. , 729:L6.

Chevallier, M. and Polarski, D. (2001). Accelerating Universes with Scaling Dark Matter. *International Journal of Modern Physics D*, 10:213–223.

Chomiuk, L., Chornock, R., Soderberg, A. M., Berger, E., Chevalier, R. A., Foley, R. J., Huber, M. E., Narayan, G., Rest, A., Gezari, S., Kirshner, R. P., Riess, A., Rodney, S. A., Smartt, S. J., Stubbs, C. W., Tonry, J. L., Wood-Vasey, W. M., Burgett, W. S., Chambers, K. C., Czekala, I., Flewelling, H., Forster, K., Kaiser, N., Kudritzki, R.-P., Magnier, E. A., Martin, D. C., Morgan, J. S., Neill, J. D., Price, P. A., Roth, K. C., Sanders, N. E., and Wainscoat, R. J. (2011). Pan-STARRS1 Discovery of Two Ultraluminous Supernovae at z 0.9. , 743:114.

Chornock, R., Berger, E., Rest, A., Milisavljevic, D., Lunnan, R., Foley, R. J., Soderberg, A. M., Smartt, S. J., Burgasser, A. J., Challis, P., Chomiuk, L., Czekala, I., Drout, M., Fong, W., Huber, M. E., Kirshner, R. P., Leibler, C., McLeod, B., Marion, G. H., Narayan, G., Riess, A. G., Roth, K. C., Sanders, N. E., Scolnic, D., Smith,

K., Stubbs, C. W., Tonry, J. L., Valenti, S., Burgett, W. S., Chambers, K. C., Hodapp, K. W., Kaiser, N., Kudritzki, R.-P., Magnier, E. A., and Price, P. A. (2013). PS1-10afx at z = 1.388: Pan-STARRS1 Discovery of a New Type of Superluminous Supernova. , 767:162.

Chornock, R., Filippenko, A. V., Foley, R. J., Perley, D. A., Silverman, J. M., Bloom, J. S., Kocevski, D., and Li, W. (2007). Supernova 2007bi. *Central Bureau Electronic Telegrams*, 929:2.

Clocchiatti, A. (2011). Type Ia Supernovae and the discovery of the Cosmic Acceleration. *ArXiv e-prints*.

Colgate, S. A. and McKee, C. (1969). Early Supernova Luminosity. , 157:623.

Conley, A., Guy, J., Sullivan, M., Regnault, N., Astier, P., Balland, C., Basa, S., Carlberg, R. G., Fouchez, D., Hardin, D., Hook, I. M., Howell, D. A., Pain, R., Palanque-Delabrouille, N., Perrett, K. M., Pritchet, C. J., Rich, J., Ruhlmann-Kleider, V., Balam, D., Baumont, S., Ellis, R. S., Fabbro, S., Fakhouri, H. K., Fourmanoit, N., González-Gaitán, S., Graham, M. L., Hudson, M. J., Hsiao, E., Kronborg, T., Lidman, C., Mourao, A. M., Neill, J. D., Perlmutter, S., Ripoche, P., Suzuki, N., and Walker, E. S. (2011). Supernova Constraints and Systematic Uncertainties from the First Three Years of the Supernova Legacy Survey. , 192:1.

Cooke, J., Sullivan, M., Gal-Yam, A., Barton, E. J., Carlberg, R. G., Ryan-Weber, E. V., Horst, C., Omori, Y., and Díaz, C. G. (2012). Superluminous supernovae at redshifts of 2.05 and 3.90. , 491:228–231.

Dawson, K. S., Aldering, G., Amanullah, R., Barbary, K., Barrientos, L. F., Brodwin, M., Connolly, N., Dey, A., Doi, M., Donahue, M., Eisenhardt, P., Ellingson, E., Faccioli, L., Fadeyev, V., Fakhouri, H. K., Fruchter, A. S., Gilbank, D. G., Gladders, M. D., Goldhaber, G., Gonzalez, A. H., Goobar, A., Gude, A., Hattori, T., Hoekstra, H., Huang, X., Ihara, Y., Jannuzi, B. T., Johnston, D., Kashikawa, K., Koester, B., Konishi, K., Kowalski, M., Lidman, C., Linder, E. V., Lubin, L., Meyers, J., Morokuma, T., Munshi, F., Mullis, C., Oda, T., Panagia, N., Perlmutter, S., Postman, M., Pritchard, T., Rhodes, J., Rosati, P., Rubin, D., Schlegel, D. J., Spadafora, A., Stanford, S. A., Stanishev, V., Stern, D., Strovink, M., Suzuki, N., Takanashi, N., Tokita, K., Wagner, M., Wang, L., Yasuda, N., Yee, H. K. C., and Supernova Cosmology Project, T. (2009). An Intensive Hubble Space Telescope Survey for z1 Type Ia Supernovae by Targeting Galaxy Clusters. , 138:1271–1283.

Dawson, K. S., Schlegel, D. J., Ahn, C. P., Anderson, S. F., Aubourg, É., Bailey, S., Barkhouser, R. H., Bautista, J. E., Beifiori, A., Berlind, A. A., Bhardwaj, V., Bizyaev, D., Blake, C. H., Blanton, M. R., Blomqvist, M., Bolton, A. S., Borde, A., Bovy, J., Brandt, W. N., Brewington, H., Brinkmann, J., Brown, P. J., Brownstein, J. R., Bundy, K., Busca, N. G., Carithers, W., Carnero, A. R., Carr, M. A., Chen, Y., Comparat, J., Connolly, N., Cope, F., Croft, R. A. C., Cuesta, A. J., da Costa, L. N., Davenport, J. R. A., Delubac, T., de Putter, R., Dhital, S., Ealet, A., Ebelke, G. L., Eisenstein, D. J., Escoffier, S., Fan, X., Filiz Ak, N., Finley, H., Font-Ribera, A., Génova-Santos, R., Gunn, J. E., Guo, H., Haggard, D., Hall, P. B., Hamilton, J.-C., Harris, B., Harris, D. W., Ho, S., Hogg, D. W., Holder, D., Honscheid, K., Huehnerhoff, J., Jordan, B., Jordan, W. P., Kauffmann, G., Kazin, E. A., Kirkby, D., Klaene, M. A., Kneib, J.-P., Le Goff, J.-M., Lee, K.-G., Long, D. C., Loomis, C. P., Lundgren, B., Lupton, R. H., Maia, M. A. G., Makler, M., Malanushenko, E., Malanushenko, V., Mandelbaum, R., Manera, M., Maraston, C., Margala, D., Masters, K. L., McBride, C. K., McDonald, P., McGreer, I. D., McMahon, R. G., Mena, O., Miralda-Escudé, J., Montero-Dorta, A. D., Montesano, F., Muna, D., Myers, A. D., Naugle, T., Nichol, R. C., Noterdaeme, P., Nuza, S. E., Olmstead, M. D., Oravetz, A., Oravetz, D. J., Owen, R., Padmanabhan, N., Palanque-Delabrouille, N., Pan, K., Parejko, J. K., Pâris, I., Percival, W. J., Pérez-Fournon, I., Pérez-Ràfols, I., Petitjean, P., Pfaffenberger, R., Pforr, J., Pieri, M. M., Prada, F., Price-Whelan, A. M., Raddick, M. J., Rebolo, R., Rich, J., Richards, G. T., Rockosi, C. M., Roe, N. A., Ross, A. J., Ross, N. P., Rossi, G., Rubiño-Martin, J. A., Samushia, L., Sánchez, A. G., Sayres, C., Schmidt, S. J., Schneider, D. P., Scóccola, C. G., Seo, H.-J., Shelden, A., Sheldon, E., Shen, Y., Shu, Y., Slosar, A., Smee, S. A., Snedden, S. A., Stauffer, F., Steele, O., Strauss, M. A., Streblyanska, A., Suzuki, N., Swanson, M. E. C., Tal, T., Tanaka, M., Thomas, D., Tinker, J. L., Tojeiro, R., Tremonti, C. A., Vargas Magaña, M., Verde, L., Viel, M., Wake, D. A., Watson, M., Weaver, B. A., Weinberg, D. H., Weiner, B. J., West, A. A., White, M., Wood-Vasey, W. M., Yeche, C., Zehavi, I., Zhao, G.-B., and Zheng, Z. (2013). The Baryon Oscillation Spectroscopic Survey of SDSS-III. , 145:10.

Delubac, T., Bautista, J. E., Busca, N. G., Rich, J., Kirkby, D., Bailey, S., Font-Ribera, A., Slosar, A., Lee, K.-G., Pieri, M. M., Hamilton, J.-C., Aubourg, É., Blomqvist, M., Bovy, J., Brinkmann, J., Carithers, W., Dawson, K. S., Eisenstein, D. J., Kneib, J.-P., Le Goff, J.-M., Margala, D., Miralda-Escudé, J., Myers, A. D., Nichol, R. C., Noterdaeme, P., O'Connell, R., Olmstead, M. D., Palanque-Delabrouille, N., Pâris, I., Petitjean, P., Ross, N. P., Rossi, G., Schlegel, D. J., Schneider, D. P., Weinberg,

D. H., Yèche, C., and York, D. G. (2014). Baryon Acoustic Oscillations in the Ly{\alpha} forest of BOSS DR11 quasars. *arxiv:1404.1801*.

Desai, S., Armstrong, R., Mohr, J. J., Semler, D. R., Liu, J., Bertin, E., Allam, S. S., Barkhouse, W. A., Bazin, G., Buckley-Geer, E. J., Cooper, M. C., Hansen, S. M., High, F. W., Lin, H., Lin, Y.-T., Ngeow, C.-C., Rest, A., Song, J., Tucker, D., and Zenteno, A. (2012). The Blanco Cosmology Survey: Data Acquisition, Processing, Calibration, Quality Diagnostics, and Data Release. , 757:83.

Diehl, H. T., Abbott, T. M. C., Annis, J., Armstrong, R., Baruah, L., Bermeo, A., Bernstein, G., Beynon, E., Bruderer, C., Buckley-Geer, E. J., Campbell, H., Capozzi, D., Carter, M., Casas, R., Clerkin, L., Covarrubias, R., Cuhna, C., D'Andrea, C., da Costa, L., Das, R., DePoy, D. L., Dietrich, J., Drlica-Wagner, A., Elliott, A., Eifler, T., Estrada, J., Etherington, J., Flaugher, B. L., Frieman, J., Fausti Neto, A., Gelman, M., Gerdes, D., Gruen, D., Gruendl, R., Hao, J., Head, H., Helsby, J., Hoffman, K., Honscheid, K., James, D., Johnson, M., Kacprzac, T., Katsaros, J., Kennedy, J., Kent, S., Kessler, R., Kim, A., Krause, E., Kron, R., Kuhlmann, S., Kunder, A., Li, T., Lin, H., MacCrann, N., March, M., Marshall, J., Neilsen, E., Nugent, P., Martini, P., Melchior, P., Menanteau, F., Nichol, R. C., Nord, B., Ogando, R., Old, L., Papadopoulos, A., Patton, K., Petravick, D., Plazas, A. A., Poulton, R., Pujol, A., Reil, K., Rigby, T., Romer, A., Roodman, A., Rooney, P., Sanchez Alvaro, E., Serrano, S., Sheldon, E., Smith, A., Smith, R. C., Soares-Santos, M., Soumagnac, M., Spinka, H., Suchyta, E., Tucker, D., Walker, A. R., Wester, W., Wiesner, M., Wilcox, H., Williams, R., Yanny, B., and Zhang, Y. . (2014). The dark energy survey and operations: Year 1. volume 9149, pages 91490V–91490V–15.

Diehl, H. T. and For the Dark Energy Survey Collaboration (2012). The Dark Energy Survey Camera (DECam). *Physics Procedia*, 37:1332.

Drake, A. J., Djorgovski, S. G., Mahabal, A., Anderson, J., Roy, R., Mohan, V., Ravindranath, S., Frail, D., Gezari, S., Neill, J. D., Ho, L. C., Prieto, J. L., Thompson, D., Thorstensen, J., Wagner, M., Kowalski, R., Chiang, J., Grove, J. E., Schinzel, F. K., Wood, D. L., Carrasco, L., Recillas, E., Kewley, L., Archana, K. N., Basu, A., Wadadekar, Y., Kumar, B., Myers, A. D., Phinney, E. S., Williams, R., Graham, M. J., Catelan, M., Beshore, E., Larson, S., and Christensen, E. (2011a). The Discovery and Nature of the Optical Transient CSS100217:102913+404220. , 735:106.

Drake, A. J., Djorgovski, S. G., Mahabal, A., Beshore, E., Larson, S., Graham, M. J., Williams, R., Christensen, E., Catelan, M., Boattini, A., Gibbs, A., Hill, R., and

Kowalski, R. (2009a). First Results from the Catalina Real-Time Transient Survey. , 696:870–884.

Drake, A. J., Djorgovski, S. G., Mahabal, A., Graham, M. J., Williams, R., Beshore, E. C., Larson, S. M., Hill, R., and Christensen, E. (2008). Supernova 2008fz. *Central Bureau Electronic Telegrams*, 1524:1.

Drake, A. J., Djorgovski, S. G., Mahabal, A., Graham, M. J., Williams, R., Catelan, M., Beshore, E. C., Larson, S. M., and Christensen, E. (2009b). Supernova 2009jh. *Central Bureau Electronic Telegrams*, 1958:1.

Drake, A. J., Djorgovski, S. G., Mahabal, A. A., Graham, M. J., Williams, R., Donalek, C., Prieto, J., Catelan, M., Christensen, E., Beshore, E. C., Larson, S. M., and Mc-Naught, R. H. (2011b). Three blue optical transients from CRTS. *The Astronomer's Telegram*, 3343:1.

Drake, A. J., Djorgovski, S. G., Mahabal, A. A., Graham, M. J., Williams, R., Prieto, J., Catelan, M., Christensen, E., Beshore, E. C., and Larson, S. M. (2012a). 33 SN Candidates from CRTS. *The Astronomer's Telegram*, 3873:1.

Drake, A. J., Djorgovski, S. G., Mahabal, A. A., Graham, M. J., Williams, R., Prieto, J., Catelan, M., Christensen, E., Larson, S. M., and Beshore, E. C. (2012b). 47 Supernova Candidates from CRTS. *The Astronomer's Telegram*, 4595:1.

Drake, A. J., Djorgovski, S. G., Prieto, J. L., Mahabal, A., Balam, D., Williams, R., Graham, M. J., Catelan, M., Beshore, E., and Larson, S. (2010). Discovery of the Extremely Energetic Supernova 2008fz. , 718:L127–L131.

Drake, A. J., Mahabal, A. A., Djorgovski, S. G., Graham, M. J., Williams, R., Prieto, J., Catelan, M., Christensen, E., Larson, S. M., and Beshore, E. C. (2012c). Classification of CRTS optical transients. *The Astronomer's Telegram*, 4498:1.

Einstein, A. (1916). The Foundation of the General Theory of Relativity. *Annalen Phys.*, 49:769–822. [Annalen Phys.14,517(2005)].

Ellis, R. S., Sullivan, M., Nugent, P. E., Howell, D. A., Gal-Yam, A., Astier, P., Balam, D., Balland, C., Basa, S., Carlberg, R. G., Conley, A., Fouchez, D., Guy, J., Hardin, D., Hook, I., Pain, R., Perrett, K., Pritchet, C. J., and Regnault, N. (2008). Verifying the Cosmological Utility of Type Ia Supernovae: Implications of a Dispersion in the Ultraviolet Spectra. , 674:51–69.

Elston, R. J., Gonzalez, A. H., McKenzie, E., Brodwin, M., Brown, M. J. I., Cardona, G., Dey, A., Dickinson, M., Eisenhardt, P. R., Jannuzi, B. T., Lin, Y.-T., Mohr, J. J., Raines, S. N., Stanford, S. A., and Stern, D. (2006). The FLAMINGOS Extragalactic Survey. , 639:816–826.

Fatkhullin, T. and Gabdeev, M. (2012). CRTS transients spectroscopic classification. *The Astronomer's Telegram*, 4599:1.

Fioc, M. and Rocca-Volmerange, B. (1997). Pegase: a uv to nir spectral evolution model of galaxies. application to the calibration of bright galaxy counts. , 326:950–962.

Flaugher, B. (2005). The Dark Energy Survey. *International Journal of Modern Physics A*, 20:3121–3123.

Flaugher, B., Diehl, H. T., Honscheid, K., Abbott, T. M. C., Alvarez, O., Angstadt, R., Annis, J. T., Antonik, M., Ballester, O., Beaufore, L., Bernstein, G. M., Bernstein, R. A., Bigelow, B., Bonati, M., Boprie, D., Brooks, D., Buckley-Geer, E. J., Campa, J., Cardiel-Sas, L., Castander, F. J., Castilla, J., Cease, H., Cela-Ruiz, J. M., Chappa, S., Chi, E., Cooper, C., da Costa, L. N., Dede, E., Derylo, G., DePoy, D. L., de Vicente, J., Doel, P., Drlica-Wagner, A., Eiting, J., Elliott, A. E., Emes, J., Estrada, J., Fausti Neto, A., Finley, D. A., Flores, R., Frieman, J., Gerdes, D., Gladders, M. D., Gregory, B., Gutierrez, G. R., Hao, J., Holland, S. E., Holm, S., Huffman, D., Jackson, C., James, D. J., Jonas, M., Karcher, A., Karliner, I., Kent, S., Kessler, R., Kozlovsky, M., Kron, R. G., Kubik, D., Kuehn, K., Kuhlmann, S., Kuk, K., Lahav, O., Lathrop, A., Lee, J., Levi, M. E., Lewis, P., Li, T. S., Mandrichenko, I., Marshall, J. L., Martinez, G., Merritt, K. W., Miquel, R., Munoz, F., Neilsen, E. H., Nichol, R. C., Nord, B., Ogando, R., Olsen, J., Palio, N., Patton, K., Peoples, J., Plazas, A. A., Rauch, J., Reil, K., Rheault, J.-P., Roe, N. A., Rogers, H., Roodman, A., Sanchez, E., Scarpine, V., Schindler, R. H., Schmidt, R., Schmitt, R., Schubnell, M., Schultz, K., Schurter, P., Scott, L., Serrano, S., Shaw, T. M., Smith, R. C., Soares-Santos, M., Stefanik, A., Stuermer, W., Suchyta, E., Sypniewski, A., Tarle, G., Thaler, J., Tighe, R., Tran, C., Tucker, D., Walker, A. R., Wang, G., Watson, M., Weaverdyck, C., Wester, W., Woods, R., and Yanny, B. (2015). The Dark Energy Camera. *ArXiv e-prints*.

Flaugher, B. L., Abbott, T. M. C., Angstadt, R., Annis, J., Antonik, M. L., Bailey, J., Ballester, O., Bernstein, J. P., Bernstein, R. A., Bonati, M., Bremer, G., Briones, J., Brooks, D., Buckley-Geer, E. J., Campa, J., Cardiel-Sas, L., Castander, F., Castilla, J., Cease, H., Chappa, S., Chi, E. C., da Costa, L., DePoy, D. L., Derylo, G., de Vicente, J., Diehl, H. T., Doel, P., Estrada, J., Eiting, J., Elliott, A. E., Finley,

D. A., Flores, R., Frieman, J., Gaztanaga, E., Gerdes, D., Gladders, M., Guarino, V., Gutierrez, G., Grudzinski, J., Hanlon, B., Hao, J., Holland, S., Honscheid, K., Huffman, D., Jackson, C., Jonas, M., Karliner, I., Kau, D., Kent, S., Kozlovsky, M., Krempetz, K., Krider, J., Kubik, D., Kuehn, K., Kuhlmann, S. E., Kuk, K., Lahav, O., Langellier, N., Lathrop, A., Lewis, P. M., Lin, H., Lorenzon, W., Martinez, G., McKay, T., Merritt, W., Meyer, M., Miquel, R., Morgan, J., Moore, P., Moore, T., Neilsen, E., Nord, B., Ogando, R., Olson, J., Patton, K., Peoples, J., Plazas, A., Qian, T., Roe, N., Roodman, A., Rossetto, B., Sanchez, E., Soares-Santos, M., Scarpine, V., Schalk, T., Schindler, R., Schmidt, R., Schmitt, R., Schubnell, M., Schultz, K., Selen, M., Serrano, S., Shaw, T., Simaitis, V., Slaughter, J., Smith, R. C., Spinka, H., Stefanik, A., Stuermer, W., Sypniewski, A., Talaga, R., Tarle, G., Thaler, J., Tucker, D., Walker, A. R., Weaverdyck, C., Wester, W., Woods, R. J., Worswick, S., and Zhao, A. (2012). Status of the Dark Energy Survey Camera (DECam) project. In *Society of Photo-Optical Instrumentation Engineers (SPIE) Conference Series*, volume 8446 of *Society of Photo-Optical Instrumentation Engineers (SPIE) Conference Series*.

Foley, R. J., Blanchard, P. K., Challis, P., Drout, M., Kirshner, R., Wolf, R. C., Fischer, J. A., Fischer, J.-L., Gladney, L., March, M., Sako, M., Brown, P. J., Krisciunas, K., Suntzeff, N., D'Andrea, C., Nichol, R., Papadopoulos, A., Smith, M., Sullivan, M., Maartens, R., Gupta, R., Kovacs, E., Kuhlmann, S., Spinka, H., Ahn, E., Finley, D. A., Frieman, J., Marriner, J., Wester, W., Aldering, G., Kim, A. G., Thomas, R. C., Barbary, K., Bloom, J. S., Goldstein, D., Nugent, P., Perlmutter, S., Castander, F. J., Desai, S., Paech, K., Smith, R. C., Schubnell, M., Kessler, R., Scolnic, D., Covarrubias, R. A., and Jarvis, M. J. (2015). Dark Energy Survey Discovery of a Likely Tidal Disruption Event. *The Astronomer's Telegram*, 6877:1.

Freedman, W. L., Madore, B. F., Gibson, B. K., Ferrarese, L., Kelson, D. D., Sakai, S., Mould, J. R., Kennicutt, Jr., R. C., Ford, H. C., Graham, J. A., Huchra, J. P., Hughes, S. M. G., Illingworth, G. D., Macri, L. M., and Stetson, P. B. (2001). Final Results from the Hubble Space Telescope Key Project to Measure the Hubble Constant. , 553:47–72.

Friedmann, A. (1924). Über die Möglichkeit einer Welt mit konstanter negativer Krümmung des Raumes. *Zeitschrift fur Physik*, 21:326–332.

Frieman, J. A., Bassett, B., Becker, A., Choi, C., Cinabro, D., DeJongh, F., Depoy, D. L., Dilday, B., Doi, M., Garnavich, P. M., Hogan, C. J., Holtzman, J., Im, M., Jha, S., Kessler, R., Konishi, K., Lampeitl, H., Marriner, J., Marshall, J. L., McGinnis, D., Miknaitis, G., Nichol, R. C., Prieto, J. L., Riess, A. G., Richmond, M. W.,

Romani, R., Sako, M., Schneider, D. P., Smith, M., Takanashi, N., Tokita, K., van der Heyden, K., Yasuda, N., Zheng, C., Adelman-McCarthy, J., Annis, J., Assef, R. J., Barentine, J., Bender, R., Blandford, R. D., Boroski, W. N., Bremer, M., Brewington, H., Collins, C. A., Crotts, A., Dembicky, J., Eastman, J., Edge, A., Edmondson, E., Elson, E., Eyler, M. E., Filippenko, A. V., Foley, R. J., Frank, S., Goobar, A., Gueth, T., Gunn, J. E., Harvanek, M., Hopp, U., Ihara, Y., Ivezić, Ž., Kahn, S., Kaplan, J., Kent, S., Ketzeback, W., Kleinman, S. J., Kollatschny, W., Kron, R. G., Krzesiński, J., Lamenti, D., Leloudas, G., Lin, H., Long, D. C., Lucey, J., Lupton, R. H., Malanushenko, E., Malanushenko, V., McMillan, R. J., Mendez, J., Morgan, C. W., Morokuma, T., Nitta, A., Ostman, L., Pan, K., Rockosi, C. M., Romer, A. K., Ruiz-Lapuente, P., Saurage, G., Schlesinger, K., Snedden, S. A., Sollerman, J., Stoughton, C., Stritzinger, M., Subba Rao, M., Tucker, D., Vaisanen, P., Watson, L. C., Watters, S., Wheeler, J. C., Yanny, B., and York, D. (2008). The Sloan Digital Sky Survey-II Supernova Survey: Technical Summary. , 135:338–347.

Gal-Yam, A. (2012). Luminous Supernovae. *Science*, 337:927–.

Gal-Yam, A., Mazzali, P., Ofek, E. O., Nugent, P. E., Kulkarni, S. R., Kasliwal, M. M., Quimby, R. M., Filippenko, A. V., Cenko, S. B., Chornock, R., Waldman, R., Kasen, D., Sullivan, M., Beshore, E. C., Drake, A. J., Thomas, R. C., Bloom, J. S., Poznanski, D., Miller, A. A., Foley, R. J., Silverman, J. M., Arcavi, I., Ellis, R. S., and Deng, J. (2009). Supernova 2007bi as a pair-instability explosion. , 462:624–627.

Gezari, S., Halpern, J. P., Grupe, D., Yuan, F., Quimby, R., McKay, T., Chamarro, D., Sisson, M. D., Akerlof, C., Wheeler, J. C., Brown, P. J., Cenko, S. B., Rau, A., Djordjevic, J. O., and Terndrup, D. M. (2009). Discovery of the Ultra-Bright Type II-L Supernova 2008es. , 690:1313–1321.

Goldstein, D. A., D'Andrea, C. B., Fischer, J. A., Foley, R. J., Gupta, R. R., Kessler, R., Kim, A. G., Nichol, R. C., Nugent, P., Papadopoulos, A., Sako, M., Smith, M., Sullivan, M., Thomas, R. C., Wester, W., Wolf, R. C., Abdalla, F. B., Banerji, M., Benoit-Lévy, A., Bertin, E., Brooks, D., Carnero Rosell, A., Castander, F. J., da Costa, L. N., Covarrubias, R., DePoy, D. L., Desai, S., Diehl, H. T., Doel, P., Eifler, T. F., Fausti Neto, A., Finley, D. A., Flaugher, B., Fosalba, P., Frieman, J., Gerdes, D., Gruen, D., Gruendl, R. A., James, D., Kuehn, K., Kuropatkin, N., Lahav, O., Li, T. S., Maia, M. A. G., Makler, M., March, M., Marshall, J. L., Martini, P., Merritt, K. W., Miquel, R., Nord, B., Ogando, R., Plazas, A. A., Romer, A. K., Roodman, A., Sanchez, E., Scarpine, V., Schubnell, M., Sevilla-Noarbe, I., Smith, R. C., Soares-Santos, M., Sobreira, F., Suchyta, E., Swanson, M. E. C., Tarle, G.,

Thaler, J., and Walker, A. R. (2015). Automated Transient Identification in the Dark Energy Survey. *ArXiv e-prints*.

Graham, M. L., Zheng, W., Filippenko, A. V., Challis, P., Kirshner, R., Parrent, J., Castander, F. J., Casas, R., Garcia-Alvarez, D., Perez-Valladares, D., Miquel, R., Smith, R. C., Schubnell, M., Kessler, R., Scolnic, D., Covarrubias, R. A., Wolf, R. C., Fischer, J. A., Fischer, J.-L., Gladney, L., March, M., Sako, M., Brown, P. J., Krisciunas, K., Suntzeff, N., D'Andrea, C., Nichol, R., Papadopoulos, A., Smith, M., Sullivan, M., Maartens, R., Gupta, R., Kovacs, E., Kuhlmann, S., Spinka, H., Ahn, E., Finley, D. A., Frieman, J., Marriner, J., Wester, W., Aldering, G., Kim, A. G., Thomas, R. C., Barbary, K., Bloom, J. S., Goldstein, D., Nugent, P., Perlmutter, S., Foley, R. J., Desai, S., and Paech, K. (2014). Discovery of the z = 0.869 Superluminous Supernova DES14X2byo. *The Astronomer's Telegram*, 6635:1.

Gunn, J. E., Siegmund, W. A., Mannery, E. J., Owen, R. E., Hull, C. L., Leger, R. F., Carey, L. N., Knapp, G. R., York, D. G., Boroski, W. N., Kent, S. M., Lupton, R. H., Rockosi, C. M., Evans, M. L., Waddell, P., Anderson, J. E., Annis, J., Barentine, J. C., Bartoszek, L. M., Bastian, S., Bracker, S. B., Brewington, H. J., Briegel, C. I., Brinkmann, J., Brown, Y. J., Carr, M. A., Czarapata, P. C., Drennan, C. C., Dombeck, T., Federwitz, G. R., Gillespie, B. A., Gonzales, C., Hansen, S. U., Harvanek, M., Hayes, J., Jordan, W., Kinney, E., Klaene, M., Kleinman, S. J., Kron, R. G., Kresinski, J., Lee, G., Limmongkol, S., Lindenmeyer, C. W., Long, D. C., Loomis, C. L., McGehee, P. M., Mantsch, P. M., Neilsen, Jr., E. H., Neswold, R. M., Newman, P. R., Nitta, A., Peoples, Jr., J., Pier, J. R., Prieto, P. S., Prosapio, A., Rivetta, C., Schneider, D. P., Snedden, S., and Wang, S.-i. (2006). The 2.5 m Telescope of the Sloan Digital Sky Survey. , 131:2332–2359.

Gwyn, S. D. J. (2008). MegaPipe: The MegaCam Image Stacking Pipeline at the Canadian Astronomical Data Centre. , 120:212–223.

Hatano, K., Branch, D., Nomoto, K., Deng, J. S., Maeda, K., Nugent, P., and Aldering, G. (2001). The Type Ic Hypernova SN 1999as. In *American Astronomical Society Meeting Abstracts #198*, volume 33 of *Bulletin of the American Astronomical Society*, page 838.

Heger, A., Fryer, C. L., Woosley, S. E., Langer, N., and Hartmann, D. H. (2003). How Massive Single Stars End Their Life. , 591:288–300.

Heger, A. and Woosley, S. E. (2002). The Nucleosynthetic Signature of Population III. , 567:532–543.

Hinshaw, G., Larson, D., Komatsu, E., Spergel, D. N., Bennett, C. L., Dunkley, J., Nolta, M. R., Halpern, M., Hill, R. S., Odegard, N., Page, L., Smith, K. M., Weiland, J. L., Gold, B., Jarosik, N., Kogut, A., Limon, M., Meyer, S. S., Tucker, G. S., Wollack, E., and Wright, E. L. (2013). Nine-year Wilkinson Microwave Anisotropy Probe (WMAP) Observations: Cosmological Parameter Results. , 208:19.

Howell, D. A., Kasen, D., Lidman, C., Sullivan, M., Conley, A., Astier, P., Balland, C., Carlberg, R. G., Fouchez, D., Guy, J., Hardin, D., Pain, R., Palanque-Delabrouille, N., Perrett, K., Pritchet, C. J., Regnault, N., Rich, J., and Ruhlmann-Kleider, V. (2013). Two Superluminous Supernovae from the Early Universe Discovered by the Supernova Legacy Survey. , 779:98.

Howell, D. A., Sullivan, M., Perrett, K., Bronder, T. J., Hook, I. M., Astier, P., Aubourg, E., Balam, D., Basa, S., Carlberg, R. G., Fabbro, S., Fouchez, D., Guy, J., Lafoux, H., Neill, J. D., Pain, R., Palanque-Delabrouille, N., Pritchet, C. J., Regnault, N., Rich, J., Taillet, R., Knop, R., McMahon, R. G., Perlmutter, S., and Walton, N. A. (2005). Gemini Spectroscopy of Supernovae from the Supernova Legacy Survey: Improving High-Redshift Supernova Selection and Classification. , 634:1190–1201.

Hubble, E. (1929). A Relation between Distance and Radial Velocity among Extra-Galactic Nebulae. *Proceedings of the National Academy of Science*, 15:168–173.

Inserra, C. and Smartt, S. J. (2014). Superluminous Supernovae as Standardizable Candles and High-redshift Distance Probes. , 796:87.

Inserra, C., Smartt, S. J., Fraser, M., Wright, D., Young, D. R., Smith, K. W., Cellier-Holzem, F., Pastorello, A., Valenti, S., Benetti, S., Taubenberger, S., Sullivan, M., Gal-Yam, A., Yaron, O., Baltay, C., Ellman, N., Hadjiyska, E., McKinnon, R., Rabinowitz, D., Feindt, U., Kowalski, M., and Nugent, P. (2012). Further spectral classification of PESSTO blue transients. *The Astronomer's Telegram*, 4329:1.

Inserra, C., Smartt, S. J., Jerkstrand, A., Valenti, S., Fraser, M., Wright, D., Smith, K., Chen, T.-W., Kotak, R., Pastorello, A., Nicholl, M., Bresolin, F., Kudritzki, R. P., Benetti, S., Botticella, M. T., Burgett, W. S., Chambers, K. C., Ergon, M., Flewelling, H., Fynbo, J. P. U., Geier, S., Hodapp, K. W., Howell, D. A., Huber, M., Kaiser, N., Leloudas, G., Magill, L., Magnier, E. A., McCrum, M. G., Metcalfe, N., Price, P. A., Rest, A., Sollerman, J., Sweeney, W., Taddia, F., Taubenberger, S., Tonry, J. L., Wainscoat, R. J., Waters, C., and Young, D. (2013). Super-luminous Type Ic Supernovae: Catching a Magnetar by the Tail. , 770:128.

Kaiser, N., Burgett, W., Chambers, K., Denneau, L., Heasley, J., Jedicke, R., Magnier, E., Morgan, J., Onaka, P., and Tonry, J. (2010). The Pan-STARRS wide-field optical/NIR imaging survey. In *Society of Photo-Optical Instrumentation Engineers (SPIE) Conference Series*, volume 7733 of *Society of Photo-Optical Instrumentation Engineers (SPIE) Conference Series*, page 0.

Kasen, D. and Bildsten, L. (2010). Supernova Light Curves Powered by Young Magnetars. , 717:245–249.

Kelly, P. L., Rodney, S. A., Treu, T., Foley, R. J., Brammer, G., Schmidt, K. B., Zitrin, A., Sonnenfeld, A., Strolger, L.-G., Graur, O., Filippenko, A. V., Jha, S. W., Riess, A. G., Bradac, M., Weiner, B. J., Scolnic, D., Malkan, M. A., von der Linden, A., Trenti, M., Hjorth, J., Gavazzi, R., Fontana, A., Merten, J. C., McCully, C., Jones, T., Postman, M., Dressler, A., Patel, B., Cenko, S. B., Graham, M. L., and Tucker, B. E. (2015). Multiple images of a highly magnified supernova formed by an early-type cluster galaxy lens. *Science*, 347:1123–1126.

Kelson, D. D. (2003). Optimal Techniques in Two-dimensional Spectroscopy: Background Subtraction for the 21st Century. , 115:688–699.

Kessler, R., Becker, A. C., Cinabro, D., Vanderplas, J., Frieman, J. A., Marriner, J., Davis, T. M., Dilday, B., Holtzman, J., Jha, S. W., Lampeitl, H., Sako, M., Smith, M., Zheng, C., Nichol, R. C., Bassett, B., Bender, R., Depoy, D. L., Doi, M., Elson, E., Filippenko, A. V., Foley, R. J., Garnavich, P. M., Hopp, U., Ihara, Y., Ketzeback, W., Kollatschny, W., Konishi, K., Marshall, J. L., McMillan, R. J., Miknaitis, G., Morokuma, T., Mörtsell, E., Pan, K., Prieto, J. L., Richmond, M. W., Riess, A. G., Romani, R., Schneider, D. P., Sollerman, J., Takanashi, N., Tokita, K., van der Heyden, K., Wheeler, J. C., Yasuda, N., and York, D. (2009a). First-Year Sloan Digital Sky Survey-II Supernova Results: Hubble Diagram and Cosmological Parameters. , 185:32–84.

Kessler, R., Bernstein, J. P., Cinabro, D., Dilday, B., Frieman, J. A., Jha, S., Kuhlmann, S., Miknaitis, G., Sako, M., Taylor, M., and Vanderplas, J. (2009b). SNANA: A Public Software Package for Supernova Analysis. , 121:1028–1035.

Kessler, R., Marriner, J., Childress, M., Covarrubias, R., D'Andrea, C. B., Finley, D. A., Fischer, J., Foley, R. J., Goldstein, D., Gupta, R. R., Kuehn, K., Marcha, M., Nichol, R. C., Papadopoulos, A., Sako, M., Scolnic, D., Smith, M., Sullivan, M., Wester, W., Yuan, F., Abbott, T., Abdalla, F. B., Allam, S., Benoit-Levy, A., Bernstein, G. M., Bertin, E., Brooks, D., Carnero Rosell, A., Carrasco Kind, M., Castander, F. J.,

Crocce, M., da Costa, L. N., Desai, S., Diehl, H. T., Eifler, T. F., Fausti Neto, A., Flaugher, B., Frieman, J., Gruen, D., Gruendl, R. A., Honscheid, K., James, D. J., Kuropatkin, N., Li, T. S., Maia, M. A. G., Marshall, J. L., Martini, P., Miller, C. J., Miquel, R., Ogando, R., Plazas, A. A., Romer, A. K., Roodman, A., Sanchez, E., Sevilla-Noarbe, I., Smith, R. C., Soares-Santos, M., Sobreira, F., Tarle, G., Thaler, J., Thomas, R. C., Tucker, D., and Walker, A. R. (2015). The Difference Imaging Pipeline for the Transient Search in the Dark Energy Survey. *ArXiv e-prints*.

Kewley, L. J. and Dopita, M. A. (2002). Using Strong Lines to Estimate Abundances in Extragalactic H II Regions and Starburst Galaxies. , 142:35–52.

Kewley, L. J. and Ellison, S. L. (2008). Metallicity Calibrations and the Mass-Metallicity Relation for Star-forming Galaxies. , 681:1183–1204.

King, A. L., Davis, T. M., Denney, K. D., Vestergaard, M., and Watson, D. (2014). High-redshift standard candles: predicted cosmological constraints. , 441:3454–3476.

King, A. L., Martini, P., Davis, T. M., Denney, K. D., Kochanek, C. S., Peterson, B. M., Skielboe, A., Vestergaard, M., Huff, E., Watson, D., Banerji, M., McMahon, R., Sharp, R., and Lidman, C. (2015). Simulations of the OzDES AGN Reverberation Mapping Project. *ArXiv e-prints*.

Knop, R., Aldering, G., Deustua, S., Goldhaber, G., Kim, M., Nugent, P., Helin, E., Pravdo, S., Rabinowitz, D., and Lawrence, K. (1999). Supernovae 1999as and 1999at in Anonymous Galaxies. , 7128:1.

Kobulnicky, H. A. and Kewley, L. J. (2004). Metallicities of 0.3z1.0 Galaxies in the GOODS-North Field. , 617:240–261.

Komatsu, E., Dunkley, J., Nolta, M. R., Bennett, C. L., Gold, B., Hinshaw, G., Jarosik, N., Larson, D., Limon, M., Page, L., Spergel, D. N., Halpern, M., Hill, R. S., Kogut, A., Meyer, S. S., Tucker, G. S., Weiland, J. L., Wollack, E., and Wright, E. L. (2009). Five-Year Wilkinson Microwave Anisotropy Probe Observations: Cosmological Interpretation. , 180:330–376.

Kostrzewa-Rutkowska, Z., Kozłowski, S., Wyrzykowski, Ł., Djorgovski, S. G., Glikman, E., Mahabal, A. A., and Koposov, S. (2013). A Plausible (Overlooked) Super-luminous Supernova in the Sloan Digital Sky Survey Stripe 82 Data. , 778:168.

Kowal, C. T. (1968). Absolute magnitudes of supernovae. , 73:1021–1024.

Krause, O., Tanaka, M., Usuda, T., Hattori, T., Goto, M., Birkmann, S., and Nomoto, K. (2008). Tycho Brahe's 1572 supernova as a standard typeIa as revealed by its light-echo spectrum. , 456:617–619.

Law, N. M., Kulkarni, S. R., Dekany, R. G., Ofek, E. O., Quimby, R. M., Nugent, P. E., Surace, J., Grillmair, C. C., Bloom, J. S., Kasliwal, M. M., Bildsten, L., Brown, T., Cenko, S. B., Ciardi, D., Croner, E., Djorgovski, S. G., van Eyken, J., Filippenko, A. V., Fox, D. B., Gal-Yam, A., Hale, D., Hamam, N., Helou, G., Henning, J., Howell, D. A., Jacobsen, J., Laher, R., Mattingly, S., McKenna, D., Pickles, A., Poznanski, D., Rahmer, G., Rau, A., Rosing, W., Shara, M., Smith, R., Starr, D., Sullivan, M., Velur, V., Walters, R., and Zolkower, J. (2009). The Palomar Transient Factory: System Overview, Performance, and First Results. , 121:1395–1408.

Leloudas, G., Chatzopoulos, E., Dilday, B., Gorosabel, J., Vinko, J., Gallazzi, A., Wheeler, J. C., Bassett, B., Fischer, J. A., Frieman, J. A., Fynbo, J. P. U., Goobar, A., Jelínek, M., Malesani, D., Nichol, R. C., Nordin, J., Östman, L., Sako, M., Schneider, D. P., Smith, M., Sollerman, J., Stritzinger, M. D., Thöne, C. C., and de Ugarte Postigo, A. (2012). SN 2006oz: rise of a super-luminous supernova observed by the SDSS-II SN Survey. , 541:A129.

Leloudas, G., Schulze, S., Krühler, T., Gorosabel, J., Christensen, L., Mehner, A., de Ugarte Postigo, A., Amorín, R., Thöne, C. C., Anderson, J. P., Bauer, F. E., Gallazzi, A., Hełminiak, K. G., Hjorth, J., Ibar, E., Malesani, D., Morell, N., Vinko, J., and Wheeler, J. C. (2015). Spectroscopy of superluminous supernova host galaxies. A preference of hydrogen-poor events for extreme emission line galaxies. , 449:917–932.

Lewis, I. J., Cannon, R. D., Taylor, K., Glazebrook, K., Bailey, J. A., Baldry, I. K., Barton, J. R., Bridges, T. J., Dalton, G. B., Farrell, T. J., Gray, P. M., Lankshear, A., McCowage, C., Parry, I. R., Sharples, R. M., Shortridge, K., Smith, G. A., Stevenson, J., Straede, J. O., Waller, L. G., Whittard, J. D., Wilcox, J. K., and Willis, K. C. (2002). The Anglo-Australian Observatory 2dF facility. , 333:279–299.

Liddle, A. (2003). *An Introduction to Modern Cosmology, Second Edition*.

Lidman, C., Ruhlmann-Kleider, V., Sullivan, M., Myzska, J., Dobbie, P., Glazebrook, K., Mould, J., Astier, P., Balland, C., Betoule, M., Carlberg, R., Conley, A., Fouchez, D., Guy, J., Hardin, D., Hook, I., Howell, D. A., Pain, R., Palanque-Delabrouille, N., Perrett, K., Pritchet, C., Regnault, N., and Rich, J. (2013). An Efficient Approach to Obtaining Large Numbers of Distant Supernova Host Galaxy Redshifts. , 30:1.

Linder, E. V. (2003). Exploring the Expansion History of the Universe. *Physical Review Letters*, 90(9):091301.

Lunnan, R., Chornock, R., Berger, E., Laskar, T., Fong, W., Rest, A., Sanders, N. E., Challis, P. M., Drout, M. R., Foley, R. J., Huber, M. E., Kirshner, R. P., Leibler, C., Marion, G. H., McCrum, M., Milisavljevic, D., Narayan, G., Scolnic, D., Smartt, S. J., Smith, K. W., Soderberg, A. M., Tonry, J. L., Burgett, W. S., Chambers, K. C., Flewelling, H., Hodapp, K. W., Kaiser, N., Magnier, E. A., Price, P. A., and Wainscoat, R. J. (2014a). Hydrogen-poor Superluminous Supernovae and Long-duration Gamma-Ray Bursts Have Similar Host Galaxies. , 787:138.

Lunnan, R., Chornock, R., Berger, E., Milisavljevic, D., Drout, M., Sanders, N. E., Challis, P. M., Czekala, I., Foley, R. J., Fong, W., Huber, M. E., Kirshner, R. P., Leibler, C., Marion, G. H., McCrum, M., Narayan, G., Rest, A., Roth, K. C., Scolnic, D., Smartt, S. J., Smith, K., Soderberg, A. M., Stubbs, C. W., Tonry, J. L., Burgett, W. S., Chambers, K. C., Kudritzki, R.-P., Magnier, E. A., and Price, P. A. (2013). PS1-10bzj: A Fast, Hydrogen-poor Superluminous Supernova in a Metal-poor Host Galaxy. , 771:97.

Lunnan, R., Chornock, R., Berger, E., Rest, A., Fong, W., Scolnic, D., Jones, D., Soderberg, A. M., Challis, P. M., Drout, M. R., Foley, R. J., Huber, M. E., Kirshner, R. P., Leibler, C., Marion, G. H., McCrum, M., Milisavljevic, D., Narayan, G., Sanders, N. E., Smartt, S. J., Smith, K. W., Tonry, J. L., Burgett, W. S., Chambers, K. C., Flewelling, H., Kudritzki, R.-P., Wainscoat, R. J., and Waters, C. (2014b). Zooming In on the Progenitors of Superluminous Supernovae With HST. *ArXiv e-prints*.

Lunnan, R., Chornock, R., Berger, E., Rest, A., Fong, W., Scolnic, D., Jones, D., Soderberg, A. M., Challis, P. M., Drout, M. R., Foley, R. J., Huber, M. E., Kirshner, R. P., Leibler, C., Marion, G. H., McCrum, M., Milisavljevic, D., Narayan, G., Sanders, N. E., Smartt, S. J., Smith, K. W., Tonry, J. L., Burgett, W. S., Chambers, K. C., Flewelling, H., Kudritzki, R.-P., Wainscoat, R. J., and Waters, C. (2014c). Zooming In on the Progenitors of Superluminous Supernovae With HST. *ArXiv e-prints*.

Madau, P. and Dickinson, M. (2014). Cosmic Star-Formation History. , 52:415–486.

Maeda, K., Mazzali, P. A., Deng, J., Nomoto, K., Yoshii, Y., Tomita, H., and Kobayashi, Y. (2003). A Two-Component Model for the Light Curves of Hypernovae. , 593:931–940.

Maguire, K., Sullivan, M., Ellis, R. S., Nugent, P. E., Howell, D. A., Gal-Yam, A., Cooke, J., Mazzali, P., Pan, Y.-C., Dilday, B., Thomas, R. C., Arcavi, I., Ben-Ami, S.,

Bersier, D., Bianco, F. B., Fulton, B. J., Hook, I., Horesh, A., Hsiao, E., James, P. A., Podsiadlowski, P., Walker, E. S., Yaron, O., Kasliwal, M. M., Laher, R. R., Law, N. M., Ofek, E. O., Poznanski, D., and Surace, J. (2012). Hubble Space Telescope studies of low-redshift Type Ia supernovae: evolution with redshift and ultraviolet spectral trends. , 426:2359–2379.

Mahabal, A. A., Drake, A. J., Djorgovski, S. G., Graham, M. J., Williams, R., Myers, A., Prieto, J., Catelan, M., Christensen, E., Mohan, V., Ravindranath, S., Beshore, E. C., and Larson, S. M. (2010). Supernova Candidates and Classifications from CRTS. *The Astronomer's Telegram*, 2490:1.

Maraston, C. (2005). Evolutionary population synthesis: models, analysis of the ingredients and application to high-z galaxies. , 362:799–825.

Margutti, R., Milisavljevic, D., Soderberg, A. M., Chornock, R., Zauderer, B. A., Murase, K., Guidorzi, C., Sanders, N. E., Kuin, P., Fransson, C., Levesque, E. M., Chandra, P., Berger, E., Bianco, F. B., Brown, P. J., Challis, P., Chatzopoulos, E., Cheung, C. C., Choi, C., Chomiuk, L., Chugai, N., Contreras, C., Drout, M. R., Fesen, R., Foley, R. J., Fong, W., Friedman, A. S., Gall, C., Gehrels, N., Hjorth, J., Hsiao, E., Kirshner, R., Im, M., Leloudas, G., Lunnan, R., Marion, G. H., Martin, J., Morrell, N., Neugent, K. F., Omodei, N., Phillips, M. M., Rest, A., Silverman, J. M., Strader, J., Stritzinger, M. D., Szalai, T., Utterback, N. B., Vinko, J., Wheeler, J. C., Arnett, D., Campana, S., Chevalier, R., Ginsburg, A., Kamble, A., Roming, P. W. A., Pritchard, T., and Stringfellow, G. (2014). A Panchromatic View of the Restless SN 2009ip Reveals the Explosive Ejection of a Massive Star Envelope. , 780:21.

Markwardt, C. B. (2009). Non-linear Least-squares Fitting in IDL with MPFIT. In Bohlender, D. A., Durand, D., and Dowler, P., editors, *Astronomical Data Analysis Software and Systems XVIII*, volume 411 of *Astronomical Society of the Pacific Conference Series*, page 251.

Mazzali, P. A., Walker, E. S., Pian, E., Tanaka, M., Corsi, A., Hattori, T., and Gal-Yam, A. (2013). The very energetic, broad-lined Type Ic supernova 2010ah (PTF10bzf) in the context of GRB/SNe. , 432:2463–2473.

McCrum, M., Smartt, S. J., Kotak, R., Rest, A., Jerkstrand, A., Inserra, C., Rodney, S. A., Chen, T.-W., Howell, D. A., Huber, M. E., Pastorello, A., Tonry, J. L., Bresolin, F., Kudritzki, R.-P., Chornock, R., Berger, E., Smith, K., Botticella, M. T., Foley, R. J., Fraser, M., Milisavljevic, D., Nicholl, M., Riess, A. G., Stubbs, C. W., Valenti, S., Wood-Vasey, W. M., Wright, D., Young, D. R., Drout, M., Czekala, I., Burgett,

W. S., Chambers, K. C., Draper, P., Flewelling, H., Hodapp, K. W., Kaiser, N., Magnier, E. A., Metcalfe, N., Price, P. A., Sweeney, W., and Wainscoat, R. J. (2014). The superluminous supernova PS1-11ap: bridging the gap between low and high redshift. , 437:656–674.

McCrum, M., Smartt, S. J., Rest, A., Smith, K., Kotak, R., Rodney, S. A., Young, D. R., Chornock, R., Berger, E., Foley, R. J., Fraser, M., Wright, D., Scolnic, D., Tonry, J. L., Urata, Y., Huang, K., Pastorello, A., Botticella, M. T., Valenti, S., Mattila, S., Kankare, E., Farrow, D. J., Huber, M. E., Stubbs, C. W., Kirshner, R. P., Bresolin, F., Burgett, W. S., Chambers, K. C., Draper, P. W., Flewelling, H., Jedicke, R., Kaiser, N., Magnier, E. A., Metcalfe, N., Morgan, J. S., Price, P. A., Sweeney, W., Wainscoat, R. J., and Waters, C. (2015). Selecting superluminous supernovae in faint galaxies from the first year of the Pan-STARRS1 Medium Deep Survey. , 448:1206–1231.

McGaugh, S. S. (1991). H II region abundances - Model oxygen line ratios. , 380:140–150.

Miknaitis, G., Pignata, G., Rest, A., Wood-Vasey, W. M., Blondin, S., Challis, P., Smith, R. C., Stubbs, C. W., Suntzeff, N. B., Foley, R. J., Matheson, T., Tonry, J. L., Aguilera, C., Blackman, J. W., Becker, A. C., Clocchiatti, A., Covarrubias, R., Davis, T. M., Filippenko, A. V., Garg, A., Garnavich, P. M., Hicken, M., Jha, S., Krisciunas, K., Kirshner, R. P., Leibundgut, B., Li, W., Miceli, A., Narayan, G., Prieto, J. L., Riess, A. G., Salvo, M. E., Schmidt, B. P., Sollerman, J., Spyromilio, J., and Zenteno, A. (2007). The ESSENCE Supernova Survey: Survey Optimization, Observations, and Supernova Photometry. , 666:674–693.

Miller, A. A., Chornock, R., Perley, D. A., Ganeshalingam, M., Li, W., Butler, N. R., Bloom, J. S., Smith, N., Modjaz, M., Poznanski, D., Filippenko, A. V., Griffith, C. V., Shiode, J. H., and Silverman, J. M. (2009). The Exceptionally Luminous Type II-Linear Supernova 2008es. , 690:1303–1312.

Miller, A. A., Smith, N., Li, W., Bloom, J. S., Chornock, R., Filippenko, A. V., and Prochaska, J. X. (2010). New Observations of the Very Luminous Supernova 2006gy: Evidence for Echoes. , 139:2218–2229.

Minkowski, R. (1941). Spectra of Supernovae. , 53:224.

Modjaz, M., Blondin, S., Kirshner, R. P., Matheson, T., Berlind, P., Bianco, F. B., Calkins, M. L., Challis, P., Garnavich, P., Hicken, M., Jha, S., Liu, Y. Q., and Marion,

G. H. (2014). Optical Spectra of 73 Stripped-envelope Core-collapse Supernovae. , 147:99.

Mohr, J. J., Armstrong, R., Bertin, E., Daues, G., Desai, S., Gower, M., Gruendl, R., Hanlon, W., Kuropatkin, N., Lin, H., Marriner, J., Petravic, D., Sevilla, I., Swanson, M., Tomashek, T., Tucker, D., and Yanny, B. (2012). The Dark Energy Survey data processing and calibration system. In *Society of Photo-Optical Instrumentation Engineers (SPIE) Conference Series*, volume 8451 of *Society of Photo-Optical Instrumentation Engineers (SPIE) Conference Series*.

Neill, J. D., Sullivan, M., Gal-Yam, A., Quimby, R., Ofek, E., Wyder, T. K., Howell, D. A., Nugent, P., Seibert, M., Martin, D. C., Overzier, R., Barlow, T. A., Foster, K., Friedman, P. G., Morrissey, P., Neff, S. G., Schiminovich, D., Bianchi, L., Donas, J., Heckman, T. M., Lee, Y.-W., Madore, B. F., Milliard, B., Rich, R. M., and Szalay, A. S. (2011). The Extreme Hosts of Extreme Supernovae. , 727:15.

Neilsen, E. and Annis, J. (2014). ObsTac: Automated Execution of Dark Energy Survey Observing Tactics. In Manset, N. and Forshay, P., editors, *Astronomical Data Analysis Software and Systems XXIII*, volume 485 of *Astronomical Society of the Pacific Conference Series*, page 77.

Nicholl, M., Smartt, S. J., Jerkstrand, A., Inserra, C., Anderson, J. P., Baltay, C., Benetti, S., Chen, T.-W., Elias-Rosa, N., Feindt, U., Fraser, M., Gal-Yam, A., Hadjiyska, E., Howell, D. A., Kotak, R., Lawrence, A., Leloudas, G., Margheim, S., Mattila, S., McKinnon, R., McCrum, M., Mead, A., Nugent, P., Rabinowitz, D., Rest, A., Smith, K. W., Sollerman, J., Sullivan, M., Taddia, F., Valenti, S., Walker, E. S., and Young, D. R. (2014). Super-luminous supernovae from PESSTO. *ArXiv e-prints*.

Nicholl, M., Smartt, S. J., Jerkstrand, A., Inserra, C., McCrum, M., Kotak, R., Fraser, M., Wright, D., Chen, T.-W., Smith, K., Young, D. R., Sim, S. A., Valenti, S., Howell, D. A., Bresolin, F., Kudritzki, R. P., Tonry, J. L., Huber, M. E., Rest, A., Pastorello, A., Tomasella, L., Cappellaro, E., Benetti, S., Mattila, S., Kankare, E., Kangas, T., Leloudas, G., Sollerman, J., Taddia, F., Berger, E., Chornock, R., Narayan, G., Stubbs, C. W., Foley, R. J., Lunnan, R., Soderberg, A., Sanders, N., Milisavljevic, D., Margutti, R., Kirshner, R. P., Elias-Rosa, N., Morales-Garoffolo, A., Taubenberger, S., Botticella, M. T., Gezari, S., Urata, Y., Rodney, S., Riess, A. G., Scolnic, D., Wood-Vasey, W. M., Burgett, W. S., Chambers, K., Flewelling, H. A., Magnier, E. A., Kaiser, N., Metcalfe, N., Morgan, J., Price, P. A., Sweeney, W., and Waters, C. (2013). Slowly fading super-luminous supernovae that are not pair-instability explosions. , 502:346–349.

Ofek, E. O., Cameron, P. B., Kasliwal, M. M., Gal-Yam, A., Rau, A., Kulkarni, S. R., Frail, D. A., Chandra, P., Cenko, S. B., Soderberg, A. M., and Immler, S. (2007). SN 2006gy: An Extremely Luminous Supernova in the Galaxy NGC 1260. , 659:L13–L16.

Ofek, E. O., Sullivan, M., Cenko, S. B., Kasliwal, M. M., Gal-Yam, A., Kulkarni, S. R., Arcavi, I., Bildsten, L., Bloom, J. S., Horesh, A., Howell, D. A., Filippenko, A. V., Laher, R., Murray, D., Nakar, E., Nugent, P. E., Silverman, J. M., Shaviv, N. J., Surace, J., and Yaron, O. (2013). An outburst from a massive star 40days before a supernova explosion. , 494:65–67.

Oke, J. B., Cohen, J. G., Carr, M., Cromer, J., Dingizian, A., Harris, F. H., Labrecque, S., Lucinio, R., Schaal, W., Epps, H., and Miller, J. (1995). The Keck Low-Resolution Imaging Spectrometer. , 107:375.

Oke, J. B. and Gunn, J. E. (1983). Secondary standard stars for absolute spectrophotometry. , 266:713–717.

Papadopoulos, A., D'Andrea, C. B., Sullivan, M., Nichol, R. C., Barbary, K., Biswas, R., Brown, P. J., Covarrubias, R. A., Finley, D. A., Fischer, J. A., Foley, R. J., Goldstein, D., Gupta, R. R., Kessler, R., Kovacs, E., Kuhlmann, S. E., Lidman, C., March, M., Nugent, P. E., Sako, M., Smith, R. C., Spinka, H., Wester, W., Abbott, T. M. C., Abdalla, F., Allam, S. S., Banerji, M., Bernstein, J. P., Bernstein, R. A., Carnero, A., da Costa, L. N., DePoy, D. L., Desai, S., Diehl, H. T., Eifler, T., Evrard, A. E., Flaugher, B., Frieman, J. A., Gerdes, D., Gruen, D., Honscheid, K., James, D., Kuehn, K., Kuropatkin, N., Lahav, O., Maia, M. A. G., Makler, M., Marshall, J. L., Merritt, K. W., Miller, C. J., Miquel, R., Ogando, R., Plazas, A. A., Roe, N. A., Romer, A. K., Rykoff, E., Sanchez, E., Santiago, B. X., Scarpine, V., Schubnell, M., Sevilla, I., Soares-Santos, M., Suchyta, E., Swanson, M., Tarle, G., Thaler, J., Tucker, L. D., Wechsler, R. H., and Zuntz, J. (2015). DES13S2cmm: the first superluminous supernova from the Dark Energy Survey. , 449:1215–1227.

Pastorello, A., Smartt, S. J., Botticella, M. T., Maguire, K., Fraser, M., Smith, K., Kotak, R., Magill, L., Valenti, S., Young, D. R., Gezari, S., Bresolin, F., Kudritzki, R., Howell, D. A., Rest, A., Metcalfe, N., Mattila, S., Kankare, E., Huang, K. Y., Urata, Y., Burgett, W. S., Chambers, K. C., Dombeck, T., Flewelling, H., Grav, T., Heasley, J. N., Hodapp, K. W., Kaiser, N., Luppino, G. A., Lupton, R. H., Magnier, E. A., Monet, D. G., Morgan, J. S., Onaka, P. M., Price, P. A., Rhoads, P. H.,

Siegmund, W. A., Stubbs, C. W., Sweeney, W. E., Tonry, J. L., Wainscoat, R. J., Waterson, M. F., Waters, C., and Wynn-Williams, C. G. (2010a). Ultra-bright Optical Transients are Linked with Type Ic Supernovae. , 724:L16–L21.

Pastorello, A., Smartt, S. J., Young, D., Kankare, E., Smith, K., Botticella, M. T., Mattila, S., Kotak, R., Valenti, S., Metcalfe, N., Sweeney, W. E., Price, P. A., Magnier, E., Tonry, J., Bresolin, F., Kudritzki, R. P., Chambers, K., Stubbs, C., Rest, A., Narayan, G., Riess, A., Huber, M., and Wood-Vasey, W. M. (2010b). Detection of PTF10cwr/CSS100313 on PS1 sky survey images and host galaxy identification. *The Astronomer's Telegram*, 2504:1.

Peebles, P. J. E. (1993). *Principles of Physical Cosmology*.

Perlmutter, S., Aldering, G., Goldhaber, G., Knop, R. A., Nugent, P., Castro, P. G., Deustua, S., Fabbro, S., Goobar, A., Groom, D. E., Hook, I. M., Kim, A. G., Kim, M. Y., Lee, J. C., Nunes, N. J., Pain, R., Pennypacker, C. R., Quimby, R., Lidman, C., Ellis, R. S., Irwin, M., McMahon, R. G., Ruiz-Lapuente, P., Walton, N., Schaefer, B., Boyle, B. J., Filippenko, A. V., Matheson, T., Fruchter, A. S., Panagia, N., Newberg, H. J. M., Couch, W. J., and Project, T. S. C. (1999). Measurements of Ω and Λ from 42 High-Redshift Supernovae. , 517:565–586.

Perrett, K., Sullivan, M., Conley, A., González-Gaitán, S., Carlberg, R., Fouchez, D., Ripoche, P., Neill, J. D., Astier, P., Balam, D., Balland, C., Basa, S., Guy, J., Hardin, D., Hook, I. M., Howell, D. A., Pain, R., Palanque-Delabrouille, N., Pritchet, C., Regnault, N., Rich, J., Ruhlmann-Kleider, V., Baumont, S., Lidman, C., Perlmutter, S., and Walker, E. S. (2012). Evolution in the Volumetric Type Ia Supernova Rate from the Supernova Legacy Survey. , 144:59.

Phillips, M. M. (1993). The absolute magnitudes of Type IA supernovae. , 413:L105–L108.

Planck Collaboration, Ade, P. A. R., Aghanim, N., Armitage-Caplan, C., Arnaud, M., Ashdown, M., Atrio-Barandela, F., Aumont, J., Baccigalupi, C., Banday, A. J., and et al. (2014). Planck 2013 results. XVI. Cosmological parameters. , 571:A16.

Quimby, R. (2006a). Supernova 2006gy in NGC 1260. *Central Bureau Electronic Telegrams*, 644:1.

Quimby, R. M. (2006b). *The Texas Supernova Search*. PhD thesis, The University of Texas at Austin.

Quimby, R. M., Aldering, G., Wheeler, J. C., Höflich, P., Akerlof, C. W., and Rykoff, E. S. (2007). SN 2005ap: A Most Brilliant Explosion. , 668:L99–L102.

Quimby, R. M., Arcavi, I., Sternberg, A., Ben-Ami, S., Yaron, O., Gal-Yam, A., Graham, M., Cenko, S. B., Filippenko, A. V., Perley, D., Cao, Y., and Kulkarni, S. R. (2012). Discovery of a Super-Luminous Supernova, PTF12dam. *The Astronomer's Telegram*, 4121:1.

Quimby, R. M., Gal-Yam, A., Arcavi, I., Yaron, O., Horesh, A., and Mooley, K. (2011a). Discovery of a Luminous Supernova, PTF11rks. *The Astronomer's Telegram*, 3841:1.

Quimby, R. M., Kulkarni, S., Ofek, E., Kasliwal, M. M., Gal-Yam, A., Arcavi, I., Ben-Ami, S., Xu, D., Sternberg, A., Silverman, J. M., Cenko, S. B., Kleiser, I. K. W., Nugent, P. E., and Howell, D. A. (2010a). Discovery of a Luminous Supernova, PTF10hgi. *The Astronomer's Telegram*, 2740:1.

Quimby, R. M., Kulkarni, S. R., Kasliwal, M. M., Gal-Yam, A., Arcavi, I., Sullivan, M., Nugent, P., Thomas, R., Howell, D. A., Nakar, E., Bildsten, L., Theissen, C., Law, N. M., Dekany, R., Rahmer, G., Hale, D., Smith, R., Ofek, E. O., Zolkower, J., Velur, V., Walters, R., Henning, J., Bui, K., McKenna, D., Poznanski, D., Cenko, S. B., and Levitan, D. (2011b). Hydrogen-poor superluminous stellar explosions. , 474:487–489.

Quimby, R. M., Kulkarni, S. R., Ofek, E., Kasliwal, M. M., Levitan, D., Gal-Yam, A., and Cenko, S. B. (2010b). Discovery of a Luminous Supernova, PTF10cwr. *The Astronomer's Telegram*, 2492:1.

Quimby, R. M., Oguri, M., More, A., More, S., Moriya, T. J., Werner, M. C., Tanaka, M., Folatelli, G., Bersten, M. C., Maeda, K., and Nomoto, K. (2014). Detection of the Gravitational Lens Magnifying a Type Ia Supernova. *Science*, 344:396–399.

Quimby, R. M., Sternberg, A., and Matheson, T. (2011c). Confirmation of the Luminous Transient CSS110406:135058+261642 (=PTF11dij). *The Astronomer's Telegram*, 3344:1.

Quimby, R. M., Werner, M. C., Oguri, M., More, S., More, A., Tanaka, M., Nomoto, K., Moriya, T. J., Folatelli, G., Maeda, K., and Bersten, M. (2013a). Extraordinary Magnification of the Ordinary Type Ia Supernova PS1-10afx. , 768:L20.

Quimby, R. M., Yuan, F., Akerlof, C., and Wheeler, J. C. (2013b). Rates of superluminous supernovae at z

0.2. , 431:912–922.

Rau, A., Kulkarni, S. R., Law, N. M., Bloom, J. S., Ciardi, D., Djorgovski, G. S., Fox, D. B., Gal-Yam, A., Grillmair, C. C., Kasliwal, M. M., Nugent, P. E., Ofek, E. O., Quimby, R. M., Reach, W. T., Shara, M., Bildsten, L., Cenko, S. B., Drake, A. J., Filippenko, A. V., Helfand, D. J., Helou, G., Howell, D. A., Poznanski, D., and Sullivan, M. (2009). Exploring the Optical Transient Sky with the Palomar Transient Factory. , 121:1334–1351.

Rest, A., Foley, R. J., Gezari, S., Narayan, G., Draine, B., Olsen, K., Huber, M. E., Matheson, T., Garg, A., Welch, D. L., Becker, A. C., Challis, P., Clocchiatti, A., Cook, K. H., Damke, G., Meixner, M., Miknaitis, G., Minniti, D., Morelli, L., Nikolaev, S., Pignata, G., Prieto, J. L., Smith, R. C., Stubbs, C., Suntzeff, N. B., Walker, A. R., Wood-Vasey, W. M., Zenteno, A., Wyrzykowski, L., Udalski, A., Szymański, M. K., Kubiak, M., Pietrzyński, G., Soszyński, I., Szewczyk, O., Ulaczyk, K., and Poleski, R. (2011). Pushing the Boundaries of Conventional Core-collapse Supernovae: The Extremely Energetic Supernova SN 2003ma. , 729:88.

Riess, A. G., Filippenko, A. V., Challis, P., Clocchiatti, A., Diercks, A., Garnavich, P. M., Gilliland, R. L., Hogan, C. J., Jha, S., Kirshner, R. P., Leibundgut, B., Phillips, M. M., Reiss, D., Schmidt, B. P., Schommer, R. A., Smith, R. C., Spyromilio, J., Stubbs, C., Suntzeff, N. B., and Tonry, J. (1998). Observational Evidence from Supernovae for an Accelerating Universe and a Cosmological Constant. , 116:1009–1038.

Riess, A. G., Press, W. H., and Kirshner, R. P. (1996). A Precise Distance Indicator: Type IA Supernova Multicolor Light-Curve Shapes. , 473:88.

Sako, M., Bassett, B., Becker, A., Cinabro, D., DeJongh, F., Depoy, D. L., Dilday, B., Doi, M., Frieman, J. A., Garnavich, P. M., Hogan, C. J., Holtzman, J., Jha, S., Kessler, R., Konishi, K., Lampeitl, H., Marriner, J., Miknaitis, G., Nichol, R. C., Prieto, J. L., Riess, A. G., Richmond, M. W., Romani, R., Schneider, D. P., Smith, M., SubbaRao, M., Takanashi, N., Tokita, K., van der Heyden, K., Yasuda, N., Zheng, C., Barentine, J., Brewington, H., Choi, C., Dembicky, J., Harnavek, M., Ihara, Y., Im, M., Ketzeback, W., Kleinman, S. J., Krzesiński, J., Long, D. C., Malanushenko, E., Malanushenko, V., McMillan, R. J., Morokuma, T., Nitta, A., Pan, K., Saurage, G., and Snedden, S. A. (2008). The Sloan Digital Sky Survey-II Supernova Survey: Search Algorithm and Follow-up Observations. , 135:348–373.

Sako, M., Bassett, B., Becker, A. C., Brown, P. J., Campbell, H., Cane, R., Cinabro, D., D'Andrea, C. B., Dawson, K. S., DeJongh, F., Depoy, D. L., Dilday, B., Doi,

M., Filippenko, A. V., Fischer, J. A., Foley, R. J., Frieman, J. A., Galbany, L., Garnavich, P. M., Goobar, A., Gupta, R. R., Hill, G. J., Hayden, B. T., Hlozek, R., Holtzman, J. A., Hopp, U., Jha, S. W., Kessler, R., Kollatschny, W., Leloudas, G., Marriner, J., Marshall, J. L., Miquel, R., Morokuma, T., Mosher, J., Nichol, R. C., Nordin, J., Olmstead, M. D., Ostman, L., Prieto, J. L., Richmond, M., Romani, R. W., Sollerman, J., Stritzinger, M., Schneider, D. P., Smith, M., Wheeler, J. C., Yasuda, N., and Zheng, C. (2014). The Data Release of the Sloan Digital Sky Survey-II Supernova Survey. *ArXiv e-prints*.

Sako, M., Bassett, B., Connolly, B., Dilday, B., Cambell, H., Frieman, J. A., Gladney, L., Kessler, R., Lampeitl, H., Marriner, J., Miquel, R., Nichol, R. C., Schneider, D. P., Smith, M., and Sollerman, J. (2011). Photometric Type Ia Supernova Candidates from the Three-year SDSS-II SN Survey Data. , 738:162.

Sánchez, C., Carrasco Kind, M., Lin, H., Miquel, R., Abdalla, F. B., Amara, A., Banerji, M., Bonnett, C., Brunner, R., Capozzi, D., Carnero, A., Castander, F. J., da Costa, L. A. N., Cunha, C., Fausti, A., Gerdes, D., Greisel, N., Gschwend, J., Hartley, W., Jouvel, S., Lahav, O., Lima, M., Maia, M. A. G., Martí, P., Ogando, R. L. C., Ostrovski, F., Pellegrini, P., Rau, M. M., Sadeh, I., Seitz, S., Sevilla-Noarbe, I., Sypniewski, A., de Vicente, J., Abbot, T., Allam, S. S., Atlee, D., Bernstein, G., Bernstein, J. P., Buckley-Geer, E., Burke, D., Childress, M. J., Davis, T., DePoy, D. L., Dey, A., Desai, S., Diehl, H. T., Doel, P., Estrada, J., Evrard, A., Fernández, E., Finley, D., Flaugher, B., Frieman, J., Gaztanaga, E., Glazebrook, K., Honscheid, K., Kim, A., Kuehn, K., Kuropatkin, N., Lidman, C., Makler, M., Marshall, J. L., Nichol, R. C., Roodman, A., Sánchez, E., Santiago, B. X., Sako, M., Scalzo, R., Smith, R. C., Swanson, M. E. C., Tarle, G., Thomas, D., Tucker, D. L., Uddin, S. A., Valdés, F., Walker, A., Yuan, F., and Zuntz, J. (2014). Photometric redshift analysis in the Dark Energy Survey Science Verification data. , 445:1482–1506.

Scalzo, R. A., Aldering, G., Antilogus, P., Aragon, C., Bailey, S., Baltay, C., Bongard, S., Buton, C., Childress, M., Chotard, N., Copin, Y., Fakhouri, H. K., Gal-Yam, A., Gangler, E., Hoyer, S., Kasliwal, M., Loken, S., Nugent, P., Pain, R., Pécontal, E., Pereira, R., Perlmutter, S., Rabinowitz, D., Rau, A., Rigaudier, G., Runge, K., Smadja, G., Tao, C., Thomas, R. C., Weaver, B., and Wu, C. (2010). Nearby Supernova Factory Observations of SN 2007if: First Total Mass Measurement of a Super-Chandrasekhar-Mass Progenitor. , 713:1073–1094.

Schlafly, E. F. and Finkbeiner, D. P. (2011). Measuring Reddening with Sloan Digital Sky Survey Stellar Spectra and Recalibrating SFD. , 737:103.

Smartt, S. J., Nicholl, M., Inserra, C., Wright, D., Chen, T.-W., Lawrence, A., and Mead, A. (2013a). Classification of super-luminous SN : MLS130517:131841-070443. *The Astronomer's Telegram*, 5128:1.

Smartt, S. J., Valenti, S., Fraser, M., Inserra, C., Young, D. R., Sullivan, M., Benetti, S., Gal-Yam, A., Knapic, C., Molinaro, M., Pastorello, A., Smareglia, R., Smith, K. W., Taubenberger, S., and Yaron, O. (2013b). PESSTO: The Public ESO Spectroscopic Survey of Transient Objects. *The Messenger*, 154:50–52.

Smartt, S. J., Valenti, S., Fraser, M., Inserra, C., Young, D. R., Sullivan, M., Pastorello, A., Benetti, S., Gal-Yam, A., Knapic, C., Molinaro, M., Smareglia, R., Smith, K. W., Taubenberger, S., Yaron, O., Anderson, J. P., Ashall, C., Balland, C., Baltay, C., Barbarino, C., Bauer, F. E., Baumont, S., Bersier, D., Blagorodnova, N., Bongard, S., Botticella, M. T., Bufano, F., Bulla, M., Cappellaro, E., Campbell, H., Cellier-Holzem, F., Chen, T.-W., Childress, M. J., Clocchiatti, A., Contreras, C., Dall Ora, M., Danziger, J., de Jaeger, T., Della Valle, M., Dennefeld, M., Elias-Rosa, N., Elman, N., Feindt, U., Fleury, M., Gall, E., Gonzalez-Gaitan, S., Galbany, L., Greggio, L., Guillou, L. L., Hachinger, S., Hadjiyska, E., Hage, P. E., Hillebrandt, W., Hodgkin, S., Hsiao, E. Y., James, P. A., Jerkstrand, A., Kangas, T., Kankare, E., Kotak, R., Kromer, M., Kuncarayakti, H., Leloudas, G., Lundqvist, P., Hook, I. M., Maguire, K., Manulis, I., Margheim, S. J., Mattila, S., Maund, J. R., Mazzali, P. A., McCrum, M., McKinnon, R., Moreno-Raya, M. E., Nicholl, M., Nugent, P., Pain, R., Phillips, M. M., Pignata, G., Polshaw, J., Pumo, M. L., Rabinowitz, D., Reilly, E., Romero-Canizales, C., Scalzo, R., Schmidt, B., Schulze, S., Sim, S., Sollerman, J., Taddia, F., Tartaglia, L., Terreran, G., Tomasella, L., Turatto, M., Walker, E., Walton, N. A., Wyrzykowski, L., Yuan, F., and Zampieri, L. (2014). PESSTO : survey description and products from the first data release by the Public ESO Spectroscopic Survey of Transient Objects. *ArXiv e-prints*.

Smartt, S. J., Valenti, S., Magill, L., Smith, K., Kankare, E., Mattila, S., Kotak, R., Fraser, M., Ward, M., Hutton, S., Metcalfe, N., Bresolin, F., Kudritzki, R., Tonry, J., Magnier, E., Chambers, K., Kaiser, N., Morgan, J., Burgett, W., Heasley, J., Sweeney, W., Waters, C., Flewelling, H., Price, P. A., and Wood-Vasey, M. W. (2011). Five transients in the Pan-STARRS1 Faint Galaxy Supernova Survey. *The Astronomer's Telegram*, 3351:1.

Smartt, S. J., Wright, D., Valenti, S., Kotak, R., McCrum, M., Magill, L., Smith, K., Chen, T.-W., Fraser, M., Bresolin, F., Kudritzki, R., Tonry, J., Magnier, E., Huber, M., Chambers, K., Kaiser, N., Morgan, J., Burgett, W., Heasley, J., Sweeney, W., Waters, C., Flewelling, H., Stubbs, C., and Price, P. A. (2012). PS1-12fo

(=CSS120121): luminous Ic supernova at z=0.175 in the PS1 3Pi survey. *The Astronomer's Telegram*, 3918:1.

Smith, N., Chornock, R., Li, W., Ganeshalingam, M., Silverman, J. M., Foley, R. J., Filippenko, A. V., and Barth, A. J. (2008a). SN 2006tf: Precursor Eruptions and the Optically Thick Regime of Extremely Luminous Type IIn Supernovae. , 686:467–484.

Smith, N., Chornock, R., Silverman, J. M., Filippenko, A. V., and Foley, R. J. (2010). Spectral Evolution of the Extraordinary Type IIn Supernova 2006gy. , 709:856–883.

Smith, N., Foley, R. J., Bloom, J. S., Li, W., Filippenko, A. V., Gavazzi, R., Ghez, A., Konopacky, Q., Malkan, M. A., Marshall, P. J., Pooley, D., Treu, T., and Woo, J.-H. (2008b). Late-Time Observations of SN 2006gy: Still Going Strong. , 686:485–491.

Smith, N., Li, W., Foley, R. J., Wheeler, J. C., Pooley, D., Chornock, R., Filippenko, A. V., Silverman, J. M., Quimby, R., Bloom, J. S., and Hansen, C. (2007). SN 2006gy: Discovery of the Most Luminous Supernova Ever Recorded, Powered by the Death of an Extremely Massive Star like η Carinae. , 666:1116–1128.

Smith, N., Mauerhan, J. C., and Prieto, J. L. (2014). SN 2009ip and SN 2010mc: core-collapse Type IIn supernovae arising from blue supergiants. , 438:1191–1207.

Stritzinger, M., Sollerman, J., Goobar, A., Nichol, R., Smith, M., and Leloudas, G. (2006). Supernovae 2006oy-2006qm. *Central Bureau Electronic Telegrams*, 762:3.

Sullivan, M., Guy, J., Conley, A., Regnault, N., Astier, P., Balland, C., Basa, S., Carlberg, R. G., Fouchez, D., Hardin, D., Hook, I. M., Howell, D. A., Pain, R., Palanque-Delabrouille, N., Perrett, K. M., Pritchet, C. J., Rich, J., Ruhlmann-Kleider, V., Balam, D., Baumont, S., Ellis, R. S., Fabbro, S., Fakhouri, H. K., Fourmanoit, N., González-Gaitán, S., Graham, M. L., Hudson, M. J., Hsiao, E., Kronborg, T., Lidman, C., Mourao, A. M., Neill, J. D., Perlmutter, S., Ripoche, P., Suzuki, N., and Walker, E. S. (2011). SNLS3: Constraints on Dark Energy Combining the Supernova Legacy Survey Three-year Data with Other Probes. , 737:102.

Suzuki, N., Rubin, D., Lidman, C., Aldering, G., Amanullah, R., Barbary, K., Barrientos, L. F., Botyanszki, J., Brodwin, M., Connolly, N., Dawson, K. S., Dey, A., Doi, M., Donahue, M., Deustua, S., Eisenhardt, P., Ellingson, E., Faccioli, L., Fadeyev, V., Fakhouri, H. K., Fruchter, A. S., Gilbank, D. G., Gladders, M. D., Goldhaber, G., Gonzalez, A. H., Goobar, A., Gude, A., Hattori, T., Hoekstra, H., Hsiao, E., Huang, X., Ihara, Y., Jee, M. J., Johnston, D., Kashikawa, N., Koester, B., Konishi, K.,

Kowalski, M., Linder, E. V., Lubin, L., Melbourne, J., Meyers, J., Morokuma, T., Munshi, F., Mullis, C., Oda, T., Panagia, N., Perlmutter, S., Postman, M., Pritchard, T., Rhodes, J., Ripoche, P., Rosati, P., Schlegel, D. J., Spadafora, A., Stanford, S. A., Stanishev, V., Stern, D., Strovink, M., Takanashi, N., Tokita, K., Wagner, M., Wang, L., Yasuda, N., Yee, H. K. C., and Supernova Cosmology Project, T. (2012). The Hubble Space Telescope Cluster Supernova Survey. V. Improving the Dark-energy Constraints above z 1 and Building an Early-type-hosted Supernova Sample. , 746:85.

The Dark Energy Survey Collaboration (2005). The Dark Energy Survey. *ArXiv Astrophysics e-prints*.

Tomasella, L., Benetti, S., Pastorello, A., Cappellaro, E., Turatto, M., and Harutyunyan, A. (2012). Classification of CSS121015:004244+132827. *The Astronomer's Telegram*, 4512:1.

Umeda, H. and Nomoto, K. (2008). How Much ^{56}Ni Can Be Produced in Core-Collapse Supernovae? Evolution and Explosions of 30-100 M_{solar} Stars. , 673:1014–1022.

Vreeswijk, P. M., Savaglio, S., Gal-Yam, A., De Cia, A., Quimby, R. M., Sullivan, M., Cenko, S. B., Perley, D. A., Filippenko, A. V., Clubb, K. I., Taddia, F., Sollerman, J., Leloudas, G., Arcavi, I., Rubin, A., Kasliwal, M. M., Cao, Y., Yaron, O., Tal, D., Ofek, E. O., Capone, J., Kutyrev, A. S., Toy, V., Nugent, P. E., Laher, R., Surace, J., and Kulkarni, S. R. (2014). The Hydrogen-poor Superluminous Supernova iPTF 13ajg and its Host Galaxy in Absorption and Emission. , 797:24.

Wei, J.-J., Wu, X.-F., and Melia, F. (2015). Testing Cosmological Models with Type Ic Super Luminous Supernovae. , 149:165.

Wood-Vasey, W. M., Miknaitis, G., Stubbs, C. W., Jha, S., Riess, A. G., Garnavich, P. M., Kirshner, R. P., Aguilera, C., Becker, A. C., Blackman, J. W., Blondin, S., Challis, P., Clocchiatti, A., Conley, A., Covarrubias, R., Davis, T. M., Filippenko, A. V., Foley, R. J., Garg, A., Hicken, M., Krisciunas, K., Leibundgut, B., Li, W., Matheson, T., Miceli, A., Narayan, G., Pignata, G., Prieto, J. L., Rest, A., Salvo, M. E., Schmidt, B. P., Smith, R. C., Sollerman, J., Spyromilio, J., Tonry, J. L., Suntzeff, N. B., and Zenteno, A. (2007). Observational Constraints on the Nature of Dark Energy: First Cosmological Results from the ESSENCE Supernova Survey. , 666:694–715.

Woosley, S. E. (2010). Bright Supernovae from Magnetar Birth. , 719:L204–L207.

Woosley, S. E., Blinnikov, S., and Heger, A. (2007). Pulsational pair instability as an explanation for the most luminous supernovae. , 450:390–392.

Woosley, S. E. and Weaver, T. A. (1986). The physics of supernova explosions. , 24:205–253.

Yuan, F., Lidman, C., Davis, T. M., Childress, M., Abdalla, F. B., Banerji, M., Buckley-Geer, E., Carnero Rosell, A., Carollo, D., Castander, F. J., D'Andrea, C. B., Diehl, H. T., Cunha, C. E., Foley, R. J., Frieman, J., Glazebrook, K., Gschwend, J., Hinton, S., Jouvel, S., Kessler, R., Kim, A. G., King, A. L., Kuehn, K., Kuhlmann, S., Lewis, G. F., Lin, H., Martini, P., McMahon, R. G., Mould, J., Nichol, R. C., Norris, R. P., O'Neill, C. R., Ostrovski, F., Papadopoulos, A., Parkinson, D., Reed, S., Romer, A. K., Rooney, P. J., Rozo, E., Rykoff, E. S., Sako, M., Scalzo, R., Schmidt, B. P., Scolnic, D., Seymour, N., Sharp, R., Sobreira, F., Sullivan, M., Thomas, R. C., Tucker, D., Uddin, S. A., Wechsler, R. H., Wester, W., Wilcox, H., Zhang, B., Abbott, T., Allam, S., Bauer, A. H., Benoit-Levy, A., Bertin, E., Brooks, D., Burke, D. L., Carrasco Kind, M., Covarrubias, R., Crocce, M., da Costa, L. N., DePoy, D. L., Desai, S., Doel, P., Eifler, T. F., Evrard, A. E., Fausti Neto, A., Flaugher, B., Fosalba, P., Gaztanaga, E., Gerdes, D., Gruen, D., Gruendl, R. A., Honscheid, K., James, D., Kuropatkin, N., Lahav, O., Li, T. S., Maia, M. A. G., Makler, M., Marshall, J., Miller, C. J., Miquel, R., Ogando, R., Plazas, A. A., Roodman, A., Sanchez, E., Scarpine, V., Schubnell, M., Sevilla-Noarbe, I., Smith, R. C., Soares-Santos, M., Suchyta, E., Swanson, M. E. C., Tarle, G., Thaler, J., and Walker, A. R. (2015). OzDES multi-fibre spectroscopy for the Dark Energy Survey: first-year operation and results. *ArXiv e-prints*.

Yuan, F., Quimby, R., McKay, T., Chamarro, D., Sisson, M. D., Akerlof, C., and Wheeler, J. C. (2008a). Discovery of a possible AGN ROTSE3 J115649.1+542726. *The Astronomer's Telegram*, 1515:1.

Yuan, F., Quimby, R., Rykoff, E., Sisson, M. D., Chamarro, D., Akerlof, C., McKay, T., Miller, J. M., Wheeler, J. C., Bloom, J. S., Foley, R. J., Modjaz, M., and Brown, P. J. (2008b). Supernova 2008am. *Central Bureau Electronic Telegrams*, 1262:1.

Zhao, F.-Y., Strom, R. G., and Jiang, S.-Y. (2006). The Guest Star of AD185 must have been a Supernova. , 6:635–640.